# Lateritic palaeosols of N.E. Africa: a remote sensing study

## Thesis

# LATERITIC PALAEOSOLS OF N.E. AFRICA: A REMOTE SENSING STUDY

A thesis presented for the degree of Doctor of Philosophy

by

**M.E. Andrews Deller**

**née Margaret Elizabeth Andrews**
B.A. Hons (Open University)

Department of Environment, Earth and Ecosystems
The Open University
October 2012

**IMAGING SERVICES NORTH**
Boston Spa, Wetherby
West Yorkshire, LS23 7BQ
www.bl.uk

# CONTAINS PULLOUTS

# Abstract

Remote sensing data and image processing techniques are used increasingly to aid scientific investigation and address geological problems in areas that are difficult to map by conventional methods. This thesis explores how multispectral satellite data, supported by traditional geological techniques, facilitate a study of lateritic palaeosols. The work centres on laterites, which are thin but important elements of the Phanerozoic stratigraphy of NE Africa. They immediately pre-date mid-Oligocene flood basalts and, if mapped, can be used to delineate a flood basalt-laterite contact and define the pre-30 Ma African Surface and uplift patterns. They have important engineering properties and are key to understanding basement alteration and its associated mineralization. They affect agriculture and groundwater quality and retention - essential in Sub-Saharan Africa where access to safe water is limited. They dominate the landscape, yet are unmapped and marginalised in the literature. Their geological context supports a laterite-focused remote sensing mapping strategy.

A strategy for geologic mapping of laterites based on their simple mineralogy and spectral characteristics that distinguish them from other rocks is developed. Methods for mapping are presented using Earth Observation data. The outcome is a series of regional geological maps of Eritrea and Ethiopia. These reveal that laterite cover is more extensive than previously thought and enable further lines of research.

The maps provide a means of regional dating of laterites, which, together with ages obtained for overlying flood basalts and new basement cooling ages, indicate a major planation during the Palaeozoic and constrain the timing of associated uplift and erosion. A regional review of Mesozoic-Cenozoic climatic, stratigraphic and structural evolution is presented and a model of Neogene deformation of the laterite-flood basalt datum is produced. Finally, laterite maps, petrographic and geochemical evidence are used to access basic essentials of life: clean water, a safe environment and a sustainable economy.

## List of contents

# List of Figures

## Chapter 1



## Chapter 2

Kenya). M – Mogadishu (Somalia). Because each map has a slightly different extent a black dot at Asmara is included on them for reference.

**Figure 2.11** Adigrat quartz sandstone with *Thalassinoides* burrows, Knafna, Eritrea now lodged with the Eritrean Ministry of Energy and Mines, Asmara, Eritrea (Andrews Deller unpublished data 2001)

**Figure 2.12** Sun cracks in Adigrat Sandstone in the Blue Nile gorge, Ethiopia. Alemu Teklegiorgis, an Ethiopian colleague, is 1.7m tall

**Figure 2.13** Interbedded near-shore and shelf limestones and shales of the Jurassic Antalo Series exposed in a road cutting towards the top of the Blue Nile gorge, near Dejen, Ethiopia.

**Figure 2.14** Upper Cretaceous fluviatile sandstones of the Amba Aradom Series interbedded with lateritic palaeosols. Adi Hageray, 25km NW of Mekele, Tigray Ethiopia.

**Figure 2.15.** Typical trap topography developed on the CFBs of the Eritrean Plateau at Emba Tekera. The foreground shows laterite clay zone cut by a Neogene basaltic dyke.

**Figure 2.16**. Trachyte plugs of the Adwa area, Tigray, Ethiopia, cutting through CFBs.

**Figure 2.17** Summarised radiometric dates of CFBs and rift-related igneous rocks in NE Africa and Arabia (from Bosworth et al 2005)

**Figure 2.18** 15km east of Massawa, Eritrea, the basal conglomerate of the Lower Miocene Dogali Formation, which rests unconformably on highly faulted mid-Oligocene CFBs in the coastal lowlands of Eritrea. The inset photomicrograph shows details of clasts. Among the clasts can be seen fragments of fresh CFBs, ferricrete pisoliths (lower left of inset) and cobbles of basement: a gneiss is clearly visible at right and a deformed granite near centre of the main image.

**Figure 2.19** Four major Neoproterozoic terranes of Eritrea (after Drury & de Souza Filho 1998)

**Figure 2.20** Gneiss with vertical foliation cut by quartz veins up to 0.5m thick.

**Figure 2.21** Faulted contact of CFBs and laterites near Shiketi, Eritrea 15km southwest of Asmara, with international party of geoscientists in foreground.

**Figure 2.22** Geological map of the Axum area (after Tadesse *et al.* 1996).

**Figure 2.23** Artisanal gold panners near Adi Nebrid, Tigray, Ethiopia.

**Figure 2.24** Mountain road between Adigrat and Adwa showing the stratigraphic sequence above the basement in the eroded basaltic highlands west of Adigrat, Tigray, Ethiopia. The terraced peak on the right is typical of continental flood basalt (CFB) topography in Ethiopia. A break of slope at its base forms a large terrace underlain by lateritic ferricrete with resistant pure, white clay at the top of the cliff (inset). The upper cliff is formed by massive, iron stained Adigrat Sandstone (AS). The break in slope at the base of the cliff marks the top of the Enticho Sandstone (ES) and the Edaga Arbi Glacials, both forming the reddish ground in the valley bottom.

**Figure 2.25** Graphs showing annual variations in rainfall and day temperature for the Eritrean Plateau (Asmara) and the Red Sea lowlands (Massawa).

**Figure 2.26** Seasonal colour-coded maps of an index of green vegetation (from SPOT data), draped over side-illuminated elevation data. The images compare vegetation cover in April 2006 (end of dry season) and September 2005 (end of main wet season) showing the dramatic effect of climate on vegetation cover in the study area. Pale to dark greens indicate substantial vegetation cover, pale yellow to greysparse to no vegetation. Source: United Nations Development Programme

**Figure 2.27** Regional distribution of all localities visited. Red lines and numbers i to xi indicate reconnaissance excursions. Sampled localities are marked by coloured dots.

**Figure 2.28** Location map for all localities visited in Eritrea and place name reference.

## Chapter 3

## Chapter 4

## Maps



## Chapter 5

**Figure 5.8** ASTER 631 image showing the classified pixel results of three different SAM approaches: red using raw ASTER reflectance data for the SWIR bands (4 to 9); yellow the same, but atmospheric correction tweaked and, orange based on an ASTER spectrum from Clay Gorge, classified as alunite-bearing by Hyperion. These results prove that ASTER and laboratory spectra can be used successfully to find likely places for finding dateable alunite

**Figure 5.9** The results of spectral angle mapping of minerals in laterites using hyperspectral data from EO-1 Hyperion. The three swaths to left of the key cover the western part of the Asmara test area, whereas that to the right covers an unknown area 10km SW of the test area. Each Hyperion swath is 7.7 km wide.

**Figure 5.10 (a)** Alunite in clay zone - backscattered electron image from electron microprobe analysis, **(b)** Alunite-rich clay zone - alunite cubes in kaolinite - cross polarised light microscopy

**Figure 5.11** (a) Spectral angle mapping of ASTER reflectance data: kaolinite pixels - blue, alunite-rich pixels in red; (b) Successfully dated alunite-rich localities near Asmara

Successfully dated alunite-rich localities (Right) picked out by spectral angle mapping of ASTER reflectance data (Left): detected kaolinite pixels - blue, detected alunite-rich pixels in red.

**Figure 5.12** Mineral detection using ASTER (kaolinite – cyan; alunite – red) also showing the area covered by Hyperion compared with ASTER.

**Figure 5.13** Location and superimposed Landsat TM, ASTER, EO-1 ALI and Hyperion data sets - red box indicates test area (30km east-west x 24km north to south)

**Figure 5.14** Alunite occurrences near As Sarat, Saudi Arabia, from spectral angle mapping of ASTER reflectance data. Kaolinitic clays are highlighted in green and alunite in red in this rendition. Image width = 25km.

**Figure 5.15** Alunite Ar-Ar ages of Eritrean laterite: detected kaolinite - yellow, detected alunite - red.

**Figure 5.16** Progression of lateritisation: bottom right saprolite with core stones; centre kaolinitic clay zone; top left mottled zone with overlying nodular ferricrete and younger flood basalts.

**Figure 5.17** Spectra of minerals important in lithological discrimination in relation to ASTER and TM bands. Note: spectra are resampled to ASTER band widths and centres.

**Figure 5.18a** ASTER Relative Band Depth – kaolinite (band4 + band7)/band6 – for Asmara test area (see previous section).

**Figure 5.18b** ASTER RBD – $Fe^{3+}$ minerals (band2 + band4)/band3 – for Asmara test area.

**Figure 5.18c** ASTER RBD – jarosite (band5 + band8)/band7 – for Asmara test area.

**Figure 5.18d** ASTER RBD – C-O and Mg-OH absorption (band6 + band9)/band8 – for Asmara test area.

**Figure 5.19** Hyperion reflectance spectra for known sites compared with resampled lab spectra for kaolinite and hematite.

**Figure 5.20** Clay mineral spectra in the SWIR region: (a) lab spectra of common clay minerals; (b) Hyperion spectra from 8 randomly picked clay zone occurrences compared with lab spectrum of kaolinite (black), with positions of kaolinite SWIR absorption features (2.163 and 2.204 μm) shown as solid vertical lines for clarity.

**Figure 5.21** Iron mineral spectra in the VNIR: (a) lab spectra of hematite (H), goethite (G) and jarosite (J); (b) Hyperion spectra of ferricretes that may be dominated by each of the three minerals.

**Figure 5.22** Results of spectral angle mapping of several minerals associated with laterites using Hyperion data (5 February 2001) for an area 20 km west of Asmara (see Figure 5.23). (a) Hyperion image equivalent to ASTER 631. Image (f) shows iron minerals typical of

**Figure 6.1** SRTM DEM colour coded shaded relief location map showing the spread of localities sampled for Ar-Ar dating: sampled localities are marked by coloured dots: laterites = red, basement = blue, basalts = green.

**Figure 6.2** Energy dispersive element map with Al, S, K as RGB of a kaolinitic clay from Horizon 3 of the laterite profile showing individual and clusters of alunite crystals (blue) in a fine groundmass of kaolinte (red).

**Figure 6.3** Energy dispersive element map of laterite Horizon 3 (M33iv) with K, S, Al as RGB showing possible disordered kaolinite containing potassium in its lattice (magenta)

**Figure 6.4** (adapted from Berhe *et al.* 1987 Figure 1) Distribution of pre-1987 K-Ar ages for CFBs older than 25 Ma in the Ethiopian-Yemeni Volcanic Province. Red dots indicate localities where basalts have been successfully dated in this study using the Ar-Ar method

**Figure 6.5** (adapted from Berhe *et al.* 1987 Figure 5) Correlation chart of Cenozoic volcanic rocks in Ethiopia with special reference to the plateau flood basalts. (F), Flood Basalts; (C), Central type volcanics; (RV), Rift-related volcanics.

**Figures 6.6** Spectral distinction between basalts in (a) ETM742 and (b) ASTER 631 reflected bands as RGB perspective views of the eastern flank of Ras Dashen, Tigray, draped over SRTM elevation data. Basalts ascribed to the Ashangi formation appear as a purple hued terrace immediately above distinctive cyan lateritic clays and below well-vegetated cliffs of basalts of the Aiba formation. The highest basalts on Ras Dashen are red-hued and correspond to the mountain's Miocene shield volcano.

**Figures 6.7** Perspective view of Ras Dashen from the south showing ASTER thermal bands 14 12 and 10 as RGB draped over SRTM elevation data. The Ashangi basalts appear in pale greenish hues above white laterites and the red-hued Adigrat sandstones. Aiba basalts in the cliffs surrounding Ras Dashen show in dark-blue to purple hues. The different hues of the two basalt formation reflect the thermal responses of different proportions of ferromagnesian minerals and feldspars.

**Figure 6.8** Geological sketch map (40km wide) of northern part of the Ras Dashen volcanic massif based on ASTER 631 and 14 12 10 false-colour images. The spectral 'signatures' of the putative Ashangi basalts pinch out in the north beneath the Aiba basalts, indicating a regional unconformity separating the two main components of the Ethiopian CFBs. Viewpoint for Figure 6.6 shown.

**Figure 6.9** Roadside outcrop in the road ascending the Ethiopian escarpment from Kobo-Alomata to Mekele that shows lava flows ascribed to the Ashangi basalts, overlain by sandstones. Note the large basalt clast at the contact.

**Figure 6.10** Photomicrographs of basalt M73i from high in the flood basalt sequence on Emba Tekera 30km SW of Asmara (a) plane-polarised (b) cross-polarised. Fresh olivine basalt (plagioclase-clinopyroxene-olivine-opaques) with flow-aligned plagioclase laths. Olivine slightly altered to brown iddingsite. Scale bar = 1mm.

**Figure 6.11** Photomicrographs of the oldest flood basalt M79ii at this locality that rests directly on laterite at Dogali (a) plane-polarised (b) cross-polarised. Fresh, porphyritic olivine basalt (plagioclase-clinopyroxene-olivine-opaques) containing large (~1.5mm) olivine phenocrysts with green bowlingite alteration. Scale bar = 1mm.

**Figure 6.12** Photomicrographs of basalt M205a close to base of the flood basalt sequence at Hagere Selam near Mekele (a) plane-polarised (b) cross-polarised. Fresh, porphyritic olivine basalt (plagioclase-clinopyroxene-olivine-opaques) containing large (~1.5-2.00mm) plagioclase phenocrysts. Scale bar = 1mm.

**Figure 6.13** Photomicrographs of flood basalt M215a from the lowest flow of the Lima Limo section of Ras Dashen (a) plane-polarised (b) cross-polarised. Amygdaloidal olivine basalt (plagioclase-clinopyroxene-olivine-opaques) Scale bar = 1mm.

**Figure 6.14** Principal of cooling ages: Pink horizontal lines define the closure temperatures; diagonal red lines are different geothermal gradients; The horizontal green line is the

maximum uplift of the laterite datum, assuming it formed at sea level.

**Figure 6.15** Geological map of Eritrean basement (after Drury & de Souza Filho 1998, Figure 1) superimposed on SRTM elevation data. Orange lines are roads and tracks suitable for vehicle traffic. GD = post-tectonic (~650 Ma) granodiorite; MV = felsic metavolcanics (~750-800 Ma); B = basalts of various Cenozoic ages; M = migmatitic gneisses formed during Pan African orogeny (>650 Ma); A = superficial sediments.

**Figure 6.16** Photomicrographs of typical post-tectonic Eritrean Neoproterozoic granodiorite intrusion (M40) (a) plane-polarised (b) cross-polarised. Fresh, medium-grained granodiorite (quartz-sodium plagioclase-alkali feldspar -biotite). Scale bar = 1 mm.

**Figure 6.17** Escarpment age profiles (a) schematic plot showing episodes of uplift and (b) $^{40}Ar/^{39}Ar$ plot of whole-rock cooling ages of granodiorite samples.

**Figure 6.18** Neogene to Recent major faults and topography in eastern Eritrea. Red solid lines – normal, down-to-west, west dipping; red dotted lines – strike-slip faults; black ticked lines – normal. down-to-east, east dipping (Drury *et al.* 1994; Frazier 1970; Ghebreab & Talbot 2000); white lines – 'border faults' (Balestrieri *et al.* 2005; Abbate *et al.* 2002); hachured areas – occurrences of ~30 Ma CFBs. Topography from side-illuminated SRTM 3 arc-second digital elevation data; dark greens through yellows and browns to greys represent elevations from 0 to 2400m a.m.s.l.; magenta areas >2400m; black dash-dot line – escarpment rim. Inset shows regional location of study area.

## Chapter 7

**Figure 7.1** Late Carboniferous-Early Permian palaeogeography with palaeolatitudes, showing the distribution of Late Carboniferous-Early Permian glacigenic deposits in Gondwana. Grey star indicates position of glacigenic deposits in Northern Ethiopia and Eritrea and arrows indicate transport directions of glacigenic sediments in Ethiopia. (from Bussert & Schrank 2007).

**Figure 7.2**.Stratigraphy of Northern Ethiopia and Eritrea (from Bussert & Schrank 2007).

**Figure 7.3a** The relationships between Neoproterozoic basement, Palaeozoic and Mesozoic sediments -after Bussert &Schrank 2007

**Figure 7.3** Schematic section showing relationships between Neoproterozoic basement, Palaeozoic and Mesozoic sediments (see figure 7.3a; after Bussert & Schrank 2007), laterites and the African Surface, which is marked by unconformities beneath laterites and the Adigrat Sandstones (see figure 7.3b).

**Figure 7.3b** Vertical section through 50m of Adigrat Sandstones

**Figure 7.4** Estimated atmospheric $CO_2$ concentrations since 400 Ma (from Figure 2c in Breeker *et al.* 2010). The yellow plot is a compilation of previous estimates, that in red covers Breeker *et al.*'s revised estimates and blue shows the output ranges from the GEOCARBSULF model. The grey bar around 1000 ppmV shows the range of estimates of future $CO_2$ levels by 2100 AD.

**Figure 7.5** Chalcedony in the mottled zone (Shiketi)

**Figure 7.6** Residual quartz inherited from the parent rock: (**a**) quartz clasts in ferricrete horizon (Dairo Kaolos) (**b**) vein quartz in mottle horizon (Paradiso) (c) thick quartz vein in mottled zone (Asmara – Keren road) (d) quartz veining cutting mottled zone - ferricrete boundary

**Figure 7.7** Photomicrograph of typical relic corroded quartz grains, which are recognisable from their highly irregular shape, etch pits and re-entrant cavities: (a) ferricrete (M34i - mesa SE of Tseada Kristyan); (b) mottled zone (M58v - Areza) (c) clay zone sample (M67 - north of Mendefera). Scale bar = 1mm.

**Figure 7.8** Highly irregular and near-spherical relic quartz grains incorporated in lateritic clay zone (M67).

**Figure 7.9** Highly irregular and near-spherical relic quartz grains incorporated in lateritic (a) ferricrete (M309 - S of Himberti) (b) mottle (M66l - S of Senafe) (c) mottle (M71i - Adiguila).

**Figure 7.10** The variation of the solubilities of silica and aluminium oxide with pH. From Webb (2006), after Mason (1966).

**Fig 7.11** Mottled zone showing yellow goethite and reddish hematite, with some evidence of later leaching by reductive dissolution of iron oxyhydroxides associated with higher water table and wetter conditions.(a) Mottled zone (Himberti) (b) Photomicrograph of mottles (M18v Mereb – Tera Imni road) showing kaolinite with isolated pisoliths and relic quartz grains, stained by hematite. Scale bar = 1mm.

**Figure 7.12** Mottled zone showing sharp boundaries between iron-rich and iron-poor mottles; leached white areas formed during wet period when water table high and conditions reducing so that iron reduced from insoluble $Fe^{3+}$ to soluble $Fe^{2+}$: (a) mottle formation (Adi Teklay), (b) thin section of mottles (M315b - Embeyto) - Scale bar = 5mm, (c) vermiform mottles (Embeyto), (d) the predominance of dehydrated hematite as opposed to hydrated goethite suggests that the constantly hot humid climate was relatively drier during this episode of lateritisation (Shiketi).

**Figure 7.13** Climatic variability during the Cenozoic (Breeker *et al.* 2010).

**Figure 7.14** Features of the thick laterite clay zone at Adi Felesti: (a) figure at contact between clay zone and pink saprolite (Horizon 2) developed on granitic basement; (b) terrace developed at the clay- mottled-zone boundary; (c) alunite veining in clay-zone; (d) upper clay zone with alunite veins (inset).

**Figure 7.15** Simple sketches showing two models for Neogene uplift affecting the CFB-laterite datum in the Eritrean-Ethiopian Escarpment. Top: Major fault at base of escarpment (Drury *et al.* 1994); Bottom; monoclinal flexure (Ghebreab & Talbot 2000).

**Figure 7.16** Points where elevations of laterite occurrence were digitised (black dots) displayed over colour-coded SRTM elevation data illuminated from the north-west.

**Figure 7.17** Minimum tension surface for the base of the laterites, colour coded and 'illuminated' from the northwest. The lowest values are in purple, higher values in rainbow sequence to the highest in red.

**Figure 7.18** Perspective 3-D view from the north of the data in Figure 7.17, with vertical exaggeration of the surface 'relief' of the laterite base. The Red Sea is shown at the left.

**Figure 7.19** Profiles (a) across and (b) along the main axis of the regional structure.

**Figure 7.20** ASTER 631 image of the lowlands to the west of the Eritrean Plateau draped over an ASTER DEM to simulate a perspective aerial view of one of the prominent linear basalt outliers of the Western Lowlands.

**Figure 7.21** Artisanal miners in SW Eritrea panning alluvial sediments for gold. The stream is just below laterites, as indicated by suspended iron oxy hydroxides colouring the pond water. The stream bed is full of core stones derived from the saprolite zone.

**Figure 7.22** Map of the elevation difference between the present land surface and the surface fitted to the laterite datum, with gold and gossan occurrences (yellow and red dots, from Usoni 1952). Green areas indicate positive values, i.e. outliers of rocks overlying laterite. Pink areas are more than 250 m below the former level of laterites. Lilac areas lie between 20 m above and 250 m below the former level of laterites. See Figure N.7 for detail of the Asmara area.

**Figure 7.23** Map of the elevation difference between the present land surface and the surface of the laterite datum, for the Asmara area. Symbols and colours as on Figure 7.22

## Chapter 8

**Figure 8.1**. ASTER 631 combined as RGB simulates natural-looking vegetation and enhances rock differences in the Ethiopian Escarpment. (Key shows colours of various elements of the terrain; CFBs = continental flood basalts)

# List of Tables

## Chapter 2



## Chapter 4



## Chapter 5



## Chapter 6



## Chapter 8

## Frequently used acronyms

**AAT** – Adobha Abiy Terrane, Eritrea

**AB** – Adwa Block, Tigray

**AHB** – Adi Hageray Block, Tigray

**ALI** – Advanced Land Imager (EO-1)

**ANB** – Adi Nebrid Block, Tigray

**ANS** – African-Nubian Shield

**ASTER** – Advanced Spaceborne Thermal Emission and Reflection Radiometer

**AT** – Arag Terrane, Eritrea

**AVIRIS** – Advanced Visible / Infrared Imaging Spectrometer

**BIF** – banded iron formation

**BT** – Barka Terrane, Eritrea

**CB** – Chila Block, Tigray

**CFB** – continental flood basalt

**DEM** – digital elevation model

**DMA** – Defense Mapping Agency (USA)

**DT** – Dankil Terrane, Eritrea

**EMA** – Ethiopian Mapping Agency

**EO-1** – Earth Observing Mission-1

**ERSDAC**- Earth Remote Sensing Data Analysis Center (Japan)

**ETM+** - Enhanced Thematic Mapper Plus (Landsat)

**HT** – Hagar Terrane, Eritrea

**LIP** – large igneous province

**MB** – Mozambique Belt

**MF** – matched filter (algorithm)

**MKB** – Mai Kenetal Block, Tigray

**NER** – Northern Ethiopian Rift

**NASA** – National Aeronautic and Space Administration (USA)

**NOAA** – National Oceanic and Atmospheric Administration (USA)

**NT** – Nakfa Terrane, Eritrea

**PA** – Pan African

**RBD** – relative band depth (algorithm)

**RGB** – red- green-blue (additive colour components)

**RS** – remote sensing

**SAM** – spectral angle mapping (algorithm)

**SB** – Shiraro Block, Tigray

**SPOT** – Système Pour l'Observation de la Terre

**SRTM** – Shuttle Radar Topography Mission

**SWIR** – short-wave infrared

**TIR** – thermal infrared

**TM** – Thematic Mapper (Landsat)

**UNICEF** – United Nations Childrens' Fund

**UNOOSA** – United Nations Office for Outer Space Affairs

**USGS** – United States Geological Survey

**UTM** – Universal Transverse Mercator (map projection)

**VMS** – volcanogenic massive sulfide

**VNIR** – visible and near infrared

**WHO** – World Health Organisation

**XC** – cross correlation (algorithm)

## *Acknowledgements*

The work for this thesis was conducted in two very different places: around Asmara in the region of Eritrea in north-east Africa and in the headquarters of the Open University at the Milton Keynes campus in England. In the former I found warmth, openness and co-operation despite the ravages of war, widespread poverty and lack of institutional security. Among the many who offered help and support I would particularly like to thank: Tesfamichael Keleta and Michael Abraha (Directors of the Geological Survey of Eritrea) for providing official letters of permission, without which extensive field work would have been impossible, and ensuring that we were accompanied by Eritrean geologists acting as guides, interpreters and good company. From the Ministry of Energy and Mines, thanks to Alem Kibreab (Director General), Berhane Negassie, Mussie Tesfai and Kaleab Ghirmai (Gaala Valley guidance) and, Omar Saleh and Mbratu (rock and water sample export permits). My thanks too to those at the Ministry of Water Resources, for example, Michael Negash (Director), Mebrat Gebreab, Tekie Yemane and Fikremariam Kahsay. At Asmara University, all are remembered with affection for their support; Mengist Teklai, Beraki Woldehaimanot and Woldai Ghebreab (Geology Lecturers) for advice and Biniam Beyene and Awet Fishazion (final-year students) for especial help. Local people were always hospitable; Seife Berhe (consulting geologist) was ever on hand, children of Tseada Kristyan taught me Tigrinya for colours of variegated laterite profiles, Gidei of the Shegah and all at the Embasoira/Imperial looked after me as did Michael Dilorenzo of Leo Car Hire with reliable Toyota Land Cruisers for field reconnaissance. Always resourceful and kind, Alemu Teklegiorgis drove expertly for 6 gruelling days in Ethiopia over 2500km of high quality 'blacktop' and roads that exist only in cartographers' imaginations.

Facilitated by Dr Steve Drury (OU), I was helped by Kathryn Linge, B. Disch and J. Duffett at NERC ICP-MS and ICP-AES with well water chemistry analyses at Kingston and Royal Holloway Universities, London, which was a relaxing experience. Outside the OU the support of those like Les Moore, Sylvia Woodhead, Jim Crowley (USGS), Naz Kaliki (ENVI), Dan Taranick (Anglo American), Richard Teuww (Portsmouth University), Prof Mike Thomas (Stirling University), Michael Abrams, Bob Crippen, and Gary Geller (all of NASA/JPL), R.B. King (ODM), David Stevens (UN/ UNOOSA), Prof John McArthur (London University) Marc Goossens (Geosense), Kent Hill Park conference centre staff and, Gerard Bradey, who was particularly helpful and reassuring, was of great value.

By contrast, at Milton Keynes there were fewer who moved beyond their own preoccupations to offer help when I needed it. Among these, Steve Drury, my principal supervisor until retired, was a tower of strength throughout, risking actual bureaucratic harm for his commitment to all OU students and myself. I suppose it is inevitable that the early vision of an idealistic institution like the OU should become muddied and obscured by time-servers and self-seekers, but Steve was one who kept the faith and for that I am grateful. Unexpected kindnesses also came from Charles Turner, Liz Lomas, Marc Davies, OU library, IT and security staff and, Mrs V. Bacigalupo and Prof A. Bassindale who were surprisingly human as was Prof Nigel Harris who gave me some useful editorial advice. Others who provided welcome support were: John Watson (XRF and whole-rock major and trace-element geochemistry), Andy Tindle (electron microprobe and X-ray fluorescence spectrometry guidance), Dick Carlton, Kay Green and Simon Kelley who allowed me use of the argon mass spectrometry facilities (see Rhiannon George's thesis acknowledgements).

Here is not the place to recall institutional indifference or sometimes positive obstruction so I end by thanking Carol, loving family and friends like Dr Philip D. Phillips who more than compensated for it. All deserve a special mention, but I'd rather not write a thesis so suffice to mention four men; my father Jack Andrews (Oxford University) who never lost faith in me and taught me all that is good, my brother John Andrews (Manchester University) - long suffering and ever interested, my beloved husband, Dr William S. Deller (Oxford University) who has always sustained me and never let me down and, our son - William John Deller.

# LATERITIC PALAEOSOLS OF N.E. AFRICA: A REMOTE SENSING STUDY

This thesis is a part-time project completed over several years when university facilities could be made available for the necessary work.

CHAPTER ONE

# Lateritic palaeosols, remote sensing and mapping - prospects and possibilities

Lateritic palaeosols, a weathering product of rock, are clearly identifiable on five continents and cover a significant part of the Earth's land surface (figure 1.1, Pedro 1968; Tardy *et al* 1991; Tardy 1997; Agnew 2010) and yet they remain largely unmapped and geologically overlooked. This study examines how remotely sensed data from a variety of sensors can be used to map lateritic palaeosols (laterites) and their distinctive horizons for the first time. It establishes what geological information can be obtained by satellite remote sensing of the component units of laterites and the surrounding terrain. Specifically it presents an investigation of Eritrean laterites in the context of NE African geology, mineral exploration, palaeoclimatic fluctuation and the societal ramifications of living with laterites.

## 1.1 Introduction

In NE Africa the base of the Tertiary sequence is marked by lateritic palaeosols conformably overlain by mid-Oligocene continental flood basalts (CFBs) (see Contents for Acronym List) of the Ethiopian plateau (figure 1.2; Bohannon 1989; Drury *et al.* 1994; Andrews Deller 2000). Some of the world's most extensive, best-preserved laterites are found in Eritrea, NE Africa, where they frequently outcrop in full profile. Typical of laterites throughout the region (Chapter 2), these common palaeosols represent a poorly understood environment. They form an excellent tectonic datum and are key to understanding the evolution of uplift and configuration of the African Surface (King 1948, 1962) and local supergene alteration of the crystalline basement and its associated primary mineralisation. Moreover, an understanding of laterites is essential if local people are to live safely in lateritic terrain and exploit the resource potential of the palaeosols, yet no geological maps

exist of laterite facies in Eritrea or neighbouring Ethiopia where they have been studied only superficially. This thesis seeks to fill that gap in the literature, examine and map laterite facies throughout the region, explore the issues arising from these maps and so provide new insights into the geology of NE Africa, whilst providing a basis for future research and raising further lines of enquiry.

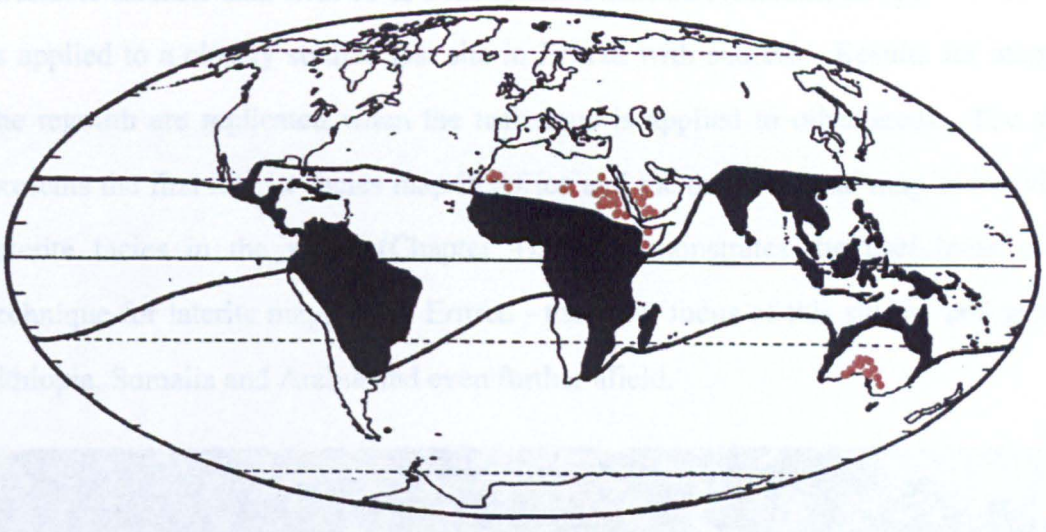

**Figure 1.1** Zone of laterite palaeosol cover - black shading - across the world (after Pedro 1968; Tardy *et al* 1991; Tardy 1997). Red-brown dots indicate laterite facies mapped in this work where laterites extend beyond and conformably underlie basalts that cover much of the region (see chapter 4) together with additional, extensive laterites noted in the thesis

However, though laterites are scientifically interesting, socio-economically important and the global distribution of the paleosols clear (Buchanan 1807; Dainelli 1943; Collenette & Grainger 1994; Mohr 1970, 2001; McFarlane 1976; Dixon 1979; Schellmann 1981, 2003; Bohannon 1989; Bird *et al.* 1990; Butt & Zeegers 1992; Drury *et al.* 1994, 2001, 2006; Vasconcelos *et al.* 1994, 2008; Ohmoto 1996; Itaya *et al.* 1996; Ollier & Pain 1996; Overstreet *et al.* 1977; Menzies *et al.* 1997; Tardy 1997; Vasconcelos 1999; Twidale 2000; Andrews Deller 2000, 2002 - 2007; Taylor & Eggleton 2001; Drury & Andrews Deller 2002; Abbate *et al.* 2003; Gunnell 2003; Vasconcelos & Conroy 2003; Andrews Deller *et al.* 2005; Balestrieri *et al.* 2005; Drury 2008; Turner 2009; Burke & Gunnell 2008; Ollier & Sheth 2008; Maiti *et al.* 2010), world-wide there are no regional maps on which their different horizons or facies appear and in practice they are commonly omitted from geological maps and

stratigraphic sections. Despite the distinctive spectra of the minerals that make up their separate horizons, there are few, if any, geoscientists who have used remote sensing to discriminate or map them and certainly none that map each horizon regionally using the tool of remotely sensed data. This research develops a strategy for such mapping based on known mineralogical variations in the profile, using freely available satellite data with 15 to 90m spatial resolution (Abrams 2000). The method is applied to a closely studied test site in Eritrea with success. Results for mapping the regolith are replicated when the technique is applied to other areas. The study presents the first laterite facies map in Africa and the only regional map of individual laterite facies in the world (Chapter 4). It demonstrates the usefulness of the technique for laterite mapping in Eritrea - the main focus of this study - and parts of Ethiopia, Somalia and Arabia and even further afield.

**Figure 1.2** Typical CFB-laterite conformable contact, Eritrea (Colouration: CFB = black; laterite = red)

## 1.2 Study area

The main area of study is situated between 13° - 16°N and 37°30' - 40°30'E, with some information gathered from more remote outlying areas of Eritrea and localities

from Addis Ababa to Mekele and Gondar to Addis Ababa in Ethiopia (figure 1.3). Although laterite exposures are spectacularly obvious in this region, there is little published work on them; in fact their presence is rarely mentioned. Nevertheless, there are helpful references to the palaeosols in the work of Merla and Minucci (1938), Dainelli (1943), Mohr (1970, 1976, 1983, 2001), Beyth (1972), Merla *et al.* (1979) and more particularly Bohannon (1989) and Drury *et al.* (1994). This research builds on that preliminary work.

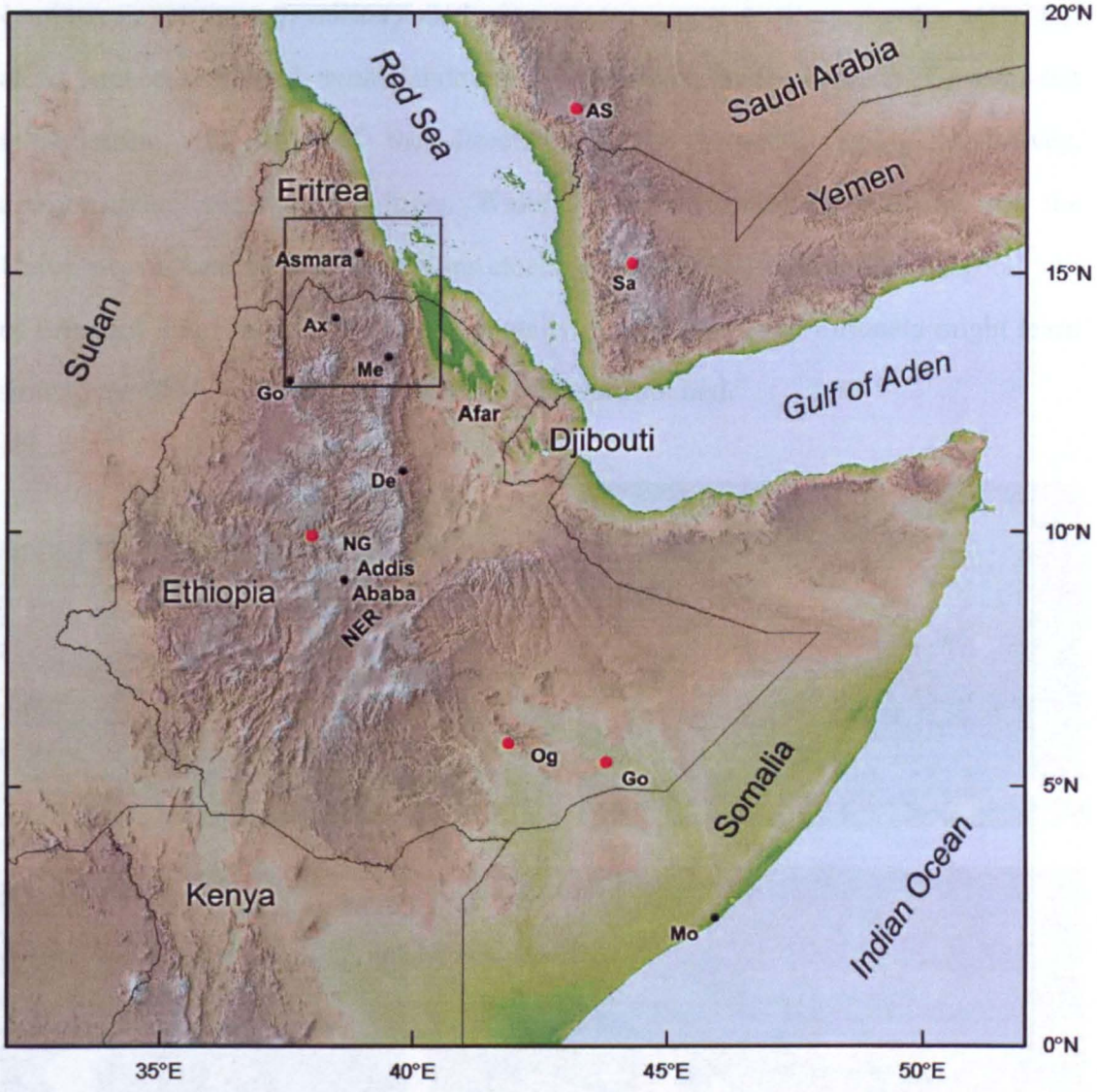


**Figure 1.3** The Horn (hill-shaded and colour-coded ~1km resolution SRTM-30): Africa's most disaster-prone region with poor map coverage. The main study area is boxed. Abbreviations: Ax = Axum; Me = Mekele; Go = Gondar; De = Dese; Mo = Mogadishu; NER = North Ethiopian Rift. Red dots indicate some distant areas studied using remote sensing: AS = As Sarat; Sa = Sa'ana; NG = Blue Nile Gorge; Og = Ogaden; Go = Gode

### 1.2.1 Accessibility

Geological work in Eritrea and Ethiopia has been hampered by military conflict over the last fifty years (see figure 1.4), but it has continued thanks to the efforts of Eritrean and Ethiopian geologists during the conflict. Even though much of the terrain is so rugged that many areas are accessible only on foot, limited vehicle access is possible along dry riverbeds, dry-season tracks and along several excellent arterial roads that span both Eritrea and Northern Ethiopia. Foreign Office guidelines cautions travel through military exclusion zones, remote territory, border areas and along traverses dotted with landmines. However, with Eritrean Government authorisation, the help of the directors of the Eritrean Geological Survey, accompanying geologists, Eritrean Water Resources staff, the blessings of the University of Asmara, United Nations clearance, authorised drivers and the good will of Eritreans and Ethiopians with a generosity of spirit the more fortunate might learn from, over 400 localities of scientific interest were studied.


**Figure 1.4** The aftermath of war: (a) Massawa bomb damage - Dr S. Muhongo for scale; (b) shelled rock store (c) unexploded grenade; (d) burnt out tank

Preliminary fieldwork was carried out in March 1998 at the end of the dry season and before the rains made work more difficult. Unfortunately, further field trips planned for 1998, 1999 and 2000 had to be cancelled. In May 1998 war broke out between Eritrean and Ethiopian forces and ongoing hostilities interrupted field studies until March 2001. In 2002 an opportunity for Ethiopian fieldwork was taken and a final field trip to Eritrea was completed in October 2003 at the start of the dry season (Chapter 2). The last three trips mentioned above were dogged by security problems over much of the study area and the 25km border exclusion zone. But although travelling after dusk was unsafe and vast distances had to be covered at dawn, preliminary results were verified by field-checks despite being hindered by 'shiftas' (bandits) and progress slowed in areas live with unexploded munitions.

## 1.3 Remote sensing data

The principal sources of multispectral digital imagery used in this project are Landsat Thematic Mapper (TM and ETM+); Advanced Spaceborne Thermal Emission and Reflection Radiometer (ASTER); Advanced Land Imager (ALI) and Hyperion hyperspectral data from NASA's experimental EO-1 mission and elevation data from the Shuttle Radar Topography Mission (SRTM).

## 1.4 Thesis plan

This work provides new data on the location, petrography, geochemistry and geochronology of laterites; the first laterite facies map in NE Africa and, illustrates the scientific and socio-economic importance of laterites and the value of using remote sensing as a mapping tool to chart distinct facies and the surrounding terrain.

### 1.4.1 Aims

- To use remotely sensed data from Landsat TM, ASTER, ALI and Hyperion and digital image processing to identify and map laterites and their component facies in Eritrea and Northern Ethiopia at scales up to 1: 200,000 and to continue mapping these palaeosols to a regional level.

- To carry out comprehensive regional fieldwork in order to document laterite facies occurrences in different geological settings, examine their stratigraphy in situ, determine the extent of the palaeosols in the region and collect samples suitable for geochemical analysis and dating.
- To design a strategy for mapping laterite facies accurately using multispectral digital imagery focused on variable laterite mineralogy and test the success/viability of the strategy by checking exposed lithologies against image data in the field before applying the technique to other areas.
- To collect geochemical data of laterite facies and associated groundwater, understand the chemical processes involved in laterite genesis and assess the risk from associated hazardous elements.
- To date laterites, the overlying CFBs and underlying basement as a means of calibrating the stratigraphic position of lateritic weathering in the geological time-scale; to determine a minimum age for laterites and infer the period of laterite evolution in the region, the duration of effusive basalt magmatism and timing of tectonic uplift.
- To use the resulting laterite facies map as:

(i) A means of detecting lateritic outcrops, delineating different parts of the profile, facies variation and different minerals present in order to select laterites for regional radiometric dating and determine regional palaeoclimatic conditions.

(ii) An indicator of the flood basalt-laterite contact as a datum across the region.

(iii) A basis for quantitative analysis of post-30 Ma tectonics over the Arabian-Nubian Shield (ANS) using the Tertiary basalt-laterite contact as a datum and digital elevation models as means of constructing a structural elevation surface on the contact in order to examine the nature of doming and uplift of the African surface using ASTER and SRTM data.

(iv) A guide to identifying potential zones of supergene enrichment of base metal and gold mineralisation using structural analysis ASTER and SRTM data, assessing groundwater quality in the light of geochemical data and determining the extent of

viable agricultural land and hazardous terrain.

- To conduct case studies on the effects of laterites on landscape and indigenous populations.

### 1.4.2 Outline

*Publications and invited presentations*

Four of the following listed papers that support the thesis are incorporated in the body of the work. They are in the name by which I am known in the scientific community; the combination of my maiden and married name lodged at the Open University, UK on my initial application for this study.

**I.** Andrews Deller, M.E. 2007. Space technology for disaster management: data access and its place in the community. In: Teeuw, R.M. (ed.) Mapping Hazardous Terrain using RS. Geological Society London (GSL), Special Publication, 283, 149–164. Published in proceedings: Geological Remote Sensing Group (GRSG), GSL, UK, 2007; 31st International Symposium for Remote Sensing of the Environment, Saint-Petersburg, Russia, 2005; United Nations (UN) International Workshop on the Use of Space Technology for Disaster Management, UN Office for Outer Space Affairs (UNOOSA), Munich, Germany, 2004.

**II.** Andrews Deller, M.E. 2006. Facies discrimination in laterites using Landsat TM, ASTER and ALI-EO1 data: examples from Eritrea and Arabia. In: International Journal of Remote Sensing, 27, 2389–2409.

**III.** Drury, S.A., Ghebreab, W., Andrews Deller, M.E., Talbot, C.J., Berhe, S.M. 2006. A comment on "Geomorphic development of the escarpment of the Eritrean margin, southern Red Sea from combined apatite fission-track and (U–Th)/He thermochronometry" by Balestrieri, M.L. *et al.* In: Earth and Planetary Science Letters, 231 (2005) 97–110, EPSL.

**IV.** Andrews Deller, M.E. 2004. Locating dateable minerals in laterites using remote sensing - an example from Eritrea, NE Africa. Oral presentation T32.03. Published in proceedings: 32$^{nd}$ International Geological Conference, Florence, 2004; GRSG, GSL, UK, 2003; University of Asmara, Eritrea, 2003; Mineralogical Society, Glasgow University, UK, 2003.

Papers not included in this study although themes developed from them are included within the thesis.

**V.** Drury, S.A., Peart, R.J. & Andrews Deller, M.E. 2001. Hydrogeological potential of major fractures in Eritrea. In: Journal of African Earth Sciences, 32, 163–177.

**VI.** Drury, S.A. & Andrews Deller, M.E. 2002. Remote sensing and locating new water sources. Oral presentation Andrews Deller, M.E. Published in proceedings: UN International Workshop for Space Technology and Disaster Management, UNOOSA, Addis Ababa, Ethiopia: http://www.unoosa.org pdf sap 2002.

**VII.** Andrews Deller, M.E. 2002. Facies discrimination in laterites using remotely sensed data; Landsat TM versus ASTER, ALI and Hyperion data: An example from Eritrea. Published in proceedings: ASTER Unveiled, GRSG, GSL, UK, 2002.

I am responsible for 100% of the work in papers I, II, IV and VII; a 50% contribution to the work in paper VI and a 30% contribution to papers III and V.

*Chapters 1-9*

The thesis is divided into nine chapters and includes sections that can be readily prepared with minor modifications for publication. Chapters 1-3 provide the framework for this study. Chapter 4 forms the core of the work and Chapters 5, 6, 7, 8 and 9 stem from the results of Chapter 4 and their application.

**Chapter 1** introduces the project.

**Chapter 2** sets the background of the thesis. The regional geology of Eritrea and Northern Ethiopia is described and laterite facies are discussed in the context of the evolution of this geological setting. Particular emphasis is placed on the geology of the palaeosols the object of this work: Laterite occurrences and their variable lithology are documented throughout the region; a working definition for Eritrean laterites presented; their petrology detailed, mineralogy established and their geochemistry examined. The chapter draws from and builds on previous published work on lateritisation that emphasises the geochemical process of intense meteoric alteration of the bedrock that results in the formation of laterites; this typifies laterites in the study area.

**Chapter 3** outlines the main research methods or techniques used in this study and briefly explains why they are used to achieve the results of strategies implemented in subsequent chapters.

**Chapter 4** discusses laterites and remote sensing (RS). A strategy for mapping laterites in a test site is developed. Semi-quantitative mineral mapping, using Landsat TM, ASTER and EO-1 ALI data is used to map laterite horizons effectively. RS data that cannot be used for mapping laterites is considered. The first geological facies map of laterites supported by ground truth is produced. The simple approach for mapping laterite facies in the test site is applied to unvisited areas in Eritrea and Arabia with success and used to determine the extent of the palaeosols throughout Eritrea and Northern Ethiopia and map them to a regional level.

**Chapter 5** uses regional maps of laterite facies (Chapter 4) as a framework for further mineral mapping and locating dateable minerals in laterites using remote sensing. Successful strategies are developed for detecting both rare and common minerals in the laterite profile. All results are illustrated and a minimum age for lateritisation is established for the first time in N.E. Africa (see also Chapters 6 & 7).

**Chapter 6** documents radiometric dating of clays, basalts and granodiorites using the $^{40}Ar$ /$^{39}Ar$ method (Chapter 3). $^{40}Ar$ /$^{39}Ar$ work on laterites is confined to representative samples selected on the basis of mineral mapping (Chapter 5) and geochemical screening (Chapter 2) for rare potassium minerals in laterites. Further evidence is obtained for the age of Eritrea and Ethiopian laterites. An estimate of the timing of ancient uplift and erosion of the basement is established as is the local time span of flood basalt eruptions. Whole rock $^{40}Ar$ /$^{39}Ar$ ages are presented for clays, basalts and granodiorites and the geological implications of all the results discussed.

**Chapter 7** deals with the palaeoclimatic and environmental setting for evolution and formation of laterites and their relationship to the African Surface (King 1948, 1962). Using the flood basalt-laterite contact as a tectonic datum, SRTM digital elevation model (DEM) data are used to construct structural elevation models of that datum to define the pre-30 Ma African surface, late-Tertiary uplift patterns and determine areas

of supergene enrichment useful for mineral exploration.

**Chapter 8** details the socio-economic benefits of mapping laterite and the surrounding terrain. Case studies on the relationship of laterite facies to groundwater, resources and hazardous terrain are presented.

**Chapter 9** concludes the study, summarises the findings of this research and recommends further lines of enquiry.

# Setting the scene: regional context and laterite petrology

Given the dearth of literature on the subject of laterites in NE Africa, this chapter places laterites of Eritrea and Tigray (a province in northern Ethiopia) in the context of their stratigraphic position (section 2.2) and the substrates (sections 2.3, 2.4; Appendix 1) from which they developed. It makes an original attempt to position laterites in the geological time-scale (Gradstein *et al.* 2004) in order to determine when they formed and the conditions necessary for their genesis (see also Chapter 7). It documents the lithologies from which laterites can be distinguished using remote sensing (RS) and sets the framework for producing detailed regional geological maps of laterite facies and determining their distribution, palaeogeographic environment and geochemistry in order to access the impact on population and landscape (Chapter 8). As the study depends on fieldwork to validate image data and interpretation, the chapter details current geological maps, regional geology, laterite geology, in particular petrology and localities where laterites outcrop (section 2.3; Appendix 1) all essential for producing a geological map and determining a RS strategy for mapping laterites.

## 2.1 Introduction

The distinctive nature of laterites in Eritrea and Tigray makes them easily identifiable in this region, which is characterised by diverse Precambrian to Mesozoic lithologies that preceded the continental flood basalts (CFBs) (Dainelli 1943; Mohr 1976; Giraud *et al.* 2005; Bosworth 2005). Following on from magmatism, sedimentation, deformation and metamorphism that shaped the regional Neoproterozoic basement, Phanerozoic evolution was tectonically simple and involved deposition of both terrestrial and marine sediments, at times in intra-cratonic rifts (Bosworth 1992).

However, there are uncertainties about the stratigraphic age of some of the sediments on which the laterites rest, the age of the laterites themselves and where they outcrop (Germann *et al.* 1993, 1994; K. Burke, pers. comm. 2001; Burke & Gunnell 2008; Moucha & Forte 2011).

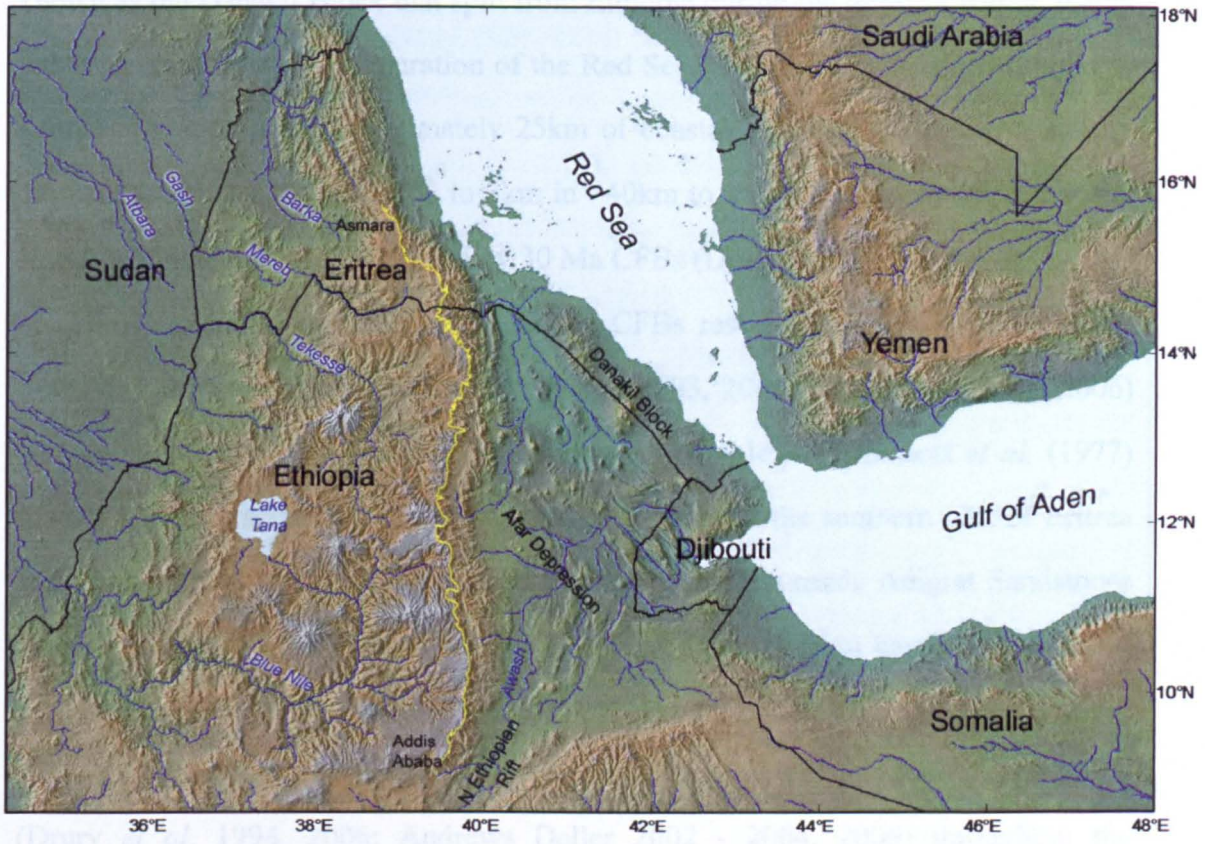


**Figure 2.1** Regional topography and drainages of NE Africa and South Western Arabia. Country boundaries, river names and names of main topographic features and tectonic boundaries are shown. Yellow line = lip of the Ethiopian-Eritrean Plateau

Figure 2.1 includes the regional study area (see also figures 1.3, 2.22) and illustrates the overall topography of NE Africa where the Barka, the Mereb-Gash, the Tekesse-Atbara and the Blue Nile or Abbai river systems (Gani & Abdelsalam 2006) have incised the Ethiopian-Eritrean Plateau. To the west of the plateau, topographic elevation descends through a series of irregular escarpments to reach an average elevation of 500 to 1000 meters in the Gash, Atbara and Nile plains. In northern Ethiopia the plateau is separated from the Red Sea to the east by the Afar Depression (Pilger & Rösler 1975; Manighetti *et al.* 2001; Wright *et al.* 2005; Barisin *et al.* 2009), a N-S zone of active extension that in some places is up to 125m below sea

level. At approximately 11.5°N, the Afar Depression Red Sea-related extension meets the NNE-SSW Northern Ethiopian Rift (NER) and the onshore extension linked to sea floor spreading in the Gulf of Aden to form a R-R-R triple junction. The Afar Depression is separated from the Red Sea by a linear fragment of thicker crust known as the Danakil Block that split from Ethiopia during the onset of rifting, which led to the present-day configuration of the Red Sea. The western Red Sea margin in Eritrea is made up of approximately 25km of coastal lowlands backed by a deeply eroded escarpment that rises 2.2 to 3km in ~40km to a plateau, locally known as the Hamasien Plateau, which is capped by 30 Ma CFBs (Drury *et al.* 1994, 2006).

Throughout northern Eritrea and Sudan CFBs rest conformably on Palaeogene (~40 Ma) lateritic palaeosols (Andrews Deller 2003, 2004, 2006; Drury *et al.* 2006) beneath which is a Neoproterozoic metamorphic complex. Overstreet *et al.* (1977) reports a similar scenario in Saudi Arabia. Whereas, in the southern part of Eritrea and northernmost Tigray discontinuous patches of early Jurassic Adigrat Sandstones and rare relics of older glaciogenic rocks separate laterites from basement in places. A thicker and more complete Mesozoic succession occurs in Ethiopia, south of Adigrat. Laterites occur in this stratigraphic position immediately beneath the CFBs (Drury *et al.* 1994, 2006; Andrews Deller 2002 - 2004, 2006) throughout the hinterland of the western Red Sea margin, from eastern Sudan (Kenea 2001), through Eritrea and northern Ethiopia (Appendix 1; Andrews Deller 2000, 2006) to the Blue Nile Gorge (Sultana & Abdelsalam 2006) and further to the south (Ebinger *et al.* 1993; Drury *et al.* 1994; George 1999); a N-S range of at least 1500km (section 5.6.1). Because they formed across most of NE Africa and western Arabia (Andrews Deller 2006) on a low-relief surface, probably close to sea level (Overstreet *et al.* 1977; Bohannon *et al.* 1989), the laterites are an important datum for assessing the effects of later regional tectonics (Drury *et al.* 1994, 2006). Post-30 Ma tectonics displace occurrences of this datum by up to 2.4km vertically between the plateau and coastal lowlands (Chapter 6; Drury *et al.* 2006).

The geology of Ethiopia and Eritrea has been the subject of many publications in

the last 25 years but there has yet to be a single account which embraces it all. An attempt is made in the next two section to present such an account in the context of the study area.

## 2.2 Regional setting - chronostratigraphic observations and the place of laterites in the geological time-scale

The 'chronostratigraphic' (Gradstein *et al.* 2004) place of laterites in a regional context is interesting. Although there are no NE African laterites recorded or observed in the Precambrian and Palaeozoic, the earliest possible occurrences in the Mesozoic are debatable and the only confirmed reports of these palaeosols place them in the Cenozoic (Dainelli 1943; Drury *et al.* 1994), there is clear evidence that laterites develop from the regional rocks (Appendix 1; Mohr 2001) of all eras except the Cenozoic. Adopting an empirical and pragmatic approach using field observations from over two hundred field sites and current literature on stratigraphic information, the chronology of lateritic palaeosols in the region is addressed here for the first time.

### 2.2.1 Precambrian

The Pan African (PA) (900-450 Ma, Kroner 1984; Kroner & Stern 2005) accretion of multiple island arcs and eventual continental collision in NE Africa and Arabia created a huge mass of new crust into which granites were intruded, the Arabian-Nubian Shield (ANS), a N-S orogenic belt of up to ~1000km across. This orogenic belt extends from Egypt to Kenya to meet the Mozambique Belt (MB) in Tanzania over a combined length of 7300km (Stern, 1994; figure 2.2). Most of this neocraton, the East African Orogen, was eroded throughout the Palaeozoic (Chapter 7). Although deposition did take place, lower Palaeozoic sediments only occur on the eastern flank of the Arabian-Nubian Shield (Giraud *et al.* 2005). Moreover, the earliest Phanerozoic sediments in NE Africa are widely considered to be of Carboniferous to Permian age.

Eritrea and Northern Ethiopia, the Yemen, Western Saudi Arabia and the Red Sea

Hills of the Sudan are part of the ANS. Its basement rocks are predominantly PA and span the transition from Neoproterozoic to Upper Ordovician. The bulk of the Neoproterozoic rocks that formed the ANS resulted from Neoproterozoic plate tectonics and microplate evolution in a predominantly oceanic setting (see Kröner & Stern 2005). Radiometric ages, isotopic and geochemical studies indicate that the cratonization process of the shield involved a progressive change in chemistry of the arc magmas, from immature, low-K, arc tholeiite, to mature, high-K, calk-alkaline

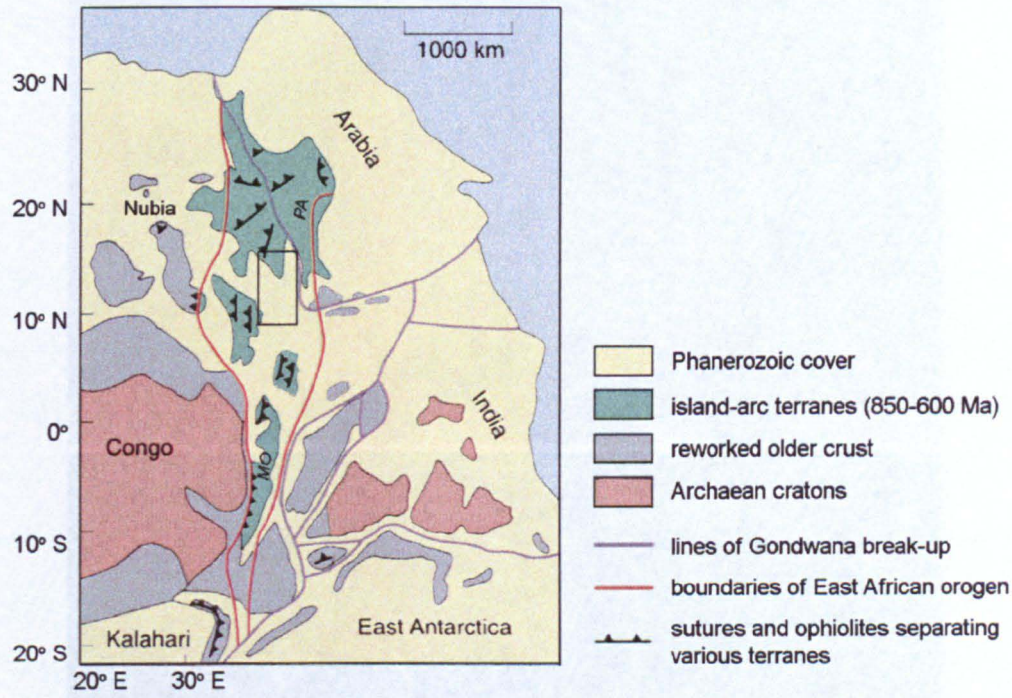


**Figure 2.2** The East African Orogen (Stern, 1994): the Pan African (PA) and Mozambique orogens (MO) (after Kröner & Stern, 2005, Figure 2). The ANS makes up the northern part of the East African Orogen where the main study area (boxed) is located

lava series. Evolution of the Pan African accreted arc terrane was terminated by continent-continent collision along the MB (Holmes 1951; Cahen 1961; Kroner & Stern 2005; figure 2.2) where Neoproterozoic crust became tectonically meshed with older continental crust (Vail 1976; Kazmin *et al.* 1978; Kröner & Stern 2005). Formed during one of the most extensive orogenic episodes in the Earth's geologic history, lithologies in the PA complex can be divided into three broad, variably deformed components, all of which predate the PA orogeny and are present in Eritrea (Drury & Berhe 1993) and northern Ethiopia (Tadesse *et al.* 2003). These Neoproterozoic assemblages are:

- volcanogenic, calc-alkaline supracrustal sequences that include both volcanic and volcano-sedimentary rocks and host various kinds of primary mineralisation;
- calc-alkaline plutonic rocks dominated by granodiorites and,
- highly deformed but layered basic to ultrabasic complexes that are often ophiolitic (Bakor *et al.* 1976; Neary *et al.* 1976; Gass 1981).

(a)

(b)

**Figure 2.3** Variably deformed Neoproterozoic rocks: (a) Stretched volcano-sedimentary conglomerate near Asmara, (b) High-grade gneiss with isoclinal folds near Keren

The magmas that make up these assemblages display a range of ages from 760 Ma in Eritrea (Teklay 1997) to 1200 Ma in Kenya (Kröner & Stern 2005). Signs of mineralisation that formed volcanogenic massive sulfide deposits where hydrothermal

fluids escaped from ocean-floor vents and instances of pervasive hydrothermal alteration of various volcanogenic rocks with associated gold mineralisation are present throughout this oceanic-arc complex (Usoni 1952; Barrie *et al.* 2007).

Deformation during the PA orogeny was variable in its intensity and episodic. In low strain areas, though signs of deformation (figure 2.3a) are obvious, original lithologies retain some of their textural features. Much larger ductile strains associated with large shear belts in the low-grade Nakfa Terrane and pervading the high-grade Barka Terrane (section 2.3; figure 2.19; Drury & De Souza Filho 1998) produced a range of schists and gneisses (figure 2.3b, figure 2.20). Throughout much of the Neoproterozoic basement compositional banding is steeply dipping with a regional ~N-S strike.

The oldest part of the PA complex is overlain, with clear unconformity in some areas, by a series of sedimentary strata (sandstones, carbonaceous phyllites and carbonates) of late Neoproterozoic to possibly early Ordovician age (Beyth 1972; Drury & de Souza 1998). This later, post-accretionary component is deformed by structures that represent the last phases of the PA orogeny, while a variety of late- to post-orogenic granitic intrusions completed the evolution of the PA complex during the Cambrian to early Ordovician (Johnson & Woldehaimanot 2003). Lithologies of all types mentioned above constitute typical parent rocks of the palaeosols throughout Eritrea and Tigray (Appendix 1) as do those of the Palaeozoic.

### 2.2.2 Palaeozoic

The complete Phanerozoic succession, the lower parts of which constitute the Palaeozoic, is only found in exploratory wells drilled in the southern Red Sea area off the Danakil Block. Figure 2.4 illustrates the stratigraphic sequence of Phanerozoic sedimentary and volcanic rocks that are known in NE Africa.

During the assembly of the supercontinent Pangaea, Africa formed the core of its southern part, Gondwana. What is now the Horn of Africa was landlocked and therefore subject to terrestrial sedimentary conditions that included the effects of Carboniferous to Permian glaciation during the longest Ice Age in geological history.

Yet Mohr in his *'Geology of Ethiopia'* (1976) writes that Carboniferous-Permian glaciation of Gondwanaland had no effect on Ethiopia. However, he does not mention the evidence cited by others for glaciogenic rocks in Ethiopia (Dow *et al.* 1971). The Tgura and Gilo Formations together with the Enticho sandstones and

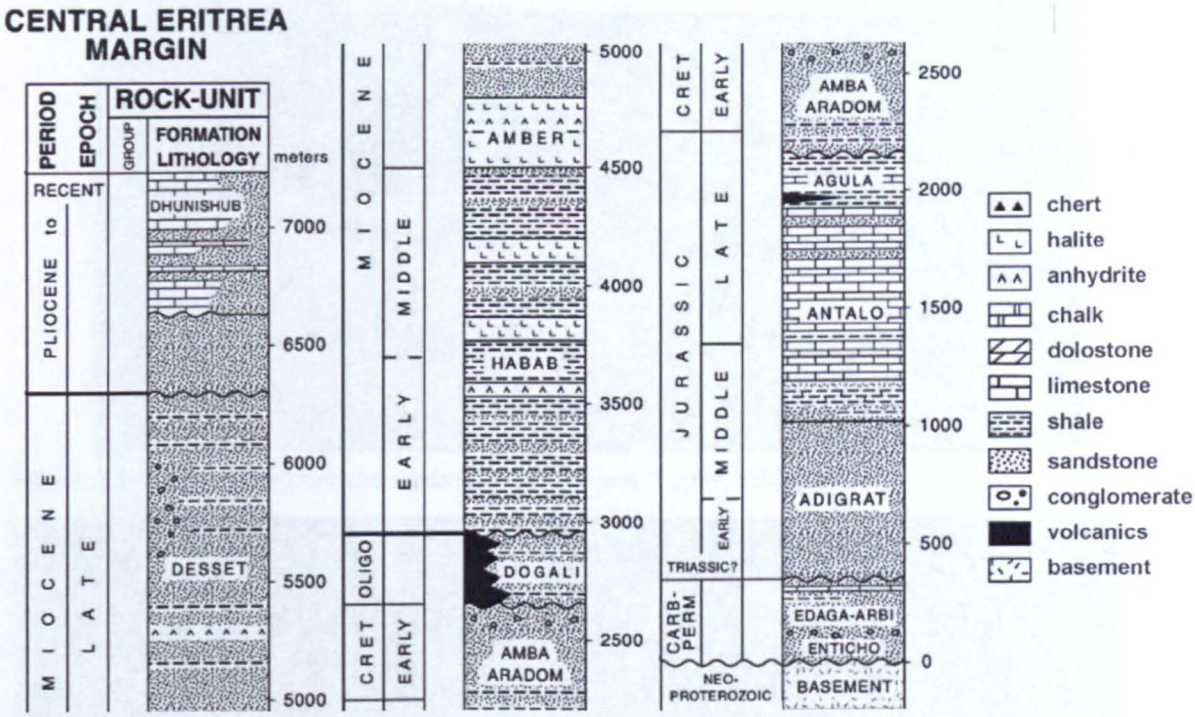


**Figure 2.4** Phanerozoic stratigraphic sequence from an exploratory well drilled in the southern Red Sea offshore of the Danakil Block (based on Bosworth *et al.* 2005, Figure 9)

**Figure 2.5** Edaga Arbi glaciogenic sediments of probable Permian age 25km SE of Adwa, Tigray Ethiopia. The tillite contains numerous rounded and angular cobbles of various basement lithologies

**Figure 2.6** cross-stratified Enticho sandstone near Adigrat, Tigray, Ethiopia

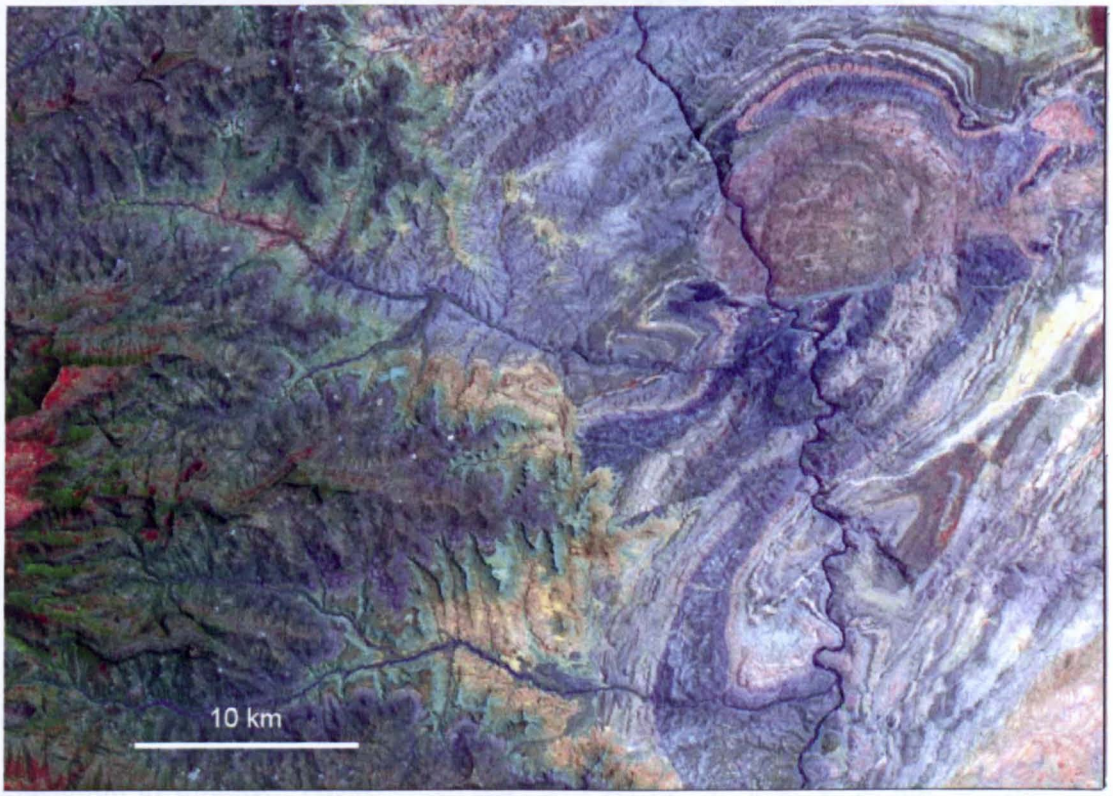


**Figure 2.7** ASTER 631 image of part of the basin of the upper Tekesse River, showing the basal unconformity of the Phanerozoic rocks. The dark area at left is the eastern flank of Ras Dashen, the highest mountain in Ethiopia, formed of mid-Oligocene CFBs capped by Miocene shield volcanics. Immediately above the highly folded Neoproterozoic metamorphic complex are Edaga Arbi glaciogenic sediments, in yellow. Note that the glaciogenic sediments pinch out towards the north of the scene. They are overlain unconformably by a thin sequence of Adigrat Sandstone (not visible) then laterites, clearly marked by the sky blue colour of their kaolinite-rich clay zone (Chapter 4)

Edaga Arbi Glacials (figure 2.6, figure 2.5), which in some parts of NE Africa form the oldest Phanerozoic rocks that rest unconformably (figure 2.7) on the Neoproterozoic basement, are just some examples of glaciogenic sediments not mentioned by Mohr (1976). Both Kazmin's (1972) and Tefera *et al's.* (1996) maps indicate that Late Palaeozoic to Triassic sediments are restricted to areas north of Mekele, whereas Merla *et al.* (1973) classify the diamictites of Tigray as Ordovician. According to the above mentioned maps, there are no glaciogenic sediments further south in the Nile gorge and sedimentary units examined there during the 2002 field season appear to be part of the Adigrat sandstone formation.

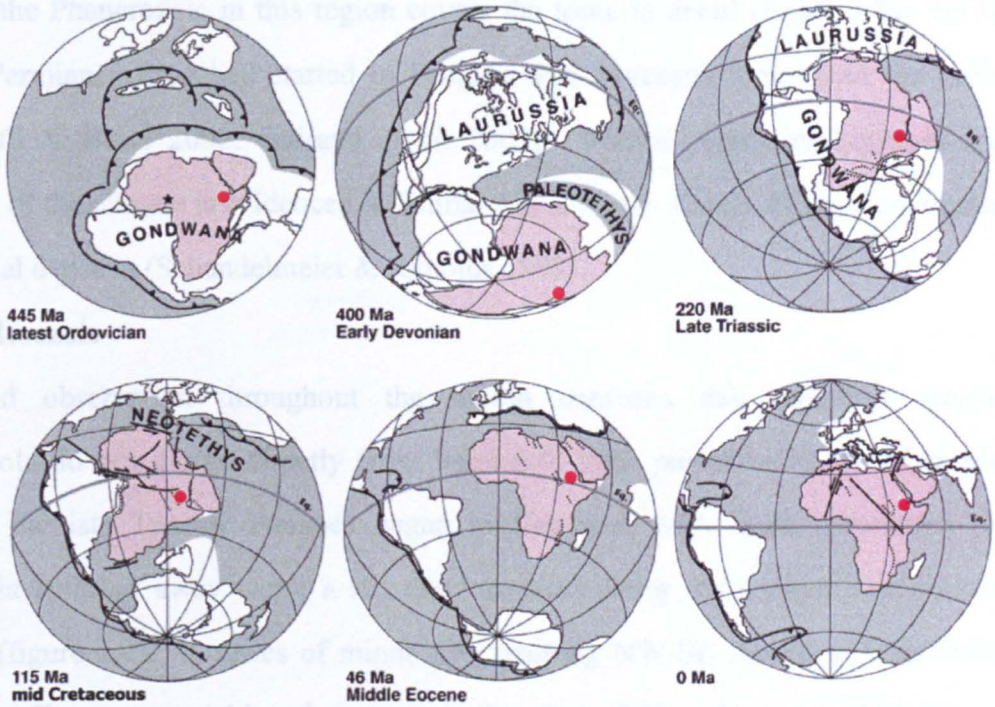


**Figure 2.8** Palaeogeographic reconstructions for Africa since the Ordovician (from Giraud et al, 2005). The approximate location of the main study area is shown by a red dot

Bosworth (1994) and Bumby and Guiraud (2005, Figure 4) document the Middle Ordovician glaciation of NW Africa and the Upper Carboniferous to Lower Permian glaciation of Southern Africa when the ANS lay at ~45 degrees south. During both periods the ANS could have been at the outermost fringe of any major glaciation of the southern hemisphere. Indeed, tillites from both episodes occur in Saudi Arabia. Furthermore, two sets of fossils from the oldest Phanerozoic sediments of NE Africa lead to contradictory findings. Trace fossils from the Adigrat Sandstone that are

younger than the glaciogenic sediments have been interpreted as trilobite tracks of Lower Palaeozoic age by Kumpulainen *et al.* (2006) who suggest that these underlying sediments formed during the Ordovician, a theory originally suggested by Dow *et al.* (1971). However, spores from sediments near the base of the Edaga Arbi Glacials have been recorded as Upper Carboniferous to Lower Permian in age (Bussert & Schrank 2007). Whichever age turns out to be valid, it is the mineralogy of the Adigrat Sandstone (Getaneh 2002) and to a lesser extent that of the glaciogenic sediments that have a bearing on the nature of the laterites formed on and from them. The informative overview of Giraud *et al.* (2005) on palaeogeographic reconstruction during the Phanerozoic in this region covers the topic in detail (figure 2.8). By the Early Permian, rifting had started in Pangaea and increased throughout the period (Stampfli & Borel 2002; Guiraud *et al.* 2005). Marine regression together with cooling of the climate is evidenced in Eritrea and southern Arabia by the development of glacial deposits (Schandelmeier & Rynolds 1998).

### 2.2.3 Mesozoic

Field observation throughout the region confirms that wherever lateritic palaeosols do not derive directly from basement, their parent rocks are Mesozoic. During the late Triassic Pangaea began to fragment, with India, Antarctica and Australia splitting away along a rift that extended along the present east coast of Africa (figure 2.9). A series of minor rifts trending NW-SE started to form in NE Africa. The most notable of these was the Anza Rift, which runs beneath the Cenozoic cover of NE Kenya (Bosworth 1992) and links with a series of roughly parallel rifts in southern Sudan. The northernmost of the minor rift 'swarm' partly controlled the lower reaches of the Blue Nile and the Mesozoic Mekele Basin that began to form in the Triassic ushering in a eustatic period characterised by repeated of marine transgression and a change in in sedimentation.

Dainelli (1943) noted this change and the presence and absence of recognisable sedimentary marine or terrestrial sedimentary units in the Mesozoic sequence at numerous localities throughout the Horn of Africa and southern Arabia. From his

findings (Figure 2.10) he reconstructed the progress of marine transgressions and regressions across the region. Based on far more extensive information than Dainelli had at his disposal, Guiraud *et al.* (2005), using results from seismic surveys and boreholes for oil exploration in southern Sudan, NE Kenya, eastern Ethiopia and Somalia, reached the same conclusions as Dainelli. Nevertheless, Dainelli's (1943) palaeogeographic maps remain the only clear account of marine transgressions and regressions for the Horn of Africa during the Mesozoic.

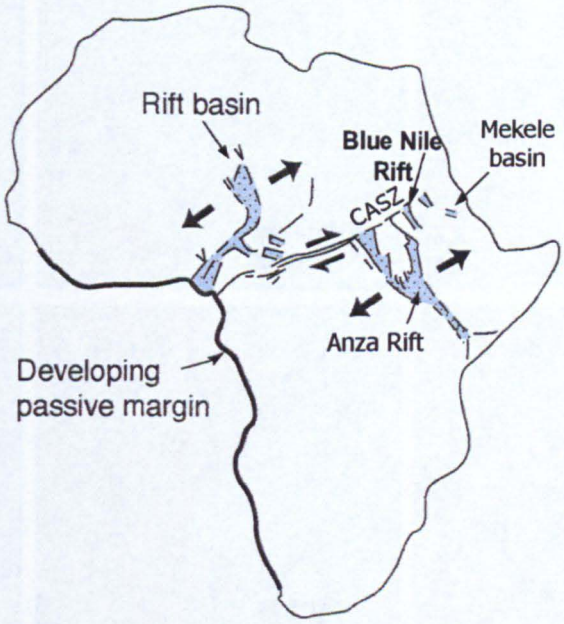


**Figure 2.9** Context for the tectonic opening of African Mesozoic rift basins (after Ghebreab 1998, Figure 1b)

The Triassic marine embayment shown in Figure 2.10 is a reflection of the influence of extensional tectonics related to break-up of Gondwana. By the end of this period, only Somalia was below sea level and occurrences of Jurassic marine sedimentation chart a protracted and extensive marine transgression that reached its maximum extent in the late Middle Jurassic. During the Upper Jurassic and the Cretaceous, renewed marine regression once again resulted in only parts of Somalia remaining below sea level. This recurrence of Mesozoic marine transgressions and retreats suggest that most of NE Africa, although often terrestrial, was very close to sea level and a regional peneplane - an ideal situation for the onset of lateritisation

(section 2.6; Chapter 7) - throughout the Mesozoic Era.

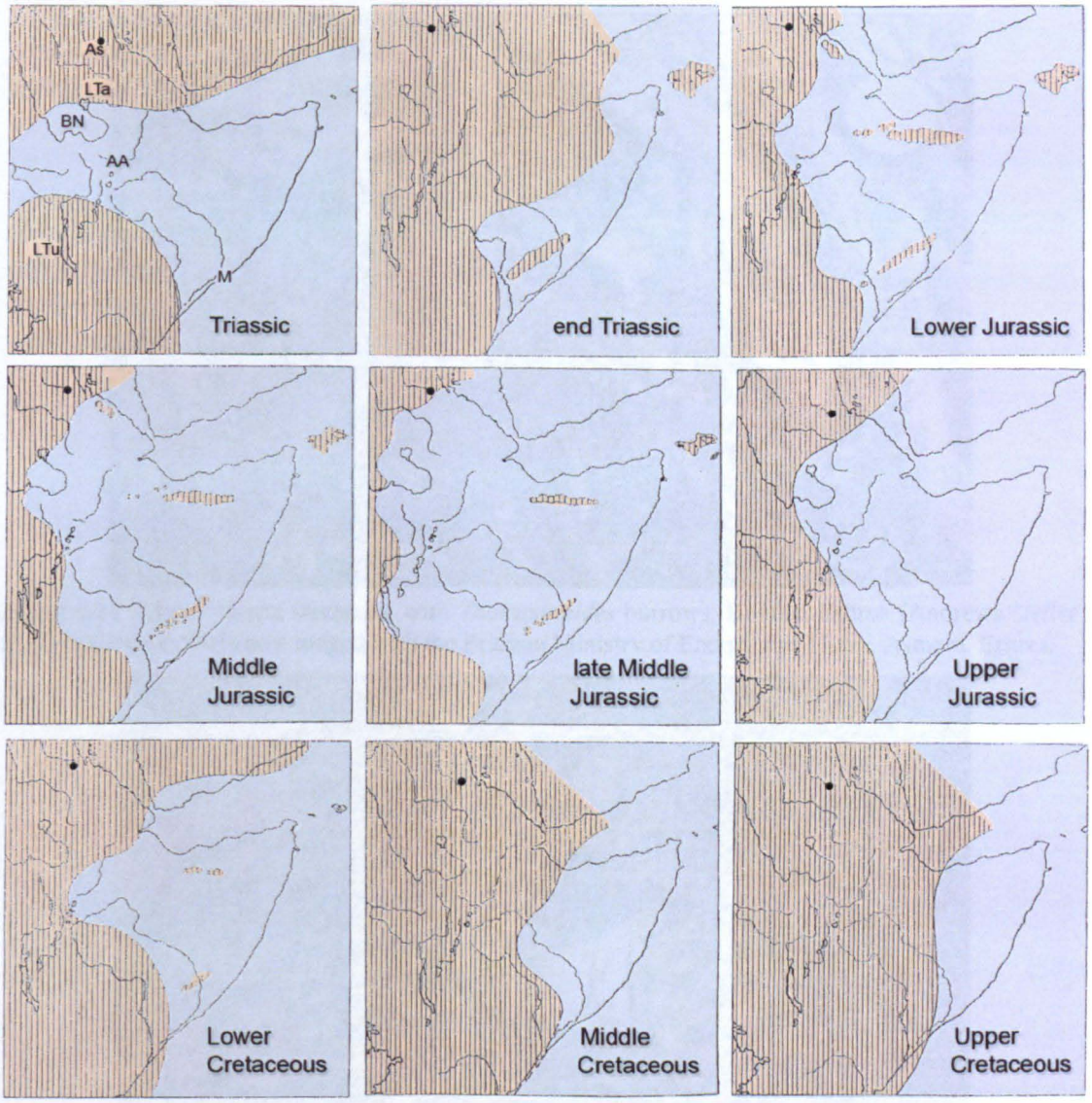


**Figure 2.10** Based on Dainelli's (1943) hand-drawn maps showing marine transgressions and regressions over the Horn of Africa and southern Arabia during the Mesozoic. Extents of terrestrial and marine conditions are indicated by pale brown and pale blue respectively. The following features are indicated for geographic reference: A – Aden (Yemen); AA – Addis Ababa; As – Asmara; BN – Blue Nile; LTa – Lake Tana; LTu – Lake Turkana (northern Kenya). M – Mogadishu (Somalia). Because each map has a slightly different extent a black dot at Asmara is included on them for reference

Taking into account the position of various ancient shorelines relative to the position of modern Asmara (figure 2.10), it becomes clear that the main study area in this thesis *was* terrestrial throughout the Mesozoic and that, given suitable climatic conditions, lateritisation in Eritrea and Tigray may have been ongoing since the Triassic. Apart from Somalia, therefore, as the entire area was above sea level from the Middle Cretaceous onwards, constraints on an absolute maximum age of laterites

could well be pushed back ~200 Ma.

**Figure 2.11** Adigrat quartz sandstone with *Thalassinoides* burrows, Knafna, Eritrea (Andrews Deller unpublished data 2001) now lodged with the Eritrean Ministry of Energy and Mines, Asmara, Eritrea

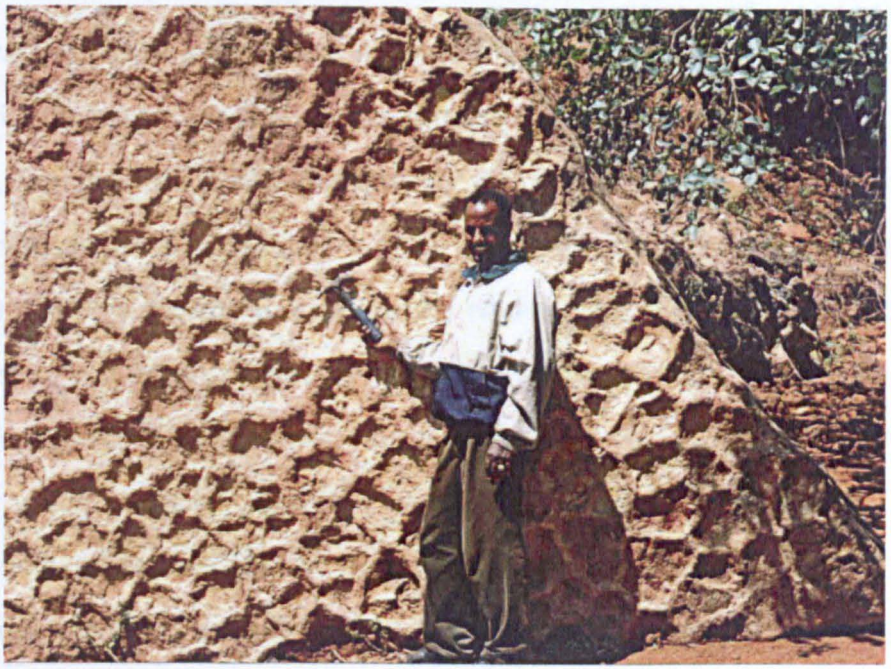

**Figure 2.12** Sun cracks in Adigrat Sandstone in the Blue Nile gorge, Ethiopia. Alemu Teklegiorgis, an Ethiopian colleague, is 1.7m tall

The major sedimentary formation of the Mesozoic succession in Eritrea and Tigray is the Adigrat Sandstone (Blanford 1870). This thick sequence that succeeds the disputed glaciogenic rocks of NE Africa is made up almost entirely of virtually pure quartz sandstones with clear fossiliferous horizons (figure 2.11) and some evidence for emergence (figure 2.12). In Ethiopia and Eritrea the age of the Adigrat

is poorly constrained (Bunter & Debretsion 1998) and there is some confusion about what constitutes the Adigrat Sandstone on existing maps and among various authors. Neither Kasmin (1972) nor Merla *et al* (1973) shows any presence of the Adigrat Sandstone in Eritrea, or for that matter at Adigrat itself. Both maps refer to these well-known sandy units as the glaciogenic Edaga Arbi Formation of Ethiopia. Conversely the Ethiopian (Tefera *et al.* 1997) and Eritrean Geological Surveys (Eritrean Ministry of Energy and Mines 1997) report the occurrence of the Adigrat Sandstone formation in northern Ethiopia and Eritrea (see Chapter 7).

South of Mekele, the Adigrat Sandstone forms the base of the Phanerozoic, but no reports exist of underlying glaciogenic rocks in this area, the Nile Gorge or in SE Ethiopia (Klein *et al.*, 2007). Kasmin (1972), Merla *et* al. (1973), Tefera *et al.* (1997) and Bosellini *et al.* (1997) suggest a Triassic to Middle Jurassic (Callovian) age for the Adigrat Sandstone, a hypothesis supported by dinosaur foot prints, fossil and plant remains in the upper reaches of the formation in Ethiopia (Klein *et al.* 2007). However, Kumpulainen *et al.* (2006) suggest that the Adigrat Sandstone exposures in Eritrea are Ordovician to Silurian, a moot hypothesis (based on marine trace fossil evidence) that they attempt to apply to the equivalent formation in Ethiopia. This leads them to suggest that higher levels of the formation in Eritrea that have been eroded may correlate with the sandstones at the base of the Adigrat Sandstone in Ethiopia, which is thicker and directly overlain by Jurassic limestones. Similar sandstones found in the Nile Gorge and SE Ethiopia that contain middle Jurassic fossils must, according to Kumpulainen *et al.* (2006), be a separate formation from that found in Tigray and in Eritrea because the trace fossil evidence differs. Kumpulainen *et al.* (2006) attempt to resolve (but in fact exacerbate) the confusion by suggesting that there are two very similar looking white sandstones lying beneath the undoubtedly Middle Jurassic limestones. Both formations, they suggest, formed in similar shallow marine environments but at very different times. Interestingly, Bosellini *et al.* (1997) provide evidence of laterites above the Adigrat sandstone in transition beds at the base of the Middle Jurassic limestones in the Nile Gorge.

Jurassic to Cretaceous sedimentation in NE Africa was restricted to intra-continental rifts, of which the large Blue Nile and minor Mekele Rifts are examples. In contrast with the view of Guiraud *et al.* (2005), Bosworth (1992, 1994) and Ghebreab (1998) document the development of these NW-SE rifts in relation to continent-wide stresses generated by the early opening of the Central and South Atlantic Oceans from the Lower Jurassic to Middle Cretaceous. In particular, the NE-SW extension across the rifts is related to dextral strike-slip movement in this period on the huge Central African Shear Zone. Except to the far SE in the Ogaden and Somalia, north of the Anza Rift (figure 2.9), there is no sign of Jurassic or Cretaceous sedimentation outside the rift basins of NE Africa.

**Figure 2.13** Interbedded near-shore and shelf limestones and shales of the Jurassic Antalo Series exposed in a road cutting towards the top of the Blue Nile gorge, near Dejen, Ethiopia

Jurassic marine sediments (Bosellini *et al.* 1997; Worash & Valera 2002) on the Ethiopian plateau are only found in Mesozoic rift basins (Giraud *et al.* 2005). The Jurassic sequence - the Antalo Series - in the minor Mekele basin consists of repeated shale-limestone near-shore and marine shelf cycles (figure 2.13) and includes evidence for evaporites. In the Mekele area Bosellini *et al.* (1997) show that these Upper Jurassic sediments are succeeded by the Cretaceous Amba Aradom Series.

The sediments are dominantly fluviatile sandstones with some evidence for aeolian deposition and lateritic palaeosols (figure 2.14) including a thick laterite at the base. The Amba Aradom Series is also correlated, by some, with sandstones in SE Ethiopia and thin limestones containing marine fossils of Aptian-Albian (middle Cretaceous) age. Bosellini *et al.* (1997) show an unconformity in the Mekele area, on which the Cretaceous rocks rest above tilted Upper Jurassic sediments. They assign this to a Lower Cretaceous uplift associated with some intra-plate deformation.

**Figure 2.14** Upper Cretaceous fluviatile sandstones of the Amba Aradom Series interbedded with lateritic palaeosols. Adi Hageray, 25km NW of Mekele, Tigray Ethiopia

Marine ups and downs of Cretaceous age are noticeable in the Ogaden and Somalia, but nowhere else in NE Africa. The Cretaceous was the time of highest sea level during the Phanerozoic over much of the Earth (~300m higher than at present), when there was large-scale marine transgression on most continents. Interestingly, the opposite was the case in the Horn of Africa with a low former sea level during a period of marine regression (Dainelli 1943) and some regional uplift. Quite possibly this extended uplift may have been related to gradual heating of the lithosphere beneath the whole of Africa, which eventually reached a climax with the Afar Plume and the flood basalts (George *et al.* 1998; Ebinger *et al.* 2000; Wright *et al.* 2005). Such uplift would not necessarily have resulted in widespread erosion (for instance of any earlier laterites). In fact, it can reasonably be argued that the lowering of the

surface by the inevitable volume loss during lateritisation could easily have kept pace with slow or protracted uplift (section 2.2.4). Moreover, loading of the lithosphere by dense CFBs erupted under the influence of the plume would tend to check any tendency for thermally induced uplift.

### 2.2.4 Cenozoic

The most important features of the Cenozoic of NE Africa and Arabia that are relevant to the discussion of laterites in this research, are the Palaeogene CFBs and the Neogene rifting and uplift in the Red Sea area. CFBs are denser than average continental crust and their excess mass would have created a positive gravity anomaly that forced down the underlying lithosphere (Leng & Zhong 2010). This would tend to check or damp down any thermal uplift associated with the Afar plume. Spread over such a broad area, any surface gradients due to thermal uplift would have been low and erosion may not have occurred. This stability over time, together with the fact that laterites are stratigraphically located between the CFBs and the underlying Neoproterozoic basement or Mesozoic sequence ensures their perfect preservation in NE Africa and Arabia, a feature unique to the region. The basal basalts have been dated at ~30 Ma (Drury *et al.* 1994) and the basement has a minimum age of ~600 Ma (Teklay *et al.* 2000) so formation of the laterites would have occurred somewhere between these two dates (see Chapters 5, 6, 7).

**Figure 2.15.** Typical trap topography developed on the CFBs of the Eritrean Plateau at Emba Tekera. The foreground shows laterite clay zone cut by a Neogene basaltic dyke

The CFBs are the dominant element in the scenery of the Ethiopian and Eritrean Plateaus. Individual flows give rise to the typical stepped topography and the common name traps, taken from the Swedish word for stairs *trappa* (figure 2.15). Following emplacement of the CFBs, the last episode of Cenozoic volcanism to affect the plateaus includes several alkaline basalt shield volcanoes of Miocene age. Punching through the traps, within the study area, Miocene alkaline volcanism is represented by spectacular trachyte plugs, which also have a dramatic effect on landforms (figure 2.16).

**Figure 2.16**. Trachyte plugs of the Adwa area, Tigray, Ethiopia, cutting through CFBs

*Dating Cenozoic tectonics – radiometric evidence*

Rifting, in its early stages, can be dated both stratigraphically and radiometrically (Bosworth *et al.* 2005; Bosworth & Burke 2004). Eritrean, Ethiopian and Yemen CFBs contain flows as young as ~26 Ma, although the bulk were erupted ~30 Ma (Drury *et al.* 1994, 2006; Hofmann *et al.* 1997; Courtillot *et al.* 1999; Andrews Deller, 2000, 2003; Davies *et al.* 2002; Ukstins *et al.* 2002; Wolfenden *et al.* 2005; Arndt & Menzies 2005 Zanettin *et al.* 2006). All CFBs and related volcanics with these documented ages are earlier than first signs of rift faulting so, 26 Ma (Upper Oligocene) is a maximum possible age for the start of rifting. Along the Arabian side of the Red Sea a massive dyke swarm parallels the coast, together with differentiated plutonic gabbros and granites (Mohr 1991). These formed during a period of major extension and have been dated at 24-20 Ma (Lower Miocene) (Zumbo *et al.* 1995),

when rifting was already underway. There are also Lower Miocene granites at the foot of the Ethiopian escarpment which possibly cut the early faults of the west flank of the Afar Depression (Drury 2004). Later volcanism (including that of the Lower to Middle Miocene Harrats of western Arabia) on both eastern and western flanks of the Red Sea occurred during episodic extension while the initial rift developed. Syn-rift volcanism on the Ethiopia-Eritrean flank was concentrated in the Afar Depression and continued from Lower Miocene to the present day (see Bosworth *et al.* 2005; figure 2.17).

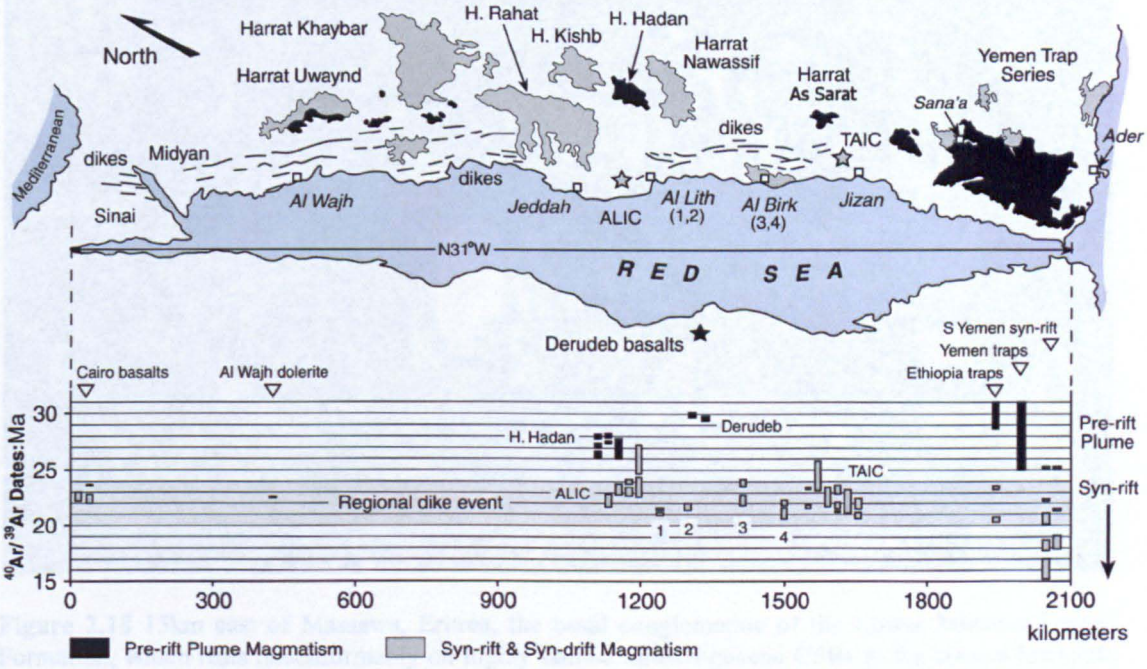


**Figure 2.17** Summarised radiometric dates of CFBs and rift-related igneous rocks in NE Africa and Arabia (from Bosworth *et al.* 2005)

Apatite fission-track (AFT) dating provides a rough guide to when uplift and erosion got underway on the flanks of the Red Sea (Bosworth *et al.* 2005). Sufficient uplift and cooling to allow apatite fission tracks to be preserved had occurred between 26 to 20 Ma in the northern Red Sea (Omar *et al* 1989; Omar & Steckler, 1995). On both sides of the southern Red Sea, AFT data suggest that major uplift and erosion had taken place between 23-17 Ma (Bohannon 1989; Menzies *et al.* 1992, 1997; Ghebreab *et al.* 2002; Abbate *et al.* 2002), with accelerated uplift after 17 Ma. Using U-Th/He thermochronometry, Balestrieri *et al.* (2005) purport that rifting began in the

Eritrean escarpment circa 15 Ma. Their findings bear no relation to other documented stratigraphic and radiometric evidence (see Drury *et al.* 2006). Actual opening and spreading of the Red Sea ('rift to drift') probably started at ~5 Ma, the age of the oldest magnetic stripes recorded over the axial zone of the Red Sea, i.e. around the Miocene-Pliocene boundary. Makris and Rhim (1991) however suggest spreading began about 10 Ma with hidden or irregular magnetic anomalies.

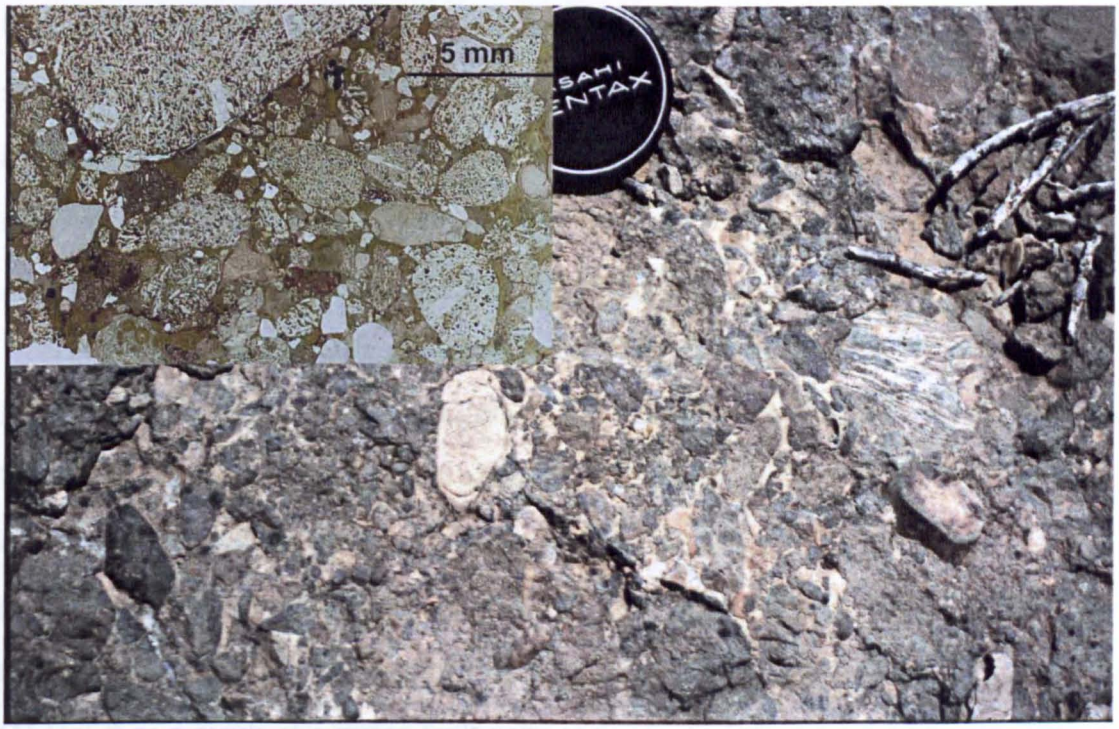


**Figure 2.18** 15km east of Massawa, Eritrea, the basal conglomerate of the Lower Miocene Dogali Formation, which rests unconformably on highly faulted mid-Oligocene CFBs in the coastal lowlands of Eritrea. The inset photomicrograph shows details of clasts. Among the clasts can be seen fragments of fresh CFBs, ferricrete pisoliths (lower left of inset) and cobbles of basement: a gneiss is clearly visible at right and a deformed granite near centre of the main image

*Dating Cenozoic tectonics - stratigraphic evidence*

The base of the Miocene in offshore exploration wells is marked by an unconformity that Bosworth *et al.* (2005) equate with the start of rifting and uplift. Bosworth and Burke (2004) hold that the Red Sea rift basin did not exist north of Eritrea until early Miocene; however, there are Upper Oligocene sediments below the Red Sea floor off Danakil (Bosworth *et al.* 2005). Onshore in the Dogali area of eastern Eritrea, the unconformity between the CFBs and the Dogali Series sediments is marked by conglomerates (Drury *et al.* 1994) containing clasts of basalt, laterite

and basement (figure 2.18). So, by the time the conglomerates were deposited, most probably in alluvial fans, uplift and erosion were well underway and had locally cut through the Eritrean Phanerozoic cover. So far, basalts immediately overlying the Dogali sediments have not been dated, but a late Oligocene to early Miocene proboscidean species (elephant) has been found in the sediments a short way from the unconformity and dated at ~26.8 Ma (Shoshani *et al.* 2006). CFBs, laterites and basement beneath the unconformity at Dogali are repeated in tilted blocks between a series of low-angled, west dipping normal faults. These are possibly the earliest faults associated with rifting, although they are interpreted in different ways (see Drury *et al.* 1994; Ghebreab & Talbot 2000; Chapter 7).

*Nature of uplift in the escarpment - Two possibilities*

The most striking feature produced by late Cenozoic tectonics in NE Africa is the Ethiopian-Eritrean Escarpment (figure 2.1). Because the CFBs and underlying laterites occur on the highest parts of the plateau and at the foot of the escarpment a down-to-east (or up-to-west) displacement, of the order of ~2.5km or more, has developed since the mid-Oligocene. Two suggestions have been made for the form taken by this large rift-related structure:

**(1)** Uplift as a result of a major fault zone at the foot of the escarpment, which has a downthrow to east (basinwards) of around 2.4km (Balestrieri *et al* 2005).

**(2)** Regional bending of continental crust by means of a crustal monocline that dips eastwards (Ghebreab and Talbot 2000), so that CFBs, laterites and other Mesozoic rocks once dipped down the escarpment. However, as there are no signs of lateritic weathering on ridge crests in the escarpment, any laterite dipping down the escarpment would have been at least 50m above that current ridge crest surface.

Little evidence exists for **(1)** (Merla *et al.* 1973; Ghebreab & Talbot 2000; Drury *et al.* 2006). However **(2)**, a crustal monocline or flexure associated with small west dipping faults that occur along the escarpment from 9° to 15°N seems a far more realistic possibility (Drury *et al.* 2006). These faults appear to have the net effect of creating a regional eastward dip of the pre-Miocene Phanerozoic cover, by tilting the

dip of strata in the opposite direction to dip of faults, a feature seen clearly at Dogali (Drury *et al.* 1994, Figure 3). In northern Ethiopia the Mesozoic cover of the Mekele basin is draped down the escarpment from an elevation of around 2.4km on the plateau to around 600m on the west flank of Afar (e.g. Merla *et al.* 1973). Although faulted, this cover is regionally bent down to east as first suggested by Ghebreab and Talbot (2000).

### 2.2.5 Conclusion

Sections 2.2 - 2.2.5 record other authors' geochronological findings in the region that are pertinent to the study of laterites in this work and establishes that laterites rest directly on basement or on patches of Mesozoic sediments. Wherever the oldest dated Tertiary rocks occur, the mid-Oligocene CFBs (Berhe *et al.* 1987; Drury *et al.* 1994; Ebinger 2000, Andrews Deller, 2003; Zanettin *et al.* 2006), laterites always occur conformably beneath them (Drury *et al.* 1994; Andrews Deller, 2006). It is worth noting that as well as the laterites beneath Cenozoic CFBs, evidence of Mesozoic lateritisation has been reported at the base of the Jurassic and beneath the Cretaceous in Ethiopia (Bosellini *et al.* 1997; see Chapter 7), showing that conditions for lateritisation in Africa existed much further back in time than many authors have realised. The age of laterites is uncertain as they have never been radiometrically dated in NE Africa, however, this study provides evidence to show that a minimum age for laterites in the region is mid-Eocene (40 to 43 Ma) (see Chapters 5, 6) and concludes that they began to evolve during the Triassic (see Chapter 7). Having positioned laterites in the geological time scale, regional maps and geology are examined below to determine the rocks from which they develop and the distribution and type of palaeosol in order to form conclusions about their formation based on field observations and data collected.

## 2.3 Geology of Eritrea and northern Ethiopia

The study area - Eritrea and Tigray (figure 1.3, 2.2) - occupies the southern part of the Arabian-Nubian Shield (ANS) and straddles the axial zone of the East African Orogen

(Stern 1994) close to the transition from the predominantly low-grade Pan African (Kennedy 1964; Johnson & Woldehaimanot 2003; Kroner & Stern 2005) assemblages to the high-grade lithologies of the Mozambique Belt (MB) first dated by Holmes (1951).

### 2.3.1 Eritrean geology

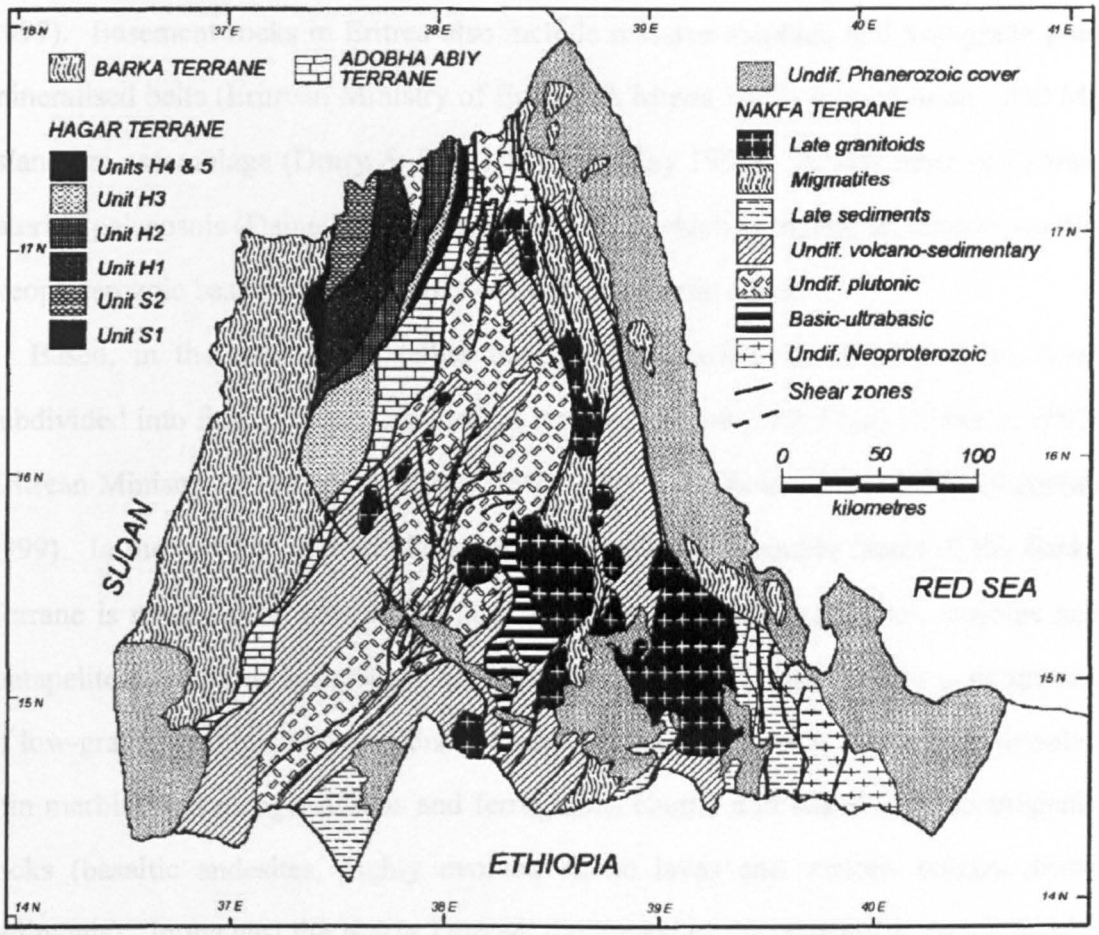


**Figure 2.19** Four major Neoproterozoic terranes of Eritrea (after Drury & de Souza Filho 1998)

At a reconnaissance level, basement geology in Eritrea is covered by Drury and Berhe (1993) and Drury and de Souza Filho (1998) who produced the first small-scale geological maps highlighting broad lithological units based largely on satellite image data. Building on their work, the Geological Survey of Eritrea (2001) compiled a The First Geological Map of Eritrea, to which the Eritrean Ministry of Energy and Mines (2009a; 2009b) have added two further basement maps at larger scales. The first covers the Gash River area in the west and the second the Mai Dima/Kohain area in the south. Throughout Eritrea, the Neoproterozoic basement is made up of

Precambrian metamorphic and igneous rocks overlain unconformably, in places, by Mesozoic sedimentary rocks and Tertiary to Quaternary volcanic and sedimentary assemblages. High-grade gneisses, low-grade volcano-sedimentary successions and mafic–ultramafic rocks make up the north–south trending crystalline basement exposed over more than 60% of the country (Eritrean Ministry of Energy & Mines 1997). Basement rocks in Eritrea also include massive sulphide and low-grade gold mineralised belts (Eritrean Ministry of Energy & Mines 1997) formed in an ~850 Ma island arc assemblage (Drury & Berhe 1993; Teklay 1997). Across most of Eritrea, lateritic palaeosols (Dainelli 1943), over 100 metres thick in places, sit directly on this Neoproterozoic basement or on relics of the Phanerozoic cover.

Based, in the main, on satellite image interpretation, the basement has been subdivided into five, possibly six distinct terranes (figure 2.19; Drury & Berhe 1993; Eritrean Ministry of Energy & Mines 1997; Drury & de Souza Filho 1998; Ghebreab 1999). In the NW the high-grade upper amphibolite to granulite facies of the Barka Terrane is made up of gneisses, (figure 2.20) amphibolites, quartzites, marbles and metapelites containing kyanite and staurolite. The central Hagar Terrane is composed of low-grade oceanic and accretionary wedge materials (chloritic schists, metabasalts, thin marbles and manganiferous and ferruginous cherts) and island-arc volcanogenic rocks (basaltic andesites, highly evolved silicic lavas and various volcanoclastic sediments). In the east the Nakfa Terrane, the largest of the terranes, is dominated by deformed granitoids, calc-alkaline metavolcanics and greenschist-facies volcanoclastic sediments. This eastern segment may incorporate, on the coast, another Precambrian terrane of high-grade gneisses, the Arag Terrane. Separating the Nakfa Terrane from the Hagar and the Barka terranes is the Adobha Abiy Terrane with a highly deformed thick carbonate-pelite-arkose sequence thought to be late Neoproterozoic to Ordovician in age (Beyth 1972). The Adobha Abiy Terrane exhibits immense ductile strains compared with the other low-grade terranes. The above mentioned terranes underlie northern and central Eritrea, whilst the last and poorly known Danakil Terrane, a tectonic inlier composed of Neoproterozoic

metamorphic rocks, occurs in the south east of Eritrea on the eastern flank of the Afar Depression (Eritrean Ministry of Energy & Mines 1997).

**Figure 2.20** Gneiss with vertical foliation cut by quartz veins up to 0.5m thick

Mesozoic sediments in Eritrea are represented by often thin and discontinuous Triassic to Jurassic sandstones of the Adigrat Formation and Jurassic Antalo Limestones. The Adigrat Sandstones (Bunter & Debretsion 1998) outcrop in Danakil and central and south Eritrea and have intercalated siltstone and hematitic layers. In places, they lie unconformably on conglomeratic sandstones, which appear to have glaciogenic characteristics (see the Edaga Arbi Formation of Ethiopia, Section 2.3.2). Trace fossils in the Adigrat Sandstones, hitherto described as terrestrial, indicate some marine influence during deposition (Andrews Deller unpublished data 2001, figure 2.11; Kumpulainen *et al.* 2006). Overlying the Adigrat Sandstone in Danakil only, the Upper Jurassic Antalo Limestone made up of shelly, fossiliferous layers interbedded with quartz sandstones, grades up into marly, gypsiferous, dolomitic beds that lie beneath the dominantly fluviatile late Cretaceous Amba Aradom Sandstone. However, over most of Eritrea apart from Danakil, Mesozoic strata are absent, except for small outliers of Adigrat Sandstone and some older glaciogenic sediments. Notably, throughout the country lateritic palaeosols rest directly on basement or upon

relics of the Mesozoic sequence. But where the oldest Tertiary rocks are found, these palaeosols always occur immediately beneath them (figure 2.21), thereby constraining the chronostratigraphic minimum age of the laterites. However, their maximum possible age in a relative, stratigraphic sense is poorly constrained in Eritrea by undated early Mesozoic sedimentary rocks of the Adigrat Sandstone that lie beneath them in places. Neither the CFBs nor laterites are present above the intensely

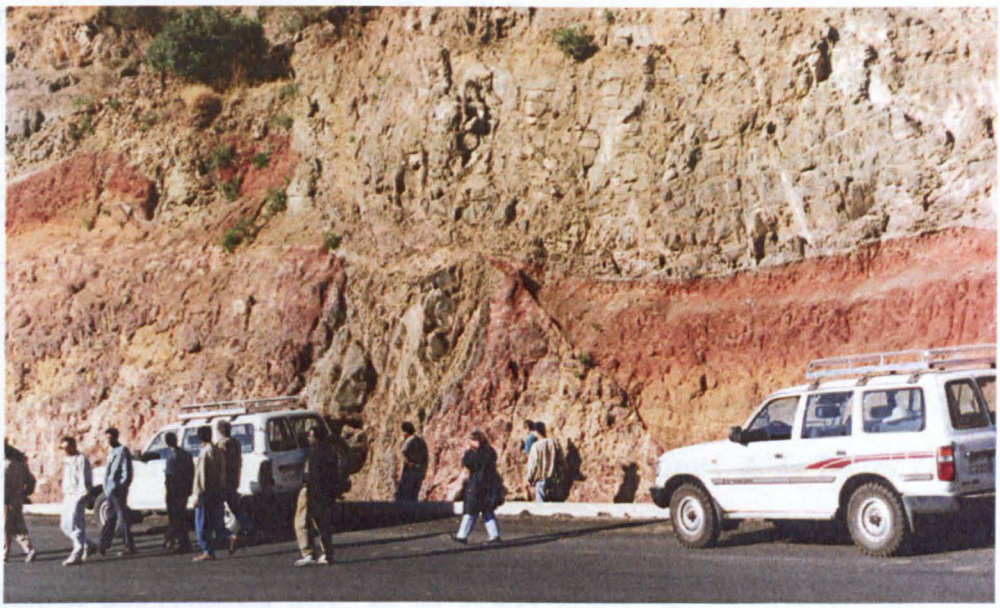

**Figure 2.21** faulted contact of CFBs and laterites near Shiketi, Eritrea 15km southwest of Asmara, with international party of geoscientists in foreground

faulted and tilted Cretaceous sandstones of Danakil that are unconformably overlain by Miocene sediments.

As well as a variety of sedimentary units, Cenozoic rocks include four main volcanic units. The earliest of these are the mid-Oligocene CFBs of the Ethiopian Igneous Province that began to erupt ~30 Ma (see Chapter 6; Drury *et al.* 1994; Hofmann *et al.* 1996) and conformably and consistently overlie the laterites wherever the CFBs occur. These are predominantly plateau forming olivine-tholeiite basalts, whose eruption is documented as spanning the period 30 to 26 Ma (Ukstins *et al.* 2002; Wolfenden 2005). Apart from scattered trachyte plugs (of possible Miocene age) and areas of Quaternary alluvial sediments, the Eritrean Plateau and Western Lowlands contain no later Cenozoic rocks. In the tectonically active Red Sea coastal plains and the Afar-Danakil Depression, Cenozoic volcanism and sedimentation

continue to the present day. The most important sedimentary units in this sequence are the Miocene (Drury *et al.* 2006) basal conglomerates of the Dogali Series in the coastal plains (also termed the Red Series, figure 8.1) and Danakil Formation. Younger volcanic units comprise the Afar Stratoid basalts (Miocene to Pliocene) and Afar basalts (Pleistocene to Recent) associated with sedimentary units, that include extensive evaporites, terrestrial clastics and tidal, reef limestones, while basaltic flows from active volcanoes of the Afar-Danakil Depression's axial zone, sheet flood terrace deposits, silt, sand and gravel dominate the Quaternary (see Bosworth *et al.* 2005, Figure 3).

### 2.3.2 Northern Ethiopian geology

The Pan African geology of Tigray, first mapped by Kazmin (1972) on his map of Ethiopia and later by Merla *et al.* (1973, 1979) on their Geological Map of Ethiopia and Somalia, has not yet been tectonically correlated across its boundary with neighbouring Eritrea (but see Drury & Berhe 1993; Drury & de Souza Filho 1998; Tadesse 1999). However, the Ethio-Eritrean border, still in some dispute, is, for the purpose of this research, taken as the course of the east to west running rivers, the Setit and the Mereb or Gash and the arbitrary political boundary that joins them between 14° - 15°N and 37°50' - 38°E (figure 2.1). This part of the study area, within the limit of the Ethiopian border and located on the Axum and Adigrat 1:250 000 topo sheets, lies north of latitude 14°N, south of the Mereb and between 37°30' to 39°00'E. It covers roughly 10,000 square kilometres, at the centre of the southernmost ANS. Although the metavolcanic rocks of Tigray support an arc accretion model (Tadesse 1996) and are geographically an extension of the Nakfa Terrane, they cannot be seen as a direct continuation of those Eritrean rocks to their north. However, the Axum area forms the southern part of this large terrane and has been subdivided into several blocks (Tadesse 1999). The western and south-eastern regions of the Axum area (figure 2.22) constitute the Shiraro Block and Mai Kenetal Block respectively, which are underlain by deformed post-accretionary clastic and shallow water carbonates that are lithologically more akin to the Eritrean Adobha Abiy Terrane. The remainder of

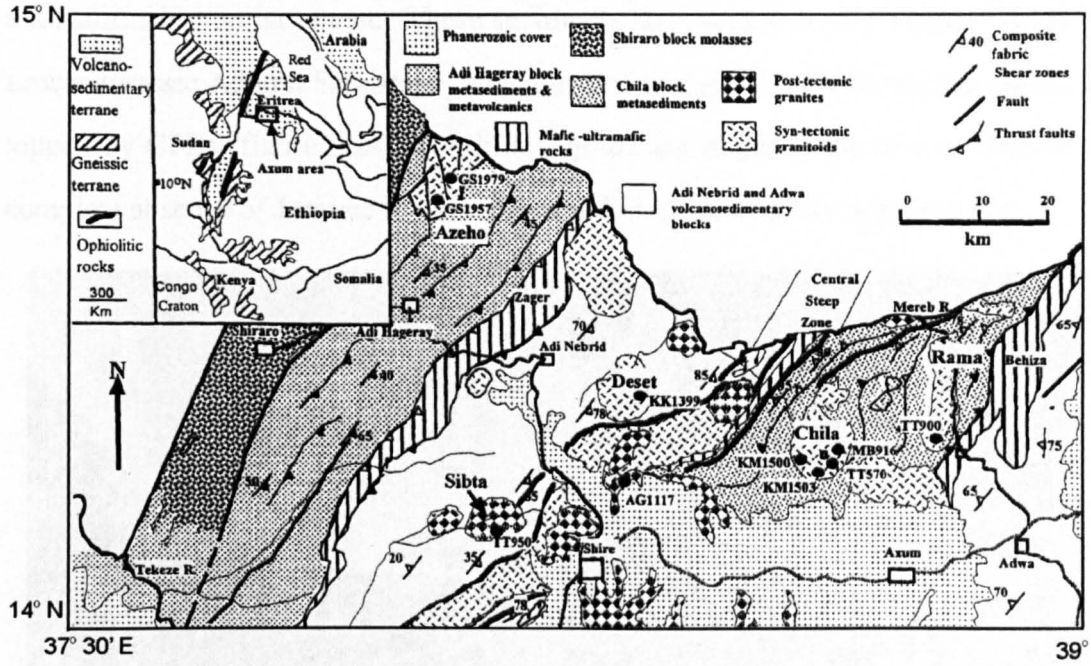


**Figure 2.22** Geological map of the Axum area (after Tadesse *et al.* 1996)

the Axum area has obvious similarities with the supra-subduction zone complexes of the Hagar Terrane in Eritrea, but is a long way east of the Hagar Terrane's southward strike continuation. The older Pan African in this area is made up of low grade metamorphic rocks of volcanic, volcanoclastic and marine sedimentary assemblages (Tadesse *et al.* 2003). Felsic and mafic intrusions are common. Six tectonostratigraphic blocks can be distinguished in the region (figure 2.22). From west to east they are: the Shiraro Block; the Adi Hageray Block that is predominantly south-east dipping and made up of deformed, >5000 metre thick greenschist facies, metavolcanic and metasedimentary rocks; the Adi Nebrid Block dominated by intermediate metavolcanics, alteration zones and gold prospect areas (figure 2.23); the Chila Block composed in the main of fine-grained sedimentary phyllites; the Adwa Block comprising Neoproterozoic clastic sediments and volcanics and the Mai Kenetal Block Block (Tadesse *et al.* 1999).

Except for a small area north of Axum, Mesozoic strata intervene between lateritic palaeosols and Pan African basement. North of the northern boundary fault of the small Mesozoic rift that contains the Mekele basin (Section 2.2.3; figure 2.9) Upper Carboniferous to Lower Permian Enticho Sandstone and Edaga Arbi Glacials rest

unconformably on basement. These sediments are overlain by the Upper Triassic to Lower Jurassic Adigrat Sandstone, which in turn is capped by lateritic palaeosols over topped by CFBs (figure 2.24) with little sign of any angular discordance despite the complete absence of Jurassic to Cretaceous sediments that occur further south.

**Figure 2.23** Artisanal gold panners near Adi Nebrid, Tigray, Ethiopia

At ~13.8°N, a large E-W trending normal fault with a large downthrow to the south marks the northern edge of the Mekele rift basin. Besides the Adigrat Sandstone and older glaciogenic sediments, the stratigraphic sequence in the Mekele basin includes the rhythmic, near-shore and shelf limestones and shales of the Jurassic Antalo Series, overlain by fluviatile sandstones of the Middle Cretaceous Amba Aradom Series (Tadesse *et al.* 2003). The upper parts of the Amba Aradom Series are dominated by laterites interbedded with sandstones (figure 2.14), whilst the uppermost laterite in the series is overlain by CFBs. Unlike the inter-rift areas of NE Africa, here lateritic palaeosols of the Mesozoic rift are separated from Pan African basement by several hundred metres of older, Carboniferous to Cretaceous sediments. It is worth noting that except in the western flank of the Afar Depression, CFBs and laterites do not occur in the Cenozoic succession to the east. As in Eritrea, Mesozoic

sequences in Afar are directly overlain unconformably by the Red Series indicating probable syn-tectonic Miocene erosion, a possible topic for further investigation.


**Figure 2.24** Mountain road between Adigrat and Adwa showing the stratigraphic sequence above the basement in the eroded basaltic highlands west of Adigrat, Tigray, Ethiopia. The terraced peak on the right is typical of continental flood basalt (CFB) topography in Ethiopia. A break of slope at its base forms a large terrace underlain by lateritic ferricrete with resistant pure white clay at the top of the cliff (inset). The upper cliff is formed by massive, iron stained Adigrat Sandstone (AS). The break in slope at the base of the cliff marks the top of the Enticho Sandstone (ES) and the Edaga Arbi Glacials, both forming the reddish ground in the valley bottom

## 2.4 Regional climate – dry season data

The seasonal requirements for image data are important and climate in the study area must be taken into account when choosing data for geological work. Dry-season, clear, cloud-free skies are necessary for satellite retrievals of high-quality remote sensing data and fieldwork is only possible before the rainy season when much of the terrain is inaccessible. Eritrea has a wide variety of climatic conditions - summed up by the popular expression, '*three seasons in two hours*' - because of the variations in altitude. Despite its position within tropics, the Eritrean Plateau is mild throughout the year because of

its high altitude. The most dramatic changes in the weather and temperature can be experienced along the Asmara - Massawa traverse. Massawa at sea level has one of the highest average temperatures in the world at ~30°C, while Asmara at 2350m above sea level and only 65km away, averages temperatures of ~16°C and experiences winter frosts. In contrast, the Danakil Depression 125m below sea level, with temperatures up to 63°C, is arguably the hottest place on Earth.

Mean annual rainfall (figure 2.25) on the plateau is from 400 to 600mm (Abdul-Haggag 1961) and decreases towards the western lowlands. On the plateau and in the western lowlands, the main rains, (*kiremti* in Tigrinya), carried on a southwesterly monsoonal airstream, fall from June to August. Precipitation and length of the rainy season decrease toward the northeastern extremes of the plateau. The dry season (November to June) falls in winter when the plateau, the escarpment and the coastal plains receive much smaller quantities of rain, the 'small rains' or *belg*, from a northeasterly airstream during October to March, whilst the regions of the Danakil-Afar Depression are practically rainless throughout the year. Precipitation on the escarpment comes from the rains and fogs caused by orographic cooling of warm moist air rising from the Red Sea.

The peculiar seasonality of the region results in complex variations in the density of green vegetation (figure 2.26) and cloud cover through the year, important for RS of rocks and superficial sediments. For the plateau and western lowlands, green

**Figure 2.25** Graphs showing annual variations in rainfall and day temperature for the Eritrean Plateau (Asmara) and the Red Sea lowlands (Massawa)

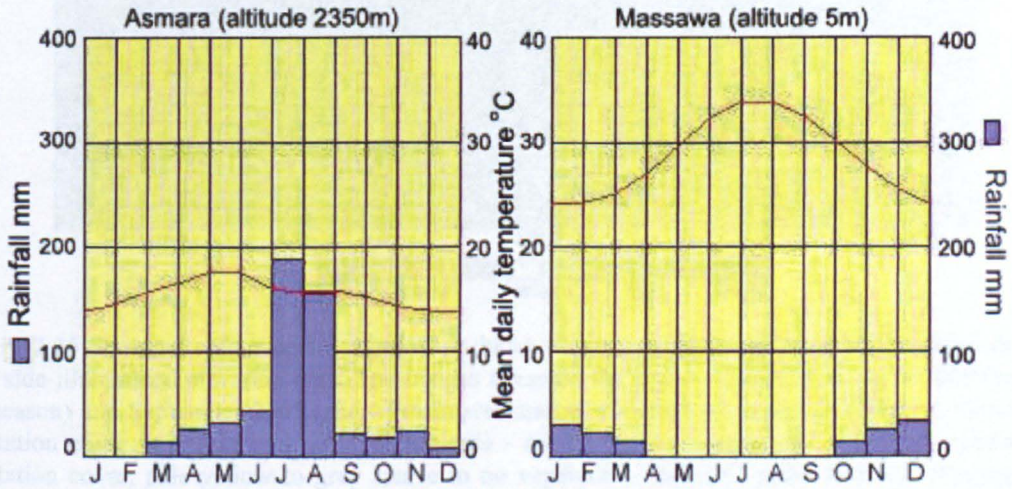

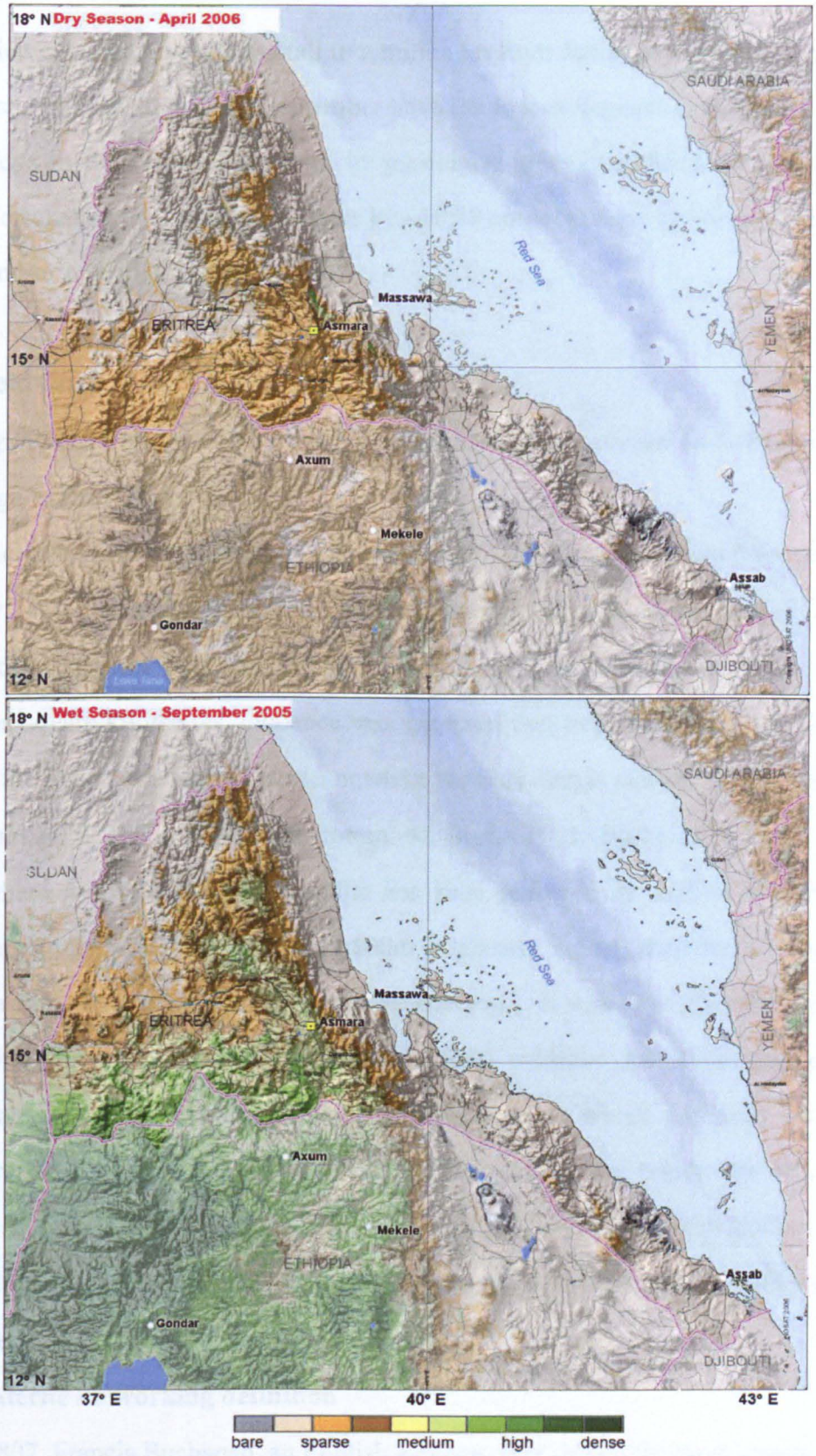


**Figure 2.26** Seasonal colour-coded maps of an index of green vegetation (from SPOT data), draped over side-illuminated elevation data. The images compare the cover vegetation in April 2006 (end of dry season) and September 2005 (end of main wet season) showing the dramatic effect of climate on vegetation cover in Eritrea and northern Ethiopia - see key: pale to dark greens indicate substantial vegetation cover, pale yellow to grey sparse to no vegetation. Source: United Nations Development Programme

vegetation cover and cloudiness fall to a minimum from January to April, whereas on the coastal plains, August and September have the lowest vegetation and cloud cover. Daily fogs in the escarpment result in substantial green vegetation throughout the year. Fortunately the fog usually clears by ~10.30 am local time: the overpass time of most land-oriented RS satellites.

## 2.5 Fieldwork

'*Making field observations is not difficult. Making appropriate field observations is a challenge.*' (Reid 2003).

Having clarified the broad stratigraphic position of laterites and examined the regional geology, comprehensive fieldwork was undertaken over a more extensive area (Appendix 1; figures 2.27 to 2.29) than is usual for a doctoral thesis. Over twenty thousand square kilometres, evidence was gathered that established that laterites did exist in the region and formed over a much larger area than is currently acknowledged (Germann *et al.* 1993, 1994; pers. comm. K. Burke 2001; Burke & Gunnell 2008). Even where part of the lateritic profile has been removed by shallow erosion, the remaining zone of deep weathering (>100m in places), signals their former presence was considerably greater than their present outcrop. It was only after the first two field trips (see section 2.5.3) that enough field evidence had been gathered to determine what features characterise Eritrean laterites on which this study focusses. The traverses covered and localities visited throughout the region are shown in Figures 2.27 to 2.29. Geocoded Landsat TM and ASTER scenes at 1:500000 and 1:250000 and 1:50000 and 1:250000 topographic maps together with a GPS receiver were used to locate road sections and localities.

### 2.5.1 Laterite - a working definition

In 1807, Francis Buchanan, an English surgeon, first coined the term laterite (from the Latin noun *later*: meaning brick or tile) to describe his observations of '*indurated clay ... diffused in immense masses, without any appearance of stratification ... placed over the granite that forms the basis of Malayala* [modern-day Kerala, South India]'

(Buchanan1807). However, J.C. Visscher (1862), whilst working for the Dutch East India Company from 1717 to 1723, made the first reference to these palaeosols when commenting on material used for building that was later referred to as laterite. On his visit to the Kerala coastal plains in South India, he wrote of the local rocks: *'the local stone is very well adapted to building. There are quarries here from which the stone is hewn; and I have seen a piece of this stone when being cut from the rock, split like wood under the stroke of an axe. The stone is reddish yellow and spotted, very porous and full of holes...'* (from Sama 1982). Subsequent publications on these palaeosols not only developed interest and increased knowledge of laterites but also created confusion (see Firman 1994; Schellmann 2003). The controversy over the definition of what exactly constitutes a laterite or its profile still rages. However, to cover every aspect of the debate one need go no further than the excellent work *'Regolith Exploration Geochemistry in Tropical and Subtropical Terrains'* edited by Butt and Zeegers (1992). Laterites and lateritisation are also described in detail by Ollier and Pain (1996) and comprehensive coverage of the topic can be found in *'Petrology of Laterites on Tropical Soils'* (Tardy 1997), the definitive work of Schellman (1981, 1986, 2003) and the extensive discussions of Firman (1994).

Adopted as a starting point for the purposes of this thesis and following the definition of Nahon and Tardy (1992); laterites are chemical entities classified as ancient residual soils (palaeosols) characterised by several distinct horizons in which the texture and mineralogy of an original parent rock has been progressively altered. In contrast with actively forming soils of modern times, laterites are indurated rocks, the ultimate products of protracted weathering in the humid tropics of the past and are consistently sharply zoned in structure. They are not to be confused with materials eroded and transported from laterites (Schellmann 1981), sometimes referred to as *'laterite'* or *'allochthonous laterites'* (e.g. Widdowson 1999), that are typical of the coastal plains of western Peninsular India or Australia, the 'Red Continent'. Much of the surface regolith of Australia, where full laterite profiles are limited in distribution, is made up of the lower horizons of laterite as the upper horizons have been eroded

and widely redistributed leaving the coarse saprolite with corestones or '*float*' in the Australian vernacular obscured by derived debris. Such reworked material is properly regarded as colluvium (material washed down slopes by sheet floods) and alluvium (materials transported and deposited by streams and rivers) and therefore excluded from the term 'laterite' in the following discussion on Eritrean laterites. Just as one would not refer to colluvial or alluvial deposits composed of quartz, feldspar and mica as an '*allochthonous granite*', in the context of laterites in NE Africa, reference to such materials as '*allochthonous laterites*' betrays a fundamental misunderstanding of the term.

### 2.5.2 Field observations

Over the course of the research fieldwork was used to:

- check the nature of laterite facies, the underlying Neoproterozoic basement and Mesozoic sediments from which laterites developed and the overlying Oligocene basaltic cover and sample each rock type for petrographic inspection, geochemical analysis and dating.
- compare the broad features of these exposures against stereoscopic aerial photographs, Landsat TM and ASTER images on site (Chapter 4);
- obtain ground truth with reference to the stratigraphy and mineralogy of laterite facies for desktop interpretation of RS data and plan further reconnaissance in order to complete the first regional geological map of laterite facies (Chapter 4) and
- sample well-water for simple on-site analysis and further detailed analysis in the UK.

Details of the lithology recorded on initial reconnaissance excursions can be found in Appendix 1. These initial excursions, on which subsequent field trips were based and new localities targeted using RS data, give an overview of the region to benefit others who may wish to follow-up this research.

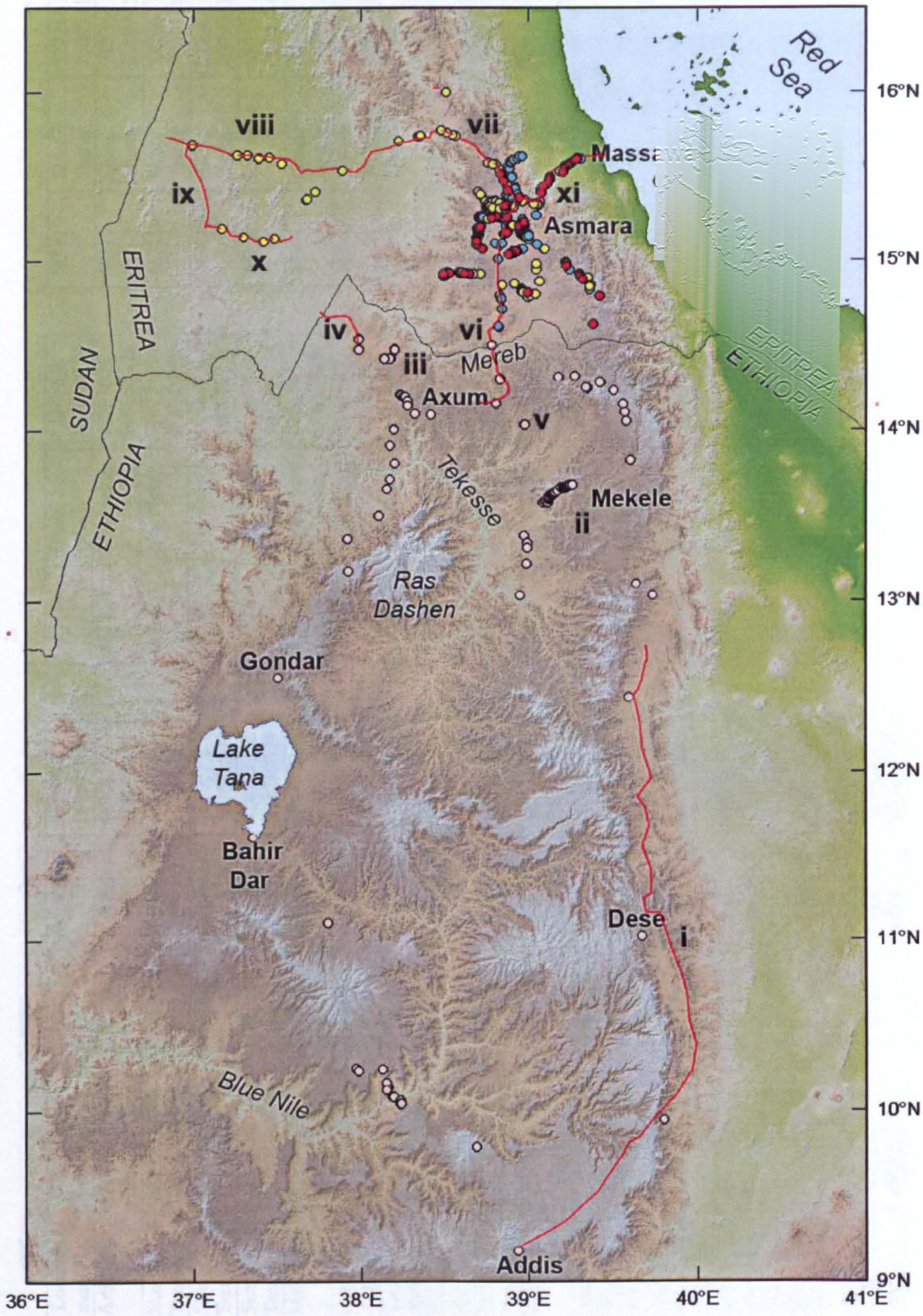


**Figure 2.27** Regional distribution of all localities visited. Red lines and numbers i to xi indicate reconnaissance excursions. Sampled localities are marked by coloured dots. See Appendix 1

| Sample no. | Location name | UTM co-ordinates* |
|---|---|---|
| M18(i) | Adi Raisi | 489060 E 1662258 N |
| M19A | 5km E Tera Emni | 487520 E 1661563 N |
| M19C (pit1) | 5km E Tera Emni | 489060 E 1662258 N |
| M19C (pit2) | 5km E Tera Emni | 489060 E 1662258 N |
| M26(ii) | Mai Nehfi | 476995 E 1685715 N |
| M29 | northern Asmara | 494200 E 1699050 N |
| M33(ii) | Tseada Kristyan | 485109 E 1693952 N |
| M33(iv) | Tseada Kristyan | 485109 E 1693952 N |
| M34 (pit2) | Dairo Kaulos | 485100 E 1693950 N |
| M45iii (pit1) | Embeyto | 496945 E 1681154 N |
| M48 | near Adi Hawesha | 497515 E 1683005 N |
| M48 | near Adi Hawesha | 497515 E 1683005 N |
| M48 | near Adi Hawesha | 497515 E 1683005 N |
| M48 | near Adi Hawesha | 497515 E 1683005 N |
| M48 (pit1) | near Adi Hawesha | 497515 E 1683005 N |
| M58c (pit1) | 5km W of Areza | 449749 E 1649237 N |
| M58c (pit2) | 5km W of Areza | 449749 E 1649237 N |
| M70a | Adi Felesti | 467067E 1670710N |
| M70A | Adi Felesti | 467067 E 1670710 N |
| M70b | Adi Felesti | 467067 E 1670710 N |
| M70B | Adi Felesti | 467067 E 1670710 N |
| M79i (pit1) | Dogali | 524952 E 1720300 N |
| M79i (pit2) | Dogali | 524 952 E 1720300 N |
| M100T | Adi Caieh | 538941 E 1641135 N |
| M101C | Adi Caieh | 538927 E 1640674 N |
| M104 | Dekemhare | 510070 E 1665052 N |
| M109 | near Adi Hawesha | 497515 E 1683005 N |
| M110E | near Adi Hawesha | 497515E 1683005N |
| M113A | 5km E Tera Emni | 487510 E 1661535 N |
| M113A | 5km E Tera Emni | 487510 E 1661535 N |
| M113A (i) | 5km E Tera Emni | 487510 E 1661535 N |
| M113A (i) | 5km E Tera Emni | 487510 E 1661535 N |
| M113B | 5km E Tera Emni | 487510 E 1661535 N |
| M113C | 5km E Tera Emni | 487510 E 1661535 N |
| M114 | Gaala valley | 489435 E 1680387 N |
| M114 | Gaala valley | 489435 E 1680387 N |
| M121B | Mai Nehfi | 479316 E 1686665 N |
| M122A | Mai Nehfi | 476774 E 1685852N |
| M125 | Adi Felesti | 466859 E 1670359 N |
| M125 | Adi Felesti | 466859 E 1670359 N |
| M125A | Adi Felesti | 466859 E 1670359 N |
| M125A | Adi Felesti | 466859 E 1670359 N |
| M125A (i) | Adi Felesti | 466859 E 1670359 N |
| M125D | Adi Felesti | 466859 E 1670359 N |
| M125D | Adi Felesti | 466859 E 1670359 N |
| M130 | Knafna | 495818 E 1638927 N |
| M131 | Knafna | 495818 E 1638927 N |
| M133 | Knafna | 496926 E 1636826 N |
| M136 | Shiketi | 485933 E 1675492 N |
| M147 | Dairo Kaulos | 477521 E 1692107 N |
| M201 | Adi Mizan nr Mekele, | 421637 E 1567575 N |
| M201a | Adi Mizan nr Mekele, | 421637 E 1567575 N |
| M211 | Shire, Tigray | 522264 E 1509741 N |
| M211 | Shire, Tigray | 522264 E 1509741 N |
| M211a | Shire, Tigray | 522264 E 1509741 N |
| M211a | Shire, Tigray | 522264 E 1509741 N |
| M320 | Embeyto | 495171 E 1676724 N |
| M344 | northern Asmara | 493998 E 1698772 N |
| M348 | Tseada Kristyan | 483797 E 1695101 N |
| M358 | Himberti | 471022 E 1686953 N |
| M359 | Wokerti | 500802 E 1675026 N |
| M361 | N of Wokerti | 497853 E 1680879 N |

**Table 2.1** Location of clays sampled from laterite profiles in Eritrea and northern Ethiopia. *UTM coordinates refer to WGS84 Datum, Zone 37 N and represent the centre point of 50 m radius location areas

### 2.5.3 The Hamasien Plateau

Reconnaissance of the region made clear that laterites are far more extensive than had previously been recorded in an area that is extremely complex geologically. More intensive fieldwork, therefore, was concentrated on and around Eritrea's Hamasien Plateau, the country's high central uplands that range from ~1,800 to ~3,000 meters above sea level. A ~6400 $km^2$ area centred on Asmara with excellent, accessible outcrops was targeted for gathering ground truth for remote sensing analysis and sampling. Exposures were located in Asmara city and its environs; along traverses from Asmara to Hagaz and Agordat, Asmara to Senafe, Mendefera to Mai Dima and Barentu, Barentu to Agordat, Asmara to Adi Kwala and Asmara to Massawa and, throughout the Gaala valley and the coastal plains near Dogali (figure 2.28). Localities were selected that offered the best opportunities to log and sample laterites in order to present a detailed picture of their textural and chemical evolution and to determine their stratigraphic relationship to other rock units with a view to constructing a detailed map of laterite facies in the region using remote sensing. It was hoped too, that by concentrated sampling in Eritrea a better understanding of the laterites' palaeo-weathering history and stratigraphic position in relation to global climate change would also emerge. Eighty localities were studied and samples were collected where appropriate (figure 2.27, 2.29; Table 2.1). Further sampling was carried out in 2001 (Eritrea), 2002 (Ethiopia) and 2003 (Eritrea) and ground checks were made at over two hundred more field sites covering an area of roughly twenty thousand square kilometres (figure 2.27). Representative specimens of lateritic composition were chosen for thin-sectioning and carbon-coated polished-section preparation and for petrographic and microprobe analysis. Some samples were designated for energy-dispersive microprobe imaging, geochemical analysis using X-ray fluorescence spectrometry (XRF) and $^{40}Ar/^{39}Ar$ dating.

Spectral analysis of laterite samples was not done because of the difficulty of obtaining a field or lab spectrometer, but more importantly, the mineralogical simplicity of laterites and the abundance of spectra in spectral libraries (e.g. USGS

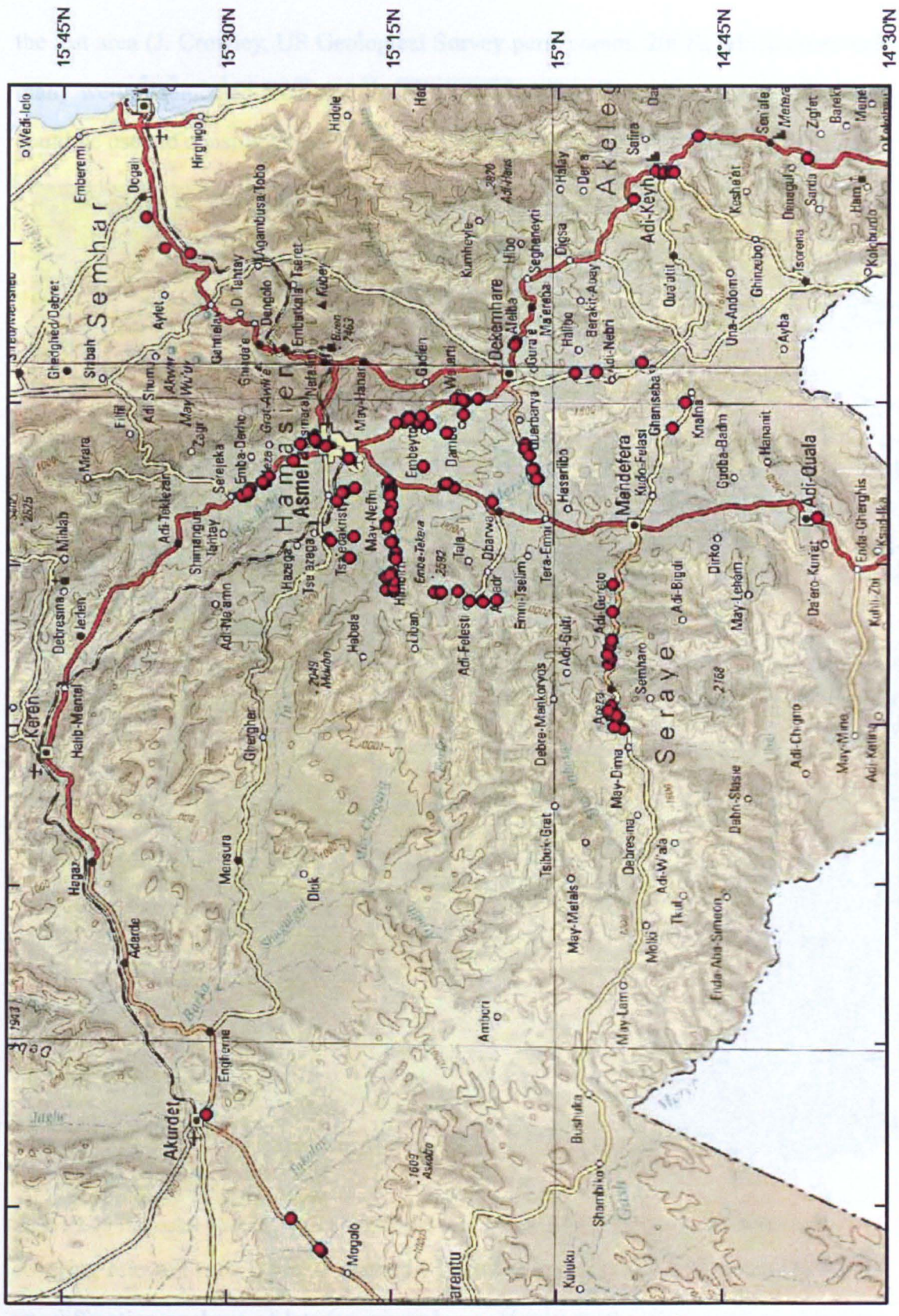


**Figure 2.28** Location map for all localities visited in Eritrea and place name reference

lateritised Archaean terrain in Western Australia that was informative. The fact that hyperspectral data from EO-1 Hyperion were acquired for two narrow swaths within

the test area (J. Crowley, US Geological Survey pers. comm. 2001), which contained many well-documented localities was a great advantage as calibrated Hyperion data could be used to construct 'real-world' reflectance spectra for 30 x 30m pixels

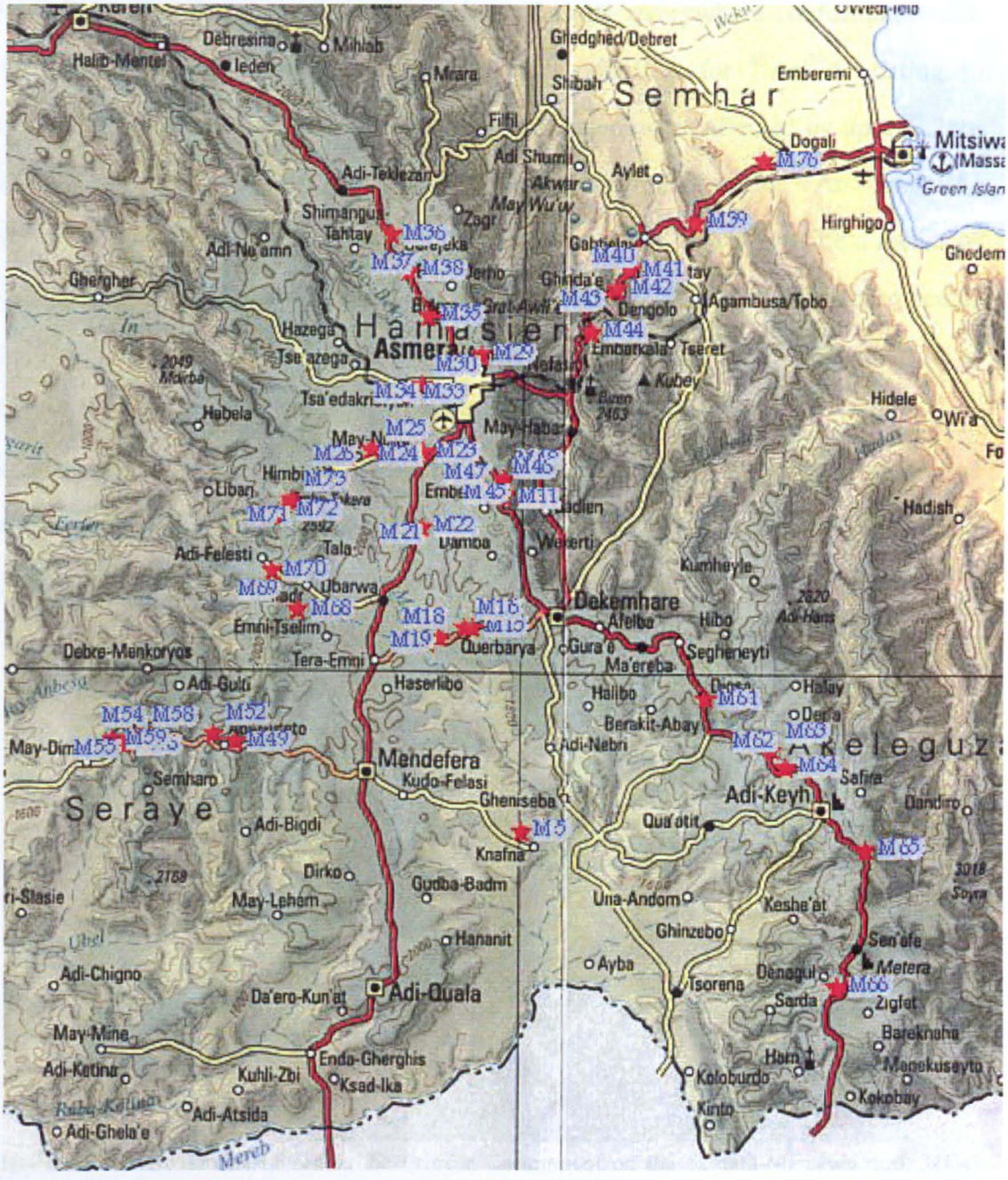


**Figure 2.29** Hamasien Plateau, Eritrea - important field and sampling localities (1998 field season)

covering relevant rock types of interest. Likewise no facilities were available for X-ray diffraction analysis of laterite mineralogy. However, the clear spectral signature over laterite clays for kaolinite in Hyperion data (see Chapter 5), compared with other clays, obviated the need for this procedure.

Laterite samples were also collected in Ethiopia to add to those from Eritrea in the hope of amassing sufficient geochronological evidence to date the palaeosols, the processes involved in their formation and to establish where possible the age of East African lateritisation throughout the region. Basalts, everywhere conformable with underlying laterites, were collected from both countries for $^{40}Ar/^{39}Ar$ dating to establish a local time span for CFB eruptions. Granodiorites affected by up to 2.2km uplift in the Red Sea escarpment (figure 2.30) were sampled too for $^{40}Ar/^{39}Ar$ dating of their cooling ages relative to topographic altitude. This was to provide a means of estimating late-Tertiary to Recent rates of uplift that had displaced the occurrence of the laterite datum at Dogali in the Eritrean escarpment (Drury *et al.* 1994) relative to that on the Hamasien Plateau. Sampled sections with relevant UTM co-ordinates are detailed where appropriate throughout the thesis. Sample locality descriptions and petrology of laterites are in the following section, whereas those for basalts and granodiorites are documented in Chapter 6.

**Figure 2.30** Granodiorite exposed in the Eritrean Escarpment on the Asmara-Massawa road, fallen blocks provide fresh samples

## 2.6 Laterite petrology

The study of laterites starts in the field and the first noticeable characteristic of these palaeosols in outcrop is that they appear to be sedimentary rocks and are often mistaken as such with horizon boundaries being interpreted as bedding planes. Often

red in colour, these palaeosols are commonly confused with many other outcrops in the area. But not all red rocks and soils are laterites. Abundant oxidised red basement rocks with hematite veneers or rinds caused by superficial oxidation of Fe silicates and sulphides (figure 2.31)

(a) (b)

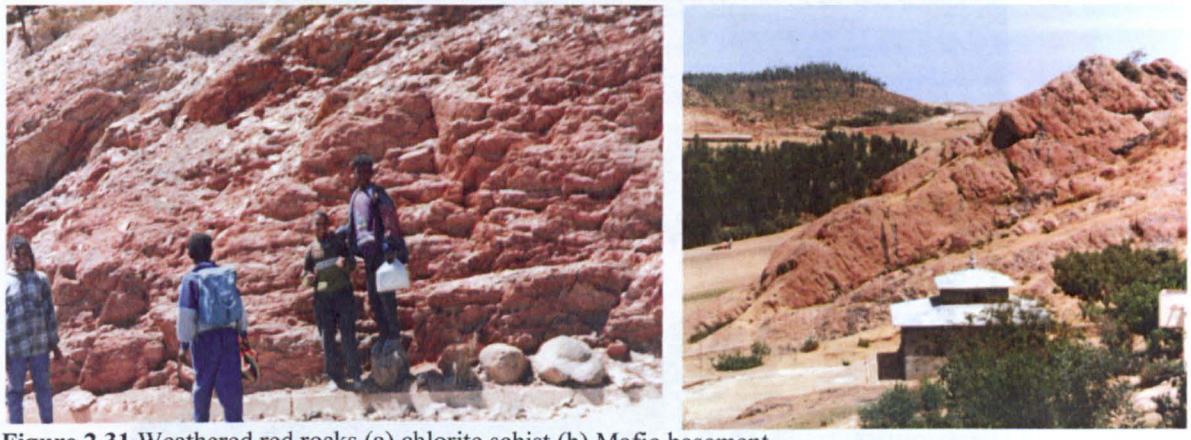

**Figure 2.31** Weathered red rocks (a) chlorite schist (b) Mafic basement

for example, are often mistaken for laterites as are the many boles (figure 2.32) developed between flood basalt flows in the area. Both are homogeneous in outcrop and neither have separate, clearly identifiable horizons. Moreover boles are often friable whereas clearly identifiable Eritrean laterites are indurated and resistant to erosion.

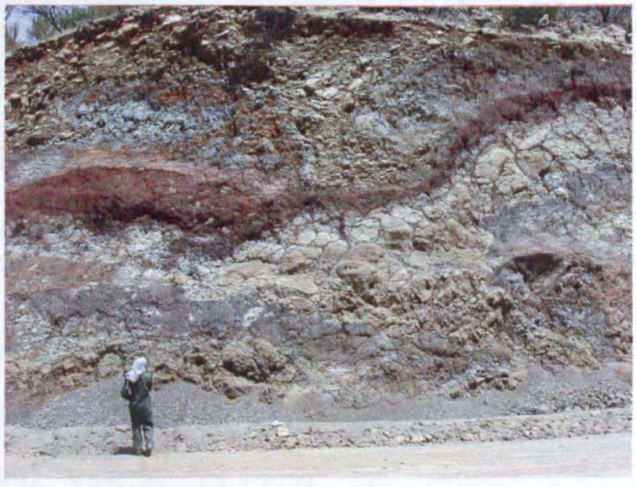

**Figure 2.32** Intraflow red fossil soil (bole) in 30 Ma slumped basalt flows

Work focusing on laterites falls into roughly two areas; that which is descriptive (McFarlane 1976), sees the palaeosols as being transported (Widdowson 1999) and forming in depositional environments and in some cases having a full profile that consists of only one horizon: this theory is largely discredited (Ollier & Sheth 2008).

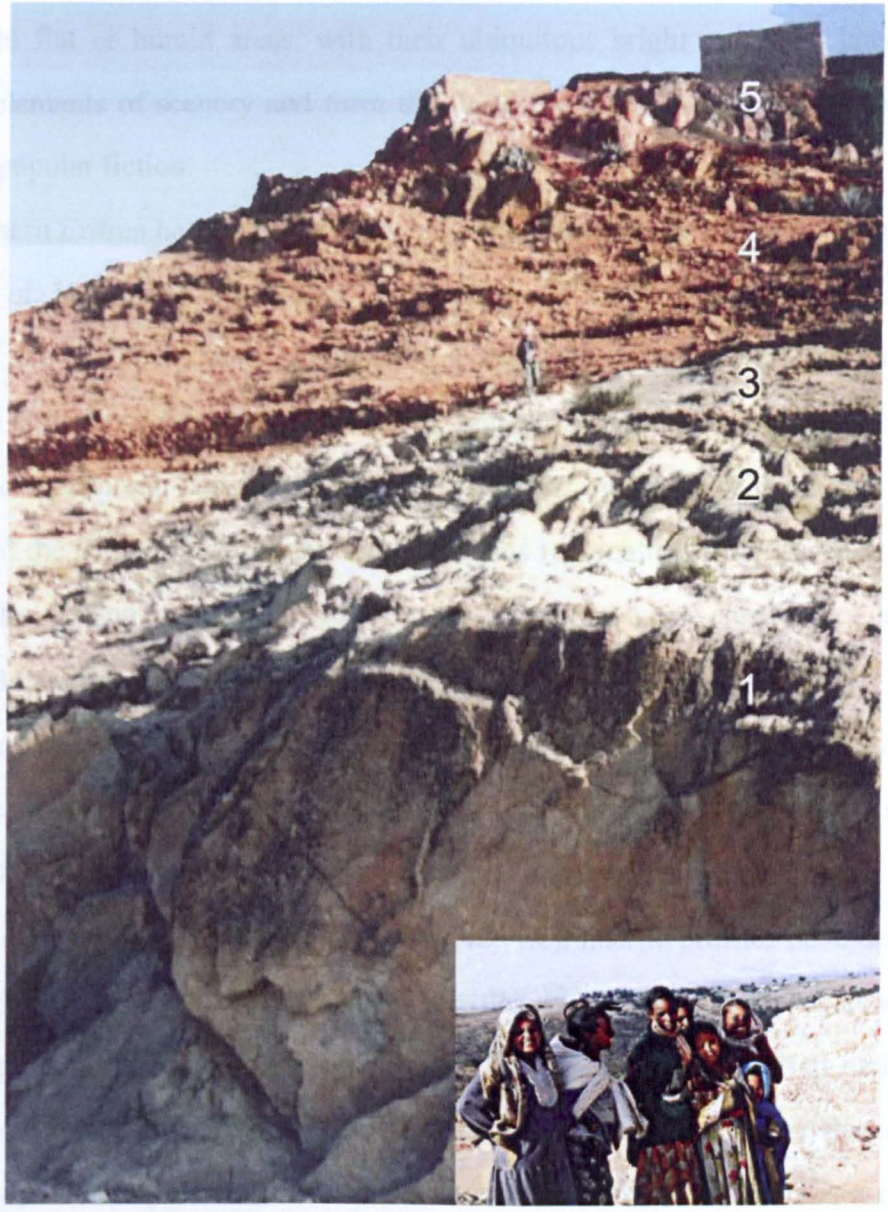


**Figure 2.33** Complete section through a laterite profile developed on Neoproterozoic granodiorite at Adi Teklay, Eritrea 22km west of Asmara. Numbers indicate the five laterite horizons. The inset shows the extent of the clay zone (Horizon 3 - foreshortened in the main figure) discussed in detail in Section 2.6.2

The only other formation process generally accepted by most workers is that laterites are chemical entities and residual rocks (Schellmann 1986; Butt & Zeegers 1992; Nahon & Tardy 1992; Vasconcelos 1999). The evidence in this study supports the latter. There are no other conceptual models of laterite formation. In practice, although Eritrean laterite horizons can be identified by their visual characteristics as Figures 2.33, 2.36 and 2.37 indicate, on close inspection they are undoubtedly an alteration product of rock that has been subjected to intense chemical weathering. In dissected semi-arid terrains, they are clearly identifiable as red, yellow and white

mesas. In flat or humid areas, with their ubiquitous bright red soils, laterites are familiar elements of scenery and form the 'bold brick red lateritic backdrop' (Boyd 1982) of popular fiction.

Southern Eritrea has extensive outcrops of Tertiary laterite. Like those in Yemen (Baker *et al.* 1996), Western Arabia (Overstreet *et al.* 1997; du Bray *et al.* 1990) and Ethiopia, the variable lateritic mineralogy in vertical and horizontal profile is preserved at its best, a feature unique to the region. Laterites form layers as resistant as their younger basalt cappings and crop out beyond the limits of the basalt. Unlike the base of the CFBs, which might be diachronous regionally and confused in outcrop with basalts of younger ages, Eritrean laterites formed on a low-elevation peneplained surface (Bohannon *et al.* 1989) and are a distinct stratigraphic unit.

Formed over tens of million years, Eritrean laterites are residual rocks, the product of long-term weathering in savannah climates with contrasting wet and dry seasons. Typical of ancient, often thick, evolved and well-preserved ferricrete-capped laterites with five distinctive horizons (figure 2.33, 2.48, 4.2), laterite profiles have developed from sandstone, schistose, granitic and metavolcanic Neoproterozoic basement rocks in this region (figure 2.35). The outcome of lateritisation is a build-up of iron and aluminium oxides at the top of the palaeosol profile, resulting in the formation of ferricretes (commonly referred to as iron crust or duricrust). Below this, a clay-rich leached zone, first mottled and then saprolitic, indicates progressive degeneration of the original bedrock (Schellmann 1986; Butt & Zeegers 1992; Nahon & Tardy 1992). The characteristic mineralogical and textural zonation in laterites (Schellmann 1986; Butt & Zeegers 1992) is caused by volume reduction resulting from solution and chemical leaching during the process of lateritisation, whilst the chemical differentiation that takes place results in marked colour zones (figure 2.36). Figures 2.34a and b graphically illustrate this process that produces a characteristic mineralogical and textural zonation within the palaeosol profile. Once exposed, a fresh rock surface is first subject to weathering to produce saprolite and core stones. Over time this weathering 'front' moves to deeper levels, while a variety of chemical

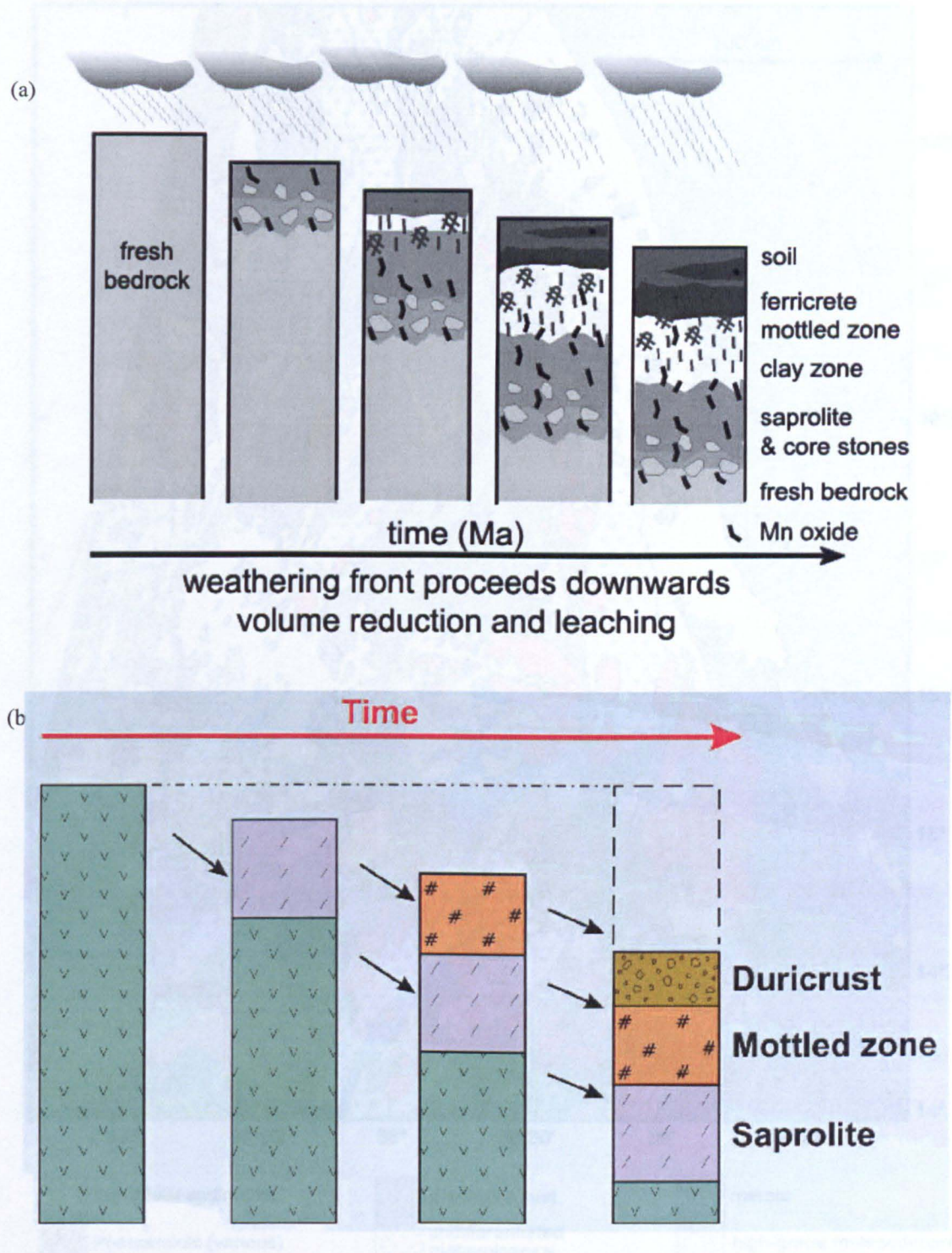


**Figure 2.34** Progressive development of zonation in laterites (involved in formation of all other soils to a lesser extent). (a) The progressive downward development of zones, the oldest forming from the first products of weathering at the top. After Vasconcelos (1999). (b) Simplified, with arrows showing the evolution of zones from earlier products of weathering. From Agnew (2010)

### 2.6.1 Introduction

Nahon and Tardy (1992) describe a typical iron-crust profile. They suggest that fully evolved laterites '*are best preserved in areas where the former*' ancient land

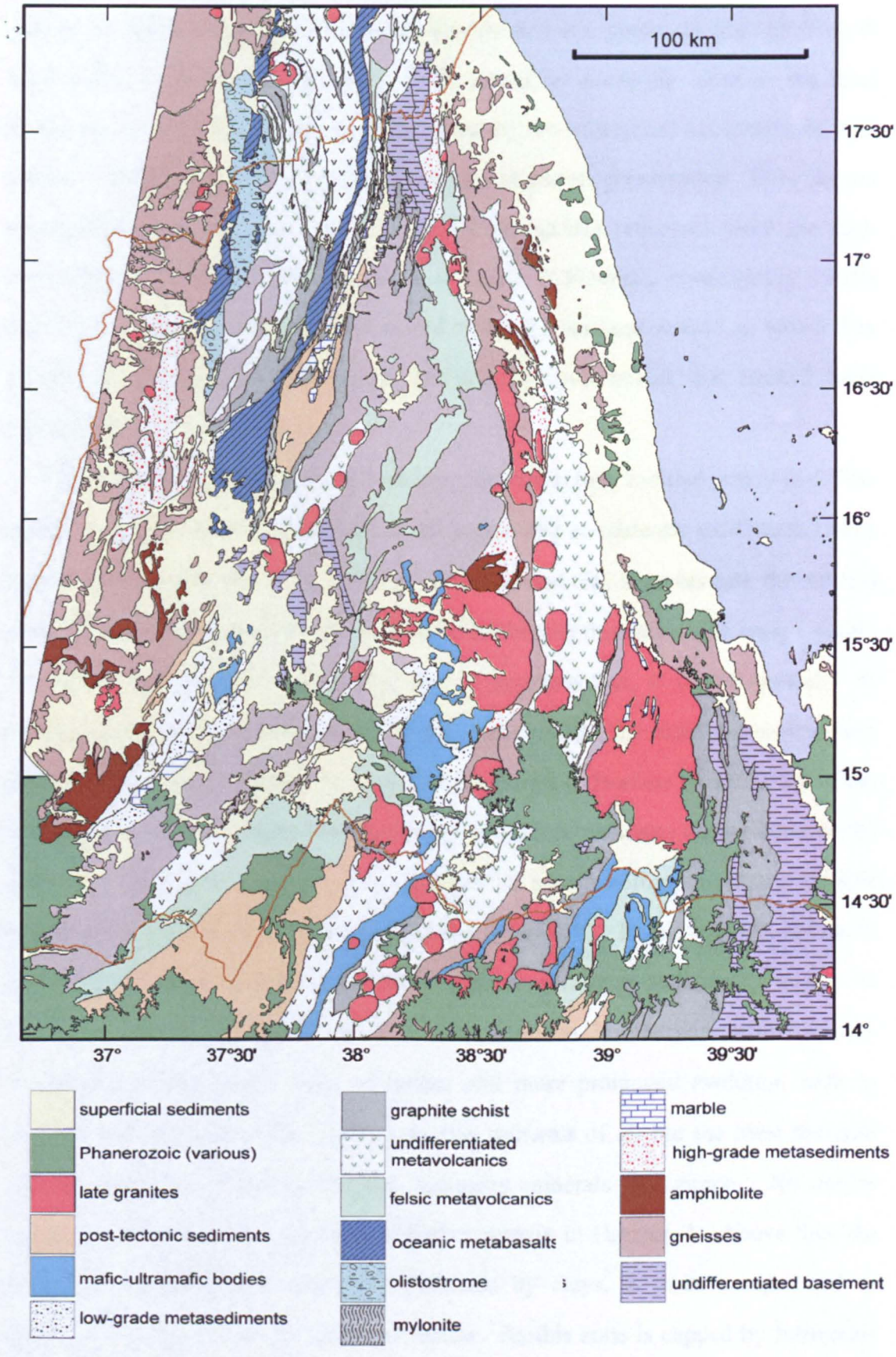


**Figure 2.35** Reconnaissance geological map of Neoproterozoic basement in Eritrea and northern Tigray (with the kind permission of Dr S.A. Drury)

surface is subject to minimal low energy erosion and is a *'gently undulating'* (Butt & Zeegers 1992; Zeegers & Lecompte 1992) low-relief peneplain close to sea level (Bohannon *et al.*1989). Eritrea is characterised by the widespread occurrence of such laterites. These often have the added advantage of perfect preservation. They are not reworked because they have been isolated from surface processes since the mid-Oligocene by the Tertiary continental flood basalts (CFBs) that conformably overlie them. Thus they preserve a pristine record of the former land surface on which they developed and provide evidence for the ancient environment that formed them (Chapter 7).

The nature of the upper three horizons, the ferricretes, mottled zones and fine-grained saprolites is similar throughout the region and consistently exhibits the same general vertical sequence, with ferricrete at the top and clay zone beneath the mottled zone. This profile is intact below the base of the basalts throughout the region Using the most simple rule of stratigraphy, that of superposition, it would normally be assumed that at progressively deeper levels in the profile, the older the sedimentary strata and structures would be. In reality, the ferricretes, (Horizon 5), at the top of the profile show textural evidence for the longest evolution. Whereas deeper down in the above the unweathered parent rock (Horizon 1), shows nothing other than the first effects of weathering of the basement (figures 2.34a & b). In this horizon, unaltered feldspars and micas persist, as do intact tectonic structures and quartz veins. At stratigraphically higher levels, the clay zone, Horizon 3, otherwise texturally and structurally simple, shows signs of further and more prolonged evolution such as pisoliths and the complete breakdown to clay minerals of all but the most resistant minerals such as residual quartz and accessory minerals like zircon. No earlier tectonic structures or features of the substrate remain in Horizon 3. Above this, the mottled zone, Horizon 4, although dominated by clays, is more complicated in structure and texture than the clay zone below. As this zone is capped by ferricretes with the most intricate of textures, Eritrean lateritic horizons become progressively more evolved and therefore *older upwards* (Schellmann 1986; Butt & Zeegers 1992;

**Figure 2.36** A typical laterite profile in Asmara City with 3 distinguishing upper horizons; from bottom to top an iron-poor clay zone, a mixed clay and iron mottled zone and an iron-rich ferricrete

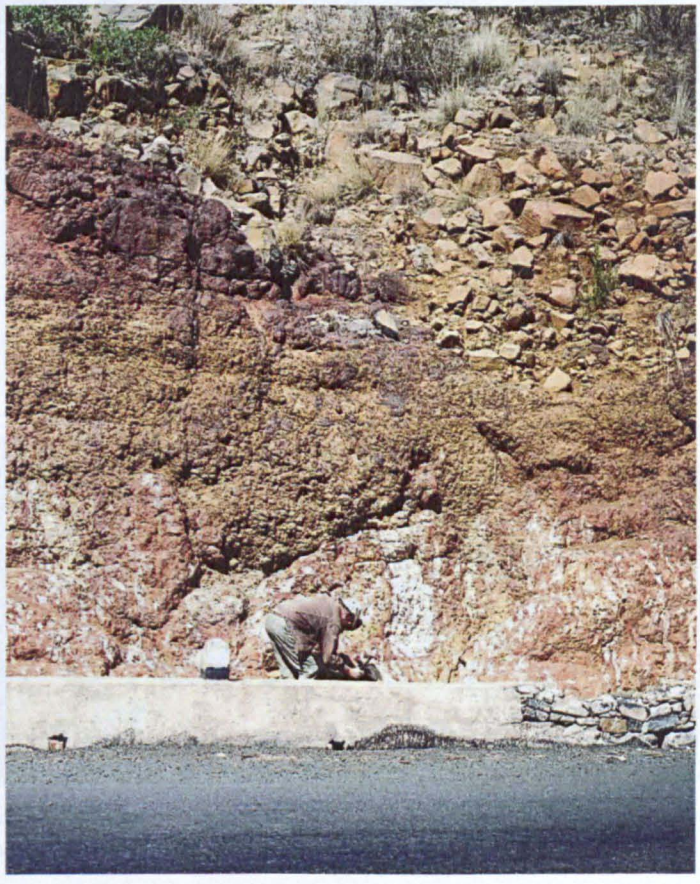

**Figure 2.37** Laterite profile beneath CFBs in road cutting near Shiketi, Eritrea. Basalt/ hematitic ferricrete contact partly obscured by fallen basalt blocks (right). Mottled zone clearly visible below goethitic ferricrete

Nahon & Tardy 1992; Firman 1994; Vasconcelos 1999). After this final stage of

maturation, completely evolved lateritised profiles were abruptly capped ~30 Myr ago by CFBs that blanketed the entire Afro-Arabian surface from Somalia to Sudan and from western Ethiopia to eastern Yemen and Saudi Arabia during the mid-Oligocene.

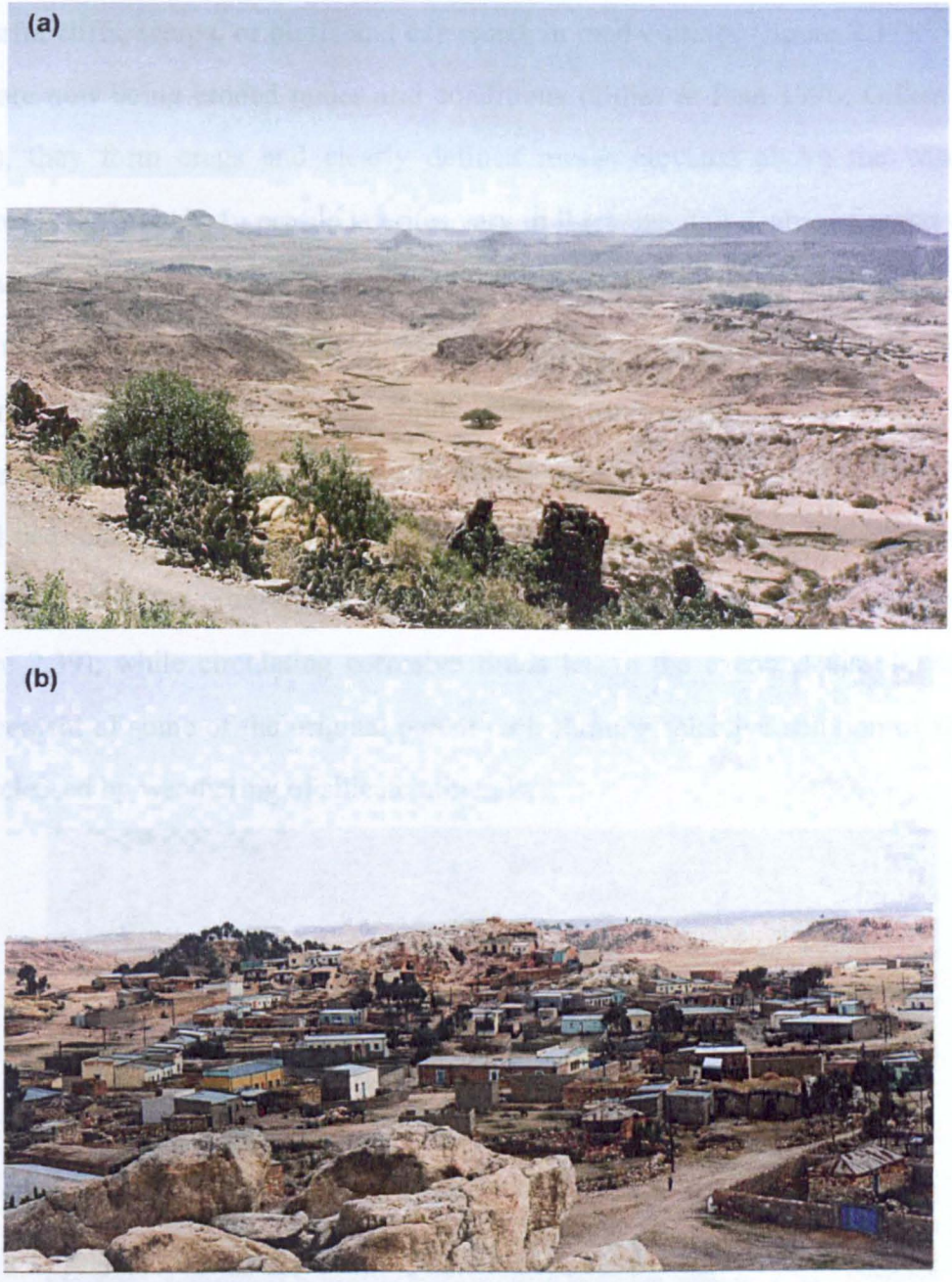


**Figure 2.38** (a) Eritrean laterite mesas: (a) Gaala valley - looking SW (b) Typical village on mesa, Eritrean plateau. Tseada Kristyan - looking SE.

As evidenced by inspection of macroscopic features of each horizon, typical laterite profiles evolve in two stages. Initially, parent rock structures, mass and volume are conserved, succeeded by the second stage affecting the upper three

horizons in particular (figure 2.36), in which the destruction of basement texture and a decrease in volume (Ambrosi & Nahon 1986) accompany the near-complete replacement of primary minerals with clay and iron oxyhydroxides.

Laterites overlain by the CFBs are conspicuous in the field, in that they form colourful cliffs, scarps, or bluffs and exposures in road cuttings (figure 2.37). Where they are now being eroded under arid conditions (Ollier & Pain 1996; Gilkes *et al.* 2003), they form crags and clearly defined mesas elevated above the basement (figures 2.38a and b). In profile laterites vary in thickness and degree of preservation but even at a distance, colour zonation is clear. On closer inspection the progression from unweathered parent rock (Horizon 1) to coarse saprolite (Horizon 2) is obvious. Original basement structures, e.g. folds, sedimentary structures and cross-cutting quartz veins, persist in Horizon 2 and fresh rock present in core-stones surrounded by rotted bed-rock indicates that alteration must have been by permeating groundwater. This resulted in the progressive replacement of primary minerals by clay minerals (figure 2.39), while circulating corrosive fluids led to the eventual dissolution and replacement of some of the original parent rock through selective solution of soluble ions released by weathering of silicate minerals.

**Figure 2.39** Coarse saprolite (Horizon 2) Asmara-Keren road. A granite dyke is completely kaolinised, while retaining its intrusive relations to Neoproterozoic meta-andesites that show fresh core stones in a rotted matrix

Occurrences of liesegang banding in this horizon further confirm the interplay

between oxidation and reduction on solubility of different ions and the reaction equilibria that are involved in chemical weathering of the substrate caused by

**Figure 2.40** Typical liesegang banding in felsic dyke cutting basement ~100m beneath laterite

percolating meteoric waters (see Butt & Zeegers 1992). The depth of ground water penetration in the basement, far beneath the upper horizons of the laterite above, is amply illustrated by the liesegang banding shown in Figure 2.40. Mineralogically simpler than the basal horizons of the full profile, Horizons 3, 4 and 5 bear little, if any, trace of the original parent rock's texture or mineralogy. Secondary minerals totally dominate the upper horizons 3, 4 and 5 and it is these three horizons, which form the basis for a laterite facies map and that are described more fully below.

The key to mapping laterites using remote sensing is to examine the spectral features of the end member iron and clays minerals that dominate the upper three horizons of the palaeosols and to identify image processing techniques that best discriminate each facies exposed at the surface (Chapters 3 to 5).

### 2.6.2 Horizon 3 - the clay zone or fine saprolite

The clay zone is very obviously exposed at the surface. Well preserved throughout the region, the fine saprolite showed no sign of containing swelling clays (i.e. smectites, that also crack when dry) in the field and was provisionally identified

as being kaolinite rich. This observation was confirmed by the Eritrean Ministry of Energy and Mines (1997) and the Geological Survey of Eritrea (1998) and is clearly identified as kaolinite by that mineral's characteristic spectrum expressed by remote sensing data from the short-wave infrared (SWIR) (Chapter 4). In Eritrea, the clay

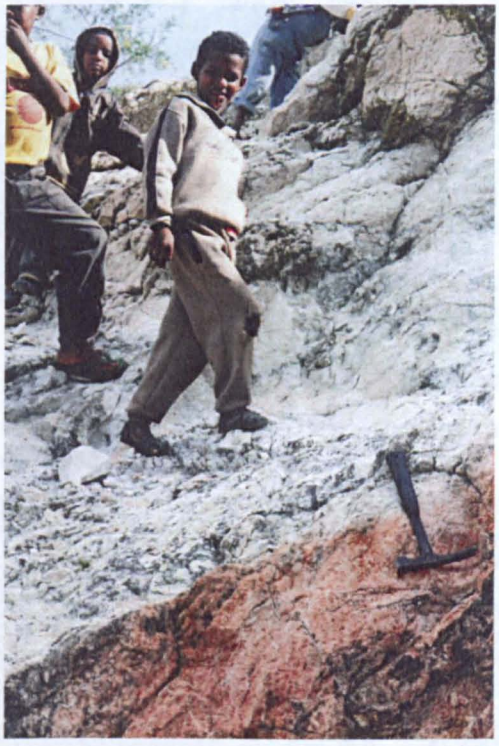

**Figure 2.41** Vegetation-free white clay facies, Tseada Kristyan: the boundary marked by the hammer indicates the distinct change in colour and mineralogy (see also figure 2.41a) between Horizons 2 and 3 typical in Eritrean laterites whilst kaolinisation in the clay facies visibly destroys previous rock fabric

**Figure 2.41a** Vegetation-free white clay facies, Adi Teklay: the boundary marked by the hammer indicates the distinct change in colour and mineralogy this time between Horizons 3 and 4 the mottled zone

**Figure 2.42** Base of massive clay facies, Adi Hawesha. Below standing children's feet is (Horizon 2) the coarse saprolite, which here is an aquifer that the fig tree roots penetrate

**Figure 2.43** Top of massive clay facies (~15m above the children in figure 2.42) outcropping beneath massive mottled facies (Horizon 4) with caves. Adi Hawesha

facies, a mineralogically distinct horizon in the laterite profile, is indurated and resistant to erosion. It frequently outcrops beyond the overlying mottled zone (Horizon 4) forming flat impermeable surfaces corrugated by rills. Almost entirely made up of pure kaolinite, the clay zone contains few, if any, nutrients and is generally bare of vegetation (figure 2.41, 2.41a).

Always pale in colour this facies is sometimes termed *pallid zone*, *argiles bariolées* or *lithomarge* (from the Greek *lithos* meaning rock and the Latin *marga* meaning clayey earth). Fine-grained, iron-poor, often flinty and porcellanous, Horizon 3 is usually white in colour though there are instances of cream, very pale yellow or fawn, purple-tinged or pinkish clay horizons. These slightly coloured variants sometimes have tiny flecks of colour derived from the weathering of ferromagnesian minerals and various degrees of staining in the form tiny hematite veinlets, pinpoint iron blemishes, patchy goethite and insignificant hematite discoloration. Pea- sized pisoliths can be found in this horizon and although they are by no means ubiquitous throughout the clays, in those profiles where they do occur, they are abundant.

There is considerable variation in the thickness of the clay horizon. It ranges from 1.5m at Adi Caieh, where laterites have developed from silicified Adigrat sandstones and are themselves silica rich, to massive ~20m facies where laterites have developed from more aluminium-rich substrates that have the potential for producing abundant kaolinite. Such substrates - granitic rocks, muscovite schists and mafic to felsic metavolcanics (figure 2.35) - are rich in the aluminous rock-forming minerals: mica, chlorite, epidote and feldspar (Pearce 1981) and are common in the Eritrean basement. Examples of thick clay facies developed on such substrates occur at Embeyto, where laterites have formed from muscovite schists and at Adi Teklay (figure 2.33), Adi Hawesha (figure 2.42; 2.43), Tseada Kristyan and Adi Felesti where laterites have developed from granodiorites. Field evidence indicates that throughout the region there is an obvious correlation between bedrock composition and the thickness of this horizon in the profile. This variation is, in turn, dependant on differences in parent rock mineralogy weathered under lateritic conditions (Butt, 1986; Hussey 1998).

*Kaolinite - provenance – selection for analysis*

A fuller understanding of Eritrean laterites and kaolinite from Horizon 3 in particular was gained by adopting a multidisciplinary approach using remote sensing,

petrographic, geochemical and geochronological data. As these palaeosols have never been dated in NE Africa, the idea of dating laterites over an entire region began as something of an experiment. If the fine-grained, iron-poor clay contained disordered kaolinite (Worrall & Cooper 1966; Crowley 1998; Melo *et al.* 2001; Beauvais & Bertaux 2002) that incorporated potassium in its structure or alunite, $KAl_3(SO_4)_2(OH)_6$, (Mondatori 1983; Bird *et al.* 1990; Germann *et al.* 1994, Figure 5; Vasconcelos 1999; Vasconcelos *et al.* 2008), dateable minerals might be found in this horizon.

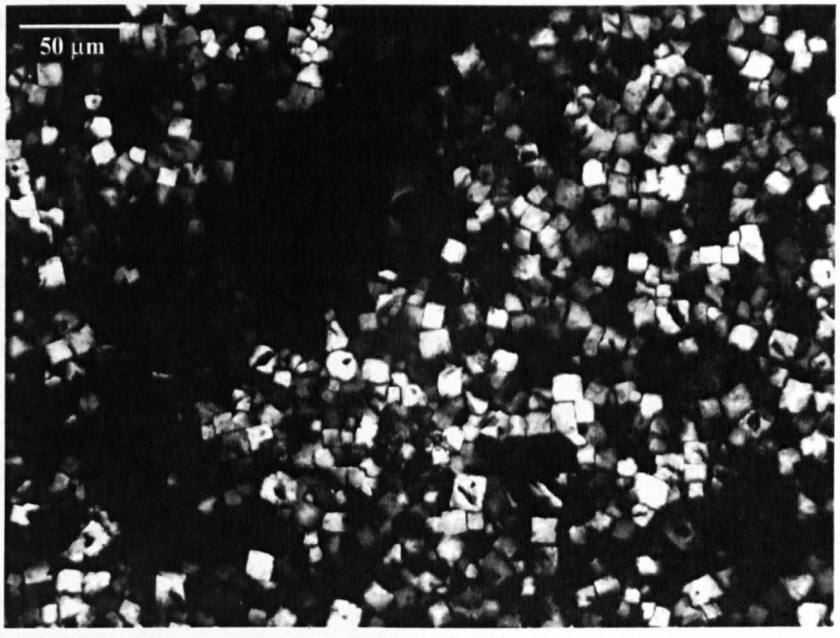


**Figure 2.44** Thin section (cross-polarised light) of sample M48 showing square cross sections of possible alunite set in very fine-grained kaolinite

At each locality (figure 2.27, 2.29; Table 2.1) the lower part of the laterite profile was checked for pure white kaolinitic clay. To ensure minimal atmospheric contamination only hard, non-friable golf ball sized samples were collected. Not only were these typical of the porcellanous clay zone and most likely to retain radiogenic argon but they were ideal for thin sectioning. Any samples containing visible pisoliths were retained for petrographic inspection though these were not used for dating. At each locality the cleanest, freshest samples were hammered out of carefully chosen kaolinitic laterite horizons in road cuttings, quarry faces or natural outcrops. All weathered surfaces were removed and samples carefully wrapped for

protection. As the kaolinite samples were so fine grained, separation and geochronological analysis of individual minerals would have proved impossible. Under laboratory conditions, thumbnail sized whole-rock chips, broken from selected field samples, were reserved for whole rock irradiation (Chapter 6) in readiness for mass spectrometry. The remaining material of these and other samples was sliced for thin sections and studied by transmitted and reflected light microscopy to determine mineralogy.

Although samples of the clay zone were from widely separated localities (Table 2.1), petrographically there is little to distinguish them. In hand specimen all samples are predominantly white or creamy indurated kaolinites. At microscopic scale, these homogenous clays are fascinating and reveal clues of their residual origin. In thin section fine-grained kaolinite is predominant in all samples and corroded quartz is common. Some specimens contained irregular fine and coarse aggregates of small white, almost cube-shaped crystals of a colourless mineral with small cut-off corners (figure 2.44), often square in cross section. To test the hypothesis that this was the characteristic texture of the rare mineral alunite (Mondatori 1983) selected samples collected in 1998 were submitted for analyses using an electron microprobe in 2000 (see below).

*Energy-dispersive electron microprobe imaging*

Alunite ($KAl_3(SO_4)_2(OH)_6$), whose common crystals are tabular to pseudo-cubic rhombohedra, is a partly dehydrated variety of one of the alums and may form as a result of precipitation from groundwater. Since the deposition of alunite accompanies silicification, it was hoped that this might give clues of the geochemical conditions during formation (Chapter 7) and induration of the clay zone. Furthermore, as alunite is potassium- rich the clay zone would provide a good candidate facies for dating.

*Confirming the presence of alunite*

Polished thin sections of selected clay samples were submitted for electron microprobe analysis (Reed 1996) using a Cameca SX100 electron microprobe, so that individual mineral grains could be chemically analysed and chemical maps of up to 4

elements could be produced for each sample together with back-scattered electron images. The last has advantages over optical petrography in that there is a greater depth of field and resolution (~1 μm) and a significantly higher magnification range that shows crystal textures on a micro-scale. As element mapping and semi-quantitative estimation of element concentrations aids detection, identification and distribution of the smallest minerals, this is especially useful when examining clays. Initially, energy-dispersive plots of electron-induced X-ray intensities were used to establish the presence of high silica (Si), aluminium (Al), and potassium (K) concentrations using the correlation of the peak height for individual elements which is roughly proportional to the concentration of the element. Besides a high abundance of K and Al, sulphur (S) was also abundant in some samples, as was titanium (Ti), which was probably inherited from the primary minerals, rutile ($TiO_2$) and ilmenite ($FeTiO_3$), in the parent rock (Tardy 1997). Electron backscatter images, maps of X-ray emissions for individual elements and colour images that combined K, Al and S X-ray emissions as red green and blue confirmed the hypothesis that the cube-shaped mineral - present as the only K-, Al- and S- rich phase in the clay - was alunite (figure 2.45).

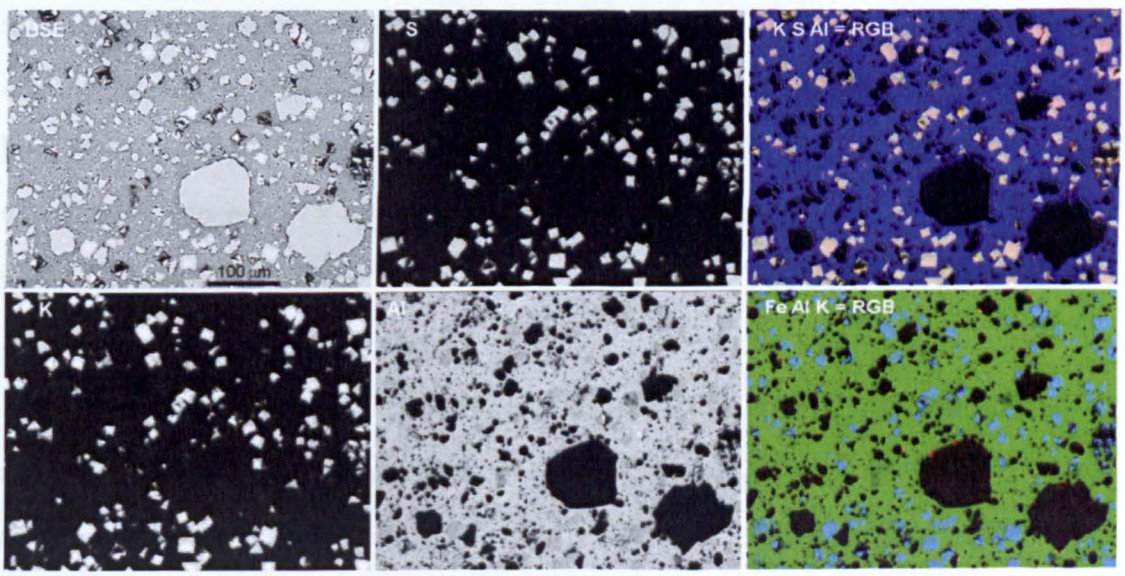


**Figure 2.45** Examples of backscattered electron image (BSE), element maps for individual elements K, Al and S, and multi-element RGB maps for K S Al – pinkish crystals have high K, S and Al – and Fe Al K – note the small red grains of an iron-rich mineral. Black grains are quartz

Samples M48, from Tusk, developed from Permian conglomeratic glaciogenic sediments rich in silica and M70, from Adi Felesti, developed from a very different substrate, granodiorite (table 2.1) are typical of samples that contain abundant alunite. Interestingly, when splitting the sample from the main outcrop a distinct, acrid odour was released at both localities. The only other locality where this aroma was obvious was at Dairo Kawlos near Asmara where sample M34 was collected from a locality where the spectral signature of alunite was very pronounced (Chapter 5). Notably in the 25th edition of Rutley's Elements of Mineralogy (Read 1962) alunite is described as giving off sulphurous fumes 'on intense heating' and it is likely that a sharp bang with a hammer - like striking a spark – produces a similar effect in the field. Table 2.1 indicates the localities where these alunite-rich samples were collected and Table 6.2 (Chapter 6) gives the locations and geochronological data of these three representative alunite-rich clays from Eritrea.

With the presence of K-bearing minerals established in some samples and the occurrence of alunite confirmed, further clay-zone sampling was carried out with the aid of satellite images on subsequent field trips. This was done to widen the area from which reliable ages for the lateritic clay zone were acquired and to determine the mineralogy and geochemistry of clays regionally. However, because alunite aggregates with very fine grain size are impossible to distinguish from their kaolinite host, it was decided to further screen all new samples for potassium and sulphur using wavelength-dispersive X-ray fluorescence spectrometry (XRF), the most rapid analytical method available.

*X-ray fluorescence spectrometry*

Lateritic clay samples, collected during March 2001 and October 2003 field seasons, were submitted for geochemical analysis using XRF (Watson, 1996). These analyses were carried out to:

- determine major and trace element variations through complete laterite sections, Horizons 1-5;

- screen kaolinite samples for potassium and sulphur that might indicate possible alunite content and,
- check for arsenic (M. Inglis, pers. comm. 2001), magnesium and iron content that may contribute to ground water contamination.

During preparation, particular care was taken to ensure that samples from different facies were kept separate to avoid one sample contaminating another and to ensure that, at every stage, samples for whole-rock geochemical analysis were representative of the different laterite facies. Preparation for XRF geochemical analysis of laterite materials was carried out as follows: each sample was crushed into fine gravel sized pieces (using a clean jaw crusher) and then placed in a new, clearly labelled sealable plastic bag. Cross contamination was kept to a minimum by cleaning the crusher after processing each sample and crushing all rocks of roughly the same composition (e.g. kaolinites) consecutively. Every crushed rock sample was ground to very fine powder using a ball mill for small samples and a TEMA for large ones. To keep the grinder thoroughly clean it was run with pure quartz sand then washed and dried after each sample. Finally, 30g of powder (the minimum requirement for each glass bead and powder pellet required for a full XRF analysis) of each sample was placed in a new, labelled container and submitted for analyses.

Of the twenty samples screened for potassium, nine were high in both K and S, a result that almost certainly signified alunite whilst another three were K rich (see table 5.1; Chapters 5 & 6). These were prepared for irradiation and mass spectrometry. A similar strategy was applied in the June 2002 field reconnaissance in Ethiopia where lateritic cover is less obvious than that in Eritrea. Moreover, the terrain in Ethiopia dotted with inaccessible steep sided canyons, sheer cliff approaches, army encampments and land-mined traverses, militated against sampling the precise localities pinpointed on satellite images. In these cases samples were collected from within the same laterite profile and horizon as the target area.

### 2.6.3 Horizons 4 and 5 - the mottled zone and ferricrete

Field studies indicate that Horizons 4 and 5, the mottled zone and indurated

ferricrete respectively are mineralogically distinct and can often be identified by their visual characteristics. They contrast starkly with the pallid clay zone beneath (figure 2.36), which outcrops beyond them and are commonly confused with other outcrops sweepingly termed laterite because of their coloration.

Horizon 4, the mottled zone, is made up of a mixture of kaolinite and the ferric oxy-hydroxides, hematite and goethite, in which kaolinite dominates. Its name derives from a range of colour variegations: rounded and elliptical features; pipe-like bodies; angular patches controlled by joints in places and diffuse variations in colour (figure 2.46). In some cases it is clear that the mottling has formed by localised leaching of an earlier red substrate; i.e. iron in its $Fe^{2+}$ (ferrous) form has been removed by dissolution. In others the reverse is the case; formerly bleached white masses are permeated by red- and yellow-brown coloured veins, tubular voids and irregular patches suggesting that iron in its $Fe^{3+}$ (ferric) form has been precipitated from solution to form hematite or goethite, depending on the position of the water table. When the water table is low, dehydrated minerals such as hematite tend to form, whereas when the water table is high, hydrated minerals like goethite dominate. Careful examination of this facies reveals further complication that signifies, for initial precipitation of ferric minerals in a nearly pure kaolinite matrix, further leaching and subsequent episodes of $Fe^{3+}$ precipitation.

**Figure 2.46** Examples of the Mottled zone – Horizon 4

The removal and addition of iron in the mottled zone almost certainly indicates changes in groundwater chemistry during the evolution of the upper laterite horizons that are dependent on the prevailing redox conditions. Given reducing conditions and the adding of electrons, insoluble $Fe^{3+}$ transforms to soluble $Fe^{2+}$, thereby leaching the weathering product. Whereas oxidising conditions and the removal of electrons from dissolved $Fe^{2+}$ ions results in the precipitation of $Fe^{3+}$ in variously coloured iron minerals (e.g. "Oxidation involves the loss of electrons, whereas reduction involves the gain of electrons: remember "OILRIG: Oxidation Is Loss; Reduction Is Gain" Drury (2006)). These shifts in water chemistry indicate repeated rises (reducing conditions) and falls (oxidising conditions) in the groundwater (Nahon & Tardy 1992; Thornber 1992; Tanner & Khalifa 2009) that is central to laterite development. Similarly, Horizon 3, which is virtually iron-free, indicates that the lower levels of the laterite profile remained saturated and starved of oxygen throughout the period of lateritisation.

**Figure 32.47** Typical Ferricrete – Horizon 5

Horizon 5, the ferricrete or iron crust, is predominantly composed of hematite and goethite with variable but less abundant clay content than Horizon 4, hence its dark

reddish-brown or yellowish-brown overall appearance. It has hard distinctive nodular iron concretions and a pisolitic texture that results in extremely irregular outcrop surfaces (figure 2.47). Although often conglomeratic in texture, it is not detrital in origin and always forms by in-situ precipitation of iron minerals that sometimes envelop material (e.g. vein quartz) that has not succumbed to pervasive dissolution processes. Ferricrete also shows signs of leaching due to reducing conditions and some dissolution of iron, but it is far less common than that in Horizon 4. Evidence for alternations between desiccation and the dehydration of goethite to form hematite is widespread, as is the hydration of hematite that results in a goethitic carapace developing in places. Although these features may signify changes in the water table during laterite formation, they could equally be due to alteration long after laterite formed and became lithified. Intermediate between the iron-rich facies above and the clay-rich facies of Horizon 3, the mottled zone is a transitional zone both in appearance and in mode of formation. Only when the three facies, Horizons 5, 4 and 3 outcrop *together* in situ (figure 2.48; Andrews Deller 1998, 2000, 2002 - 2007) is a laterite unequivocally distinguishable.

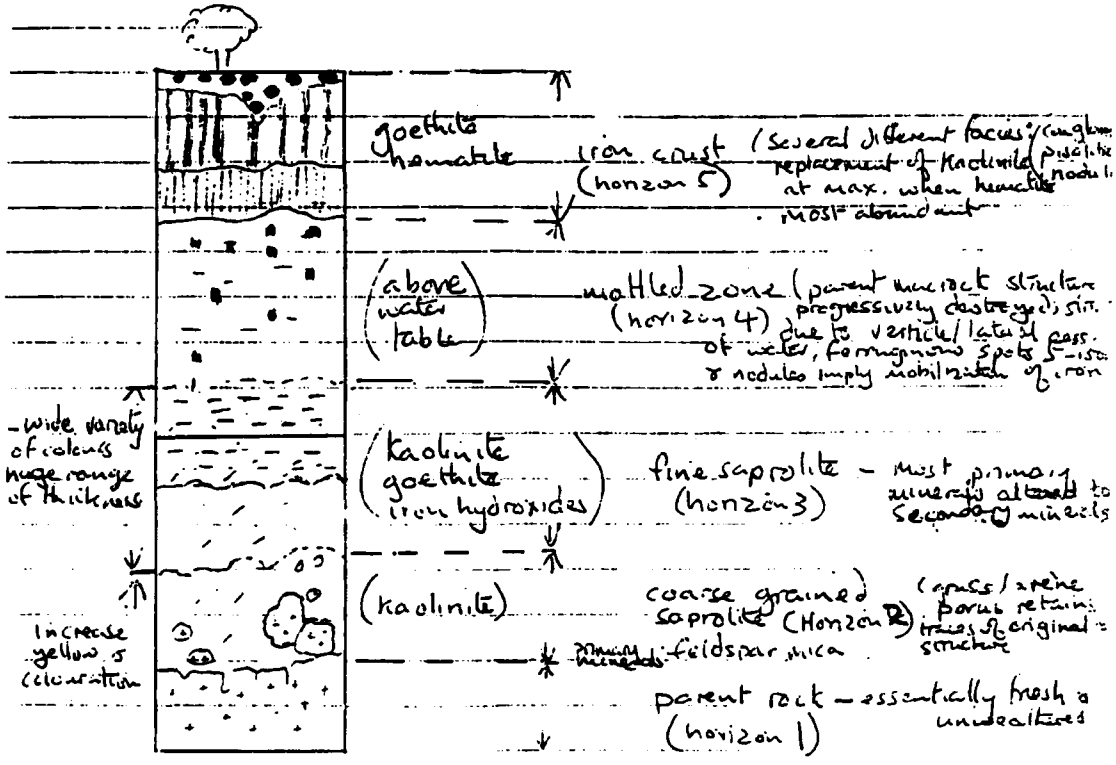


**Figure 2.48** Initial rough field sketch of a typical lateritic profile showing 5 horizons (1998) scale omitted as horizons vary greatly

No attempt was made to date the mottled zone or ferricrete at the top of the profile - see Chapters 5 and 6. Sample collection was reserved for petrographic examination and geochemical analysis and to validate remotely sensed data.

## 2.7 Geochemical variation in Eritrean laterites

The impact of coupling the geochemical movement of elements within the full profile with the distribution of laterite facies has ramifications for mineral exploration and a marked bearing on the health and social well-being of the local population (see Chapter 8). As there are no studies on the geochemistry of the full laterite profile in NE Africa, this contribution goes some way to filling that gap: the resulting data when combined with detailed laterite regolith mapping using RS may be exploited to the advantage of the indigenous population.


**Figure 2.49** Locations of geochemical sampling sites

### 2.7.1 Introduction

A total of 60 rock specimens, including those representing four full laterite profiles developed from basement rocks were analysed using wavelength dispersive X-ray fluorescence spectrometry (section 2.6.2) to:

- establish broad geochemical variations in the laterites in Eritrea;
- check for the presence of alunite in lateritic clay zones and,
- show geochemical changes through 4 distinctly different laterite sections.

All samples were collected in areas of Neoproterozoic basement apart from 4 analysed samples from the Adi Caieh (M101) and Knafna (M130, M131 and M133) districts. These 4 samples originate from the clay zones of the laterites that developed on Adigrat Sandstone Section (2.2.3) and are clay-rich silcretes collected in the hope of finding alunite suitable for Ar-Ar dating. Locations of sampling sites are shown in Figure 2.49. Sample preparation and details of the analytical technique are given in Ramsey *et al.* (1994) and Watson (1996).

### 2.7.2 Geochemical features of laterites

Broad geochemical variations in the samples are described below and changes through four laterite sections are compared with the geochemistry of basement rocks on which they developed. Major and trace elements from different levels in laterites and from fresh basement on which laterites have evolved are plotted against $Fe_2O_3$ concentrations of samples to show how they vary with depth in the laterite profiles and also to illustrate how they have responded to dominant geochemical processes involved in laterite formation. Full XRF analyses of laterite samples and fresh basement samples are given in Table 5.1 and Appendix A.

The most distinctive feature of Eritrean laterites is the concentration of iron in the uppermost ferricretes and its decrease with depth through the mottled zone and the clay zone. This iron zonation reflects two factors: the solubility of iron as Fe(II) under reducing conditions in the water-saturated parts of the palaeosol as it formed below the water table and precipitation of iron as oxy-hydroxides of Fe(III) when different horizons in the palaeosol were aerated as the water table fell and conditions

became oxidising. The mottled zone, lower down the profile, contains intermediate, variable $Fe_2O_3$ content.

The progress of lateritisation during oxidising and reducing conditions; the influence of acidic conditions and the role of hydrogen ions in breaking down silicates together with stagnation and sluggish flow in a water-saturated environment, gives clues to the probable behaviour of individual elements (Butt *et al.* 1991, 2000; Butt & Zeegers 1992) during lateritisation. Not only is the behaviour of elements controlled by Eh-pH conditions (Taylor & Eggleton 2001) and the presence or absence of various ions during lateritisation of the regolith but it is directly dependent on the specific properties of each element detailed below:

i. Highly soluble elements, such as potassium (K), sodium (Na), calcium (Ca) and magnesium (Mg) are released to solution during weathering of feldspars and ferromagnesian minerals. Any sulfides present in fresh basement rapidly break down due to initial oxidation to produce both hydrogen and sulfate ions. These major elements and trace elements that have similar chemical properties, i.e. barium (Ba), rubidium (Rb) and strontium (Sr), are likely to have become increasingly concentrated in groundwater. Their precipitation is possible only when they become saturated in solutions, usually as a result of desiccation. Rainfall will remove these elements from higher levels in the profile and the most likely site for their concentration and eventual precipitation is deep in the laterite profile.

ii. Elements whose main hosts are resistant to chemical breakdown, such as highly insoluble minerals zircon ($ZrSiO_4$ with significant uranium and thorium), apatite ($Ca_5(PO_4)_3(F,Cl,OH)$), the common titanium minerals ilmenite ($FeTiO_3$) and rutile ($TiO_2$) and monazite ($(REE,Y,Th)PO_4$) are likely to remain unaltered within the laterite. Since extreme weathering steadily reduces the volume of the remaining solids, all laterite horizons can be expected to have higher concentrations of these elements than the fresh basement from which they have formed. In contrast with the lower facies, the horizon that began to form at the onset of lateritisation and is most reduced in volume, Horizon 5 the ferricrete, is likely to contain a larger concentration

of resistant minerals and their associated elements. An upward increase of these minerals in the profile therefore seems likely.

iii. Iron oxy-hydroxides, especially goethite, efficiently adsorb elements like copper, lead, zinc, cadmium (Webster *et al* 1998) and uranium (Loganathan *et al.* 2009); complex ions of the non-metals, arsenic (As), phosphorus (P), selenium (Se) and, the metals chromium (Cr), molybdenum (Mo), vanadium (V) and tungsten (W) (Xu *et al* 2009). If these elements are readily available either from the basement or in water that percolates through the profile as it formed, they may be enriched in the more iron-rich horizons, especially the ferricrete. Potentially, therefore, laterites are a source of many pollutants should the elements adsorbed by goethite be released by the dissolution of goethite under reducing conditions (Nickson *et al.* 2000).

iv. As well as iron, several metals may occur in different valence or oxidation states that affect their solubility because of varying conditions. Most notable is manganese (Mn), which has five oxidation states (+2, +3, +4, +6 and +7). Manganese occurs most commonly in reducing natural waters as soluble Mn(II). Oxidation to Mn(IV) results in precipitation of pyrolusite ($MnO_2$). As with iron, manganese is expected to be concentrated in the upper part of laterite profiles where the oxidation potential is high and it precipitates out as an oxide or oxy-hydroxide (Taylor & Eggleton 2001). Other elements whose solubility can be controlled by oxidation state are chromium (Cr) and vanadium (V).

### 2.7.3 Results – general geochemistry

Element abundances for samples selected from laterite horizons 1-5 are plotted against $Fe_2O_3$ concentrations are detailed below (figures 2.50 to 2.54). Iron concentrations give a rough indication of the position of each sample in a generalised laterite profile (e.g. $Fe_2O_3$ <2% indicates a pure kaolinite; 2 to 10% covers the mottled zone and concentrations >10% characterise ferricrete). Figures 2.55 to 2.57 show variations between the different facies in complete laterite profiles.

*Soluble elements: K, Na, Ca, Sr and Ba*

Figure 2.50a shows clearly that, as predicted, potassium (K) and sodium (Na) are

at significantly higher concentrations in low-Fe parts of the laterites, i.e. in the clay and mottled zones, than in ferricretes. Magnesium (Mg) is also concentrated in the clay and mottled zones. However, calcium (Ca) (figure 2.50b) shows no such concentration in any laterite horizon and seems to have been lost from laterites as a whole, except for one sample with 12% CaO from Horizon 2 (highly weathered

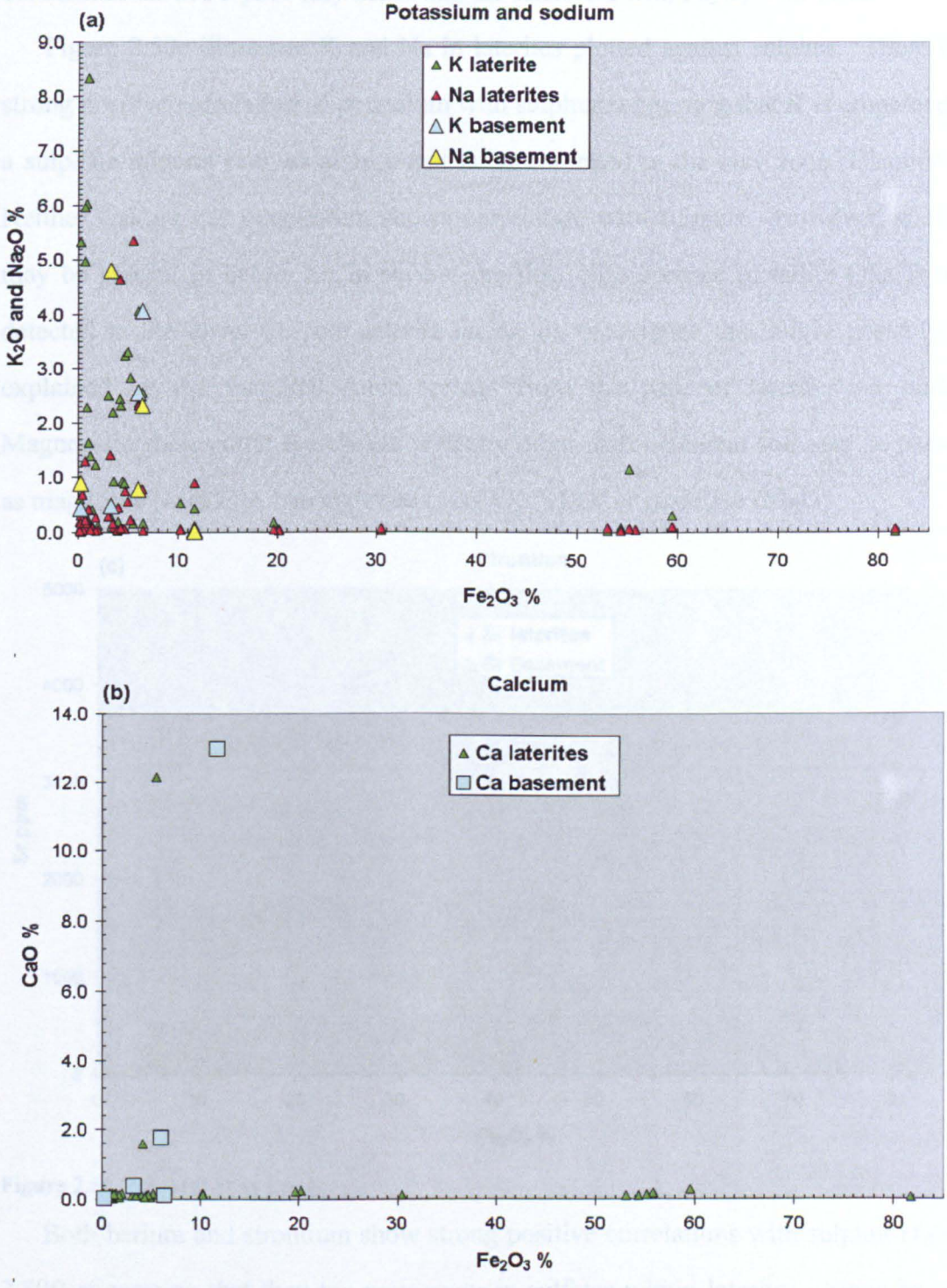


**Figure 2.50** Soluble elements (a) $K_2O$, $Na_2O$ and vs $Fe_2O_3Fe_2O_3$; (b) CaO vs $Fe_2O_3$

basement) developed on a schist with 0.1 % CaO. There was calcite veining in the outcrop, from which this sample was collected, which may have contaminated the sample. Strontium (Sr) (figure 2.50c) shows high concentrations in Fe-poor clay and mottled zones only, as predicted whilst barium (Ba) (figure 2.50d) also shows high concentrations in Fe-poor clay zones and the ferricrete with $Fe_2O_3$ = 45-60%.

Figure 2.50e illustrates K and Na in laterites plotted against sulphur. There is a strong positive correlation of potassium with sulphur suggesting that K is contained in a sulphate mineral such as alunite that is concentrated in the clay zone (Chapter 5). Neither sodium nor magnesium shows correlation with sulphur. However, sodium may be present in halite, for in several profiles, efflorescence of halite (NaCl) was detected in the lower Fe-poor laterite facies, an occurrence that might possibly be explained by the fact that some springs from the base of laterites are saline. Magnesium shows little correlation with any other major element and may be present as magnesite ($MgCO_3$), barringtonite ($MgCO_3 \cdot 2H_2O$) or periclase (MgO).

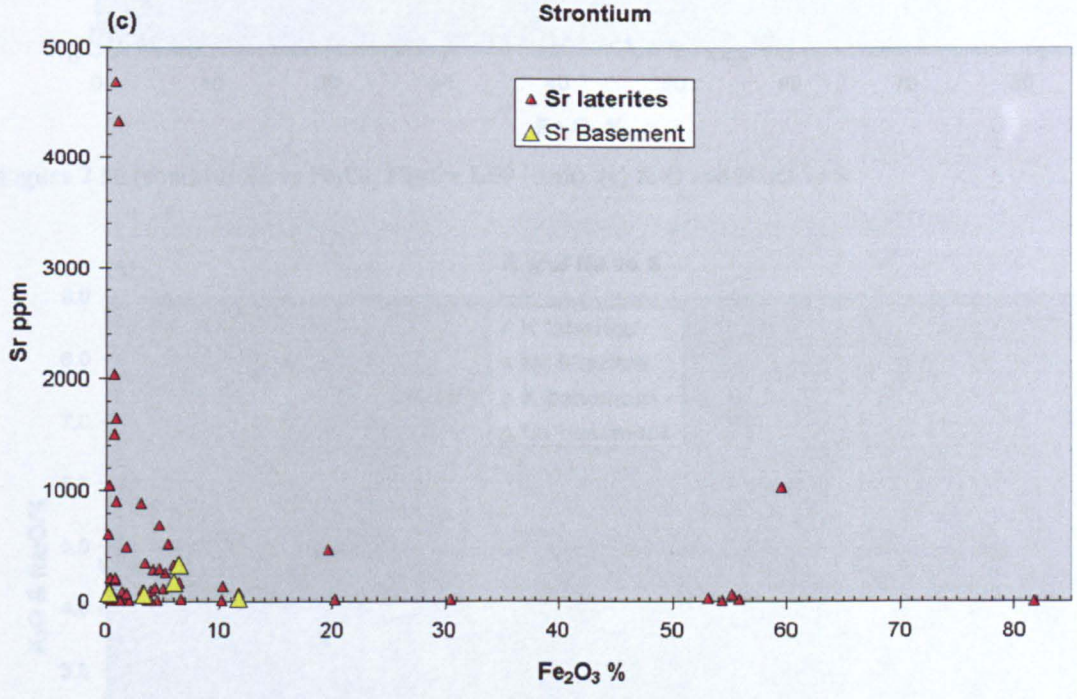


**Figure 2.50** (cont) (c) Sr vs $Fe_2O_3$

Both barium and strontium show strong positive correlations with sulphur (figure 2.50f) suggesting that they too may occur in sulfates within laterites. Since barium

tends to follow potassium because of its similar ionic radius, its concentration in Fe-poor laterite zones may be in alunite. However, the K-poor nature of Fe-rich zones indicates that barium is not present in the mottled zone of ferricrete in either alunite or jarosite. One possibility that would also explain barium's odd distribution relative to iron (figure 2.50d) is that traces of barite ($BaSO_4$) occur in the ferricretes across a specific range of $Fe_2O_3$.

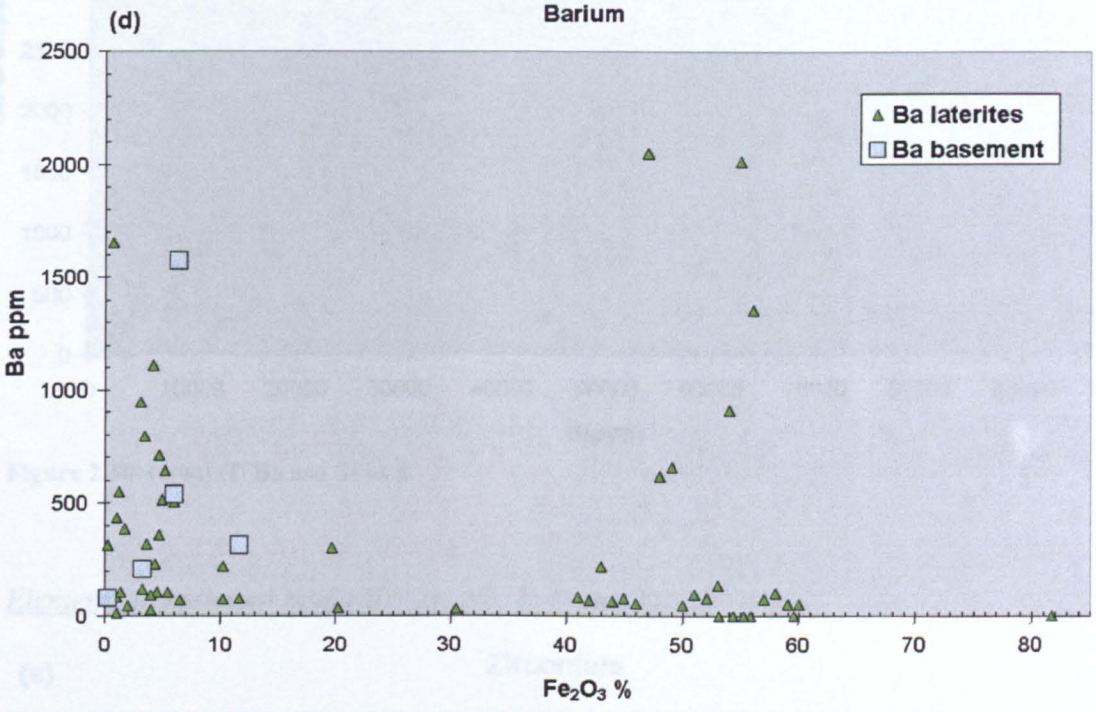


**Figure 2.50** (cont) (d) Ba vs $Fe_2O_3$; **Figure 2.50** (cont) (e) $K_2O$ and $Na_2O$ vs S

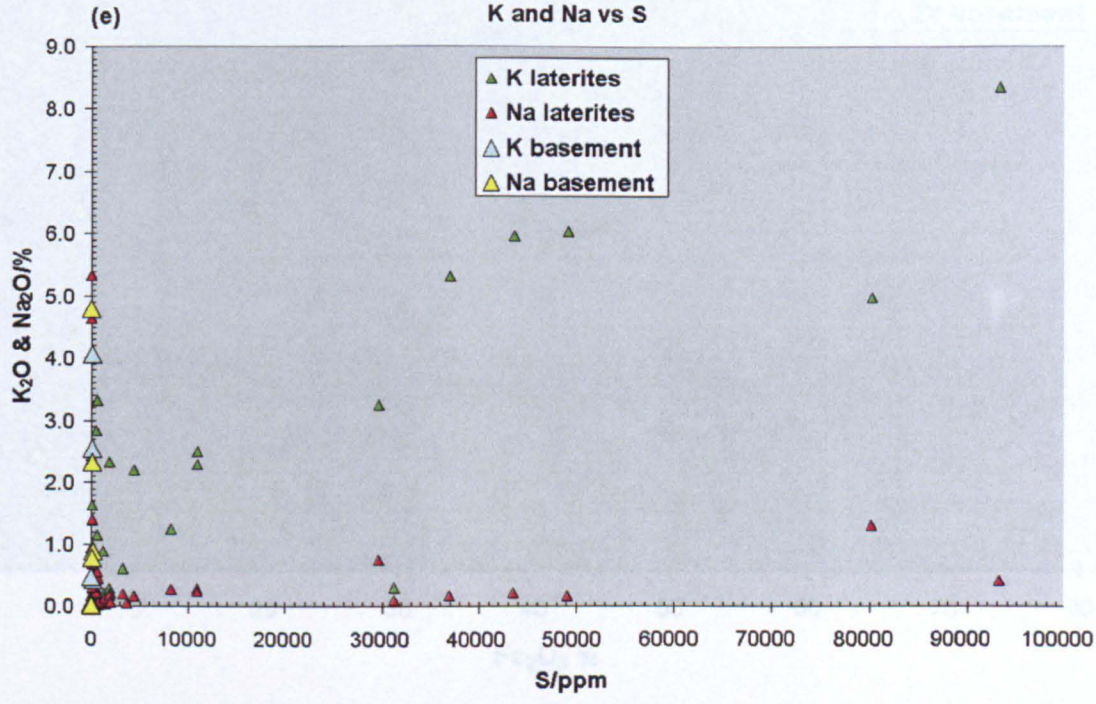

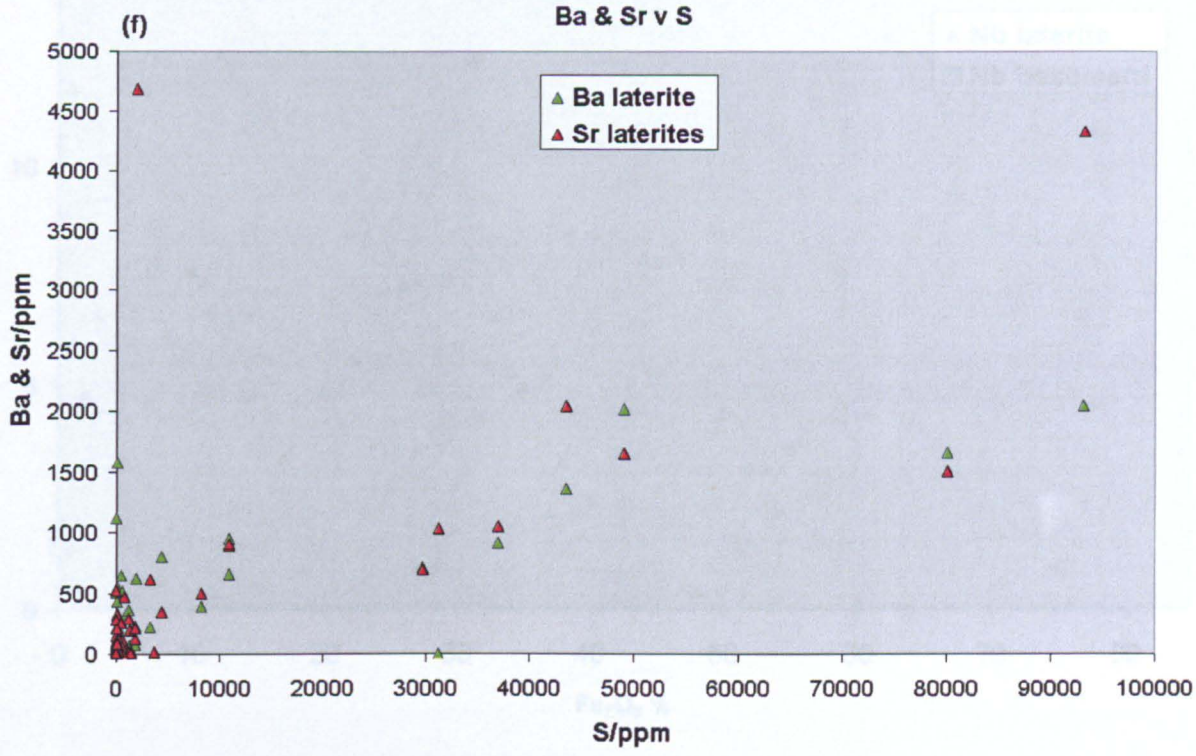


**Figure 2.50** (cont) (f) Ba and Sr vs S

*Elements in resistant minerals: Zr, Nb, Y, P and Ti*

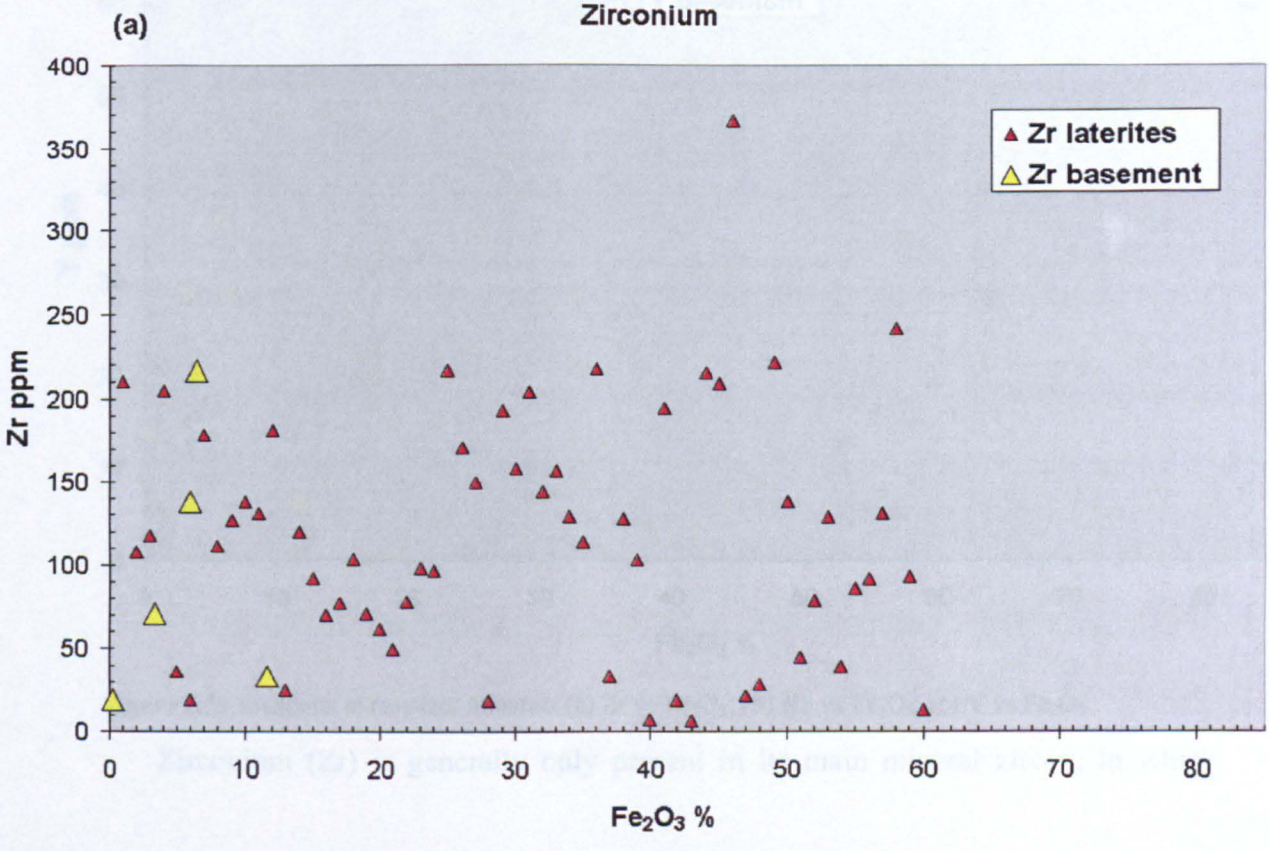

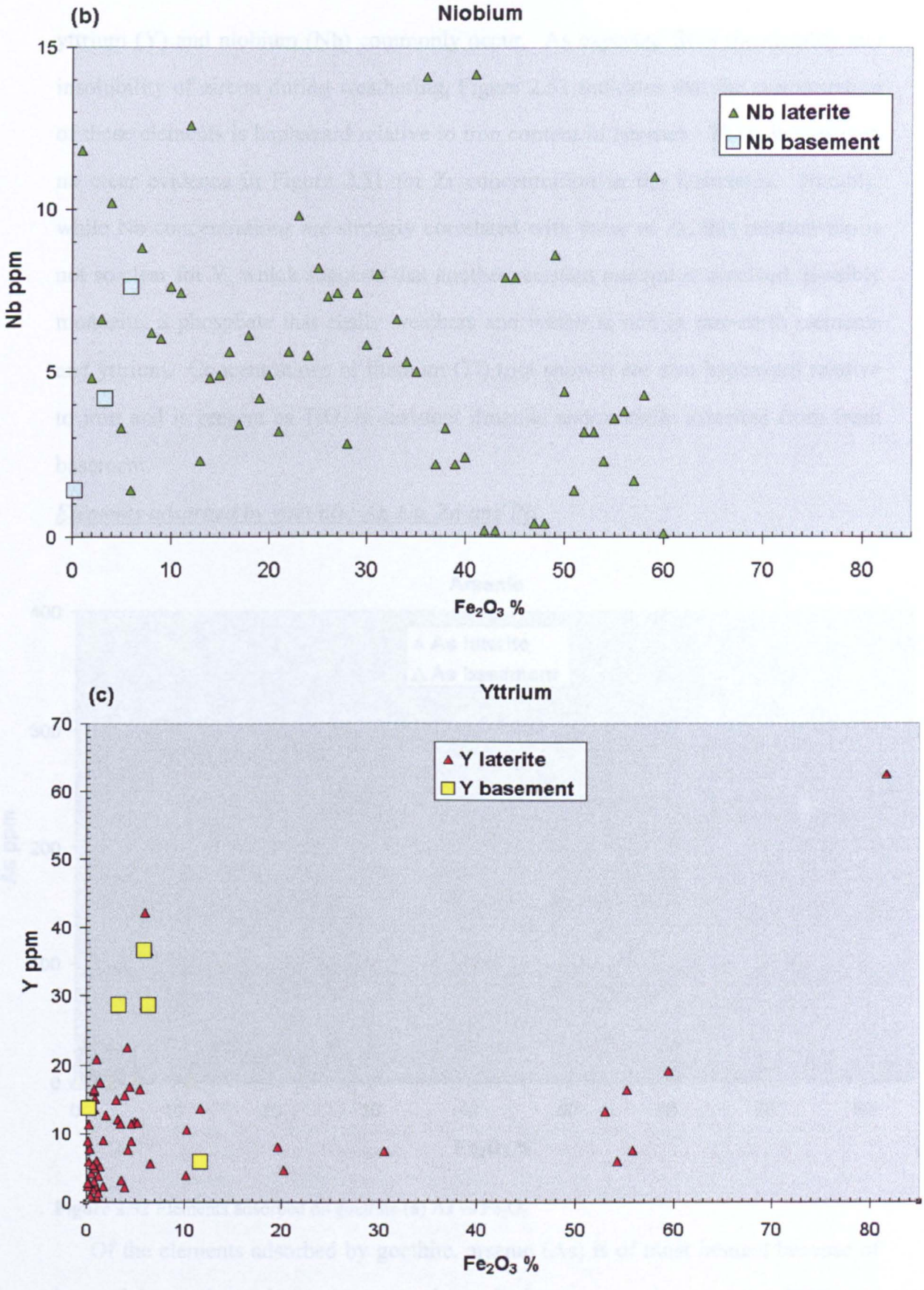


**Figure 2.51** Elements in resistant minerals (a) Zr vs $Fe_2O_3$; (b) Nb vs $Fe_2O_3$; (c) Y vs $Fe_2O_3$

Zirconium (Zr) is generally only present in its main mineral zircon, in which

yttrium (Y) and niobium (Nb) commonly occur. As expected from the stability and insolubility of zircon during weathering, Figure 2.51 indicates that the concentration of these elements is haphazard relative to iron content in laterites. There is however, no clear evidence in Figure 2.51 for Zr concentration in the ferricretes. Notably, while Nb concentrations are strongly correlated with those of Zr, this relationship is not so clear for Y, which suggests that another resistant mineral is involved, possibly monazite, a phosphate that easily weathers and which is rich in rare-earth elements and yttrium. Concentrations of titanium (Ti) (not shown) are also haphazard relative to iron and is present as $TiO_2$ in resistant ilmenite and/or rutile inherited from fresh basement.

*Elements adsorbed by goethite: As, Cu, Zn and Pb*

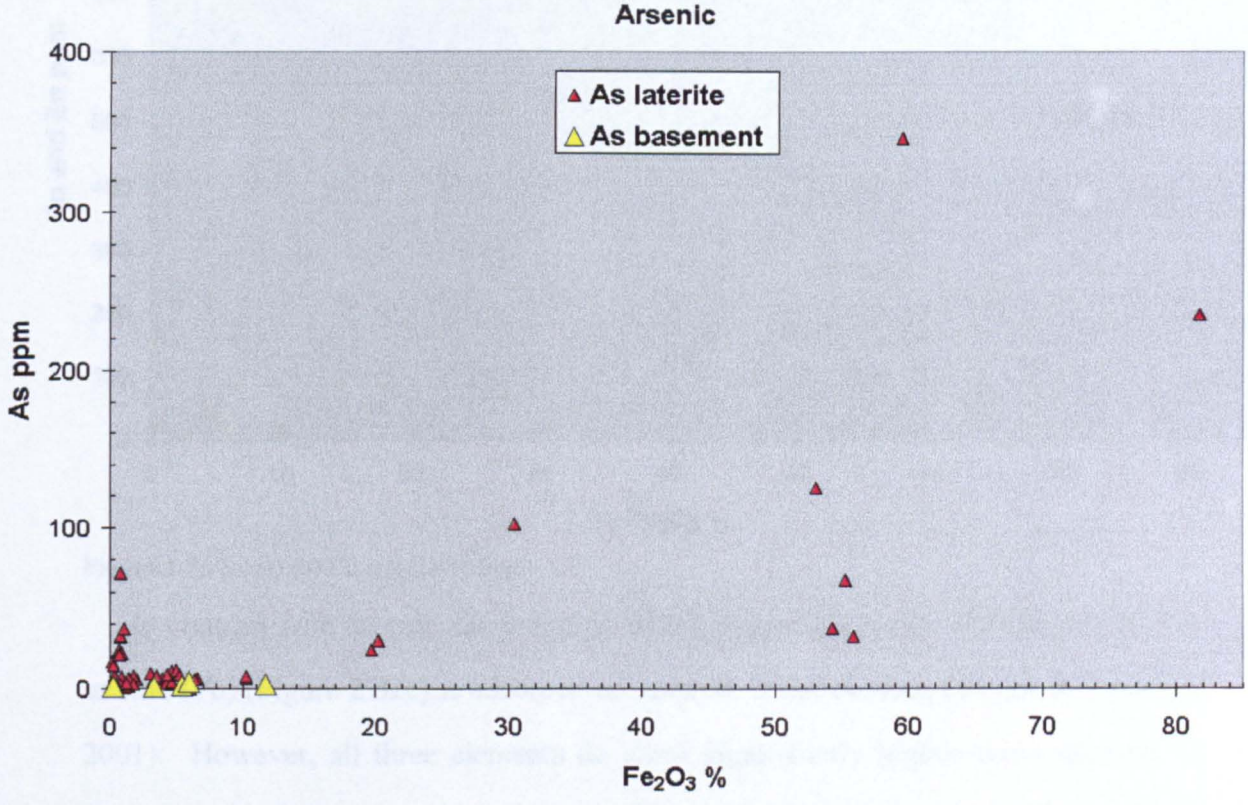


**Figure 2.52** Elements adsorbed on goethite (**a**) As vs $Fe_2O_3$

Of the elements adsorbed by goethite, arsenic (As) is of most interest because of its toxicity and carcinogenic properties. It becomes a dangerous pollutant in groundwater when goethite is dissolved under reducing conditions (Nickson *et al.*

2000; Radloff *et al.* 2011; Drury 2006, 2012).

It is clear from Figure 2.52a that arsenic occurs at significantly higher concentrations in all laterite horizons than it does in fresh basement. Moreover, it shows a rough correlation with iron content confirming that it is adsorbed on goethite. The much higher concentration than in bedrock also suggests that the laterites have efficiently scavenged arsenic from groundwater during their evolution or after their formation.

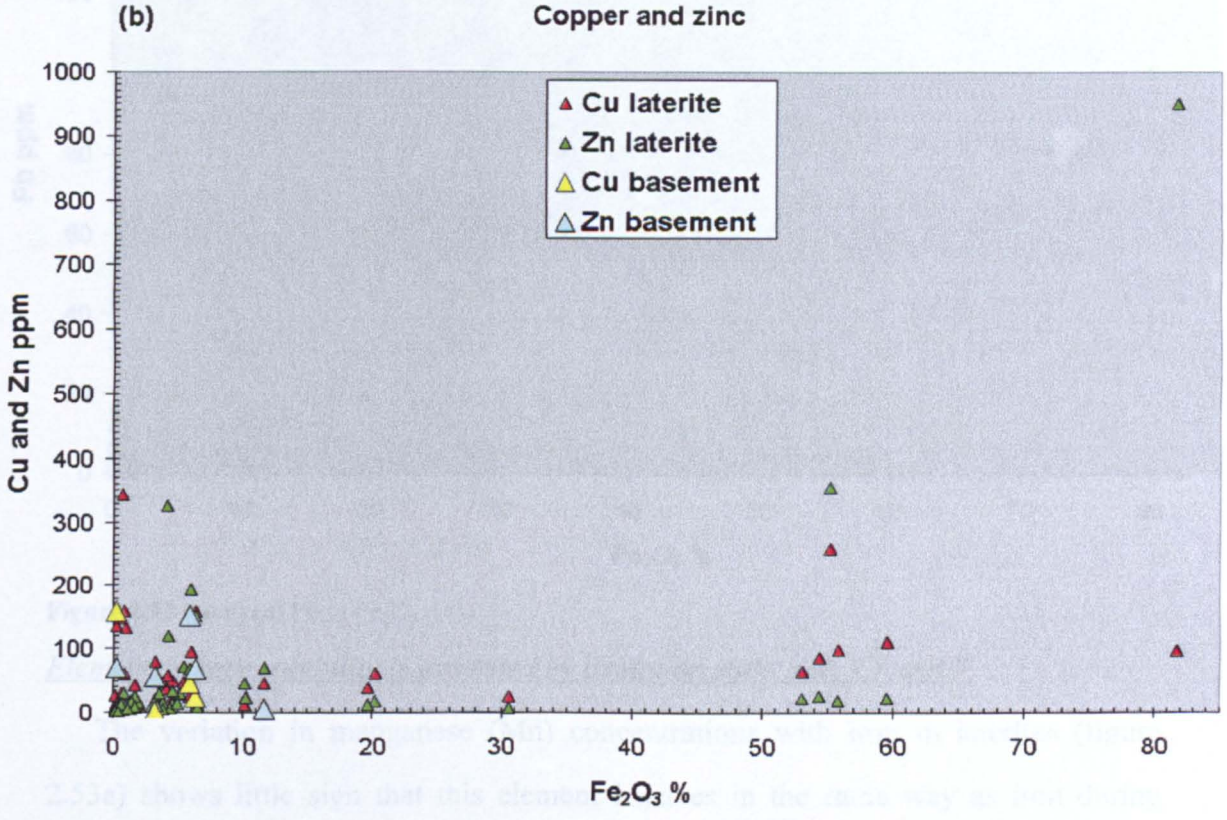


**Figure 2.52** (cont) (b) Cu and Zn vs $Fe_2O_3$

In contrast with arsenic, the extent to which copper (Cu), zinc (Zn) (figure 2.52b) or lead (Pb) (Figure 2.52c) is adsorbed on goethite is not obvious (Taylor & Eggleton 2001). However, all three elements do show significantly higher concentrations in ferricrete, mottled-zone and almost pure clays samples (to a lesser extent) than their source rocks. However, it is impossible to determine whether Cu, Zn and Pb enrichment results from the redistribution of the elements during lateritic weathering of their source rocks or from scavenging by goethite from later groundwaters. Interestingly, the samples in the clay zone that show the highest values for Pb also

have high $K_2O$ contents. The similarity of ionic radii of K and Pb allows for some substitution of Pb for K in potassium-rich minerals. High Pb contents in ferricretes are almost certainly due to adsorption on goethite as the samples have very low $K_2O$ contents.

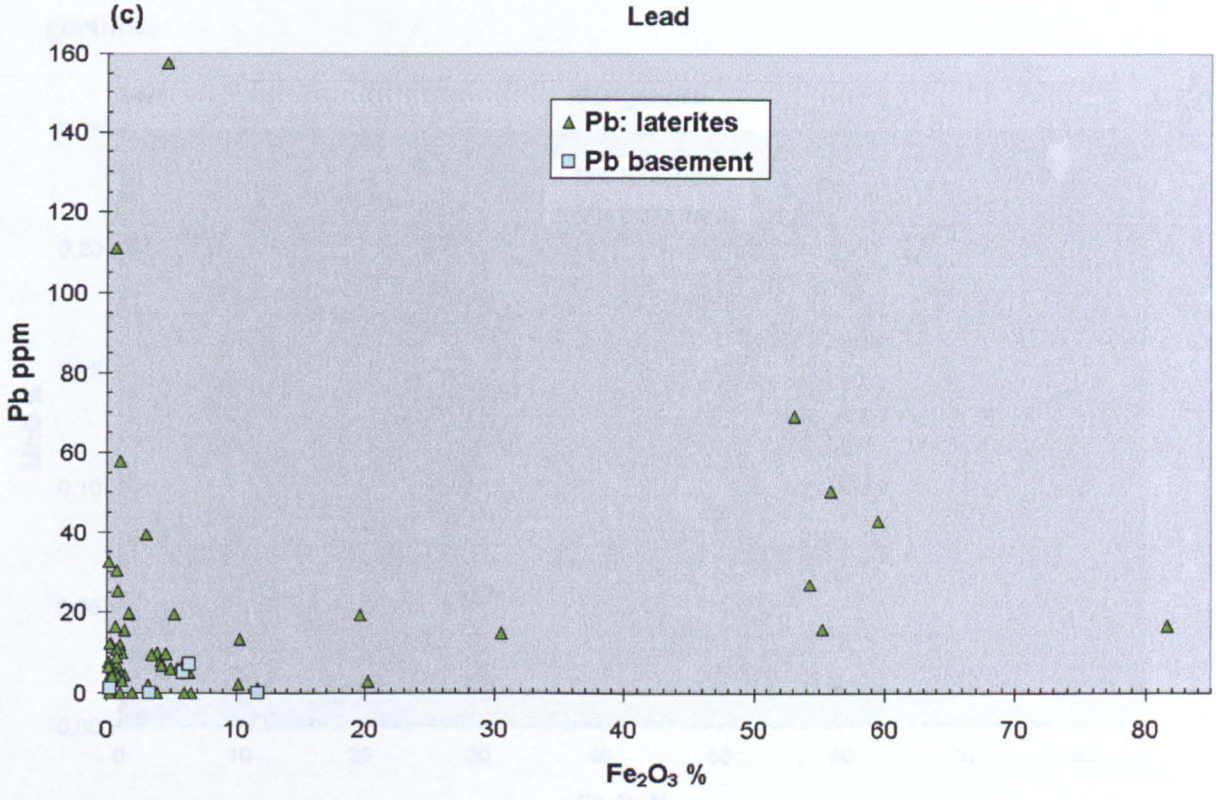


**Figure 2.52** (cont) (c) Pb vs $Fe_2O_3$

*Elements whose solubility is governed by oxidation state: Mn, Cr and V*

The variation in manganese (Mn) concentrations with iron in laterites (figure 2.53a) shows little sign that this element behaves in the same way as iron during lateritisation as ferricretes have low concentrations of this element as does the mottled zone. However, three samples from the mottled zone do show significantly higher Mn, which may be due to much later precipitation of pyrolusite ($MnO_2$) from modern groundwater: a suggestion supported by the observation that joint faces on building blocks made from the mottled-zone also show dendritic black patterns typical of recent pyrolusite deposition.

Chromium (Cr) and vanadium (V) are below detection limit in ferricretes but reach higher concentrations in mottled-zone samples than in fresh basement (figure

2.53b). This may be explained by shifts in their oxidation state during lateritization, although the mechanism is complex since there is no apparent correlation between oxidation of these elements and iron. Vanishingly low concentrations of these elements in ferricretes indicate that, unlike arsenic, they have not been adsorbed on goethite.

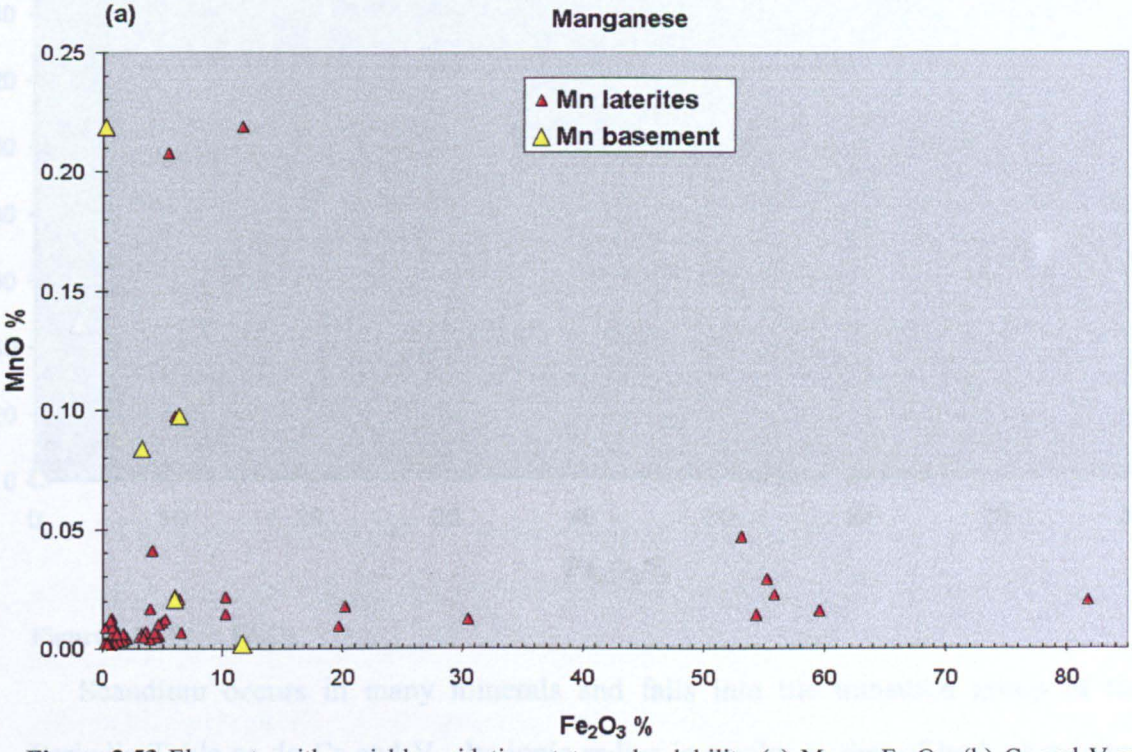


**Figure 2.53** Elements with variable oxidation state and solubility (a) Mn vs $Fe_2O_3$; (b) Cr and V vs $Fe_2O_3$

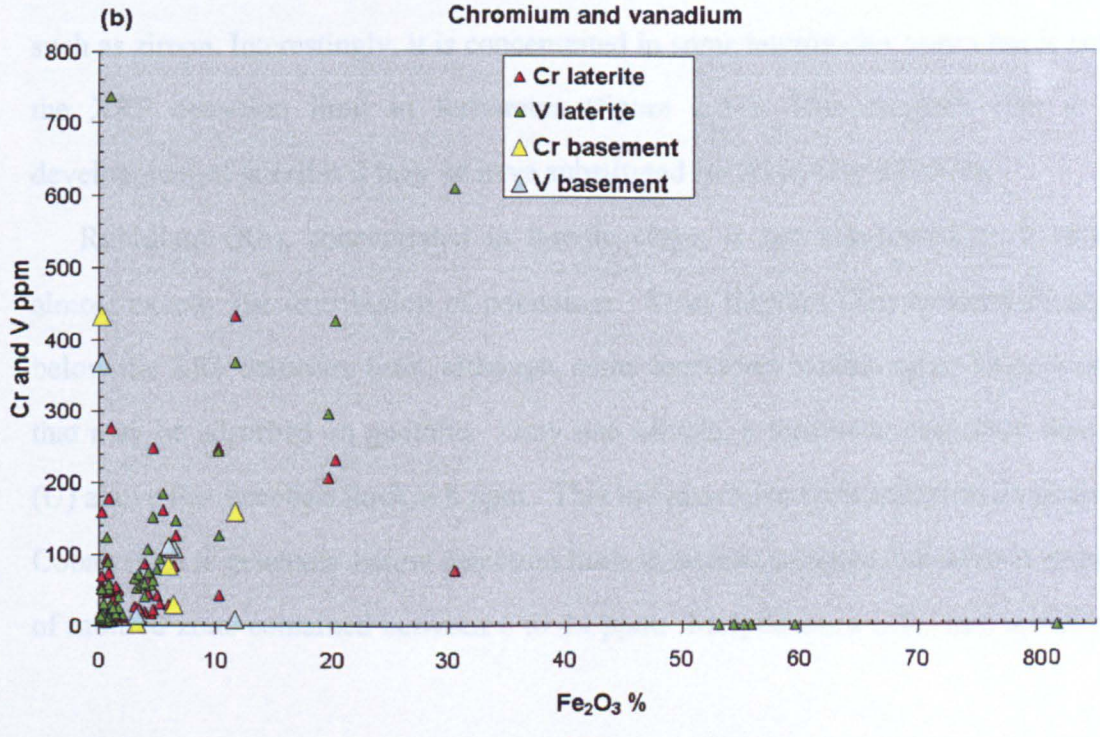

*Other elements*

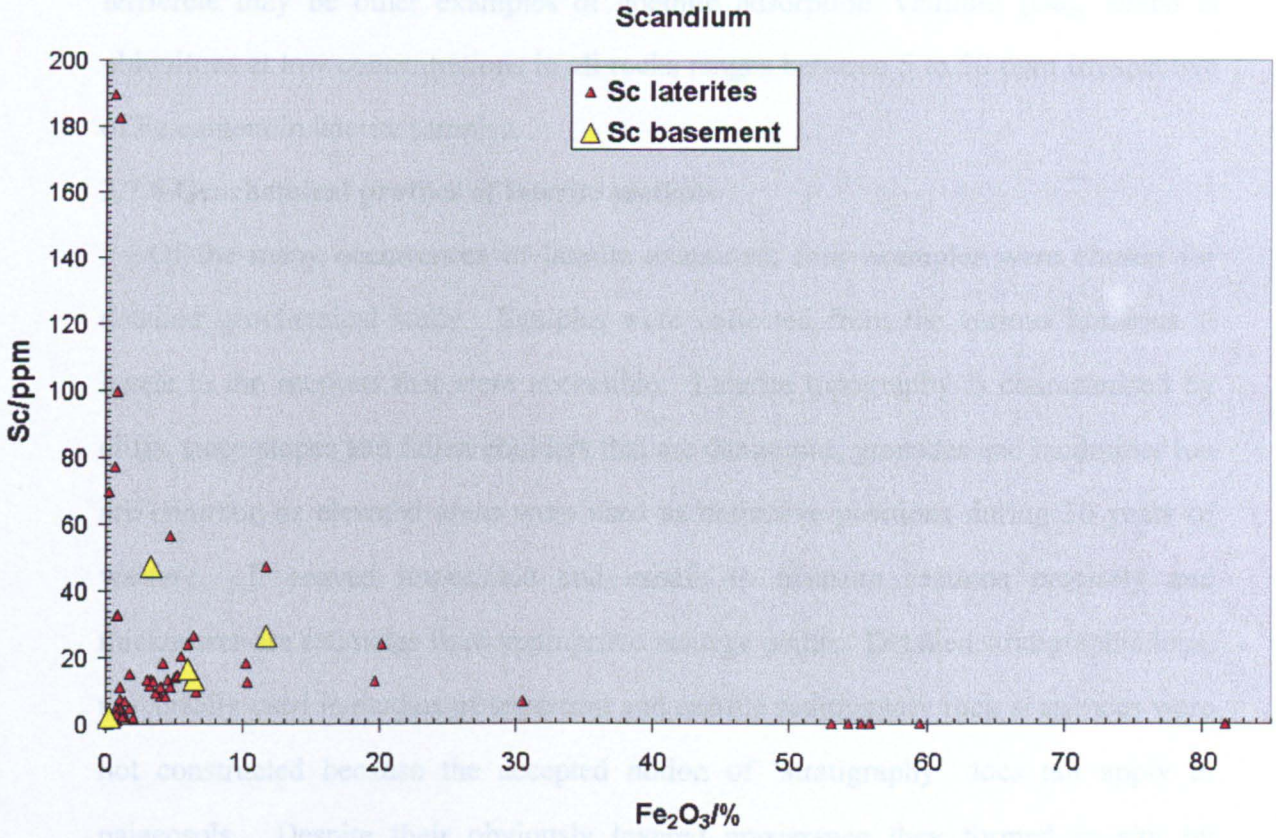


**Figure 2.54** Sc vs $Fe_2O_3$

Scandium occurs in many minerals and falls into the transition group of the Periodic Table as do Cr and V. Its ionic radius is similar to that of both aluminium (Al) and Y and may substitute for Al in minerals or follow Y in entering minerals such as zircon. Interestingly, it is concentrated in some laterite clay zones but is below the XRF detection limit in ferricretes (figure 2.54). This suggests that in the development of laterites it may be have substituted for Al in clay minerals.

Rubidium (Rb), concentrated in laterite clays, is not considered as it reflects almost exactly the distribution of potassium. Most thorium (Th) concentrations are below the XRF detection limit, although, some ferricretes contain up to 18 ppm of Th that may be adsorbed on goethite. Only one sample, a ferricrete, contained uranium (U) above the detection limit at 8 ppm. This too may have been adsorbed on goethite. Cobalt (Co) is generally below detection limit in laterite samples, but several samples of mottled zone contained between 6 to 44 ppm. Molybdenum (Mo) and nickel (Ni)

are only above their detection limits in some ferricretes. The affinity of Mo and Ni for ferricrete may be other examples of goethite adsorption. Gallium (Ga), which is ubiquitous at low concentrations in all rocks ranges between 5 to 50 ppm irrespective of Fe content in laterite samples.

### 2.7.4 Geochemical profiles of laterite sections

Of the many occurrences of laterite examined, four examples were chosen for detailed geochemical study. Samples were collected from the various horizons at levels in the sections that were accessible. Laterite topography is characterised by cliffs, steep slopes and fallen boulders that are dangerous; grenades and landmines too are common as elevated areas were used as defensive positions during 30 years of warfare. It proved impossible and unsafe to measure sections precisely and thicknesses are estimates from appropriate vantage points. Detailed stratigraphic logs, universally used in studies of terrestrial and marine sedimentary rock sequences were not constructed because the accepted notion of 'stratigraphy' does not apply to palaeosols. Despite their obviously layered appearance they formed *in situ* by processes of protracted chemical breakdown of the lithologies on which the palaeosols developed. Consequently, each small occurrence within a particular horizon results from fluctuating redox conditions and pH over millions and possibly tens of million years. As explained earlier the horizon with the longest history of geochemical and mineralogical change is that at the top of the profile - the ferricrete - whereas the clay horizon provides a minimum age for lateritisation (see Chapter 6). Each horizon, with the exception of the clay zone, is completely heterogeneous. Consequently it is impossible to representatively sample any but the clay zone. Despite this problem, sampling the most common material in each facies provides new insights into the processes operating during lateritisation that cause geochemical variations within the lateritic regolith.

*Four geochemically analysed laterite profiles*

- Wokerti (500799 E, 1675028 N, UTM Zone 37), developed on green, chloritic microdiorite at the margin of a large Neoproterozoic, post-tectonic granodiorite intrusion;
- North of Wokerti (497847 E, 1680879N, UTM Zone 37), developed on Neoproterozoic quartz schist;
- North of Shiketi (486600 E, 1676721 N, UTM Zone 37) developed on a deformed Neoproterozoic granodiorite;
- Himberti (471022 E, 1686953 N, UTM Zone 37), developed on highly deformed Neoproterozoic granodioritic gneiss.
- Except for those elements that are generally below XRF detection limits (Th, U, Co, and Mo) and Rb, Ni and Ga, Figures 2.55, 2.56 and 2.57 show how the analysed elements vary in each profile.

*Major elements (Si, Al, Fe)*

Relative to its concentration in fresh bedrock, $SiO_2$ is strongly depleted in the ferricretes of all four profiles. Except in the case of M358 (figure 2.57), the clay zone is also silica-poor. Both ferricrete and clays have lost silica by solution, presumably into alkaline groundwater as $SiO_2$ has low solubility in acid waters. High silica in the mottled zone suggests its re-precipitation in that horizon developed from earlier clay zone material during lateritisation. Profile M358 (figure 2.57), in which the clay zone is less pronounced, retains high concentrations of $SiO_2$ in the saprolite.

Alumina ($Al_2O_3$) increases in the more clay-rich areas of the profile, but remains roughly constant throughout the mottled zone and ferricrete. The exception is M361 (figure 2.56a).

As expected, $Fe_2O_3$ increases from roughly constant levels in the bedrock and lower profile to a distinct maximum in ferricretes.

*Soluble elements*

Of those elements most likely to be removed in solution during lateritisation (K, Na, Ca, Mg, Ba, Sr), $K_2O$, Ba and Sr are enriched relative to basement and the rest of

the laterite profile in most kaolinite-rich parts of the profiles. Again M361 (figure 2.56a) is the exception. In the most kaolinitic zones of M359, M136 and M358 (figures 2.55, 2.56 and 2.57) $K_2O$ and Ba correlate strongly with S, as expected, suggesting that they are probably held as sulfate in alunite and in traces of barite. The association with S applies to Sr in M359 and M136 but M358 is Sr-poor throughout the profile and is at a low concentration in fresh basement parent rock. The relationship between $K_2O$, Ba, Sr and S breaks down in M361; $K_2O$ is high in the mottled zone whereas Ba, Sr and S peak in the clay zone and are probably held in the sulfate mineral, barite. It is unclear why $K_2O$ in M361 deviates from its strong association with S in kaolinite-rich zones established in Figure 2.50e. The other soluble elements, Na, Ca and Mg, behave as expected in M359 and M358 (figures 2.55; 2.57), where high $Na_2O$, CaO and MgO in fresh basement or saprolite decline markedly in the laterite profile. In M361 (figure 2.56a), where fresh basement has low MgO, the mottled zone is highly enriched in MgO along with $K_2O$ and is equally difficult to explain.

*Elements in resistant minerals*

Elements that largely reside in resistant minor minerals (Zr, Nb, Y, P and Ti) are enriched in Horizon 5. However M136 is the only profile to show the expected enrichment of Zr, Nb, Y, and Ti in the ferricrete, whilst the other profiles exhibit haphazard distribution of Zr, Nb and Y relative to $Fe_2O_3$ in the laterites as a whole. This may be due to the difficulty of sampling the ferricretes, which are extremely heterogeneous mixtures of clay-rich iron oxy-hydroxide nodules with a matrix and irregularly distributed patches of granular debris. Nevertheless, $P_2O_5$ does follow the predicted trend in all the profiles, suggesting that apatite has accumulated with loss of mass during lateritisation. Using the ratio of $P_2O_5$ in ferricrete to that in the basement on which it developed as a measure of mass reduction during lateritisation gives values of 2.0, 5.5, 6.4 and 8.7 times for profiles M136, M358, M359 and M361 respectively. No clear trend of $P_2O_5$ increasing with $Fe_2O_3$ is shown by the laterite samples as a whole. That may be due to wide variation in $P_2O_5$ content in the 4

basement samples, from which the laterite profiles developed. $P_2O_5$ content ranges from 0.024 to 0.210 %.

*Elements adsorbed on goethite*

The elements As, Cu, Zn and Pb are representative of the many that goethite is capable of adsorbing from solution. All are expected to be abundant in ferricrete relative to basement.

Arsenic follows this association consistently in all four profiles. Its concentration increases by 42, 19, 86 and 235 times relative to its original concentration in basement samples in ferricretes M136, M358, M359 and M361 respectively. The maximum As concentration of 346 ppm in ferricrete M359N is more than 200 times greater than its average concentration in crustal rocks, so ferricrete potentially poses a health hazard, should arsenic be leached from it into groundwater (Chapter 8). Copper, Zn and Pb show concentrations above those of basement in ferricretes, as the model for goethite adsorption suggests they might. However, both Cu and Pb show increased concentrations in M359 and M136 clay zones, which contain very low $Fe_2O_3$.

None of the ferricretes show high Cr, V or Mo, which may be adsorbed on goethite as complex ions (e.g. $CrO_4^{2-}$). The ferricrete capping profile M361 contains 1364 ppm Ni, massively enriched over its concentration (4 ppm) in the basement on which it developed. Conversely, other analysed ferricretes contain far less Ni than do the basement rocks from which they developed. Nickel commonly enters sulphides and may have been released to surface- and groundwaters during lateritisation to become adsorbed locally on goethite.

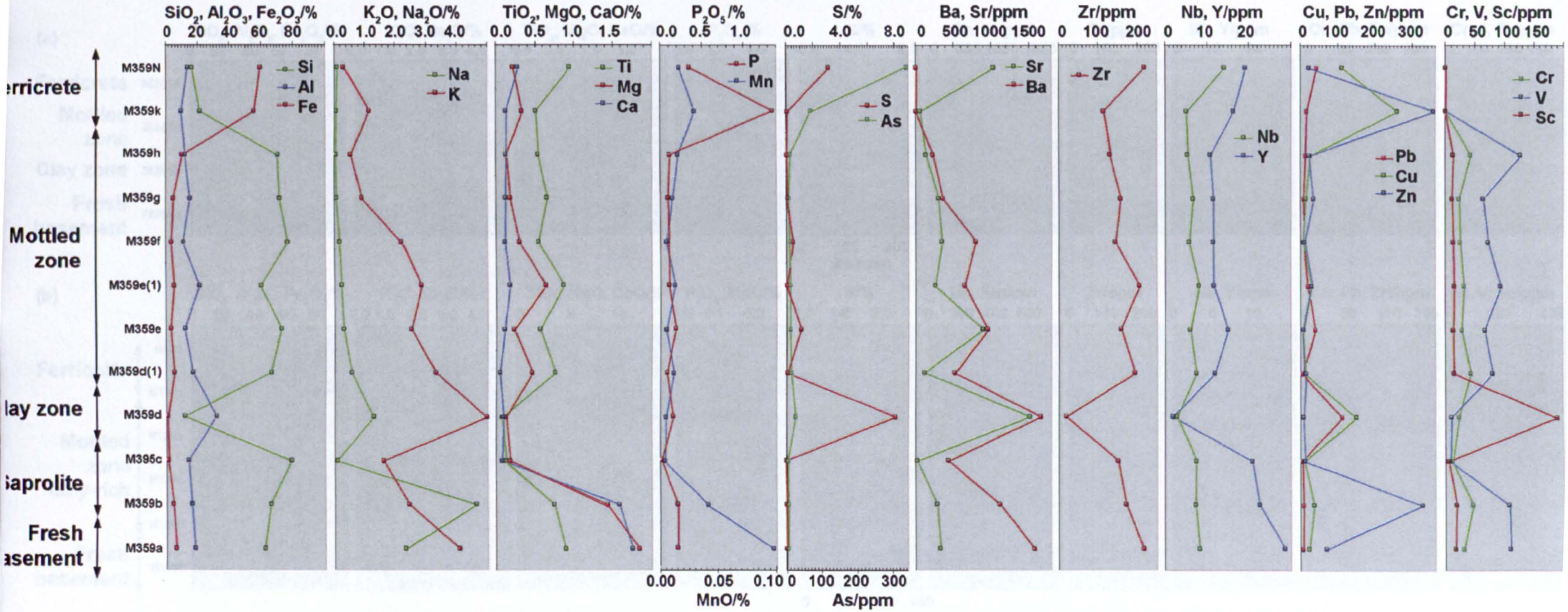


**Figure 2.55** Detailed geochemical profile through complete laterite section M359 (~35m thick – not to scale) at Wokerti (500799 E, 1675028 N, UTM Zone 37). Basement is green, chloritic microdiorite, separated by 4m of saprolite with core stones from an 8m thick pure white, kaolinitic clay zone with saline efflorescences. 15-20m of mottled zone shows evidence for repeated cycles of leaching under reducing conditions, precipitation of goethite under oxidising conditions, desiccation (hematite replacing goethite) and volume reduction that formed cavities filled with clay fragments in goethitic matrix. Iron content increases upwards in the mottled zone, which is sharply overlain by 2m of coarse, nodular ferricrete

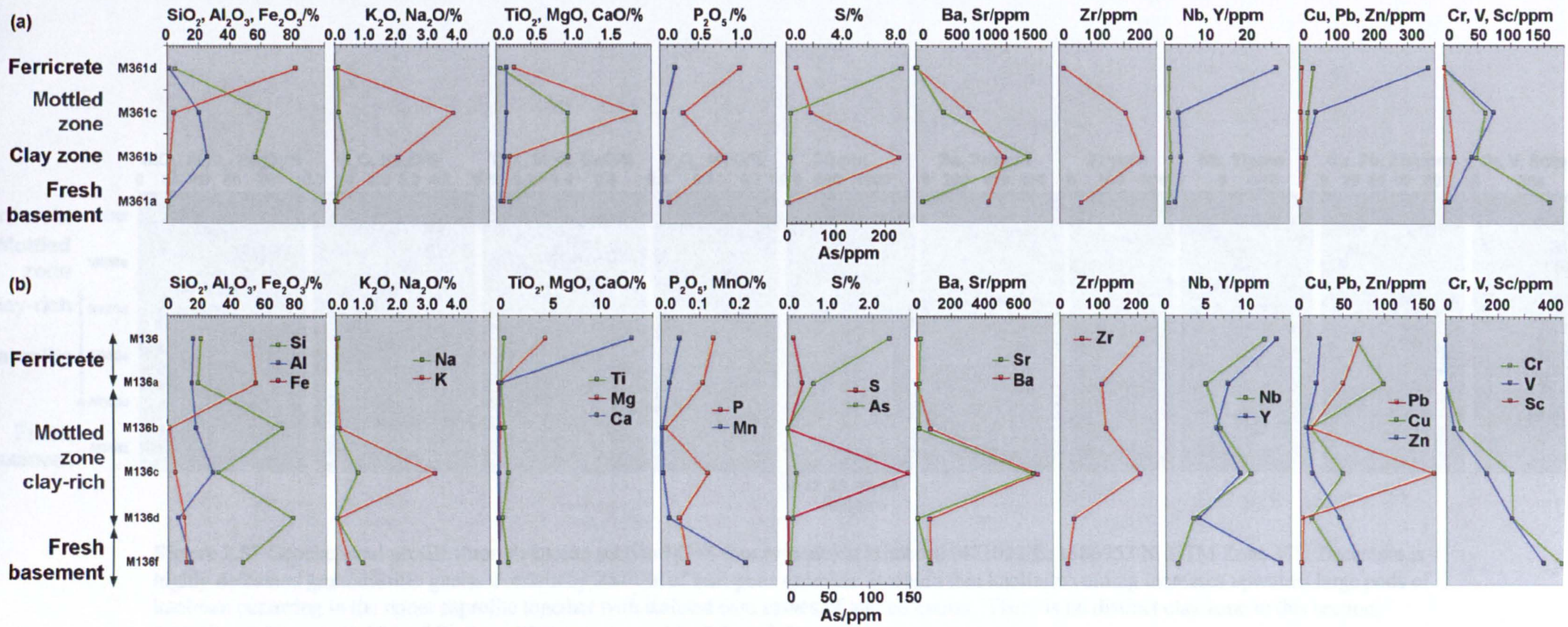


**Figure 2.56**(a) Geochemical profile through laterite section M361 (not to scale) north of Wokerti (497847 E, 1680879N, UTM Zone 37). Basement is quartz schist, overlain by 1.5m of clay zone with small goethitic mottles, 2m or clay-rich mottled zone capped by 1m of ferricrete. (b) Laterite section M136 (not to scale) north of Shiketi (486600 E, 1676721 N, UTM Zone 37). Basement is deformed granodiorite, with 2m of saprolite with cherty patches overlain by 3m of mottled zone (lower part clay-rich, upper part containing patches of chert or chalcedony),and 1.5m of ferricrete

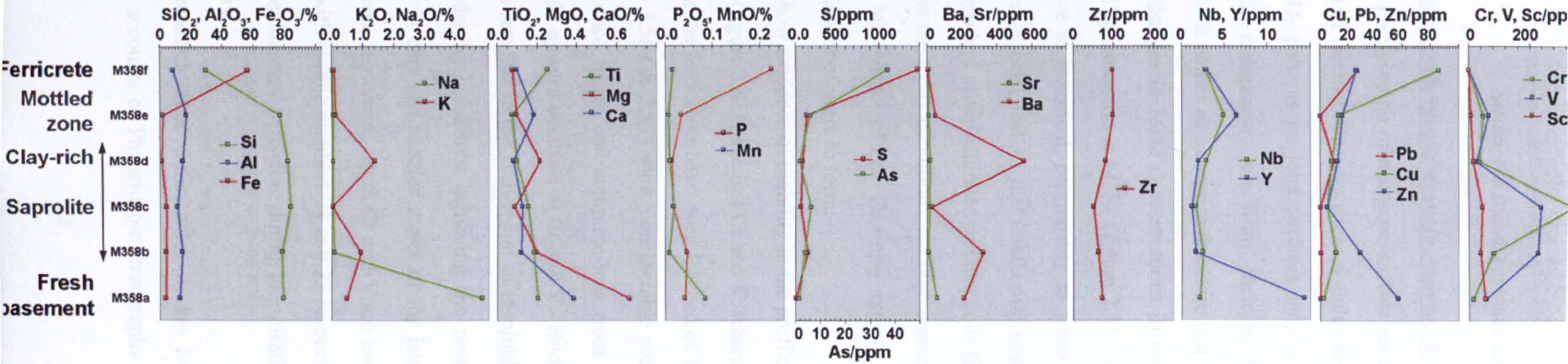


**Figure 2.57** Geochemical profile through laterite section M358 (not to scale) at Himberti (471022 E, 1686953 N, UTM Zone 37). Basement is highly deformed granodioritic gneiss overlain by 25-30m of iron-poor saprolite in which thin kaolinite veining increases upwards, large pods of kaolinite occurring in the upper saprolite together with isolated core stones of altered gneiss. There is no distinct clay zone in this section, saprolite giving way to 15m of flinty mottled zone capped by 0.5m of clay-rich ferricrete

*Common elements whose solubility is strongly governed by oxidation state*

The widespread precipitation of manganese oxide coatings on pebbles in modern lakes, the formation of ocean-floor manganese nodules and the common presence of black dendritic $MnO_2$ patterns on joint surfaces indicate how subtle variations in redox conditions shift manganese ions from their insoluble to soluble oxidation states and *vice versa*. It comes as a surprise therefore that three of the laterite profiles show virtually no changes in MnO concentrations in any horizon relative to their parent substrates. The exception is M359 (figure 2.55), where there has been a net loss of MnO relative to basement, presumably to water with reducing properties, which itself must have been lost to the weathering system. Experiments on the solubility of Mn in modern water-saturated tropical soils (Porter *et al.* 2004; Cornu *et al.* 2009) suggest that the redox conditions and high amounts of organic matter allow slow dissolution of Mn but not of Fe. This may explain the loss of Mn throughout laterites that took millions of years to form.

Both Cr and V show evidence of mobility in the profiles. The upper saprolite and clay zones in M359 (figure 2.55) have lost Cr and V, whereas there have been gains in the mottled zone but the ferricretes have been leached of both elements. Both M361 and M 358 (figures 2.56a & 2.57) show considerable concentration of Cr and V in their clay - and mottled facies and complete loss from ferricretes. M136 (figure 2.56b) shows a steady upward decrease in Cr and V. Rock *et al.* (2001) showed that oxidising conditions resulted in the conversion of insoluble Cr(III) to soluble Cr(VI) in Cr-rich soils, reducing conditions achieving the reverse. This would explain accumulation of Cr in clay and mottled zones of the laterite profile and its almost complete removal from ferricretes. Both Cr and V are transition metals (adjacent on the Periodic Table with atomic numbers 24 and 23 respectively), so it is unsurprising that they show almost identical behaviour during lateritisation.

### 2.7.5 Closing remark

During initial research three deficiencies in the literature became apparent; contrary and vague accounts of Phanerozoic stratigraphy in the study area; unclear

concepts of what constitutes a laterite and confusion regarding the planation history of the African continent. All three topics are reviewed in this study for the sake of a consistent approach. Chapter 2 is a critical review of stratigraphy in Eritrea and northern Ethiopia. It defines laterites and, equally important, illustrates what they are not. There is no evidence in the region to suggest that laterites are somehow distinct from ferricretes (Bitom *et al.* 2003; Widdowson 2007; Ollier & Sheth 2008; Tanner & Khalifa 2010). Although vestiges o f an earlier landscape and more akin to the rocks

**Figure 2. 58** A typical Eritrean road - weathered ferricrete and mottled zone on a clay horizon

on Mars in colour and composition (figures 2.58, 3.24) understanding their geological origin is dependent on many disciplines (MacDougal 2008). An understanding of the mineral distribution within the laterite profile allows for a RS strategy which can be used to facilitate field observation and discriminate and map the facies that distinguish laterites from basement rocks so that a clearer picture emerges of their nature and distribution. Moreover, the spin-off of regionally identifying laterites (Chapter 4) and determining their geochemistry proves useful when assessing their effect on the local

population, environment and regional geology (Chapter 8). Evidence for their palaeo-weathering history and geochronology in the context of regional Tertiary volcanism and tectonics (Chapter 5, 6) help resolve anomalies and contradictions in NE African geological literature. The chapter provides a basis for adding to Lester King's account (1948, 1967) of African planation and Mesozoic to Cenozoic weathering history (Chapter 7) and the necessary data to access the scientific and socio-economic impact of this research. Armed with remote sensing, petrographic, geochemical and field data, a regional map of laterite facies can be constructed with confidence (see Chapter 4) facilitating useful and rigorous investigation of laterite regolith, the object of this study.

CHAPTER THREE

# Methodology

Since the 1980s image processing methods or techniques have been developed for the analysis of remote sensing (RS) data: most were developed for broad-band data but since the advent of hyperspectral data more complex analytical techniques have been introduced. All the methods in use and their underlying theories are discussed in detail in the scientific literature (e.g. Vincent 1997). This research considers the effectiveness of the simpler methods before testing more complex ones. Until this study, no regional mapping of different laterite facies, using remote sensing, had been carried out despite the distinctive spectral characteristics of their mineralogy. Methods of particular geological relevance to this project are emphasised and their relative usefulness accessed. The chapter describes the main research methods carried out and implemented in strategies developed in subsequent chapters to achieve specific results. Image processing methodologies primarily covering RS are discussed initially followed by a brief outline of the $^{40}Ar/^{39}Ar$ dating method used for geochronological work in this research.

## 3.1 Standard image processing methods

The primary objective when selecting image processing methods was to produce informative images in order to extract qualitative and quantitative geological information from multispectral (see Drury 2001; Vincent 1997) and hyperspectral data (see Cloutis 1996) respectively, for simple and for effective visual image interpretation. A variety of methods were applied to RS data to show how laterites could be detected, discriminated and mapped using the distinctive spectral characteristics of their mineralogy.

### 3.1.1 Spectra and bands

As electromagnetic waves interact with materials at the Earth's surface, their

reflected radiance gives important information (a spectral response with identifying characteristics) about the mineral composition of exposed rocks and soils. Particular materials absorb energy in certain wavebands. And it is the reflected spectrum (Drury 1993; Spatz 1997; Vincent 1997) of each mineral detected by a remote sensing instrument, which enables materials to be identified or discriminated on an image. This unique set of *spectral characteristics* or spectral response is a 'spectral signature' (figure 3.1). All materials have a spectral signature in much the same way as a person has an identifying fingerprint. Spectral signatures are used to isolate laterite minerals in the test area, in relation to the number and widths of individual bands.

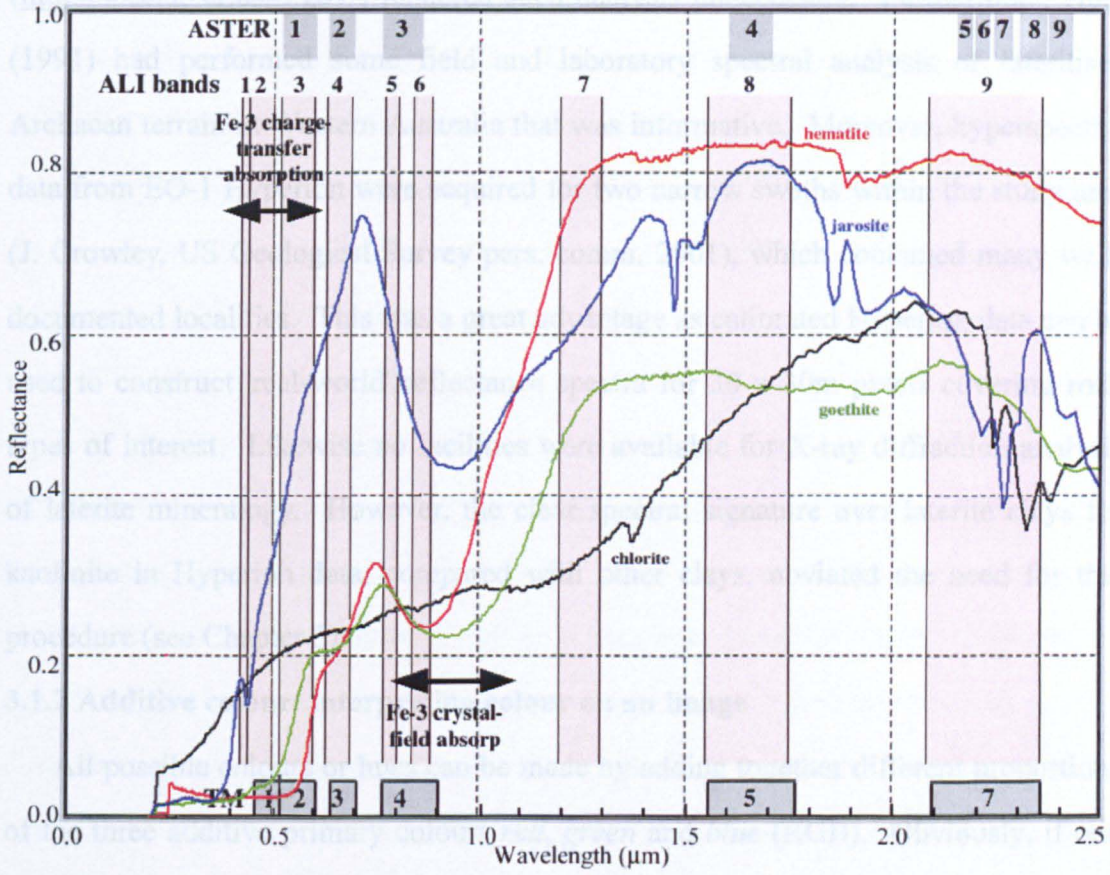


**Figure 3.1** Reflectance spectra of some iron-rich minerals in the visible and near-infrared (VNIR) and short-wave infrared (SWIR). Band widths are shown for three orbital imaging systems used in this study: Advanced Spaceborne Thermal Emission and Reflection Radiometer (ASTER); Advanced Land Imager (ALI); Landsat Thematic Mapper (TM). Spectral data from the US Geological Survey Spectral Library

A *band* (Drury 1987; Crippen 1989; Abrams *et* al. 2002; Rowan & Mars 2002), sometimes referred to a channel (Hunt *et al.* 1986; Hubbard *et al.* 2003), in remote sensing is the range of wavelengths recorded by one detector to form an image (figure

3.1). All digital remote sensing data comes as data files, arranged in a variety of digital formats, for various numbers of bands for ranges of wavelengths in the electromagnetic spectrum. The range of wavelengths covered by a single band (see figure 3.1) varies from around 0.07 - 0.27 micrometres (μm) with Landsat TM to 0.01μm with hyperspectral data (e.g. airborne AVIRIS and HyMap not covered in this work and EO-1 Hyperion which is).

Spectral analysis of laterite samples was not done because of the difficulty of obtaining a field or lab spectrometer. However, the mineralogical simplicity of laterites and the abundance of spectra available from the USGS Spectral Laboratory (http://speclab.cr.usgs.gov/) rendered such analysis unnecessary. Furthermore, Hunt (1991) had performed some field and laboratory spectral analysis of lateritised Archaean terrain in Western Australia that was informative. Moreover, hyperspectral data from EO-1 Hyperion were acquired for two narrow swaths within the study area (J. Crowley, US Geological Survey pers. comm. 2001), which contained many well-documented localities. This was a great advantage as calibrated Hyperion data can be used to construct 'real-world' reflectance spectra for 30 x 30m pixels covering rock types of interest. Likewise no facilities were available for X-ray diffraction analysis of laterite mineralogy. However, the clear spectral signature over laterite clays for kaolinite in Hyperion data, compared with other clays, obviated the need for this procedure (see Chapter 5).

### 3.1.2 Additive colour: interpreting colour on an image

All possible colours or hues can be made by adding together different proportions of the three additive primary colours *red*, *green* and *blue* (RGB). Obviously, if one component is high and the other two are low, the high primary colour will show up. Equal proportions of R, G & B give no colour at all. If all are very high, then the result is white. Intermediate values for all produce a grey, and very low values of all make a dark grey to black. If red and green are both high, but the blue component is low, the result is yellow. If red and blue are high but green is low, the result is magenta. If green and blue are high and red is low, the result is cyan or sky-blue.

These are the simplest cases. Other colours such as orange, browns and purples are more complex mixtures of all three primary colours with varying brightnesses.

### 3.1.3 Multispectral data: experimentation versus a knowledge-based technique

Experimenting with multispectral data characterised early multispectral RS. All possible combinations of available bands and their permutations in threes as red, green, blue (RGB) were examined for a scene when the number of bands acquired by a sensor was limited. For example with 3 bands (SPOT-1 data), there is only 1 combination, but there are 6 possible RGB permutations or 3! differently coloured images using the same data (123, 231, 312, 132, 321 and 213 as RGB). The greater the number of bands, the more complicated the situation. Therefore, with 4 bands (Landsat MSS data; see Rothery 1982, 1984) there are 4 combinations of 3 bands. In general, the number of combinations of n bands in groups of 3 is: $n!/(n-3)!3! = n!/6(n-3)!$ so for the 6 reflected bands of Landsat TM and ETM+, the number of 3-band combinations is 20 and for the 9 reflected bands of ASTER 84. Taking the 6 possible RGB permutations of one set of three bands, 120 possible colour images are obtained using TM and 504 using ASTER.

This simple "experimentation" method becomes increasingly unwieldy as the number of bands increases; a problem exacerbated by adding all possible ratios between available bands and all the principal components derived from the data by re-plotting the n-dimensional data 'cloud' on n axes at right angles (Drury 2001). More complex "experimentation" soon makes pure empiricism inefficient, time consuming, directionless and at worst unworkable. Such a method would be essential if nothing was known about the way radiation interacts with materials on the Earth's surface. However, this very basic technique (and some still find a place for it) has been superseded by knowledge-based analytical techniques using RS data adopted in this thesis, based on spectral properties of specific minerals found in laterites facies (e.g. Crowley *et al.* 1989; Rowan & Mars 2003).

Given the spectral features of a particular material and multispectral data, it is possible to select bands that can be expected to distinguish one material from another.

It is useful to consider the mineralogical make-up of a rock in terms of its constituent minerals, which are general referred to in remote sensing parlance as *end members* (it is important to note that, in practice, vegetation is often an end member in surface materials as well as minerals). For instance, in a weathered iron-rich schist containing sulfides there may be 4 end members in the soil above it: chlorite; hematite, goethite and jarosite ($KFe_3^{3+}(OH)_6(SO_4)_2$). The spectrum of jarosite compared with the other three iron-rich minerals on Figure 3.1 suggests that using TM bands 2, 4 and 7 should distinguish it clearly from the others. Image processing methods enable a user to predict the range of colours that a particular material will show in an RGB image using the simple principles of additive colour theory (Section 3.1.2). Surfaces are explored for the presence of specific materials in sufficient abundance to stand out spectrally. The method is context-based and in this study dependent on the presence or absence of laterites and mineral variations between their different facies. Field observations are then used to validate image data interpretation.

### 3.1.4 3-band false-colour composites

The method employed, simply involves using spectral features of the main laterite minerals to select TM or ASTER band combinations as red (R) green (G) and blue (B) components of a colour image to highlight or best emphasise each facies on the image. For layman and expert alike, the most informative, visually pleasing and readily understood colour combinations are 3-band composites where the arrangement of spectral bands determines the perceived colour. If one component is high and the other two low, the high primary colour shows up whereas if there are high values for two primary colours and a low value for the third component, hues (a characteristic of the colour of an image pixel which is the measure of the relative amount of red, green and blue that contribute to colour (Drury 2001; Vincent 1997) are generated at different intensities, dependant on the assignment of bands to RGB. Combined with field evidence, 3-band false-colour composites are a reliable and simple method of isolating the clay horizon.

### 3.1.5 Band ratios

The band-ratioing method (Crippen 1998), emphasises spectral contrast between different facies. Using reference spectra, numerator and denominator bands can be selected to highlight subtle mineralogical differences on the surface imaged. For instance, from figure 3.1, the ratio between TM bands 7 and 5 (usually represented as 7/5) would be much lower for jarosite than for hematite or goethite, but possibly similar to that for chlorite, jarosite and chlorite both absorbing strongly in band 7. Band-ratios displayed as RGB colour combinations may more effectively detect mineral mixtures than would 3-band colour composites. This is because band-ratios use two bands that express differences in reflected radiance from surfaces composed of pure end members more strongly (Drury & Hunt 1989). So that when one band is divided by the other, the value of the ratio for one end member is ideally different from all the others. No single band-ratio separates one end member from the rest, as in the case of jarosite above, except the Landsat TM band-ratio 4/3 for green vegetation, so several ratios have to be combined to map lithologies. Figure 3.1 shows that this particular method is useful for distinguishing between iron rich horizons and is used in this work to separate the mottled zone from the ferricrete in laterites.

### 3.1.6 Principal component analysis (PCA)

The use of PCA 'is an analytical technique based on the transformation of spectral axes such that spectral variability is maximised' (Cloutis 1995). It renders highly correlated reflected data in a decorrelated form (Soha & Schwartz 1978) so that combinations in RGB of those PCs with high loadings for different groups of bands (related to different surface types), separate otherwise subtle spectral variations in vivid colours. Full statistical details can be found in any standard text (e.g. Drury 2001; Vincent 1997).

PCAs, by definition, rearrange the 6-band data of Landsat TM into 6 new, completely uncorrelated variables using a statistical analysis of the means of all bands and the covariances between all the bands in pairs. (Variance of a single band

expresses the spread of DN either side of the mean value; covariance is the variation together of two bands - a positive value indicates some degree of correlation, while a negative value indicates anti-correlation). The statistics that drive the PCA are in a covariance matrix for all the bands arranged in pairs. The simplest case involves just two bands (figure 3.2).

The first step in this method is to set the origin of the distribution to the point defined by the mean values of both bands (all bands in 6-band case) (figure 3.2a), i.e. the means are all set to zero. Using the covariance statistics between the two bands, a line of best fit through this origin and the cloud of data is calculated (figure 3.2b red line). By definition this is the line that encompasses the greatest variance between the bands and expresses the strong correlation among all the bands. It is the principle axis or the first principal component (PC1) of the data distribution, along which there is the greatest spread of information. All points can be projected at right angles onto this axis, but that still leaves some covariance unaccounted for. A second axis at right angles to the first one (figure 3.2b green line) consumes this remaining covariance, again by projection down right angles to this second principle component (PC2). Because this part of the covariance in PC2 could not be projected onto PC1, the values along it for each pixel bear no correlation with those along PC1. They are decorrelated and represent the "oddest" pixels in the 2-band plot.

The PC1 axis is at an angle to the original band axes and the final step is a rotation of the two PC axes so that values for each can be expressed as numbers in a new 2-D space (figure 3.2c). Roughly half the values in each PC will have positive numbers and the rest negative numbers. They can be used like that, but usually the range is converted to a positive 8-bit range of DN from 0 to 255.

For the 6-band case, covariance remains after PC2 is created and that is consumed progressively by further axes at right angles to all the others. A 6-band input always has a 6 PC output, and the higher the order of a PC the less a fraction of the variance it will contain. With increasing order the more 'odd' the information in a PC becomes and the less organised. Being decorrelated, combining PCs in threes as RGB images

guarantees brightly coloured images, but understanding them is difficult. This is explained by the eigenvector matrix, which shows the relative contribution or weighting of each band to each of the PCs that occurred during the projection process.

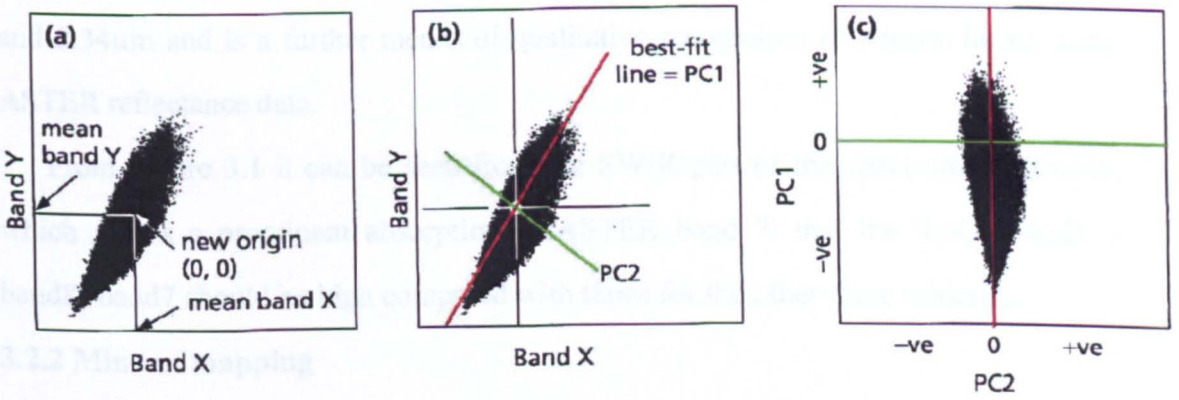


**Figure 3.2** The principle of PCA (for 2 bands). Note that the original data are highly correlated (a), whereas when rearranged on principal component axes (c) they are decorrelated

Bands used for PCA can also be restricted to those that might be affected by a particular end member (Crosta & Moore1989; Loughlin 1991; de Sousa & Drury 1998), hence the Fe-oriented and OH-oriented directed PCA approach. Unfortunately, PCAs are scene- and season-dependent – statistics vary a lot from scene to scene and also according to the effect of seasonal vegetation - and their values cannot be correlated quantitatively from one area to another. So, conventional principal component analyses are used in this study only qualitatively to discriminate urban areas (Chapters 4 & 8) and pure kaolinites as it is important to know where population areas occur on laterite terrain.

## 3.2 Advanced image-processing methods

More complex techniques, based on similar mineral-spectra considerations to those discussed in section 3.1 are now discussed the context of the thesis.

### 3.2.1 Relative band depth (RBD) method (Crowley *et al.* 1989)

This extension of the qualitative band ratio method expresses the magnitude of mineralogically distinctive absorption features contained in a particular band (band A) relative to bands unaffected by the feature, i.e. on either 'shoulder' of the feature

(bands $S_L$ and $S_R$):

Therefore, relative band depth or RBD = $(S_L + S_R)/A$.

The method largely depends on narrow bands that subdivide the short-wave infrared (SWIR) region that is covered by 5 ASTER bands and Hyperion bands between 2.1 and 2.34μm and is a further means of qualitative recognition of laterite facies using ASTER reflectance data.

From Figure 3.1 it can be seen from the SWIR part of the spectrum of jarosite, which shows a prominent absorption in ASTER band 7, that the RBD (band5 + band8)/band7 should be high compared with those for the other three minerals.

### 3.2.2 Mineral mapping

This semi-quantitative approach uses several techniques to establish the occurrence of minerals by assessing the closeness of pixel spectra shapes to those of pure minerals. The method uses three algorithms, originally developed for hyperspectral data, which describe spectral shapes mathematically, thereby allowing the spectra of unknown materials to be matched with library spectra (see Cloutis 1996; Smith 2001). In principle these methods should also be useful with ASTER's 5 SWIR bands that cover distinguishing spectral features of many minerals. The entire available spectral range can be used, though in practice better results emerge by comparing parts of the range that contain distinct spectral features of the materials of interest.

*Matched filtering (MF)*

The target for matching in this method is a lab spectrum from a pure sample of a particular mineral resampled to match the band-widths and band centres of bands deployed by a remote sensing instrument. The spectrum of each pixel in an image is assumed to be a linear mixture of the target spectrum (from 0 to 100%) with spectra of other materials that make up the surface contained within a pixel. Such mixing could be within one dominant material sampled by a pixel, or amongst several small areas of different materials. The process identifies what proportion (if any) of each composite pixel spectrum could be produced by the target spectrum (end member). A

good match yields a large *positive* output value, while poor matches yield low positive or even negative values.

*Cross-correlation (XC)*

This analytical technique calculates the correlation coefficient between the spectrum from each image pixel and that of a target mineral spectrum – i.e. spectra are treated as linear, one-dimensional waveforms – to estimate the degree of similarity in shape. A spectrum completely dissimilar to that of the target has a value of 0.0, whereas an identical pixel yields a value of 1.0.

*Spectral angle mapping (SAM)*

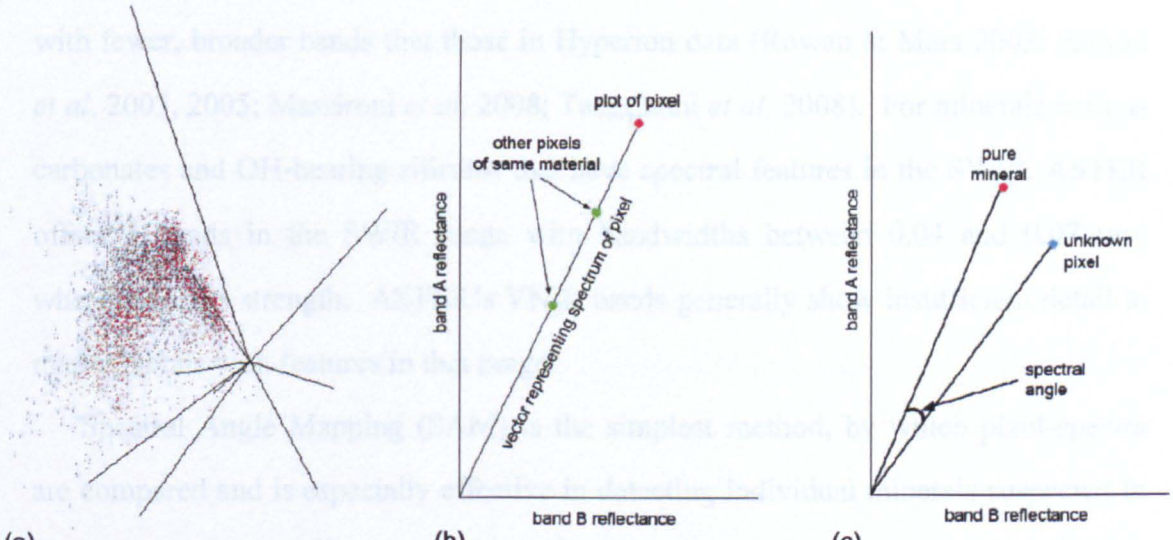


**Figure 3.3** Principle of the Spectral Angle Mapper: (a) simulation of many pixels plotted in 9-dimensional space; (b) two-band plot of spectral data for pixels containing a pure mineral; (c) the spectral angle between an unknown pixel and a pure mineral

Spectral angle mapping treats the data in target spectra and pixel spectra as plots that define a point in n-dimensional spectral space (figure 3.3a). Each point is the end of a line or vector through n-dimensional space that begins at the origin of the co-ordinate system. The angle between such a line vector for an unknown pixel and that of a target material is a measure of the similarity of the unknown spectrum to that of the target material: *smaller* spectral angles indicate greater similarity. Figure 3.3b shows the case for two bands and shows pixels of a pure mineral with different overall brightness. Figure 3.3c shows a pixel whose mineralogy is unknown compared

with a pure mineral, and the spectral angle between each mineral's vector.

Figure 3.3b shows that this method is insensitive to differences in average brightness between spectra that may be due to topographic or instrumental effects, because these factors change the length of a spectral vector - but not its orientation. A threshold for the spectral angle value is generally used and highlighted pixels with lower values are most likely to match the target spectrum. It is common practice to use the same threshold for each target spectrum, so that all results have comparable significance.

Several authors have discussed the use of hyperspectral analysis tools, such as Spectral Angle Mapper, for the detection of spectrally distinctive minerals using data with fewer, broader bands that those in Hyperion data (Rowan & Mars 2003; Rowan *et al.* 2003, 2005; Massironi *et al.* 2008; Tangestani *et al.* 2008). For minerals such as carbonates and OH-bearing silicates that have spectral features in the SWIR, ASTER offers 5 bands in the SWIR range with bandwidths between 0.04 and 0.07 μm, wherein lies its strength. ASTER's VNIR bands generally show insufficient detail to map minerals with features in that range.

Spectral Angle Mapping (SAM) is the simplest method, by which pixel-spectra are compared and is especially effective in detecting individual minerals suspected in various rocks. It also illustrates some points about mineral mapping in general:
SAM processing is initiated by choosing one of the following *target spectra*:

- the lab spectrum of a pure mineral – produced under controlled conditions;
- a spectrum produced by mathematically mixing proportions of the lab spectra of two or more minerals – potentially useful for rocks or soils with simple mineralogy;
- the field spectrum of a specific rock type or soil – 'ground truth' in the sense that the analysed material can be known in every detail although very small areas do not represent large remotely sensed pixels that are mixtures of materials;
- a spectrum derived from a pixel of known mineralogical composition by the imaging system itself – 'ground truth' in the sense that the pixel's actual

composition is known and it has the same area as other pixels, thereby allowing comparison of like-with-like – although 'pure' pixels are uncommon

Ensuring like-with-like comparison between a target spectrum and that of an unknown pixel requires the matching of the spectral resolution of the target spectrum (the number of bands, their central wavelengths and wavelength range) to that captured by the imaging system. This is achieved by *resampling* the target spectrum to the wavelength ranges of each band used by the remote sensing instrument. Effectively, resampling averages the target's reflectance only over the wavelength range covered by each band used by the instrument, discarding the rest of the information in the target spectrum.

In practice, spectral angle mapping involves several processing steps:

- *Selection of a suitable target spectru* (see above).
- *Selection and radiometric correction of appropriate data.* In the case of Hyperion and ALI data, pixel radiance values have to be converted to reflectance to remove atmospheric effects and those of the solar spectrum (ASTER reflectance data are readily available from the suppliers). One method is to calibrate the data relative to spectrally featureless or 'flat' materials that occur in the scene. A common choice, where available, is evaporitic halite (NaCl) in dried lake beds or areas of pure quartz. Neither of these is present in the area covered by Hyperion data available for this study so the calibration method known as *Equal Area Normalisation* (see below) was used.
- *Selection of appropriate bands.*
- *Running spectral angle mapper software and analysing output.* The method of calibration of bands considered and the suitably resampled reflectance spectrum of the mineral of interest are specified as parameters to be applied by the software (within TNTmips). The output is a 32-bit, floating-point image file of spectral angle saved with an appropriate name. A grey-tone or colour density-sliced image of this can then be compared with an RGB image that is useful in qualitative mapping of laterite facies.

- The next step is to choose a value for spectral angle. This upper limit is a threshold value, below which pixels can confidently be assumed to contain high proportions of the chosen mineral. The choice of this threshold depends partly on the shape of the histogram of spectral angle. A high proportion of almost pure pixels is signified by a 'tail' at low values that is distinct from the main spread of values elsewhere in the scene - the peak in the histogram - and from a high-value 'tail' of pixels that are most unlike the chosen mineral (figure 3.4). The other criterion is that pixels with values below the threshold in a well-known area make geological 'sense', for instance where a laterite clay zone is known to be present. The software produces some misdetection due to areas of superficial sediment derived from laterite, dust that coats vegetation, small outliers equivalent to only a few pixels and noise in the data. Misdetected pixels are generally scattered in a 'salt and pepper' fashion and can be reduced by lowering the threshold or by post-processing filters. Small areas of properly detected pixels usually form coherent clusters.

There are other techniques to spectrally oriented mineral mapping and variants of the three outlined above. Use of all of them for a range of minerals can lead to confusion, even for those experienced in this field. Only the three cases described above are used in this study in order to determine the most effective method. The mineral spectra illustrated in Figure 3.5 are sufficiently different to expect a useful outcome from such data 'mining'. Yet it has to be remembered that natural surfaces are almost always complex mixtures of many minerals that contribute to the spectrum of a pixel; pure pixels are the exception rather than the rule. In certain cases this 'mixed pixel' effect can be addressed by creating spectra of mineral composites as targets or by using the spectra of pixels with known mineralogy.

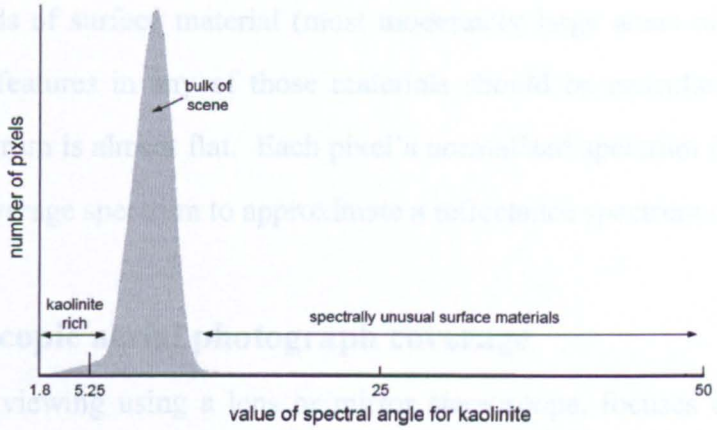


**Figure 3.4** Histogram of spectral angle values from Figure 4.21, indicating the main features of interest

### 3.2.3 Calibration to reflectance by Equal Area Normalisation

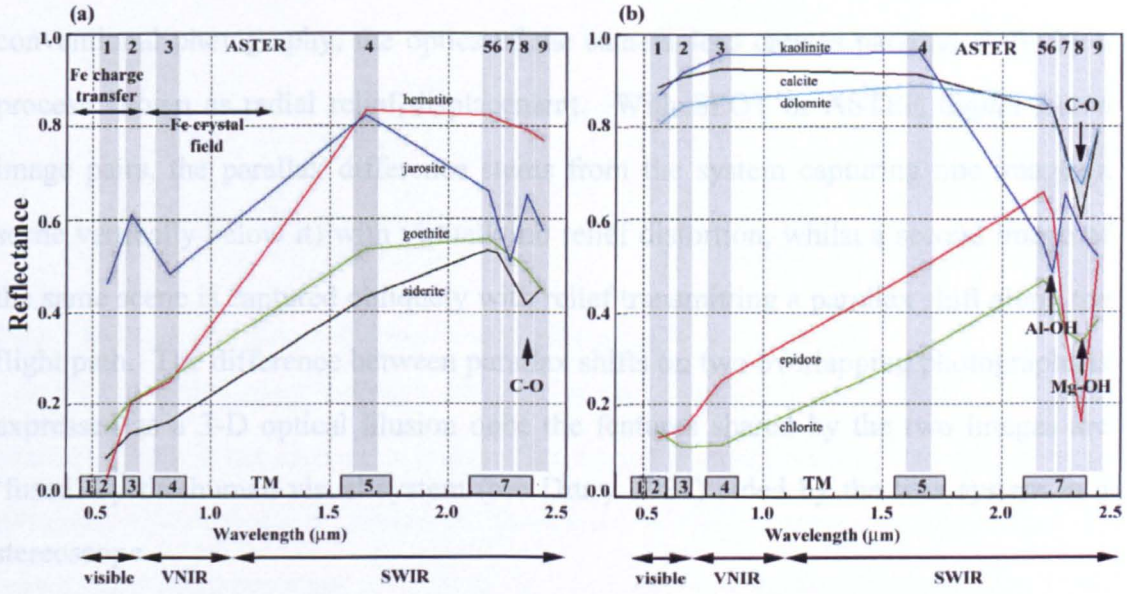


**Figure 3.5** Spectra of minerals important in lithological discrimination in relation to ASTER and TM bands. Note: spectra are resampled to ASTER band widths and centres

In this method, the radiance values for the bands for each pixel (i.e. points in the pixel's spectrum) are first normalised so that the sum of all the values for each band in every pixel is constant over the entire scene. This shifts all spectra in the image to approximately the same relative brightness, thereby removing differences in overall brightness between materials as well as illumination differences caused by topography. An average spectrum for the entire scene is then calculated from the

normalized spectra. The reasoning behind this is that if the scene includes many different kinds of surface material (most moderately large areas of the land surface do) spectral features in any of those materials should be cancelled out so that the average spectrum is almost flat. Each pixel's normalized spectrum is then divided by the scene's average spectrum to approximate a reflectance spectrum (Smith 2001).

## 3.3 Stereoscopic aerial photograph coverage

Stereoscopic viewing using a lens or mirror stereoscope, focuses the left and right eyes separately on the area shared by two overlapping images taken from slightly different positions along the system's flight path. Each image contains a parallax shift proportional to the height of objects relative to their surroundings. In the case of conventional photography, the optics of the camera lens creates parallax shifts by a process known as radial relief displacement. With SPOT or ASTER digital stereo image pairs, the parallax difference stems from the system capturing one image (a scene vertically below it) with virtually no relief distortion, whilst a second image of the same scene is captured obliquely with relief transmitting a parallax shift along the flight path. The difference between parallax shifts on two overlapping photographs is expressed as a 3-D optical illusion once the features shared by the two images are 'fused' by the human visual system (see Drury 1987) aided by the lens system in a stereoscope.

ASTER data include two infrared bands, one of which is captured along with the other bands through an optical system pointing vertically downwards (Abrams *et al.* 2002). The remaining infrared band is captured by a separate optical system that points obliquely backwards along the flight path to image the same scene acquired by the main system, several seconds later. These stereoscopic ASTER scenes have a resolution of 15m that approximates to a 60 x 60km aerial stereopair.

Stereo pairs of both ASTER and digitally scanned aerial photographs can be combined as RGB in anaglyph images (left-eye view as red and right as both green and blue to give a cyan tint), which produce the 3-D illusion of topography by

viewing through a red filter for the left eye and a cyan one for the right. Anaglyphs are invaluable as a means of graphically illustrating specific features or for geological mapping when other methods are inconclusive, particularly as they are portable and easy to use.

## 3.4 Radar

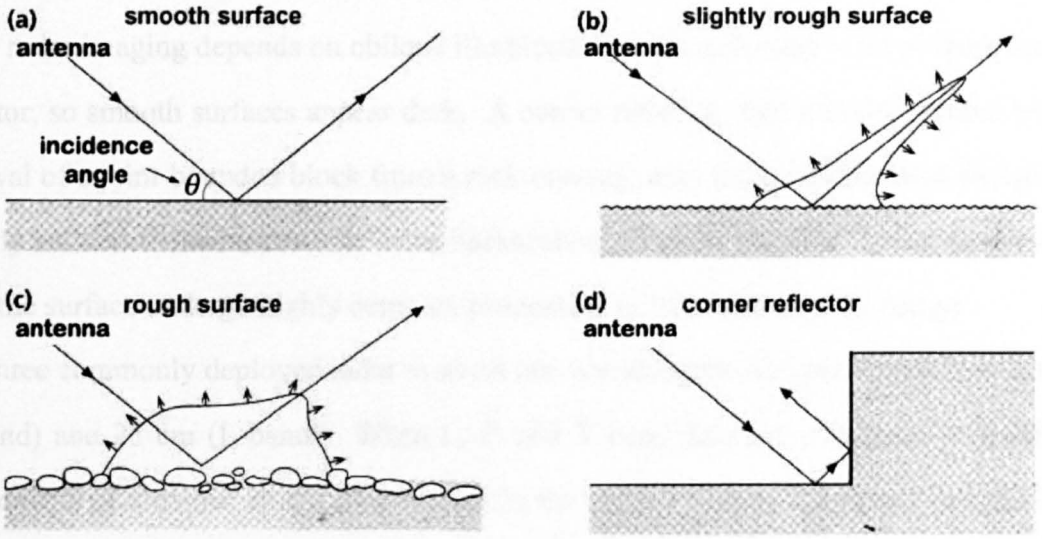


**Figure 3.6** Interaction of radar illumination with surfaces of different roughness.

The way in which radar interacts with land surfaces makes it unsuitable for mapping laterites. This is because radar images distinguish texture and roughness but not the minerals with distinctive reflectance spectra that identify laterites. The method, by which radar produces images, depends on illumination of the land surface using radar microwaves: this results in images that are entirely different from those based on multispectral reflected data (for details see Drury 1993). Instead, radar images show the influence of surface texture (figure 3.6) and, to a lesser extent, soil moisture on scattering of microwave energy back to the detector (backscatter). Their response is dependent on the wavelength of the signal used. So a surface that appears rough to X-band microwaves (3cm wavelength) will not respond in that way to C-Band (6cm) and L-band (23cm) if the surface micro-relief has dimensions that fall below the roughness criterion for those wavelengths. Generally radar imaging reveals

differences in the surface micro-relief where surface irregularity ($h$) is greater than the Rayleigh roughness criterion [$h > \lambda/4.4.\sin\theta$] for the wavelength ($\lambda$) used (Fung & Ulaby 1983) and ($\theta$) is the radar incidence angle. A rough surface will reflect more energy back to the sensor than a smooth surface. If surface irregularity is greater than $\lambda/4.4.\sin\theta$, then it acts as rough to radar. The rougher the surface relative to radar wavelength, the more energy backscattered so that radar-rough surfaces show brightly on an image. Radar-smooth surfaces tend to reflect energy in a mirror-like fashion. Since radar imaging depends on oblique illumination, such reflection is away from the detector, so smooth surfaces appear dark. A corner reflector, like a cavity formed by removal of a joint-bounded block from a rock outcrop, may reflect all incident energy directly back to the radar receiver. The backscattered signals received by the antenna from the surface undergo highly complex processing to be rendered as an image.

Three commonly deployed radar systems use wavelengths of 3 cm (X-band), 6 cm (C-band) and 23 cm (L-band). When L, C and X band data are combined as RGB components of a colour image (Section 3.1.2) the surface texture may ~~to~~ be analysed from the resulting hues in the image. An RGB combination of L-, C- and X-bands, for example, gives the following results. A surface rough to L-band, will show as white, since it will also be rough to C- and X-band, from the Rayleigh roughness criterion; a cyan hue results from low red and equally high green and blue, in this case from a surface that is rough to C-and X-bands but which is smooth as regards L-band; a blue response signifies a surface which is only rough to X-band radar. Results from using multi-frequency radar data covering Eritrean laterites are given in Chapter 4.

## 3.5 $^{40}Ar/^{39}Ar$ dating method

The technique, based on the decay of the naturally occurring parent isotope of potassium ($^{40}K$) to its argon daughter isotope ($^{40}Ar$), involves subjecting irradiated samples to incremental or step heating analyses (Merrihue & Turner 1966). This releases argon from the mineral–lattice to reveal the date or time at which argon became trapped in the sample as well as an original cooling age for disturbed samples

(Kelley 1995). The history and development of $^{40}Ar/^{39}Ar$ dating techniques, the method and the analytical procedures involved together with its advantages, are covered in detail by Merrihue and Turner (1966), Faure (1977), McDougall and Harrison (1998, 1999) and Kelley (1995, 2002). An outline of the method follows.

The initial irradiation step in $^{40}Ar/^{39}Ar$ dating allows a more precise measurement of $^{39}K$ – the dominant isotope of potassium. Each sample is initially irradiated in a nuclear reactor by bombardment of fast neutrons (Merrihue & Turner 1966). A proportion of $^{39}K$ is converted to $^{39}Ar$ in the nuclear reaction:

$_{19}{}^{39}K(n,p)\,{}^{39}{}_{18}Ar$

where *n* is the neutron and *p* is the proton. During the short period of analysis, $^{39}Ar$ (a proxy for $^{39}K$) can then be treated as a stable isotope in mass spectrometry because it has a half-life of 269 years. Samples are then heated, in an ultra-high vacuum system using a directed continuous wave laser beam to release gas, including $H_2O$, $CO_2$, $CH_4$ that are removed in the system, and admitted into the mass spectrometer where isotopes of argon are measured.

Of the extracted argon isotopically analysed in the mass spectrometer, $^{36}Ar$ indicates the atmospheric contamination, $^{39}Ar$ is used to measure potassium and $^{40}Ar$ gives an indication of the sample's age. Analyses of $^{40}Ar$ are corrected for atmospheric contamination by assuming the standard $^{40}Ar/^{36}Ar$ ratio in air is 295.5 (Steiger & Jageer 1977; Kelley 2002) using the equation:

$$^{40}Ar^{*}/^{39}Ar = [^{40}Ar/^{39}Ar]_m - 295.5[^{40}Ar/^{36}Ar]_m$$

where the subscript *m* signifies measured ratios and * signifies the corrected value for $^{40}Ar$, gives the corrected ratio of the daughter $^{40}Ar^*$ to parent potassium, represented by $^{39}Ar$. The $^{40}Ar^*/^{39}Ar$ ratio of these two isotopes is proportional to the age of the sample and can be used to date the sample using the equation:

$$t = 1/\lambda \log(1+[(^{40}Ar^{*}/^{39}Ar) \times J]).$$

Here $t$ is the sample age in Ma; $\lambda$ the decay constant of $^{40}K$ and J a dimensionless irradiation parameter (an estimate of the neutron flux). The J value is calculated using mineral standards of known ages and appropriate to the sample in a given irradiation.

In this case J values (Appendix B) were derived using the biotite standard GA1550. Background argon levels are monitored by blanks and calcium (Ca) and K corrections are applied for interference reactions where appropriate (Appendix B).

The $^{40}Ar/^{39}Ar$ dating method is used in this study because it is less prone to error than other radiometric dating techniques and provides the most precise geochronological results to date.

## 3.6 End note

Each of the methods listed above, apart from radar which was not used eventually, has its place in this study and is appropriate to aims of the thesis, although some, depending on the part of the research project tackled, are not as useful as others, as documented above. Standard image processing methods, which are simple, effective and inexpensive, were used with freely available RS data to detect and map laterite facies that have never been discriminated and mapped before using remote sensing. Sophisticated advanced techniques such as SAM used with hyperspectral data, to which few people in laterite-encrusted areas would have access, illustrate the important possibility of mapping individual minerals within laterites and extend the knowledge base as does the method for radiometric dating.

# Mapping laterite facies from space

Geologists depend on maps, especially where investigations need to cover large and/or remote areas. Satellite remote sensing (RS) provides a viable means of producing such maps and offers considerable advantages over traditional ground-based techniques (Sheffield 1981; Drury 1987, 2001, 2005; Gupta 1991; Vincent 1997; Abrams 2000; Andrews Deller 2000, 2005; Teeuw 2007). As well as providing access to inaccessible, inhospitable or war-ravaged terrain, satellite coverage (Stoney 2008) and data provide a practical tool for detailed mapping and lithological analysis. Useful geological maps produced from integrating disciplines such as RS and regolith studies (e.g. Drury & Hunt 1988 1989; Stamoulis 2009; Teeuw 2004), using mid to high resolution satellite data at minimal cost when funding is limited, are therefore valuable for providing a regional perspective of the land surface.

A growing number of satellite sensors measure the amount of radiation reflected and emitted from the Earth's surface in an increasing range and number of spectral wavebands and so provide a stream of updated information of the land's surface (Gaber *et al.* 2009). At the simplest level, RS data and multispectral image analysis can be used to delineate: stratigraphic, intrusive and tectonic boundaries; structural trends, faults and fracture systems; various lithologies and mineral concentrations and the extent and distribution of geological features, while highlighting many more outcrops than those already mapped (Drury & Holt 1980; Sheffield 1981; Drury 1983, 1986, 1987, 1993, 1998, 2001; Rothery & Drury 1884; Hunt *et al.* 1986; Drury & Hunt 1987, 1988; Taranik *et al.* 1991; Hunt 1991; Drury & Berhe 1993; Drury *et al.* 1994, 2006; Denniss 1994; Vincent 1997; Drury & de Souza Filo 1998; Abrams 2000; Crippen *et al.* 2000; Andrews Deller 2000, 2002, 2003, 2006; Goossens 2002; Chavez *et al.* 2002; Rowan & Mars 2003; Hubbard & Crowley 2005; Rowan *et al.* 2005; Solomon & Ghebreab 2006). Yet even though spectral data from existing optical and

microwave imaging systems have proved useful in mapping the distribution of common rock types no one has mapped laterite facies.

Edited extracts (Sections 4.1 - 4.4) from the published paper Andrews Deller (2006) illustrate how laterite facies can be mapped using RS and image processing methods outlined in Chapter 3. Ideas explored in the manuscript form the core of the thesis, all subsequent research stemming from the work documented in the paper. The study demonstrates that Landsat Thematic Mapper (TM) can be used to identify different facies within the laterite profile. Its suitability lies in that it provides data in six visible and near infrared (VNIR) and short-wave infrared (SWIR) wavebands that are affected by the spectral features of clay and iron minerals that dominate laterites. Data from the Advanced Spaceborne Thermal Emission and Reflection Radiometer (ASTER) and the EO-1 Advanced Land Imager (ALI) instruments are used to complement TM data (table 4.1).

**Table 4.1** Details of Landsat TM/ETM+, ASTER and EO-1 ALI (Andrews Deller 2006)

| **Landsat-7 ETM+ (Landsat-4 & 5 TM bands 1-7 only)** | | **Terra ASTER** | | **EO-1 ALI** | |
|---|---|---|---|---|---|
| **Band** | **Range (μm)** | **Band** | **Range (μm)** | **Band** | **Range (μm)** |
| 1 (30 m) | 0.45-0.52 | 1 (15 m) | 0.52-0.60 | 1 (30 m) | 0.43-0.45 |
| 2 (30 m) | 0.52-0.60 | 2 (15 m) | 0.63-0.69 | 2 (30 m) | 0.45-0.515 |
| 3 (30 m) | 0.63-0.69 | 3 (15 m) | 0.76-0.86 | 3 (30 m) | 0.525-0.605 |
| 4 (30 m) | 0.76-0.90 | 4 (30 m) | 1.600-1.700 | 4 (30 m) | 0.63-0.69 |
| 5 (30 m) | 1.55-1.75 | 5 (30 m) | 2.145-2.185 | 5 (30 m) | 0.775-0.805 |
| 7 (30 m) | 2.08-2.35 | 6 (30 m) | 2.185-2.225 | 6 (30 m) | 0.845-0.89 |
| Pan (15 m) | 0.52-0.90 | 7 (30 m) | 1.235-2.285 | 7 (30 m) | 1.2-1.3 |
| | | 8 (30 m) | 2.295-2.365 | 8 (30 m) | 1.55-1.75 |
| | | 9 (30 m) | 2.360-2.430 | 9 (30 m) | 2.08-2.35 |
| | | | | Pan (10 m) | 0.48-0.69 |

Spectral bands in the reflected region captured by Landsat TM and ETM (http://ltpwww.gsfc.nasa.gov/IAS/handbook/handbook_toc.html); ASTER (Abrams, 2000) and EO-1 ALI (http://edc.usgs.gov/products/satellite/eo1.html). Other data used in preparing this paper are panchromatic aerial photographs, flown for the Ethiopian Mapping Agency in 1964–1967, and multi-frequency imaging radar data from the NASA/JPL SIR-C and German and Italian Space Agencies' (DLR and ASI) X-SAR missions carried by the Space Shuttle in September 1994. Digital SIR-C/X-SAR data are L- (23.5cm), C- (5.8cm) and X-band (3.1cm) synthetic-aperture radar images

Sections 4.5, 4.6 and 4.7 build on the strategy established in Andrews Deller (2006) and show how the continuity of laterite facies sequences extends far beyond the test area to a regional level.

*Facies discrimination in laterites using Landsat Thematic Mapper, ASTER and ALI data—examples from Eritrea and Arabia*

M. E. Andrews Deller

(Received 20 August 2004; in final form 17 January 2006).
Published in the International Journal of Remote Sensing Vol. 27, No. 12, 20 June 2006, 2389–2409

*Abstract:*

Lateritic palaeosols cover roughly 33% of Earth's land surface. In spite of this, laterite facies remain largely unmapped. This paper illustrates how spectral properties of clays and iron minerals guide the mapping of three laterite facies using remote sensing as a mapping tool. Remotely sensed data and image processing techniques prove ideal for effective mapping of laterites over large areas and difficult terrain so that their economic importance can be evaluated. Several types of remote sensing data are considered and the most appropriate selected. A 700km$^2$ area in Eritrea is used as a test site. A laterite facies map derived from remotely sensed data is presented for the first time. Methods of mapping are given using Landsat Thematic Mapper (TM), Advanced Spaceborne Thermal Emission and Reflection Radiometer (ASTER) and Advanced Land Imager (ALI) data. Field evidence supports observations. Remote sensing methodology developed for the test site is applied to unvisited areas in Eritrea and Saudi Arabia. The results indicate that laterite facies maps can be produced easily and used to highlight palaeosols hosting known ore deposits and commodities such as base metals or building resources as well as targeting further potential sites. A reliable, inexpensive means of mapping laterites is demonstrated, which can be used to focus on regions where problems (landslides, groundwater quality and non-viable agricultural land) identified in lateritised terrain can be assessed and favourable areas and those of risk established. Mapping laterite distribution in relation to topography also sheds light on the tectonic evolution of NE Africa, whilst the presence of laterites gives clues to ancient terrestrial climate.

## 4.1 Introduction

This paper demonstrates how to identify and map facies variation in lateritic palaeosols (laterites), using freely available remote sensing data at little or no cost. Simple digital image processing techniques are used to give scientists, engineers, managers, teachers and non-governmental organisation (NGO) personnel ways to generate laterite facies maps for socio-economic benefit. Image interpretation is limited by the spectral capability of the data in the context of laterites' characteristic assemblage of the secondary minerals, kaolinite, hematite, goethite and residual

quartz, whose concentrations vary through laterite profiles with ferricrete, mottled and clay horizons. (Chapter 2; Schellmann 1986; Butt & Zeegers 1992).

Facies maps of laterites are important. They can be used to plan infrastructure and target resources, mineral wealth and safe water supplies. Lateritisation produces infertile, poorly draining, kaolinitic soils and affects groundwater. Strategic placing of wells is therefore important as lateritic ferricretes and mottled zones are potential aquifers. High ferric hydroxide content in some lateritised terrain produces pipe blockages and red-stained supplies (e.g. Ogaden, Ethiopia - Oxfam, personal communication 2001). Goethite, formed during lateritisation, concentrates arsenic which can affect localised ground water (Chapter 8; Smedley *et al.* 1996; Kinniburgh & Smedley 2001) and magnesium sulphate (epsomite or Epsom salts) and sodium chloride in groundwater from lateritised basement cause diarrhoea. However, epsomite in drinking water may be beneficial in countries where drugs are expensive, as Mg sulphates benefit women with eclampsia or pre-eclampsia and their babies (Magpie 2002). As a resource, laterite clay-rich horizons can be used for brick making or building blocks, ferricrete for low-cost road surfacing or hard core and kaolinite for porcelain. Engineering properties of laterites are important, as failure in the clay zone results in subsidence or landslides (Chapter 8; Temesgen *et al.* 2001; Andrews Deller 2002; Singhroy & Molch 2004). Laterites concentrate gold, silver, copper, zinc, nickel, cobalt, bauxite, lead and manganese in ore deposits associated with particular settings in Precambrian basement rocks (Tadesse *et al.* 2003). A regional map of laterite facies, together with digital elevation data, can be used by exploration geologists to identify zones of gold and base metal enrichment associated with lateritisation of mineralised zones (Chapters 7, 8; Edwards & Atkinson 1986; Butt 1986, Taranik *et al.* 1991; Smith *et al.* 2000).

Eritrean laterites, conformably underlying mid-Oligocene flood basalts, are interesting from a scientific standpoint. By mapping this flood basalt-laterite contact as a datum, it is possible to estimate variation in average rates of tectonic uplift (Chapter 7; Drury *et al.* 1994; Ghebreab & Talbot 2000; Ghebreab *et al.* 2002) and

denudation, important in NE Africa where Miocene to Recent opening of the Red Sea has deformed the pre-30 Ma African surface (Bohannon *et al.* 1989). Laterites also shed light on early-Tertiary climate and the ancient terrestrial environment (Chapter 7). Furthermore, dating laterites (Chapters 5, 6; Andrews Deller 2003) provides time constraints on lateritic evolution in NE Africa and Red Sea geology (e.g. Baker *et al.* 1996). Given the scientific value and the socio-economic importance of mapping laterites, remotely sensed laterite facies maps have potential. To date no regional mapping of different laterite facies, using remote sensing has been done despite the distinctive spectral characteristics of their mineralogy and their common occurrence. A geological map distinguishing laterite facies from common rocks in the Eritrean Highlands is presented. The method is then shown to hold good regionally.

## 4.2 Test site - lithologies imaged

The centre of the test site (700 $km^2$) is located 10km south west of Asmara, Eritrea's capital (figure 4.1). Bordered to the west by the Mensura Plain and to the east by the Red Sea Escarpment, it is situated in the semi-arid central highland region of the Neoproterozoic Nakfa Terrane (Drury & Berhe 1993; Teklay *et al.* 1997; Drury & de Souza Filo 1998; Ghebreab 1999; Johnson & Woldehaimanot 2003). It is a lightly vegetated region dominated by stark outcrops, ideal for detailed field studies of the facies variation within the laterites and perfect for remote sensing.

Lithologies imaged are typical of the highlands of Eritrea (Chapter 2). Granitic intrusive rocks in the west of the test area dominate the local basement, whereas a variety of metasedimentary and metavolcanic rocks outcrop in the east. In places, small remnants of Phanerozoic cover occur but there are no Mesozoic sediments. Scattered outliers of Tertiary laterite are common as well as the main outcrop in which the variable lateritic mineralogy in vertical and horizontal profile is preserved

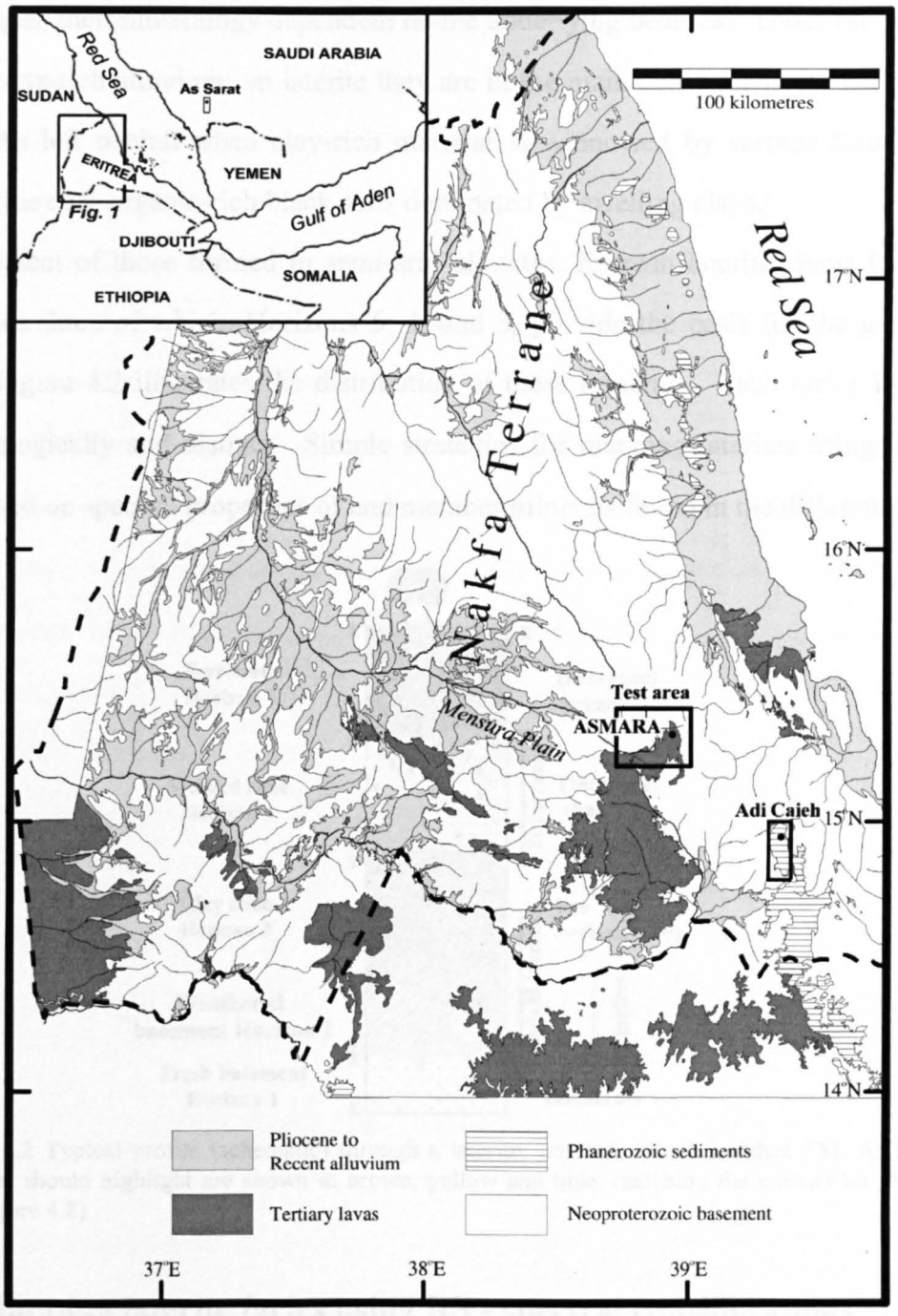


**Figure 4.1** Location map showing the test site and Adi Caieh, Eritrea and As Sarat, Saudi Arabia (see inset)

immediately beneath the 30 Ma continental flood basalts (CFBs) that occupy much of the southern part of the test area. Basement outcrops beyond the laterite whose clay horizon outcrops beyond the mottled zone, which in turn outcrops beyond the ferricrete and basalt. Patchy colluvium on slopes consists of material washed down from bedrock forming higher ground. Substantial modern soils occur only in

drainages, their mineralogy dependent on the underlying bedrock. Those on basement are quartz-rich alluvium; on laterite they are in the main dense ferricrete cobbles and pisoliths left behind when clay-rich material is winnowed by surface flow and on basalt they are organic-rich black soils dominated by swelling clays.

Typical of those formed in semi-arid climates, Eritrean laterites have five main horizons three of which, Horizons 5, 4, and 3, provide the basis for the geological map. Figure 4.2 illustrates the distribution of these minerals. Each facies is simple mineralogically and distinct. Simple strategies for mapping laterites using RS data are based on spectral properties of end member minerals found in the different facies.

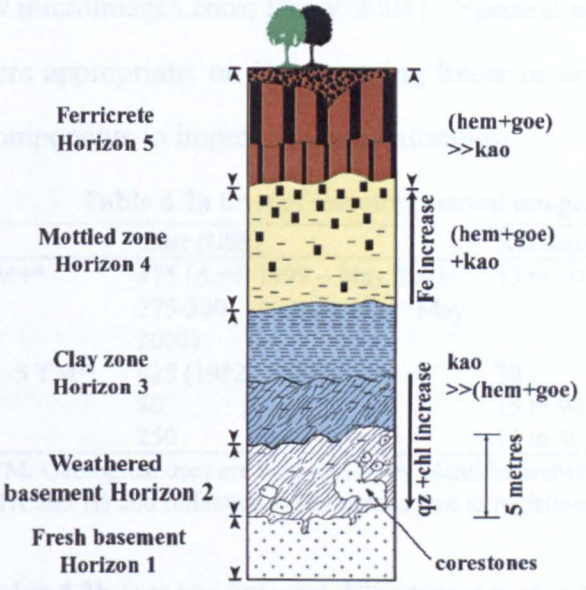


**Figure 4.2** Typical profile (schematic) through a laterite: horizons which Landsat TM, ASTER and ALI data should highlight are shown in brown, yellow and blue, matching the colours on geological map (figure 4.8)

## 4.3 Mapping laterite facies using RS - spectral considerations

Geological interpretation of the test area is based on remote sensing data and field studies. In 1998, 2001 and 2002, two hundred field sites were established to validate remotely sensed data. Laterite facies were sampled and logged so that areas with predicted responses on images could be related to exposures of each facies. As mixed vegetation cover mutes and camouflages the response of image data to the local geology (section 2.4), dry-season data were used to reduce the complication of further

spectral mixing by the influence of vegetation.

Georeferenced images used in this study cover a 30.7 by 25.6 km test area centred at 38° 50'N, 15° 20'E (figure 4.1). The data comprise: Landsat-5 TM (path 169/row 049, 18 April 1986), Landsat-7 ETM (15 and 31 March 2000), Level-1B ASTER (dates between November 2000–June 2002) and ALI (18 and 23 March 2001 overpasses). Except for acquisition during the dry season, the age of the data is unimportant. Landsat TM/ETM and ASTER are freely available (table 4.2a and b) and ALI data were acquired for the study during the early phase of NASA's Earth Observation (EO-1) mission. TNTlite and TNTmips software was used for image processing (www.microimages.com; Drury 2001). Spectral contrast of all lithologies is enhanced, where appropriate, on images using linear or normalised stretch of red, green and blue components to improve colour saturation.

**Table 4.2a** Cost of remotely sensed images

| Instrument | Cost (US$) | Resolution (m) | Swath (km) |
|---|---|---|---|
| **Landsat-7 ETM+*** | 475 (April 1999 – May 2003) 275-300 (scenes after May 2003) | 15 to 30 | 180 |
| **Landsat-4 and -5 TM*** | 425 (1982 – 2005) | 30 | 180 |
| **ASTER**** | 80 | 15 to 90 | 60 |
| **EO-1 ALI** | 250 | 10 to 30 | 37 |

*Landsat TM/ETM: Geological uses are well served by plentiful archives of cloud-free scenes.
**ASTER level 1A and 1B and reflectance data scenes free to registered educational users.

**Table 4.2b** Free and low-cost data sources used in this study

| Web site | Brief description of available data |
|---|---|
| **USGS -** http://landsat.usgs.gov | Landsat 7 ETM+ to purchase, browse and ordering facilities |
| | Some free orthorectified Landsat |
| http://edcsns17.cr.usgs.gov/EarthExplorer/ | TM/ETM+ scenes - other scenes: TM and ETM+. EO-1 ALI data - See Table 2a |
| **Global Land Cover Facility (University of Maryland, US) -** http://glcfapp.umiacs.umd.edu:8080/esdi/index.jsp | Free Landsat TM and ETM+ 742 compressed mosaics; free Landsat TM/ETM+ scenes |
| **NASA Earth Observing System Data Gateway (EROS Data Center) -** http://edcimswww.cr.usgs.gov/pub/imswelcome/ | Low-cost or free ASTER, MODIS & AVHRR data; other data, browse and ordering facilities |
| **Google Earth -** http://earth.google.com/ | Free on-line TM natural colour world, perspective views of topography |

Selection of data and image processing techniques (Chapter 3) used to identify

and map different laterite facies is based on the distinct spectral responses of light and dark minerals that typify laterites (figure 4.3). These are clay and iron minerals with strong hydroxyl absorption features (reflectance minima) in the SWIR and Fe-3 crystal-field absorption features in the VNIR respectively. The spectral plots for light and dark coloured lateritic minerals compared with those of green vegetation, Fe-chlorite in the basement and the flat featureless spectra of quartz with high reflectance are presented in Figure 4.3a & 4.3b. RS bands (table 4.1) that measure the distinctive spectral characteristics of laterite minerals, are selected to highlight individual facies. Red, green, blue (RGB) colour combinations of bands and band-ratios are used to display spectral characteristics of laterite end-member minerals. Band combinations that emphasise hematite, goethite and kaolinite are selected. Mixtures of these minerals, identified by their coloration on RS images are used to detect each facies. After checking with known field occurrences, each colour is interpreted as a map unit and a geological map of laterite facies is produced by on-screen digitising of these units. All three facies must occur together so that lateritic palaeosols are not confused with gossans (Abdelsalam *et al.* 2000), banded ironstone formations (BIFs) or detrital kaolinitic and ferruginous deposits formed from transported debris eroded from laterite.

Field studies demonstrate that soils developed on laterite facies have similar mineralogy to that of the underlying laterite horizon. In sparsely vegetated areas, there are relatively few common minerals with distinct spectral features that occur in the top few micrometres of rock and soil surface (Drury 1993; Spatz 1997; Vincent 1997). Clays, iron oxy-hydroxides, quartz, feldspars, carbonates, chlorite, amphiboles and various hydrated ultramafic minerals are some examples. Each mineral can be an end member in a physical and a spectral mixture (Crippen 1989). A spectrum in the visible and near infrared (VNIR) to short-wave infrared (SWIR) range for any surface is a spectral mixture that depends on the proportions of distinct materials. For

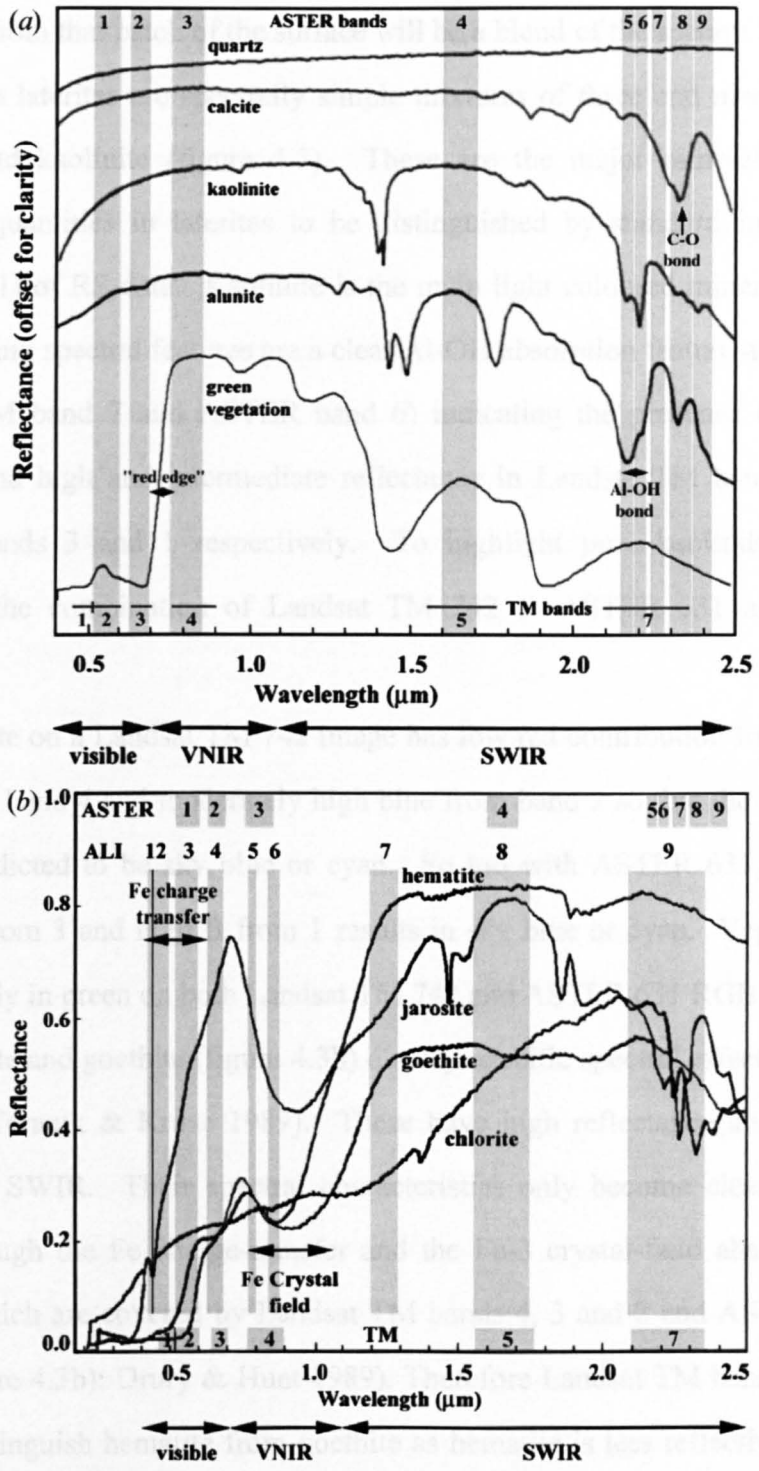


**Figure 4.3** Spectra of main minerals in laterites showing particular features that can be analysed. Vegetation and other minerals referred to in this paper included: (a) Visible, VNIR and SWIR reflectance curves of light minerals and vegetation with positions of their main absorptions in relation to Landsat TM and ASTER bands; (b) Visible VNIR and SWIR reflectance curves of dark iron-rich minerals and chlorite with positions of their main absorptions in relation to Landsat TM, ASTER and EO-1 ALI bands

instance the proportion might be 25% grass, 25% quartz, 25% goethite and 25% kaolinite. In this case 4 end members are mixed in equal proportions so a spectrum

generated from that patch of the surface will be a blend of the spectra for all four.

Eritrean laterites are spectrally simple mixtures of three end members: hematite, goethite and kaolinite (figure 4.3). These are the major minerals that occur in sufficient quantities in laterites to be distinguished by standard image processing (Section 3.1) of RS data. Kaolinite is the main light coloured mineral (figure 4.3a). Its identifying spectral features are a clear Al-OH absorption feature around 2.2μm (in Landsat TM band 7 and ASTER band 6) indicating the presence of hydroxylated minerals and high and intermediate reflectance in Landsat TM bands 4 and 2 and ASTER bands 3 and 1 respectively. To highlight pure kaolinite in Horizon 3 therefore, the combination of Landsat TM 742 or ASTER 631 as RGB is most effective.

Kaolinite on a Landsat TM 742 image has low red contribution from band 7, high green from band 4 and moderately high blue from band 2 so that the combined result can be predicted to be sky blue or cyan. So too with ASTER 631; low R from 6, higher G from 3 and high B from 1 results in sky blue or cyan. Vegetation appears comfortingly in green on both Landsat TM 742 and ASTER 631 RGB renditions.

Hematite and goethite (figure 4.3b) display specific spectral effects linked to Fe-3 minerals (Taranik & Kruse 1989). These have high reflectance and no distinctive features in SWIR. Their spectral characteristics only become clear in visible and VNIR through the Fe charge-transfer and the Fe-3 crystal-field absorption features parts of which are covered by Landsat TM bands 4, 3 and 2 and ASTER bands 3, 2 and 1 (figure 4.3b); Drury & Hunt 1989). Therefore Landsat TM band 2 and ASTER band 1 distinguish hematite from goethite as hematite is less reflective in the visible green region. Visual inspection of spectra (figure 4.3) reveals Landsat TM band 3 (ASTER band 2) highlights high reflectance for quartz and kaolinite. Landsat TM band 4 (ASTER band 3) is important in that the iron oxy-hydroxides with the distinctive crystal-field absorption feature are separated from kaolinite and quartz. Landsat TM band 5 (ASTER band 4), with the highest reflectance for all iron minerals but low reflectance for vegetation, is useful for band-ratios. The broad Fe-3

crystal-field absorption of all Fe-3 minerals is only covered adequately by EO-1 ALI data which can be used to differentiate further between light and dark minerals. Although RGB colour combination images adequately detect kaolinite of Horizon 3, hematite and goethite are only subtly different from each other and can be confused with local chloritic meta-igneous crystalline basement rocks or chlorites common in soils developed on them. Horizons 4 and 5 are mixtures of the end member minerals goethite and hematite (figure 4.3) and band-ratios displayed as RGB colour combinations (table 4.3) effectively detect the mineral mixtures that distinguish Horizon 4 (mottled zone) more clearly from Horizon 5 (ferricrete zone).

**Table 4.3** Numeric ratio values for laterite minerals, based on USGS reflectance spectra re-sampled to TM and ASTER wavebands

| Mineral | TM 5/4 AST 4/3 ratio (red) | TM 3/2 AST 2/1 ratio (green) | TM 7/5 AST 6/4 ratio (blue) |
|---|---|---|---|
| Quartz | 1.0 1.0 | 1.0 1.0 | 0.99 1.0 |
| Hematite | 3.4 3.4 | 5.1 5.1 | 0.98 0.96 |
| Goethite | 2.1 2.1 | 1.4 1.4 | 1.0 0.93 |
| Fe chlorite | 2.8 2.8 | 0.76 0.76 | 1.5 1.3 |
| Kaolinite | 1.0 1.0 | 1.1 1.1 | 0.50 0.48 |
| Green vegetation | 0.48 0.48 | 0.44 0.44 | 0.48 0.40 |

Not all remote sensing data measures the spectral features of the main minerals in the reflected region. Individual laterite facies cannot be distinguished using high resolution (< 2 metres), panchromatic aerial photographs because they show only differences in albedo and not spectral variation related to mineralogy. Aerial photographs, together with field observations, indicate that laterites form distinctive flat-topped mesas with sharp terraces covering basement. Their prime advantage, stereoscopic viewing, is outweighed by the stereoscopic potential of ASTER, bands 3N and 3B (15m) and Google Earth (table 4.2b), which covers the whole planet. Although aerial photographs highlight geological relationships and topography (section 4.5; Drury 1993), they are expensive, dependent on aircraft access and subject to turbulence, which affects image scale.

Radar too has drawbacks. It is useful in resolving geological structures (Spatz 1997) but unreliable for laterite facies mapping (section 4.6). SIR-C/XSAR images

distinguish surface texture and roughness (Chapter 3) but not the mineralogy that identifies laterites. In the Eritrean highlands most rock exposures have a micro-relief greater than 10cm and are rough in all radar bands. Alluvium and flat areas of soils derived from saprolite, have a micro-relief which is less than the roughness criteria for radar bands, so these appear as dark grey when L, C and X bands are used as RGB colour combinations. Some ferricrete breaks down to a surface composed of pisoliths about 1cm in diameter and on LCX RGB colour combinations these do show up clearly. However, not all ferricrete surfaces break down to pisolitic gravels hence results are inconsistent. Multi-wavelength colour radar images make no distinction between pisolitic surfaces and gravel roads, clay zones and alluvial flats, or flood basalts and blocky ferricrete.

### 4.3.1 Landsat TM

Landsat TM can be used to map laterite facies successfully.

*Landsat TM 742 images* (figure 4.4) provide an excellent basis for overall geological interpretation and also highlight laterite occurrences in the test area. Predicted colours for all major surface types are given in Table 4.4. The Mai Nehfi reservoir (black in the south west), the airport runway and asphalt roads (blue in the south east) and a north–south trending vertical fault with downthrow to the east, position the scene. Green vegetation is obvious in the drainages, particularly in the top right hand corner of the image and in the circular market garden area north of the airport. Chloritic soils together with the quartz-rich granitic and andesitic metavolcanic rock in the NW quadrant are a complex mixture of pink and pastel shades. Tertiary basalts in the south-east quadrant have a texture different from that of the underlying laterites and display colours ranging from mottled grey to pastel magenta. Highly organic black-cotton soils in some basalt drainages show up as dark brown. Laterite exposures are extensive in the south and east and there are also laterite outliers in the west. The 742 Landsat TM image, focusing on low SWIR reflectance in band 7, highlights the kaolinite-rich clay zone uniquely in cyan or sky blue but the distinction

between the mottled zone in dull brown and the ferricrete in dull red is not obvious. However, the confusion is resolved using Landsat TM band-ratio images.

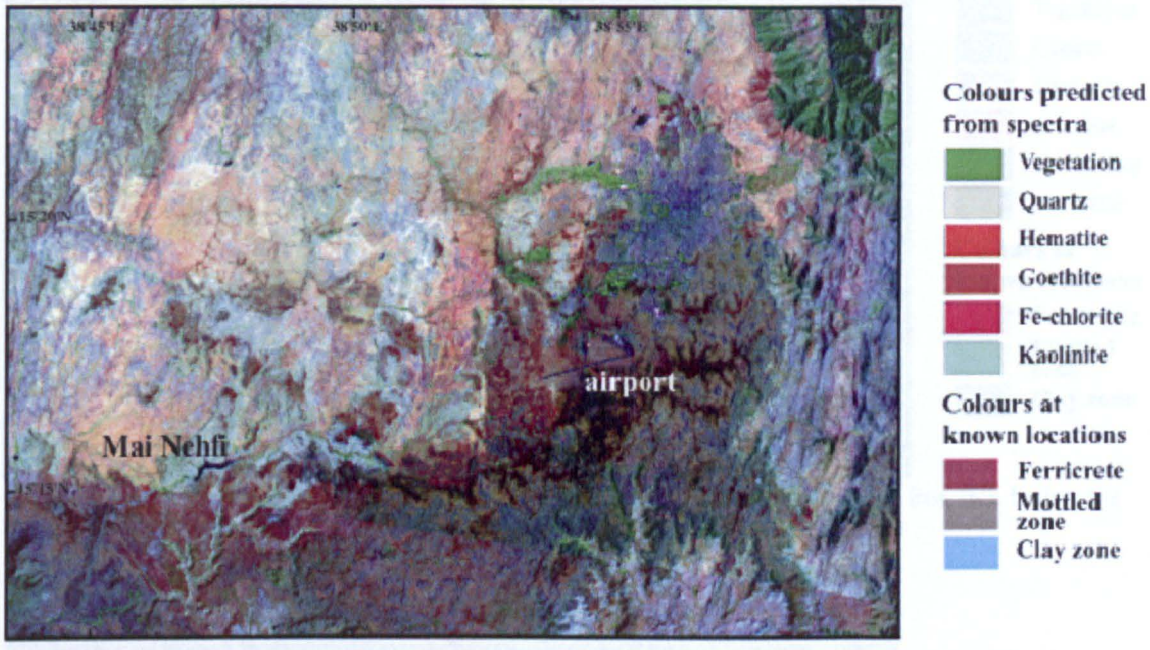


**Figure 4.4** Landsat TM 742 image of the test area: This image shows kaolinite (Horizon 3) uniquely in cyan or sky blue

*Landsat TM 5/4–3/2–7/5 band-ratio images* (figure 4.5) further discriminate between the two iron-rich laterite facies. Facies rich in hematite and goethite with variable kaolinite, the ferricrete and mottled zones, are successfully identified because the chosen Landsat TM band-ratios focus on the iron minerals' crystal-field features (5/4), charge-transfer absorptions of iron minerals (3/2) and the absorption feature of kaolinite (7/5) (see figure 4.3). Since Horizon 5 and Horizon 4 are mixtures of both Fe-3 minerals and kaolinite in different proportions, it is necessary to combine several band-ratios, Landsat TM 5/4, 3/2 and 7/5 as RGB, to discriminate these facies (figure 4.5, table 4.3). Pure clay (Horizon 3) in this rendition is dark green. Vegetation is black whilst urban Asmara is dark blue. The mottled, iron-stained clay facies (Horizon 4) is yellow whilst the iron-rich ferricrete, (Horizon 5) with a dominance of Fe-3 oxides/hydroxides and far less clay, is orange-red and so distinctly different from the mottled zone. The basalts are nondescript and variegated. However, using this

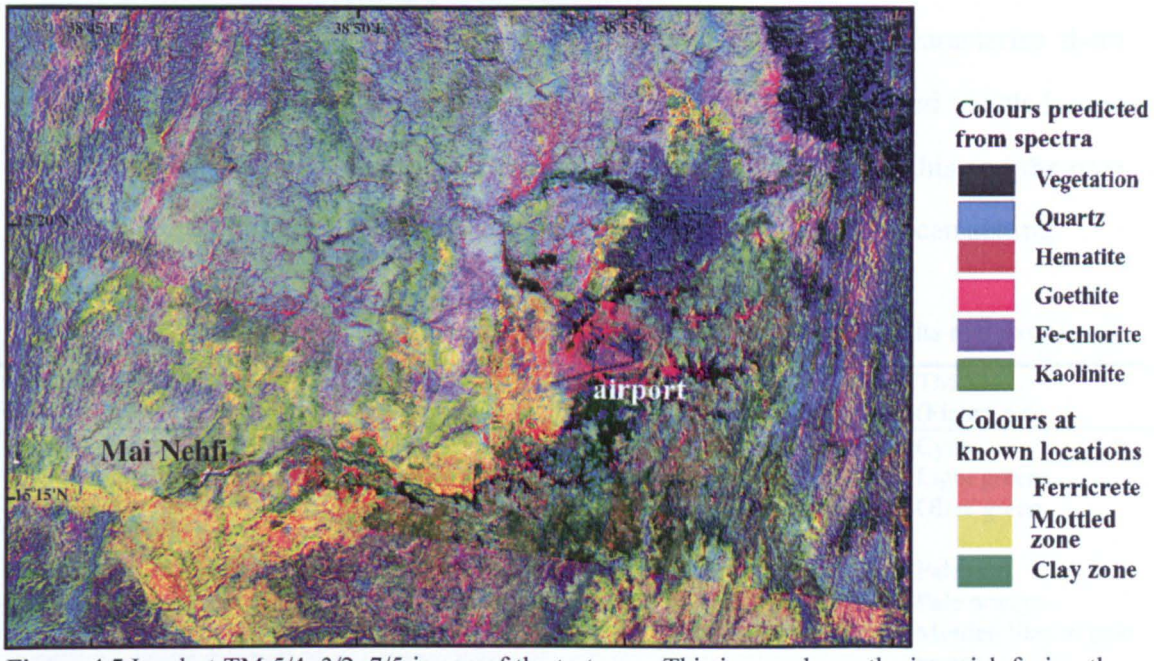


**Figure 4.5** Landsat TM 5/4, 3/2, 7/5 image of the test area: This image shows the iron rich facies; the mottled zone (Horizon 4) clearly in yellow and ferricrete (Horizon 5), in orange-red

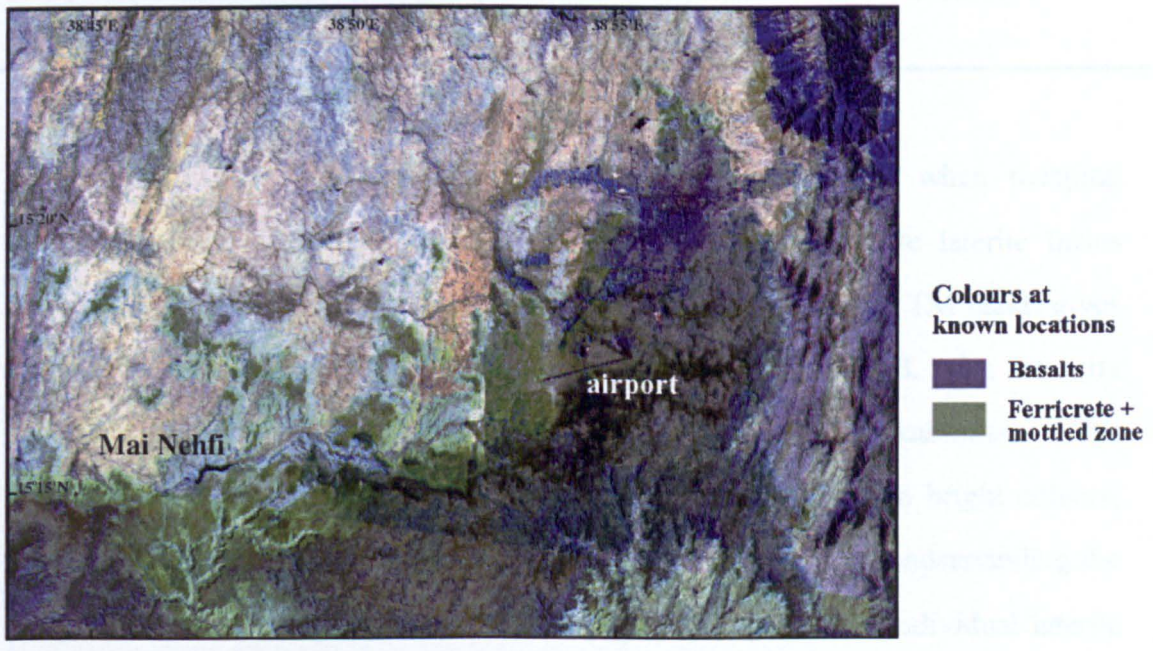


**Figure 4.6** Landsat TM 754 image of the test area: This image distinguishes the basalts from the underlying laterites

band-ratio image, not only are horizon 4 and horizon 5 clearly distinct, but the basalts are easily distinguished from all laterite facies, as they contrast with the green, yellow and orange of the laterite facies

*Landsat TM 754 images* (figure 4.6, table 4.4) are a simple means of distinguishing laterite facies from basalts. Basement surfaces with complex geochemistry (Teklay

1997) show in highly variable hues and no attempt is made to characterise them spectrally. The clay zone is displayed as cyan and the ferricrete and mottled zone appear in olive greens, whilst the overlying basalts are mauve. Both this and the next image are useful but not essential when mapping laterites in a NE African setting.

**Table 4.4** Colours (TM-5) associated with soils above field-checked rock units and exposures

| **Field unit** | TM 742 (figure 4.4) | TM 5/4 3/2 7/5 (Figure 4.5) | TM 754 (Figure 4.6) |
|---|---|---|---|
| Pure kaolinite (Horizon 3) | Cyan | Dark green | Cyan |
| Fe-rich kaolinite (Horizon 4) | Brown/Grey-brown | Yellow-orange | Light green |
| Ferricrete (Horizon 5) | Maroon/dark red brown | Orange-red | Olive green |
| Quartz + clay soil (saprolite) (Horizon 2) | Pink to white | Pale green-cyan | Pale pink |
| Chloritic soil (metavolcanics) (Horizon 1) | Reddish | Purple | Pale orange |
| Soil over granitic rocks ) (Horizon 1) | Pastel orange-red | Blues | Mottled lilac to pale brown |
| Basalts | Mottled grey t pastel magenta | Mottled various | Mottled brown |
| Black, montmorillonite soil (basalts i places) | Dark brown | Black | Dark brown |
| Vegetation | Green | Black | |

*Landsat TM PC2–PC3–PC4 images* (figure 4.7) are useful when mapping urbanised laterite areas (see Chapter 8), they do not discriminate laterite facies successfully. Conventional principal component analysis of Landsat TM bands gives interesting results. Landsat TM PC2–PC3–PC4 combined as RGB, with intensity controlled by PC1, strongly discriminate urban areas and pure kaolinites. This rendition discriminates a large range of subtly different surfaces in bright colours, urban areas showing up as yellow and pure clays in red; however, understanding the image in terms of end members and spectra and relating these to individual laterite horizons is almost impossible.

*Landsat TM Results*: the 742, 5/4–3/2–7/5 and 754 Landsat TM images highlight most spectral characteristics of laterites extremely well and distinguish their different facies from other rock types. Together, these renditions provide the basis for the first geological map of Eritrean laterites (figure 4.8) on which all interpretations are verified by field studies.


**Figure 4.7** Landsat TM PC2, PC3, PC4 with intensity controlled by PC1 image of the test area: This image discriminates much in bright colours, urban areas show up uniquely as yellow and brown, and clay zone in red

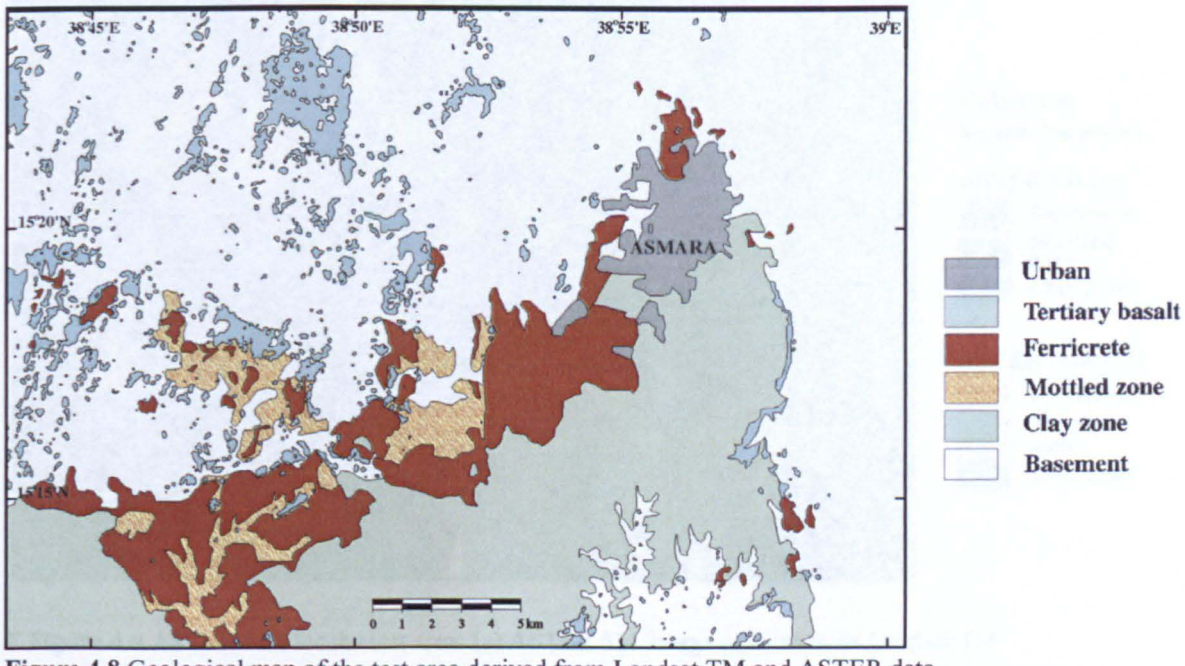


**Figure 4.8** Geological map of the test area derived from Landsat TM and ASTER data

### 4.3.2 ASTER

ASTER (Abrams & Hook 1995; Thome 1999; Abrams 2000) has superseded Landsat TM and provides equivalent images for mapping laterite facies. Interpretations from ASTER data like those of Landsat TM data are incorporated in Figure 4.8 yet in terms of the spectral capabilities of RS data ASTER offers little

more than Landsat TM. Landsat TM data are useful in broadly discriminating lithological differences in most surfaces with little vegetation cover. However, although Al-OH, Mg-OH and C-O features are sharp and distinguishable in spectra by their characteristic wavelengths, they all fall within Landsat TM band 7, which is so broad that the C-O absorption of carbonates and the Mg-OH absorption of hydrated ferromagnesian minerals also affect it (Drury 1993). Landsat TM data therefore blur mineralogical differences, however, ASTER, in contrast, has nine reflected bands (table 4.1), five of which (SWIR 5-9) span the range of Landsat TM band 7 and in this respect is more useful. Although ASTER VNIR data (15m) have twice the spatial resolution of Landsat TM (28.5m) this serves only to render topographic features more sharply.

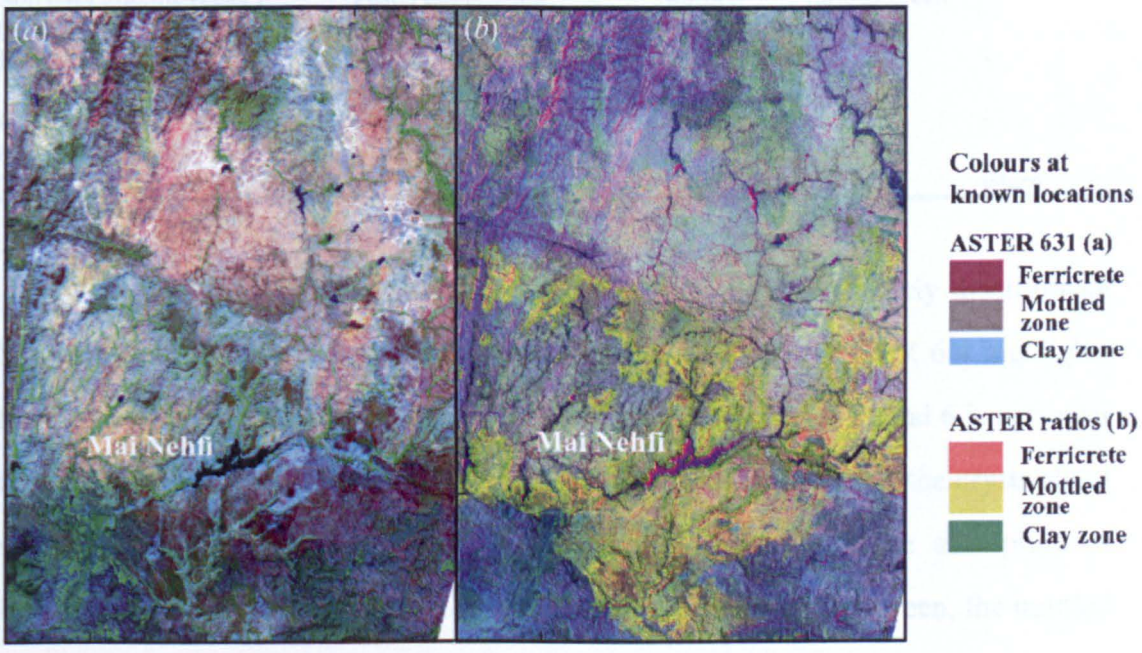


**F Figure 4.9** ASTER data for the test area: (a) ASTER 631 image equivalent to Landsat TM 742 (figure 4.4); (b) ASTER 4/3, 2/1, 6/4 image equivalent to Landsat TM 5/4, 3/2, 7/5 (figure 4.5)

*ASTER 631 images* focus on low SWIR reflectance of kaolinite in band 6 and highlight the clay-rich zone of Horizon 3 in cyan or sky blue uniquely (figure 4.9a, table 4.5). The rough equivalent of the 742 Landsat TM image, this rendition provides the basis for the facies map and discriminates the three laterite facies clearly. ASTER's improved spatial resolution sharpens the images to such an extent that even

unpaved roads show up. Iron-rich facies mimic the same reddish brown tones of the 742 Landsat TM, but because hematite and goethite lack any spectral features in the region covered by ASTER's narrow SWIR bands, mottled and ferricrete zones are not clearly separated and in this respect ASTER offers little more than Landsat TM.

**Table 4.5** Colours (ASTER, ALI) associated with soils above field-checked rock units and exposures

| Field unit | ASTER 631 (figure 4.9a) | ASTER 4/3 2/1 6/4 (figure 4.9b) | EO-1 ALI 765 (figure 4.11) |
|---|---|---|---|
| Pure kaolinite (Horizon 3) | Pale blue | Green | - |
| Fe-rich kaolinite (Horizon 4) | Brown/Grey-brown | Yellow | Reddish magentas |
| Ferricrete (Horizon 5) | Maroon/dark red-brown | Orange | Reddish magentas |
| Quartz + clay soil (saprolite (Horizon 2) | Pink to white | Pale pink Pale green-cyan | - |
| Chloritic soil (metavolcanics (Horizon 1) | Reddish | Purple | - |
| Soil over granitic rocks ) (Horizon 1) | Pastel pinkish-red | Mottled various/green pink | - |
| Basalts | Mottled grey to pastel magenta | Blues /purples | - |
| Black, montmorillonite soil (basalts in places) | Dark brown | Dark brown Black | - |
| Vegetation | | Black | Blues |

*ASTER 4/3–2/1–6/4 images* (figure 4.9b, table 4.5) however clearly discriminate between the ferricrete and mottled zone (Horizons 5 and 4). ASTER 6/4 highlights the Al-OH feature in kaolinite better than TM 7/5 because ASTER band 6 is narrower than Landsat TM band 7. As with the Landsat TM band-ratio image, the crystal-field and charge-transfer absorptions of iron minerals together with the absorption of kaolinite in band 6 are highlighted. Pure clays in this rendition are green, the mottled zone is yellow, clearly separated from the bright reddish orange ferricretes and the basalts are blue. The dynamic range of radiance values in individual ASTER SWIR bands is about half that in TM bands 5 and 7, which may explain why, together with different soil moisture and vegetation cover on dates of Landsat TM and ASTER acquisition, ASTER band-ratios give slightly poorer results than Landsat TM band-ratios.

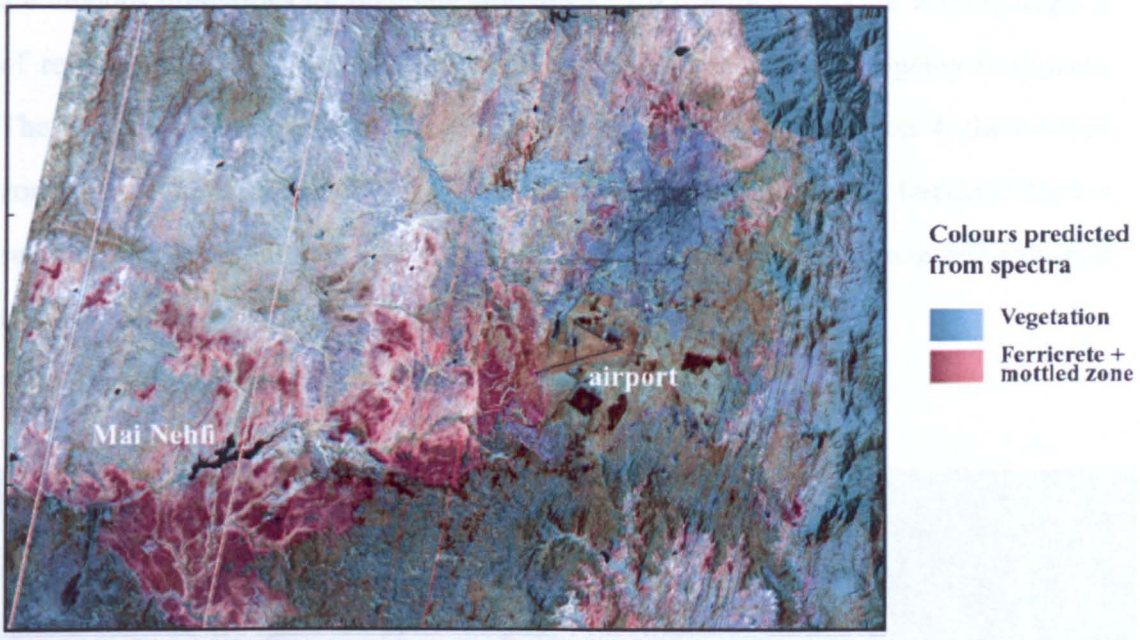


**Figure 4.10**. EO-1 ALI 765 image of test area. Iron-rich laterite zones show uniquely in reds

### 4.3.3 EO-1 ALI

ALI data are more costly than ASTER (table 4.2a) and not readily available unless acquisition is requested. EO-1 ALI data, as a possible replacement for Landsat-7 ETM data, prove effective for highlighting the iron-rich facies. However, the final design of Landsat-8 will use the ALI band configuration in the Operational Land Imager that replaced the ETM+ on Landsat-7 but unfortunately will omit ALI bands 6 and 7 and so any opportunity for further detailed mapping of iron oxy-hydroxides from orbit. ALI bands 1, 2, 3 and 4 give more comprehensive coverage of the iron-mineral charge-transfer absorption feature than Landsat TM or ASTER and can be used to discriminate between hematite, goethite and jarosite (figure 4.3b). These minerals have important implications for mineral exploration (Taranik *et al.* 1991) and water quality (McArthur *et al.* 2001). Three of the 9 ALI bands (5, 6 and 7) are more appropriately placed than Landsat TM and ASTER to cover the Fe-3 crystal field absorption of hematite, goethite and jarosite. The 765 ALI image (figure 4.10) illustrates beautifully the potential of using ALI data to detect iron oxy-hydroxides (Andrews Deller 2002; Hubbard *et al.* 2003). Only Fe-3 minerals show as red-magenta. Vegetation is blue in this rendition and as the clay zone remains blue there

are obvious limitations for mapping Horizon 3. All iron-rich soils are varying degrees of red-magenta. The more iron-rich the facies, the deeper red-magenta it appears. The very darkest red coloration is the ferricrete, Horizon 5. Horizon 4, the mottled zone, is a somewhat lighter red and modern soils developed on the ferricrete have a salmon pink tinge due to some iron staining derived from the ferricrete and iron-rich clays on which they develop.

### 4.3.4 Unvisited areas

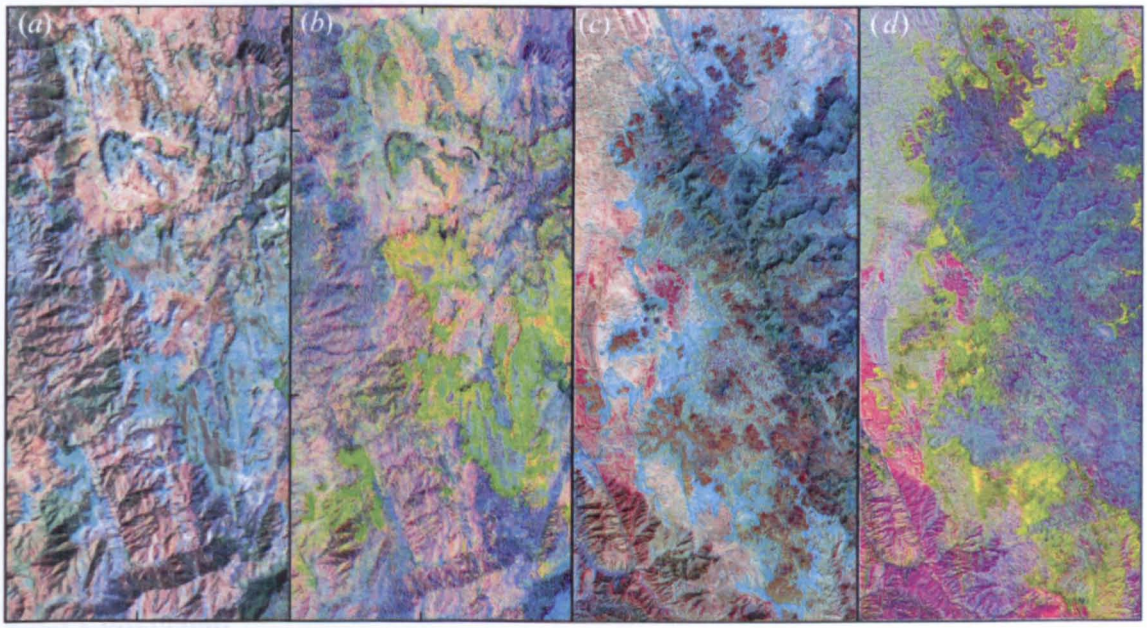


**Figure 4.11** Remote sensing images of unvisited areas - each image is 10km wide: (a) Landsat TM 742 image of Adi Caieh; (b) Landsat TM 5/4, 3/2, 7/5 image of Adi Caieh; (c) ASTER 631 image of As Sarat; (d) ASTER 4/3, 2/1, 6/4 image of As Sarat

To ensure that the strategy holds good for any locality, an unvisited area, Adi Caieh (figure 4.1), 100km south east of the test site was selected. Landsat TM 742 and band-ratio images highlight clearly three laterite facies (figure 4. 11a and b): sky blue for the kaolinitic Horizon 3 (figure 4.11a); yellow for the mottled zone and, bright reddish orange for the ferricrete (figure 4.11b), each clearly interpretable as units on a geological map. In situ evidence was then collected to verify the efficiency of image processing. Kaolinite-rich zones were picked out precisely (figure 4.11a) and the iron-rich facies were also clearly displayed (figure 4.11b). Fieldwork around Adi Caieh

indicates that the laterite cover had developed from iron- and feldspar-poor Adigrat Triassic sandstones (Tadesse *et al.* 2003) and is much thinner than that of the Asmara test area. In the Adi Caieh area silica mobilised during lateritisation has resulted in pervasive silicification. However, the flat spectrum of quartz (figure 4.2a) has no marked effect on the spectral dominance by iron minerals and kaolinite. Potentially, these silcrete variants of laterite can be discriminated from 'normal laterite' occurrences using ASTER thermal infrared (TIR) bands in a 14-12-10 ASTER colour combination image to reveal the distinctive red hues typical of silica (e.g. Gillespie 1986).

On an even larger scale, a completely unknown area As Sarat in Arabia, on the other side of the Red Sea (figure 4.1), documented only by a USGS clay resources report (Overstreet *et al.* 1977), supports the hypothesis that mapping laterite facies using remotely sensed data is regionally effective. The ASTER 631 image (figure 4.11c), picks out the blue coloured clay zone beneath flood basalts, in the same way as in the Eritrean test area roughly 650km to the south west, whilst the ASTER band-ratio image (figure 4.11d) highlights the iron- rich facies in yellow and reddish orange.

**4.3.5 Conclusion**

Using Landsat TM, ASTER and ALI data, laterite facies can be identified regionally. Mineral variations in the laterite profile can be mapped in considerable detail because of their distinctive spectra. Simple RGB colour combinations of bands and band-ratios are the most effective means of mapping these palaeosols. In situ data comprehensively validates this image processing technique, which can be used to map laterites in any arid, semi-arid or sparsely vegetated area world wide using freely available data. Once the three main laterite facies are mapped, mineral wealth and resources can be appropriately targeted; agricultural and water problems associated with ferricrete, mottled and clay horizons contained and hazardous situations avoided. Both Landsat TM and ASTER satisfy the needs for low-cost, rapid, accurate, regional mapping of laterites, the value of which should not be underestimated.

*Acknowledgements*

Enduring thanks to W.S. Deller and S.A. Drury for the benefit of their individual expertise, appropriate hardware and software facilities, editorial advice and encouragement throughout. I am indebted to the Mines Department of Eritrea and particularly to T. Keleta and M. Abreha, Directors of the Geological Survey, for their help and for making it possible for me to work in Eritrea. Both S.A. Drury's comprehensive knowledge of Eritrea and B. Negash's expertise in fieldwork are much appreciated. The work was funded in part by the Open University Research Development Fund (OU Grant 2001-2003; BR68***SC025) for which I am grateful. My thanks to J. Crowley (US Geological Survey) for his generosity in providing EO-1 ALI data and to NASA, whose extraordinarily altruistic Open Skies policy makes satellite data freely available. My thanks also go to M. G. Abdelsalam for his invaluable comments.

## 4.4 Regional mapping

Using simple RGB band combinations of Landsat TM, ASTER and ALI data Andrews Deller (2006) demonstrates how laterite facies in a well-known test site can be detected, discriminated and mapped accurately using standard techniques. Progressing to mapping laterites on a regional level without the luxury of detailed ground truth, stereoscopic, aerial and ASTER images (section 4.5) are used to help add structural detail; the mapping potential of radar is considered in more detail (section 4.6) and a tool developed for hyperspectral analysis is used for regional detection of the pure kaolinite Horizon 3 using ASTER reflectance data and EO-1 ALI data (section 4.7).

## 4.5 Stereoscopic images

Stereoscopic aerial photograph coverage of most of northern Ethiopia and Eritrea was acquired between 1963 and 1966 by a US contractor for the US Defence Mapping Agency in collaboration with the Ethiopian Mapping Agency. These aerial

photographs were taken from high altitude using a standard aerial survey camera with a 152mm focal length lens and a film-frame size of 9 x 9 inches. These were the basis for creating the DMA/EMA 1:250 000 topographic map series of the country. Panchromatic film was used through a yellow filter to reduce atmospheric haze and the approximate scale of contact prints is 1:50 000.

Giorgio Pietrangeli (Studio Pietrangeli, Rome), kindly provided prints for the area of study. Scanned at 300 dots per inch (an approximation to the grain size of the prints), the images have a resolution of ~4m per pixel. This is less than the best available Quickbird natural colour images of ~2.4m resolution satellite images of Eritrea from Google Earth and roughly the same as the more commonly available high-resolution Ikonos natural colour data from Google Earth. However, the main advantage of aerial photography over free Google Earth data is its stereoscopic coverage, presented in this study in the form of anaglyphs (see also Chapter 8). A simple anaglyph viewer can be found in a pocket on the back binding of the thesis.

Aerial and ASTER anaglyph images are used in this study for mapping the regional laterite regolith in cases where methods that exploited lithological discrimination with multispectral data were unable to resolve geological boundaries. Their main advantage lies in revealing the breaks in slope that coincide with boundaries between rocks of different resistance to erosion (figure 4.12). The most important of these stratigraphically-related features are: the unconformity at the base of the Adigrat sandstone where that unit overlies basement; the base of the laterite clay zone; the bases of the laterite mottled zone and ferricrete; the boundary between CFBs and the laterite ferricrete. Several examples are given below:

Figure 4.12a shows major boundaries in an area near Shire in Tigray, where relic ridges of flood basalts overlie an extensive terrace of resistant laterite clay zone. This in turn unconformably overlies more easily eroded basement in the canyon at the bottom of the image. Individual flows in the flood basalts are well marked because in this area each is separated by a distinctive, weakly altered palaeosol or bole. Ferricrete and mottled zones outcrop at the base of the flood basalt ridges, forming

patchy dark veneers over the clay zone.

Figure 4.12b in Eritrea shows the same relationships but in a distinctive outlier of laterites capped by a conical hill of flood basalt. The laterites occur as irregular terraces and flat-topped ridges. Both ferricrete and clay zones are more resistant to erosion relative to mottled zone and the underlying basement. The steep compositional banding in the basement, which controls NW-SE linear features, emphasises the unconformable relationship with laterites.

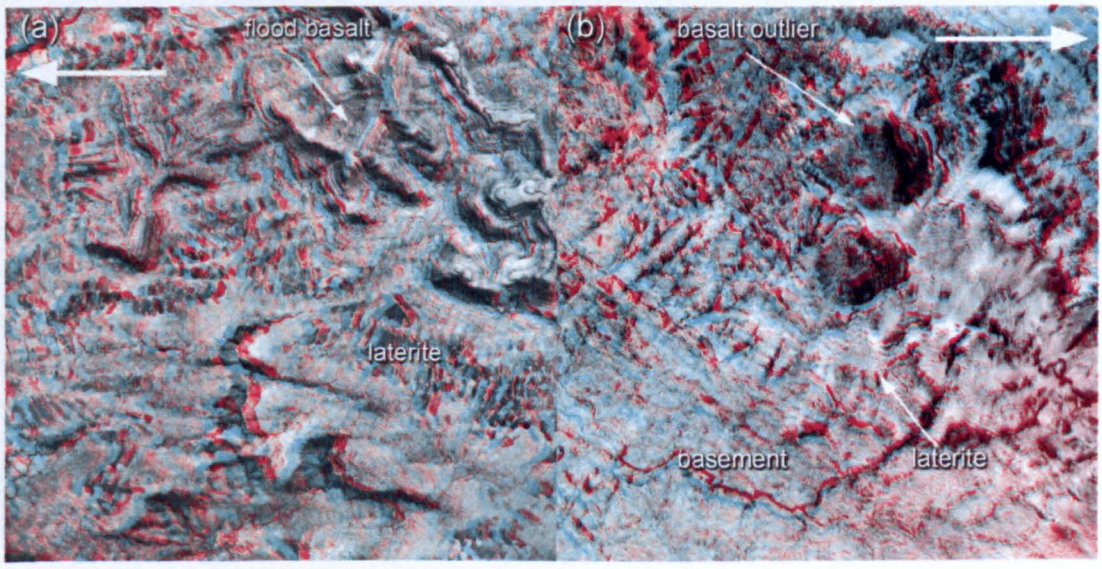


**Figure 4.12** Stereo anaglyphs of high-altitude, panchromatic aerial photographs (viewer in pocket at rear of thesis) illustrating relationships between flood basalts, laterites, and basement. (a) 5km north of Shire, Tigray Ethiopia. (b) 20km south of Asmara, Eritrea. Each image is about 5km across

ASTER images offer a wide-area, synoptic view of relationships at a pixel size about three times that of available aerial photographs. Mapping could be done using GeoEye or Quickbird data but these would give too much intricate detail for the regional maps intended for this work. No high-resolution images (better than 5m resolution) are currently available that improve on black and white panchromatic, natural colour or VNIR false colour renditions and none of these are useful for mapping different laterite lithologies. ASTER however is useful as it combines stereo with excellent multispectral capabilities.

Figure 4.13 shows the thickest sequence of flood basalts in Eritrea, exposed on Emba Tekera (lower left). They are surrounded by irregular outcrops of laterite,

which form irregular terraces, plateaus and mesas that rest unconformably on basement rocks. As with aerial photographs, the lack of spectral information other than albedo makes confident discrimination between lithologies difficult.

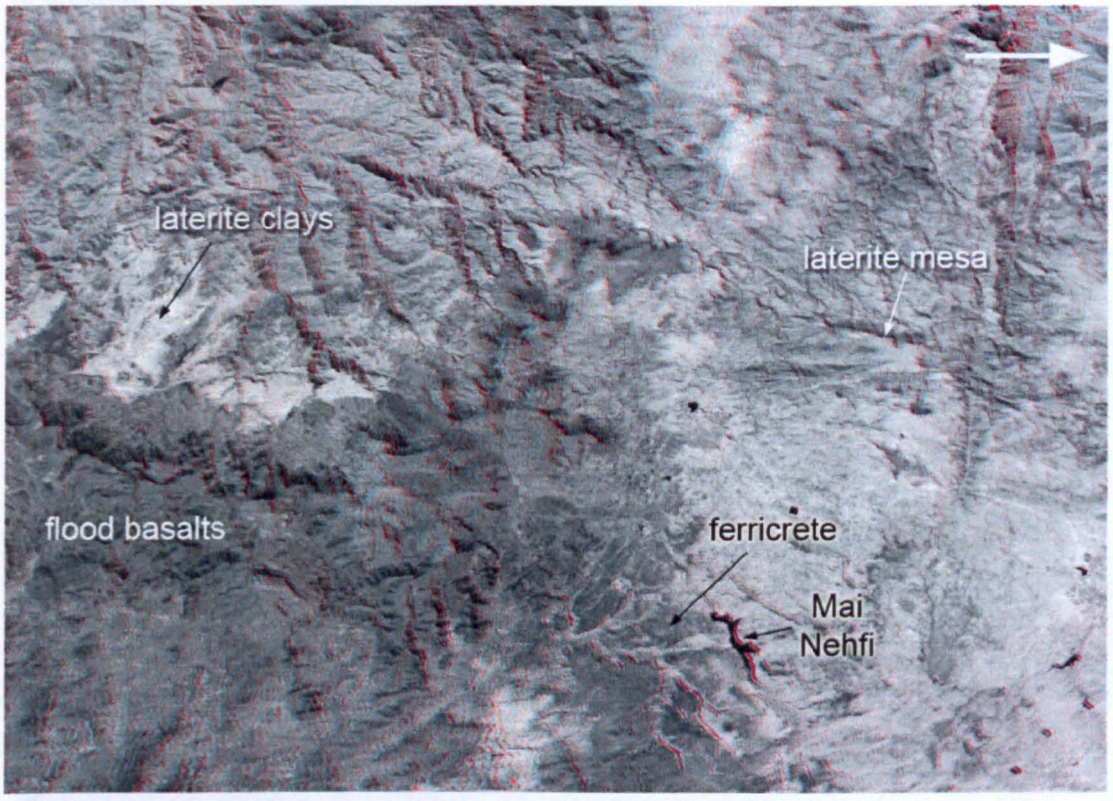


**Figure 4.13** Stereo anaglyph of ASTER data for part of the test area near Asmara (note the prominent reservoir of Mai Nehfi for reference to images in Andrews Deller (2006)). Image is about 25km wide. West is at the top since parallax shifts in stereo images must be arranged with left- and right-eye views along the flight path, i.e. NNE-SSW in the case of ASTER data

Figure 4.13 shows the thickest sequence of flood basalts in Eritrea, exposed on Emba Tekera (lower left). They are surrounded by irregular outcrops of laterite, which form irregular terraces, plateaus and mesas that rest unconformably on basement rocks. As with aerial photographs, the lack of spectral information other than albedo makes confident discrimination between lithologies difficult.

Figure 4.14 is close to the area of maximum thickness of the flood basalts in the Ethiopian Plateau, where the Tekesse river has incised a valley around 2000m deep to expose their base. Immediately beneath them are laterites that outcrop as a series of terraces above cliffs that descend to tributaries of the Tekesse River. Here the cliffs are in Adigrat sandstones and glaciogenic rocks (Chapter 2), over which the laterites

rest with slight angular unconformity. In turn they are profoundly unconformable upon the Neoproterozoic basement complex. The intricacy of some of the relic ridges of basalts at lower left seems to be a result of the resistance of the underlying laterites to erosion.

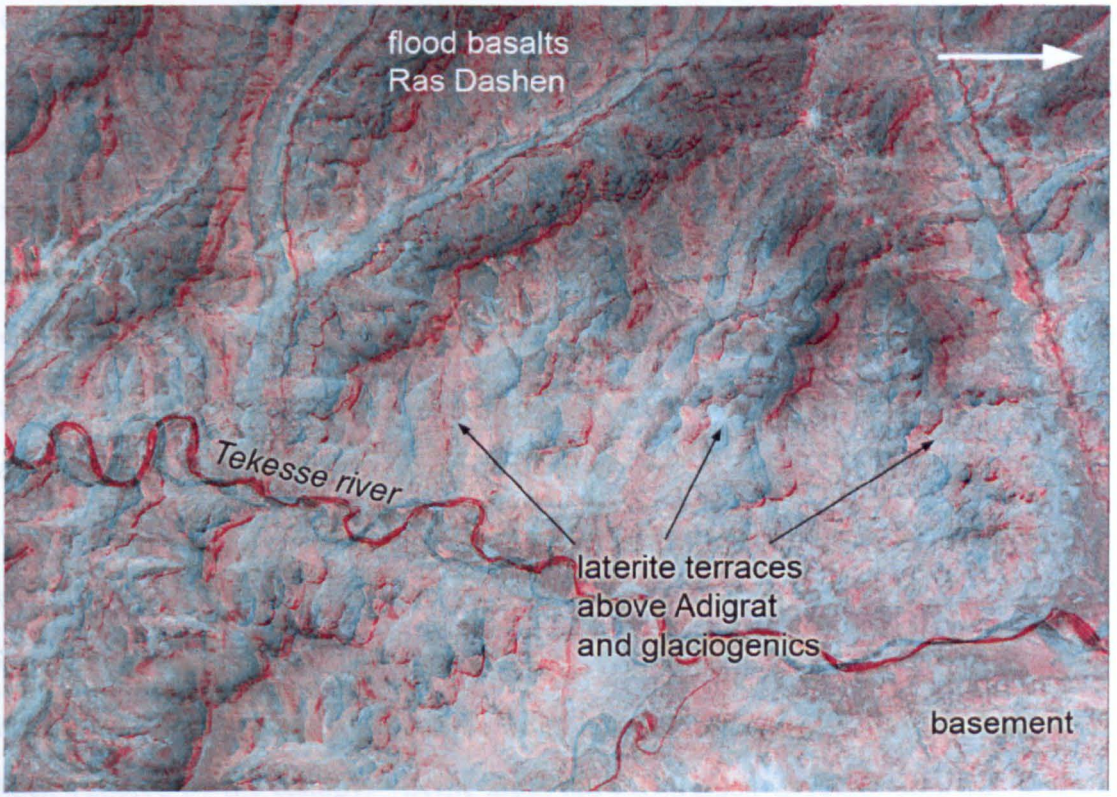


**Figure 4.14** Stereo anaglyph of ASTER data in the headwaters of the Tekesse river in Tigray, Ethiopia, about 40km west of Mekele with the eastern flank of Ras Dashen at the top. Image is about 25km wide

## 4.6 Multi-frequency radar images

This section presents results based on the analytical methodology for radar imaging outlined in Section 3.4. All three radar bands were deployed by the joint US-German SIR-C/XSAR experiment carried by the Space Shuttle Endeavour in 1994, which deployed X-, C- and L-band radar (3, 6 and 23cm wavelengths respectively). It is possible to access the effectiveness of multi-frequency radar for laterite facies mapping by combining L-, C- and X-band as RGB in a false-colour image (figure 4.15).

On the Eritrean plateau flat-topped mesas and more extensive areas have

developed on the highly resistant ferricretes to form almost horizontal surfaces that roughly mark the former laterite-CFB boundary. Because of their abundant iron-rich nodules that resist erosion while clay-rich patches are etched out, ferricrete surfaces usually appear rougher in the field than those on the more homogeneous mottled and clay zones. These differences in surface roughness affect radar microwaves.

Dark areas in Figure 4.15 are smooth to all three wavelengths, and include the open water of Main Nehfi reservoir in the SW quadrant, Asmara airport's main runway and irregular patches of recent alluvium in drainages. Asmara city appears in cream to white, showing that it contains features that are rough to all three wavelengths, i.e. buildings with many corner reflectors. Reddish to brown areas signify that more L-band than X- and C-band energy is backscattered to the radar antenna, which is impossible for areas of rough solid surfaces. In fact they coincide with areas with vegetation, dense prickly pear plantations on the rugged topography east of Asmara and patches of low bush elsewhere. The coloration may be explained by shorter wavelength X- and C-band having passed through the canopy of branches and twigs and being absorbed, while longer wavelength L-band has been backscattered by the canopy. Some areas are highlighted as bright blue due to their high X-band backscatter and 'smoother' responses to C- and L-band. These areas correspond to surfaces on top of ferricrete that have a covering of loose, pisolitic nodules of iron minerals. Ferricrete grains are about 1cm in diameter; rough to X-band but smooth to C- and L-band, which explains their bright blue hues on Figure 4.15. Ferricrete surfaces show in this way, to the east and north of Asmara as do pisolitic gravels derived from the mottled zone. Areas completely lacking laterite are also misidentified. Despite being widespread, areas of laterite clay zone are unrecognisable on Figure 4.15 in contrast with other images in section 4.3. In fact in the north quadrant of Figure 4.15, outliers of the clay zone and saprolite have a similar blue signature to ferricrete surfaces. Radar images lack any direct relation to unique mineral assemblages, as the same radar responses can occur on widely different rock types.

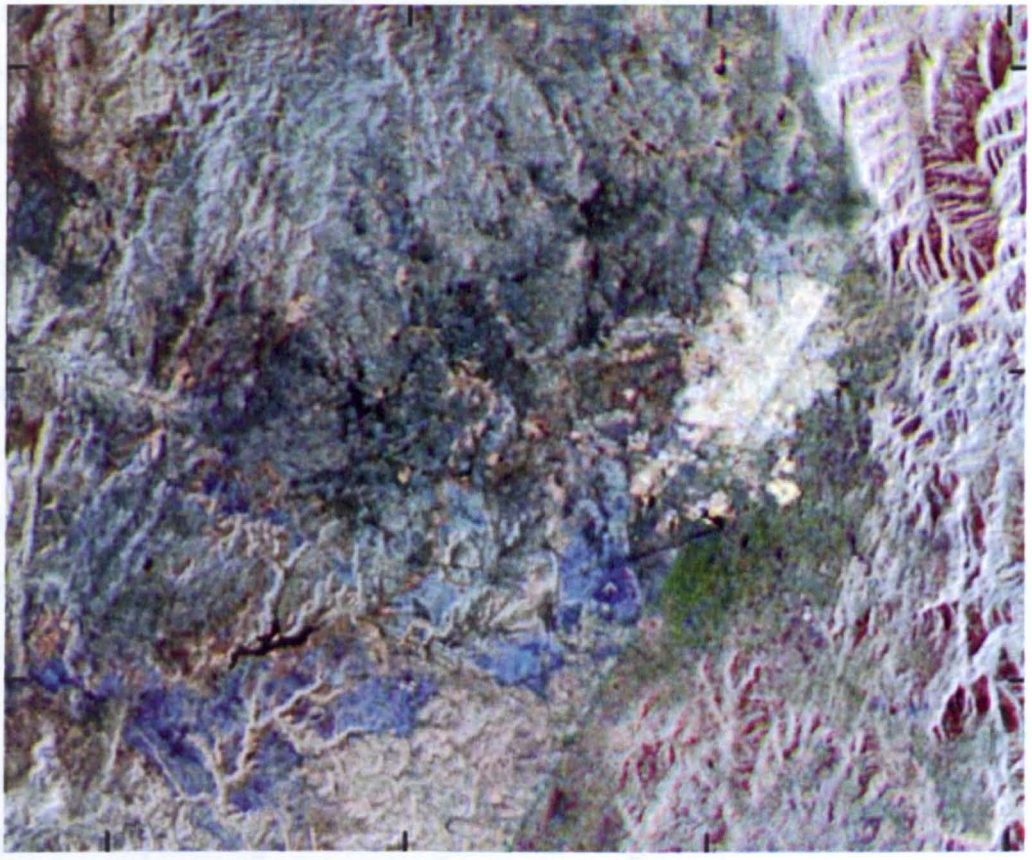

**Figure 4.15** Image of SIR-C/XSAR data using L-, C- and X-band data in RGB, covering part of the Asmara test area (compare with figure 4.8).

## 4.7 Earth Observing Mission 1 (EO-1)

NASA launched the experimental EO-1 mission on 21 November 2000. This mission took satellite remote sensing a step further. It carried two instruments; the broad-band, multispectral Advanced Land Imager (ALI) in preparation for the replacement of Landsat-7 and Hyperion, the first Earth- orbiting hyperspectral system to test on a global scale methodology developed for similar airborne technology.

*The EO-1 Advanced Land Imager (ALI)*

EO-1 (ALI) was aimed at testing sensors that could be used on future Landsat instruments. Five of these (ALI 2, 3, 4, 8 and 9) are approximately the same as Landsat-7 ETM+ and Landsat-4 and -5 TM bands1, 2, 3, 5 and 7. ALI 1 (blue-violet) explores possibilities for measuring depths of clear-water bodies and assessing haze. Two bands (ALI 5 and 6) split Landsat TM band 4 into two, in order to avoid a minor

water absorption band. ALI 7 covers an atmospheric window in the SWIR, unaffected by water vapour. Table 4.1 compares the bandwidths from ALI, ETM+ and ASTER, while Figure 4.3b shows ALI band widths compared with spectral plots of four common iron minerals - hematite, goethite, jarosite and iron-rich chlorite. ALI images are in 150km wide swaths that comprise four abutting 37km wide data strips. The only advance that ALI data presents for geological work is the split of the wavelength range of TM band 4 into ALI 5 and 6 and the addition of ALI 7. These cover the range of the $Fe^{3+}$ crystal-field effect absorption feature and may discriminate them (see figure 4.3b). Analysis of ALI data is covered in Chapter 5.

*The EO-1 Hyperion instrument*

Hyperion is NASA's second attempt at launching a hyperspectral imaging system into orbit. The previous Lewis mission was destroyed on 28 September 1997 before gathering any data, when its control system failed. Hyperion aims to investigate the possibilities of providing low-cost global coverage, equivalent to airborne hyperspectral systems, such as AVIRIS, which have opened up new possibilities for recognising and quantitatively mapping different minerals and varieties of vegetation, including plants that are stressed by excess water, drought and toxic metals.

Hyperion's hyperspectral imaging system focuses radiation from the Earth's surface onto a block made up of 220 narrow-waveband detectors. As the block of detectors sweeps over the ground beneath, it records data for each waveband in lines 256 pixels wide across the flight path with a pixel size of 30m, in a 7.7 x 42km image swath. Each image pixel obtains data from 220 individual narrow wavebands of between 0.35 and 2.58μm, so covering roughly the same range of visible, near infrared and short-wave infrared as TM, ASTER and ALI. The wavelength range of individual sensors ranges from 0.01μm in the VNIR to 0.03μm in the SWIR is comparable with the spectral resolution of a laboratory or field spectrometer. Of the 220 Hyperion bands, 63 either contain no data or duplicate other bands, in effect leaving 157 bands containing valid data for reconstructing surface spectra.

Hyperion data can be used in two ways:

- To provide a spectral plot in the reflected 0.4 to 2.4μm region for each pixel imaged by the system, which can be compared with field- or standard laboratory spectra - e.g. by using spectral angle mapping whereby image pixels whose spectra resemble that of a single mineral or mixture of minerals are found and,
- To highlight specific types of surface material, either by spectral classification methods or by choosing 3 of the bands that cover specific spectral features to use in an RGB display.

In brief, hyperspectral image data are aimed at quantitatively mapping the surface according to the actual materials from which it is composed. For geological applications such data provide a means of mineral mapping (Chapter 5).

As with all remotely sensed 'raw' image data, the values recorded in a Hyperion band represent *radiance* - the energy received from the ground by the sensor. Each band is differently affected by solar radiation having passed through the atmosphere twice, once from the Sun to the surface and again after reflection from the surface to the sensor. Measurement of radiance from orbit introduces a number of factors that obscure the true spectra of surface materials. For example, the amount of solar energy illuminating the surface varies with wavelength and with the sun's height in the sky when the image was acquired. Other factors include wavelength-selective absorption and scattering by atmospheric gases and particulates and illumination differences due to topography (direction and angle of slope, and shadowing). In order to make meaningful comparisons between image spectra and laboratory reflectance spectra, the image radiance values must be corrected or calibrated to *reflectance* (Thome 1999) by removing these other contributing effects. This is essential because lab- and field spectra, with which hyperspectral data need to be compared, are expressed as reflectance: the proportion of incoming solar radiation (*irradiance*) that a surface reflects in each narrow band, i.e. radiance divided by irradiance in the range 0.0 to 1.0. In the lab or the field this involves measuring the solar radiation reflected by a perfect reflecting surface, a measurement which gives the irradiance for each band. Radiance from the natural surface is then divided by irradiance to give each band a

value for reflectance. This is rarely possible for data gathered by satellite, as one would need to use a spectrometer to measure irradiance at the exact time the satellite passed over as atmospheric and illumination conditions vary with time. Fortunately, ASTER VNIR and SWIR data calibrated to reflectance are available from NASA and ERSDAC so the method known as *Equal Area Normalisation* (section 3.2.3) was used as an alternative.

### 4.7.1 Hyperspectral image analysis

Hyperspectral imaging systems that cover the reflected region produce data for each pixel that closely resemble those produced by a field- or lab spectrometer when plotted as reflectance against wavelength. They are effectively reflectance spectra of patches of the Earth's surface that correspond to the dimensions of an image pixel and can be directly compared with spectra of rocks, soil or plants obtained under controlled conditions, thereby opening the possibility of mapping the distribution of similar materials over vast areas. Even with broad-waveband data and limited numbers of bands (e.g. Landsat and SPOT), such '*supervised classification*' has produced considerable success in mapping distributions of plant communities. Although there has been some success in lithological mapping of areas of bare rock and soil (Drury & Holt 1997; Abrams *et al.* 1988), several factors have conspired against accurate mapping using simple classification. These are:

- mixtures of several dominant minerals producing complex spectra;
- occurrences of identical rocks that are variably weathered, coated with lichens or masked by plants yielding very different spectra;
- disproportionate spectral effects by minor minerals, e.g. reduced albedo by minor amounts of organic carbon or sulfides;
- spectrally bland mixtures of rocks such as anhydrous silicates and carbonates;
- Reflected radiation emanating from the top few micrometres of natural surfaces e.g. dusts or 'desert varnish' (Rivard *et al.* 1992).

A more fruitful approach has been to match remote sensing spectra to those of pure minerals or mixtures of several minerals that resulted in successful mapping of

hydrothermal alteration zones of Cuprite in Nevada (Kruse *et al.* 1990; Rowan *et al.* 2003; Cloutis 1996).

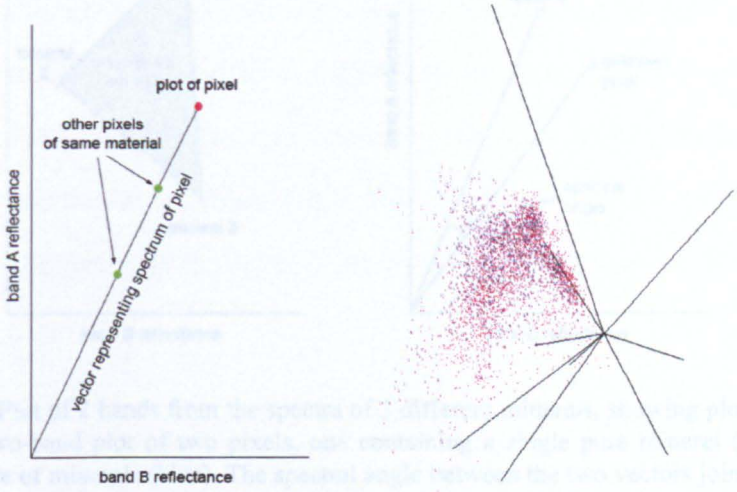


**Figure 4.16** (a) Two-band plot of spectral data from a pixel; (b) A graphical simulation of many pixels plotted for 9 spectral bands

Another kind of spectral plot is more appropriate for computer analysis of hyperspectral data. Figure 4.16 shows a simple two-band example and one that visualises 9 bands. In this format, the spectrum of a pixel may also be considered as the end point of a line through hyperspace that begins at the origin of the co-ordinate system. Spectra with exactly the same shape but with different overall reflectance (albedo) or illumination (as a result of topographic shadowing) plot as points on the same vector at different distances from the origin – the further from the origin the higher the albedo of the pixel. It is important to note that every natural mineral is compositionally and spectrally variable. So the vector shown on Figure 4.16a would in practice be an acute-angled triangle whose most acute apex is at the origin.

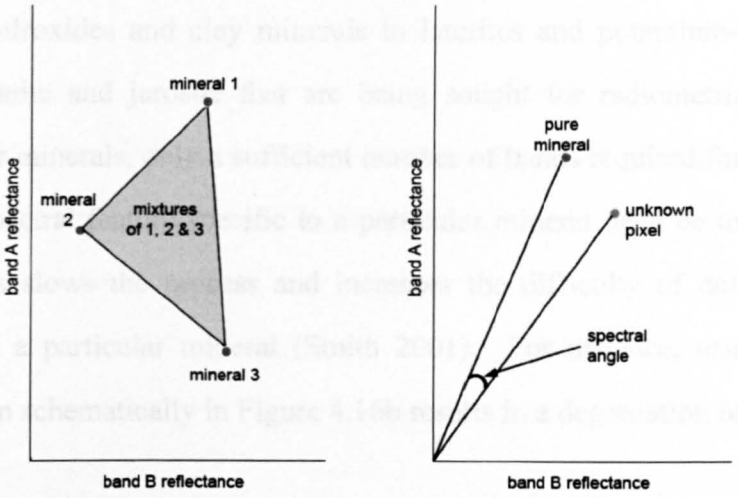


**Figure 4.17** (a) Plot of 2 bands from the spectra of 3 different minerals, showing plots of the three end members (b) Two-band plot of two pixels, one containing a single pure mineral (red), the other an unknown mixture of minerals (blue). The spectral angle between the two vectors joining the pixel plots to the origin is a measure of the likelihood that the unknown pixel contains a proportion of the pure mineral

Although some rocks are made of a single mineral (e.g. pure limestone or quartzite), the pixel sizes of most imaging devices generally ensure that more than one material contributes to a pixel-spectrum measured by the sensors. The resulting spectrum is a mixture of the spectra of each component (figure 4.17a) that depends on the relative proportions of the end members. Where one of the end members has a strong feature at some wavelength in its spectrum, and others do not, even small proportions of each end member will show in the combined spectrum. Spectra of such 'mixed pixels' will plot on a different line in hyperspace from that of the pure mineral. Consequently there will be a mathematically definable angle between the two spectra (figure 4.17b). The smaller that '*spectral angle*' (Smith 2001) is, the more likely that the surface consists of a high proportion of the pure mineral. The larger the angle, the less likely is the presence of that mineral in a ground pixel. In practice there will be a spectral angle beyond which spectral vectors of other pixels do not contain the mineral in question. Minerals with highly distinctive spectra and intricately marked spectral features that cover specific wavelengths are more easily distinguished than those with featureless spectra or broad features.

*Spectral Angle Mapping* (see Chapter 3) can be used to locate zones that contain iron oxy-hydroxides and clay minerals in laterites and potassium-bearing minerals such as alunite and jarosite that are being sought for radiometric dating. When mapping for minerals, only a sufficient number of bands required for the algorithm to resolve a spectral feature specific to a particular mineral need be used. The use of many bands slows the process and increases the difficulty of defining pixels that characterise a particular mineral (Smith 2001). For instance, using all 9 ASTER bands shown schematically in Figure 4.16b results in a degradation of the results.

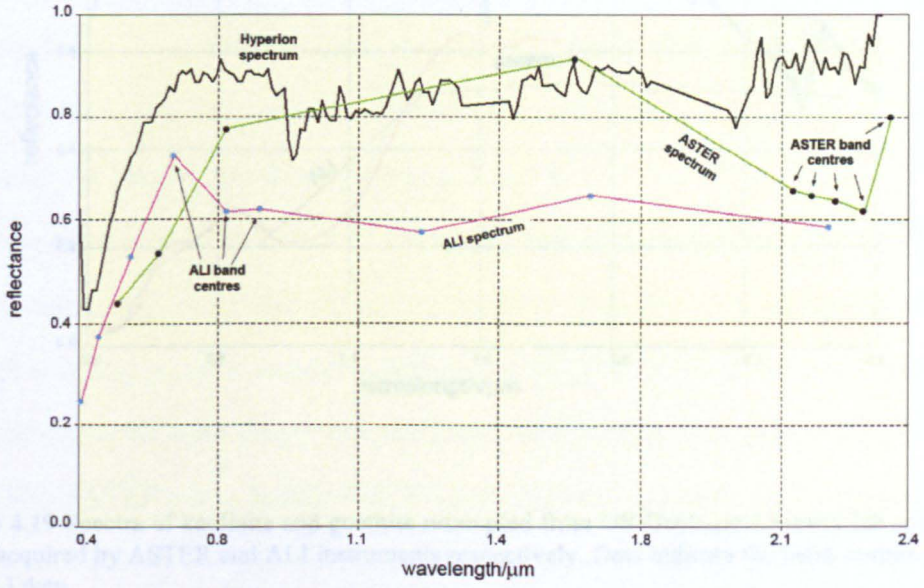


**Figure 4.18** Comparison of reflectance spectra produced by the Hyperion (black), ALI (magenta) and ASTER (green) instruments for a single pixel located on weathered, partly vegetated flood basalts 20km SW of Asmara. Note: reflectance calculated using the equal-area normalisation method

Figure 4.18 compares the spectra produced by Hyperion, ASTER and ALI for one pixel in an area in Eritrea where all three instruments have recorded data. The general shapes are similar. The ALI spectrum shows lower overall reflectance than that produced by Hyperion, despite both data sets being recorded at the same time. This probably results from the different designs of the two EO-1 instruments; the Hyperion sensors produce a stronger response to reflected radiance than those carried by ALI.

Figure 4.19 compares two mineral spectra that have been resampled to ALI and ASTER bands with the lab spectra from which they were derived. Although highly

stylised relative to the full USGS spectra, the ASTER kaolinite spectrum shows its strong Al-OH feature at 2.20μm. The ALI goethite spectrum shows part of the mineral's prominent crystal-field feature in the VNIR and the distinctive charge-transfer feature that gives goethite its yellow-brown colour. These results (see Chapter 5) indicate that both minerals can be detected applying the Spectral Angle Mapper to ASTER and ALI data.

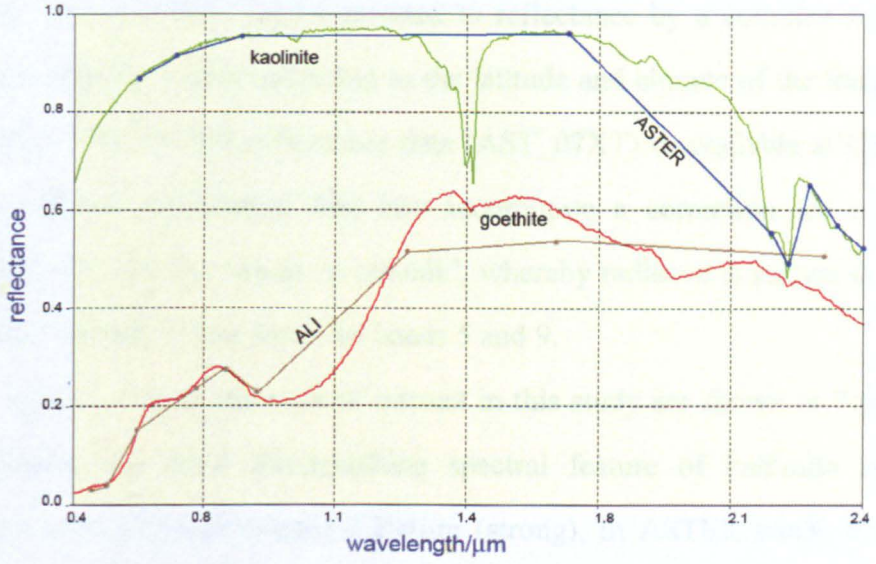


**Figure 4.19** Spectra of kaolinite and goethite resampled from US Geological Survey lab spectra to the bands acquired by ASTER and ALI instruments respectively. Dots indicate the band centres of ASTER and ALI data

Because the ASTER and EO-1 data used in this study consisted of scenes captured on a range of dates, it was most expedient to use the same resampled lab spectra for the minerals of interest consistently, i.e. those for kaolinite, alunite, hematite, goethite and jarosite from the USGS spectral library. This ensured a consistent approach to the analysis, which aimed at detecting rocks containing significant amounts of the minerals, rather than areas of pure minerals. Given the suite of minerals selected, the most likely rocks to be detected would be the lateritic clay zone, mottled zone and ferricretes. Ideally, representative spectra of each laterite horizon should have been acquired in the field at the time the data were captured. This was impossible because

of the irregular timing of ASTER data collection for all the scenes used and because the EO-1 data were acquired when an opportunity presented itself: neither coincided with opportunities for fieldwork.

Experiments were carried out with the spectrally most detailed data, Hyperion, which seemed to offer the greatest potential for identifying the selected minerals. The same calibration method was used for the broader band EO-1 ALI data.

ASTER data are generally available as radiance data, but the USGS offers 'on-demand' data that have been converted to reflectance by a complex algorithm that uses atmospheric models according to the latitude and climate of the imaged area. A summary of the ASTER reflectance data (AST_07XT) is available at USGS (2009). The on-demand reflectance data also incorporate a correction for a problem in ASTER SWIR data known as 'cross-talk', whereby radiance is known to 'leak' from the sensor for band 4 into those for bands 5 and 9.

Lab spectra of pure minerals of interest in this study are shown in Figure 4.3. As an example, the main distinguishing spectral feature of kaolinite is a pair of absorptions at 2.163μm (weak) 2.204μm (strong), in ASTER bands 5 and 6. For Hyperion data the wavelength range chosen for kaolinite detection was 2.02-2.34μm, while for ASTER, data bands 4 to 8 (1.65-2.33μm) proved most effective. These ranges also include Al-OH related features for alunite, jarosite, chlorite and saponite (an Fe,Mg smectite clay) and the distinguishing C-O features for several carbonates (Andrews Deller 2006, Figures 4.3a and b). The appropriate spectral range for the broad crystal-field and charge-transfer features that characterise the iron minerals expected in the ferricrete and mottled zone is 0.7 to 1.6μm (Andrews Deller 2006, Figure 4.2b). These are only covered usefully by EO-1 ALI bands 4 to 8 among the non-hyperspectral data sets. Table 4.6 itemises the wavelengths of the main spectral features that form the basis for spectral angle mapping of several minerals. However, as the kaolinite-rich laterite clay zone is the key to regional mapping of laterites, this section concludes by discussing the use of spectral angle mapping (SAM) for mapping kaolinite, while other minerals are covered in Chapter 5.

**Table 4.6** Main spectral features of minerals of interest in this study, the ASTER and ALI bands in which they occur and the ranges of bands/wavelengths in ASTER, ALI and Hyperion data used for spectral angle mapping. CF = crystal-field

| Mineral | Main spectral features (μm) | ASTER bands | ALI bands | Hyperion range (μm) |
|---|---|---|---|---|
| Kaolinite<br>$Al_2Si_2O_5(OH)_4$ | 2.163 (weak)<br>2.204 (strong) | 5<br>6<br>4-8 used | 9<br>9<br>not used | 2.10-2.34 |
| Alunite<br>$KAl_3(SO_4)_2(OH)_6$ | 2.168 (broad)<br>2.322 | 5<br>8<br>4-8 used | 9<br>not used | 2.10-2.34 |
| Hematite<br>$Fe_2O_3$ | Broad CF 0.7-1.0 | 2, 3, 4<br>1-4 used | 4, 5, 6, 7<br>2-7 used | 0.70-0.93 |
| Goethite<br>FeO.OH | Broad CF 0.7-1.2 | 2, 3, 4<br>1-4 used | 4, 5, 6, 7, 8<br>2-7 used | 0.70-0.93 |
| Jarosite<br>$KFe_3(SO_4)_2(OH)_6$ | Broad CF 0.7-1.2<br>2.265 (broad) | 2, 3, 4<br>6, 7<br>1.4 and 4-8 used | 4, 5, 6, 7, 8<br>9<br>2-7 used | 0.70-0.93<br>2.25-2.34 |
| Chlorite<br>$(Fe,Mg,Al)_6(Si,Al)_4O_{10}(OH)_8$ | 2.245 (strong)<br>2.325 (strong) | 7<br>8<br>4-9 used | 9<br>not used | 2.25-2.34 |
| Saponite<br>$(Mg,Fe)_3(Al,Si)_4O_{10}(OH)_2(Ca,Na)_{0.3}.4H_2O$ | 2.315 (strong) | 8<br>4-9 used | 9<br>not used | 2.10-2.34 |
| Dolomite | 2.320 (strong) | 8<br>4-8 used | 9<br>not used | 2.10-2.34 |

ASTER 631, ALI 765 or the equivalent much narrower bands in Hyperion data displayed in RGB illustrate the usefulness of grey-tone or colour density-sliced images for checking the consistency of SAM results. Figure 4.20 compares a kaolinite spectral angle image derived from ASTER bands 4-8 with an ASTER 631 image. Note that the darkest areas of Figure 4.20a coincide with the distinctive laterite facies on Figure 4.20b, as expected from the clay-rich nature of all the laterite facies.

Figure 4.21a shows Figure 4.20a with spectral angle values less than a chosen threshold set to a bright colour with higher values showing as grey levels. Setting all values below the threshold to 1 and those above the threshold to 0 creates a 1-bit file that defines all pixels deemed to be significantly rich in the chosen mineral (figure 4.21b). This bit-map then forms the basis for simple boundary-detection software that converts the raster image to vector polygons for use in map creation.

Unfortunately, the automated USGS calibration of ASTER data to reflectance does not always fully allow for atmospheric effects. However, this is only noticeable

where extreme differences in elevation separated occurrences of laterites, for example between those on the plateau and those at the foot of the Escarpment at Massawa. Satisfactory results for the two elevation extremes were achieved by using slightly different thresholds.

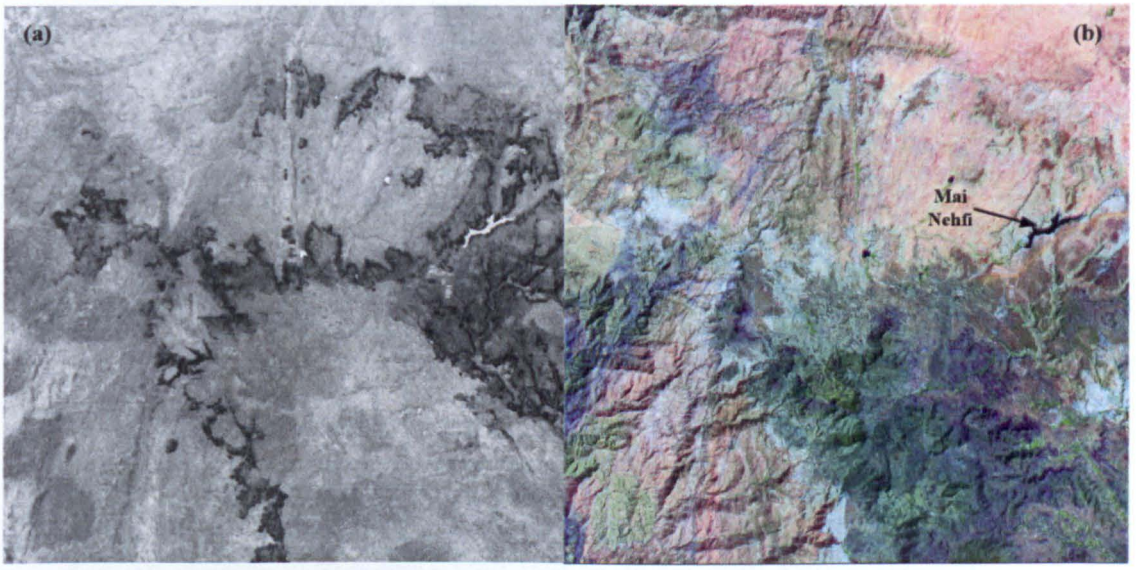


**Figure 4.20** (a) Grey-tone rendition, with stretched contrast, of an image of kaolinite spectral angle derived from ASTER data, which includes part of the Asmara test area. (b) ASTER 631 RGB image of the same area (for reference to figures in Andrews Deller 2006, note the black reservoir of Mai Nehfi)

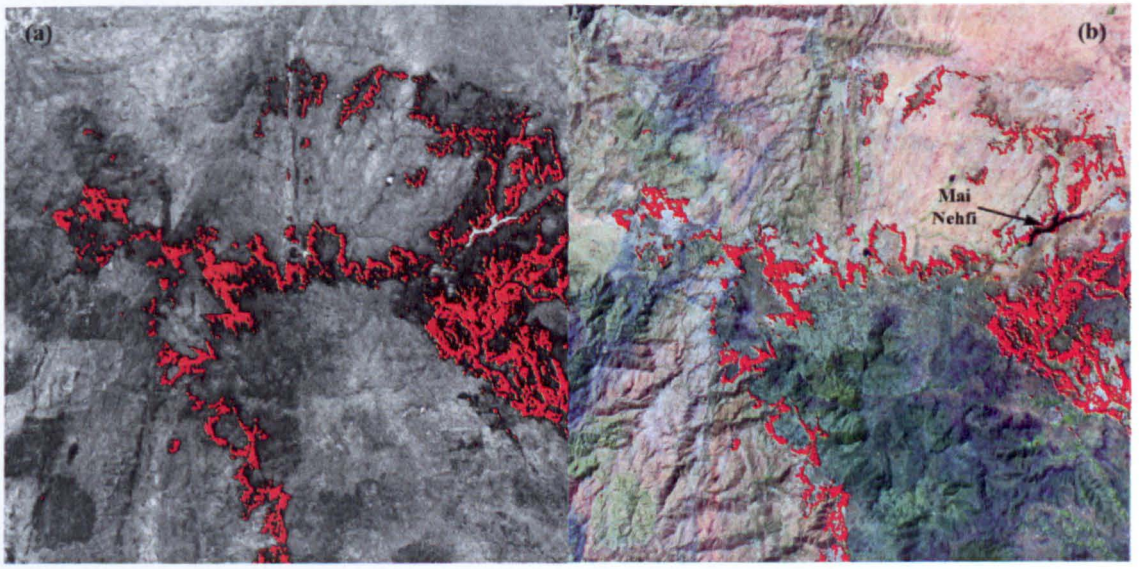


**Figure 4.21** (a) Image of kaolinite spectral angle (figure 4.21a) in which pixels with values below a threshold of 5.5 have been set to red. (b) Bit-map of (a) with kaolinite pixels superimposed on ASTER 631 image

The efficiency and accuracy of spectral angle mapping for detecting kaolinite, in particular, lays a firm basis for rapid regional mapping of the laterite facies and their local context. A vector map of the clay zone then forms a guide for manually

mapping mottled and ferricrete facies.

## 4.8 Concluding remarks

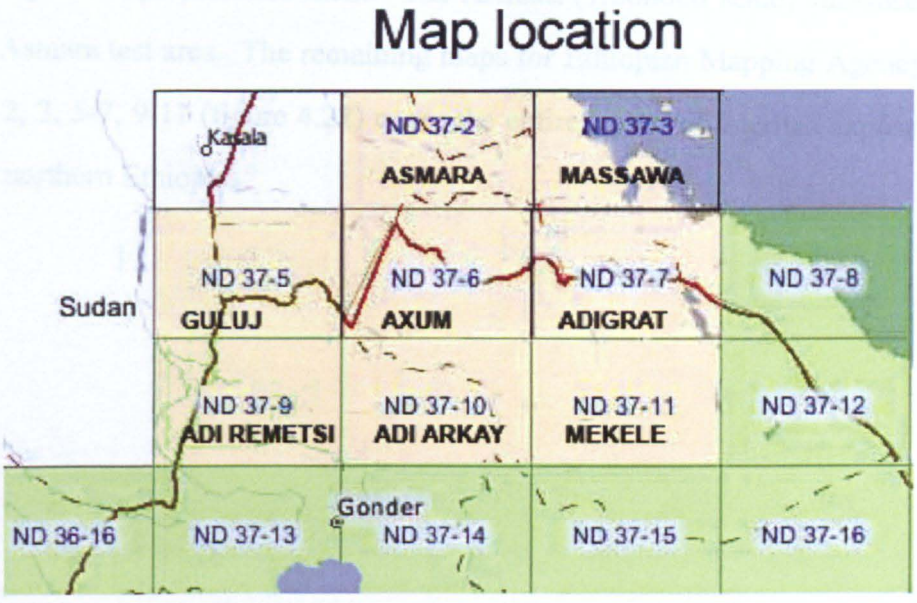


**Figure 4.22** Laterite map sheets

Like most well preserved iron-crusted laterite palaeosols, those in Eritrea and Tigray have the classic laterite profile with five main horizons. The excellent preservation of the upper three horizons allows for their ready identification on digitised satellite data and geological mapping of the palaeosols throughout the region (figure 4.2; sheets ND 37: 2, 3, 5-7, 9-11; Asmara sub-sheet). The mapping of laterite facies is fundamentally controlled by their simple mineralogy and the distinct spectral properties of those minerals. These are well-matched to the spectral coverage of freely available Landsat TM, ASTER and ALI data, which exploit and uniquely discriminate different laterite horizons. Although there are many sophisticated methods which might be employed for regolith mapping, these are not accessible to many who might benefit from laterite facies maps (see Chapter 8). Therefore a simple method of isolating laterite horizons on free satellite images is designed here together with a cheap and novel means of mapping the laterite regolith for those who live and work in such areas.

Five geological maps of laterite facies and four image maps that highlight the distribution of the clay zone (Horizon 3) conclude this chapter. These nine maps, each presented in A3 format, are bound between Pages 159 and 160; a legend for the geological maps precedes them. The Asmara (1:200000 scale) sub-sheet highlights the Asmara test area. The remaining maps for Ethiopian Mapping Agency sheets ND 37: 2, 3, 5-7, 9-11 (figure 4.22) cover the entire extent of laterites exposed in Eritrea and northern Ethiopia.

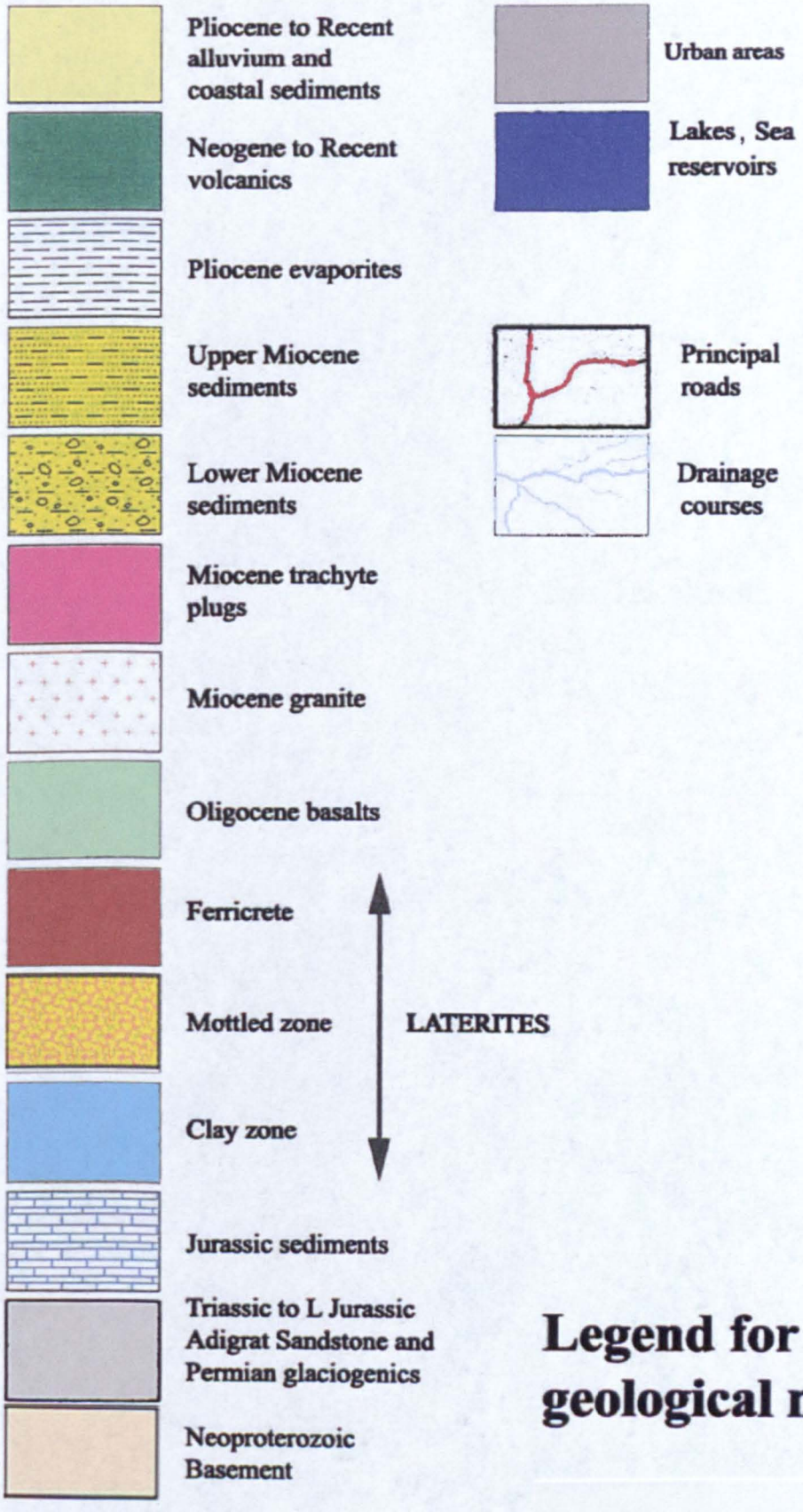


# Legend for geological maps

1:250 000 versions of Sheets ND 37-2, -3, -6, -7 in pocket at rear of thesis

37°30'E
38°E
38°30'E
39°E
16°N
15°30'N
15°N

KEREN

Barka River

Akurdet

Adi Tekelezan

ASMARA

Mai Nefhi

Barentu

0 10 20 30 40 50 km

Sheet
ND 37-2

ASMARA

37°30'E 38°E 38°30'E 39°E

16°N

15°30'N

15°N

KEREN

Adi Tekelezan

Barka River

Akurdet

ASMARA

Mai Nefhi

Barentu

Sheet
ND 37-2

Scale: 1:250 000

0 10 20 30 40 50 km

# ASMARA

39°E
39°30'E
40°E
40°30'E
16°N
15°30'N
15°N

Wik'ro
MASSAWA
Dogali
Hirgigo
Ginda
Dekemhare

Sheet
ND 37-3

0 10 20 30 40 50 km

# MASSAWA

39°E 39°30'E 40°E 40°30'E

16°N

15°30'N

15°N

Wik'ro

Dogali

MASSAWA

Hirgigo

Ginda

Dekemhare

Scale: 1:250 000

0 10 20 30 40 50 km

Sheet
ND 37-3

# MASSAWA

37°30'E
38°E
38°30'E
39°E
15°N
14°30'N
14°N

Tera Imni
Arena
MENDEFERA
Mereb River
Shiraro
Shilalo
Shiyaboni
Adi Hageray
Adi Nebrid
Adi Quala
ERITREA
ETHIOPIA
AXUM
Adwa
Shire

0 10 20 30 40 50 km

Sheet
ND 37-6

AXUM

37°30'E 38°E 38°30'E 39°E

15°N 14°30'N 14°N

Tera Imni

Areza

MENDEFERA

Mereb River

Shilalo

Shiraro

Adi Quala

Shiyaboni

Adi Hagoray

Adi Nebrid

ERITREA

ETHIOPIA

Adwa

AXUM

Shire

Scale: 1:250 000

0 10 20 30 40 50 km

Sheet
ND 37-6

# AXUM

39°E
39°30'E
40°E
40°30'E
15°N
14°30'N
14°N

Mersa Fatma

ADI KAIEH

Senafe

ERITREA

ETHIOPIA

Enticcio

ADIGRAT

0 10 20 30 40 50 km

Sheet
ND 37-7

# ADIGRAT

39°E 39°30'E 40°E 40°30'E

15°N

14°30'N

14°N

ADIG'AEH

Senafe

Mersa Fatma

ERITREA

ETHIOPIA

Enticcio

ADIGRAT

Scale: 1:250 000

0 10 20 30 40 50 km

Sheet
ND 37-7

# ADIGRAT

# ASMARA
## Sub-Sheet

Scale: 1:200 000

0 2 4 6 8 10 km

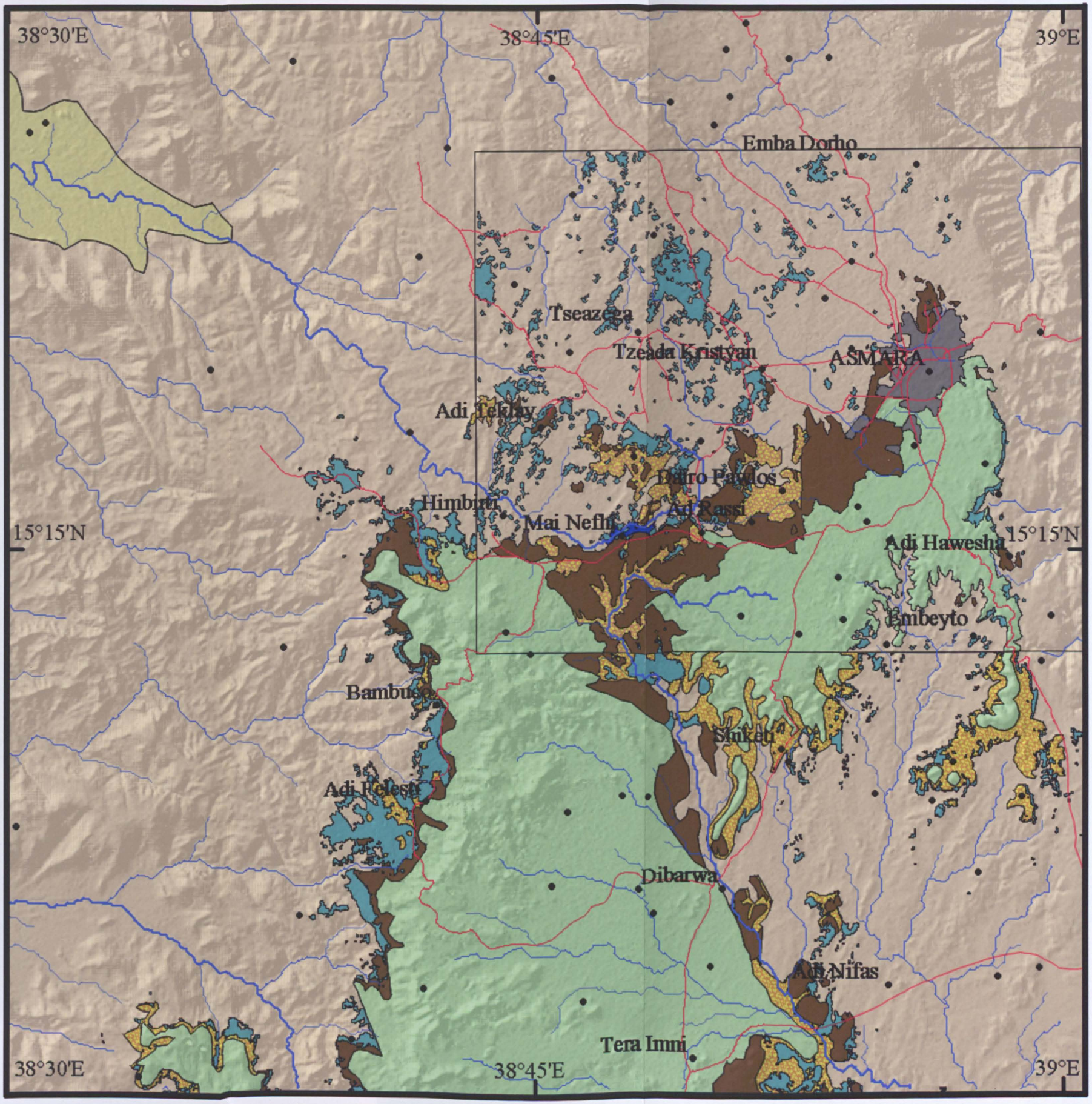

15°N
36°E
36°30'E
37°E
37°30'E
15°N
Guluj
ERITREA
14°30'N
14°30'N
SUDAN
Um Hajer
Tekesse/Setit
River
Humera
ETHIOPIA
14°N
36°E
36°30'E
37°E
37°30'E
14°N

Sheet
ND 37-5

0 10 20 30 40 50 km

# GULUJ

36°E
14°N
36°30'E
37°E
37°30'E
14°N
Adi Remetsi
13°30'N
13°30'N
13°N
36°E
36°30'E
37°E
37°30'E
13°N

Sheet
ND 37-9

0 10 20 30 40 50 km

# ADI REMETSI

37°30'E
38°E
38°30'E
39°E
14°N
13°30'N
13°N

Tekesse River

Adi Arkay

Ras Dashen

DEBARK

0 10 20 30 40 50 km

Sheet
ND 37-10

# ADI ARKAY

39°E
14°N
39°30'E
40°E
40°30'E
14°N
Erta Ale volcano
Hagere Selam
MEKELE
13°30'N
13°30'
13°N
13°N
39°E
39°30'E
40°E
40°30'E

Sheet
ND 37-11

0 10 20 30 40 50 km

MEKELE

CHAPTER FIVE

# Mineral mapping - dateable and widespread mineral detection

Laterites facies mapping described in previous chapters is discussed here in the context of using remote sensing (RS) to map *and* target specific minerals. A pilot study (figure 5.1) that documents targeting dateable potassium-bearing minerals in Eritrean laterites and accesses whether the age of laterites that have never been dated in NE Africa can be determined regionally is presented. As remote sensing has never been used to isolate minerals for radiometric dating, the success of the strategy chosen for locating areas containing the minor mineral, alunite, using ASTER and EO-1 Hyperion data led to the use of this and other mineral mapping tools to locate more common laterite minerals. Specifically, these tools are used to assess the composition of clay minerals, the targeting of kaolinite and iron-3 minerals and the whereabouts of other minerals produced by lateritisation of unusual basement rocks. These results follow a peer-reviewed discussion below on alunite (Andrews Deller 2003). $^{40}Ar/^{39}Ar$ dates for the minimum age of lateritisation are presented. A full investigation on the timing and duration of lateritisation is explored in Chapter 6.

*Locating dateable minerals in laterites using remote sensing - an example from Eritrea, NE Africa.*

M. E. Andrews Deller

Published in proceedings: Geological Remote Sensing Group, Geological Society London, Burlington House, London, 2003; 32nd International Geological Conference, Florence, 2004

*Abstract:*

Dating laterites is difficult. The problem lies in finding dateable minerals formed in these palaeosols during lateritisation. Such minerals are rare, randomly distributed and impossible to distinguish in hand specimen from surrounding lateritic minerals. Unlike igneous rocks, which contain several common minerals formed at the time of crystallisation that are suitable for radiometric dating, palaeosols are dominated by secondary minerals with no unstable

isotopes. New analytical techniques using TM, ASTER, ALI and Hyperion data from NASA's experimental EO-1 mission, enable geologists to pinpoint locations of dateable minerals in laterites over entire countries by focusing on characteristic mineral spectra which uniquely identify appropriate minerals. This revolutionises the dating of laterites, which have been dated, crudely in places, by the age of the rocks on which they develop and that of rocks that overlie them. Dating of potassium-bearing minerals in the lateritic profile, consistently indicates that the minimum age for lateritisation in Eritrea is mid-Eocene (40 to 43 Ma), not as suggested by other scientists, mid-Oligocene (30 Ma). As a result, long-accepted notions on the evolution of the Ethiopian Igneous Province (Menzies *et al.* 1990; Hofmann *et al.* 1997; Courtillot *et al.* 1999; Burke & Gunnell 2008) are thrown into question and time constraints are placed on supergene enrichment of gold and base metal mineralisation in the area. The results, backed by ground truth, confirm that screening for dateable minerals in laterites using remote sensing, enables systematic regional dating of them and makes field work more efficient.

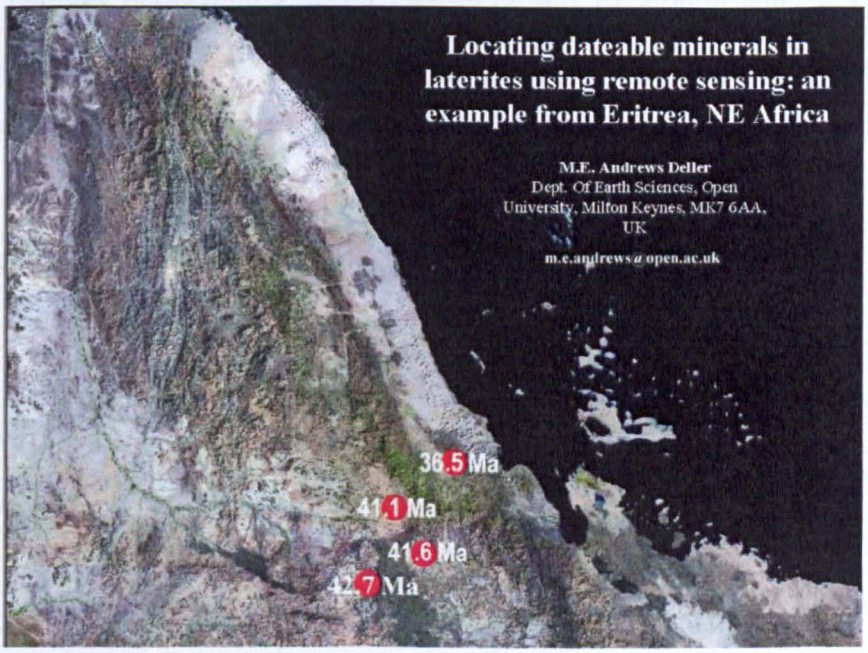


**Figure 5.1** Results of pilot study on dating laterites: Andrews Deller (2003)

## 5. 1. Introduction

In NE Africa and the Arabian Peninsula laterites are crudely dated by the age of the rocks that overlie them and that of rocks on which they develop because dateable minerals formed in these palaeosols are hard to find. Two rare potassium (K) minerals, cryptomelane and alunite allow $^{40}Ar$ /$^{39}Ar$ dating of laterites (Bird *et al.* 1990; Vasconcelos 1992; Vasconcelos *et al.* 1994; Rufett *et al.* 1996; Henocque *et al.*

1998). Both minerals are difficult to detect in situ and neither mineral is widely distributed in laterites. Cryptomelane (potassium manganese oxide, $KMn_8O_{16}$) is black and occasionally found in the dark ferricretes of the topmost laterite facies. Its spectrum is featureless and in terms of remote sensing, it is spectrally flat and lacks features essential for mineral detection. Alunite (hydrated potassium aluminium sulphate, $KAl_3(SO_4)_2(OH)_6$) is white and sometimes occurs in the white kaolinitic horizon of the saprolite lower down the profile in a typical laterite. In contrast with cryptomelane, alunite has clear identifying spectral features which can be exploited in the analysis of remotely sensed ASTER and hyperspectral EO-1 Hyperion data rather than relying on lucky finds of the mineral in the field. This study illustrates a strategy whereby laterites containing isolated concentrations of alunite can be highlighted using RS and once detected, targeted for collection and regional dating of the palaeosols, which has never been attempted.

## 5.2 Spectral properties of alunite - targeting the mineral

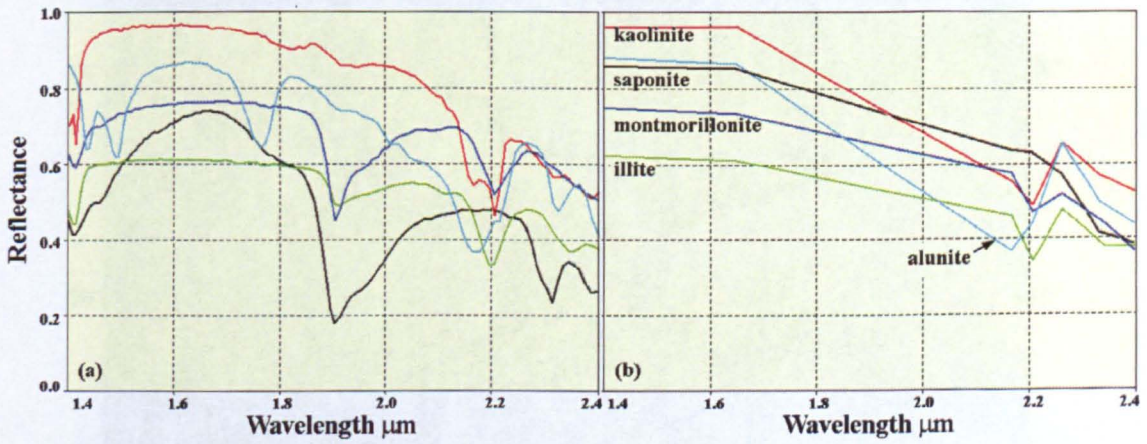


Figure **5.2** SWIR lab spectra comparing alunite with common clay minerals: (a) full USGS spectra; (b) resampled to the band centres of ASTER bands

Often associated with argillic hydrothermal alteration, alunite is a mineral widely sought by exploration geologists using remote sensing. As a potassium mineral, it can be radiometrically dated - one of the aims of this thesis on laterites - using the Ar-Ar method (Chapter 3). In a feasibility study for dating Eritrean laterites, clay-zone specimens revealed clusters of small alunite crystals that yielded meaningful Ar-Ar

ages (Andrews Deller 2003). Alunite therefore, became a target in this remote sensing work. Figure 5.2 shows that, like clay minerals, alunite has a SWIR Al-OH absorption, but at 2.17μm rather than close to 2.2μm for the main absorptions of kaolinite, illite and montmorillonite; i.e. in ASTER band 5 rather than band 6. In both Hyperion and ASTER SWIR data, alunite should therefore be readily detectable and distinguishable from other clay minerals. Given this observation, it should be possible to indicate sites where dateable samples might be collected on a regional basis using remote sensing.


**Figure 5.3** Location map based on colour coded, side-illuminated GTOPO30 DEM data

Figure 5.3 depicts the area where the lateritic clay zone was targeted in the pilot study and As Sarat, a remote area used to test the strategy established in Eritrea. For ground truth to support satellite image observation, laterite clays were sampled at 137 field sites (figure 5.4). Alunite, if formed in the regolith during lateritisation, occurs in this zone, however its presence is masked by the kaolinitic clay of Horizons 3 which is often up to several metres thick (figure 5.5). Figure 5.6 indicates underlying basement and the clay zone clearly in sky blue outcropping beyond overlying laterite horizons and basalts, a necessary feature if it is to be imaged. The basalts in Eritrea have been dated at ~30Ma (Drury *et al.* 1994) and the basement has a minimum age of ~650Ma (Teklay 1997; Drury and de Souza Filo 1998; Ghebreab 1999; Johnson and Woldehaimanot 2003), consequently laterites will have formed at a time somewhere in between.


**Figure 5.4** Field localities in Eritrea; Sampling for alunite - green stars samples collected 2001. Blue M numbers - samples collected 1998, see also Figure 2.25

**Figure 5. 5** Laterite kaolinitic clay zone - the extent of this horizon is indicated by B. Negash Dr S.A. Drury for scale.

**Figure 5.6** Laterites of the Eritrean Plateau view west (simulated aerial oblique view of Landsat 742 image draped over SRTM DEM data). Note the underlying multi-coloured NeoProterozoic basement and overlying laterite clay zone showing in sky blue outcropping beyond the ferricrete and basalts

## 5.3. Finding alunite

To find alunite using RS, the upper three laterite facies (figure 4.2), in particular the clay zone, have to be mapped out initially using image processing methods described

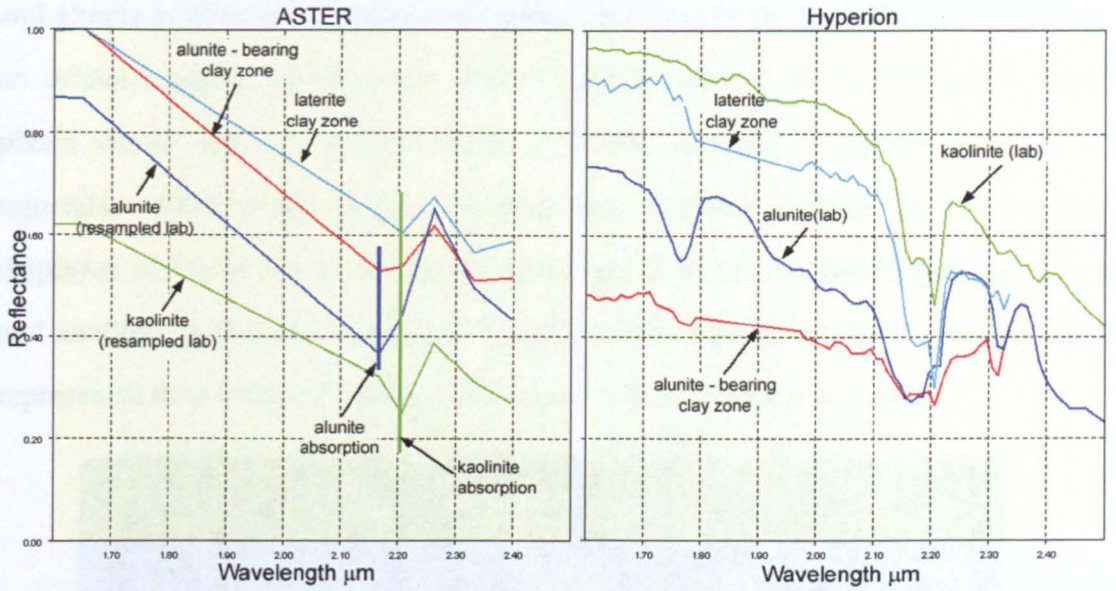


**Figure 5.7** Detailed lab spectra from ASTER & Hyperion compared with spectra at well-studied sites in Eritrea

in Chapter 3 where satellite data detects minerals on a ground surface because of their unique, sufficiently pronounced spectral features. With the resulting laterite facies map (Chapter 4), the clay horizon was targeted in order to pinpoint and isolate dateable minerals in situ. This was done using EO1-Hyperion and ASTER reflectance data with

spectral angle mapping (SAM) (Smith 2001), which is especially effective for detecting small occurrences of a mineral. Applying SAM, lab spectra of kaolinite and alunite (resampled from the USGS spectral library to the band-widths and centres of ASTER and Hyperion data) were compared with ASTER and Hyperion individual pixel spectra from well-studied sites. The marked difference between the target spectra of kaolinite and alunite illustrated by Figure 5.7 is evident as is the clear distinction between the main SWIR absorption features of alunite and kaolinite using both ASTER and Hyperion. Vertical bars mark absorption features of these minerals important in the analysis of remotely sensed data. ASTER spectra for kaolinite and alunite compared with lab spectra resampled to ASTER bands also indicate that even with ASTER's 6 SWIR bands, alunite is distinguishable from kaolinite as evidenced by results illustrated in Figure 5.8. The distinction between the spectra of kaolinite

and alunite is even more pronounced using data from hyperspectral EO-1 Hyperion, an orbital imaging spectrometer with 178 useful narrow bands that define image pixels whose spectra resemble those of single minerals or simple mixtures of minerals. SAM results using Hyperion data, superimposed on an EO-1 image displayed in Figure 5.9 show that the difference in the absorption features of alunite and kaolinite at Hyperion's spectral resolution does distinguish alunite-bearing clays represented here in blue from clays composed of pure kaolinite in green.

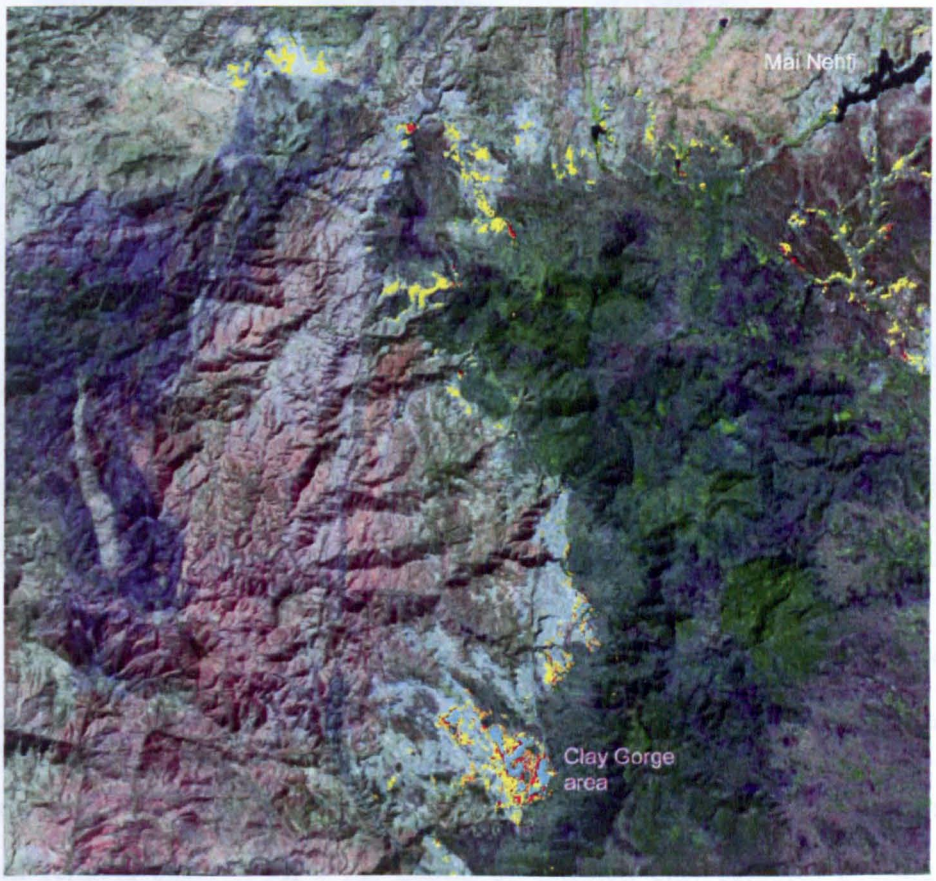


**Figure 5.8** ASTER 631 image showing the classified pixel results of three different SAM approaches: red using raw ASTER reflectance data for the SWIR bands (4 to 9); yellow the same, but atmospheric correction tweaked and, orange based on an ASTER spectrum from Clay Gorge, classified as alunite-bearing by Hyperion. These results prove that ASTER and laboratory spectra can be used successfully to find likely places for finding dateable alunite

Samples were then collected from those localities identified on image data as being alunite rich. Thin-sections and electron-microprobe analysis of selected samples indicated distinct cubic alunite crystals in all samples (figure 5.10 a, b), confirming convincingly that the strategy worked on Eritrean laterites using hyperspectral data (for results using ASTER reflectance data see below). To further

screen the targeted samples detected by RS for dating and narrow down the selection to those most likely to yield reliable radiometric ages these specimens were submitted for XRF analysis. Only samples high in potassium ($K_2O$) - greater than 0.10 % - and high in sulfur (S) – greater than 100 parts per million (ppm) - were chosen (table 5.1) as the combination of these elements almost certainly signified the presence of

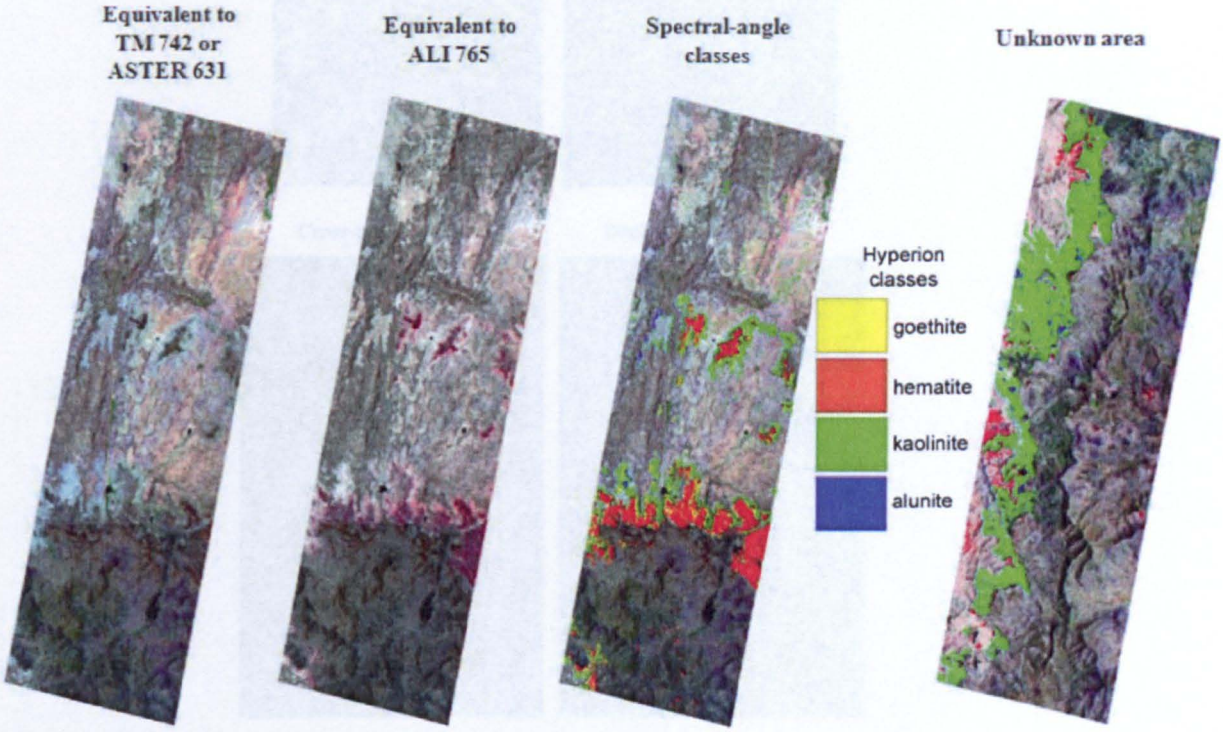


**Figure 5.9** The results of spectral angle mapping of minerals in laterites using hyperspectral data from EO-1 Hyperion. The three swaths to left of the key cover the western part of the Asmara test area, whereas that to the right covers an unknown area 10km SW of the test area. Each Hyperion swath is 7.7km wide

alunite ($KAl_3(SO_4)_2(OH)_6$), whereas high potassium marked out samples most likely to yield reliable ages. $^{40}Ar$ /$^{39}Ar$ dating of selected clay samples bearing alunite yielded reproducible and reliable ages. Sites where samples had previously been dated successfully were also pin-pointed using SAM of ASTER reflectance data over a well-known ~80 $km^2$ area near Eritrea's capital Asmara (figure 5. 11). Reinforcing earlier results, Figure 5.11a defines the extent of the kaolinite clearly in sky blue in contrast with the alunite detected in red. All results (figure 5. 11b) indicate consistently that quantitative mineral mapping using remotely sensed data is a valuable and viable tool for extending laterite dating from what would previously

have been one lucky sample in the field to systematic regional dating based on many samples pinpointed by RS.

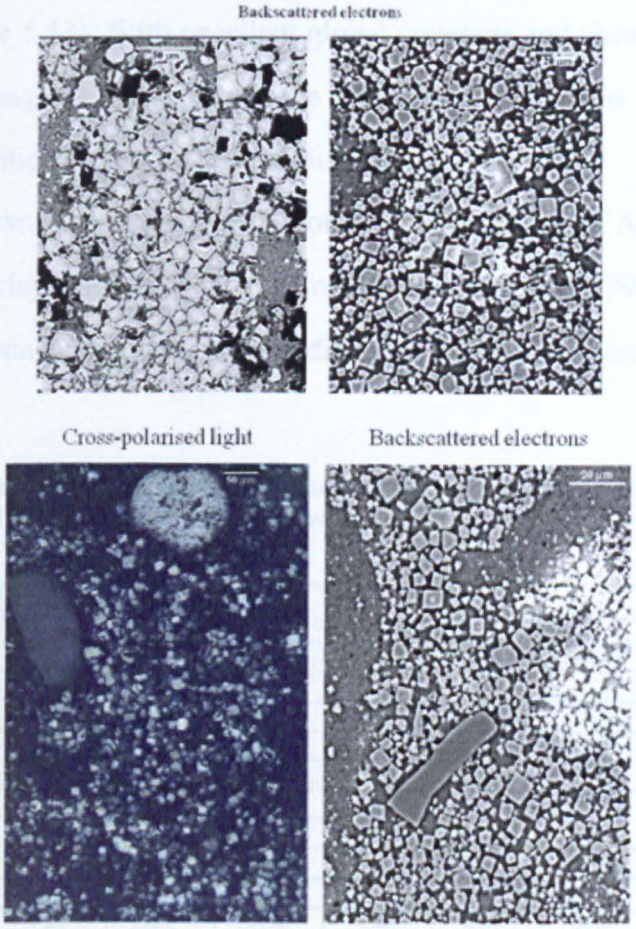


**Figure 5.10** Alunite in clay zone - backscattered electron image from electron microprobe analysis, Alunite-rich clay zone - alunite cubes in kaolinite - cross polarised light microscopy

However, not only should the above strategy work, but it must also be cost-effective especially where funds are limited, so the price of remotely sensed images should be taken into account. Moreover, to be regionally useful the chosen data should be available for all areas of interest. Hyperion and probably any future orbital hyperspectral system, acquire such large volumes of data for narrow swaths, that full coverage, even of geographically small areas, will take a long time to acquire, if at all. The value, therefore, in using broad rather than narrow spectral band data sets is outlined for the regional area on Figures 5.12 and 5.13, where the coverage of Hyperion is compared with that of local ASTER scenes. Both image systems have comparable spatial resolution, but ASTER at US$85 per 60km swath with the

capability of revisiting any place on Earth at least every 16 days compared with Hyperion at US $1000 per 7.7km swath is the better option from a regional perspective (figure 5.13). With excellent global coverage and cheap readily available high-resolution images ASTER reflectance data can be used to test the method used to find dateable lateritic clays in any arid region.

The strategy was therefore tested around As Sarat, Saudi Arabia (figure 5.3), where the USGS clay resources survey (Collenette & Grainger 1994; Overstreet *et al.* 1997), reported abundant patches of sporadic alunite found in a hardened fine, white

**Table 5.1** Detected and analysed clay-zone samples using XRF - samples high in K highlighted in green / samples with high S highlighted in yellow

| X1168M | MEAD | | 7/6/01 | | | | | | | |
|---|---|---|---|---|---|---|---|---|---|---|
| | | | | | | | | | | |
| Sample | M101c | M104 | M109 | M110e | M110t | M113 | M113a | M113b | M113c | M114 |
| wt. % | | | | | | | | | | |
| SiO2 | 94.40 | 70.42 | 41.97 | 65.79 | 64.66 | 54.88 | 0.31 | 43.25 | 40.08 | 77.83 |
| TiO2 | 0.805 | 0.037 | 0.016 | 1.006 | 1.003 | 1.474 | 0.075 | 0.034 | 0.855 | 0.571 |
| Al2 O3 | 2.51 | 19.67 | 39.09 | 22.05 | 23.31 | 30.21 | 35.53 | 38.51 | 33.03 | 14.82 |
| Fe2O3 | 0.32 | 0.79 | 0.19 | 0.80 | 0.78 | 1.43 | 1.04 | 0.78 | 0.89 | 0.77 |
| MnO | 0.002 | 0.002 | 0.002 | 0.002 | 0.002 | 0.003 | 0.002 | 0.013 | 0.006 | 0.001 |
| MgO | 0.03 | 0.05 | 0.03 | 0.03 | 0.00 | 0.12 | 0.00 | 0.02 | 0.06 | 0.06 |
| CaO | 0.08 | 0.18 | 0.09 | 0.07 | 0.06 | 0.18 | 0.03 | 0.13 | 0.10 | 0.12 |
| Na2 O | 0.04 | 0.05 | 0.20 | 0.12 | 0.17 | 0.08 | 0.42 | 0.07 | 0.24 | 0.08 |
| K2 O | 0.21 | 0.12 | 0.61 | 0.21 | 0.28 | 0.05 | 8.34 | 0.21 | 2.29 | 0.07 |
| P2 O5 | 0.053 | 0.022 | 0.099 | 0.035 | 0.039 | 0.031 | 0.137 | 0.506 | 0.155 | 0.014 |
| LOI | 2.05 | 8.40 | 17.10 | 9.47 | 10.19 | 11.73 | 41.24 | 15.49 | 21.21 | 6.26 |
| | | | | | | | | | | |
| Total | 100.49 | 99.73 | 99.39 | 99.58 | 100.50 | 100.19 | 87.12 | 99.00 | 98.92 | 100.60 |
| | | | | | | | | | | |
| S ppm | 122 | 278 | 3304 | 1358 | 1899 | 62 | 93174 | 1983 | 10890 | 64 |
| | | | | | | | | | | |
| | | | | | | | | | | |
| | | | | | | | | | | |
| Sample | M121a | M121b | M122a | M125 | M125a | M125d | M130 | M131 | M133 | M147 |
| Wt. % | | | | | | | | | | |
| SiO2 | 79.05 | 81.25 | 76.02 | 40.57 | 18.05 | 31.82 | 84.45 | 93.14 | 71.13 | 78.20 |
| TiO2 | 0.323 | 0.288 | 0.553 | 0.175 | 0.337 | 0.323 | 0.123 | 0.323 | 1.185 | 0.256 |
| Al2 O3 | 13.58 | 12.83 | 15.92 | 21.27 | 32.76 | 23.40 | 10.48 | 5.28 | 19.48 | 14.62 |
| Fe2O3 | 1.72 | 0.56 | 0.30 | 0.29 | 0.87 | 0.71 | 0.15 | 0.14 | 1.20 | 0.42 |
| MnO | 0.006 | 0.002 | 0.002 | 0.009 | 0.009 | 0.012 | 0.002 | 0.002 | 0.006 | 0.002 |
| MgO | 0.04 | 0.06 | 0.03 | 0.01 | 0.03 | 0.02 | 0.05 | 0.04 | 0.05 | 0.04 |
| CaO | 0.13 | 0.12 | 0.08 | 0.07 | 0.05 | 0.09 | 0.18 | 0.06 | 0.15 | 0.12 |
| Na2 O | 0.04 | 0.04 | 0.31 | 0.17 | 0.18 | 0.22 | 0.03 | 0.03 | 0.04 | 0.69 |
| K2 O | 0.03 | 0.19 | 0.20 | 5.33 | 6.03 | 5.96 | 0.06 | 0.05 | 0.05 | 0.12 |
| P2 O5 | 0.045 | 0.017 | 0.027 | 0.294 | 0.229 | 0.525 | 0.040 | 0.019 | 0.021 | 0.006 |
| LOI | 6.01 | 5.50 | 6.28 | 26.51 | 36.14 | 30.13 | 4.81 | 2.20 | 7.67 | 5.47 |
| | | | | | | | | | | |
| Total | 100.97 | 100.85 | 99.72 | 94.70 | 94.70 | 93.21 | 100.38 | 101.29 | 100.98 | 99.94 |
| | | | | | | | | | | |
| S ppm | 105 | 85 | 61 | 36962 | 49094 | 43530 | 53 | 45 | 28 | 62 |

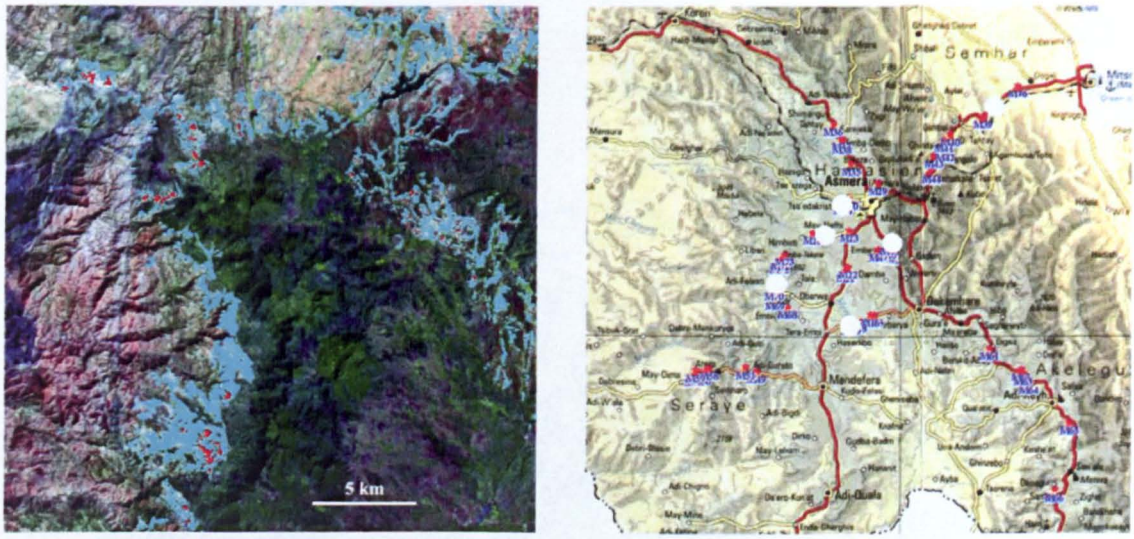


(a) (b)

**Figure 5.11** (a) Spectral angle mapping of ASTER reflectance data: kaolinite pixels - blue, alunite-rich pixels in red; (b) Successfully dated alunite-rich localities near Asmara

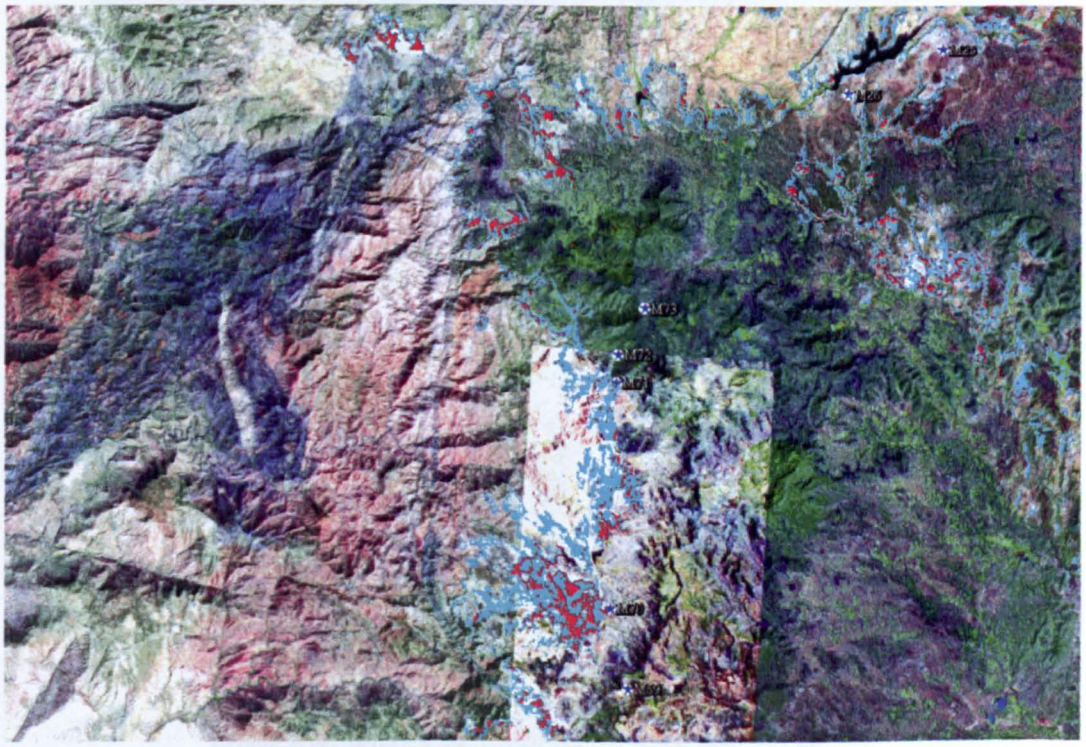

**Figure 5.12** Mineral detection using ASTER (kaolinite – cyan; alunite – red) also showing the area covered by Hyperion (lighter hues) compared with ASTER

clay rock in the laterite sequence overlain by flood basalts. USGS investigations into the laterite in this area were concerned with evaluating the amount of alunite present, in the hope that if there were sufficient quantities of the mineral they might serve as an ore for potash fertiliser.

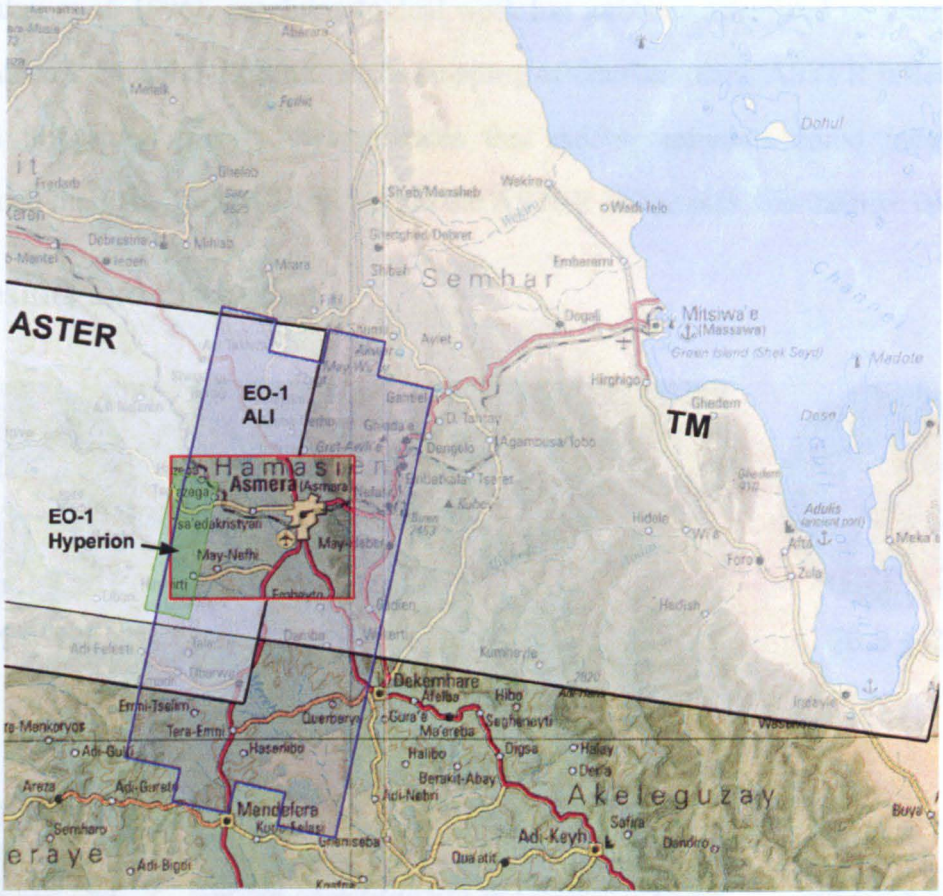


**Figure 5.13** Location and superimposed Landsat TM, ASTER, EO-1 ALI and Hyperion data sets - red box indicates test area (30km east-west x 24km north to south)

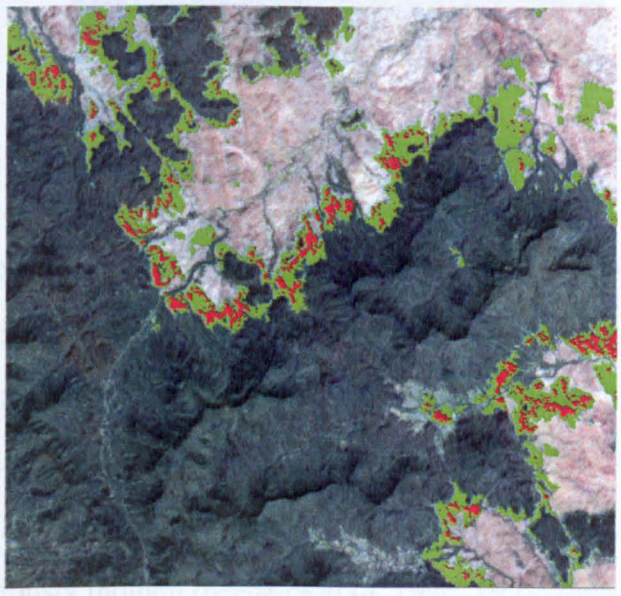

**Figure 5.14** Alunite occurrences near As Sarat, Saudi Arabia, from spectral angle mapping of ASTER reflectance data. Kaolinitic clays are highlighted in green and alunite in red in this rendition. Image width = 25km

Although flood basalts in the Yemen Igneous Province have been dated circa 30

Ma (Baker *et al.* 1996), geochronological work has not been attempted on laterites in the Arabian Peninsula. Spectral angle mapping of laterites using ASTER reflectance data in this area however, demonstrates that datable minerals could indeed be pinpointed there too (figure 5.14). Again the ASTER image picks out laterite facies

## 5.4 Results and discussion

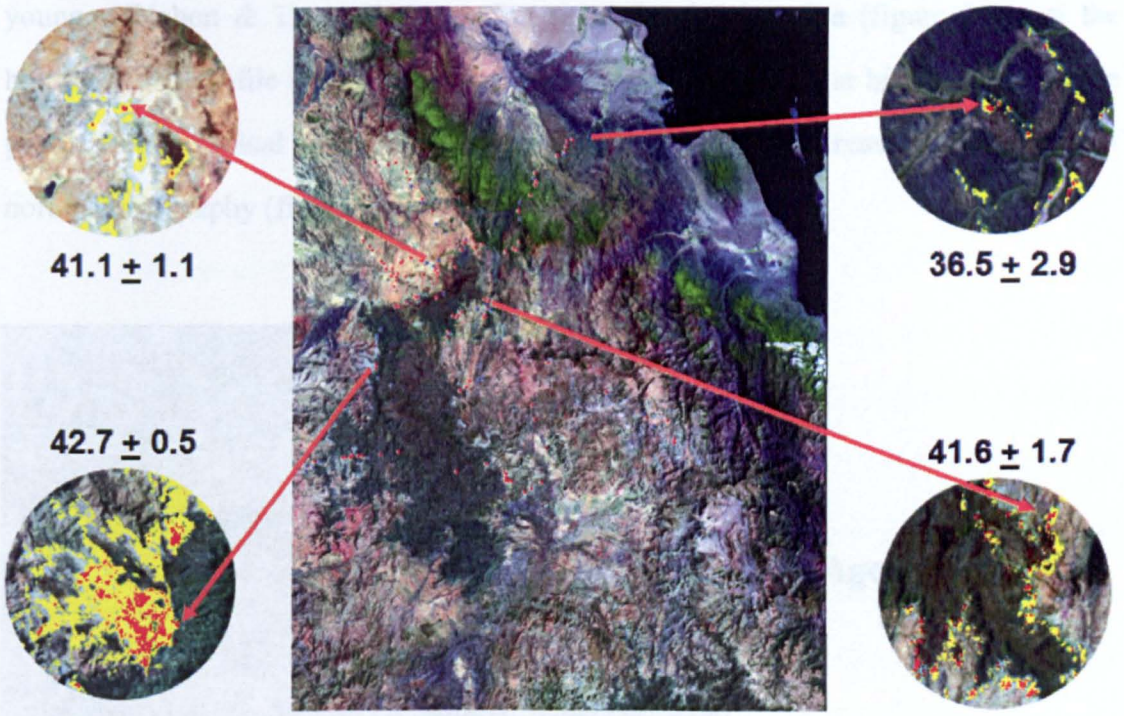


**Figure 5.15** Alunite Ar-Ar ages of Eritrean laterite: detected kaolinite - yellow, detected alunite - red

Alunite-bearing clay samples from Horizon 3 in typical Eritrean laterites spread over ~6400 square kilometres yielded well-constrained mid-Eocene $^{40}Ar$ /$^{39}Ar$ ages. Examples of successfully dated laterites in this experiment and their distribution over the region are illustrated in Figure 5.15. All results indicate that the *minimum* age for lateritisation in Eritrea is mid-Eocene (~40 to ~43 Ma) and *not* mid-Oligocene (~30Ma), as previously thought (Menzies *et al.* 1990, 1997; Burke & Gunnell 2008).

The reason that this can only be regarded as a minimum age for lateritisation is because of the counter-intuitive way in which laterites form. In a layered sequence, a conventional stratigraphic view would be that age increases downwards, from top to

bottom of the weathered profile. This logical expectation is not played out in the gradual evolution and formation of laterites. Horizon 5 (figure 4.**2**), the topmost ferricrete subjected to the longest chemical weathering, is the product of all weathering and precipitation of iron minerals since weathering first began - and is therefore the most evolved - and so the oldest laterite horizon (figure 5.16). Lower horizons, subjected only to early stages of weathering, are less evolved and therefore younger (Nahon & Tardy, 1992). Consequently, the saprolite (figure 2.39) at the bottom of the profile is the youngest facies in any laterite and at higher levels in the profile as the residual palaeosol becomes more evolved, age increases - the reverse of normal stratigraphy (figure 2.34).

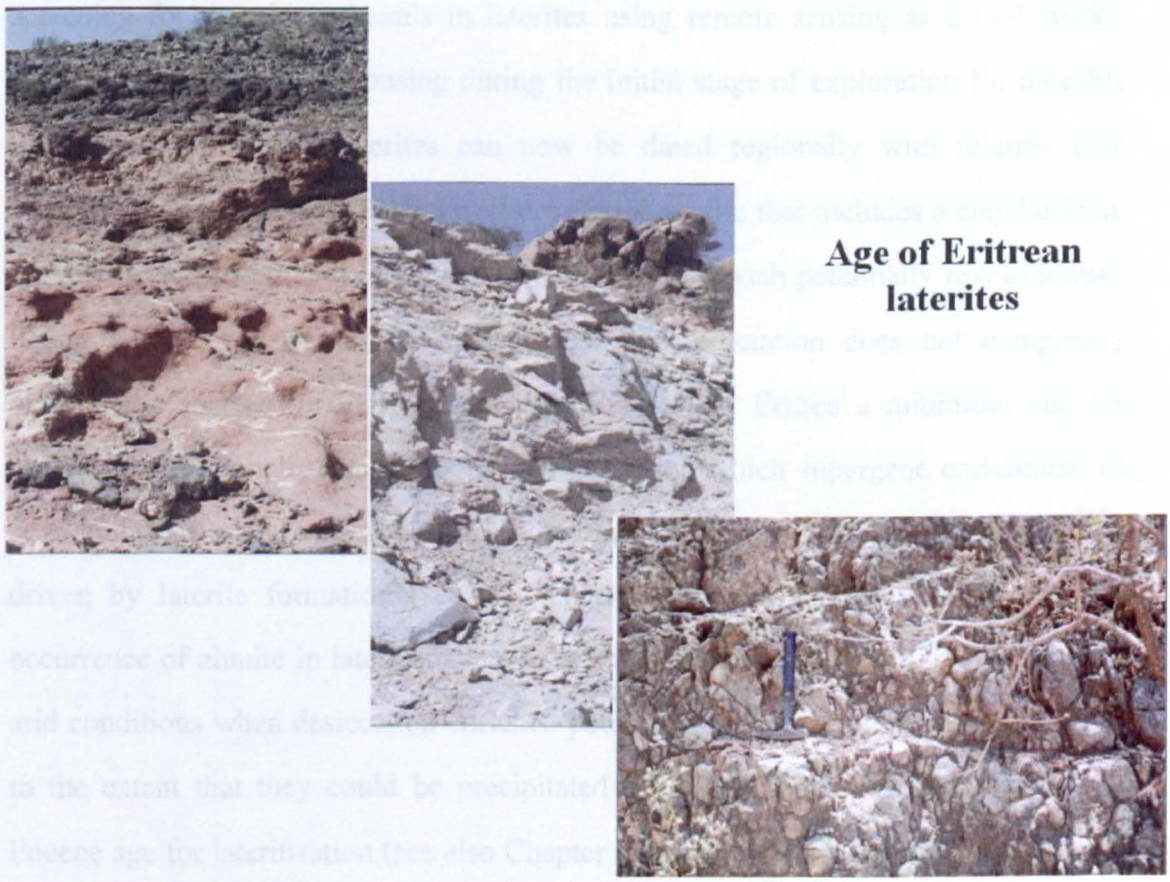


**Figure 5.16** Progression of laterisation: bottom right saprolite with core stones; centre kaolinitic clay zone; top left mottled zone with overlying nodular ferricrete and younger flood basalts

To sum up the age of the palaeosols is intrinsically linked to the evolution of the profile. The saprolitic kaolinitic clay, exhibiting only early signs of laterite

weathering is the host for alunite. Alunite occurs in it as crystals that formed *after* that clay had developed. As a sulfate, it is likely that alunite was precipitated from groundwater carrying abundant potassium and sulfate ions during a final period of desiccation of the palaeosol. Because alunite crystallised in pre-existing kaolinitic clay zone, itself the youngest laterite horizon proper to form during downward weathering, any ages obtained from alunite cannot be older than the clay horizon. Hence, $^{40}Ar/^{39}Ar$ ages of alunite from this horizon only give a minimum age for the alaeosol. Future work will hopefully determine a maximum age for lateritisation by dating the ferricretes (see also chapter 7).

### 5.4.1 Conclusion

The findings of this pilot study, validated by field evidence, prove that regional screening for dateable minerals in laterites using remote sensing as a tool works. Innovative use of remote sensing during the initial stage of exploration for dateable minerals indicates that laterites can now be dated regionally with relative ease wherever these palaeosols have a well-developed profile that includes a clay horizon, in which dateable minerals can be detected. This approach potentially revolutionises dating laterites wherever such rocks occur and vegetation does not completely obscure the surface for at least part of the year. In Eritrea a minimum age for lateritisation regionally constrains the period during which supergene enrichment of gold and base metal mineralisation in the sub-laterite Pan African basement was driven by laterite formation (see also chapter 8). Furthermore, the widespread occurrence of alunite in laterites signifies a marked change in palaeoclimate to more arid conditions when desiccation enriched potassium and sulfate ions in groundwater to the extent that they could be precipitated as alunite. The evidence for a mid-Eocene age for lateritisation (see also Chapter 6) contradicts the current consensus on Red Sea geology that Tertiary evolution of the land surface, on which the Arabian, Yemen and Ethiopian Traps erupted occurred only in a brief episode of the mid-Oligocene shortly before flood volcanism (Menzies *et al.* 1990; Burke & Gunnell 2008).

*Acknowledgements*

My sincere thanks to those who have encouraged, supported and advised me, especially W.S. Deller and S.A. Drury. The generosity of J. Crowley (USGS) and J Watson (OU) for providing Hyperion and XRF data respectively is much appreciated as is the help of the Mines Department and Geological Survey of Eritrea and the use of OU lab facilities provided by A. Tindle and S. Kelley. The work was funded in part by an award from the GRSG affiliated to the Geological Society London, for which I am grateful as I am for the invaluable support of N. Kaliki (ENVI), D Taranick (Anglo American) and R Teuww (Portsmouth University). Finally my thanks to my reviewers particularly Prof. M.F. Thomas (Stirling University) who stated that he 'cannot fault the science'.

## 5.5 Advanced techniques -widespread mineral detection

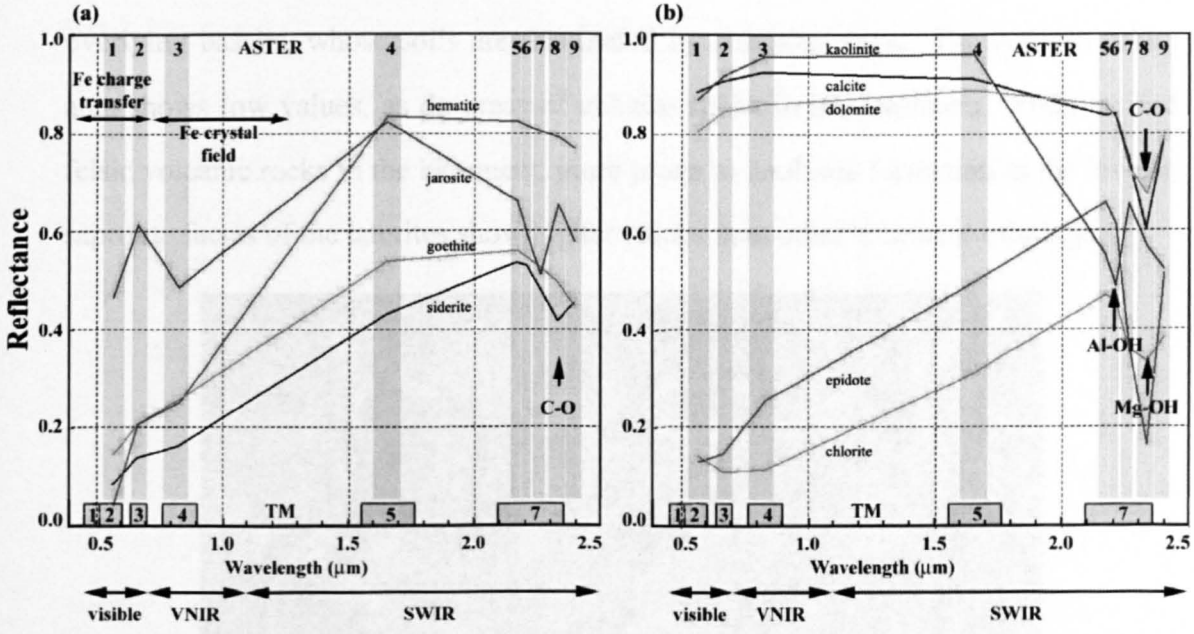


**Figure 5.17** Spectra of minerals important in lithological discrimination in relation to ASTER and TM bands. Note: spectra are resampled to ASTER band widths and centres

Andrews Deller (2006) aimed at illustrating how free and low-cost RS data, simple image processing techniques (Chapter 3; 3-band false-colour composites and band ratios) and a strategy oriented by the spectral features of minerals in laterites allows their rapid mapping. This strategy was augmented using SAM with ASTER to target

the kaolinitic clay facies as a guide for mapping other laterite facies using the qualitative approach described in Chapter 4. Results of more complex approaches based on similar mineral-spectra considerations and the strategy adopted for alunite detection are now discussed in the context of the thesis. These approaches depend on the short-wave infrared (SWIR) region that is covered by 5 ASTER bands and Hyperion bands between 2.1 and 2.34μm. Figure 5.17 shows lab spectra, both full and resampled to ASTER bands, of some important minerals in laterites and the Neoproterozoic basement. The chapter concludes with mapping results for various minerals using EO-1 ALI and ASTER data.

### 5.5.1 Uses of the relative band depth (RBD) method (Crowley *et al.* 1989)

Figures 5.18a-d shows examples of RBD images for the Asmara test area (compare with figure 4.8). The rendition for kaolinite (figure 5.18a) clearly shows the expected relationship of high (bright) values to exposures of laterite, especially the clay zone facies. Both mottled zone and ferricrete show higher values than do the overlying basalts, whose soils are dominated by smectite clays. The Asmara urban area shows low values, as do areas of chlorite schist in the basement. Granitic and felsic volcanic rocks in the basement, more prone to kaolinite formation in the lowest, saprolite facies of the laterites show higher values than other basement lithologies.

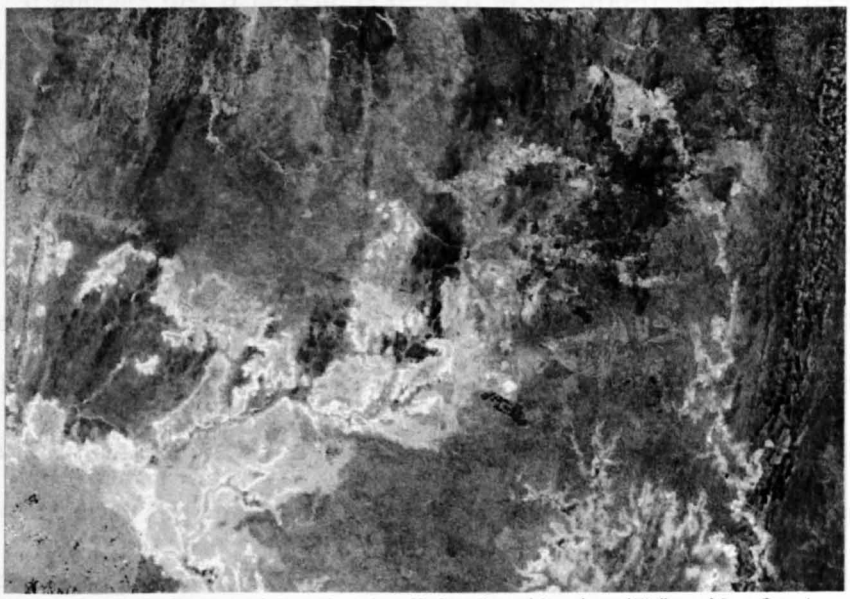

**Figure 5.18a** ASTER Relative Band Depth – kaolinite (band4 + band7)/band6 – for Asmara test area (see previous section)

**Figure 5.18b** ASTER RBD – $Fe^{3+}$ minerals (band2 + band4)/band3 – for Asmara test area

The ASTER RBD image for the $Fe^{3+}$ mineral crystal-field absorption in the VNIR – (band 2 + band 4)/band3 (figure 5.18b) – is poor in quality, as anticipated, although higher values are roughly associated with laterite mottled zone and ferricretes. The RBD for jarosite's distinctive SWIR absorption in ASTER band 7 (figure 5.18c) is instructive in that most areas of laterite in the Asmara test area show lower values than do basement and CFBs. Highest values are in the soils of the more humid escarpment to the east, and in an area of colonial gold-mining operations in the NW quadrant. It appears that if jarosite is present in the iron-rich laterite facies, it is in small amounts.

Figure 5.18d targets absorption in ASTER band 8 that is common to carbonates and to minerals containing Mg- or Fe-OH bonds, including the smectite saponite. Exposed laterites of all facies show low values, as expected. The light areas in the west of the test area coincide with pinkish areas on the Landsat 742 image (figure 4.4) and probably highlight chloritic and/or epidotic basement rocks. Light areas in the eastern part of the test area, within the Eritrean escarpment clearly pick out the roughly N-S trend of the basement compositional banding. Landsat 742 and ASTER 631 images (figures 4.4 and 4.9) shows little sign of pinkish hues in this area and the light bands probably represent thin marbles in the basement, which outcrop in road

cuttings along the Asmara to Massawa road, but have not been mapped extensively.

**Figure 5.18c** ASTER RBD – jarosite (band5 + band8)/band7 – for Asmara test are

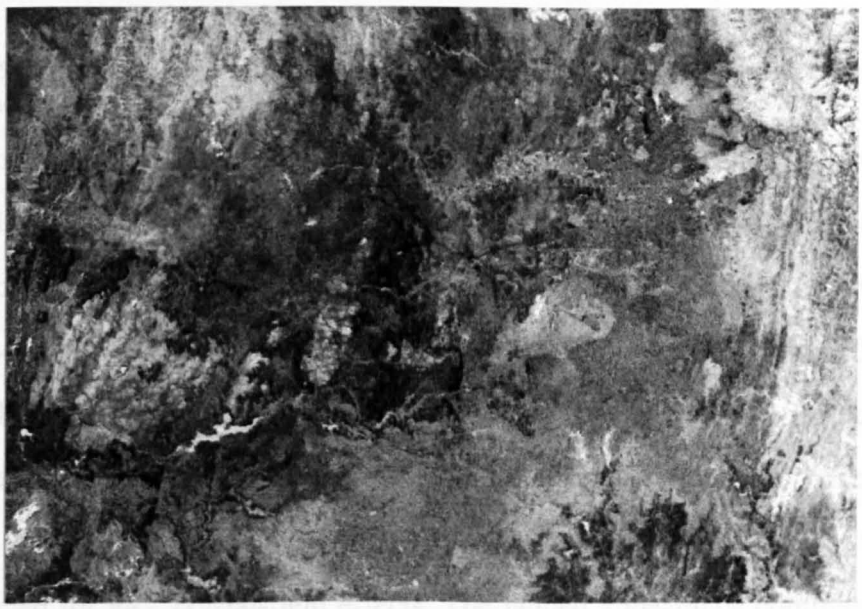

**Figure 5.18d** ASTER RBD – C-O and Mg-OH absorption (band6 + band9)/band8 – for Asmara test area

### 5.5.2 Spectral analysis results

In the absence of XRD analyses of laterites, the hypotheses that can be tested with Hyperion spectra are that:

- The iron-rich facies contain mixtures of hematite, goethite and possibly jarosite;

- The clay content of the Eritrean laterites is dominated by kaolinite, the stable end-product of breakdown of all other clay minerals originally formed by silicate weathering (Butt & Zeeger, 1993) having evolved over at least tens of million years.

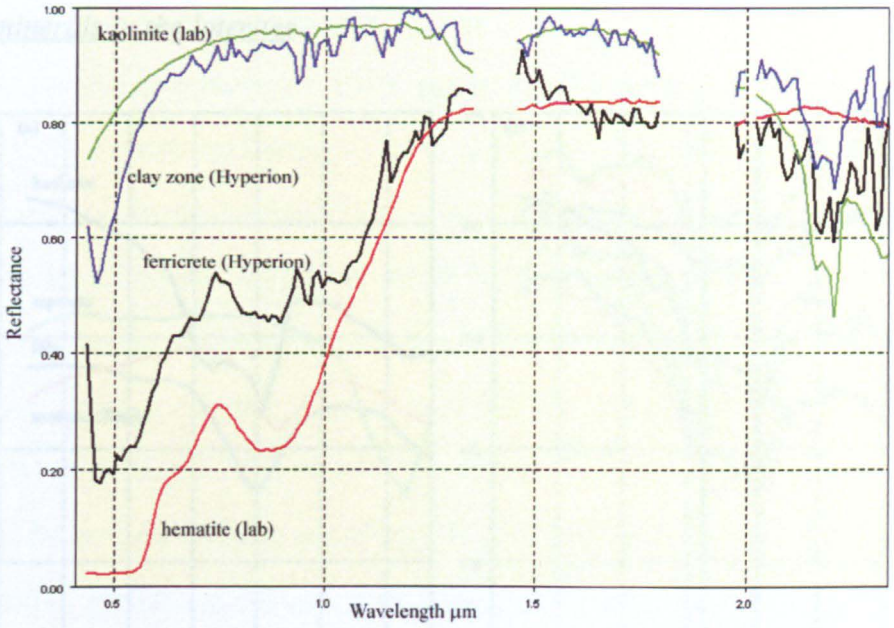


**Figure 5.19** Hyperion reflectance spectra for known sites compared with resampled lab spectra for kaolinite and hematite

Figure 5.19 shows full Hyperion spectra of known ferricrete and clay zone pixels, compared with resampled lab spectra of hematite and kaolinite. The most obvious attribute of the Hyperion ferricrete spectrum is how noisy it is compared with the lab spectra. Most of the sharply defined features in the 0.4 to 1.4µm region (the VNIR) are probably spurious, perhaps resulting from problems with the sensor or deficiencies in the simple atmospheric correction applied to convert radiance to reflectance. However, the general shape followed in the VNIR, especially up to 0.9µm, is close to that expected for $Fe^{3+}$ crystal-field effects. The jagged appearance continues through to the SWIR. Two specific features coincide with the kaolinite absorptions and almost all ferricrete spectra show that kaolinite is a major component of the rock. The Hyperion spectrum of a virtually iron-free clay zone locality shows a good fit overall to the kaolinite lab spectrum, especially in the SWIR, where the unique doublet of kaolinite absorption features at 2.163 and 2.204µm is matched well. This suggests that

whatever causes the poor quality of the VNIR part of the Hyperion spectra (acquired by a separate Hyperion sensor bank from that used for SWIR), information in the SWIR region is probably valid.

*Clay minerals in the laterites*

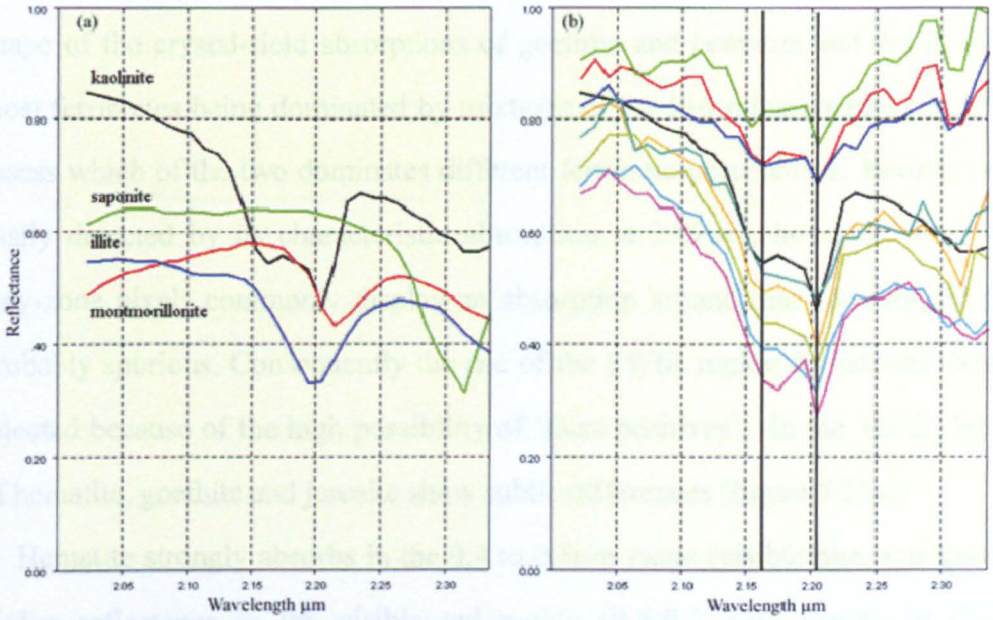


**Figure 5.20** Clay mineral spectra in the SWIR region: (a) lab spectra of common clay minerals; (b) Hyperion spectra from 8 randomly picked clay zone occurrences compared with lab spectrum of kaolinite (black), with positions of kaolinite SWIR absorption features (2.163 and 2.204 µm) shown as solid vertical lines for clarity

Figure 5.20a shows laboratory SWIR spectra of four common clay minerals – kaolinite, illite, montmorillonite (Na-,Ca-rich smectite) and saponite (Mg-, Fe-rich smectite). Each of these minerals has a characteristic spectral shape and placement of spectral features in the SWIR. Kaolinite is most distinct because of its doublet of features. Figure 5.20b shows SWIR spectra derived from Hyperion data at 8 randomly chosen localities in known areas of iron-free clay zone (no spectra have been omitted, these being the first 8 pixels chosen), together with the lab spectrum of kaolinite with its two absorption features marked. Clearly there is a very close match between the Hyperion spectra of randomly chosen field occurrences of clay zone and the pure kaolinite spectrum. Conceivably some of the clay-zone spectra could result from mineral mixtures between kaolinite and a mineral with a single absorption around

2.16μm, but the broad illite feature and those of smectites are absent. In the case of clay minerals, these findings give grounds for confidence in results from knowledge-based mineral mapping presented later.

*Iron minerals in ferricrete and mottled zone*

The prominent noise in the VNIR region of all Hyperion spectra, the similarity in shape of the crystal-field absorptions of goethite and hematite and the likelihood of most ferricretes being dominated by mixtures of the two minerals make it difficult to assess which of the two dominates different ferricrete occurrences. Jarosite should be easily detected by its characteristic absorption at 2.27μm, however, even iron-free clay-zone pixels commonly display an absorption around that wavelength, which is probably spurious. Consequently the use of the SWIR region for jarosite detection is rejected because of the high possibility of 'false positives'. In the VNIR, lab spectra of hematite, goethite and jarosite show subtle differences (figure 5.21a):

- Hematite strongly absorbs in the 0.4 to 0.6μm range (visible blue and green), with higher reflectance in the visible red region (0.6-0.7 μm), giving its cherry red coloration. Its crystal-field effect results in a reflectance peak at ~0.745μm and a minimum at ~0.86 μm;
- Goethite's main absorption is in the visible blue, resulting in its common yellow-brown colour. Its crystal-field effect peaks at ~0.765 and the broad absorption is at its lowest ~0.92μm;
- In the visible region, the reflectance of jarosite falls steadily from 0.7 to 0.4μm, resulting in its distinct yellow-orange colour. It has a much more pronounced crystal-field effect than the other two oxidised iron oxy-hydroxides, with a peak at 0.715μm.

Patient collection of numerous Hyperion spectra from pixels at ferricrete occurrences does show that there are examples that possibly contain dominantly goethite, hematite or jarosite in mixtures with kaolinite (figure 5.21b), although the first two cases are far more common than jarosite-rich ferricretes. The result gives some confidence that semi-quantitative mapping of these minerals' proportions based on Hyperion data could prove fruitful.

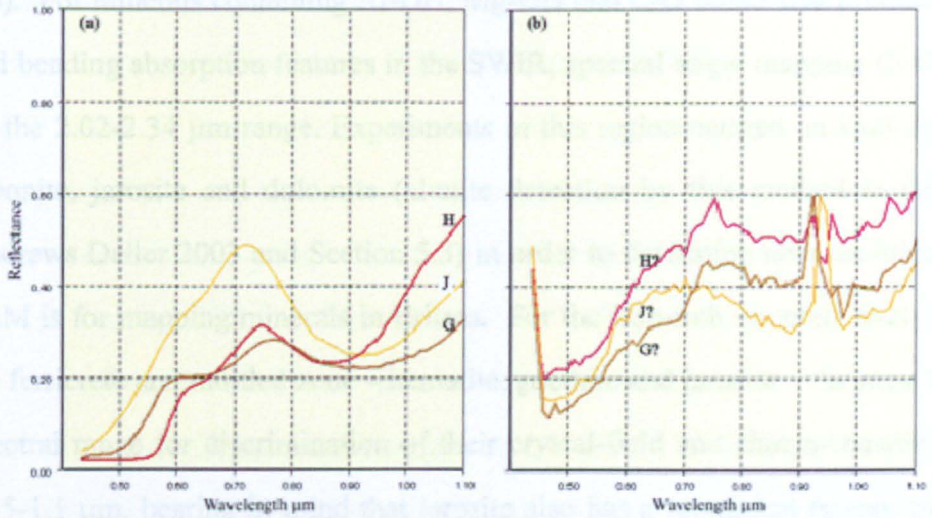


**Figure 5.21** Iron mineral spectra in the VNIR: (a) lab spectra of hematite (H), goethite (G) and jarosite (J); (b) Hyperion spectra of ferricretes that may be dominated by each of the three minerals

Having demonstrated the spectral dominance of kaolinite over less evolved clay minerals in the laterite clay-zone, and that hyperspectral data do present a chance of distinguishing the minerals making up the bulk of the saprolite, clay, mottled and ferricrete facies, it remains to examine three possibilities that:

- spectrally distinct, dominant minerals in the laterites can be mapped over large areas using their spectral properties;
- other possibly important minerals that occur in lesser proportions can be detected in laterites, given sufficient differences from the main laterite-forming minerals;
- both possibilities may also be achieved using less spectrally resolving, but widely available ASTER data.

### 5.5.3 Mineral mapping

*Hyperion data (spectral angle mapping)*

Because hyperspectral Hyperion data contains a large number of narrow spectral bands from 0.4 to 2.4 µm (Section 4.7), they offer the best chance of accurate mineral detection using spectral angle mapping (SAM). However, as Figure 4.18 shows, some regions contain noise. Because of this and the need to avoid computational confusion, discussed above, it is more effective to restrict the analysed spectral range in Hyperion data to that which brackets mineralogical features of interest (see Table

4.6). For minerals containing Al-OH, Mg-OH and C-O bonds that produce stretching and bending absorption features in the SWIR, spectral angle mapping (SAM) focused on the 2.02-2.34 μm range. Experiments in this region centred on kaolinite, chlorite, saponite, jarosite and dolomite (alunite detection by this method is dealt with in Andrews Deller 2003 and Section 5.3) in order to determine how useful in each case SAM is for mapping minerals in Eritrea. For the iron-rich minerals likely to occur in the ferricrete and mottled zone – hematite, goethite and jarosite – the most appropriate spectral range for discrimination of their crystal-field and charge-transfer features is 0.45-1.1 μm, bearing in mind that jarosite also has a prominent feature in the SWIR (see below). Figure 5.22 shows spectral angle mapping results based on Hyperion data for an area to the west of Asmara. Several of the images highlight the 'noisy' nature of some bands in these experimental data.

The dominant mineral throughout laterite profiles, kaolinite (figure 5.22b), is extremely well mapped using Hyperion data, to the extent that choosing a spectral-angle threshold of 7.5 from a range of 4.0 to 53.1 restricts its detection to the clay zone only. Raising the threshold to 9.0 shows kaolinite in saprolite, mottled zone and ferricrete, except for the most iron rich types, with little misidentification in either basalts (with illite-rich soils) or in fresh basement occurrences. Hyperspectral data, should they ever become widely and cheaply available would therefore be an excellent tool for both mapping lateritic clay zone and also assessing the variation in kaolinite content throughout laterite profiles.

Iron minerals too are well identified by Hyperion-based spectral angle mapping (figure 5.22.c to f), and carefully selected thresholds easily restrict results to the iron-rich parts of the laterite occurrences, although there are speckles recorded in the areas of basalt, which have modern weathered surfaces containing the same iron minerals. Despite the abundant field evidence for the presence of goethite in hand specimens of ferricretes, it is far less prominent using remote sensing than is hematite (compare Figure 5.22d with c). This is almost certainly due to the dominance of hematite in the bulk of ferricrete and mottled zone and the tendency for modern dehydration, on the

exposed surfaces of goethite, to produce ubiquitous hematite-rich surface veneers.

In contrast, jarosite is only detected in small quantities using the 0.70-0.93 μm VNIR bands (figure 5.22e) and when detecting jarosite using its broad SWIR absorption (figure 5.22g) all identified pixels lie outside laterite occurrences. Indeed, laterites as a whole have a higher spectral angle than their surroundings and the jarosite pixels on Figure 5.22g cluster consistently on pinkish areas of basement that are iron-rich chlorite schists (figure 5.22a). Since no pixels within the laterites are highlighted as jarosite, it is safe to presume that jarosite is absent from their iron-rich upper horizons and that what appears to be jarosite detected in Figure 5.22e, is in fact hematite or goethite. Furthermore, the pattern of pixels highlighted by Hyperion SWIR as jarosite closely resembles that for chlorite (Figure 5.22b), whose narrow absorption feature at 2.245μm is on the short-wavelength shoulder of jarosite's broad feature (figure 4.3). Moreover, Hyperion spectra of pixels highlighted as jarosite in the SWIR also resemble the spectrum of epidote ($Ca_2(Al,Fe)_3(SiO_4)_3(OH)$), which commonly accompanies chlorite in the low-grade mafic metavolcanic rocks of the basement. As a means of determining this particular iron sulfate mineral therefore results are not as clear-cut as they are for the main laterite minerals.

Saponite, a Mg-rich variety of the clay mineral montmorillonite (a smectite), is a common product of lateritic weathering of ultramafic igneous rocks, particularly in the saprolite zone (Gaudin et al. 2005) however in Eritrea, saponite forms well away from laterite exposures and is found exclusively over basement ultramafic rocks. Figure 5.22h shows pixels identified as saponite by spectral angle mapping in a zone of basement that also contains patches of chlorite and dolomite (figures 5.22 i & j), as well as probable epidote misidentified as jarosite. This association is compatible with the presence in the basement of greenschist-grade metamorphosed mafic and ultramafic igneous rocks. The elevation is close to that of the base of the laterites and saponite and dolomite are compatible with protracted weathering of such Mg-rich rocks. Both Tadesse et al. (1998) and Teklay (pers. comm. 2001) report narrow linear bodies of highly deformed mafic-ultramafic rocks in the basement of Eritrea and

Tigray, tentatively suggested as ophiolite relics. The area has low relief and extensive colluvium cover lacking outcrops of such rocks though metabasalt clasts occur in the soil.

The narrowness of Hyperion data swaths (~8km) clearly does not offer any regional mapping potential. But the close resemblance of the reflectance-calibrated hyperspectral data to detailed mineral spectra and successful mapping of some minerals allows Hyperion to be used as a check for results using less revealing data such as those from ASTER and EO-1 ALI.

*ASTER data (spectral angle mapping)*

Demonstrating the usefulness of ASTER data for mineral mapping has been pioneered by groups associated with the US Geological Survey (e.g. Rowan & Mars 2003; Rowan et al 2003, 2005, Hubbard & Crowley 2005). It has also become a low-cost means of assessing exploration potential for a variety of metal ore deposits, focussing on alteration associated with hydrothermal and porphyry-style mineralisation. Yet little about that application has been published in peer-reviewed journals (but see GRSG 2003): perhaps a measure of its success in the commercial field. Figure 5.23 gives some examples of laterite-related minerals detected by spectral angle mapping applied to ASTER reflectance data.

Like the results from Hyperion data, those for kaolinite are excellent. As Figure 5.23 b shows, spectral angle mapping detects all known clay zone occurrences in the Asmara area with few pixels outside laterite areas falling below the threshold. This mineralogical accuracy is further emphasised by the results for illite (figure 5.23 c), with few illite pixels falling in areas of laterite. Andrews Deller (2006, Section 2)

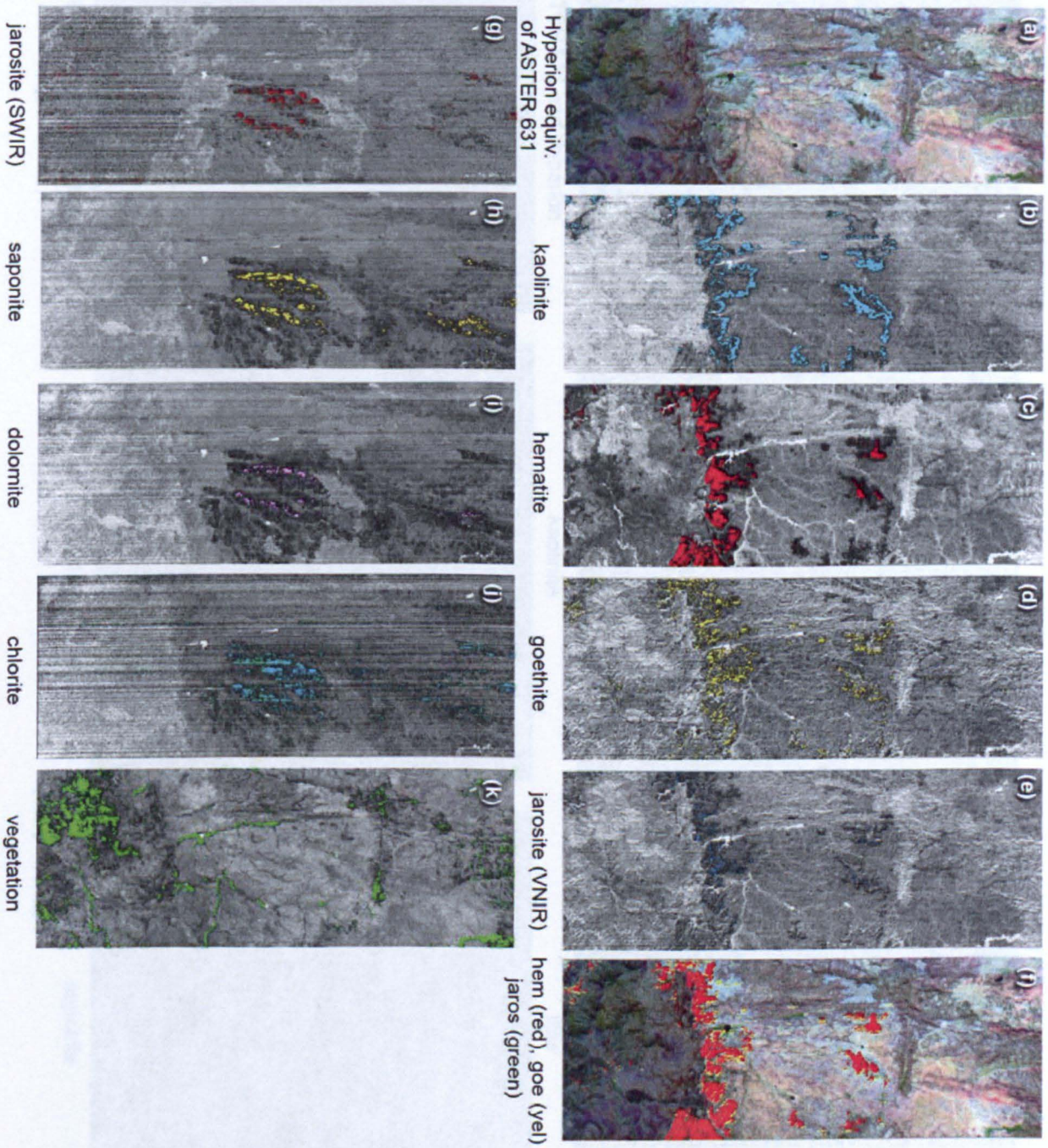


**Figure 5.22** Results of spectral angle mapping of several minerals associated with laterites using Hyperion data (5 February 2001) for an area 20 km west of Asmara (see Figure 5.23). (a) Hyperion image equivalent to ASTER 631. Image (f) shows iron minerals typical of ferricretes superimposed on (a). Image (k) shows the success of Hyperion in detecting areas of vegetation: a means of validating the method – note that other dark areas follow drainage courses: typical of vegetation in Eritrea

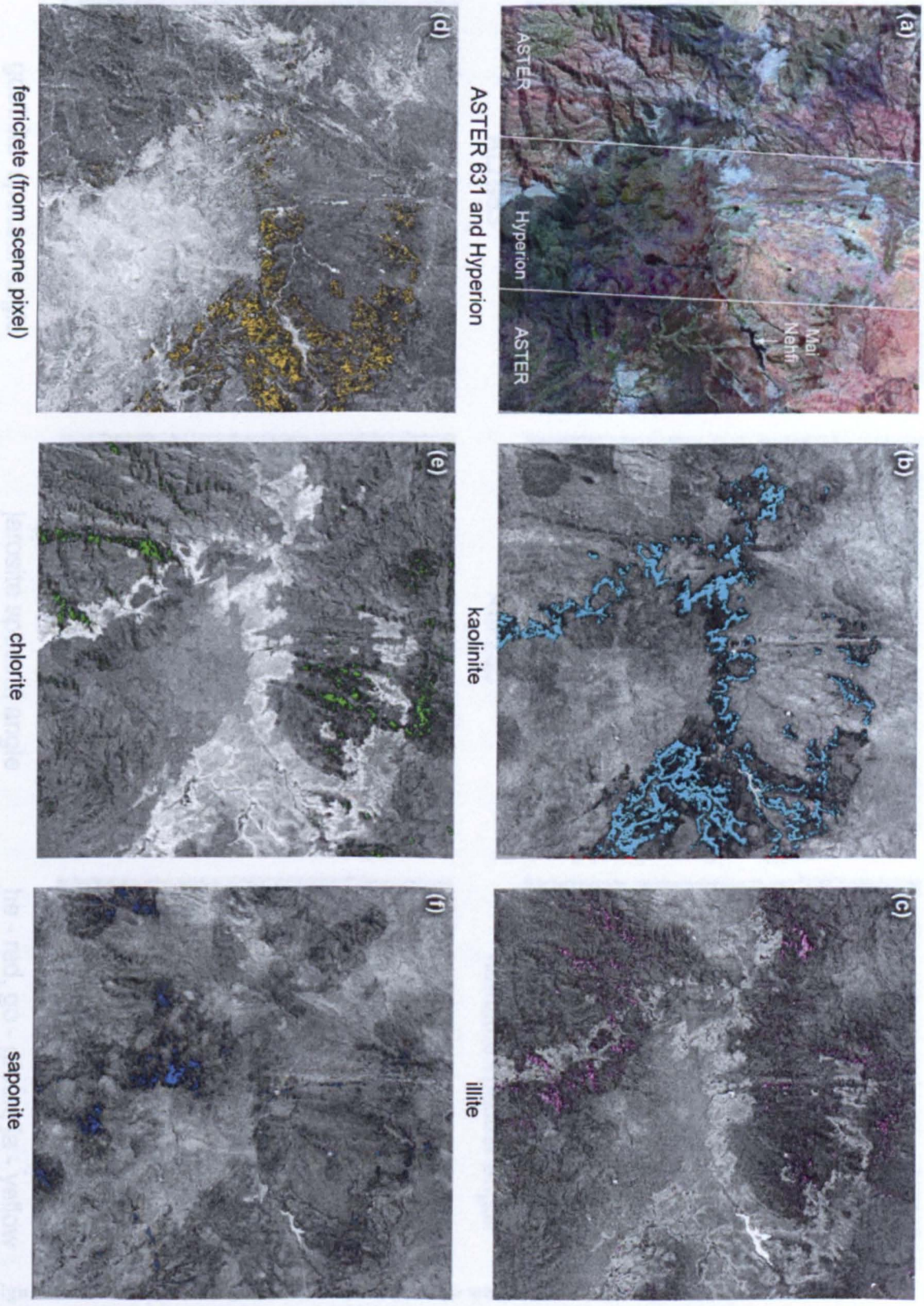


**Figure 5.23** Examples of spectral angle mapping using ASTER data. (a) ASTER 631 image (14 February 2004) of an area west of Asmara – note the position of the Mai Nehfi reservoir – with the Hyperion swath discussed in the last section. (b to f) Images of spectral angle for several minerals, with values below chosen thresholds highlighted in colour

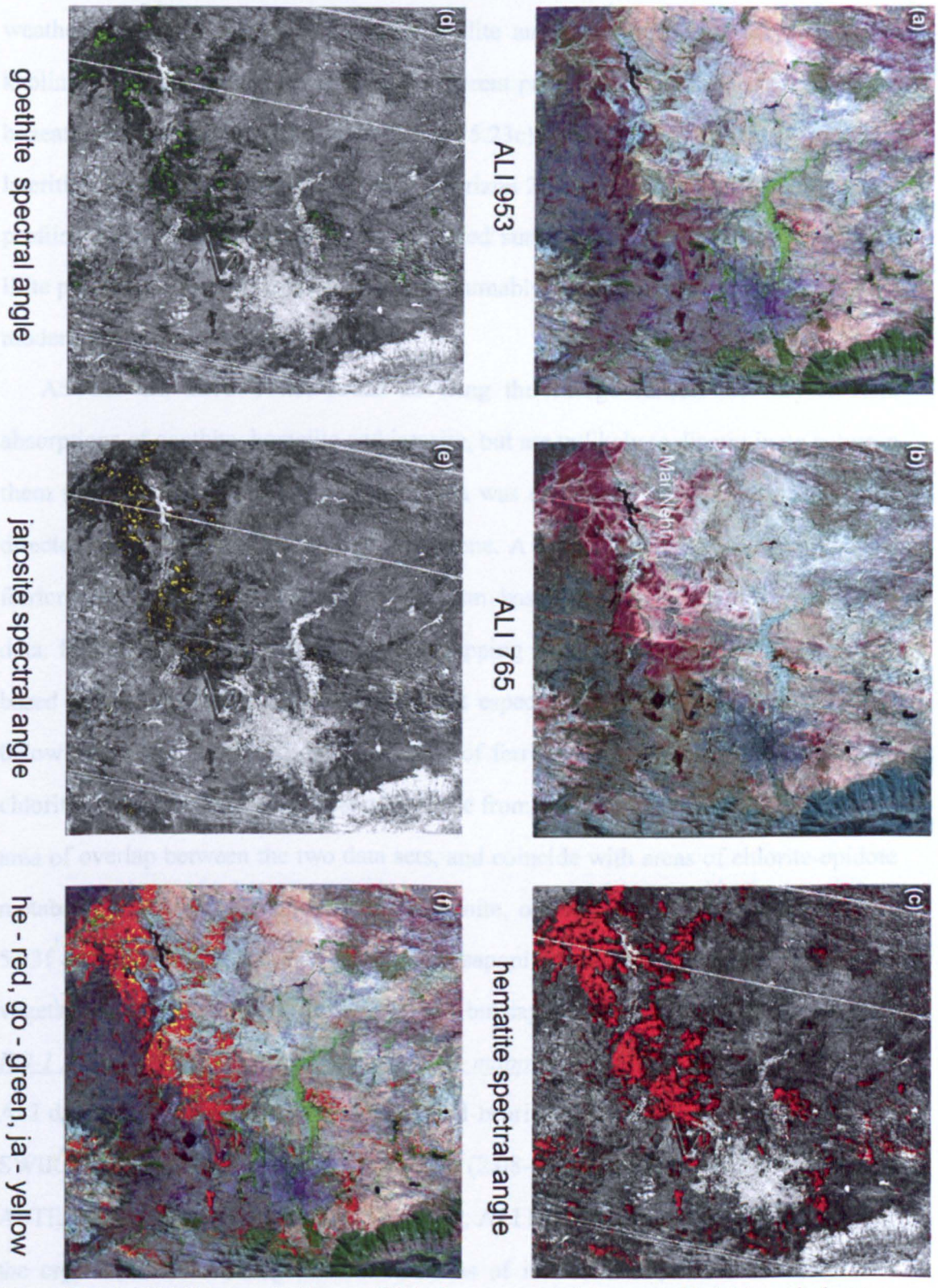


**Figure 5.24** a) ALI 953 image (5 February 2001) of an area around Asmara (mid-right): equivalent to Landsat TM 742. (b) ALI 765 image that highlights surfaces rich in iron oxy-hydroxides. (c to e) Images of spectral angle for hematite, goethite and jarosite with pixels below chosen thresholds highlighted in colour. (f) ALI 953 image with results of spectral angle mapping for iron minerals superimposed.

contains a brief account of the evolution of clay minerals during protracted lateritic

weathering, which eventually transforms illite and montmorillonite clays to stable kaolinite. Interestingly, there are some coherent patches of illite in the basement just beneath the laterites (upper left, figure 5.23c), which may reflect incomplete lateritisation in the weathered basement (Horizon 2, the 'youngest' part of the laterite profile) that was arrested when the lateritised surface was smothered by the CFBs. Illite pixels also show in areas of basalt, presumably as an important component of the modern fertile black soils or *tselima.*

ASTER has three VNIR bands covering the charge-transfer and crystal-field absorptions of goethite, hematite and jarosite, but are unlikely to discriminate between them (figure 5.17). So, a different approach was chosen for spectral angle mapping directed at lateritic ferricrete and mottled zone. A pixel from a known area of dense ferricrete provided a representative spectrum based on USGS ASTER reflectance data. Figure 5.23d shows spectral angle mapping results from ASTER bands 1 to 5 based on that spectrum. The results are not especially good, but the bulk of pixels below the chosen threshold do lie in areas of ferricrete or mottled zone. Results for chlorite (Figure 5.23e) closely resemble those from Hyperion data (figure 5.22j) in the area of overlap between the two data sets, and coincide with areas of chlorite-epidote metabasalt fragments in modern soil. Saponite, on the other hand (compare figure 5.23f & 5.22h) shows no such match and saponite pixel clusters occur in areas of vegetation. Chlorite is successfully detected, but saponite is not: it may not be present.

*EO-1 Advanced Land Imager (spectral angle mapping)*

ALI data are of little use in investigating OH-bearing minerals, band 9 being the only SWIR band and has a broad spectral range (2.08-2.35 μm) that covers all 5 narrow ASTER bands in the SWIR region. However, ALI has 7 bands in the VNIR that cover the crystal-field and charge-transfer features of iron-rich minerals reasonably well (Andrews Deller 2006, Section 3.3) and they should be well-suited to discrimination of iron-rich laterite facies and iron minerals. Figure 5.24 shows spectral angle mapper results from this iron-oriented instrument.

Hematite (figure 5.24c) is the most convincingly detected of the three minerals,

large, coherent clusters of pixels that fell below the chosen threshold mainly falling within areas of known ferricrete or mottled zone. There are pixels in areas of basalt, most probably because of the red hematitic weathering of exposed basalt. Other 'false positives', in the context of laterite mapping occur in the areas of basement, and these pixels are probably areas of ferricrete pisoliths transported from active erosion of laterites: being very dense they do not travel far from their source on the plateau surface.

As with results using Hyperion, those based on ALI data for goethite and jarosite (figures 5.24d & e) are patchy. However pixels below the chosen thresholds form coherent clusters within the areas of laterite outcrop, but not in the clay zone. Figure 5.24f combines bitmaps for the three minerals overlaying the ALI 953 image.

*Hyperion data (matched filtering and cross correlation)*

Two further approaches were applied to hyperspectral EO-1 Hyperion data in the context of iron and clay minerals that dominate laterites. The analyses focused on the 2.12 to 2.23μm range for kaolinite, illite and smectites – specifically montmorillonite (figure 5.20) – and the 0.5 to 0.9μm range for hematite, goethite and jarosite (figure 5.21). Detection of jarosite was also attempted on the basis of its unique SWIR absorption, using the 2.20 to 2.34μm range. The results presented here are from the western part of the Asmara test area (figure 4.8).

Hematite and jarosite (figures 5.25b & d) show high values for matched filtering (MF) in the areas of known laterite, correlating strongly with ferricrete and mottled zone, with intermediate values over the flood basalts and generally low ones over the lower horizons in the laterite profile and basement. There are however poor results in the SWIR range for jarosite. Goethite (figure 5.25c), despite its known presence in ferricretes and mottled zone, is no more abundant there than it is over basalts and basement. A colour rendition of the MF results for hematite, goethite and jarosite in RGB order (figure 5.25e), emphasises in yellow 'false positives' for hematite and goethite in some areas of living vegetation (figure 5.25j). The strong red signature over many known exposures of ferricretes and mottled zone indicates the dominance

of hematite in these facies, but an associated speckling of blues suggests that jarosite is abundant in places. The magenta hues with further blue speckling over flood basalts indicates hematitic soils with some influence of sulfate ions from the break-down of pyrite in the basalts. Goethite clearly dominates as a colorant in the modern soils and ancient saprolite developed on much of the basement judging by the prominent greens north of the flood basalt and laterite exposures. As expected, areas of clay zone, which show clearly in cyan on Figure 5.25a, have no iron-mineral signature.

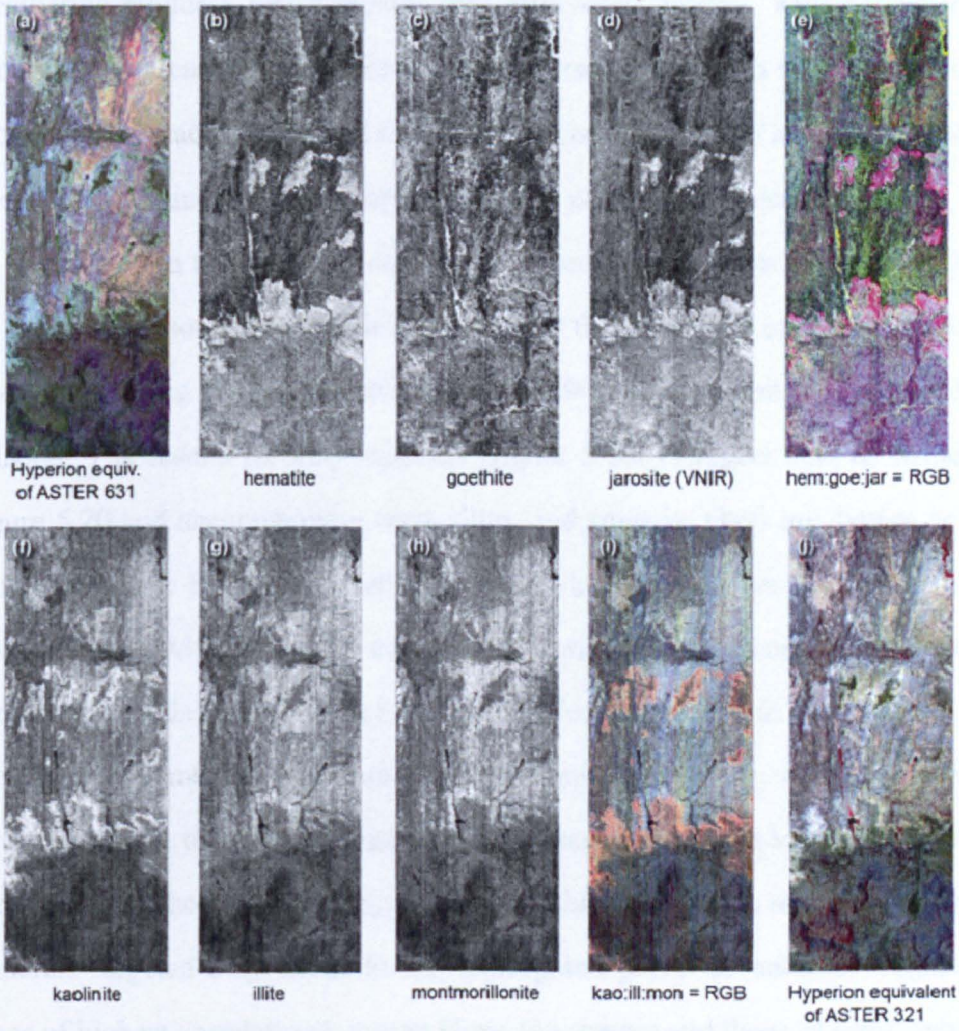


**Figure 5.25** Results from matched filtering of Hyperion data: (a) Hyperion equivalents of ASTER 631 and ETM+ 742 – general geological rendition and (j) of ASTER 321 and ETM+ 432 – standard false-colour composite showing vegetation as red, are for reference. The MF results are shown with a normalised contrast stretch. The width of the area is 7.7 km (256 x 30m pixels)

All three clay minerals (figure 5.25f-h) exhibit a similar pattern with each

showing the highest values for MF around laterites, but kaolinite clearly dominates the clay zone proper as a more sharply defined bright strip. This is borne out in Figure 5.25i by the red to orange fringe to all laterite occurrences, though that hue does suggest the possible presence of some illite in the clay zone. Illite and montmorillonite dominate the coarse saprolite (laterite Horizon 2) and modern soils over basement, as indicated by the cyan-blue hues in Figure 5.25i. Notably, the lowermost flood basalts, adjacent to the south of the laterites show dark blue hues commensurate with dominant montmorillonite (smectite) clays in their Neogene weathering products, which include the fertile black '*tselima*' soils characterising low ground on Eritrean and Ethiopian basalts. These organic-rich soils naturally break up along myriad cracks during the dry season, a characteristic of swelling smectite clays, and a further inducement to tillage as minimal ploughing is necessary.

Results from the cross-correlation (XC) method are shown in Figure 5.26. Instead of using continuous grey-tone images to show the results for each mineral, only those pixels containing cross-correlation values >0.90 are displayed for the output of each mineral. The results for clay minerals (figure 5.26b) suggest that, as suspected (see figure 5.20 and accompanying text), illite- and smectite clays are cannot be recorded with confidence by the XC method, whereas kaolinite shows strong correlations for pixels located within the clay and mottled zone facies of laterites. Cross-correlation for iron minerals (figure 5.26c) reveals dominant hematite in the upper two laterite facies, with some patches dominated by goethit and only very sparse patches of jarosite. Again the SWIR range gives poor results for jarosite, however, the results for the XC method given in Figure 5.26 should not be taken as confirmation that the minerals targeted *only* occur in the highlighted pixels as coloured regions display areas of highest correlation between Hyperion spectra and those of target minerals. The results using the spectral angle mapper approach (figure 5.22) broadly correspond with those achieved by the other two methods with the exception of jarosite.

Despite the presence of noise in Hyperion data, they are clearly capable of detecting a wide range of common minerals, specifically the iron- and clay minerals

that dominate laterites. The cross-correlation and spectral angle mapping approaches help to confirm this. As predicted, kaolinite is the overwhelmingly dominant clay mineral in the upper three laterite facies. Where illite and smectite clays do show up, most notably though spectral angle mapping, the pixels most likely to contain them are in the lowest coarse saprolite facies where weathering of basement has not reached completion (section 3.1). Hematite dominates the Fe-rich laterite facies, with patchy goethite, but jarosite is not widespread. Indeed, this iron-rich member of the alums occurs over sulfide-rich schists-and may be a product of current weathering.

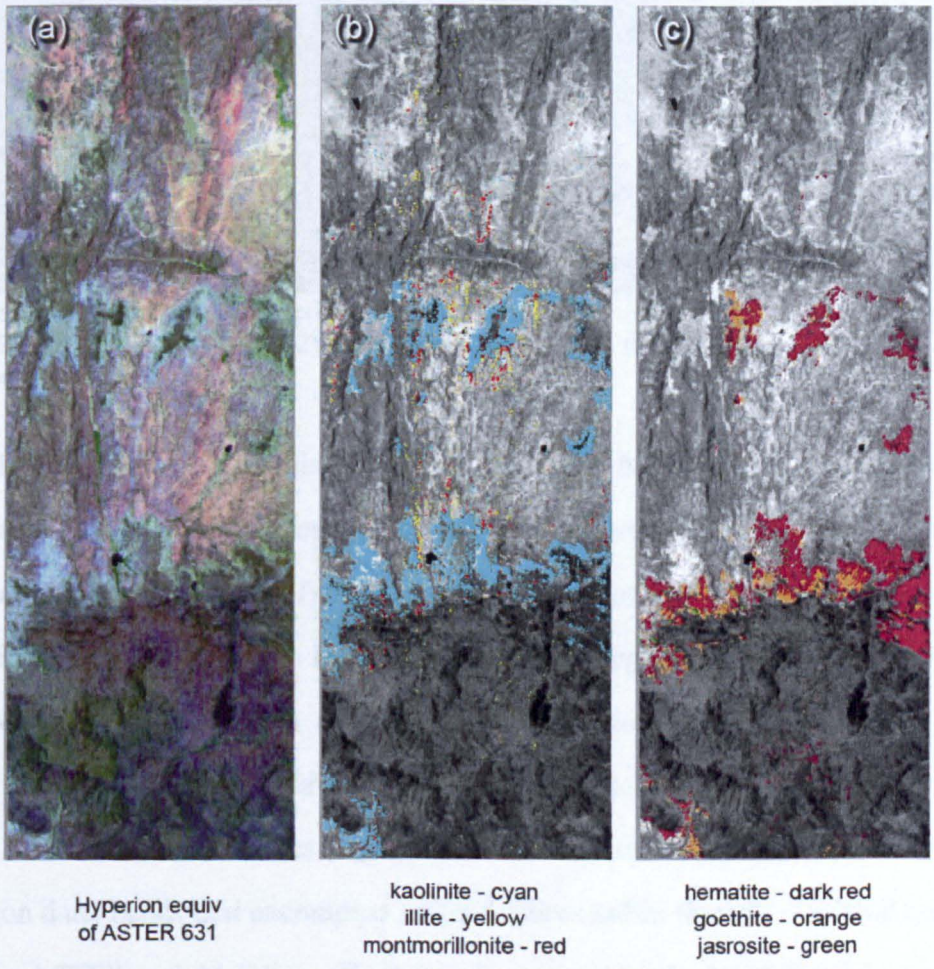


**Figure 5.26** Results from cross-correlation of Hyperion data. (a) Hyperion equivalents of ASTER 631 and ETM+ 742 – general geological rendition, for reference; (b) clay mineral pixels with correlation coefficients >0.90; (c) Fe minerals with correlation coefficients >0.90. (a) and (b) results superimposed on image of Hyperion visible red reflectance

As Hyperion data are only produced on demand in narrow (7.7km) swathes, it is unsuited for regional mapping purposes, despite the obvious promise that these pilot

studies have shown. ASTER with its 5 narrow bands in the SWIR and the provision by the USGS and ERSDAC of data calibrated to reflectance does offer a chance of fulfilling a mineral mapping role globally, using the same data analysis methods as applied to Hyperion. The outlook, however, is optimistic for laterites, as most of the associated minerals (figure 5.17) still show spectral differences despite the poorer spectral resolution of the ASTER sensors.

*ASTER and EO-1 ALI data (matched filtering and cross correlation)*

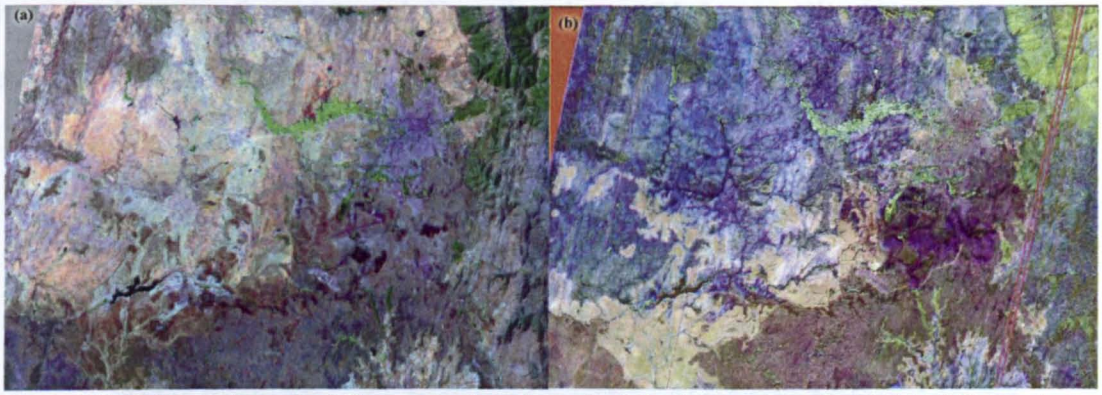


**Figure 5.27** EO-1 ALI matched filtering in detection of oxidised iron minerals. (a) ALI 942 (equivalent to ASTER 631 and Landsat TM 742) for reference. (b) Matched filtering results for hematite, goethite and jarosite as RGB

Only one broad-band multispectral instrument has bands that adequately cover the distinctive Fe-3 charge-transfer and crystal-field absorptions in the VNIR, the EO-1 Advanced Land Imager (ALI) that covers that region with 7 bands with variable bandwidths (see figure 4.3). In the critical SWIR region ASTER deploys 5 bands (bandwidths 0.04 – 0.07μm) compared with Hyperion's 19 (0.01μm) and clearly cannot show the same spectral detail, yet convolution of mineral spectra to ASTER SWIR band widths and centres (figure 5.17) does retain distinctive features. As with Hyperion data, bands that encompass target features rather than all available bands are used for ASTER and ALI data. Therefore for iron minerals ASTER bands 1 to 5 and ALI 1 to 7 are employed and for -OH and C-O features, ASTER bands 4 to 9 are used.

As regards detection and discrimination of oxidised iron minerals, the salient features of hematite, goethite and jarosite are better covered by EO-1 ALI bands 1 to

7 than by ASTER bands 1 to 5 so analyses of ALI data are described initially. On Figure 5.27b, known laterite occurrences show as pale yellows suggesting all three iron minerals are abundant. Basement and saprolite are dominated by dark blues, cyans and greens, suggesting a deficit of hematite relative to goethite and/or jarosite in modern soils and saprolite. Deep magenta coincides with the *tselima* soils developed on basalts and vegetation appears in pale yellowish-greens. This rendition distinguishes sharply laterites from overlying basalts that have a speckled brownish hue. In the area of overlap with Hyperion data, ALI data predictably do not perform as well as those from Hyperion in matched filtering of iron minerals (figure 5.25e).

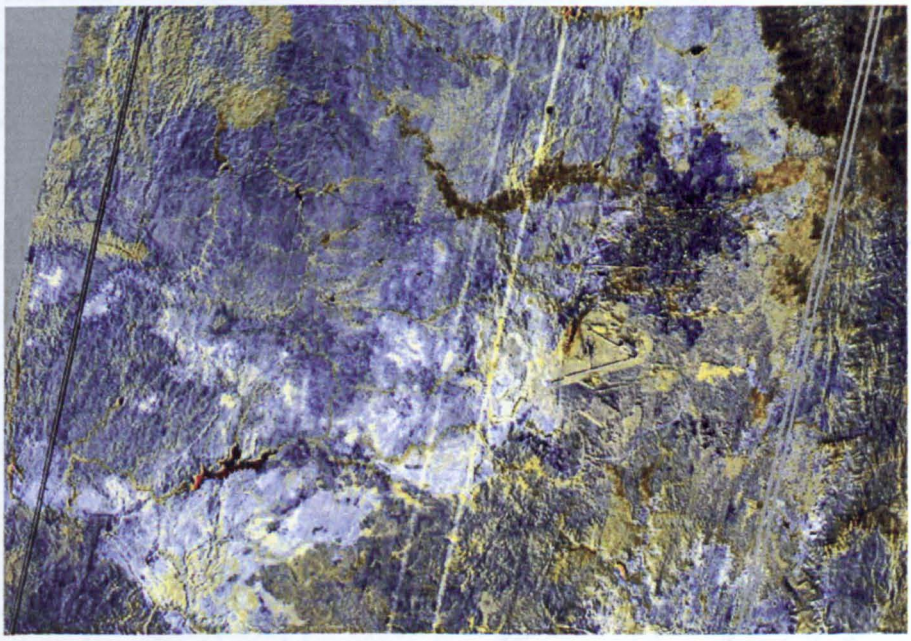

**Figure 5.28** EO-1 ALI cross correlation results for iron minerals: hematite, goethite and jarosite as RGB

The cross correlation method used for Hyperion data (figure 5.26c) demonstrates nicely that hyperspectral data successfully discriminate and map the main iron minerals in laterites. The same cannot be said for ALI data. Although Figure 5.28 does highlight areas of laterite in pale hues, some ferricretes and the most iron-rich mottled zone show as white: suggesting high proportions of all three minerals. Thresholding cross-correlation results for the three minerals outlines the iron-rich laterite facies in each case, but jarosite is indicated as the dominant one with

goethite and hematite substantially less-well correlated with their lab spectra. In fact this result is probably deceptive, as Figure 5.29 suggests. Clearly, ALI picks out the main crystal-field absorption (in ALI band 6) associated with the three minerals but fails to recognise the differences as regards charge-transfer features in ALI bands 1 to 4, thereby confusing the three sought-after iron minerals. ALI is good for mapping oxidised iron minerals in general, but not for discriminating them in detail.

Matched filtering of ASTER data for the three oxidised iron minerals does not produce useful results for hematite, goethite and jarosite. The probable reason for this is that ASTER VNIR band 3 is not affected much by the crystal-field absorptions of goethite and hematite, though that of jarosite does produce a marked signal (figure 5.17a). None of the ASTER pixel spectra for known ferricretes that were examined reveal the strong band 7 absorption of jarosite (figure 5.17a) and if present in the laterites, it is rare. An alternative tactic is called for using an ASTER spectrum from a pixel in a known area of iron-rich laterite facies bare of other cover – a crude proxy for field spectroscopy. Little improvement was achieved using the MF approach, but cross-correlation highlighted effectively all iron-rich laterite facies in the test area (figure 5.30) with ferricretes showing very high correlation (>0.99)

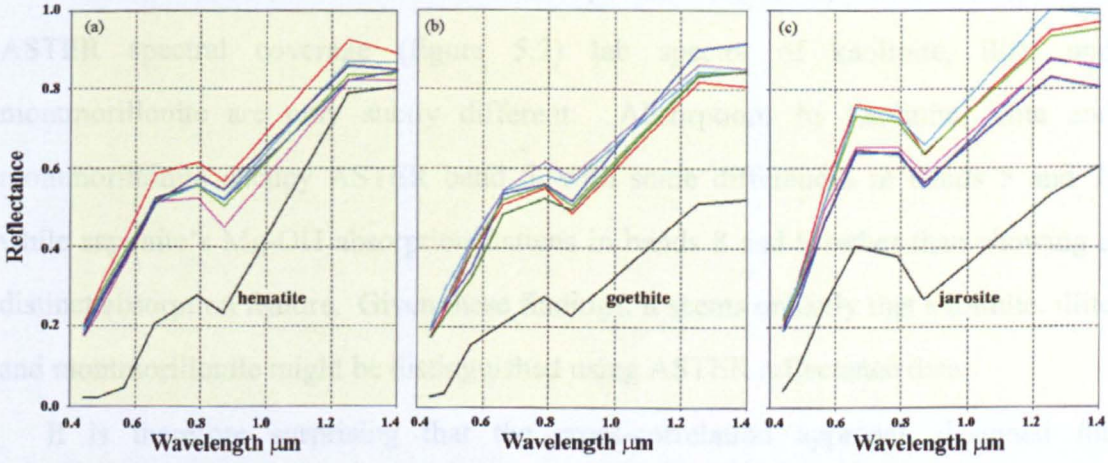


**Figure 5.29** ALI spectra from six of the most highly correlated pixels for each iron mineral, compared with lab spectra resampled to ALI specifications

Interestingly a proxy spectrum derived from ASTER data for a pixel on a known area of bare ferricrete pays dividends when used for SAM (figure 5.30). Spectral

angle values below 2.0 with a very close fit of pixels to that for a ferricrete in 9-dimensional spectral space are abundant. By choosing a threshold of 2.75, all ferricretes and the most iron-rich mottled zone occurrences are highlighted with few pixels outside known areas of laterite. Increasing the threshold above 3.0 however, shows many patches of basement outside lateritic areas; not unexpected in a terrain in which many of the schists and metavolcanics are pyritic and have iron-rich weathered surfaces and modern soil cover.

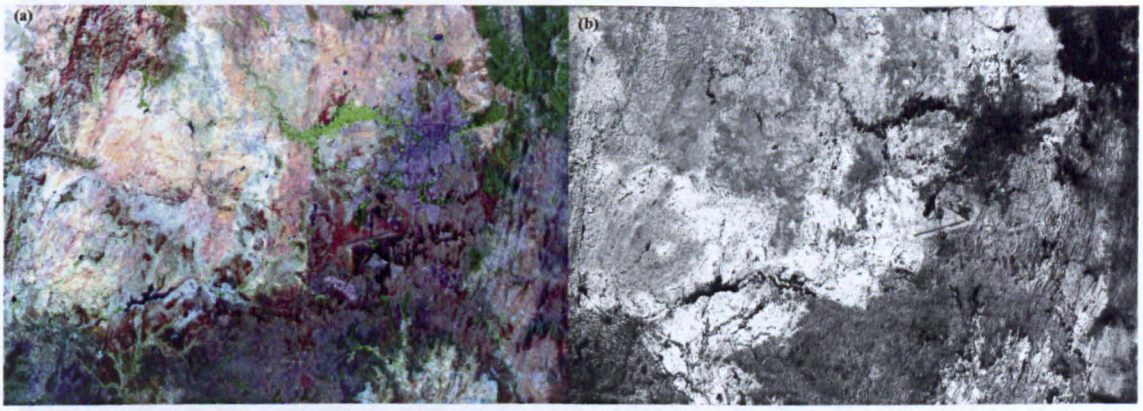


**Figure 5.30** Detection of iron-rich laterite facies using ASTER reflectance data. (a) ASTER 631image for reference. (b) Cross correlation of ASTER data with spectrum derived from typical ferricrete occurrence

ASTER's five SWIR bands cover that region where various minerals carrying – OH and C-O bonds have distinctive lab spectra. However, when resampled to ASTER spectral coverage (figure 5.2) lab spectra of kaolinite, illite and montmorillonite are only subtly different. Absorptions by kaolinite, illite and montmorillonite occupy ASTER band 6, with some differences in bands 5 and 7, while saponite's Mg-OH absorption flattens in bands 8 and 9 rather than showing a distinct absorption feature. Given these findings, it seems unlikely that kaolinite, illite and montmorillonite might be distinguished using ASTER reflectance data.

It is therefore surprising that the cross-correlation approach designed for hyperspectral data is capable of successfully discriminating kaolinite, illite and montmorillonite – though not illite from montmorillonite as Figure 5.31 illustrates convincingly. Much of the area of laterites and saprolite developed on basement of the Hamasien Plateau is seen on Figure 5.31a to show a high SWIR correlation with

the kaolinite spectrum. Most of the basement areas where correlation is markedly lower has been incised through the saprolite by Neogene to Recent erosion. In contrast, the main areas of laterite and saprolite on Figure 5.31b show low SWIR correlation with the spectra of montmorillonite as is also the case for illite; a similar observation to that revealed by Hyperion data (figures 5.22, 5.24 & 5.25). In contrast, the matched filtering approach fails to distinguish significantly between kaolinite, illite and montmorillonite, perhaps to be explained by the different algorithm used by the method.

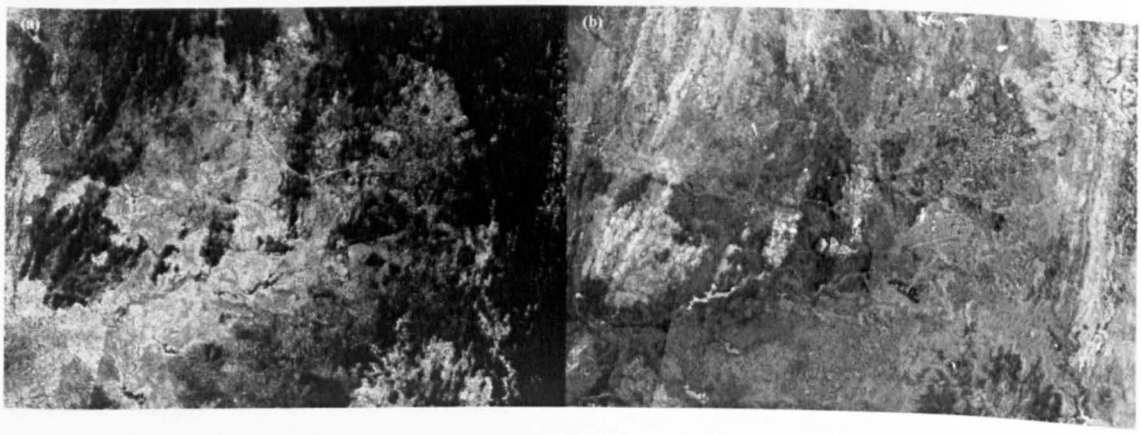


**Figure 5.31** ASTER cross-correlation images for (kaolinite), (b) montmorillonite. Note: that for illite is barely distinguishable from (b)

Figure 5.32 displays SAM results for the three clay minerals with very similar spectra in the ASTER spectral range suggest that this method confuses kaolinite and illite, in fact a lower threshold for illite than for kaolinite is required to highlight the laterite clay zone. However, even though montmorillonite shows lower spectral angle values over the clay zone than for most non-lateritic areas, a threshold of 9.5 is required to highlight any pixels in this facies and to show them as clearly as Figure 5.32b and c where a threshold of 10.5 wrongly highlights larger areas of vegetation. The cross-correlation method used for ASTER on the other hand clearly shows kaolinite dominance in the clay zone, in common with several approaches using Hyperion data. Validated by ground truth, the weight of remotely sensed evidence on the Asmara test area therefore, strongly supports the anticipated dominance of kaolinite in the Eritrean laterites and the absence from them of smectites.

Analysis for the distribution of another smectite, saponite, detected using

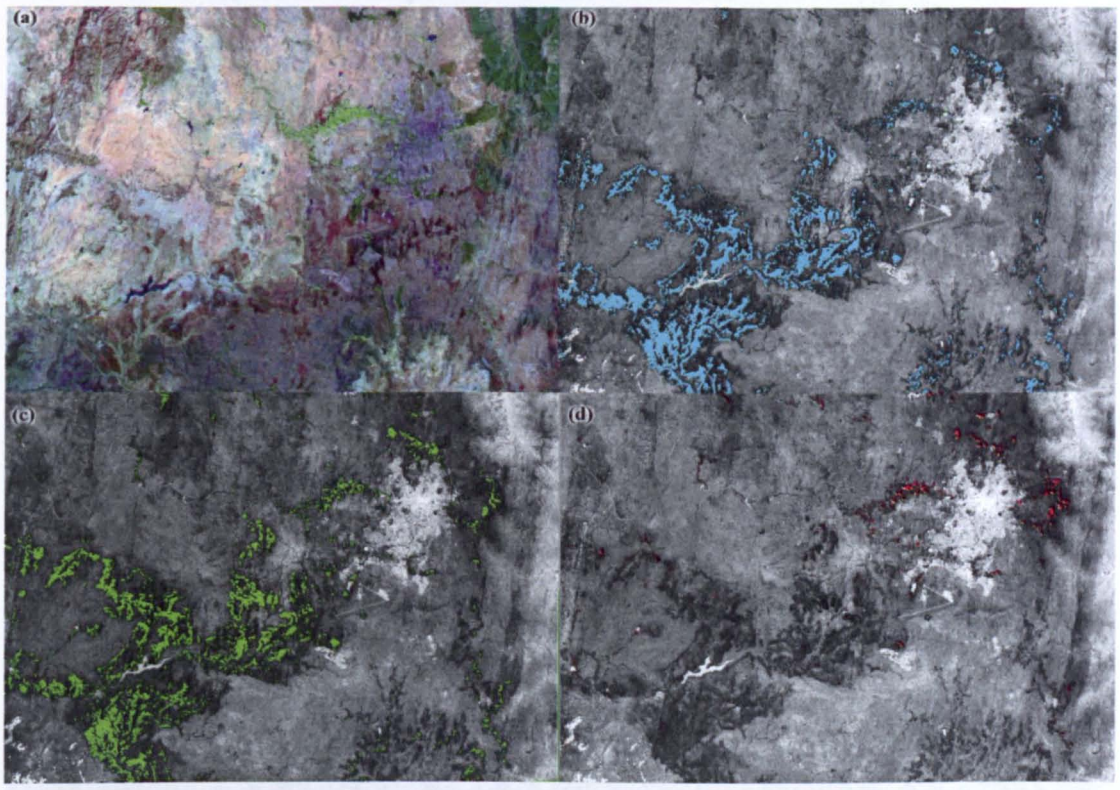


**Figure 5.32** ASTER spectral angle mapping. (a) ASTER 631; (b) kaolinite – threshold 9; (c) illite – threshold 7.75; (d) montmorillonite – threshold 9.5

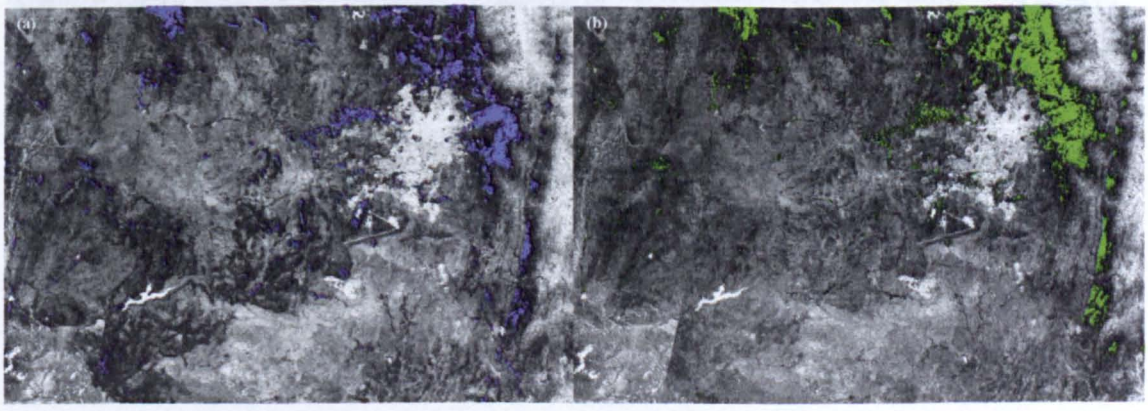


**Figure 5.33** ASTER spectral angle mapping of Mg-OH minerals. (a) saponite (Mg-, Fe-rich smectite clay) – threshold 12; (b) talc – threshold 9.4. Compare with Figure 5.32a

Hyperion data (see figure 5.25i) led to the surprise find that (figure 5.33a) saponite shows no systematic correspondence with laterites and is confused with some types of vegetation (see figure 5.32a). However, saponite is signaled in a clear NNE-SSW line in the east of Figure 5.33a, parallel to the regional strike of the basement, where serpentinite has been reported (T. Keleta. & M. Teklay, pers. comm. 1998, 2001).

Indications of saponite correspond with those for talc, whose spectrum is similar (figure 5.33b), but not with chlorite. An interesting observation is that where the trend disappears beneath laterite in the SE corner of Figure 5.33, neither mineral is indicated in the laterite clay zone. The only difference in the laterite profile there is that clay and mottled zones are markedly thinner than elsewhere.

### 5.5.4 Results in other areas

Results of SAM using ASTER reflectance data, applied to other areas in NE Africa and the Arabian Peninsula show clearly, in the examples given below, the consistency of this approach and the fact that it works in any arid or semi-arid area.

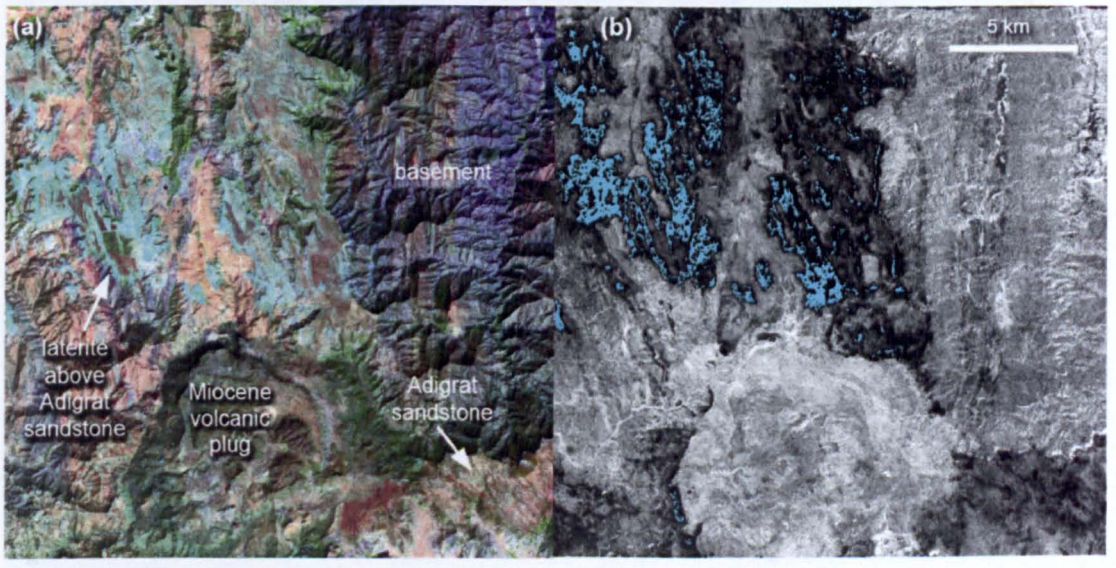


**Figure 5.34** The Adi Caieh area in Eritrea, 30 km SSE of Asmara (see Figure 4.11 in Andrews Deller 2006). (a) ASTER 631 image (22 January 2001). (b) Spectral angle image for kaolinite, with pixels below a threshold of 5.5 highlighted

The laterites of Adi Caieh (figure 5.34), unlike those of the Asmara area, developed on the Adigrat Sandstone, an almost pure quartz sandstone. Consequently, they are far thinner than laterites that formed on basement rocks. The clay zone is highly siliceous and is a flinty silcrete as are the overlying, iron-bearing equivalents of mottled zone and ferricrete that are less than 2m thick. Despite this, the high kaolinite content of the lowest horizon shows up extremely well in the image of spectral angle (figure 5.34b). The iron-rich horizons also have low spectral angles and show dark. The pervasive kaolinite signature is so wide in this case as the laterites outcrop on

three plateaus separated by down-to-west normal faults: a clear example of the usefulness of the clay zone as a datum for analysing structure (Chapter 7).

Figure 4.11 in Andrews Deller (2006) also illustrates another example of laterites from As Sarat in Saudi Arabia that developed on Neoproterozoic basement rocks and were smothered by CFBs of the Yemeni large igneous province that are coeval with those of the Ethiopian province (i.e. in the same stratigraphic setting as those of Eritrea). This area is on the arid Arabian Plateau and almost devoid of vegetation. As a result, Figure 5.35 shows perhaps the best available example of the power of kaolinite mapping using the spectral angle mapper approach.

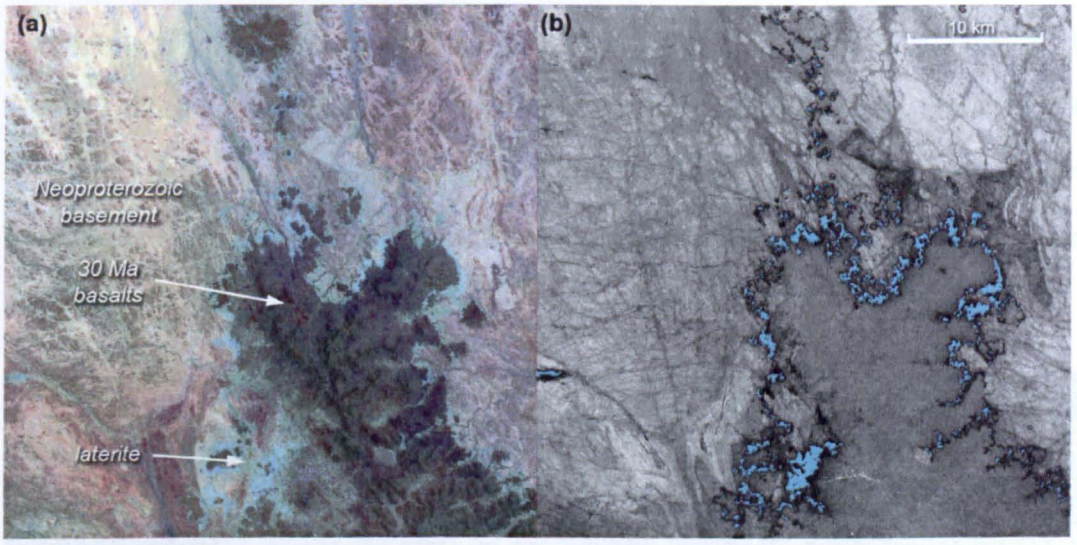


**Figure 5.35** The As Sarat area in Saudi Arabia. (a) ASTER 631 image (7 May 2001). (b) Kaolinite spectral angle image

Kaolinite detected using spectral angle mapping occurs consistently at the base of CFB outliers over a span of 400km from its easternmost occurrence in Eritrea into the valley of the Atbara River in eastern Sudan and up to 330km to the south of Asmara where laterites disappear beneath the main mass of the Ethiopian flood basalts. Figure 5.36 shows results from the eastern flank of Ras Dashen, a huge pile of CFBs capped by a Miocene shield volcano of alkaline basalts and trachytes that rises to 4543m. This area is close to the southern limit of laterite occurrences before the blanket of CFBs. Figure 5.36a clearly shows structurally complex basement unconformably overlain by yellow-brown glaciogenic sediments and Adigrat Sandstone. They, in

turn, are overlain by a bluish unit (possible laterite clay zone) then a reddish brown unit (ferricrete) capped by dark purple CFBs. The reddish unit high on the slope of Ras Dashen is probably a highly weathered alkaline basalt. Spectral angle mapping (figure 5.36b) shows clearly that the bluish unit is indeed the kaolinite-rich lateritic clay zone. The view that laterites were removed by erosion during crustal bulging prior to eruption of the CFBs of the Ethiopian large igneous province (Burke & Gunnell 2008; Ukstins *et al.* 2004) is hard to accept on evidence of their presence from so close to the central zone of CFB eruption. The only sign of unconformity, other than that at the base of the Adigrat and glaciogenics, is the pinching out of these Permian to early Jurassic strata in the northern part of this area (figure 5.36a).

Field evidence from the gorge of the Blue Nile 300km further south of Ras Dashen indicates the presence of laterites at the base of CFBs on both northern and southern lips of the gorge. Unfortunately, the terrain there is so steep and vegetated that the laterites barely show at the resolution of ASTER data, so spectral angle mapping was not attempted in that area.

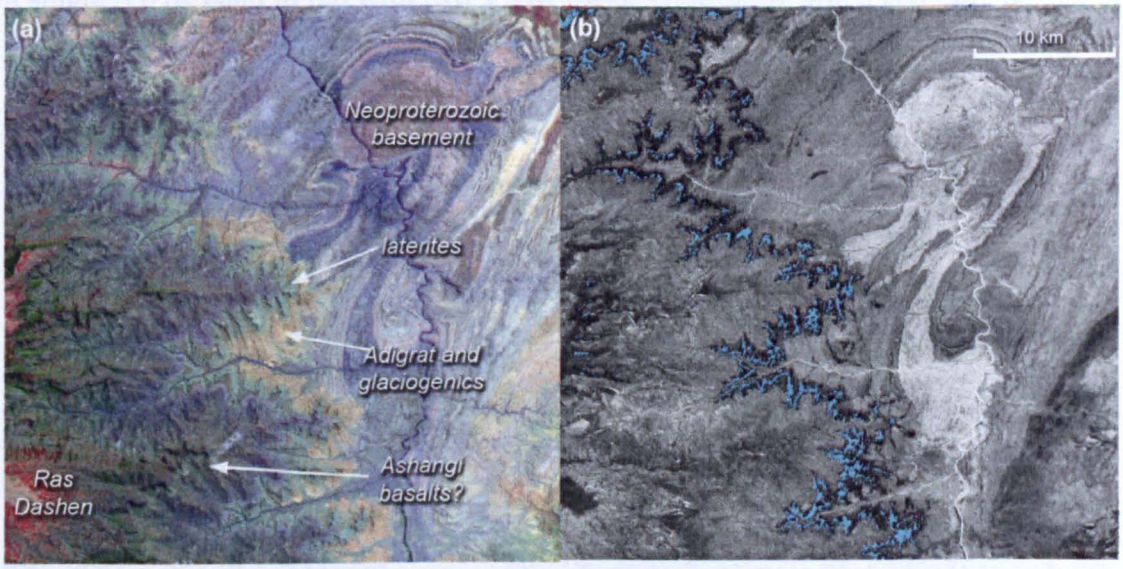


**Figure 5.36** The eastern flank of Ras Dashen in southern Tigray province, Ethiopia. (a) ASTER 631 image (24 May 2004). (b) Distribution of kaolinite as revealed by spectral angle mapping

The total lack of any significant uplift and erosion between the close of lateritisation and the onset of flood-basalt volcanism is further confirmed by Figure 5.37, in the plain of the Wabi Shebelle River in Ogaden province Ethiopia, close to

the Somali border. This is on the eastern side of the Main Ethiopian Rift, around 850km from the location of Figure 5.36. Upper Jurassic to Lower Cretaceous interbedded limestones, mudstones and beds of evaporitic gypsum dominate the area (Merla *et al.* 1973). Overlying them are outliers of basalts, possibly distal flows of the Ethiopian CFB province but undated.

Once again the presence of abundant kaolinite suggests the likely presence of laterites beneath basalts of the Ogaden, and their vast regional extent. Other outliers of similar basalts in the Ogaden also prove to overlie probable lateritic palaeosols. Interestingly, the bluish unit showing at bottom right of Figure 5.37a is not picked up as resembling kaolinite, indeed it has high values for the spectral angle (Figure 5.37b). This is probably gypsum that is the only other common mineral that appears in sky blue on Landsat ETM 742 and ASTER 631 images. Both minerals have overall high albedo, so are reflective across the spectrum, but kaolinite has two distinct absorption features in the SWIR (in ASTER bands 5 and 6) whereas gypsum has broadly low reflectance in the SWIR compared with the VNIR region. For this reason, combining a single SWIR band in red with two VNIR bands controlling green and blue results in a sky blue or cyan appearance for both minerals: use of spectral techniques, such as the spectral angle mapper is a accurate way of distinguishing the two.

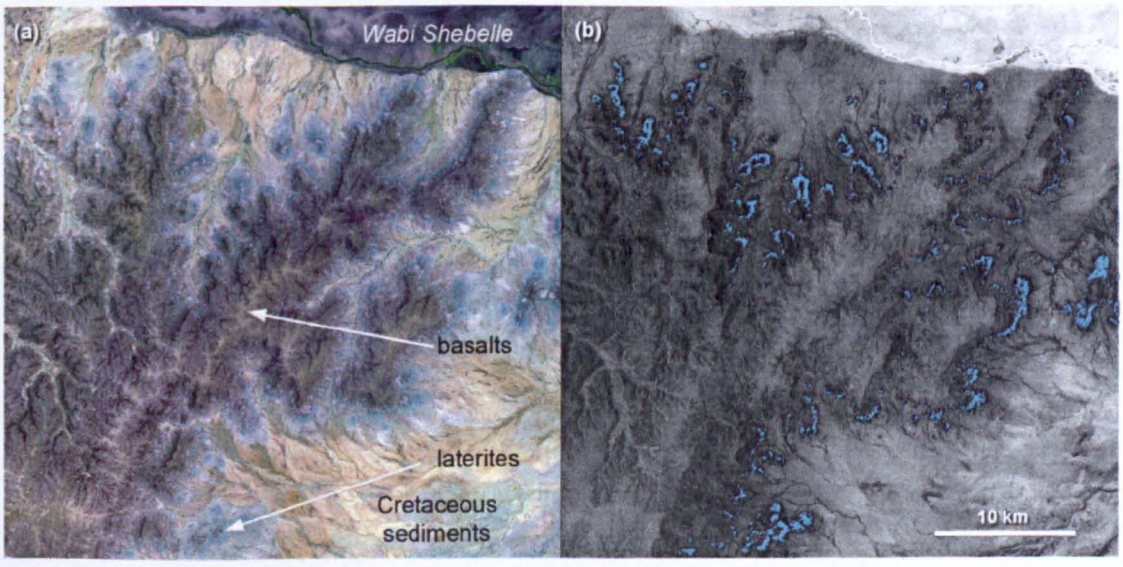


**Figure 5.37** Part of the Ogaden close to the Ethiopia-Somalia border on the south bank of the Wabi Shebelle and close to the Gode refugee camp. (a) ASTER 631 image (26 March 2006). (b) Kaolinite occurrences on spectral angle image.

### 5.5.5 Discussion

A firm basis for rapid regional mapping of the laterite facies is provided by combining the efficiency and accuracy of SAM for detecting kaolinite with visual discrimination of laterite facies from each other and from other rocks.

Importantly, SAM of kaolinite also detects small occurrences of the lateritic clay zone, far from larger laterite occurrences and close to the lower margin of the CFBs thus identifing small outliers, which would otherwise go unnoticed in 3-band RGB images. Insignificant as they might seem, such isolated patches define the elevation of the regional tectonic datum that combined with regional digital elevation data can be used to model the structural shape of the datum and the nature of Miocene uplift (Chapter 7). In turn, such a model provides the key for investigating the regional effect of secondary enrichment during lateritisation. Finally, accurate geological maps of the distribution of laterites are a basis for assessing any health hazards that may stem from the palaeosols' particular chemistry (Chapter 8).

# $^{40}Ar/^{39}Ar$ dating: evidence for the timing and formation of laterites in Eritrea

Laterites in Arabia, Yemen, East Africa and more particularly in Eritrea and Ethiopia have never been dated. Where they have been dated in other parts of the world, notably South America, West Africa and Australia (Bird *et al.* 1990; Vasconcelos 1999; Gunnell 2003; Vasconcelos *et al.* 2008), geochronological work has been confined in the main to small pockets of outcrop, remnants of lateritic caprock or localised mineral-rich seams that have been altered and enriched by presumed laterite-forming processes. In contrast, this chapter sets out to establish the minimum age of lateritisation using remote sensing (RS) to pin-point dateable laterite facies over the region, roughly the size of Wales, UK, the Hamasien Plateau, part of the Nakfa Terrane, Eritrea (see figure 2.29).

## 6.1 Introduction

The results of a laser $^{40}Ar/^{39}Ar$ geochronological study are presented for samples collected throughout the area in order to determine the timing and duration of lateritisation using the particular resolution afforded by the $^{40}Ar/^{39}Ar$ dating technique. This establishes a reliable geochronological database for laterites which, devoid of fossils, have only been crudely dated by being bracketed in local stratigraphic sequences in Eritrea, Ethiopia and the Yemen (Baker *et al.* 1996; Menzies *et al.* 1990, 1997; Drury *et al.* 1994).

Stratigraphically located above the Neoproterozoic basement and isolated relics of the Mesozoic sequence and below the mid-Oligocene plateau basalts of the Ethiopian Igneous Province, laterites conformably underlie the CFBs and blanket sizeable areas of the region thus forming a clear datum (Drury *et al.* 1994). In this chapter, $^{40}Ar/^{39}Ar$ ages for lateritic palaeosols confirm this tectonic marker. Furthermore,

inasmuch as *'an age ...represents the best estimate of when a geological phenomenon took place'* (Vasconcelos 1999), these new geochronological data shed light on the tectonic and palaeo-weathering history implicit in the evolution of Eritrean laterites. The findings may be extrapolated to Ethiopia where lateritic cover is obscured over large areas by CFBs. Following a discussion on $^{40}Ar/^{39}Ar$ dating, the body of this chapter is divided into 5 major sections. The first 3 deal with $^{40}Ar/^{39}Ar$ data acquired for laterite, basalt and basement samples. Each section is self-contained and can be readily prepared for publication. The 4th is a discussion by Drury *et al.* (2006) printed below to further the debate. An overall appraisal of the research topics covered in Chapter 6 concludes the chapter.

- Section 6.4, building on the previous chapter, establishes the minimum age of lateritisation in the region. To avoid repetition, the conclusions drawn in the section directly relate to radiometric dating of the laterites and not to the RS strategy for targeting minerals. Conclusions for the RS minerals targeting strategy are found in Chapter 4, which detailed the detection of laterite facies and Chapter 5, in which the RS targeting of the dateable mineral alunite is developed.
- Section 6.5 focuses on flood basalt effusion in Eritrea and Tigray. The maximum age of CFBs compared with the minimum age for lateritisation indicates the time lag between the close of deep weathering and the influence of the mantle plume that generated the lavas. A minimum age for the lavas constrains the timing for the start of Neogene uplift and Red Sea rifting.
- Section 6.6 provides $^{40}Ar/^{39}Ar$ cooling ages of granitic basement as evidence for episodes of regional tectonics, which suggests a much earlier and perhaps more widespread episode connected with the development of the peneplain on which laterites began to form.
- Section 6.7 outlines evidence accumulated in this and earlier studies that bears on the initiation of Red Sea rifting and major uplift that is studied in Chapter 7 using the laterites as a tectonic datum. It takes the form of a discussion on Balestrieri *et al.* (2005) that uses U-Th/He dating of apatites to model basement

cooling associated with Neogene uplift in eastern Eritrea. In it the authors (including the author of this thesis) present a critique of Balestrieri *et al.*'s (2005) interpretation of regional Neogene tectonics, thereby creating a context for the latter parts of Chapter 7.

## 6.2 Strategy

There is no systematic geochronological research published on laterites in East Africa, despite their widespread occurrence. However, given that both underlying basement and basalts that cap the laterites in Eritrea have been dated at ~650 Ma (Teklay 1997) and ~30 Ma (Drury *et al.* 1994) respectively - a time gap of more than half a billion years - the idea of determining the age of the laterites sandwiched in-between was a challenge. During the first field trip in March 1998, one aim was to collect suitable samples for $^{40}Ar/^{39}Ar$ dating. The primary objective was to select specific laterite samples, which it was hoped would contain potassium-bearing minerals that after irradiation could be used to obtain valid ages for these palaeosols. Should this objective be achieved, multispectral RS would be used to locate further localities with datable minerals (see Chapter 5) even though this approach had never been tried before this study. A second objective was to collect samples of basement rocks exposed in the Eritrean escarpment to see if they provided radiometric constraints on regional unroofing and uplift history in relation to the formation of the African Surface (King 1948) from which laterites developed. This information would be used to examine post-laterite uplift associated with Red Sea rifting, an objective attempted by Mock *et al.* (1999) without success. A third objective was to collect samples from the highest and lowest CFB flows. These would be used to establish the local time span of flood basalt eruptions and check the initial discovery by Drury *et al.* (1994) of a ~30 Ma maximum age for Oligocene volcanism in Eritrea, which in turn would place constraints on the absolute minimum age for lateritisation (Bird *et al.* 1990).

## 6.3 $^{40}Ar/^{39}Ar$ Dating

New whole rock $^{40}Ar/^{39}Ar$ ages were acquired for representative samples of: (i) clays from horizon 3 within the laterites; (ii) granodiorites from the Red Sea escarpment intruded into the basement underlying the laterites and, (iii) basalts overlying the laterites (Mohr 1970) using the Ar/Ar dating method (section 3.5). After irradiation at the McMaster University reactor, Canada, laser spot step-heating analyses were carried out on whole-rock samples at the Open University mass spectrometry laboratory. Using an infrared (IR) continuous wave (CW) Nd YAG laser system with a 25-micron diameter beam and 80 watt power, argon was released from each sample in steps at increasing temperatures.

It should be noted that alunite-bearing samples are difficult to analyse using laser heating. The samples do not release argon slowly by diffusion or melting. They break down and disintegrate suddenly and often violently, vibrating and migrating as they release gas. Most of the gas released is probably $SO_2$ but it happens so rapidly that it makes analysing the alunite challenging. Initial gas release originates from the grain surface and from sites within the sample that lose gas readily whereas at higher temperatures, gas is released from more retentive sites of the sample. The $^{40}Ar/^{39}Ar$ ratio of gas released from the sample at each step was used to calculate its apparent age (the date corresponding to one analysed step; section 3.5). Apparent $^{40}Ar^{*}/^{39}Ar$ ages for each step were plotted against the cumulative percent of $^{39}Ar$ released to produce an age spectrum (McDougall & Harrison 1999; Vasconcelos 1999).

Three age estimates may be obtained from these analyses: plateau ages, integrated and isochron ages (Tables 6.1, 6.2, 6.3; Appendix B). A *plateau age* is defined as two or more consecutive steps that correspond to at least 50% of the total $^{39}Ar$ released (Feng & Vasconcelos 2001). An *integrated age* is the apparent age calculated from the total gas yield of the sample (Girard and Onstott 1991; Vasconcelos 1999). An *isochron age* is that derived from a plot of $^{36}Ar/^{40}Ar$ against $^{39}Ar/^{40}Ar$ for all heating steps where the age is given by a best-fit line between the plots. Where results from steps were inconsistent because of recoil (Kelley 2002), atmospheric contamination or

excess argon, the weighted mean (to $^{39}Ar$ yield) of data selected heating steps for a particular sample, was used to give an *estimated age*. In certain cases however, most of the argon was given off in one step so effectively making these results *total fusion ages*. Such a result is the equivalent of a K/Ar age, relying on wholesale release of argon in a single heating step. However, these analyses also resulted in meaningful ages and are taken into consideration. Similar considerations apply to the basalt and basement dating.

## 6.4 The laterite group

### 6.4.1 Previous published research

In the early stages it was uncertain whether or not Eritrean laterites contained any potassium-bearing minerals. The only mention of dateable minerals occurring in East African laterites comes from Germann *et al.* (1993, 1994) who were not concerned with dating laterites. Furthermore their statements that, *' in north-east Africa ...no or only thin relics of kaolinitic..saprolite'* exist, together with their subsequent observation that, *'the **sole** complete lateritic weathering profile known at present from north-east Africa exists in the Jebal Tawiga area of north-west Sudan'* (Germann *et al.* 1993. 1994) was not encouraging. More promisingly, they did find strata-bound alunite-bearing lateritic kaolinites with alunite-enriched veinlets and fissures in the Gedaref area of the Sudan close to the Ethiopian border (Germann et al. 1994). Drury *et al.* (1994) countered initial claims made by Germann *et al.* (1994) by confirming the clear presence of Eritrean laterites based on field observations, so reinforcing the findings of Dainelli (1943), Mohr (1970, 1976, 1979), Bohannon (1989), Drury and Berhe (1993) and Burke (1996).

At the time of the first field trip (March 1998), the only work done on radiometric dating of laterites was confined to Australia, (Bird *et al.* 1990), West Africa, (Vasconcelos *et al.* 1994) and Brazil (Vasconcelos *et al.* 1994; Rufett *et al.* 1996). Bird *et al.* (1990) were the first to date alunite in a laterite profile, one sample yielding a K/Ar early Tertiary minimum age for the profile in which it was found. In West

Africa Vasconcelos *et al.* (1994) carried out $^{40}Ar/^{39}Ar$ dating of jarosite ($KFe(III)_3(OH)_6(SO4)_2$) at one locality in order to study primarily, weathering and secondly laterite formation. In Brazil, Vasconcelos *et al.* (1994), again with the same objectives, used the $^{40}Ar/^{39}Ar$ technique to date cryptomelane (a complex potassium-manganese oxide ($K(Mn(IV), Mn(II))_8O_{16}$) in laterites, as did Rufett *et al.* (1996) who dated cryptomelane in one manganese-rich lateritised deposit. Two further publications followed in 1998. In Botswana, Gutzmer & Buekes (1998) reported a ~2.0-2.2 billion year-old laterite. They however, based their age estimation on the stratigraphic position of the palaeosol in relation to the age of the surface on which it rested and the age of overlying materials (Bird *et al.* 1990; Bourman 1993; Andrews Deller 2003). Somewhat later, Henocque *et al.* (1998) dated two samples of cryptomelane in a Burkina Faso laterite using their $^{40}Ar/^{39}Ar$ study of this mineral to place geochronological constrains on tropical weathering there.

Jarosite, cryptomelane and alunite have all been found in laterites. However, in this study, jarosite, concentrated in the ferricrete, was ruled out because of the problems of mineral identification and surface contamination of the upper ferricretes since their formation, which would greatly affect ability to measure a true age. Furthermore no comprehensive $^{40}Ar/^{39}Ar$ analyses of jarosite existed - results worldwide being based on a few samples from a few localities in gossans (Vasconcelos 1999; McDougall & Harrison 1999). In Eritrea then, only two rare potassium minerals in laterites, cryptomelane ($KMn_8O_{16}$) and alunite ($KAl_3(SO_4)_2(OH)_6$), allow $^{40}Ar/^{39}Ar$ dating, but both are difficult to detect in laterites. Cryptomelane is black and only occurs in dark ferricretes that form over Mn-rich bedrock, whilst alunite, which may occurs in saprolites, is white and difficult to detect in white kaolinites. Cryptomelane, like jarosite, is difficult to identify in the iron-rich crust. If concentrated in Horizon 5 of the laterite profile and constantly subjected to surface weathering and in NE Africa to re-heating by the overlying CFB lavas, it too would be subject to surface contamination. Furthermore, manganese is extremely susceptible to reduction, dissolution and leaching in lateritic systems and as there are

no Mn-rich rocks in the Eritrean Precambrian basement from which the ferricretes evolved, cryptomelane would be difficult to find. Although alunite is not as abundant as the potassium manganese oxides, in Eritrean laterites it remained the only potassium-bearing mineral that, if present, would be concentrated away from the present day weathering front in kaolinitic clay horizon 3.

The oldest material in laterite profiles is located in the uppermost ferruginous horizon 5 - the inversion of normal stratigraphy so to speak (figure 2.34; section 5.4). In these ferricretes minerals such as cryptomelane and jarosite that may be dated in the absence of problems would, if feasible, provide a *maximum* age for lateritisation. However, when determining the age of the lateritic weathering profile, it has to be remembered that laterites are *not* the product of a single weathering event (Vasconcelos 1999). Horizon 5, the oldest part of the profile is therefore the wrong facies in which to search for dateable minerals if a *minimum* age for laterisation is required. Rather, it is the youngest part of the laterite proper - Horizon 3 - where dateable minerals must be located, if *'direct isotopic age measurements of the rock'*, here palaeosols, (McDougall 2008) are to be used to provide a minimum age for lateritisation and its relation to the African surface. Alunite therefore, already radiometrically dated in Australia (Bird *et al.* 1990) and discovered in lateritic clay horizons in the Sudan (Germann *et al.* 1994) was the preferred mineral to select for dating Eritrean laterites.

Despite the rarity of $^{40}Ar/^{39}Ar$ dating of hydrated potassium aluminium sulphate in laterites, *'few minerals have as many geological applications for K/Ar or $^{40}Ar/^{39}Ar$ dating as alunite'* (Itaya *et al.* 1996). First used as a geochronometer over forty years ago (Shanin *et al.* 1968; Webb & McDougall 1968; Chuchrov *et al.* 1969; Silberman & Ashley 1970), radiometric dating of alunite has long provided reliable information about weathered ore bodies and associated base mineralisation (Ashley & Silberman 1976; Alpers & Brimhall 1988). Several geochronological studies indicated that supergene alunite is Ar retentive at relatively low temperatures, <50 °C, in the surficial environments that resulted in its genesis (Gustafson & Hunt 1975; Bird *et al.*

1990; Itaya *et al.* 1996; Vasconcelos 1999) and Sillitoe and McKee (1996) noted its stability in geological weathering environments. Indeed, Landis *et al.* (2004) report, *'...at <200–220 °C, the alunite will retain Ar almost indefinitely'*. In 1992, Vasconcelos dated a single crystal of alunite using the laser-heating $^{40}Ar/^{39}Ar$ technique and more recently, $^{40}Ar/^{39}Ar$ ages of alunite have been used to research palaeoclimate and environment (Itaya *et al.* 1996; Vasconcelos 1999, 2008; Vasconcelos & Conroy 2003; Vasconcelos *et al.* 1994, 2008).

### 6.4.2 Provenance / selection

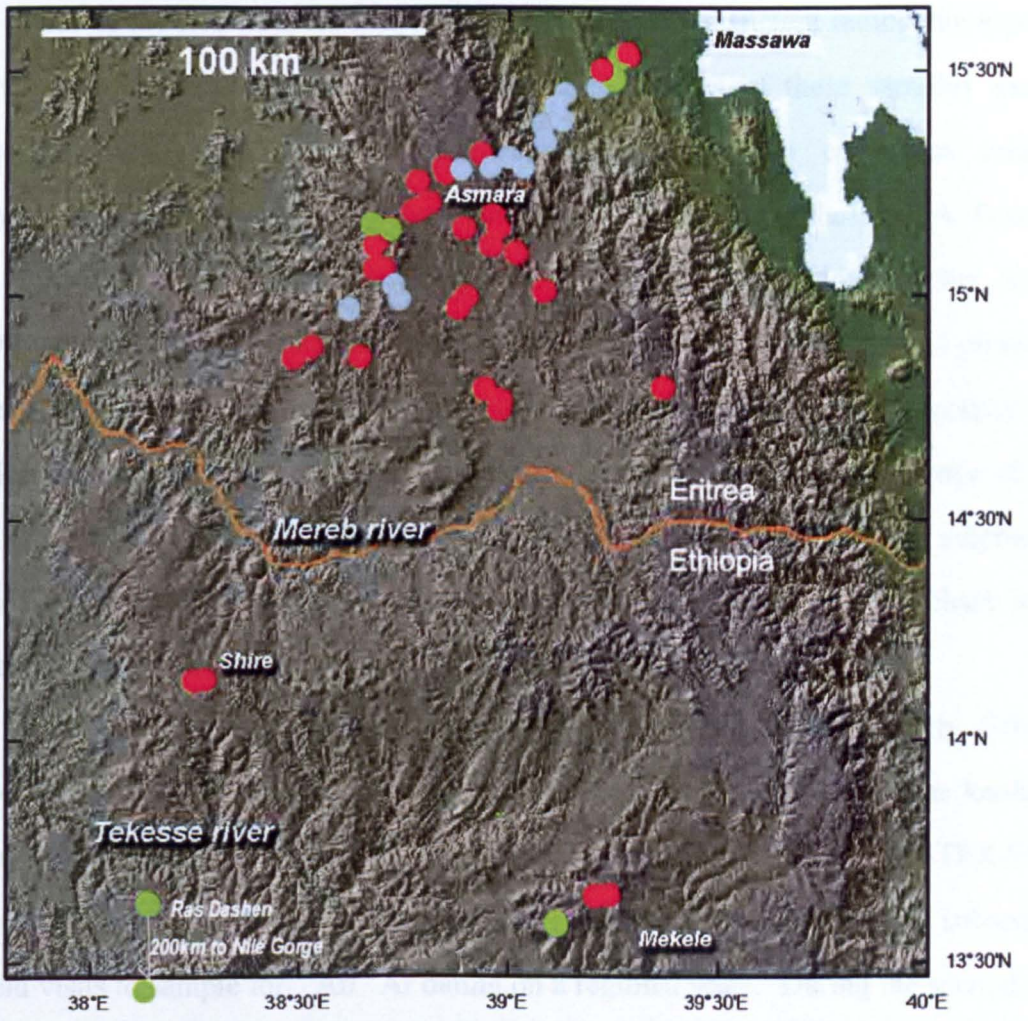


**Figure 6.1** SRTM DEM colour coded shaded relief location map showing the spread of localities sampled for Ar-Ar dating marked by coloured dots: laterites = red, basement = blue, basalts = green

Figure 6.1 shows the distribution of samples collected for Ar-Ar dating and indicates the sites that were targeted for laterite clays containing alunite (red dots) using RS. The best candidate facies for sample selection for Ar-Ar dating is the

clearly identifiable mineralogically distinct clay (Horizon 3) in the laterite profile that is resistant to erosion. This fine-grained, iron-poor, flinty, porcellanous clay was most likely to contain disordered kaolinite that may incorporate K in its structure or alunite, thus potentially providing dateable minerals. At each locality (figure 6.1, table 6.1), Horizon 3 was checked for pure white kaolinitic clay. As the most suitable horizons for geochronology are indurated (Vasconcelos 1999), only hard samples with minimal atmospheric contamination which were most likely to retain radiogenic argon were collected for irradiation and mass spectrometry.

Four of the five samples irradiated in 1998 yielded sufficient radiogenic argon to give well-constrained ages (Chapter 5). Thin sections of these samples showed irregular aggregates of small cube-shaped crystals of a colourless mineral. Suggestions were made that this was authigenic K-feldspar (adularia) (S.A. Drury & A. Tindle pers. comm. 1999) or allanite (S.P. Kelley & M. Widdowson pers. comm. 1999), so to test the hypothesis that the simpler mineral alunite was in fact present in the samples, polished thin sections were prepared for optical petrography and microprobe analysis (Reed 1996). These procedures established the presence of high silica (Si), aluminium (Al), potassium (K) and, in some samples abundant sulphur (S) and confirmed that the *only* mineral present as a K-, Al- and S-bearing phase in the clay that could be dated using the $^{40}Ar/^{39}Ar$ method, *was* indeed alunite.

As detailed in Chapters 4 and 5, kaolinite and alunite have distinctly different spectra in the short-wave infrared. Alunite-rich occurrences in the laterite kaolinitic clay zone could therefore be detected using digital image processing of ASTER SWIR data. Such areas once detected on satellite images were targeted during subsequent field visits to sample for $^{40}Ar/^{39}Ar$ dating on a regional scale. During the second field season in March 2001 several such localities were visited and clay-zone samples collected, using the above criteria. Localities that had already yielded samples that produced good ages (Chapter 5) were revisited in order to obtain a wider sample spread and provide an opportunity for testing the reproducibility of results within a given area. In these cases samples were collected from within the same laterite

profile and horizon as the target area. Where conditions precluded access to RS target sites alternative areas were selected. Furthermore, given the predominance of quartz and the very fine grained nature of supergene alunite in these samples, careful screening and selection further complicated sample choice. Given time constraints on laboratory use, only samples from two areas were irradiated for analysis. Any inconclusive results or outstanding uncertainties that arise from analysis of the Ethiopian samples therefore, may only be resolved by further sample collection and future work.

### 6.4.3 Results and discussion

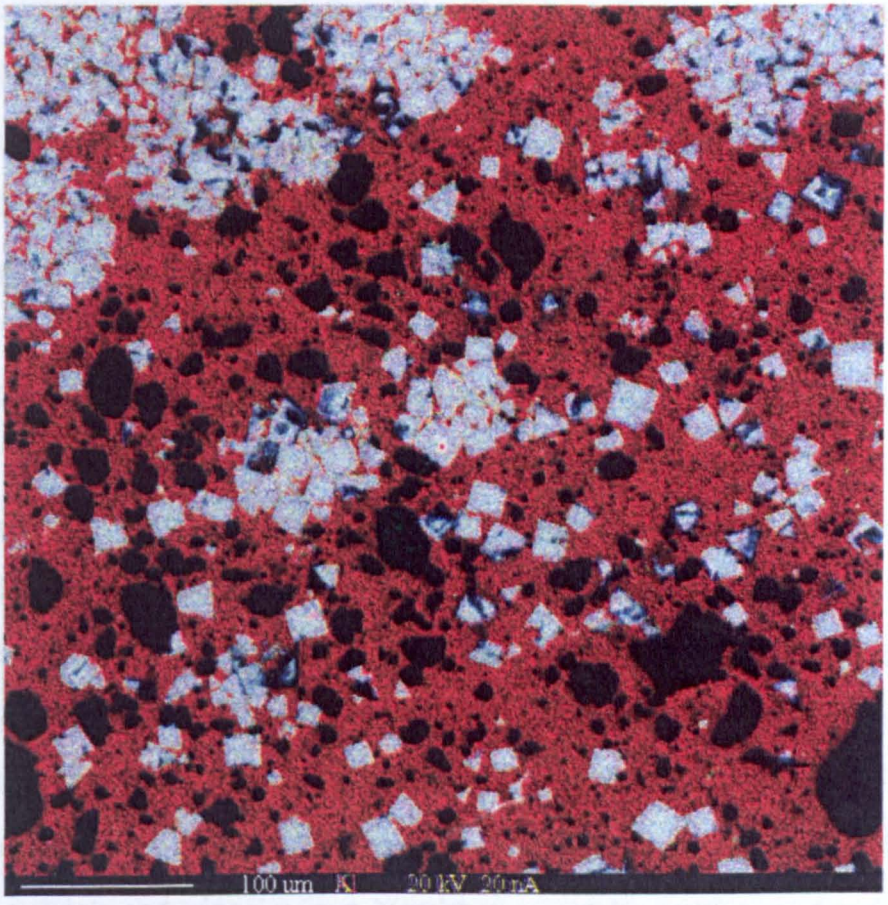


**Figure 6.2** Energy dispersive element map with Al, S, K as RGB of a kaolinitic clay from Horizon 3 of the laterite profile showing individual and clusters of alunite crystals (blue) in a fine groundmass of kaolinte (red)

New $^{40}Ar/^{39}Ar$ dates were acquired for thirty-five representative samples from the clay zone (Horizon 3) of lateritic palaeosols in Eritrea and Tigray. Age constraints for the minimum age of lateritisation over an area of roughly twenty thousand square

kilometres were obtained from twenty-two samples using whole-rock laser spot analysis (table 6.1). Despite the difficulties encountered in analysing these samples, the reproducibility of these results was confirmed when further analyses were carried out on different whole-rock samples from ten of the successfully dated laterite localities. Four types of data (plateau, integrated, isochron and total fusion ages) are used where appropriate to date laterite samples from Horizon 3, in which the occurrence of alunite (figure 6.2) in some areas in the region is now established. However, major and trace element XRF analysis of powdered samples (table 5.1) also indicated that in spite of the presence of potassium, abundances of these elements are not always sufficient to allow dating. $^{40}Ar$ /$^{39}Ar$ data, discussed below, indicate that the analysed clays can be divided into three broad categories; those selected from sites where samples yielded good ages, those from localities where samples yielded both good and variably old ages and, those from areas where samples failed.

*The failures - samples that did not yield geologically meaningful ages*

$^{40}Ar/^{39}Ar$ results for the samples in this category are disappointing. Samples M18i, M29, M45iii, M58 and M122A yielded old, basement-like ages of 821.8 ± 3.6, 609.5 ± 3.1, 719.6 ± 3.4, 438± 290 and 871± 15 Ma respectively, whilst samples M26ii and M121B yielded no ages at all. Although samples are from widely separated localities (figures 2.28, 2.29, 6.1), petrographically there is little to distinguish the samples that did not yield meaningful information from those that yielded good ages. In hand specimen, all samples are predominantly white or creamy, porcellanous kaolinites from laterite Horizon 3. Apart from samples that are particularly white and flinty, others display various degrees of iron staining from tiny hematite veinlets and pinpoint iron blemishes to patchy goethite and insignificant hematite discoloration. In thin section fine-grained kaolinite is predominant in all samples and only four (see below) contain visible alunite crystals. The most likely reason for samples that yield poorly constrained ages is that they contained very little potassium and laser heating released extremely small amounts of argon often dominated by atmospheric contamination and restite minerals in the laterite.

Anomalously old $^{40}Ar/^{39}Ar$ ages can therefore, in some instances, be explained by the chemistry of the failed laterite sample and the bedrock from which it developed (Chapter 2).

M18i and M45iii are samples from laterites, which developed on the chlorite schists of the volcano-sedimentary sequences of the Nakfa terrain that are known to have low K levels. M29 also low in K is underlain by diorite containing sodium-rich feldspars, whereas M26ii, M121B and M122A, from the Mai Nehfi area, formed on trondjhemite, a sodium-rich granite that contains little K. M58 however, derived from granite that contains K-feldspar, may have been dateable had alunite been present. However, like samples M121B and M122A that in later XRF analysis were shown to contain 81.25% and 76.02% SiO2 respectively, M58 was silica-rich. It should be noted that *initially* remote sensing was not used to target localities where samples M18 (i), M29 M45iii and M58 had been collected in 1998 as ASTER data was unavailable. However, they were targeted after the launch of ASTER to help check that the results were geologically consistent.

Given that this was the first time remote sensing has been used in a dating project, ASTER data were used to determine retrospectively whether the alunite signature was apparent at localities where samples failed to provide reliable ages. Interestingly, no alunite signature was registered at any of the failed sample locations. Fifty metres to the east of locality for M58 a good alunite signature was apparent but this was on the inaccessible side of a mountain col. Of the localities from which samples were collected that did not yield meaningful ages, only the Mai Nehfi area was revisited because within a kilometre of the M26ii locality, the alunite spectral signature occurs in abundance. However, the patchy nature of alunite precipitation and the fact that the concentration of the mineral decreases rapidly suggests that sampling needs to be within areas on images that are clearly alunite bearing.

All the failed samples show a similar release pattern during laser heating, with very low $^{39}Ar$ released in all of the steps. Quartz contamination is a possible explanation for this result although it is equally possible that contamination problems

are caused by relics of basement muscovite retained in the clay. Furthermore, it is noticeable that the lower temperature gas extractions that correspond to the release of argon from the grain surface and yield anomalously old apparent ages, can be explained by $^{39}Ar$ recoil (Kelley 2002; Vasconcelos *et al.* 2008). This can be expected in any potassium-bearing samples but it is a particular problem with very fine-grained clay minerals like kaolinite.

*Geologically meaningful and variably old ages*

With the exception of M33iv, M19A and M19C collected in 1998, lateritic kaolinites in this section were selected for dating on the basis of geochemical and image processing data. Clays with high $K_2O$ and S were preferentially selected (Table 5.1). Any samples with less than 0.10 % of $K_2O$ and less than 100 parts per million (ppm) of sulfur were rejected as being unlikely to give well-constrained ages.

Analysis of M101C with $K_2O$ (>0.10 %) but with lowish S (<1000 ppm) like 121B and 122A discussed above, was attempted as the chemistry suggested that it contained some alunite, but it failed to yield a reliable age.

The analysed clay samples in this section come from five widely spaced general areas (figure 6.1, 2.29). Samples from three of these areas: M100T and M101C from Adi Caieh, Eritrea; M201 and M201a from Adi Mizan, Ethiopia and, M211 and M211a from Shire, Ethiopia yield similar results and are discussed together. Laterites at all six localities are silica enriched and developed on relics of the Mesozoic sequence that occurs mainly in the south of Eritrea and in Tigray, Ethiopia. Laterites at the Ethiopian Adi Mizan localities developed on silicified Cretaceous sandstones whilst analysed clays from Adi Caieh and Shire developed on the Late Triassic to Early Jurassic Adigrat formation, a nearly pure quartz sandstone. Although the laterite profiles at each locality are complete, each horizon looks very different from the horizons of those laterites that developed on basement. All horizons in these laterites are particularly flinty or chert-like and typical of intense tropical weathering of quartz-rich rocks. Nevertheless, the clay-rich horizon cemented by fine-grained silica does appear to contain alunite since they can be dated using the $^{40}Ar$ /$^{39}Ar$

method. M100T, M201a and M211 yielded well constrained circa 40 Ma ages (table 6.1) yet within fifty meters of each sample that yielded a reliable Eocene age very similar samples failed to yield geologically meaningful ages. The conclusion to be drawn appears to be that quick chemical and remote sensing screening does work, but that the small fragments chosen for irradiation must be selected with great care in silica-rich laterites. This can be difficult as quartz may very easily be mistaken for alunite in hand specimens. The problem is exacerbated by the fine-grained nature of these samples, as individual laser spot s may comprise mixtures of the whole rock.

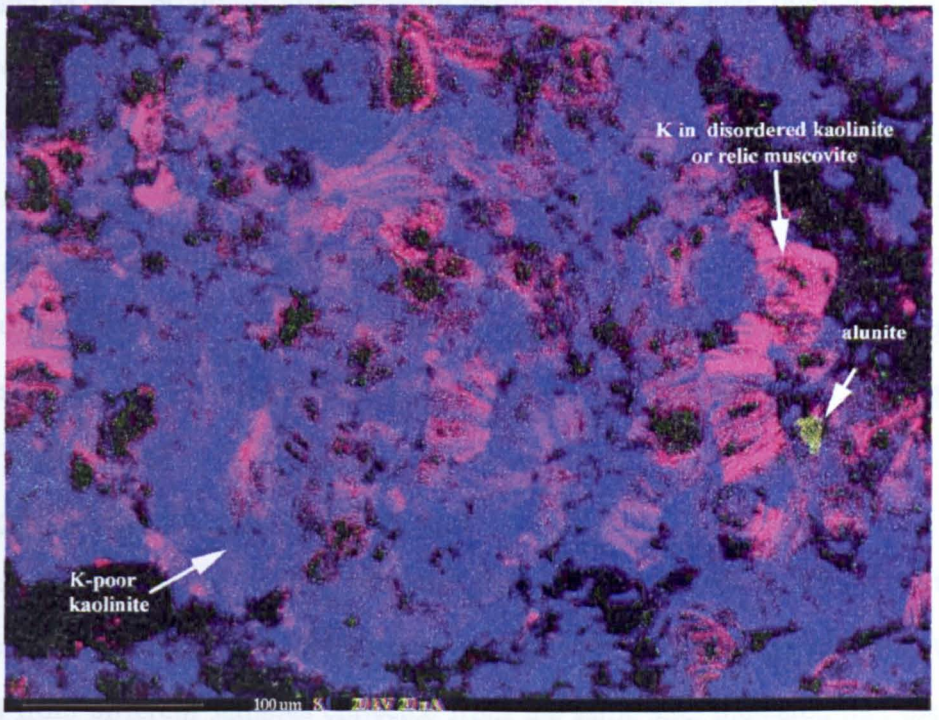


**Figure 6.3** Energy dispersive element map of laterite Horizon 3 (M33iv) with K, S, Al as RGB showing possible disordered kaolinite containing potassium in its lattice (magenta)

However as alunite has a low outgassing temperature compared with silicates, all the argon is often released from the alunite crystals in the low temperature steps and these reveal the age of the sample. Sample M33iv was the oddity in this section. No alunite was detected by post-dating remote sensing or geochemistry, yet sample M33iv produced an unlikely old age (~387 Ma) that was far less old than anomalously older ages from other sampled localities (table 6.1). The only explanation for these results seemed to be the presence of significant amounts of potassium in a disordered

kaolinite lattice (Worrall & Cooper 1996; Melo *et al.* 2001; figure 6.3) resulting in this anomaly. However, there is no indication of potassium in such kaolinite lattices in other samples and significantly, none of the samples analysed produced markedly younger Oligocene ages that might represent younger kaolinitic clays.

Analysed samples M19A and M19C, M113A, M113B and M113C (table 6.1) were collected from laterite profiles developed on sulfide and potassium-rich felsic metavolcanics bordering the River Mereb, which host a major Neoproterozoic volcanogenic massive sulfide deposit about 10km north of the locality. Samples M19A and M19C, produced unexpectedly variably old ages even though the alunite signature in the RS data and the bulk chemical analysis of samples from this locality indicated that there were alunite-rich, dateable phase in the laterite profile. Armed with this evidence, the area was revisited and the selected clay samples (M113A, M113B and M113C) that were analysed corroborated the success of the strategy developed in Chapter 5. All three samples yielded consistent results confirming the hypothesis that $^{40}Ar/^{39}Ar$ geochronology could be used to determine the ages of laterites in the region.

*The successes: geologically meaningful ages*

All samples analysed in this category were high in K and S, almost certainly contained alunite and yielded well-constrained ages (table 6.1). Reproducible results obtained from different samples collected from the same site, indicated that the ages reflected reliable and reproducible ages for precipitation of the mineral alunite. Seven samples (M70a, M70b, M70A, M70B, M125, M125A and M125D) collected from sites up to one kilometre apart were analysed from laterite profiles centred round Adi Felesti, some thirty-five kilometres south west of Asmara. At Dogali, forty kilometres north east of Asmara one sample (M79i) was analysed and at Tusk, twelve kilometres south east of Asmara, three widely distributed samples (M48, M109 and M110E) were analysed. All samples yielded Eocene ages providing clear evidence for the minimum age for lateritisation. Different irradiated grains 5-10 microns across, were also analysed from samples M34 (Dairo Karlos), M48 and M125 and

reproducible Eocene ages were again obtained indicating that supergene alunite is a reliable geochronometer in lateritic palaeosols.

**Table 6.1** $^{40}Ar$-$^{39}Ar$ ages for alunite-bearing kaolinites from Horizon 3 of laterite profiles in Eritrea and northern Ethiopia. UTM co-ordinates refer to WGS84 Datum, Zone 37 N.

| Analysed sample no. | Location name | * UTM coordinates | Integrated (Total gas) age (Ma)[1] |
|---|---|---|---|
| M18(i) | Adi Raisi | 489060 E 1662258 N | 821.8 ± 3.6 |
| M19A | Mereb. | 487520 E 1661563 N | 597.8 ±2.6 |
| M19C(pit2) | Mereb | 489060 E 1662258 N | 413.7 ± 9.8 |
| M26(ii) | Mai Nehfi | 476995 E 1685715 N | None |
| M29 | Paradiso | 494200 E 1699050 N | 609.5 ± 3.1 |
| M33(iv) | Tseada Kristyan | 485109 E 1693952 N | 387.1 ± 6.8 |
| M34(pit1) | Dairo Karlos SE | 485100 E 1693950 N | 41.1 ± 1.1 |
| M34(pit2) | Dairo Karlos | 485109 E 1693952 N | 38.4± 0.2 |
| M45iii(pit1) | Embeyto | 496945 E 1681154 N | 719.6 ± 3.4 |
| M48 | Tusk | 497515 E 1683005 N | 36.1 ± 0.2 |
| M48a | Tusk | 497515 E 1683005 N | 39.5 ± 0.2 |
| M48a(i) | Tusk | 497515 E 1683005 N | 41.6± 1.7 |
| M48a(ii) | Tusk | 497515 E 1683005 N | 40.8 ± 0.2 |
| M58c(pit2) | Areza | 449749 E 1649237 N | 438 ± 290 |
| M70a | Adi Felesti | 467067E 1670710N | 52.0 ± 0.3 |
| M70b | Adi Felesti | 467067 E 1670710 N | 39.2 ± 1.0 |
| M70A | Adi Felesti | 467067 E 1670710 N | 42.3 ± 0.3 |
| M70B | Adi Felesti | 467067 E 1670710 N | 44.2±0.2 |
| M70B(i) | Adi Felesti | 467067 E 1670710 N | 43.4 ±;1.6 |
| M79i | Dogali | 524952E 1720300 N | 36.5±2.9 |
| M100T | Adi Caieh | 538941 1641135 | 44.2±5.3 |
| M101C | Adi Caieh | 538927 E 1640674 N | Negative age |
| M109 | Embeyto NE | 497515 E 1683005 N | 39 ± 12.0 |

| | | | |
|---|---|---|---|
| M110E | Tusk | 497515E 1683005N | 44.3±4.0 |
| M113A | Mereb | 487510E 1661535 N | 39.1 ± 0.2 |
| M113A(1) | Mereb | 487510E 1661535 N | 35.8±0.2 |
| M113A(i) | Mereb | 487510E 1661535 N | 37.7 ± 0.2 |
| M113A(i1) | Mereb | 487510E 1661535 N | 53.9±4.1 |
| M113B | Mereb | 487510E 1661535 N | 44.5 ± 2.8 |
| M113B(i) | Mereb | 487510E 1661535 N | 51.27±15.24 |
| M113C | Mereb | 487510E 1661535 N | 41.2 ± 0.6 |
| M113Ci | Mereb | 487510E 1661535 N | 39.9 ± 0.6 |
| M121B | Mai Nehfi | 479316 E 1686665 N | none |
| M122A | Mai Nehfi | 476774 E 1685852N | 871±15 |
| M125 | Adi Felesti | 466859E 1670359 N | 40.9 ± 0.6 |
| M125(i) | Adi Felesti | 466859E 1670359 N | 46.0 ± 2.4 |
| M125A | Adi Felesti | 466859E 1670359 N | 38.4 ± 0.2 |
| M125A(1) | Adi Felesti | 466859E 1670359 N | 38.7±0.2 |
| M125A(i) | Adi Felesti | 466859E 1670359 N | 39.8 ± 0.2 |
| M125A(i)b | Adi Felesti | 466859E 1670359 N | 41.36 ±0.96 |
| M125D | Adi Felesti | 466859E 1670359 N | 43.5±1.5 |
| M125D(i) | Adi Felesti | 466859E 1670359 N | 45.2±0.9 |
| M201 | Adi Mizan nr. Hagare Selem | 421637 E 1567575 N | none |
| M201a | Adi Mizan nr. Hagare Selem | 421637 E 1567575 N | 45.6 ± 2.3 |
| M211 | Shire | 522264 E 1509741 N | 35.0 ± 0.6 |
| M211a | Shire | 522264 E 1509741 N | 289 ±11 |

* UTM co-ordinates represent the centre point of 50m radius location areas
[1] An integrated age is the apparent age calculated from the total gas yield of the sample

### 6.4.4 Conclusion

These Ar-Ar results provide reasonable constraints for a minimum mid-to late Eocene age for lateritisation in the region (Table 6.1). Given the excellent correlation

between the new Ar-Ar ages, K-bearing minerals in laterite samples consistently demonstrate that the minimum age for lateritisation in Eritrea and Ethiopia is Eocene and not Oligocene as previously thought (Table 6.1). Moreover, an important implication of this work is that the long held view that laterites formed over a very short period (Menzies *et al.* 1990, 1997) is not credible given the evidence to the contrary that laterites formed over a much longer time-span (Dainelli 1943) than previously thought possible.

## 6.5 The Basalt group

### 6.5.1 Previous research

The most comprehensive study of the Eritrean continental flood basalt composition and stratigraphy was carried out by Mengist Teklay of the University of Asmara, Eritrea between 2001 and 2004 (M. Teklay unpublished data 2003, 2004). Although a start was made on sharing this research with the international scientific community (Teklay *et al.* 2002, 2005), Teklay was unable to date the full sequence and his work has yet to be published (M. Teklay pers. comm. 2003, 2008). McDougall and Harrison (1999) note the importance of dating *'samples in known stratigraphic relationship to one another other'* and it is this approach that is used *'as a means of ascertaining the consistency of derived ages'* for Eritrean and Ethiopian CFB data presented in this section. Blanford (1869), Dainelli (1943), Mohr (1971), Kazmin (1972) and Bohannon (1989) reported Oligocene flood basalts in Eritrea so placing constraints on the age of the CFBs by the Epoch in which they occurred. However, only Drury *et al.* (1994) and Zanettin *et al.* (2006), radiometrically dated flows in the Eritrean flood basalt sequence that conformably overlie the lateritised peneplain prior to this study.

Drury *et al.* (1994) were the first to date the flood basalts in Eritrea using four whole-rock samples collected from within 100 meters of the base of the ~650m thick flood volcanic pile. Two from the Mogolo area between Acordat and Barentu yielded $^{40}Ar/^{39}Ar$ ages of 32.9 ± 2.6 and 29.7 ± 3.7 Ma respectively. The third from

Mendefera was dated at 28.5 ± 3.2 Ma, whilst a fourth from Dogali yielded a 28.0 ± 2.5 Ma age. Isochron ages of these four samples gave a mean age of 29.8 Ma, which within error, suggests a maximum age for flood volcanism in Eritrea of ~30 Ma (Drury *et al.* 1994). A fifth whole rock sample, from an isolated olivine basalt flow near Massawa, the stratigraphy of which is unclear, yielded a $^{40}Ar/^{39}Ar$ age of 18.0 ± 1.6 Ma. In contrast to the four samples mentioned above, the younger age of this sample was interpreted by Drury *et al.* (1994) as a possible minimum age for flood volcanism in Eritrea. But, this basalt flow, sitting on top of the sediments of the Dogali Formation that rest unconformably on the faulted CFBs and laterites at Dogali, is clearly younger than the faulting that affects those CFBs and laterites. Consequently, because this 18 Ma flow occurs near the top of the early Miocene, it is clearly not part of the flood basalt sequence.

Twelve years later, Zanettin *et al.* (2006) confirmed the overall findings of Drury *et al.* (1994) and the observations made on geochronology of Eritrean basalts in this study. Again illustrating the importance of collecting samples from known stratigraphic positions, Zanettin *et al.* (2006) selected three samples from the plateau-forming Tertiary flood basalts of central Eritrea (the counterpart of the Aiba/Alaji basalts of Ethiopia), that outcrop along the Asmara to Adi Quala road. One sample came from the upper CFB flows near Mendefera (Adi Ugri) and the other two from lower flows of the flood basaltic pile located at Tera Emni (Teramni) and Adi Quala respectively. The Mendefera sample yielded a K/Ar age of 22.72 ± 0.33 Ma and a $^{40}Ar/^{39}Ar$ age of 22.15 ± 0.18 Ma. Both were consistent with the occurrence of a 24 Ma Deinotherium tooth from an Early Miocene elephant-like mammal, *Dinotherium hobleyi* (Andrews 1911, Vialli 1966), found in interflow sediments of the upper part of the Mendefera basaltic pile. Roughly 15 kilometres north of Mendefera, the Tera Emni sample taken from a few meters above the laterite yielded a $^{40}Ar/^{39}Ar$ age of 29.6 ± 0.6 Ma. Approximately 30 kilometres south of Mendefera, the Adi Quala sample selected from the third flow above the laterite gave a K /Ar age of 28.6 ± 0.3 Ma. Both lower basalt ages were coeval with those ages obtained by Drury *et al.*

(1994), thus reinforcing the ~30 Ma maximum age for Oligocene CFB volcanism in Eritrea. However the dates given by Zanettin *et al.* (2006) suggest that flood volcanism in Eritrea spanned an interval at least from 30 – 22 Ma (mid-Oligocene to Early Miocene).

In contrast with the paucity of radiometric data on Eritrean CFBs, the story is very different in Ethiopia where geochronological studies have a long history. Zanettin *et al.* (1974), preceded only by Grasty *et al.* (1963), were among the first to undertake K /Ar dating of Ethiopian basalts. Berhe *et al.* (1987) provide the most comprehensive geochronological review of the Ethiopian Cenozoic volcanics, i.e. that of the flood basalts and distinctly younger volcanic events (see Berhe *et al.* 1987 for discussion). Even though they and their sources use the K/Ar method, which is somewhat less precise than the $^{40}Ar/^{39}Ar$ method and more prone to error, their work provides a useful geochronological overview of the entire region, which has yet to be followed up with more accurate radiometric dating. Berhe *et al.*'s (1987) Figure 1 (reproduced here as figure 6.4), illustrates the widespread occurrence of CFBs and documents all pre-25 Ma ages, as does their Figure 5 (reproduced here as figure 6.5), which shows an early attempt at Ethiopia-wide correlation between the regionally important volcanic groups. To these they add 15 new K /Ar dates for volcanism that enable them to distinguish between underlying CFBs and later shield volcanics in the province. Their coverage (figure 6.4) includes the main Ethiopian Plateau, the Ethiopian rift, SW, SE, NW and Central Ethiopia and Afar, extending into Djibouti and Somalia. K/Ar ages for CFB volcanism on the main Ethiopian Plateau and Northern Rift are between 25 Ma and 32 Ma and coincide with the range of ages reported by Bohannon (1989), Bohannon *et al.* (1989) and Woldegabriel *et al.* (1990), as do the $^{40}Ar/^{39}Ar$ ages for flood basalt volcanism by other workers (Ethiopian Geological Survey 1996; Haggerty 1996; Hoffman *et al.* 1997; Courtillot *et al.* 1999; Kenea *et al.* 2001; Coulie *et al.* 2003; Arndt and Menzies 2005). The Royal Holloway University of London (RHUL) group (Menzies *et al.* 1997; Ebinger 2000; Ukstins *et al.* 2002; Wolfenden *et al.*2005), rather than discrediting previous K/Ar

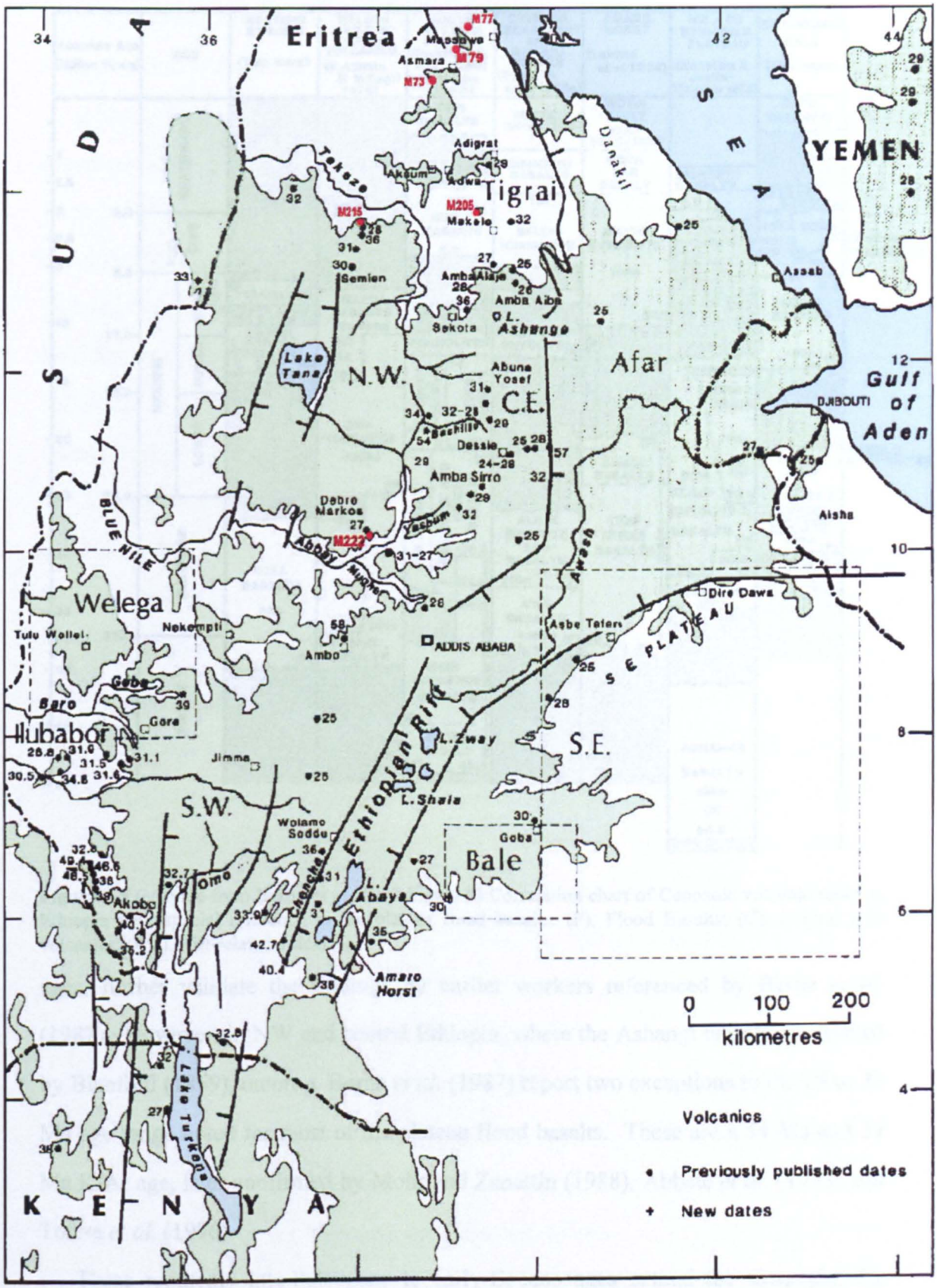


**Figure 6.4** (adapted from Berhe *et al.* 1987 Figure 1) Distribution of pre-1987 K-Ar ages for CFBs older than 25 Ma in the Ethiopian-Yemeni Volcanic Province. Red dots indicate localities where basalts have been successfully dated in this study using the Ar-Ar method

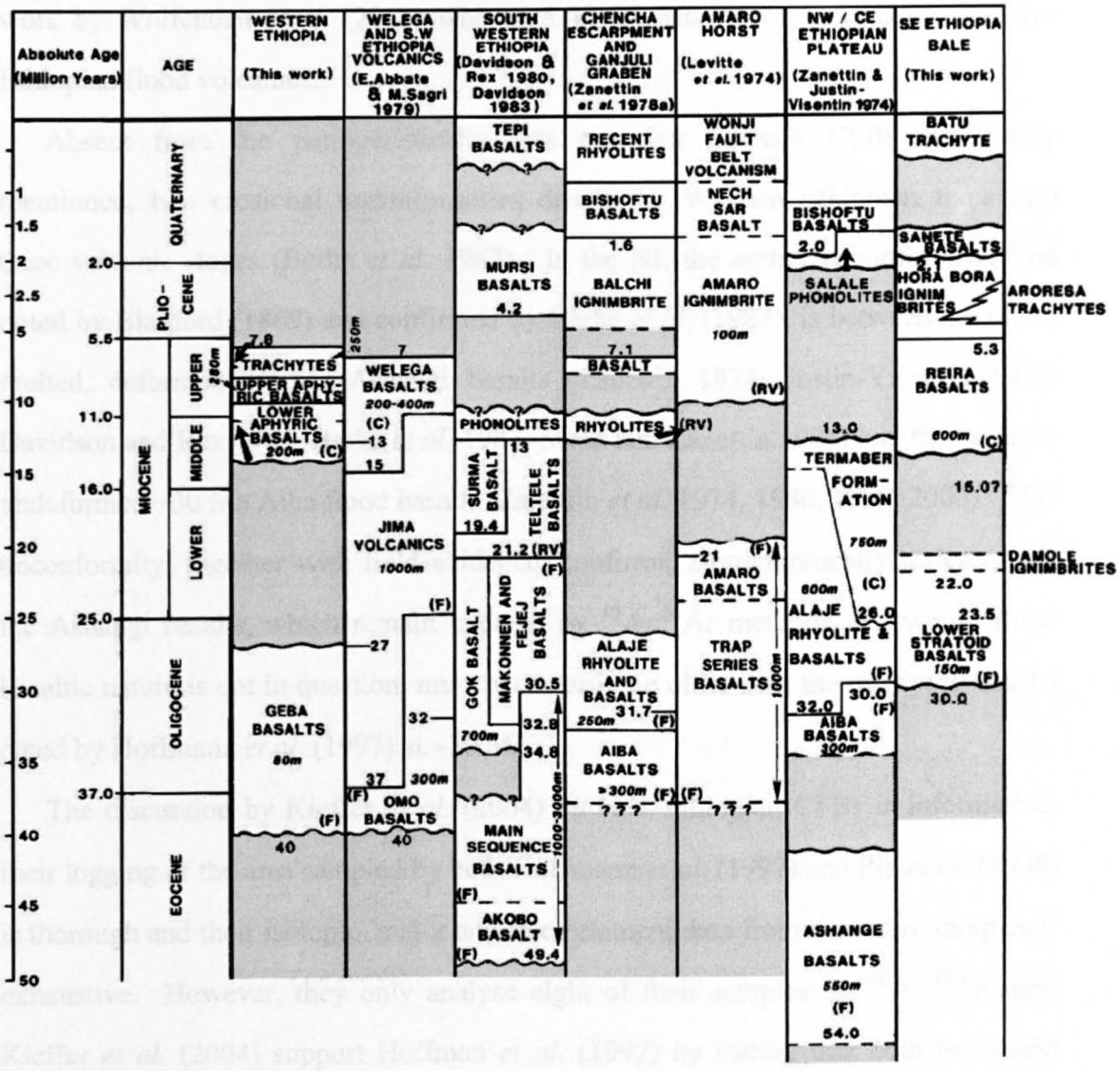


**Figure 6.5** (adapted from Berhe *et al.* 1987 Figure 5) Correlation chart of Cenozoic volcanic rocks in Ethiopia with special reference to the plateau flood basalts. (F), Flood Basalts; (C), Central type volcanics; (RV), Rift-related volcanics

ages, further validate the findings by earlier workers referenced by Berhe *et al.* (1987). However, in NW and central Ethiopia, where the Ashangi basalts, as defined by Blanford (1869), outcrop, Berhe *et al.* (1987) report two exceptions to the 25 to 32 Ma age range noted for most of the plateau flood basalts. These are a 54 Ma and 57 Ma K/Ar age, later confirmed by Mohr and Zanettin (1988), Abbate *et al.* (1993) and Tefera *et al.* (1996).

These reputedly late-Paleocene to early-Eocene ages extend the time-span for Tertiary flood basalt emplacement in Ethiopia, as does work on the Amaro flood basalts of Southern Ethiopia (Ebinger *et al.* 1993, 2000; George 1997, 1998) and the

work by Wolfenden *et al.* (2005) who note 42–22 Ma $^{40}Ar/^{39}Ar$ ages for northern Ethiopian flood volcanics.

Absent from the petrogenetically less complex Eritrean CFBs and rarely mentioned, two erosional unconformities divide the Western Ethiopian traps into three volcanic stages (Berhe *et al.* 1987). In the NE the earlier unconformity, first noted by Blanford (1869) and confirmed by Berhe *et al.* (1987), is between the older, faulted, deformed 54 Ma Ashangi basalts (Zanettin 1974; Justin-Visentin 1974; Davidson and Rex 1980; Berhe *et al.* 1987; Mohr and Zanettin 1988) and the younger undeformed ~30 Ma Aiba flood basalts (Zanettin *et al.* 1974, 1980, 1999, 2006). This unconformity, together with field evidence, confirms, stratigraphically at least, that the Ashangi basalts, which remain undated by $^{40}Ar/^{39}Ar$ methods, but whose flood basaltic nature is not in question, must necessarily be older than the overlying basalts dated by Hoffmann *et al.* (1997) at ~30 Ma.

The discussion by Kieffer *et al.* (2004) on NW Ethiopian CFBs is informative: their logging of the area sampled by both Hoffmann *et al.* (1997) and Pik *et al.* (1998) is thorough and their isotopic, major and trace element data from the many samples is exhaustive. However, they only analyse eight of their samples for $^{40}Ar/^{39}Ar$ ages. Kieffer *et al.* (2004) support Hoffman *et al.* (1997) by stating that both the shield volcanics and the Aiba flood basalts of the Simien mountains are 30 Ma, despite the fact that they themselves report a Miocene $^{40}Ar/^{39}Ar$ age of 18.65 ± 0.19 Ma for one alkaline shield basalt high on the flanks of Ras Dashen, the highest peak in the Simiens. Kieffer *et al.* (2004) do not discuss the >10 Ma age difference between their findings (18.65 ± 0.19 Ma) for shield basalts from Ras Dashen and those (~30 Ma) by Hoffman *et al.* (1997), Rochette *et al.* (1998) and Coulié *et al.* (2003) whose data and conclusions they accept. Further confusion results when those rocks crowning Ras Dashen are variously described by Kieffer *et al.* (2004, Figure 2 and Figure 3) as both flood basalts (the product of effusion from many long fissures) and shield basalts (in a low angled cone fed by a single vent). Kieffer *et al.* (2004), then criticise the precedent set by other geologists that the Ashangi basalts of W Ethiopia,

the Central Plateau and the western escarpment of the Afar Depression may be markedly older than 30 Ma being unconformably overlain by the Aiba basalts, despite their having no data from the area reputedly exposing the Ashangi basalts. Instead they maintain that the Ashangi and Aiba basalts are not widely differentiated by age and that the difference between Aiba and Ashangi formations is primarily geomorphological. Like Pik *et al.* (1998), who later part ways with Kieffer *et al.* (2004) by contradicting their hypothesis on the composition of flood volcanics (Pik *et al.* 2006), Kieffer *et al.* (2004) avoid well established formation names. They reclassify the CFB formations of the Northern plateau as Upper and Lower flood basalt formations (Arndt & Menzies 2005). This categorisation is not adopted in this study for the following reasons:

(1) Satellite imagery clearly distinguishes between two separate CFB formations (historically named the Ashangi and Aiba) in the northern part of the Ethiopian Plateau. The Ashangi basalts, mapped by Merla *et al.* (1973) and Tefera *et al.* (1996), are spectrally different from the overlying Aiba basalts in the reflected region (Landsat 742 and ASTER 631 as RGB, figure 6.6). Moreover, images in the thermally emitted region (ASTER bands 14 12 and 10 as RGB, figure 6.7) reveal the two basalt suites to be fundamentally different in their proportions of ferromagnesian minerals and feldspars. No such spectral distinction can be found in the continental flood basalts of Eritrea (S.A. Drury pers. comm. 2008). Both Figures 6.6 and 6.7 show clearly that the lower basalt unit mapped as Ashangi, pinches out on the eastern flank of Ras Dashen and to its north (figure 6.8). Using elevations of upper and lower contacts from SRTM digital elevation data, the Ashangi basalts can be seen to thin from 675m on the SE of Ras Dashen to 151m on its northern flank. Furthermore, they are not present beneath the Aiba basalts of the Shire-Axum area, only 30km further north. This suggests a low-angle unconformity between the mapped Ashangi and Aiba basalts on the northern Ethiopian Plateau: an observation that is at odds with both Kieffer *et al.*

(2004) and Pik *et al.* (1998) who *'suggest the existence of a continuous lava sequence ... rather than two ... stratigraphically distinct units'.*

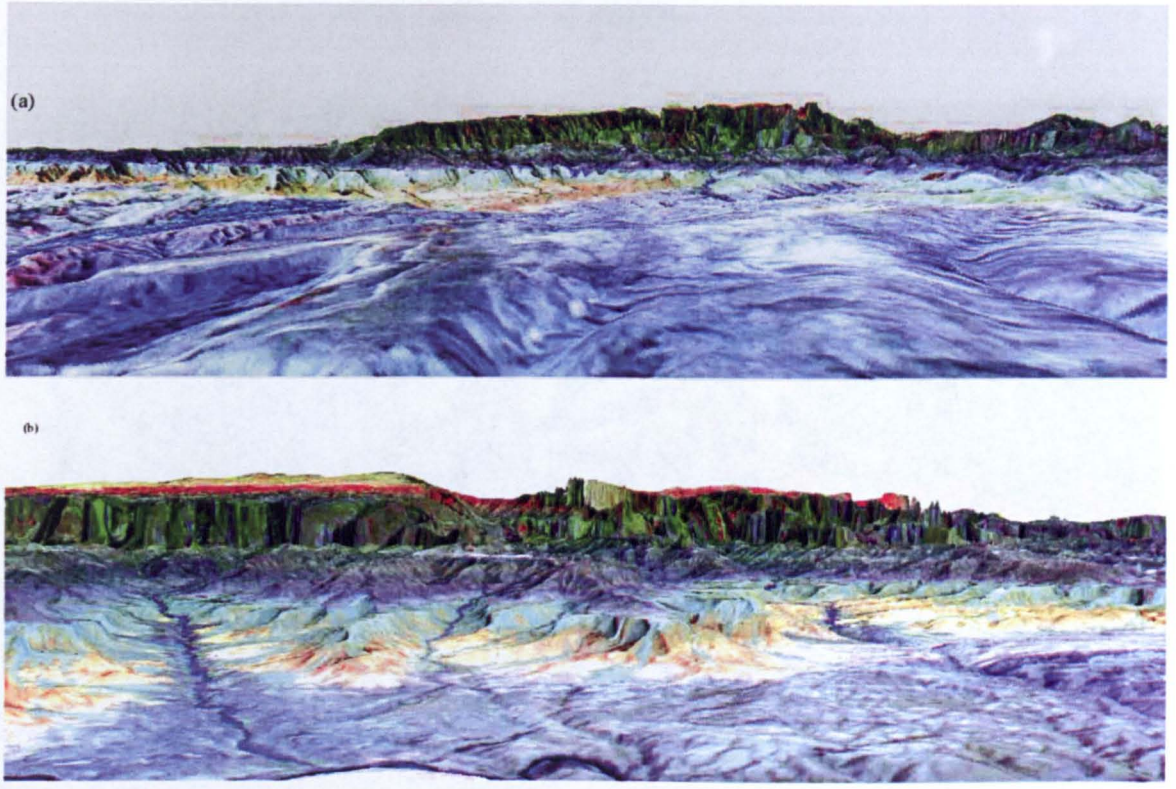


**Figures 6.6** Spectral distinction between basalts in (a) ETM742 and (& b below ) ASTER 631 reflected bands as RGB perspective views of the eastern flank of Ras Dashen, Tigray, draped over SRTM elevation data. Basalts ascribed to the Ashangi formation appear as a purple hued terrace immediately above distinctive cyan lateritic clays and below well-vegetated cliffs of basalts of the Aiba formation. The highest basalts on Ras Dashen are red-hued and correspond to the mountain's Miocene shield volcano

2) The distinction by Kieffer *et al.* (2004) between Lower CFBs, Upper CFBs, Lower / Upper CFBs, or any other combination thereof is confusing when regional formation names are well established.

(3) Clearly at odds with Kieffer *et al.'s* (2004) proposition, supporting Hofmann *et al.* (1997) and Courtillot *et al.* (1999) that the traps erupted ~30 Ma ago, are the conclusions of the Ethiopian Geological Survey (see Berhe *et al.* 1987) together with the weight of published work (Blanford 1870, Merla *et al.,* 1973, 1979, Mohr 1980, Berhe *et al.* 1987 and references therein, Zanettin 1993, Abbate *et al.* 1993, Tadessi *et al.* 2003) that emphasises that mid-Oligocene flood basalts are underlain by Eocene flood basalts. In the Mekele area of Tigray, Ethiopian

geologists report basalts interleaved with lacustrine sediments that contain Eocene gastropods (Russo *et al.* 1997), an observation confirmed in the field by this study (2002) and by Nyssen *et al.* (2002).

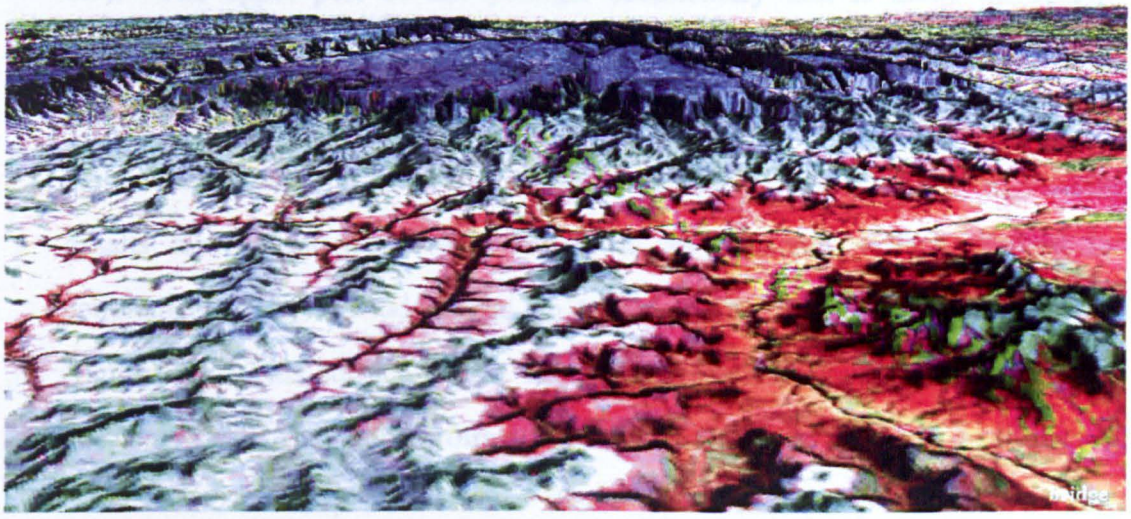

**Figures 6.7** Perspective view of Ras Dashen from the south showing ASTER thermal bands 14 12 and 10 as RGB draped over SRTM elevation data. The Ashangi basalts appear in pale greenish hues above white laterites and the red-hued Adigrat sandstones. Aiba basalts in the cliffs surrounding Ras Dashen show in dark-blue to purple hues. The different hues of the two basalt formation reflect the thermal responses of different proportions of ferromagnesian minerals and feldspars

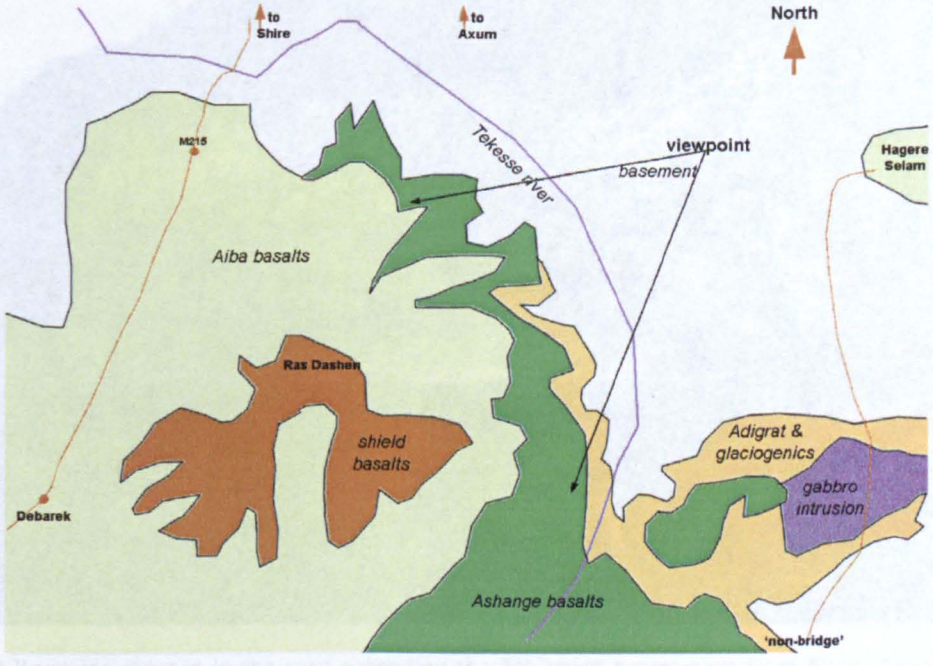


**Figure 6.8** Geological sketch map (40km wide) of northern part of the Ras Dashen volcanic massif based on ASTER 631 and 14 12 10 false-colour images. The spectral 'signatures' of the putative Ashangi basalts pinch out in the north beneath the Aiba basalts, indicating a regional unconformity separating the two main components of the Ethiopian CFBs. Viewpoint for Figure 6.6 shown

(4) Finally, fresh cuttings along a new E-W road up the main escarpment from

the Kobo-Alamata valley to Mekele now reveal that the regionally lowest basalts (named Ashangi basalts on all Ethiopian geological maps) are overlain by a 100-200m thick sequence of fluviatile, clay-rich sandstones and conglomerates (figure 6.9). The upper part of this younger sedimentary unit is made up of thin sandstone beds topped by a lateritic palaeosol. In turn, this lateritic top is overlain by the distinctive Aiba flood basalts, which rise to almost 4000m at the crest of the escarpment. A close examination of the contact between Ashangi basalts and sandstones reveals that it is an erosional surface marked by conglomerates that include clasts up to 1m across of the underlying basalts (figure 6.9). This surface almost certainly represents a period of uplift of the Ashangi basalts and their protracted erosion before 100-200m of sedimentary cover could be deposited above them. This relationship almost certainly corresponds to Blanford's (1870) report of an unconformity that separates the lower, Ashangi flood basalt sequence from the younger, Aiba flood basalts.

**Figure 6.9** Roadside outcrop in the road ascending the Ethiopian escarpment from Kobo-Alomata to Mekele that shows lava flows ascribed to the Ashangi basalts, overlain by sandstones. Note the large basalt clast at the contact

All that remains is to obtain a geologically meaningful $^{40}Ar/^{39}Ar$ age for the Ashangi flood basalts, which to date has not been attempted. Notably, the Ashangi basalts

overlie laterites in the upper Tekesse basin (figure 6.7) as do the Eocene basalts of southern Ethiopia (George 1997).

In SW Ethiopia the Akobo (49.4-46 Ma) and Main Sequence flood basalts (perhaps lateral equivalents of the Ashangi basalts) are unconformably overlain by the younger basalts of the Omo and Gok formations (Davidson 1983, Berhe *et al.* 1987). Along the Ilubabor to Addis Abba road there is also an extensive, clearly visible unconformity between the underlying tilted Jima volcanics (30-21 Ma) of the Gibe Valley and the far younger 15-7 Ma Welega volcanics (Merla *et al.* 1979, Abbate & Sagri 1983, 1993, Zanettin 1993). These findings, albeit from K-Ar dating, again extend the duration and timing of CFB volcanism yet further, as does the work on the west flank of the Afar Depression of Ukstins *et al.* (2002).

Unfortunately, the incorrect and confused assertions: '*Flood volcanic rocks in Ethiopia were unconformably emplaced on a regional lateritized sandstone horizon. This sandstone unit covers an area of 90 000 km$^2$...and represents a period of palaeosol development prior to initiation of flood volcanism...*' made by Ukstins *et al.* (2002) and wrongly attributed to Drury *et al.* (1994), Berhe *et al.* (1987), Davidson & Rex (1980) and Woldegabriel *et al.* (1990) are misleading. Nevertheless, the geochronological work of Ukstins *et al.* (2002) is interesting and furthers the debate. Ukstins *et al.* (2002), who incorporate the data (delayed in publication) of Wolfenden *et al.* (2005), confine their work to localities that roughly follow 250km of the Adis Abba to Desi road running from the Main Ethiopian Rift (MER) and along the eastern escarpment of the central Ethiopian Plateau. They date one possible continental flood basalt at 25.0 ± 2.2 to 29.34 ± 0.15 Ma from their Desi-Bati profile that fits in remarkably well with the findings of earlier workers in the same area (Berhe *et al.* 1987). They recognise unconformities within the basaltic pile of the rift-margin flood volcanics. They date ignimbrites, localised basaltic and felsic flows that overlie the flood basalts; their 'pre-rift' volcanics yielding dates of 29 to 25 Ma extend to well before 30.9 Ma the age of the underlying undated sequence of CFBs, which they estimate as ~800m thick. Ukstins *et al* (2002) find '*a dramatic decrease in volcanic*

*activity in Ethiopia between 25 and 20 Ma,*' a '*volcanic gap*' marking '*the transition from pre to syn-rift*' or shield volcanism. Significantly, the 18 Ma basalt near Massawa, Eritrea, (Drury *et al.* 1994) correlates geohronologically with this syn-rift volcanism (Ukstins *et al.* 2002) and indicates that 750km further north, there were similar Miocene volcanic outpourings in Eritrea. Wolfenden *et al.* (2005) reinforce the findings of Ukstins *et al.* (2002) by confining their observations to localities that almost mirror those of Ukstins *et al.* (2002) and producing similar isotopic ages for flood volcanism.

The debate on the framework of volcanic evolution that emerges from regional work on the flood basalts centres on two opposing propositions: Hofmann *et al.* (1997), Courtillot *et al.* (1999) and Coulie *et al.* (2003) postulated that the Ethiopian traps erupted in ~1 Ma. Whereas Berhe *et al.* (1987), later reinforced by Mohr and Zanettin (1988), Zanettin (1992 1993), Kazmin and Byakov (1999) and Ebinger *et al.* (2000), who questioned a 1 Ma age-spread for flood volcanism, prefer a much longer Eocene to Miocene time-span. In Eritrea, both Drury *et al.* (1994), who suggest the Eritrean CFBs, erupted over a minimum of ~ 4 Ma and Zanettin *et al.* (2006), who propose an Oligocene to Lower Miocene duration for flood volcanism of at least ~7 Ma, lend weight to the work of Berhe *et al* (1987). However, the problem with placing time constraints on Tertiary volcanism based on the scientific literature is compounded by the limited number of localities studied and repeatedly re-sampled, by the difficult terrain (Mohr 1980) and by warfare that has made much of the territory inaccessible (Zanettin *et al.* 2006). Given the vast extent of the province (Baker *et al.* 1996), it is '*unwise to distort the facts to support the theory*' (Christie 1940) or to extrapolate from the findings of a few sections and presume that they characterise the entire region. New $^{40}Ar$ /$^{39}Ar$ ages presented here indicate that CFB volcanism in the Ethiopian Igneous province may not have been quite as brief an episode as has been suggested in some studies.

**6.5.2 Provenance / selection**

Basalt sampling for $^{40}Ar$ /$^{39}Ar$ dating was the simplest of the three collection

strategies (see Section 6.2). Fresh samples are obvious in outcrop and, unlike laterites, basalts contain common minerals formed during crystallisation, namely feldspars, that are suitable for $^{40}Ar$ /$^{39}Ar$ dating. Only continental flood basalts were analysed and these were selected on the basis of their position with reference to laterites. In all cases, except at one locality, samples were chosen from sites as close as possible to the base of the flood basalt sequence conformably overlying the laterites in both Eritrea and Ethiopia. The exception was a locality within 100m of the top of the sequence of the CFB pile in central Eritrea 30km SW of Asmara on Emba Tekera, the thickest flood basalt section with more than fifty-eight flows (Teklay *et al.* 2002), where three samples (M73i, M73ii and M73iii) were collected. This well-exposed basalt sequence shows no sign of an unconformity or significant dips of the upper flows that might be expected of shield lavas.

Six localities were sampled in all. In Eritrea two localities at the base of the escarpment along the Dogali-Massawa traverse and one, mentioned above, at the top of the escarpment in the uppermost CFBs. In Ethiopia the first locality selected was near the Tigrayan capital of Mekele where the Ethiopian laterite cover is most ubiquitous. The second sampled locality, 130km west of Mekele, was at the base of the Lima Limo area on Ras Dashen in the Simien mountains, the main section investigated by Hofmann, Courtillot, Pik and workers (Hofmann *et al.* 1997), who determined that the age-spread of Ethiopian CFB volcanism was limited to ~1 Ma. The third locality, sampled 340km south of Ras Dashen, was in the Blue Nile gorge near Degen in Welega where the laterite-basalt contact again becomes obvious.

The least glassy, uncontaminated samples, without vesicles or amygdales were selected where possible for whole-rock laser $^{40}Ar$ /$^{39}Ar$ step-heating analysis (see section 6.3). The chosen samples were fresh in hand specimen, ranged from light to dark grey in colour and in thin section showed little sign of hydrous alteration, except for some minor serpentinisation of olivine. Although the samples had slightly different textures all the basalts were olivine basalts, with varying proportions of plagioclase, clinopyroxene, olivine and the opaques including ilmenite.

Stratigraphically and petrographically, they were typical continental flood basalts. Figures 6.10, 6.11, 6.12 and 6.13 show photomicrographs of representative samples of basalts from Eritrea and Ethiopia used in this study. Mineral separates were not used, as the basalts were fine-grained. Fortunately, $^{39}Ar$ recoil was not a problem, though all samples were corrected for calcium by correcting $^{39}Ar$ and $^{36}Ar$ peaks before calculating ages (table 6.2).

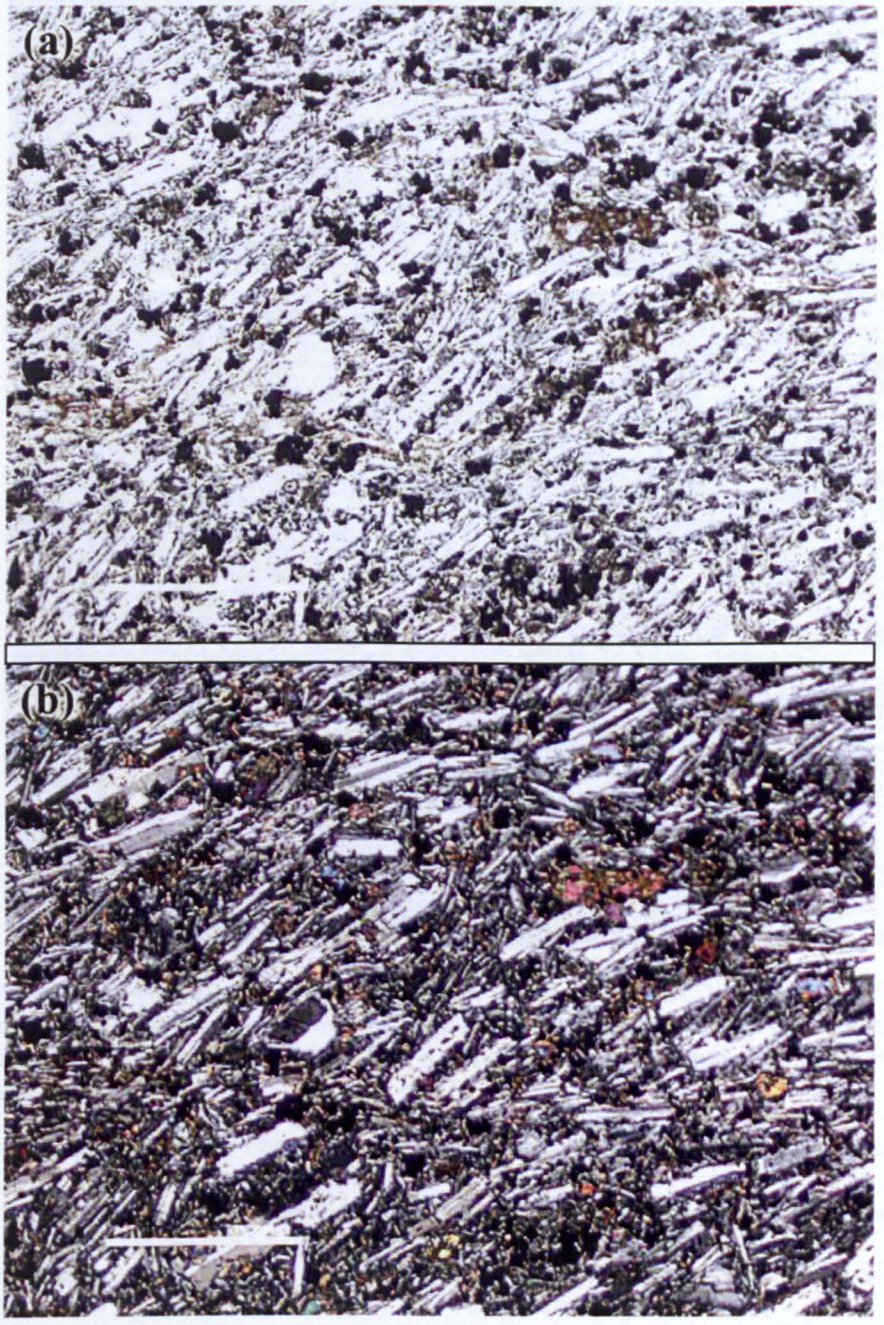


**Figure 6.10** Photomicrographs of basalt M73i from high in the flood basalt sequence on Emba Tekera 30km SW of Asmara (a) plane-polarised (b) cross-polarised. Fresh olivine basalt (plagioclase-clinopyroxene-olivine-opaques) with flow-aligned plagioclase laths. Olivine slightly altered to brown iddingsite. Scale bar = 1mm

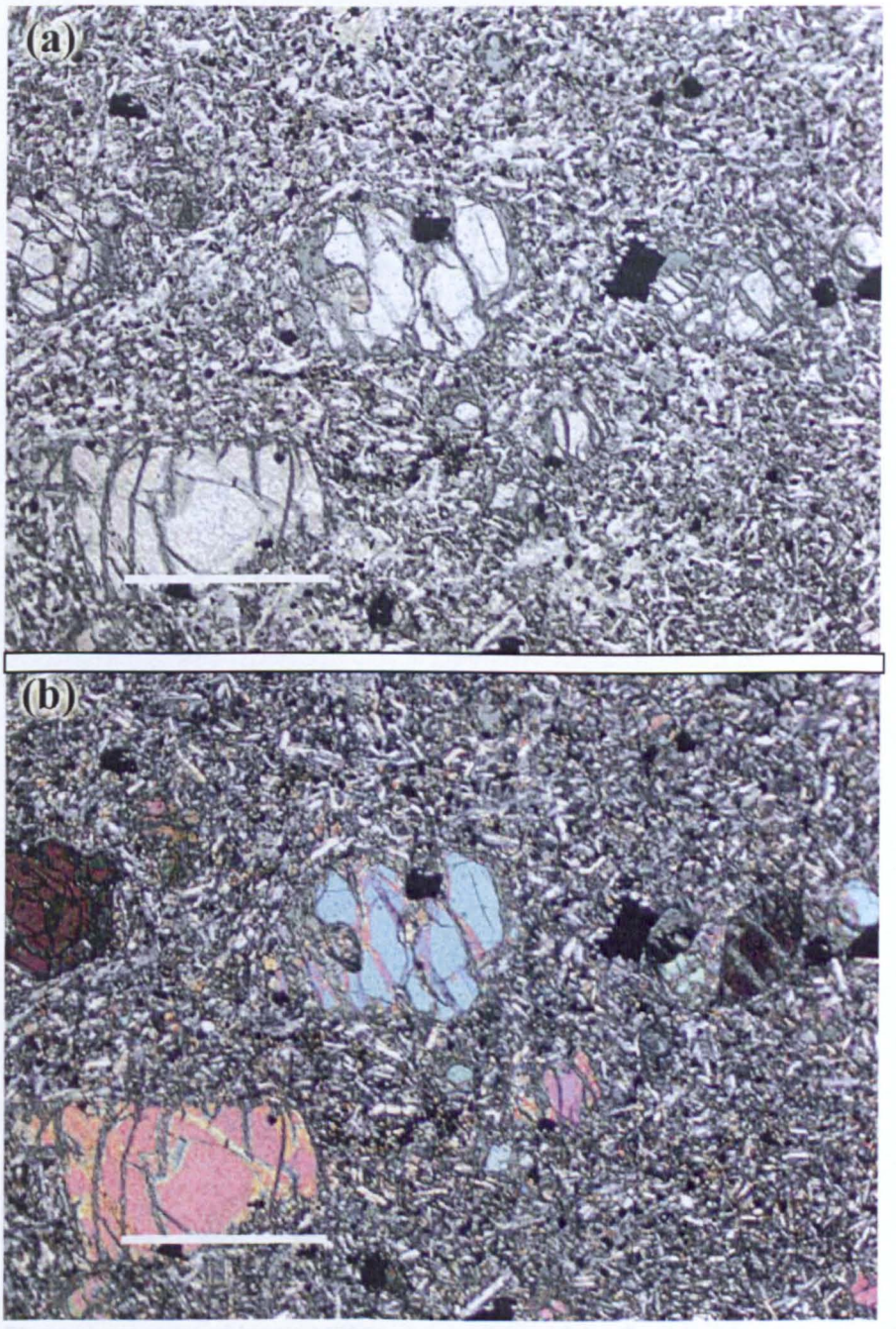


**Figure 6.11** Photomicrographs of the oldest flood basalt M79ii at this locality that rests directly on laterite at Dogali (a) plane-polarised (b) cross-polarised. Fresh, porphyritic olivine basalt (plagioclase-clinopyroxene-olivine-opaques) containing large (~1.5mm) olivine phenocrysts with green bowlingite alteration. Scale bar = 1mm

The five Eritrean basalt samples (M73i, M73ii, M73iii, M77, M79ii) that were irradiated, were collected in 1998 before the recommencement of war and the three-year interruption to field work in Eritrea. M73i (figure 6.10) at 2411 metres elevation is typical of the three samples collected from the upper basalt flows of the 600-meter thick volcanics of Emba Tekera between Adi Felesti and Asmara at the highest point

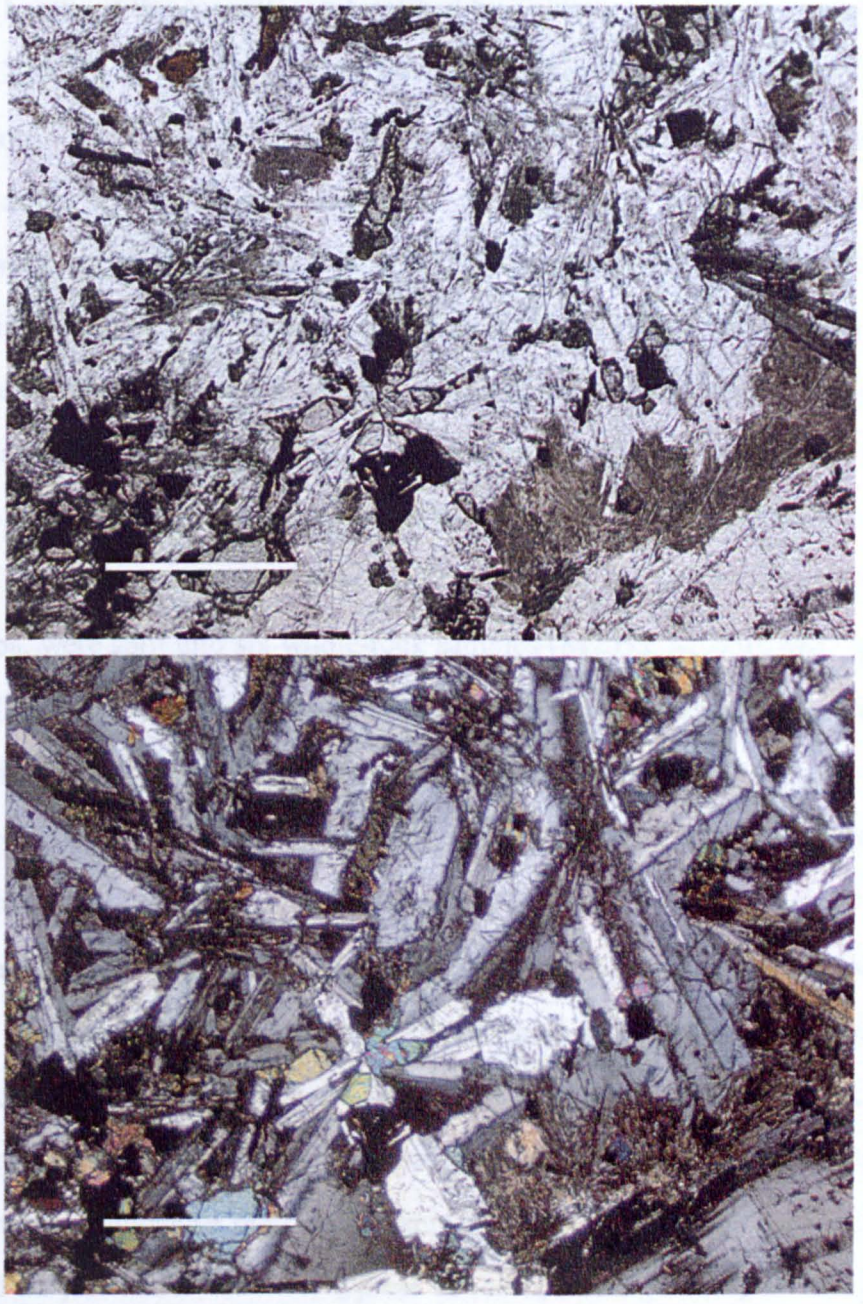

**Figure 6.12** Photomicrographs of basalt M205a close to base of the flood basalt sequence at Hagere Selam near Mekele (a) plane-polarised (b) cross-polarised. Fresh, porphyritic olivine basalt (plagioclase-clinopyroxene-olivine-opaques) containing large (~1.5-2.00mm) plagioclase phenocrysts. Scale bar = 1mm

reached on Adi Felesti-Mai Nehfi pass 380 metres above the laterites. Light grey in hand specimen and in thin section richer in feldspar than any of the basalts collected close to the base of the flood basalt sequence, flow-aligned plagioclase laths are clear in this fresh, very fine-grained (~0.1-0.3mm), olivine basalt with few phenocrysts. The assemblage includes plagioclase-clinopyroxene-olivine-opaques and some brown iddingsitized olivine. Although geochemical data for basalts were not acquired in this

study, the basalts at this locality are described by Teklay *et al.* (2002) as alkaline with higher $TiO_2$ (1.90-3.17 wt%) than the lower tholeiitic flows and elevated Sr and Nd isotopic ratios. Samples M77 from Massawa and M79ii from Dogali, 17km west of Massawa at the base of the escarpment and directly above ferricrete, are dark grey, fine- grained, porphyritic olivine basalts. M79ii (figure 6.11), characteristic of both samples, is very fresh and in thin section phenocrysts of augite and fresh olivine (grain size ~1.5mm) are abundant in a groundmass of plagioclase-clinopyroxene-olivine-opaques (grain size ~0.05mm). Olivine in the matrix is altered to brownish serpentine and there is some greenish metastasis - possibly devitrified glass.

Three Ethiopian basalts, collected in 2002 prior to the UNOOSA conference in Addis Abba, were split into six whole-rock samples (M205a, M205b, M215a M215b, M222a, M222b) for irradiation - two samples from each basalt specimen. All samples are from the lowest flows of the Aiba basalt formation. Their petrography has been well described by Mohr & Zanettin (1988), Zanettin (1993), Pik *et al.* (1998, 1999) and Zanettin *et al.* (2006). M205a (figure 6.12) is representative of the samples collected at Hagere Selam NW of Mekele and close to the base of CFBs. Fresh, very dark grey and the coarsest of the samples in hand specimen, in thin section this porphyritic olivine basalt shows a groundmass of clear low-Ti clinopyroxene, olivine, opaques and fresh plagioclase (grain size ~0.1-0.4mm) containing phenocrysts of slightly altered plagioclase of (~1.5-2.0mm). M215a (figure 6.13) from the basal flow of CFBs just above laterites, typical of the remaining Ethiopian samples, was collected on the flanks of Ras Dashen on the well-documented Lima Limo section (Hofmann *et al.* 1997), south of the Tekesse Bridge on the Shire-Gonder road. A light grey, clearly amygdaloidal, olivine basalt with no phenocrysts comprising plagioclase-clinopyroxene-olivine-opaques, it has an ophitic texture in which brownish high-titanium clinopyroxene (grain size up to 1mm) encloses earlier plagioclase laths (grain size ~0.2-0.3mm). Interestingly Pik *et al.* (1998) describe the Lima Lima section as being Low-Ti basalts, whereas other workers report Ashangi basalts, as geochemically High-Ti; yet this particular sample is titanium- rich.

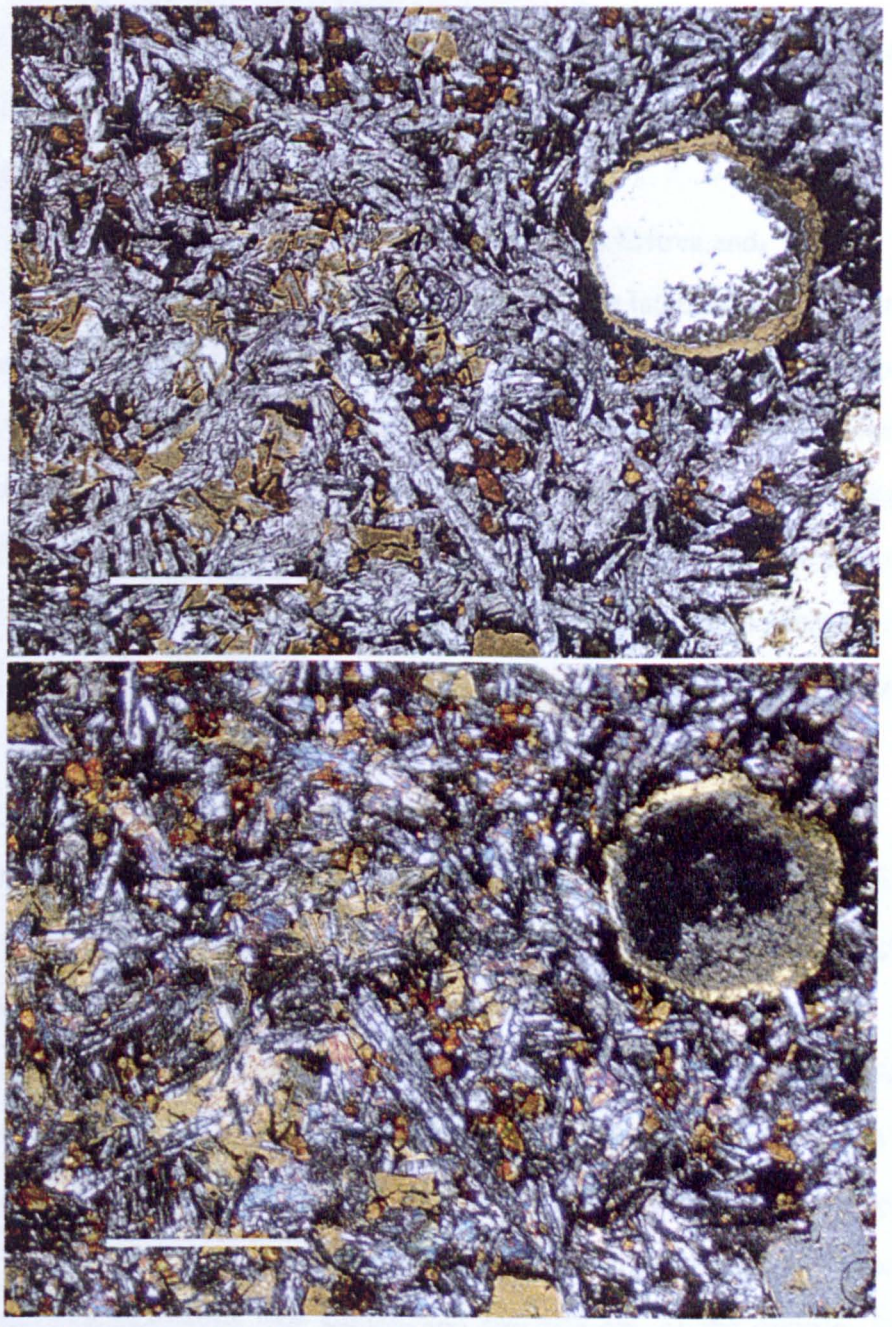

**Figure 6.13** Photomicrographs of flood basalt M215a from the lowest flow of the Lima Limo section of Ras Dashen (a) plane-polarised (b) cross-polarised. Amygdaloidal olivine basalt (plagioclase-clinopyroxene-olivine-opaques) Scale bar = 1mm

### 6.5.3 Results and discussion

The ten new $^{40}Ar/^{39}Ar$ ages presented here (table 6.2) provide further evidence for the timing and duration of flood basalt volcanism proper being a far longer lived event than the relatively short episode that Hofmann *et al.* (1997) or Courtillot *et al.* (1999) put forward. Of the eleven whole rock Eritrean and Northern Ethiopian CFB samples irradiated, ten yielded geologically meaningful ages (Table 6.2). These results

(1) validate the initial discovery by Drury *et al.* (1994) of a ~30 Ma maximum age for Oligocene volcanism in Eritrea;

(2) corroborate the findings of Zanettin *et al.* (2006);

(3) establish a local time span for flood basalt eruptions in Eritrea and,

(4) place time constraints on an absolute minimum age for lateritisation in the region. $^{40}Ar$ /$^{39}Ar$ ages of the Ethiopian basalt samples collected from flows just above the laterites tally, within error, with the results given for Eritrean samples in similar flows and correlate well with K/Ar ages of earlier workers (Berhe *et al.* 1987). Integrated, plateau, isochron and total fusion ages (table 6.2) are used where appropriate, to date selected samples. Where an excess argon signature is apparent, the lowest number is used as the best estimate of the age and in some cases the weighted mean of selected steps are used to back up the findings. The results are encouraging.

*The Eritrean basalts - geologically meaningful ages*

Four out of the five Eritrean samples yielded geologically meaningful $^{40}Ar/^{39}Ar$ ages (table 6.2). The very low potassium content of M73iii produced too little gas for good measurements making the resultant age meaningless. Yet within the ~50m radius location area, M73i and M73ii yielded well-constrained ages for samples from the upper part of the basalt sequence on Emba Tekera. Interestingly, although M73i yielded a geologically meaningful age, it had a classic excess argon signature (Appendix B), in which ages started high because of excess argon and reduced to reasonable ages in the centre that approached the true age of the sample (Kelley, 2002) before rising again. In this event the best estimate of a $^{40}Ar/^{39}Ar$ age is 22.4 ± 1.0 Ma. However, as Ar - Ar stepped heating used on these samples *'provides a physical technique'* (Kelley 2002) for selecting steps with the most useful release patterns for reliable ages, the very high first and last steps of this 7-step analysis were omitted. A weighted mean age for the 5 remaining steps gave a total gas or integrated $^{40}Ar/^{39}Ar$ age of 22.9 ± 0.3 Ma that reinforced the initial single-step (total fusion age) result (table 6.2; Appendix B). M73ii yielded an $^{40}Ar/^{39}Ar$ age of 21.3 ± 1.01 Ma, the weighted mean of all 12 steps in the analysis and a 19.4 ± 0.3 Ma $^{40}Ar$ /$^{39}Ar$ age based

on the weighted mean of all the steps without significant errors. Both $^{40}Ar/^{39}Ar$ ages for basalts from this locality establish a new minimum age in the early Miocene for flood volcanism in Eritrea and compare extremely well with K/Ar and $^{40}Ar/^{39}Ar$ ages for the upper flows of the Adi Ugri basalts further south in Eritrea (Zanettin *et al.* 2006: see section 6.5.1). Furthermore, the young dates of Zanettin *et al.* (2006) for the upper Eritrean lavas together with the even younger dates presented in this study tend to close the 'volcanic gap' between the Oligicene CFBs and Miocene shield volcanism (Ukstins *et al* 2002).

**Table 6.2** $^{40}Ar/^{39}Ar$ ages for basalts that conformably overlie laterites in Eritrea and northern Ethiopia. UTM co-ordinates refer to WGS84 Datum, Zone 37 N

| Analysed sample no. | Location name | *UTM coordinates | Integrated (Total gas) age (Ma)[1] | Plateau age (Ma) | Isochron age (Ma) |
|---|---|---|---|---|---|
| | | | | | |
| M73i | Emba Tekera | 469607E 1680012N | 22.9 ± 0.3. | | |
| M73ii | Emba Tekera | 469607E 1680012N | 19.4 ± 0.3 | | |
| M77 | Dogali | 531087E 1724789N | 31.5 ± 1.8 | | |
| M79ii | Dogali area | 524952E 1720300N | 32.0 ± 2.2 | | |
| M205 a | Hagere Selam | 510711E 1500669N | 31.2 ± 0.2 | 32.8 ±0.8 | 34.0 ± 1.8 |
| M205 b | Hagere Selam | 510711E 1500669N | 32.3 ± 0.3 | | 33.7 ± 4.3 |
| M215a | Ras Dashen Lowest flow | 408679E 1508638N | 31.8 ± 0.5 | | 34.0 ± 5.0 |
| M215b | Ras Dashen Lowest flow | 408679E 1508638N | 29.50 ± 0.2 | | |
| M222a | Nile Gorge Lowest flow | 408679E 1120351N | 27.6 ±0.2 | | 31.1 ± 5.1 |
| M222b | Nile Gorge Lowest flow | 408679E 1120351N | 16.2 ± 0.2 | | 21.7 ± 0.3 |

* UTM co-ordinates represent the centre point of 50m radius location areas

[1] An integrated age is the apparent age calculated from the total gas yield of the sample

Collected from the lowest CFB flows above the laterites in the Dogali area at the base of the escarpment, sample M77 with an excess argon signature yielded a $^{40}Ar/^{39}Ar$ age of 31.5 ± 1.8 Ma, whilst M79 yielded an integrated age of 32.0± 2.2 Ma. Given the amount of faulting and warping at the base of the escarpment (Drury *et al.* 2005), potential fluid pathways might be expected to lead to excess argon. For

this reason M77 and M79 were chosen from specific localities to check the $^{40}Ar/^{39}Ar$ ages that Drury *et al.* (1994) reported for the same area. Both samples M77 and M79 yielded Oligocene ages (circa ~30 Ma) that were consistent with the 28.0 ± 2.5 Ma age established by Drury *et al.* (1994) at the base of the escarpment and that correlated with recorded radiometric ages - circa ~30 Ma - for all basal flows of the plateau basalts directly above laterite in Eritrea (Drury *et al.* 1994; Zanettin *et al.* 2006). As the geochronological evidence illustrates, Eritrean CFBs are at most Lower Oligocene, it is suggested that the absolute minimum age for lateritisation is indeed ~30 Ma. However, the maximum $^{40}Ar/^{39}Ar$ age for a CBF sample in this study is 32.0 ± 2.2 Ma and it is arguable that an absolute minimum age for lateritisation can be set at 32.0 ± 2.2 Ma. Similarly, the minimum valid $^{40}Ar/^{39}Ar$ age acquired for basalts in the upper flows is 19.4 ± 0.3 Ma, younger by 3 Ma then any CFB dated in Eritrea. Therefore the overall range of flood basalt eruptions in Eritrea is ~13 Myrs.

$^{40}Ar/^{39}Ar$ ages for both samples from the Emba Tekera basalt sequence are Lower Miocene, younger than the youngest flood basalts in the Ethiopian Rift (Ebinger *et al.* 1994) and indicate that flood basalt volcanism lasted far longer in Eritrea than in Northern Ethiopia (Hofmann *et al* 1997). As Eritrea is ~400km from the centre of the Ethiopia LIP (Kieffer *et al.*2004), it is surprising that the 600m thick CFB sequence near Asmara should take ~13 Ma to form, whilst the 2km thick section at Ras Dashen should erupt in ~1 Ma (Hofmann *et al.* 1997; Courtillot *et al.*1999). Moreover even if the ~1 Ma timing and duration for the eruption of the Ethiopian traps is not questioned (Coulié *et al* 2003; Arndt & Menzies 2005), the situation is further complicated as Miocene shield volcanism in Ethiopia would appear to have had a flood volcanism counterpart in Eritrea.

*The Ethiopian basalts - geologically meaningful ages*

All six samples from the Ethiopian Plateau (see Davies *et al.* 2003) yielded results with reproducible and well-constrained $^{40}Ar/^{39}Ar$ ages. M205a, M205b collected from basalt flows immediately above the laterites at Hagere Selam, NW of Mekele gave particularly good sets of ages. In this area Ethiopian geologists have long

questioned the dating of Courtillot *et al.* (1999) and Coulie *et al.* (2003) and maintained that mid-Oligocene flood basalts are underlain by Eocene basalts that contain fossiliferous lacustrine beds (see section 6.5.1) so the results in this study were enlightening. M205a with an integrated, plateau and isochron age of 31.2 ± 0.2 Ma, 32.8 ± 0.8 Ma and 34.0 ± 1.8 Ma respectively and M205b with an integrated age of 32.3 ± 0.3 Ma and an isochron age of 33.7 ± 4.3 Ma extend the age of the earliest flood volcanism in this area. Within error, the $^{40}Ar/^{39}Ar$ data indicate that the CFBs in Tigray do indeed border on the Eocene. However, they do not approach the Palaeocene/ Eocene ages reported for the Ashangi basalts.

Similar results were obtained for samples M215a and M215b collected from the lowest visible CFB flow on the north-western flank of Ras Dashen. Coeval with the samples from Hagere Selam, M215a yielded an integrated age of 31.8 ± 0.5 Ma and an isochron age of 34.0 ± 5.0 Ma, whilst M215b yielded an integrated age of 29.5 ± 2.0 Ma. Taken together, these four sets of data push back the age of the earliest flood volcanism by up to 4 Ma, raise doubts about the short (1 –2 Ma) duration of Ethiopian flood volcanism and support the findings of Ebinger's group's work in the Eastern Ethiopian Escarpment (Ebinger *et al.* 2000). M222a and M222b, the Nile Gorge basalts, were collected at a locality that had been drilled for palaeomagnetic analysis and was coincidentally only ~300m from one of Pik *et al.*'s (1998) sampling areas (See E70 in Pik *et al.* 1998). The most geologically meaningful age yielded by this specimen was a $^{40}Ar/^{39}Ar$ age of 31.1 ± 5.1 Ma for sample M222a. Low $^{39}Ar$ release was apparent for sample M222b which yielded a $^{40}Ar/^{39}Ar$ age of 21.7 ± 0.3 Ma.

### 6.5.4 Conclusion

Given the validity of $^{40}Ar/^{39}Ar$ ages for the Ethiopian basalts in this study and, by extending the field area from Eritrea to Northern Ethiopia, an absolute minimum age for lateritisation can be pushed back from ~30Ma to ~34Ma in the Upper Eocene. Furthermore, since ground checks at over two hundred field sites from Addis Ababa to the River Mereb and northwards to Asmara establish that continental flood basalts conformably overlie laterites, it is with some confidence that the minimum date for

lateritisation in this work can be regarded as regional. Given the amount of criticism levelled at earlier workers in the province (section 6.5.1), it is hoped that the excellent correlation between new $^{40}Ar/^{39}Ar$ ages in this study and previously published K/Ar and $^{40}Ar/^{39}Ar$ dates goes some way to redress the balance. $^{40}Ar/^{39}Ar$ dates presented here reinforce the notion that the bulk of the Ethiopian traps erupted over a much longer time than ~1 Ma, but they do not resolve the Ashangi basalt problem. Since remote sensing highlights two mineralogically distinct basalt formations in part of Tigray Province, Ethiopia (figures 6.6 & 6.7), further work on that widespread occurrence is needed to establish a reliable time-span for the duration and timing of CBF volcanism. Whatever the outcome, the evidence from this study suggests with some confidence that the basalt pile is more complex than some previous workers have suggested.

## 6.6 The Basement group

### 6.6.1 Preamble / previous research

Satellite, field and aerial photographic data together show that laterites not only cover large tracts of basement but also form a number of outliers (Chapters 2 & 3). These outcrops are present at different elevations, from sea-level to more than 3km above it, resulting from post-Oligocene rifting and uplift related to the initial rifting of the Red Sea. They outcrop in steep, unvegetated slopes and irregular cliffs on the plateau and at the base of the escarpment. Because laterites formed close to sea level on a peneplane (Overstreet *et al.* 1977; Bohannon *et al.* 1989), variations in their present elevation indicate that there has been significant uplift associated with Red Sea rifting in this region of up to 3km. Taking into account the occurrence of laterite described above, this exercise began as a trial to assess whether dating basement granodiorites at varying elevations from the top to the bottom of the eastern Eritrean escarpment, might reveal signs of uplift history and erosional unroofing in the area.

Radiometric methods used to date episodes of uplift and erosion rely on naturally occurring, isotopes that decay to produce daughter isotopes of a gas, for example, $^{40}K$,

that decays to $^{40}Ar$ and is employed in the $^{40}Ar/^{39}Ar$ method. Others are $^{238}U$, $^{235}U$ and $^{232}Th$ with decay schemes that emit helium (He) nuclei in the form of alpha particles and form the basis for U-Th/He dating. Minerals that contain potassium, uranium or thorium retain their gaseous daughter isotopes *only* if they remain below a temperature above which the thermal vibration of the argon or helium atoms allows those atoms to escape from the mineral lattice. Above that *closure temperature*, radiogenic daughter isotopes escape rapidly from the mineral into the grain boundary network (McDougall & Harrison 1999). Once the mineral has cooled below its closure temperature, the daughter gas isotope can accumulate in the 'parent' mineral over time and dating will give a cooling age i.e. the age at which the mineral cooled below its closure temperature. A similar principle applies to apatite fission track (AFT) dating, where fission tracks created by high-energy emissions from radioactive isotopes in minerals, such as apatite or zircon, anneal rapidly and disappear above the mineral's closure temperature. Below the closure temperature, the accumulated tracks can be counted to estimate a cooling age.

Different minerals have different closure temperatures for argon, helium or fission tracks. For U-Th/He dating of apatite, the closure temperature of around 70° C for He loss from apatite is exploited. The closure temperature of around 120° C for fission tracks is employed in AFT dating. Feldspars and micas with closure temperatures from 150-240° C and 330-350° C respectively, are commonly used to obtain $^{40}Ar/^{39}Ar$ cooling ages (figure 6.14). Radiometric dating, using a decay scheme that involves a gaseous daughter isotope, only provides the 'true' age of a mineral if it formed or cooled rapidly below its closure temperature and remained cooler than that temperature to the present day. A rock buried by accumulation of younger material above it or by tectonic thickening of the crust is heated. The temperature that it then attains depends on depth of burial and the geothermal gradient. Figure 6.14 shows that if the geothermal gradient is 20° C $km^{-1}$, the mean for continental plate interiors, burial to more than 8km will result in heating above the closure temperatures for helium, fission tracks in apatite and argon in feldspars. Burial to ~5km under a

geothermal gradient of 70° C $km^{-1}$ exceeds even the closure temperature for argon in micas. Consequently, 'true' ages of rock genesis for all dating systems shown in Figure 6.14 may be *re-set* to zero by burial, because any radiogenic gases that had previously accumulated in the minerals will have been driven off or fission tracks will have been sealed. Finally, minerals that crystallised deep in the crust in plutonic igneous intrusions or during metamorphism (starting at ~300° C) only begin to accumulate radiogenic gases or fission tracks after they are uplifted to depths where temperatures are below the appropriate closure temperature. It is this last process that allows $^{40}Ar/^{39}Ar$; U-Th/He and AFT dating to be used to track the rate at which once deeply buried rocks rise to be exposed at the surface because of uplift and erosion.

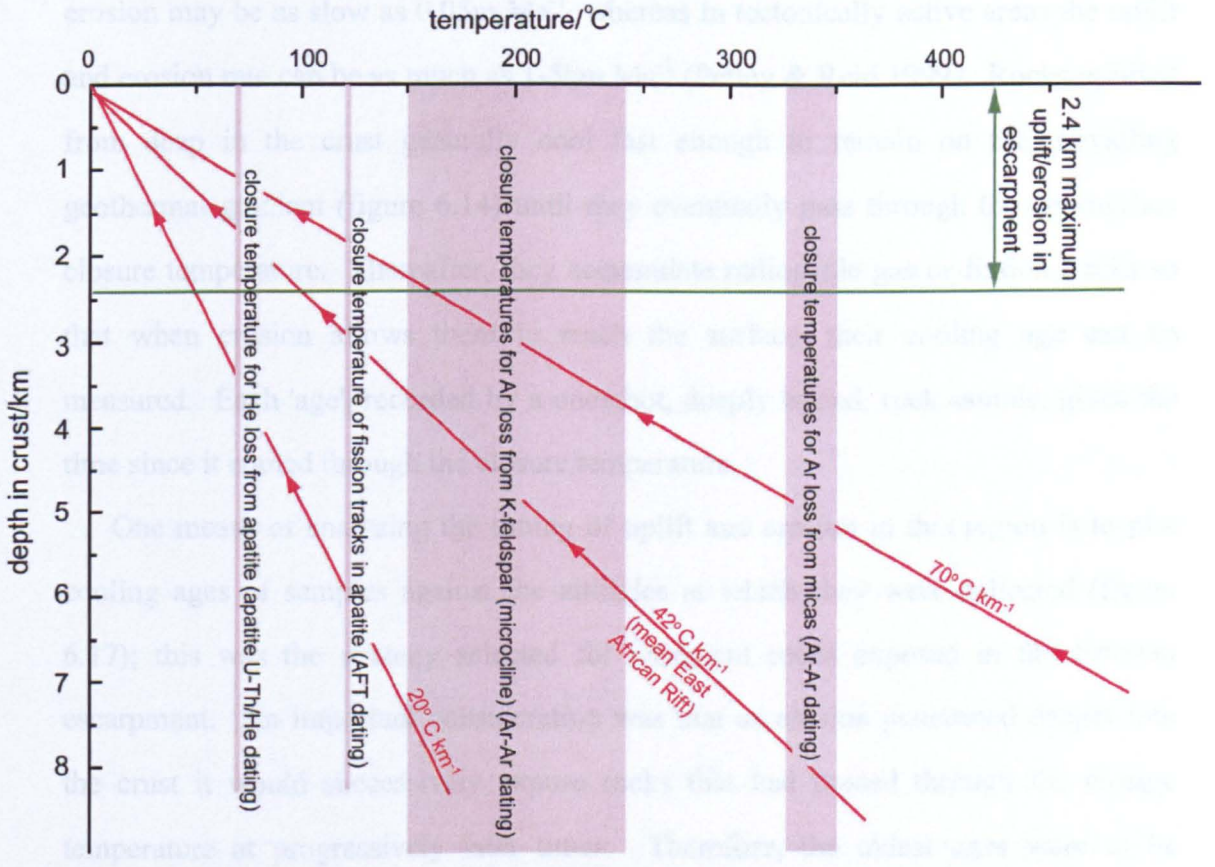


**Figure 6.14** Principal of cooling ages: Pink vertical lines define the closure temperatures; diagonal red lines are different geothermal gradients; The horizontal green line is the maximum uplift of the laterite datum, assuming it formed at sea level

An opportunity arose for collaborative work when the Scottish Universities Research Reactor Centre (SURRC) offered training in how to recognise and select apatites in Neoproterozoic basement samples collected for this study. These samples

would then be dated using SURRC U-Th/He dating facilities to estimate timing and uplift rates on the Western flank of the Red Sea. The interest of SURRC was primarily in developing the technique that was seen to be very much in the development stage with only a small chance of success and that the results should not be reorted in this thesis. Unfortunately the logistics involved proved impracticable and it was decided to confine the dating of uplift and erosion of the Eritrean Neoproterozoic basement to $^{40}Ar/^{39}Ar$ methods (section 3.5).

The rate at which buried rocks make their way to the Earth's surface is controlled by the erosion of overlying rocks in this area. The global mean rate of erosion and related uplift is 10.7 ± 1.6m $Ma^{-1}$ (Portenga *et al.* 2009). In tectonically stable areas, erosion may be as slow as 0.05m $Ma^{-1}$, whereas in tectonically active areas the uplift and erosion rate can be as much as 1-5km $Ma^{-1}$ (Petley & Reid 1999). Rocks uplifted from deep in the crust generally cool fast enough to remain on the prevailing geothermal gradient (figure 6.14) until they eventually pass through the appropriate closure temperature. Thereafter, they accumulate radiogenic gas or fission tracks so that when erosion allows them to reach the surface, their cooling age can be measured. Each 'age', recorded by a once hot, deeply buried, rock sample, gives the time since it cooled through the closure temperature.

One means of analysing the timing of uplift and erosion in this region is to plot cooling ages of samples against the altitudes at which they were collected (figure 6.17); this was the strategy selected for basement rocks exposed in the Eritrean escarpment. An important consideration was that as erosion penetrated deeper into the crust it would successively expose rocks that had passed through the closure temperature at progressively later times. Therefore, the oldest ages were to be expected from samples collected at the highest altitudes where there had been least erosion and the youngest ages anticipated should be from areas where erosion has penetrated most deeply at the lowest altitudes. Following on from this, if erosion had been constant over a long period, there would be a single best-fit line through the data and the lower the gradient of the line, the slower the rate of erosion and uplift.

Conversely, the steeper the gradient the more rapid the rate of erosion and a significant change in the gradient of the plotted data would signify the duration of a change in the rate of uplift and erosion (figure 6.17).

Basement rock formations in Eritrea range between 650-850 Ma (Teklay 1997; Ghebreab 1999; Johnson and Woldehaimanot 2003). Miller *et al.* (1967) obtained K/Ar whole rock ages of ~627 ~670 and ~690 Ma for granodiorites in southern Eritrea. The mylonites of Mount Ghedem (900m) near the coast of eastern Eritrea have yielded $^{40}Ar/^{39}Ar$ average plateau cooling ages of age of ~579 Ma (Ghebreab *et al.* 2005) and the gneisses from which they formed were dated by Teklay (1997) at 796 ± 0.7 Ma using a single zircon Pb-Pb method. Syn-kinematic granitoid rocks in central Eritrea and granitoid rocks near Nakfa have been dated using a single zircon U-Pb method at 585 Ma and ~630 Ma respectively (Teklay *et al.* 2002, 2003). In northernmost Eritrea, near Felcat, two high-grade metagranitoids analysed using U-Pb SIMS zircon geochronology yielded ages of 838 ± 17 Ma and 814 ± 15 Ma, respectively, whilst a late syn-kinematic granite from the same area yielded an age of 603 ± 5 Ma (Andersson *et al.* 2008).

No attempt has been made here (but see Chapter 7) to quantify uplift from cooling ages(see Pik *et al* 2003) or detail the basement geology in Ethiopia in detail (Teklay *et al.* 1998; Tadesse *et al.* 2000; Grenne *et al.* 2003). However interestingly, the findings of Teklay (1997) on the Eritrean basement tally with those documented for Ethiopia. In southern and eastern Ethiopia, Teklay *et al.* (1998) reported Pb-Pb single zircon ages of ~850, ~750-700 and ~650-550 Ma for highly deformed gneisses that showed three periods of granitic magmatism that contributed to Neoproterozoic crustal growth. In northern Ethiopia, Tadesse *et al.* (2000) reported ~750-800 Ma ages for deformed granitic plutons and circa ~550 to ~541 Ma ages for undeformed granites, whereas Grenne *et al.* (2003) reported a zircon U–Pb age of 866 ± 20 Ma for a deformed plutonic igneous complex in western Ethiopia. These age ranges are similar to those of the Eritrean Neoproterozoic basement, although one late syn-kinematic granitoid age (550 Ma) in Tigray is not contemporaneous with its Eritrean

counterpart (Teklay *et al.* 2002). Mock (1999) who worked with mineral separates from late tectonic granitoids at high elevations in Ethiopia reported $^{40}Ar/^{39}Ar$ ages that ranged from 462 to 679 Ma but none of her samples either stayed deep in the crust following the Pan African orogeny, or underwent any later re-heating above the closure temperatures.

**6.6.2 Provenance / selection**

Basement samples collected during the 1998 and 2001 field trips were selected from similar lithologies exposed in the uplifted and dissected escarpment along the Asmara to Massawa road (figure 6.15) that descends 2km over a distance of 35km, from the outskirts of Asmara to the flat coastal area around Dogali. Lithologies chosen were predominantly late-Neoproterozoic granodiorites that form a large intrusion, a diorite body in felsic metavolcanics and a granodioritic gneiss from the coastal high-grade terrain (Ghebreab & Talbot 1997). Together with the basement diorite sample from the Eritrean Plateau near Debarwa, sample localities spanned the full range of topographic elevations along the Asmara-Massawa road. These samples, it was hoped, would give a range of ages indicating when the feldspars in these granitic rocks had passed through the mineral's argon closure temperature (150° to 250° C) during basement unroofing and thus provide a clue to the erosional and uplift history in the escarpment. Samples were collected, terrain permitting, at locations vertically spaced as evenly as possible, every 200m over a vertical distance of ~2000m.

All samples, except for M68 located off a dirt road, were collected from recent road cuttings along the asphalt Asmara-Massawa road (figure 2.30, 6.15). The lowest sample, M39, was a gneiss containing deformed K-feldspar, M96, the sample selected from the highest elevation, was a felsic diorite and samples M40 to M44 and M94 were fresh granodiorites from the Dekemhare granodiorite - a large pluton intruded into Neoproterozoic volcano-sedimentary metamorphic rocks (figure 6.15). The granodiorite intrusion has yielded single-zircon U-Pb ages of ~650 Ma (Teklay 1998). Sampling these intrusions ensured that all cooling ages would represent rocks with the

same absolute age, chemical composition and mineralogy. As these granodiorites contained little mica (figure 6.16) all ages probably reflect the decay of $^{40}K$ in feldspars that would accumulate radiogenic $^{40}Ar$ once the host rocks had cooled during uplift to less than 150°- 240° C. Only rocks that showed no visible sign of weathering were sampled. For most of the vertical section, samples were non-porphyritic, K-feldspar-bearing granodiorites with a 5 to 15mm grain size. With the exception of M96, which was an amphibole-bearing metadiorite, the samples showed few signs of deformation during the Pan-African orogeny, which ended shortly after

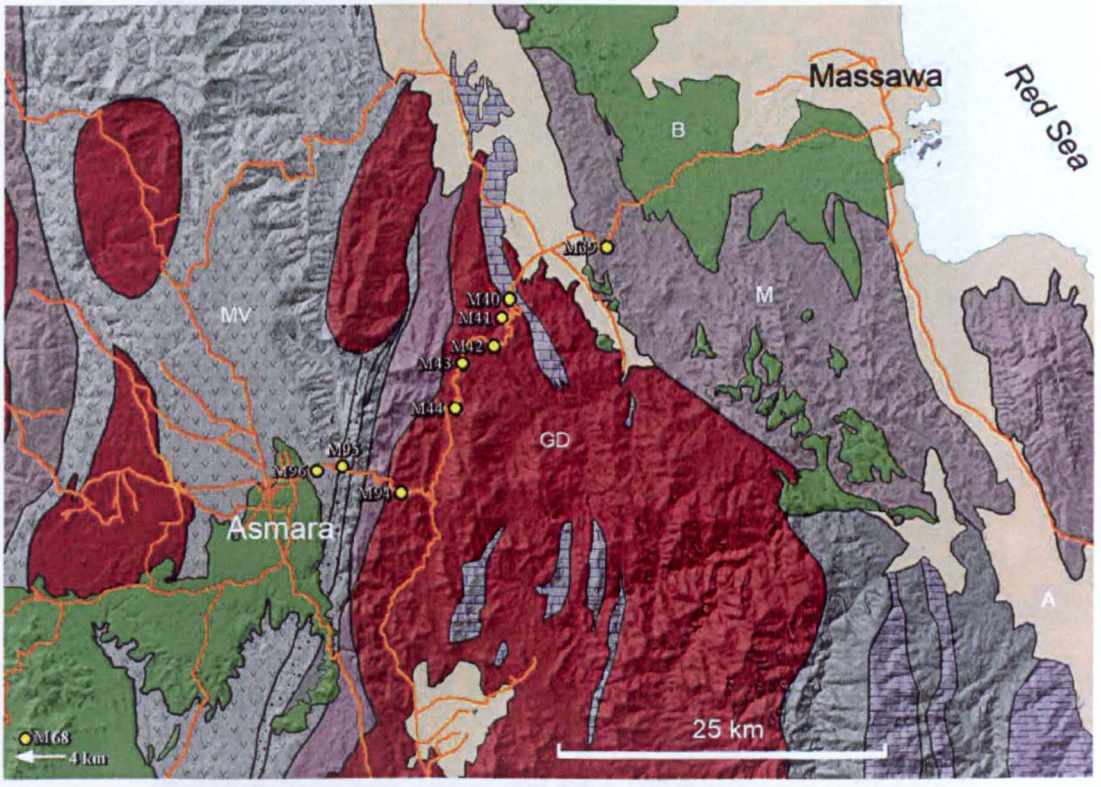


**Figure 6.15** Geological map of Eritrean basement (after Drury & de Souza Filho 1998, Figure 1) superimposed on SRTM elevation data. Orange lines are roads and tracks suitable for vehicle traffic. GD = post-tectonic (~650 Ma) granodiorite; MV = felsic metavolcanics (~750-800 Ma); B = basalts of various Cenozoic ages; M = migmatitic gneisses formed during Pan African orogeny (>650 Ma); A = superficial sediments

their emplacement ~650 Ma (Teklay, 1997). The chosen samples were fresh in hand specimen and their thin sections showed few signs of hydrous alteration of feldspars. A typical intrusive basement granodiorite, M40 (figure 6.16), is representative of the irradiated samples. Figure 6.16 illustrates a fresh, medium-grained (2 - 4mm), quartz-rich granodiorite, with the assemblage of quartz, sodic plagioclase and K-feldspar

(microcline) with minimal biotite. Microcline, with distinctive 'tartan' twinning, occurs in small interstices in dominant quartz-plagioclase and was probably the last mineral to crystallise. The potassium in microcline made it possible to obtain $^{40}Ar/^{39}Ar$ cooling ages from the granodiorites. In the diorite either plagioclase or hornblende provided the dateable phase.

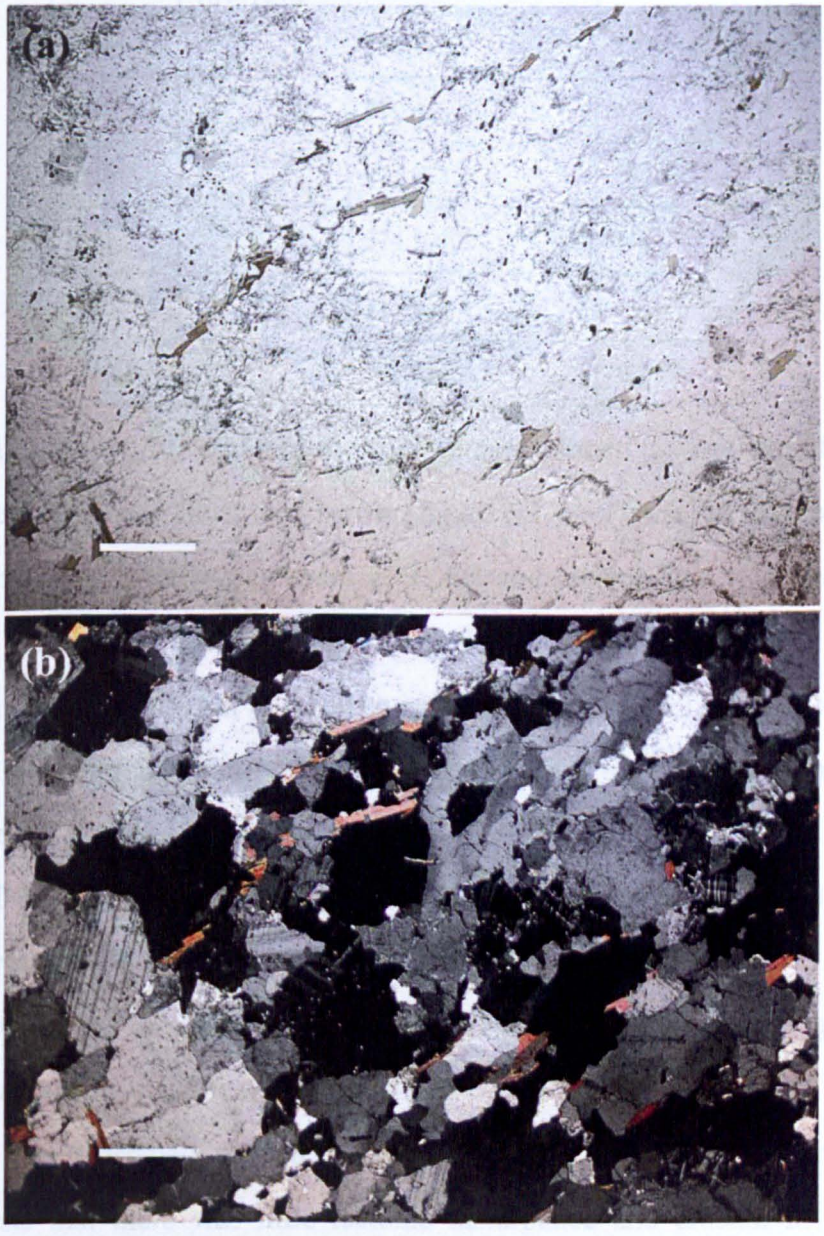


**Figure 6.16** Photomicrographs of typical post-tectonic Eritrean Neoproterozoic granodiorite intrusion (M40) (a) plane-polarised (b) cross-polarised. Fresh, medium-grained granodiorite (quartz-sodium plagioclase-alkali feldspar -biotite). Scale bar = 1mm

### 6.6.3 Results and discussion

Nine new whole rock $^{40}Ar$ /$^{39}Ar$ ages are presented for representative basement samples that were systematically collected from the Eritrean Escarpment (table 6.3).

**Table 6.3** $^{40}Ar/^{39}Ar$ cooling ages for Neoproterozoic granitic samples from the Eritrean Escarpment and Plateau. Coordinates correspond to UTM Zone 37 North

| Sample | UTM co-ordinates | $^{40}Ar/^{39}Ar$ cooling age (Ma) | Altitude (m) |
|---|---|---|---|
| M96 | 496160E 1696650N | 692.1±3.1 | 2420 |
| M68 | 470541E 1665652N | 546.5±3.7 | 2166 |
| M94 | 503684E 1694715N | 454.9±5.7 | 2112 |
| M44 | 508523 E 1702306 N | 350.1±1.7 | 1329 |
| M43 | 509201 E 1706314 N | 310.4±1.8 | 973 |
| M42 | 512033 E 1707837 N | 271.6±1.4 | 960 |
| M41 | 551713 E 1710367 N | 274.5±1.5 | 684 |
| M40 | 513397 E 1711998 N | 315.8±1.8 | 451 |
| M39 | 522030E 1716591N | 261.4±1.3 | 333 |

Geologically meaningful results of the cooling ages plotted against altitude for these samples are figuratively illustrated below (figure 6.17). Figure 6.17a is a schematic plot showing three idealised episodes of uplift and erosion that involved different uplift rates (see section 6.6.1). Line B-C on Figure 6.17a suggests that the rate of erosion and uplift increased at B, when an episode of tectonic uplift began and that the new, faster rate continued until C. Subsequently, from C to D, the rate of erosion and uplift slowed. Figure 6.17b is a plot of $^{40}Ar/^{39}Ar$ whole-rock cooling ages of samples (table 6.3) from the crystalline basement in the Red Sea Escarpment of Eritrea against sample elevation in the escarpment.

The plot of well-constrained $^{40}Ar/^{39}Ar$ cooling ages presented in Figure 6.17b, indicates that Neoproterozoic ages are retained by the $^{40}Ar/^{39}Ar$ system at the highest altitudes in the escarpment and on the Eritrean Plateau (see also Mock *et al.* 1999). This suggests that there was little tectonic disturbance and erosion in NE Africa during the Lower Palaeozoic. However in the more deeply eroded parts of the escarpment, between altitudes of 300-1500m, a steep well-defined trend in the data (figure 6.17), indicates an episode of accelerated uplift and erosion between 350 and 260 Ma (Lower Carboniferous to Middle Permian). The gradient of the best-fit line

through these data gives an estimated rate of uplift and erosion of 22.6 m $Ma^{-1}$ during this episode, which is more than twice the average of 10.7m $Ma^{-1}$ (Portenga *et al.* 2009) for the continental crust.

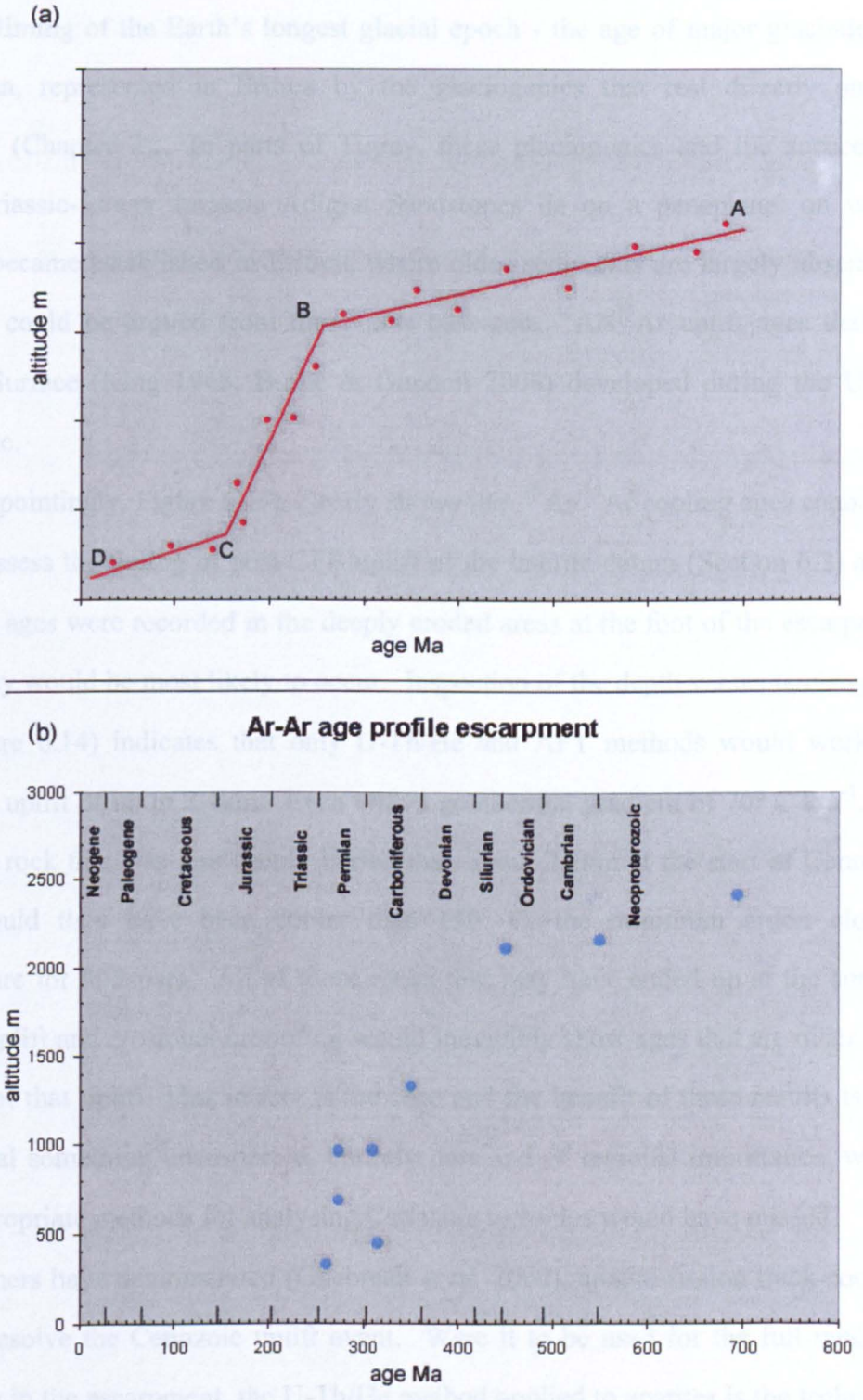


**Figure 6.17** Escarpment age profiles (a) schematic plot showing episodes of uplift and (b) $^{40}Ar/^{39}Ar$ plot of whole-rock cooling ages of granodiorite samples

Surprisingly, the basement data show a clear trend of decreasing age with

decreasing altitude that spans an 80 Ma Carboniferous to Permian episode. Significantly, the episode of accelerated uplift and erosion recorded by $^{40}Ar/^{39}Ar$ cooling ages from the Eritrean crystalline basement in this study roughly coincides with the timing of the Earth's longest glacial epoch - the age of major glaciation in Gondwana, represented in Eritrea by the glaciogenics that rest directly on the basement (Chapter 2). In parts of Tigray, these glaciogenics and the succeeding Upper Triassic-Lower Jurassic Adigrat Sandstones lie on a peneplane, on which laterites became established in Eritrea, where older sediments are largely absent. It therefore could be argued from these new basement $^{40}Ar/^{39}Ar$ uplift ages that the African Surface (King 1948; Burke & Gunnell 2008) developed during the Upper Palaeozoic.

Disappointingly, Figure 6.17b clearly shows that $^{40}Ar/^{39}Ar$ cooling ages cannot be used to assess the timing of post-CFB uplift of the laterite datum (Section 6.2) as no Cenozoic ages were recorded in the deeply eroded areas at the foot of the escarpment where they would be most likely to occur. Inspection of the depth versus temperature plot (figure 6.14) indicates that only U-Th/He and AFT methods would work for Cenozoic uplift of up to 2.4km. Even with a geothermal gradient of 70° C $km^{-1}$, any basement rock that was less deeply buried than about 2.2km at the start of Cenozoic uplift would then have been cooler than 150° C, the minimum argon closure temperature for feldspars. All of those rocks that may have ended up at the surface through uplift and erosional unroofing would inevitably show ages that are older than the start of that uplift. This in fact is the case and the benefit of these results is that they reveal something unsuspected, entirely new and of regional importance, which more appropriate methods for analysing Cenozoic tectonics would have missed.

As others have demonstrated (Ghebreab *et al.* 2002), apatite fission track cooling ages do resolve the Cenozoic uplift event. Were it to be used for the full range of elevations in the escarpment, the U-Th/He method applied to apatites is the technique most likely to trace that event in detail. Unfortunately, the only attempt to use that approach on the western side of the Red Sea was flawed (Balestrieri *et al.* 2005;

section 6.7) as indicated in Drury *et al.* (2006) reproduced below, which discusses and comments on the apatite fission-track results for Eritrea (Balestrieri *et al.* 2005).

## 6.7 Uplift and timing

*A comment on "Geomorphic development of the escarpment of the Eritrean margin, southern Red Sea from combined apatite fission-track and (U–Th)/He thermochronometry" by Balestrieri, M.L. et al. [Earth Planet. Sci. Lett. 231 (2005) 97–110]*

S.A. Drury, W. Ghebreab, M.E. Andrews Deller, C.J. Talbot, S.M. Berhe

(Received 26 April 2005; in final form 18 October 2005)
Published in: Earth Planetary Science Letters 242 (2006) 428–432 Editor: Courtillot, V.

### 6.7.1. Introduction

The western Red Sea margin in Eritrea comprises ~25km of coastal lowlands backed by a deeply eroded escarpment that rises >2.2km in ~40km. The plateau atop this zone of Neogene uplift is capped by ~30 Ma continental flood basalts (CFB). The CFBs rest conformably on thin Palaeogene (> 40 Ma) lateritic palaeosols (Andrews Deller 2004), beneath which is a Neoproterozoic metamorphic complex. In the southern part, the laterites are separated from basement by discontinuous patches of Jurassic sandstones.

The laterites observed in the field and on satellite images occur in this stratigraphic position throughout the hinterland of the western Red Sea margin from eastern Sudan (Kenea 2001) through Eritrea and northern Ethiopia (Andrews Deller 2000) to the Blue Nile Gorge (Sultana & Abdelsalam 2005) (a N-S range of >800km) and further to the south (Ebinger *et al.* 1993). Because they formed on a low-relief surface close to sea-level (Bohannon *et al.* 1989) across most of NE Africa and western Arabia (Andrews Deller in press), the laterites are an important datum for assessing the later effects of regional tectonics (Andrews Deller 2000; Drury *et al.* 1994). Post-30 Ma tectonics has displaced occurrences of this datum on the plateau and coastal lowlands by 2.2 - 2.8km vertically. The opportunities presented by the laterite datum clearly encouraged Balestrieri *et al.* (2005) and Abbate *et al.* (2002) to

analyse geomorphic processes at the western Red Sea margin thermochronologically. So too did previous work on the initiation of rifting in the Red Sea and Gulf of Aden areas (Bohannon *et al.* 1989; Ghebreab *et al.* 2002; Omar *et al.* 1989; Abbate *et al.* 2001), which converged on initiation of uplift and erosion from 25 to 20 Ma. On the basis of 13 apatite (U-Th)/He cooling ages (apatite He ages) from the Eritrean escarpment, Balestrieri *et al.* (2005) conclude a 10 Ma younger age for the start of rifting in the southern Red Sea.

Fig. 6.18 shows a variety of evidence referred to in this Comment, which we believe casts doubt on the geological context used by Balestrieri et al (2005) and by an earlier paper using apatite fission-track (AFT) dating (Abbate *et al.* 2002) upon which they rely.

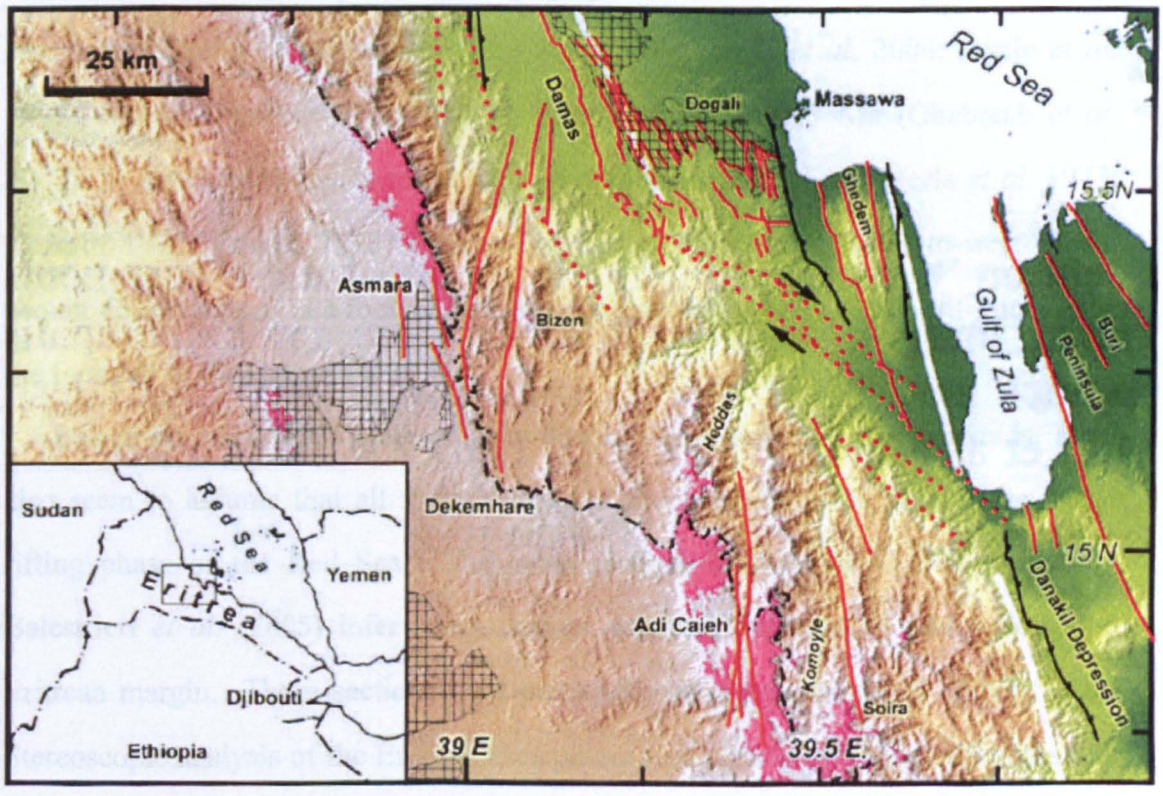


**Figure 6.18** Neogene to Recent major faults and topography in eastern Eritrea. Red solid lines – normal, down-to-west, west dipping; red dotted lines – strike-slip faults; black ticked lines – normal. down-to-east, east dipping (Drury *et al.* 1994; Frazier 1970; Ghebreab & Talbot 2000); white lines – 'border faults' (Balestrieri *et al.* 2005; Abbate *et al.* 2002); hachured areas – occurrences of ~30 Ma CFBs. Topography from side-illuminated SRTM 3 arc-second digital elevation data; dark greens through yellows and browns to greys represent elevations from 0 to 2400m a.m.s.l.; magenta areas >2400m; black dash-dot line – escarpment rim. Inset shows regional location of study area

### 6.7.2 Regional tectonics

Balestrieri *et al.* (2005; Abbate *et al.* 2002) assume that major, down-to-east 'border faults', form the western margins of major basins. Their plots of AFT and apatite He ages against distance from such inferred faults (Balestrieri *et al.* 2005, Figures 1c & 3) are compared with surface age distributions that would result from simple denudation models. They locate one such 'border fault' at the basement-cover boundary in the footwall of the active, down-to-west faulted margin of the Damas Basin. Despite continuous exposure, there is no evidence for such a fault. Instead, a duplex of down-to-west faults repeat the basement-cover boundary in a series of east-dipping blocks (Drury *et al.* 1994; Sagri *et al.* 1998). The 'border fault' in their southernmost transect (Balestrieri *et al.* 2005) links the western margins of the Gulf of Zula and the Danakil Depression. Topographic features there do suggest down-to-east normal faults. However, they are active (Ogubazghi *et al.* 2004; Ayele *et al.* 1997), Mount Ghedem (910m) having been uplifted since 3 Ma (Ghebreab *et al.* 2002). In the Buri Peninsula to the east, several basement inliers (Merla *et al.* 1973; Kazmin 1972; Frazier 1970) indicate the footwalls of large down-to-west faults. Mount Ghedem itself is a footwall inlier analogous to the larger extent of gneisses in the footwall of the Damas Fault.

Balestrieri *et al.* (2005) refer only to down-to-east faulting, i.e. basinwards. They also seem to assume that all faults formed at the same time, i.e. during the initial rifting phase of the Red Sea. The cross sections (Abbate *et al.* 2002) used by Balestrieri *et al.* (2005) infer steep, mainly eastward dips for all faults along the Eritrean margin. Those sections omit many important exposed faults (figure 6.18). Stereoscopic analysis of the Eritrean escarpment and plateau reveals many faults that dip westwards, some at angles less than 45° (Drury *et al.* 1994; Ghebreab & Talbot 2000). Also omitted is evidence for low-angled, structurally necessary extensional detachments (Drury *et al.* 1994; Talbot & Ghebreab 1997; Ghebreab & Talbot 2000), which plausibly explain basement inliers in the Red Sea lowlands as extensional core complexes (Ghebreab & Talbot 2000).

The active Damas Fault is not simple. Its rising footwall has progressively displaced the course of the Damas River some 40km NNW from its original direct course to the Red Sea, so that its tip is propagating northwards (Drury *et al.* 1994). The SSE end of its footwall now reaches ~300m above the Damas Basin, and carries uplifted lavas and undissected cinder cones at high elevations, one sample of which yielded an Ar-Ar total fusion age of 1 Ma (unpublished data of Drury, Berhe and Kelley). Westward projection of the base of the Tertiary cover around Dogali suggests a cumulative displacement of 0.5 to 1.0km (Drury *et al.* 1994) in very recent times. Interestingly, the youngest apatite He age (5.5 Ma) Balestrieri *et al.* (2005) is from a sample (Balestrieri *et al.* 2005, ER167, Table 1) in the footwall of the active Damas Fault. We suggest that its young age is a result of active uplift and erosion. Trending SE of the Damas Fault's southern termination are further uplifted lavas and volcanoes, each at different elevations. This zone and several faults form a link from the Damas Basin to the western boundary of the Danakil Depression. This is a dextral zone of transpression (Drury *et al.* 1994), the Damas Basin being a linked transtensional zone. This tectonic transfer system forms the transition between Red Sea extension to the north and that of Danakil-Afar to the south: Eritrea is structurally the most complex sector of the southern Red Sea's west flank.

### 6.7.3. Stratigraphy

In discussing evidence for a 15 Ma onset of post break-up erosion in this area, Balestrieri *et al.* (2005) refer to Late Miocene conglomerates of the Upper Dogali Formation in the footwall of the Damas Fault. The Dogali Formation rests unconformably upon the ~30 Ma CFBs, showing no sign of the underlying intense faulting. Its *basal* conglomerate contains large clasts of CFBs and basement rocks in prominent roadside exposures (Drury *et al.* 1994). This is not recorded in an earlier work involving two of the present authors (Sagri *et al.* 1998), the Lower Dogali Formation being said to be exclusively a 'volcano-lacustrine' sequence. This basal conglomerate clearly demonstrates that erosion of uplifted crust was well established at the time of its deposition. The age range of the Dogali Formation is poorly

constrained. However, a basalt flow in the Upper Dogali Formation has yielded an Ar-Ar total fusion age of 18±1.6 Ma (Drury *et al.* 1994) corresponding to nearby Middle Miocene coral faunas (Sagri *et al.* 1998). The basal conglomerate of the Dogali Formation is clearly older than that age. Deep incision of the Eritrean escarpment had been achieved by 18 Ma at the latest.

Balestrieri *et al.* (2005) claim that there are no sediments derived by erosion of the escarpment that are older than Early Pleistocene on the floor of the northern Danakil Depression. In fact thick sequences of the Miocene-Pliocene 'Red Series' (probably coeval with the Dogali Formation) occur extensively on both flanks of that basin (Barberi *et al.* 1972).

**6.7.4. Geomorphology**

Balestrieri *et al.* (2005, pp 101, 108) suggest that uplift of the Ethiopian and Eritrean plateaux produced radial drainage on a dome centred at the eruptive axis of the CFBs. If that were so, initial drainage in Eritrea would be approximately northwards. They cite as relics northward trends in the upper Komoyle and Heddas rivers. In fact, the headwaters of the Komoyle and Heddas follow down-to-west N-S faults with throws of several hundred metres (figure 6.18; Drury *et al.* 1994; Ghebreab & Talbot 2000). Other major rivers in the escarpment clearly show dendritic patterns.

Drainage throughout the Ethiopian-Eritrean plateau does not correspond to a simple dome. The plateau carries several large shield volcanoes of Early to Middle Miocene age (Berhe *et al.* 1987). These have had a profound effect on the post-Miocene drainage and erosion of the plateau (Gani & Abdelsalam in press), giving rise to the curiously circuitous courses of the Blue Nile and Tekesse-Setit. Assuming a simple dome seems unfortunate, when regional landforms are the object of the investigation of Balestrieri *et al.* (2005).

Balestrieri *et al.* (2005) regard 'a series of marginal highs that often reach greater altitude than the (escarpment's) rim' as an 'antecedent drainage divide'. Such a divide is a central requirement of the 'plateau degradation/downwearing' model that

their data are said to support. Some isolated and irregularly distributed peaks seaward of the escarpment's rim do out-top its elevation locally (figure 6.18). Because a vast volume of upper crust has been removed from deep valleys that separate these peaks, a more plausible explanation of 'the eastern marginal belt' is local isostatic response to lithospheric unloading by erosion (England & Molnar 1990).

**6.7.5. Strategy**

Balestrieri *et al.* (2005) and Abbate *et al.* (2002) constrain the position of their inferred 'border faults' by assuming that the youngest AFT and apatite He ages occur in their footwalls. Only one sample is from the footwall of the Damas Fault, in which they locate such a 'border fault'. The 'border fault' to the east of Ghedem (Balestrieri *et al.* 2005; Abbate *et al.* 2002) has no apatite He age constraint. The youngest AFT ages (3-5 Ma at 910m) on Ghedem (Ghebreab *et al.* 2002) occur in the footwalls of down-to-west faults, whose hanging walls show older ages (22-32 Ma) at elevations down to 200m (Ghebreab *et al.* 2002). Data from the escarpment also contradict an age-elevation correlation (Balestrieri *et al.* 2005; Abbate *et al.* 2002). An AFT age of 23 Ma at 2465m on Mount Bizen contrasts with 350 Ma at 760m elevation on its northern flank (Ghebreab *et al.* 2002). Balestrieri *et al* (2005) also report an extremely young apatite He age from the >3000m summit of Mount Soira.

The stratigraphic argument for a ~15 Ma initiation of erosion at the Eritrean margin (Balestrieri *et al.* 2005) is at variance with evidence from the Dogali Formation (Section 6.7.3), as well as previous estimates for a 5-10 Ma earlier start of Red Sea rifting (Bohannon *et al.* 1989; Ghebreab *et al.* 2002; Omar *et al.* 1989). Thermochronologically that age also seems flawed by assumption of an unrealistically low geothermal gradient of 25°C $km^{-1}$ (Balestrieri *et al.* 2005, p. 101). The minimum value for the *western* Ethiopian plateau is 35°C $km^{-1}$ (Pik *et al.* 2003), and the geothermally active Eritrean margin undoubtedly must have a much higher geothermal gradient, which would seriously affect the conclusions of Balestrieri *et al.* (2005). So too might sampling problems: replicate ages reported from each sample site (Balestrieri *et al.* 2005, Table 1) deviate from one another by >20 Ma in some

cases.

### 6.7.6. Conclusion

Structural, stratigraphic and geomorphological details of the area studied by Balestrieri *et al.* (2005) demonstrate complex tectonic and erosional evolution through Neogene times. These arose from the area's situation at the transition between Red Sea and Danakil-Afar rifting, where tectonic motions are accommodated by strain transfer oblique to the main trend of the Red Sea (Drury *et al.* 1994). Their approach may be appropriate for less complex scenarios, but not for this setting, each of their traverses being in different sectors of an exemplary tectonic transfer zone. Episodic extension of the Red Sea, well-established on both its flanks (Bohannon *et al.* 1989; Drury *et al.* 1994; Ghebreab *et al.* 2002; Ghebreab *et al.* 2000; Omar *et al.* 1989; Abbate *et al.* 2001; Berhe 1986), in segments with different fault polarities and cooling histories cannot be ignored in planning and interpreting thermochronometry.

## 6.8 Conclusions on the chapter as a whole

*Laterites*

The strategy of using remote sensing to detect alunite-bearing occurrences of Horizon 3 clay zone proves to be successful. Moreover, the abundance in the study area of pixel clusters in which alunite can be detected suggests that, given access to argon mass spectrometry, dating programmes can be achieved at a variety of sample spacings from a kilometre to regional levels. Such is the accuracy of alunite detection, given sparse vegetation cover, that wherever well developed laterites occur it should be possible to identify localities with a good chance of yielding ages. Indeed, alunite has a spectrum sufficiently different from other light-coloured minerals, such as clays, that a reconnaissance approach to finding occurrences using ASTER data would benefit dating programmes in other terrains, such as those affected by hydrothermal and porphyry-style mineralisation where abundant sulphate and potassium ions in mineralising fluids sometimes produce alunite in alteration zones.

In the study area, a minimum age for lateritisation, associated with final

desiccation of the laterite profile, has been defined at between 35 and 51 Ma, with most well-dated samples falling between 38 and 42 Ma. Intense tropical weathering in Eritrea and Tigray appears to have ended in the mid-Eocene (Bartonian to late-Lutetian).

*Continental flood basalts*

Ten new $^{40}Ar/^{39}Ar$ ages from Eritrean and northern Ethiopian flood basalts span a far longer time span (32.3±0.3 to 19.4±0.3 Ma) than those sampled by others in the Ras Dashen area. Dates for the basal flows confirm the roughly 30 Ma age for the initiation of flood volcanism in this part of the Yemeni-Ethiopian large igneous province (Drury *et al.* 1994) but the better precision of ages in this study yields an integrated-age range between 27.6 ±0.2 to 32.3±0.3 Ma. This suggests a range of early Oligocene ages for magmatic initiation over this large area, which may reflect shifting locations – probably fissures – for the source of different flows; a likely scenario for the build-up of such a thick lava sequence over a huge area. Two $^{40}Ar/^{39}Ar$ isochron ages suggesting late Eocene ages have large errors, and may confirm the early Eocene Ashangi basalts of other workers. However, a new exposure in the Tigrayan escarpment of flood basalts beneath an erosional surface and thick fluviatile sediments (figure 6.9) provides an excellent target for future dating.

The youngest flood basalts sampled from the 600m thick sequence on Emba Tekera in Eritrea gave a lower Miocene (Burdigalian) age of 19.4 ± 0.3 Ma, confirms the work in Southern Eritrea by Zanettin *et al.* (2006) and extends the duration of flood basalt effusion in Eritrea to 13 Ma, compared with the 1 Ma suggested for the thicker Ras Dashen sequence (Hofmann *et al* 1997). The lower Miocene age also places an upper limit on the initiation of extensional tectonics that marked the onset of Red Sea rifting, which from apatite fission-track dating is widely believed to been around 25 Ma ago (Bohannon *et al.* 1989; Omar *et al.* 1989; Abbate *et al.* 2001; Ghebreab *et al.* 2002).

The consistent occurrence of laterites beneath the lowest CFB flows in the study area and the roughly 10 Ma difference between the minimum age of lateritisation and

the maximum age of basalt effusion refutes the notion of Menzies *et al.* (1990, 1997) that thermal uplift associated with CFB initiation started a brief episode of tropical weathering of underlying rocks that produced laterites. Furthermore, the time lag between lateritisation and CFB effusion and the ubiquitous occurrence of laterites are totally inconsistent with the hypothesis by Burke (1996) and Burke & Gunnell (2008) that the CFBs must have been preceded by thermal doming and erosion so that laterites must be absent from the stratigraphy of the whole Ethiopian plateau.

*Basement*

The 2.4km high Eritrean Escarpment, which exists as a consequence of Neogene uplift and erosion, exposes lithologically and metamorphically diverse Neoproterozoic basement, including compositionally uniform granitoid intrusions and gneisses from which the laterites evolve. It presents an excellent opportunity for studying uplift history by dating the cooling of rocks through minerals' closure temperatures for degassing of gaseous daughter products of radioactive decay or annealing of tracks produced by particles released by radioactive isotopes. During this study, it was found that the $^{40}Ar$ /$^{39}Ar$ method of cooling age dating of granitic rocks over an altitude range of 2.2km was, inappropriate for Cenozoic uplift because the closure temperatures of K-bearing minerals in the granites were too high for the prevailing geothermal conditions.

However, a plot of cooling age versus elevation revealed strong evidence for a much earlier episode of uplift and erosion. Devonian to Neoproterozoic cooling ages against altitude obtained suggest sluggish uplift since their formation during the Lower Palaeozoic. The regional significance of this observation of Upper Palaeozoic uplift and erosion is discussed in Chapter 7 in the context of the surface on which laterites developed.

*Discussion of regional Neogene tectonics*

The more appropriate use of U-Th/He cooling age dating in basement apatites, combined with earlier apatite fission track dating, conducted in the Eritrean escarpment by Balestrieri *et al.* (2005) prompted the discussion here (Drury *et al.*

2005) that emphasises the complexity of the Neogene tectonic setting of the Eritrean flank of the Red Sea, lying at the transition between the rifting of the Red Sea proper and that in the Danakil-Afar Depression. This is a zone of tectonic accommodation where strain was taken up oblique to the main NNW-SSE trend of the Red Sea by a major strike-slip transfer zone which bisects Balestrieri *et al.*s (2005) radiometric traverse, thereby casting doubt on their findings and interpretations. The discussion bears directly on the 3-dimensional analysis of the laterite datum covered in Chapter 7, which reveals the complex pattern of Neogene uplift in this region.

From a stratigraphic standpoint this discussion establishes that conglomerates resting unconformably on CFBs (see Chapter 2) at the foot of the Escarpment post-date uplift and high-energy erosion that had already cut through the CFB sequence at higher altitudes to expose laterites and basement. The conglomerate is succeeded by terrestrial sediments capped by 18 Ma old Miocene lavas and marine coral limestones (Chapter 2). Together with the 19.4 Ma minimum age of CFB effusion on the Eritrean Plateau, these observations establish the most likely age for the onset of Neogene uplift and erosion and the extremely rapid pace at which it took place.

# Laterites and the African Surface - a possible new chapter

*'The poetry of earth is never dead'* {Keats 1816}

## 7.1 Introduction

The cratonization of the continental crust of NE Africa (Kroner & Stern 2005), the formation of laterites, the emergence of man (Wood 1997; Abbate *et al.* 1998; White *et al.* 2003) and the birth of a new ocean (Wright *et al.* 2005) unfold between latitudes 20°N and 10°N, where the study area of this thesis is concentrated. Apart from notable gossans and remnants of Upper Palaeozoic glacials, the only geological exposures stratigraphically in place between Mesozoic sedimentary sequences and the Trap basalts are the laterites, most of which developed from Neoproterozoic basement exhumed during regional peneplanation that produced an erosional land surface famously dubbed the African Surface. Although few remote sensing studies aim at understanding the geological controls on the distribution of the lateritic regolith, this chapter, in part, attempts that. Widely distributed in Eritrea and northern Ethiopia the study of laterites provides geological clues about the age and formation of the palaeosols and the evolution of the African Surface (King 1948, 1950, 1962, 1967, 1973 Ollier & Marker 1985; Bohannon 1986, 1989; Twidale 1992, 1998; Marker & McFarlane 1997; Partridge 1998; Marker *et al.* 2002; Chardon *et al.* 2006; Coltorti *et al.* 2007; Burke & Gunnell 2008; Oard 2011).

Field, petrographic, microprobe, geochemical, geochronological data and the first regional geological maps of laterite facies (Chapter 4 - sheets ND37-2, -3, -6, -7; Asmara sub-sheet) are used as indicators of the palaeoenvironment in which the lateritic regolith formed and of the palaeo-surface from which it developed. Evidence presented here places constraints on regional uplift and the glacial epoch that predates the laterites and sculpted the African continent. Multispectral digital imagery and digital elevation data are used to map the post-uplift pre-erosion interface between the

flood basalts and laterites as a datum (Drury *et al.* 1994) to reconstruct the shape taken by post-Oligocene crustal doming and extension and estimate average rates of Neogene uplift of the African Surface. This structural analysis not only provides a means of mapping the continent-wide planation that shaped the African Surface but furnishes guidelines for determining potential zones of supergene enrichment of metalliferous deposits in the Neoproterozoic basement in the highly dissected terrain.

## 7.2 Evolution of a landscape - an overview

The connection between regional palaeogeography, palaeoenvironment and palaeoclimate and Eritrean and Ethiopian laterites and their chronostratigraphy (Chapter 2) in relation to the African Surface (King 1962) is informative. There are no recorded occurrences of Palaeozoic lateritisation in the region. This is consistent with the investigation made in this study which found no evidence of pre-Mesozoic lateritic palaeosols in Eritrea or Tigray using remotely sensed data, the regional map of laterite facies and comprehensive field work (Chapters 2). After the Permian however, regionally extensive laterites, often with deep weathering profiles and invariably characterised by distinctive horizons 3, 4 and 5, outcrop throughout the area an observation supported by field evidence and remotely sensed digital imaging data.

As noted in previous chapters, ideal conditions required for the formation of deeply weathered laterites include; humid tropical seasonal climatic regimes (Butt *et al.* 2000), a stable almost flat continental surface close to sea level (Dainelli 1943; Bohannon 1989; Drury *et al.* 1994) and a lengthy period of time. Laterite palaeosols take several millions of years to develop (Fookes 1997; Budel 1982; Nahon & Tardy 1992). In Africa, Australia, Asia, South America and India laterites have formed and evolved for over 100 Ma (Butt *et al.* 2000; Rossetti 2004). However, the suggestion that the average rate of laterite weathering is 20m/Ma (Nahon & Tardy 1992) or the revised conclusion that a 20m-thick laterite takes 500 Kyr to form (Nahon 2003) is not supported in this study. Dependent on parent rock-type in the study area, laterites

range in thickness from a few metres to over 100 metres in full profile (Chapter 2; Butt & Zeegers 1992; Drury *et al.* 1994; Tardy 1997; Vasconcelos 1999). Furthermore, minimum ages for laterites throughout the region established as predominantly mid-Eocene, (~40 to ~43 Ma, Chapter 5) extend into the early Eocene with minimum ages for laterite formation of 52.0 ± 0.3 Ma and 53.9 ± 4.1 Ma at two widely separated localities (Chapter 6). Consequently, contrary to the suggestions of previous workers (Menzies *et al.* 1990, 1997; Thiry & Simon-Coinçon 1999; Schwartz & Germann 1999; Abbate *et al.* 2002 and others), it is advanced that laterites in the region formed over a substantially longer period than has previously been suggested. Moreover, the time gap must have been long enough - several tens of millions of years prior to mid-Oligocene CFB volcanism - for the rotting of the regolith to take place when palaeogeography, palaeoclimate and palaeoenvironment were conducive to the formation of mature laterite profiles. This interplay of conditions necessary for the formation of laterites played itself out *across* the African Surface.

*The African Surface in NE Africa*

The African Surface, also referred to as the Gondwana Surface (King 1948, 1962; Chardon *et al.* 2006), is at the base of the Mesozoic in NE Africa. It is an erosion surface developed on crystalline Precambrian basement and late Palaeozoic glaciogenic sediments (Bussert & Schrank 2007) that are unconformably overlain by Triassic to middle Jurassic Adigrat sandstones thought to be diachronous throughout NE Africa (Mohr 1962; Bosellini 1989; Coltorti *et al.* 2007). At, or close to sea level, the bevelled peneplain surface, believed to slope gently from the centre of the continent towards its margins, where exposed, was subsequently lateritised (Mohr 1999).

A wealth of confusion surrounds the term African Surface first coined by King (1942), who also used the terms Gondwanaland Surface, African Land-Surfaces and African Erosion Surface. This situation is not aided by Burke & Gunnell's (2008) attempted refutation of King's work (1930 - 1983) and most other authors' views, or

their insistence on "*the absence of a laterite-covered African Surface from a roughly circular area ~1000km in diameter centred on the Afar Dome*" - an area incorporating Eritrea and Tigray; the study area. Yet despite seeming indications of novelty, their position, inconsistent in places like King's (1948, 1967), almost exactly follows that of earlier workers. Nevertheless, Burke & Gunnell's (2008) broad synthesis of the subject of the African Surface is informative from a historical perspective and they themselves admit to "*increasing similarities in the use of the term, if not as yet a consensus*". Most workers do not dispute the existence of the African Surface; the problem lies rather in defining it. By and large, King's framework (1948, 1950, 1962) for an erosionally exhumed, bevelled, peneplained frequently duricrusted and lateritised African Surface, of obvious continent-wide aerial extent still stands.

On one level at least, there is a consensus, which is that the African Surface is marked by laterites. In fact throughout Africa, laterites are diagnostic of and characterise the African Surface (Bohannon 1986; Marker & McFarlane 1997; Chardon *et al.* 2006; Burke & Gunnell 2008; Oard 2011). Unlike South Africa where several distinct planation surfaces occur, field evidence indicates that only one peneplained surface characterised by lateritisation exists in NE Africa; this to all intents and purposes is the African Surface that arguably resulted from late Palaeozoic glaciation (section 7.2.1). This simpler scenario contradicts the multi-peneplained model suggested for Northern Ethiopia by Coltorti *et al.* (2007) and has parallels with Australia where Permian glaciogenics rest on a similar continent-wide surface subjected to prolonged lateritisation (Twidale 2000).

### 7.2.1 Palaeogeography

During the Upper Palaeozoic Africa was incorporated in the Gondwana supercontinent, when NE Africa lay south of the palaeo-Equator (figure 7.1). It remained at low- to mid- palaeolatitudes (~35-45°S) during the Late Carboniferous and Early Permian (Scotese & Golonka 1992; Scotese 1994; Bunter *et al.* 1998; Stampfli *et al.* 2001; Ziegler & Stampfli 2001; Bussert & Schrank 2007). But by the Triassic, Africa had drifted north to straddle the Equator, much as it does today.

Figure 2.8, depicting the plate tectonic evolution of Africa, shows the gradual emergence of Africa as it was 'freed' first by the separation of India, then Australia, Antarctica and South America in the polyphased break-up of Gondwana (Guiraud *et al.* 2005) during the mid Cretaceous. By the Middle Eocene, continent-configuration was close to that of the present day but it was not until the late Miocene that Africa rifted from Arabia. However, it is worth noting that the palaeogeographic position of Africa remained roughly the same with very little shift of the study area relative to the Equator over the last 250 Ma (figure 2.8, red dot). The movement of NE Africa to the inter-tropical belt where it remained throughout the Mesozoic and Cenozoic eras, signalled a marked change in conditions and placed Africa in the optimum palaeogeographic position in which laterites could develop given appropriate environmental constraints.

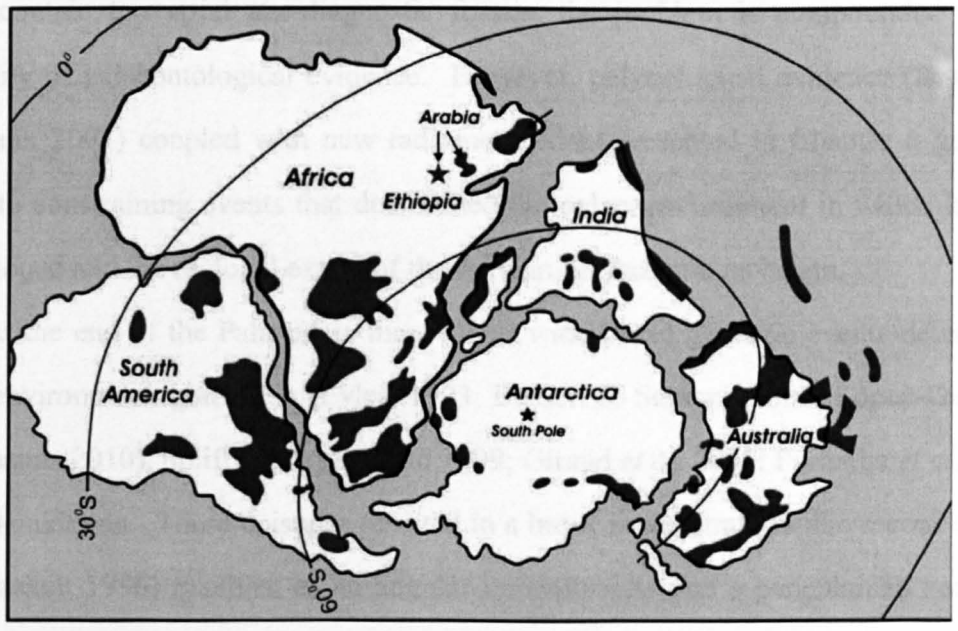


**Figure 7.1** Late Carboniferous-Early Permian palaeogeography with palaeolatitudes, showing the distribution of Late Carboniferous-Early Permian glacigenic deposits in Gondwana. Grey star indicates position of glacigenic deposits in Northern Ethiopia and Eritrea and arrows indicate transport directions of glacigenic sediments in Ethiopia (from Kruck & Thiele 1983; Al-Belushi *et al.* 1996; Wopfner & Casshyap 1997;Bussert & Schrank 2007)

### 7.2.2 Palaeoenvironment and palaeoclimate

Geology, palaeogeography and palaeoclimate within the Phanerozoic help determine the palaeoenvironment in NE Africa. Even though chronostratigraphic

boundaries are not arbitrary and correlate geological time with global episodes and significant regional change (Rampino & Caldeira 1993) generalised observation based on subdivisions within the geologic time scale are more useful if they can be substantiated *locally* by field evidence, scientific data and experimentation. The challenge in this region is that there is little to go on. Radiometric dating is patchy for the Upper Palaeozoic to Lower Mesozoic. There are '*neglected intervals*' of time (e.g. the Upper Jurassic-Lower Cretaceous) where there is no detailed dating at all (Gradstein *et al.* 2004). '*Correlative events*', primarily marked by marine zone fossils (e.g. Jurassic ammonites at Robin Hood's Bay, Yorkshire, UK), so important in the absence of radiometric data, are few and far between in the Mesozoic of sub-Saharan Africa (Bosellini *et al.* 2001; Klein *et al.* 2007) and certainly absent in laterites. Since reconstructing environments depends primarily on the presence of sedimentary rocks that contain terrestrial age-diagnostic fossils, the problem is compounded by the scarcity of palaeontological evidence. However, palynological evidence (Bussert & Schrank 2007) coupled with new radiometric data presented in Chapter 6 go some way to constraining events that determined the palaeoenvironment in which laterites developed and the regional extent of the African Surface and its origin.

At the end of the Palaeozoic three major widespread geologic events determined that environment: glaciation (Eyles, 1993; Bussert & Schrank 2007; López-Gamundí & Buatois 2010), uplift (Petley & Reid 1999; Giraud *et al.* 2005; Portenga *et al.* 2009) and denudation. These episodes resulted in a break in the stratigraphic record (Visser & Praekelt 1996) manifest as an angular unconformity and a peneplained basement throughout NE Africa. Geochronological data (section 6.6.3) confirm that the Lower Palaeozoic was tectonically quiescent while the scatter of younger basement cooling ages obtained for the Upper Palaeozoic (figure 6.17) is convincing evidence that at least one major period of uplift and protracted erosion took place during the Carboniferous to early Permian. Furthermore the Late Palaeozoic cooling ages are a strong indication that ancient glacial deposits in the region (section 2.2.2) are indeed of Carboniferous-Permian age. There is general accord within the literature that the

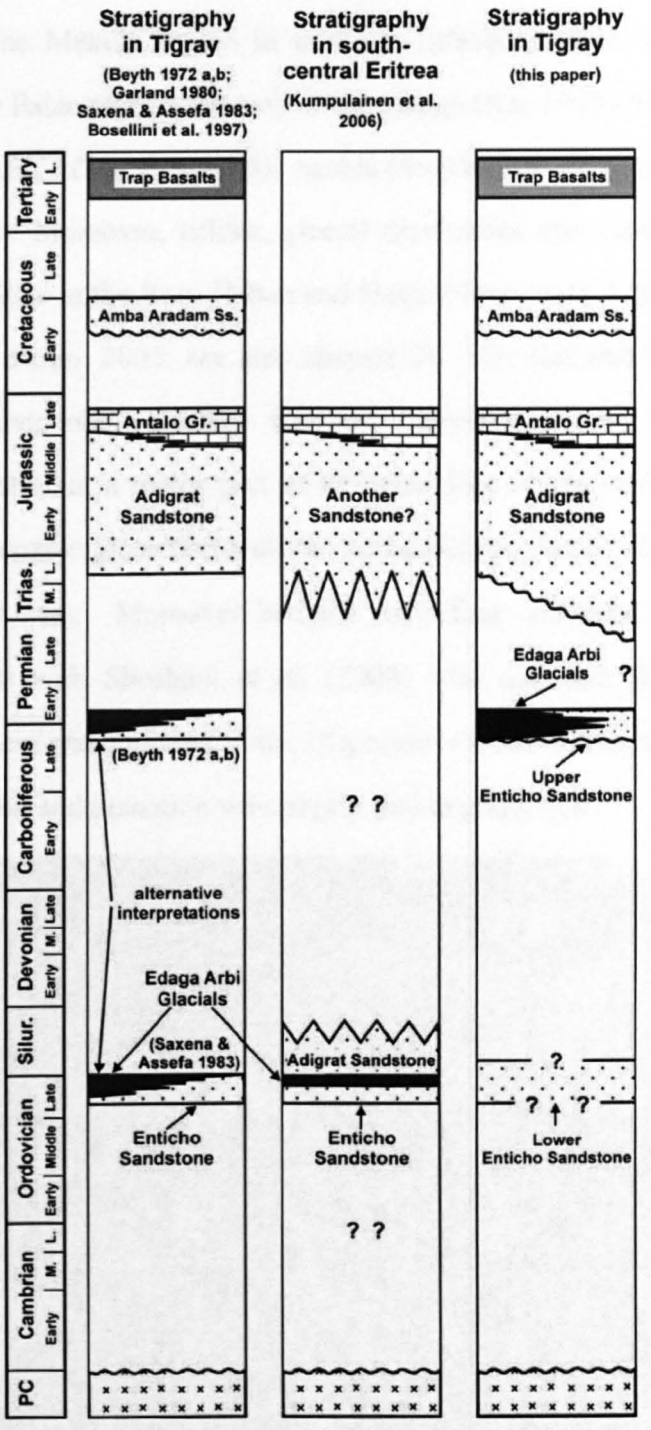


**Figure 7.2**.Stratigraphy of Northern Ethiopia and Eritrea (from Bussert & Schrank 2007)

Gondwanan Supercontinent was extensively glaciated in the Late Palaeozoic (López-Gamundí & Buatois 2012). What is in dispute is to what extent and when, if at all, land ice formed in Eritrea or Tigray. Bussert and Schrank (2007) summarise nicely the status of existing ideas on glaciogenics in the area (figure 7.2). They report a broad range of Carboniferous-Early Permian spores and pollen in glaciogenic

sediments of the Mekele region in northern Ethiopia which correlate with fossils found in Upper Palaeozoic sediments of the Congo (Kar 1969), Katanga (Maheshwari 1969), South Africa (MacRae 1988); Arabia (Stephenson & Osterlo 2002) and Gabon (Jardine 1974). Moreover, tillites, glacial diamictites and sandstones are found in Eritrea at localities in the Rora Habab and Hagar Neus areas, Tusk and Adi Caieh (A. Kibreab, pers. comm. 2005; see also chapter 2). The fact that Bussert & Schrank's (2007) fossil evidence coincides with the basement cooling ages (figure 6.17b) strongly suggests that a major part of the unroofing of the crust in Eritrea resulted from Late Palaeozoic glaciation and that that unroofing lasted about 90 million years (~350 to ~260 Ma). Moreover because unroofing coincided with glaciation - a finding at odds with Shoshani *et al.* (2006) who maintain that unroofing of the Eritrean basement was initiated in the Oligocene - it seems reasonable to assume that extensive erosion and planation was largely due to glaciation.

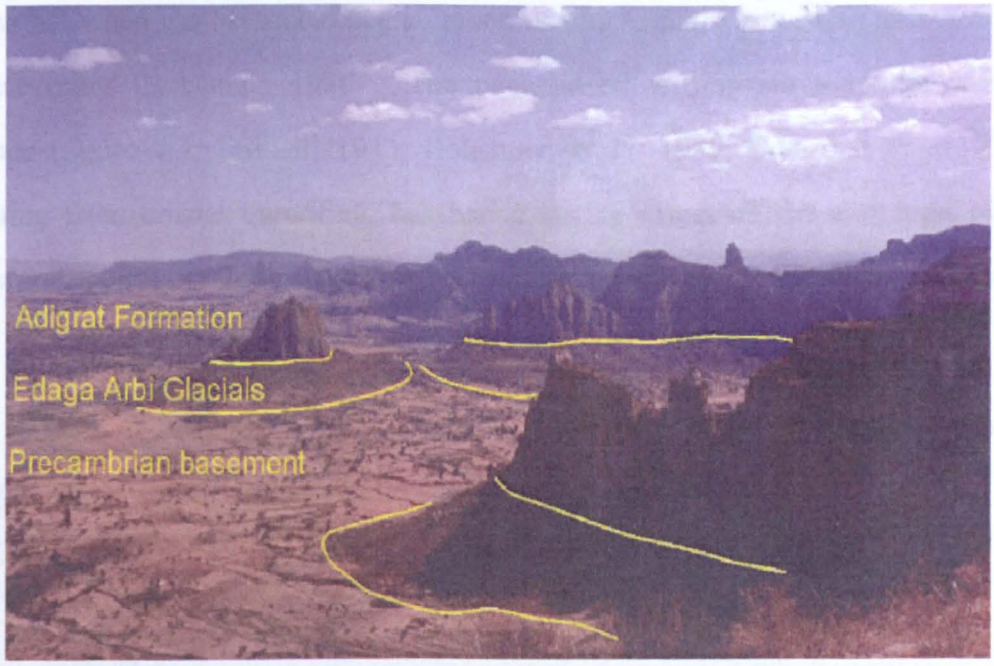


**Figure 7.3a** The relationships between Neoproterozoic basement, Palaeozoic and Mesozoic sediments –from Bussert 2007

Throughout the region glaciogenic sediments filled glacial channels and troughs etched in the Neoproterozoic basement (figure 7.3, 7.3a; Beyth 1972) whereas the higher ground supported discontinuous ice sheets due to the palaeo-position of NE Africa. However, glaciogenic sediments only occur in uneven patches (some of which

are lateritised) and where they are found under the Adigrat Sandstone (figure 7.3b) the contact is unconformable (Dow *et al.* 1971; Arkin *et al.* 1971; Beyth 1972; Bosellini *et al.* 1997; Getaneh 2002; Garland *et al.* 1978; Bussert & Schrank 2007). Initial distribution of the glaciogenic sediments may have been irregular but since much of those deposited have been removed the conclusion here is that erosion continued after glaciation stopped. This is clearly shown on the latest Ethiopian Geological Survey map (Tefera *et al.* 1996) and on localised maps of the immediate area (Russo *et al.* 1997). One of the best places to examine the relationship between Permian to Cretaceous sedimentation and weathering is the Upper Tekesse basin - a potential site for future work.

Given the clear interaction between tectonics and erosion (Todd *et al.* 2003; Rossetti 2004) and the evidence that uplift and denudation at twice the average rate for continental crust (section 6.6.3) spanned a ~90 million year period, it seems very likely that when the Mesozoic began, much of NE Africa was a peneplain with low surface relief (Bohannon 1986). The peneplained erosion surface - the *African Surface* (figure 7.3; Dainelli 1943; Bohannon *et al.* 1989; Bosworth *et al.* 2005) resulting from crustal unroofing, has had a lasting effect on the evolution of the landscape, continues long-lived and essentially unchanged despite modification by

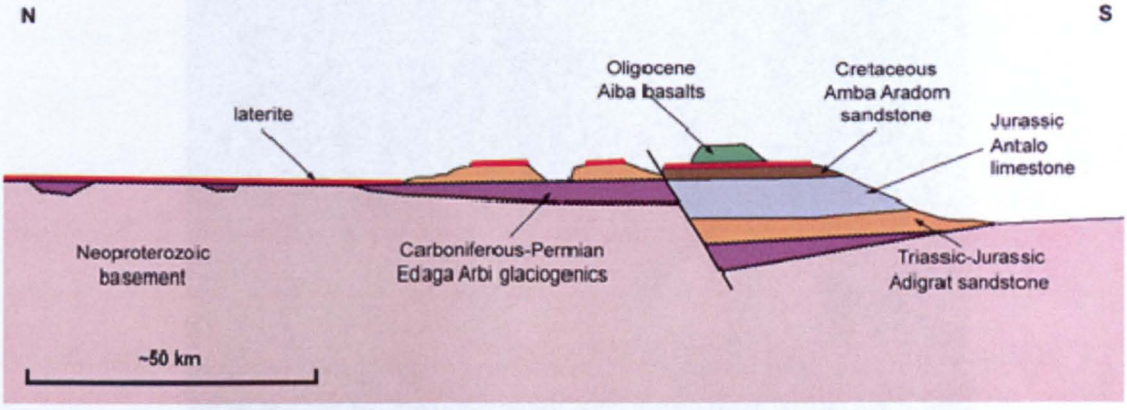


**Figure 7.3** Schematic section showing relationships between Neoproterozoic basement, Palaeozoic and Mesozoic sediments (see figure 7.3a; Bussert 2007), laterites and the African Surface, which is marked by unconformities beneath laterites and the Adigrat Sandstones (see figure 7.3b)

lateritisation, Mesozoic deposition and erosion. Moreover, it can be traced with some confidence wherever laterites have developed from crystalline basement or glaciogenic sediments. Relics of this surface are widespread (Schwartz & Germann

1999) and can be identified on satellite images as near-planar surfaces above which outcrop the glaciogenics and the Adigrat Sandstone - see the middle reaches of the Tekesse River basin, Chapter 4 (sheets ND37: 6, 7, 10) and Figure 5.36. Oligocene to Recent volcanism, sedimentation and erosion obscure it in other places.

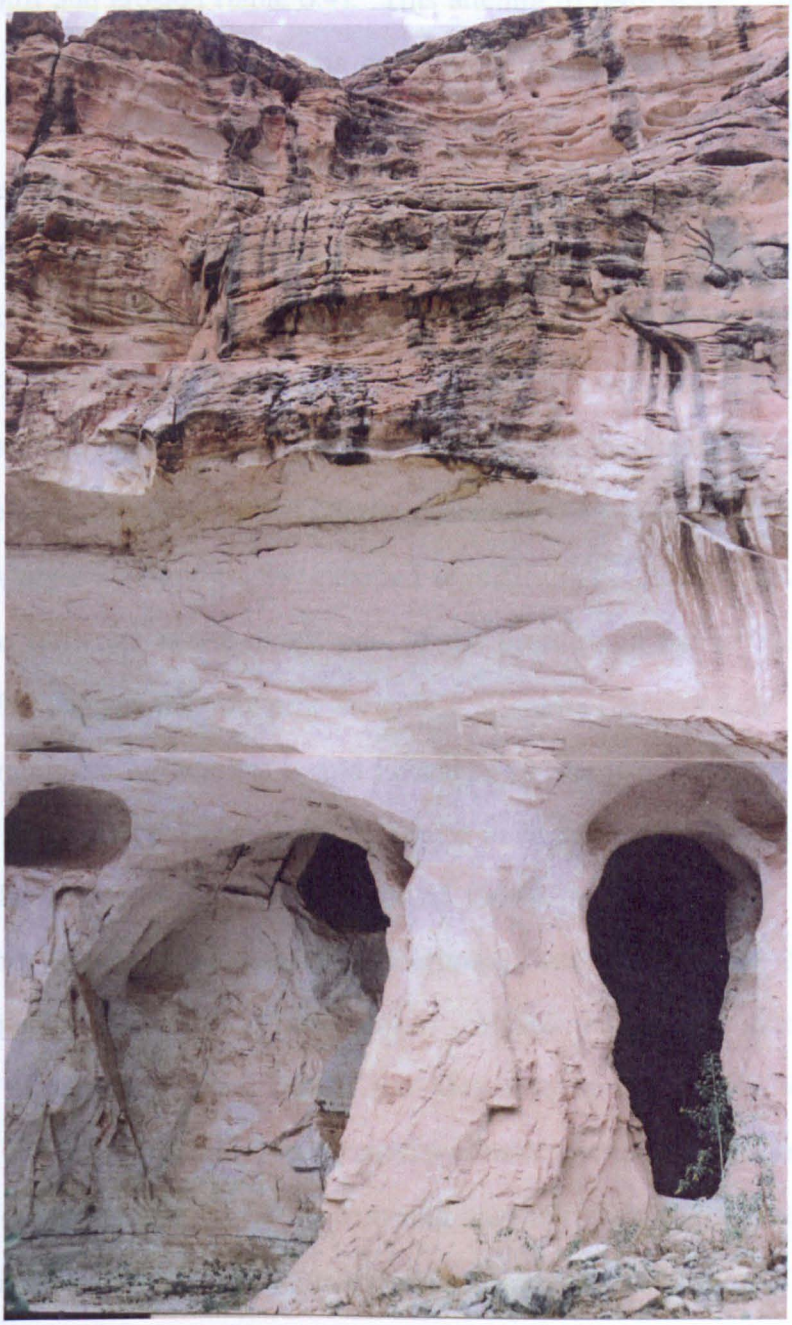

**Figure 7.3b** Vertical section through 50m of Adigrat Sandstones

In the light of the above discussion it is proposed that $^{40}Ar/^{39}Ar$ cooling-age data (section 6.6) from recently exposed basement granodiorites in the Red Sea Escarpment support the hypothesis that the African Surface is Carboniferous to

Permian in origin. Basement uplift ages record the initial formation of that surface, which has a maximum age circa 261 Ma. This is based on the terminal age for the period of uplift and erosion taken from the plot of age against altitude where a position correlation between age and altitude provides a record of the time span of the episode of uplift and erosion (table 6.4). This attempt to resolve the debate about a definition of the African Surface runs contrary to Burke & Gunnell (2008) who maintain that the African Surface is a composite erosion surface of about 30 Ma. Their hypothesis is backed by the received – but not evidentially supported – wisdom that lateritisation is coeval with CFB volcanism (Menzies *et al.* 1990, 1997; Burke 1996; Bosellini *et al.* 2001; Ukstins *et al.* 2002; Bosworth *et al.* 2005; Burke & Gunnell 2008). Perhaps one drawback to *their* assertion is that the African Surface is an erosional surface represented in places by ferricrete at the top of laterite profiles. The fundamental misconception that laterite constitutes an erosional ~30 Ma surface because of its *apparent* stratigraphic position is misleading. Laterite palaeosols are residual. The ferricrete is the oldest part of the profile and not as Schwartz and Germann (1999) suggest the youngest horizon in a laterite (Section 5.4). As already noted, a minimum age for laterites is mid Eocene, ~40 Ma, (Chapters 5 & 6) not ~30 Ma. What in fact Burke & Gunnell (2008) appear to be calling the African Surface is a construct - the laterite-CFB datum (Drury *et al.* 1994).

During the Upper Palaeozoic global climate was dictated by the longest continuous glaciation in the Phanerozoic. Hence conditions precluded the development of laterites. In contrast, the Mesozoic in NE Africa was an era characterised by tectonic stability, an equatorial climate and low-lying relief. Devoid of topographic barriers and subject to recurrent marine transgression and regression Eritrea and Tigray had moved to the tropics where laterites could form if it was wet enough. Palaeoclimatic indicators such as tillites and glacial diamictites were replaced by arkosic fluviatile sequences, beach sand and shallow-marine quartz sandstone which thin westwards (Beyth 1972; Bosellini *et al.* 1997; Bunter *et al.* 1998; Getaneh 2002; Bosworth *et al.* 2005). Deposition of the up to 680m thick

Adigrat Sandstone Formation, dominated the Triassic, early and mid-Jurassic (Mohr 1962). It was the first sedimentary sequence unconformably overlying the African Surface (figure 7.3). It was succeeded conformably in rift zones, such as the Mekele and Blue Nile basins, by Late Jurassic limestones, mudstones and evaporites of the Antalo Group. That in turn, is unconformably overlain by Cretaceous Amba Aradam unfossiliferous sandy sediments (figure 7.2; Beyth 1972; Merla1979; Bunter *et al.* 1998). The stratigraphic relationship between the different Mesozoic sedimentary units can be clearly traced in the Mesozoic rift of the Mekele Basin and Eritrea's Danakil Alps. There are no dates for the lower boundary of the Adigrat Sandstone (Bosellini *et al.* 2001) although in Tigray an amphibian mandible discovered in one basal facies indicates a Late Triassic age limit (Warren *et al.* 1998). Part continental, part marine in origin (Klein *et al.* 2007), much of the Adigrat Sandstone, which includes siliciclastic horizons that contain silicified fossil wood fragments, consists of well-rounded, well-sorted, white sandstone facies that vary hugely in thickness (figure 7.3b). In the absence of marine body fossils, intense bioturbation (figure 2.11) evenly distributed through several homogenous horizons in the basal and middle part of the sandstone reflect slow sedimentation rates (Tucker 1985), shallow marine incursion across a possible deltaic setting. A warm humid climate in the Late Jurassic is indicated by near-shore shelf limestones, shales and evaporites of the Antalo Group. Abundant lateritisation of the Adigrat Sandstone is identified throughout the region (section 4.3.4) while laterites pervade the Amba Aradam Formation conformably underlying the Tertiary Aiba flood basalts in the Mekele Basin (section 6.5; Beyth 1972; Bosellini *et al.* 1997). Predominantly fluvial with lacustrine and floodplain deposits the Amba Aradam Formation is continental in origin, whereas the palaeo-depositional environment of the Adigrat Sandstone is thought to be continental fluvio-deltaic to shallow marine (figure 2.11, 2.12; Mohr 1962; Beyth 1972; Bosellini *et al.* 2001).

Palaeogeographic constraints, the Mesozoic sedimentary package and the presence of laterite, suggest a uniformity of palaeoclimate and terrestrial

palaeoenvironment throughout the era, that may have been partly due to the peneplained African Surface and allowed for lateritisation of that surface from the Triassic onwards. This begs the question as to whether laterites were forming in the Mesozoic. The evidence amassed throughout this study, which suggests that they were forming can be grouped into four broad categories; compelling visual evidence, prerequisite conditions for Mesozoic to late Eocene lateritisation, evidence for Mesozoic laterites in other regions and reliable radiometric data.

*Compelling visual evidence*

Geologists who have visited the area report laterites stratigraphically in place within the Adigrat Sandstone and the Cretaceous Amba Aradam Formation (Beyth 1972; Bosellini *et al.* 1997; Getaneh 2002; Bussert & Schrank 2007). This study finds similar evidence (e.g. at the base of the Adigrat Sandstone in the Blue Nile gorge; see also figure 2.14, 2.24; section 4.3.4). At over 500 field localities, laterites are observed to develop from Mesozoic sediments or Neoproterozoic crystalline basement and Palaeozoic glacial sediments of the African Surface at the base of the Mesozoic. In itself, this observation is inconclusive. However, the trap basalts are never in direct contact with basement or glacial rocks and they never conformably overlie Mesozoic sediments. The important inference therefore is that laterite cover must have blanketed the region - just as it does in Saudi Arabia at As Sarat (Overstreet *et al.* 1977) - and remained intact (section 6.7.1). The laterite mantle always intervenes between CFBs and stratigraphically lower exposures so the deeply lateritised pre-volcanic surface - the laterite-basalt contact - is invariably in place. Where CFBs have been later removed by large-scale Neogene denudation, that laterite-basalt interface (Drury *et al.* 1994) is marked by vast lateritic floors such as the Shire, Shiraro and Adwa peneplains of Tigray and the sub-volcanic Shiketi plain (Mohr 2001) of the Eritrean plateau. These plains indicate long periods of tectonic stability and are in themselves an expression of the lateritised African Surface and the manner in which it evolved.

Further evidence for the emergence of laterites in the Mesozoic comes from

macroscopic and microscopic features of different horizons within the laterite profile itself (figure 4.2). Only then were conditions favourable for the development of the oldest parts of the profile, i.e. the ferricrete and mottle zone. There is abundant evidence of alternating continental aridity and humidity in Africa at the time (Fawcett & Barron 1998) and different laterite formations have been correlated with climate typical of the era by many (McFarlane 1983; Tardy *et al.* 1991; Rossetti 2004; Burke & Gunnell 2008). Across the region chemical weathering resulting in the dissolution of silica under alkaline conditions and the breakdown of feldspar and ferromagnesian silicates under acid conditions central to the formation of laterites could now take place given a suitable geochemical environment. Although acid conditions result from the influence of bacteria breaking down organic matter to produce organic acids and the oxidation of pyrite, an accessory mineral in many rocks, the most widespread source of acid waters, and thus hydrogen ions needed for silicate weathering, is atmospheric carbon dioxide ($CO_2$). When dissolved in rainwater $CO_2$ produces weak carbonic acid ($H_2CO_3$). Estimates of atmospheric $CO_2$ concentrations in the past have been based on a wide variety of proxies, each resulting in different ranges of maximum $CO_2$ concentrations. As yet, there is no universal agreement on $CO_2$ palaeo-levels except that they were far higher than the present value of 395 parts per million by volume (ppmV) for lengthy periods of the Phanerozoic. To resolve the issue, Breeker *et al.* (2010) compiled estimates of atmospheric $CO_2$ concentrations from 450 Ma to the present (figure 7.4) using a method based on the carbon-isotope proportions of carbonates found as nodules in a variety of palaeosols and a new calibration method. They assessed their findings by comparing their recalibration and previous soil-carbonate estimates of atmospheric $CO_2$ with a model of variations in the carbon cycle (GEOCARBSULF) linked to known episodes of Phanerozoic glaciation and other global climate indicators.

Figure 7.4 (red data) illustrates their findings. It shows clearly that since the end of the Carboniferous-Permian Gondwana glacial episode, atmospheric $CO_2$ levels from the Triassic to the end of the Palaeogene were at least 3 to 4 times higher than

that at present. From 200 Ma to ~35 Ma, greenhouse conditions prevailed reaching a maximum in the mid- to late Cretaceous according to Breeker *et al.*'s (2010) revised data. An increased delivery of acid rain and hydrogen ions to the weathering surface during the Mesozoic supports the hypothesis proposed here that intense tropical weathering and therefore lateritisation did take place in Eritrea and Tigray during this period and would do so in any region at suitable latitude with abundant rainfall. Higher global mean temperatures would also have ensured higher precipitation levels caused by greater evaporation of the ocean surface in the intertropical belt.

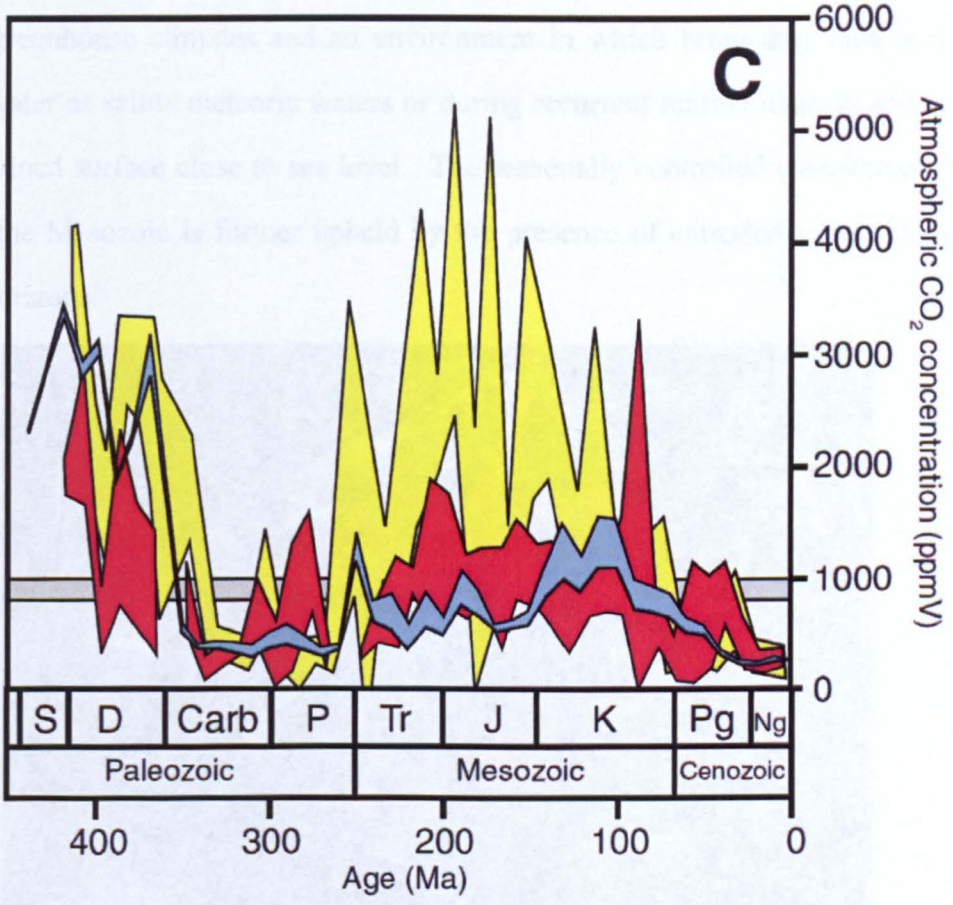


**Figure 7.4** Estimated atmospheric $CO_2$ concentrations since 400 Ma (from Figure 2c, Breeker *et al.* 2010). The yellow plot is a compilation of previous estimates, that in red covers Breeker *et al.*'s revised estimates and blue shows the output ranges from the GEOCARBSULF model. The grey bar around 1000 ppmV shows the range of estimates of future $CO_2$ levels by 2100 AD.

Minerals in the upper laterite horizons are characteristic of the seasonally fluctuating, hot, humid, greenhouse conditions that prevailed from the Triassic onwards. Throughout the region chalcedony (Kerr 1959; Mondadori 1983; Allaby

2008), is often found in the mottled facies (figure 7.5, 3.22b). Although the precise conditions needed for opaline quartz formation are unclear and reflect various chemical conditions such as a shift from alkaline to acidic conditions (N.B.W Harris, pers. comm. 2011) and the presence of salts and Fe oxide, if excess silica is available chalcedony can form (Whitten & Brooks 1987). Figure 2.56b illustrates that given salt, and thus alkaline conditions, in groundwater, all the necessary chemical conditions are met (i.e. a sufficiency of solute silica (Si) and iron (Fe) relative to depleted aluminium (Al)) for the deposition of chalcedony. Moreover, its deposition in laterites is indicative of an episode of percolating acid ground waters typical of ancient greenhouse climates and an environment in which brine may have entered ground water as saline meteoric waters or during recurrent marine transgression over a peneplained surface close to sea level. The seasonally controlled environment that typified the Mesozoic is further upheld by the presence of corroded quartz in upper laterite horizons.

**Figure 7.5** Chalcedony in the mottled zone (Shiketi)

Like the deposition of chalcedony the solubility of quartz by hydrolysis is a function of pH (Thornber 1992; Schulz & White 1998). These processes take place because of the environmental precondition for lateritisation that the land surface must

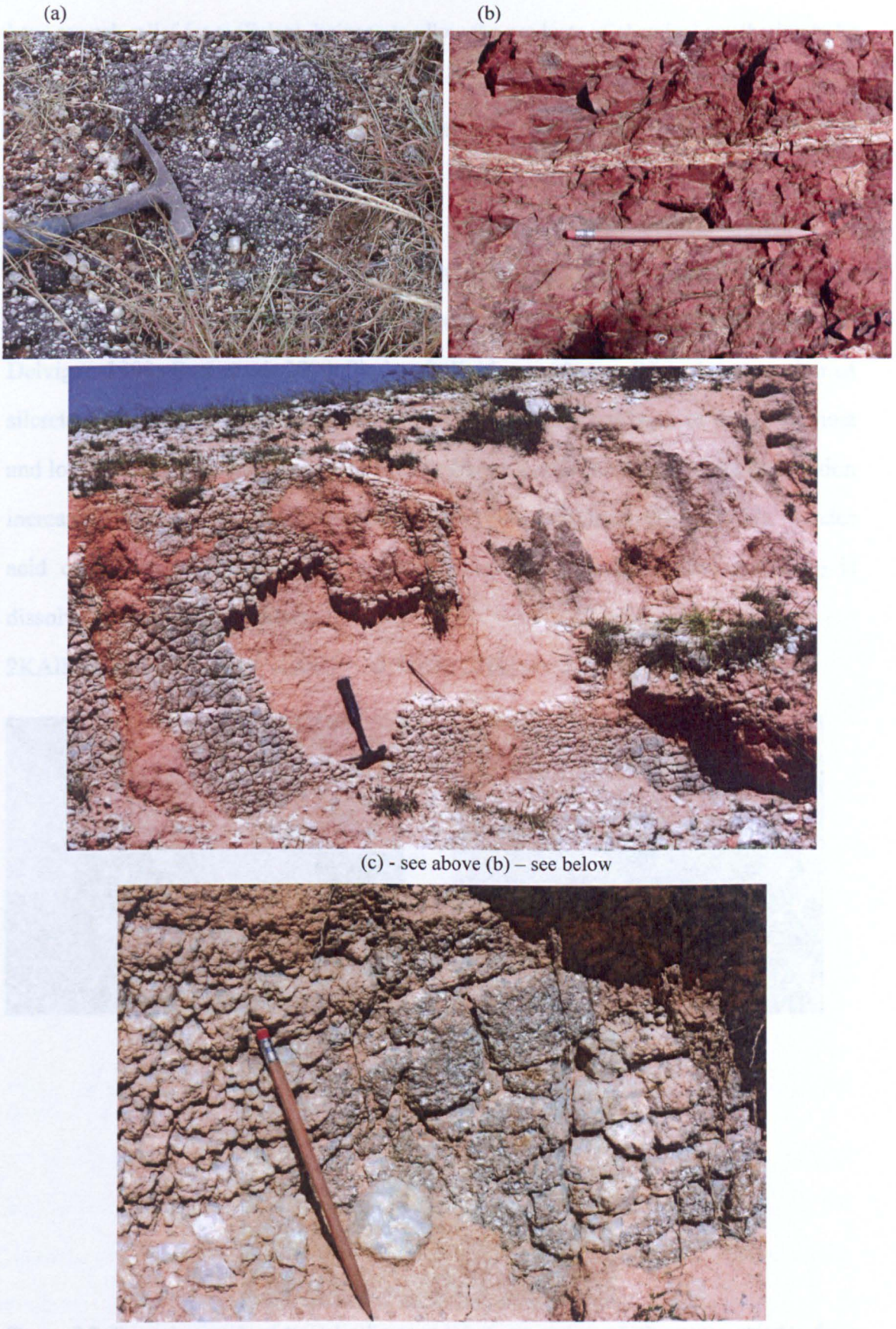


**Figure 7.6** Residual quartz inherited from the parent rock: (**a**) quartz clasts in ferricrete horizon (Dairo Kaolos) (**b**) vein quartz in mottle horizon (Paradiso) (c) thick quartz vein in mottled zone (Asmara – Keren road) (d) quartz veining cutting mottled zone - ferricrete boundary

have enough relief for sufficient drainage to allow the products of chemical weathering to be mobilised and leached (Butt & Zeegers 1992). If there is low relief the water tables remain static and there is no drainage; with strong relief and/or tectonic instability regolith erosion precludes lateritisation (Butt *et al.* 2000).

An important process in the formation of laterites under tropical conditions is volume decrease or shrinkage due to dissolution that partly results from quartz dissolution in the upper horizons of the laterite profile (Trescases 1992; Tardy 1997; Delvigne 1998; Butt *et al.* 2000; Taylor & Eggleton 2001). With the exception of silcretes (section 4.3.4), silica is usually at its lowest concentration in the uppermost and longest-lived ferricrete facies indicating that as depth decreases quartz dissolution increases (figures 2.55 - 2.57; Brantley *et al.* 1986; Schulz & White 1999). Under acid conditions, K-feldspars breakdown to clay minerals (kaolinite) and $SiO_2$ is dissolved in acid groundwater:

$$2KAlSi_3O_8(s) + 2H^+(aq) + H_2O(l) = Al_2Si_2O_5(OH)_4(s) + 2K^+(aq) + 4SiO_2(aq)$$

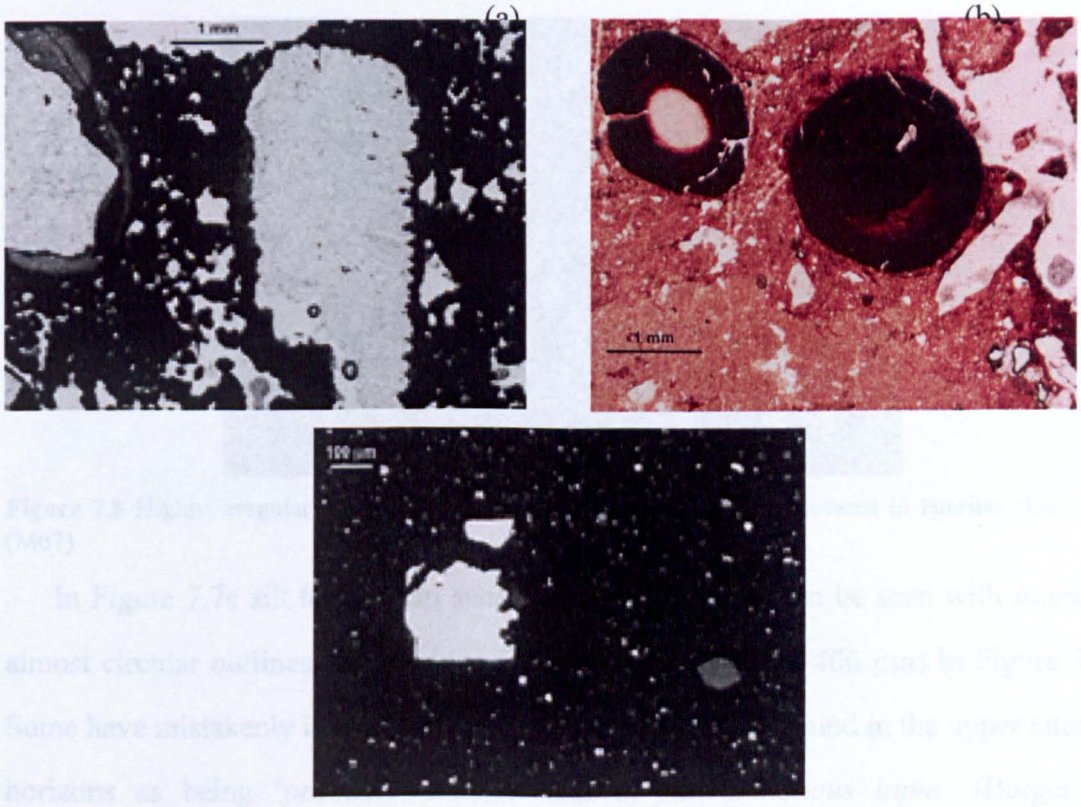


**Figure 7.7** Photomicrograph of typical relic corroded quartz grains, which are recognisable from theirhighly irregular shape, etch pits and re-entrant cavities: (**a**) ferricrete (M34i - mesa SE of Tseada Kristyan) (**b**) mottled zone (M58v - Areza) (**c**) clay zone sample (M67 - north of Mendefera). Scale bar = 1mm

Under alkaline conditions quartz is corroded and may be ultimately dissolved (Tardy 1997). Dissolved silica is also derived during lateritisation from the weathering of other silicates but if these are not available, quartz is dissolved by percolating alkaline waters enriched with potassium and sodium ions released during lateritisation of the alkaline-feldspar rich rocks granite and granodiorite.

In laterites formed from Neoproterozoic basement intact quartz veins in Horizon 2 and skeletal fragments, tusk-like clasts and residual vein quartz in Horizons 3, 4 and 5 (figure 7.6) are often visible, so dissolution of quartz, as opposed to release of silica to solution, is not consistent throughout the laterite profile. Thin sections of ferricrete containing quartz fragments show that they often have highly complex grain boundaries with re-entrant cavities (figure 7.7a, b). Similar grains, albeit much smaller, are common in Horizons 3 (figure 7.7c) that developed from quart-rich bedrock, such as granitic basement. Such grains show convincing evidence of having been corroded by partial dissolution.

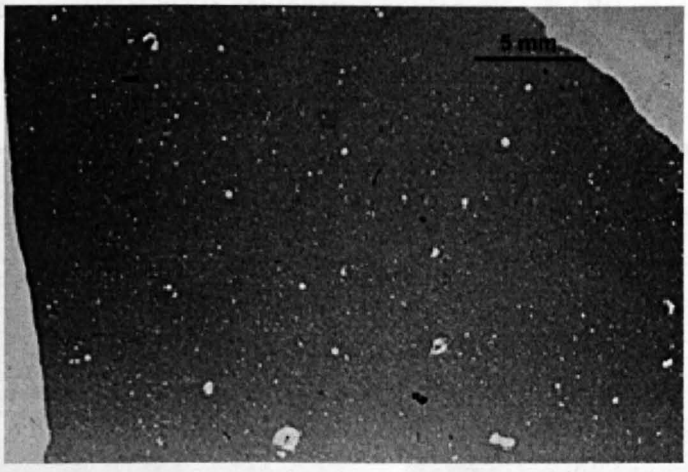


**Figure 7.8** Highly irregular and near-spherical relic quartz grains incorporated in lateritic clay zone (M67)

In Figure 7.7c silt to medium sand-sized quartz grains can be seen with rounded almost circular outlines, better viewed at a larger scale (~60-400 μm) in Figure 7.8. Some have mistakenly identified these near spherical grains found in the upper laterite horizons as being '*probably aeolian*' and of '*allochthonous input*' (Borger & Widdowson 2001). Evidence that windblown sand grains of desert origin have penetrated 10 or more metres downwards through residual soil forming in a humid

seasonal climate has not been found in this study and is unlikely. Most authors accept that quartz in laterites is residual (Firman 1993; Schellmann 2002, 2003; Butt & Zeegers 1992; Nahon & Tardy 1992; Delvigne 1998; Butt *et al.* 2000; Andrews Deller 2006) and has a direct relation to its silicic parent rock (Tardy 1997; Trescases 1992; Vasconcelos 1999; Butt *et al.* 2000). During sub-surface laterite formation, quartz veins or fragments of quartz commonly preserved throughout the profile are strongly corroded but never displaced (figure 7.6b; Nahon & Tardy 1992) convincing evidence that this mineral has *not* been imported. Spherical grains and fragments of quartz partially trapped in and between pisoliths or fully incorporated in their cortex, which developed in situ, also proves that the quartz was not introduced later (figure 7.9 a, b, c; Delvigne 1998). Solution rounding of minute quartz clasts, like etch pitting, results from corrosion-dissolution. Angular surfaces of each grain are dissolved leading to the formation of sub-rounded to near perfect spheres of quartz (Crook 1968; Schulz & White 1999; Lidmar-Bergstrom *et al.* 1999; Taylor & Eggleton 2001) a somewhat more convincing explanation for the common presence of round quartz grains in laterites observed in the Eritrea.

(a) (b)

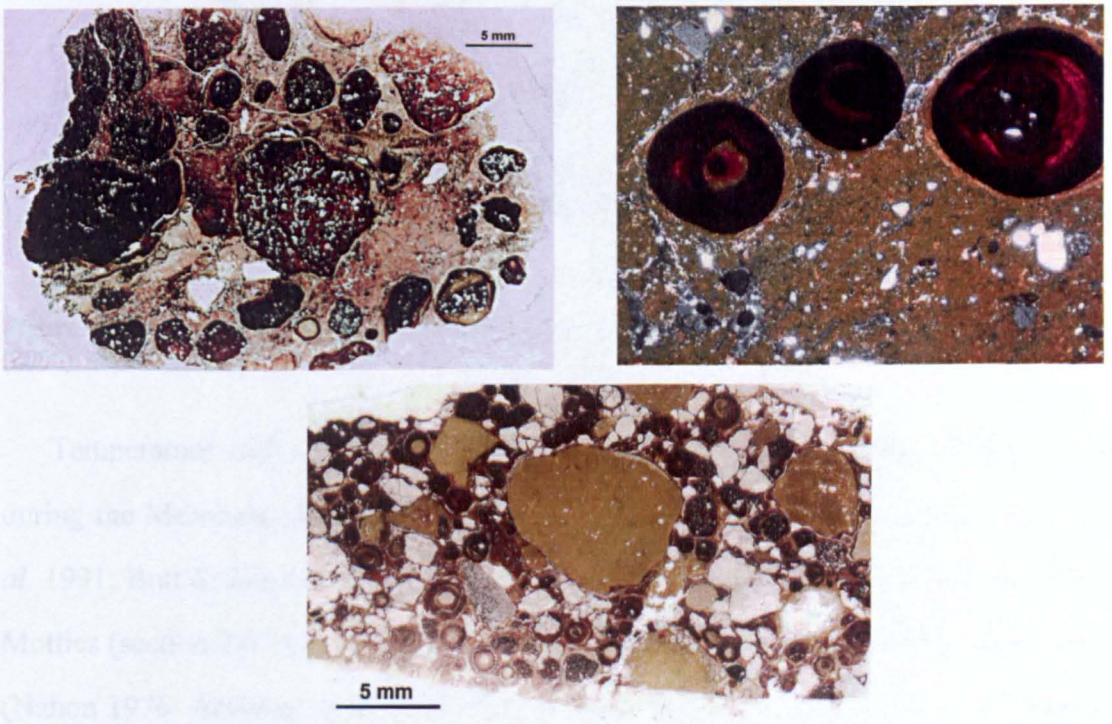


**Figure 7.9** Highly irregular and near-spherical relic quartz grains incorporated in lateritic (a) ferricrete (M309 - S of Himberti) (b) mottle (M66I - S of Senafe) (c) mottle (M71i - Adiguila)

Mason (1966) in his authoritative book on the basic principles of geochemistry provides experimental evidence for a process that explains dissolution of quartz during lateritisation. Figure 7.10 shows that the solubilities of quartz and aluminium oxide vary with pH. For silica, solubility increases steadily as conditions become increasing alkaline, until at ~pH 10.0 it increases rapidly and is joined by aluminium oxide that is insoluble under natural conditions. As groundwater becomes more saturated with dissolved anions (e.g. $HCO_3^-$, $SO_4^{2-}$) their negative charges neutralise the hydrogen ions ($H^+$), driving up pH and so increasing alkaline conditions and allowing for quartz corrosion.

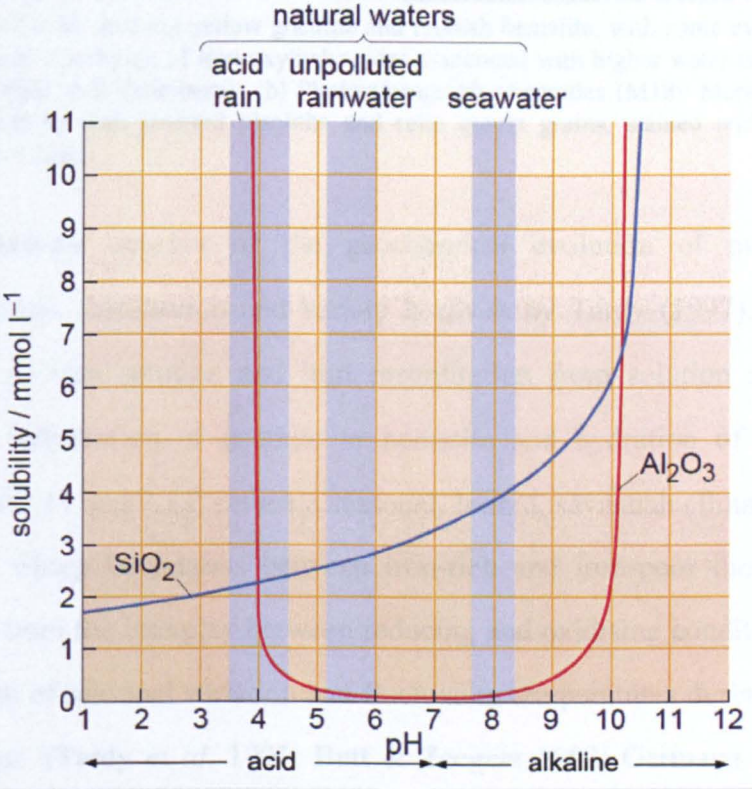


**Figure 7.10** The variation of the solubilities of silica and aluminium oxide with pH. From Webb (2006), after Mason (1966).

Temperature and water determine the rate of chemical reactions, which is why during the Mesozoic, geochemical weathering predominated in the tropics (Tardy *et al.* 1991; Butt & Zeegers 1992; Germann *et al.* 1994; Butt *et al.* 2000; Renton 2006). Mottles (section 2.6.3) in horizons 4 are further evidence of such a weathering regime (Nahon 1976; Ambrosi *et al.* 1986; Nahon & Tardy 1992; Tardy 1997). Fluctuation between oxidation and reduction is clearly visible in the colour changes or mottles it

causes in the profile (Trescases 1992) the redistribution of iron being manifest as splotches of colour.

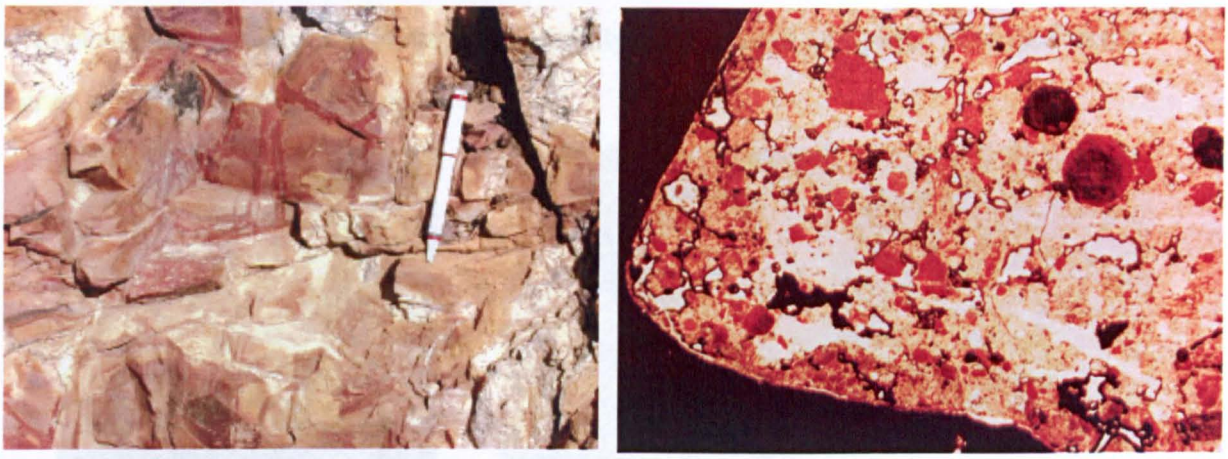

**Figure 7.11** Mottled zone showing yellow goethite and reddish hematite, with some evidence of later leaching by reductive dissolution of iron oxyhydroxides associated with higher water table and wetter conditions. (a) Mottled zone (Himberti) (b) Photomicrograph of mottles (M18v Mereb – Tera Imni road) showing kaolinite with isolated pisoliths and relic quartz grains, stained and cemented by hematite. Scale bar = 1mm

A comprehensive account of the geochemical evolution of mottles, their complexity, genesis, distribution and variety is given by Tardy (1997). Suffice to state here that as iron solution and iron precipitation from solution over several generations of dehydration of goethite to hematite and hydration of hematite to goethite (figures 7.11 and 7.12) reflect a seasonal, humid, savannah climate typical of the Mesozoic. Sharp boundaries between iron-rich and iron-poor mottles (figure 7.12), resulting from the interplay between reducing and oxidising condition, are also a clear indication of seasonal variation and fluctuating temperatures during protracted laterite evolution (Tardy *et al.* 1991; Butt & Zeegers 1992; Germann *et al.* 1994; Tardy 1997; Vasconcelos 1999; Burke & Gunnell 2008). Leached zones, recognised as palaeoenvironmental indicators and a component feature of the African Surface (Marker *et al.* 2002), result from reductive dissolution of iron oxyhydroxides as $Fe^{2+}$ becomes soluble during a wetter climate associated with a higher water table. In contrast, iron-stained mottles develop with the onset of oxidizing conditions and a fall in the water table, causing insoluble $Fe^{3+}$ to precipitate. Although Si, Al and Fe dominate the ferricrete and mottled horizons - an important identifying characteristic

of laterites - other elements are also precipitated or redissolved according to redox conditions which may affect modern groundwater chemistry (Chapters 2, 8). However, no element in laterites is ever totally immobile or completely leached (Butt *et al.* 1991, 2000; Butt & Zeegers 1992).

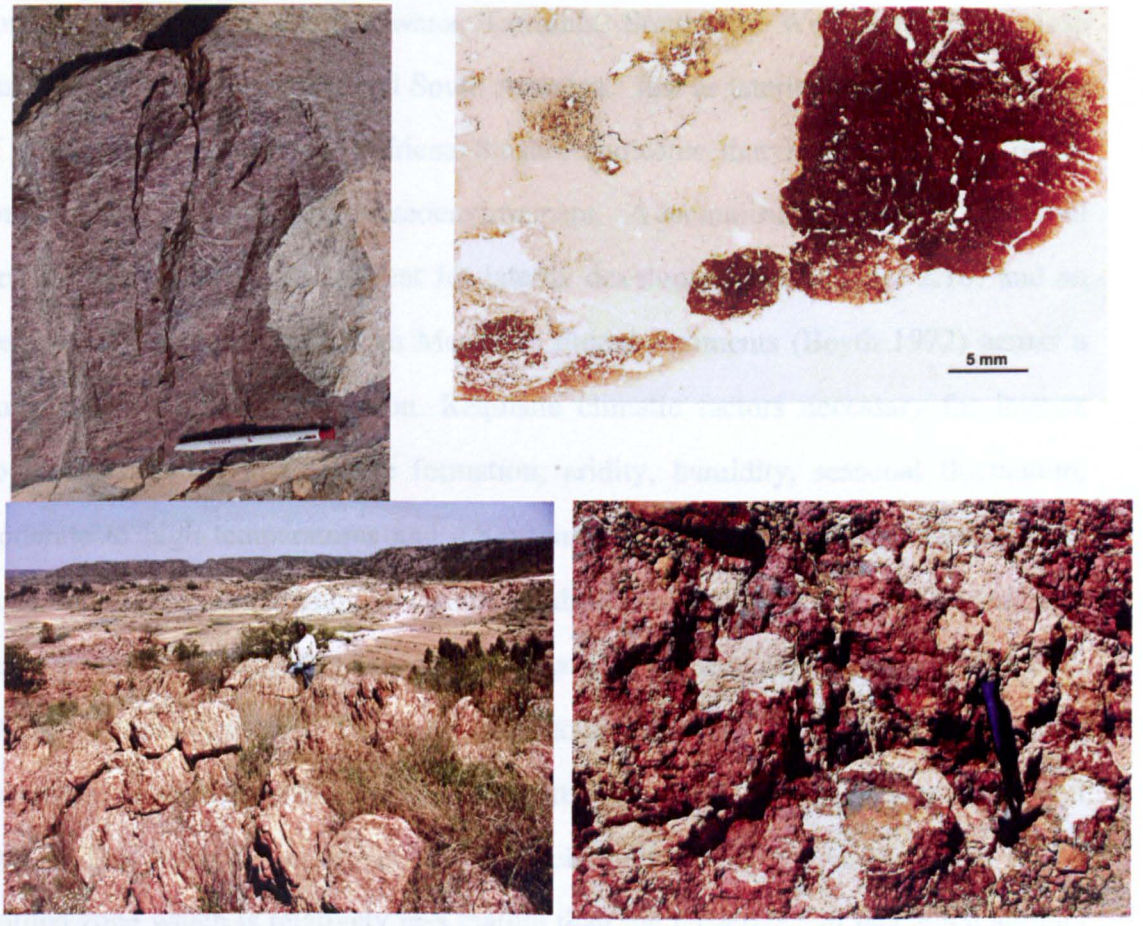


**Figure 7.12** Mottled zone showing sharp boundaries between iron-rich and iron-poor mottles; leached white areas formed during wet period when water table high and conditions reducing so that iron reduced from insoluble $Fe^{3+}$ to soluble $Fe^{2+}$: (a) mottle formation (Adi Teklay) (b) thin section of mottles (M315b - Embeyto) - Scale bar = 5mm, (c) vermiform mottles (Embeyto) (d) the predominance of dehydrated hematite as opposed to hydrated goethite suggests that the constantly hot humid climate was relatively drier during this episode of lateritisation (Shiketi).

*Prerequisite conditions for Mesozoic lateritisation*

All necessary conditions (section 7.2) for the formation of laterites in NE Africa are met in the Mesozoic. The African Surface, across which later events are preserved as rocks, including the laterites, was ground flat by the glaciation and progressive later erosion providing a necessary condition essential for laterite formation - a flat or gently undulating peneplain marginally above sea level (Dainelli

1943; Bohannon *et al.* 1989) since the Triassic. The very presence of laterites is a good guide to ancient peneplains and the coexistence of both is evident throughout Africa (section 7.2; Chapters 2, 4) an observation accepted by the majority of geologists. Examples of this relationship (detected using ASTER images) occur in Somalia, Sudan, Ogaden, Botswana, Tanzania, South and West Africa and close parallels are found in Arabia and South America. Just as laterites signal the presence of peneplains, arguably the African Surface indicates that laterites were a major component of the Mesozoic palaeoenvironment. A tectonically quiescent, terrestrial land surface is also a requirement for laterite development (see figure 2.10) and an absence of calcareous cement in Mesozoic fluvial sediments (Beyth 1972) across a study region fulfils this criterion. Requisite climatic factors necessary for intense tropical weathering and laterite formation; aridity, humidity, seasonal fluctuation, moderate to high temperatures and a savannah environment - already discussed in some detail - are all evident. More arid conditions prevailed during the Triassic and Jurassic when it is suggested here that, (Horizon 5), the ferricrete formed (Tardy *et al.* 1991). Moreover, there is ample evidence to suggest that the Cretaceous, although interrupted by cooler episodes, was much hotter and wetter overall (Burke & Gunnell 2008). This being the case, conditions would be ideal for the development of the mottled zone which is relatively less mature than the ferricrete. In fact some authors suggest that dehydrated hematite would have formed when prevailing temperatures were generally hotter whereas hydrated goethitic mottles are the product of episodes when temperatures were cooler (Tardy 1997; Burke & Gunnell 2008). Finally the progress of chemical weathering is slow and for a thick laterite profile to form a very long time is required (Butt & Zeegers 1992; Trescases 1992; Vasconcelos 1999; Butt *et al.* 2000). The Mesozoic lasted some 190 million years, which seems adequate time for each phase (Horizons 4 and 5) of the profile to develop.

*Convincing evidence for Mesozoic laterites in other regions*

Although inter-regional and continental correlation of lateritic occurrences throughout the world is at best speculative, many authors provide convincingly

evidence for the presence of Mesozoic laterites in other regions (Dainelli 1943; Tardy *et al.* 1991; McFarlane 1991; Bird & Chivas 1993; Merino 1993; Thomas 1994; Tsekhovskii *et al.* 1995; Ruffet *et al.* 1996; Tardy 1997; Mohr 1971, 1999; Twidale 2000; Thiry 2000; Feng & Vasconcelos 2001; Temgoua *et al.* 2002, 2003; Gilkes *et al.* 2003; Pillans 2004; Rossetti 2004; Skarpelis 2005; Chandran *et al.* 2005; Retallack 2010).

Carboniferous to early Permian glaciation of NE Africa affected most of Gondwanaland (Ziegler *et al.* 1997). West, South and Central Africa, Australia, South America and Arabia were all subjected to massive denudation, erosion and the subsequent lateritisation of a Mesozoic landscape (figure 2.8). Lateritisation is documented with radiometric ages from: South Australia (Bird & Chivas 1993; Twidale 2000; Gilkes *et al.* 2003), Eastern Australia (Feng & Vasconcelos 2001) and the Yilgarn Block of Western Australia (Drury & Hunt 1988, 1989; Twidale 2000). The laterites of Kangaroo Island, South Australia are overlain by mid-Jurassic basalts, confirming the true antiquity of Gondwanan lateritisation (Twidale 2000). As NE Africa was part of the same landmass as Australia, during the Triassic and Jurassic, it is entirely possible that laterites were also forming during this period in Eritrea and Tigray.

After fragmentation of the super-continent of Gondwana during the Cretaceous (Partridge 1998; Guiraud 2005; McDougall 2008) lateritisation is documented as continuing in Amazonia (Rossetti 2004) and Cameroon (Temgoua *et al. et al.* 2002, 2003), whereas Ruffet *et al.* (1996) produce radiometric ages in Brazil. It seems highly likely therefore, that as Eritrea and Tigray were subject to the same geological controls as the rest of Africa and South America, lateritisation would also continue throughout the Cretaceous.

Even though laterite occurrences are documented and reported in India (P.D. Phillips, pers. comm. 1998; Chandran *et al.* 2005; Ranganathan & Jayaram 2006), further work is required before meaningful comparisons can be dawn here with other continents. Although India entered the tropics during the Cretaceous following final

break-up of Gondwana (Tardy *et al.* 1991) and Cretaceous lateritised surfaces are reported as widespread on the Deccan Traps (Widdowson 1997, 2007; Gunnell & Widdowson 1999), Ollier and Sheth (2008) in their detailed fieldwork in the area find no evidence of what is commonly accepted as laterite. They report a total absence of the clay zone and only rare occurrences of underdeveloped mottle. For these reasons, and the fact that as yet there are no documented instances of radiometric ages of laterites in India, that continent is not considered further.

*The ancient palaeosols are long-lived: reliable radiometric data*

In Eritrea and Tigray reliable radiometric dates indicate an Early Eocene minimum age limit for the clay zone (Chapters 5, 6), the least evolved horizon in the laterite profile. Consequently higher and therefore older mottled and ferricrete facies may tentatively be ascribed to the time span between circa 52 Ma and 261 Ma, the maximum age for the African Surface. Weathering is most advanced in the ferricretes so a maximum radiometric age for laterites in the region would necessarily come from Horizon 5. The oldest minimum ages obtained in this study are obtained from laterites that are the product of basement lithologies (Chapter 6). Arguably therefore laterites evolved from Neoproterozoic basement rather than from the Mesozoic sediments that elsewhere unconformably overlie the peneplained African Surface. Moreover the thickest weathering profiles derive from granitic rocks. All estimates by others indicate that granite-sourced laterites form more slowly than those from other lithologies (Butt *et al.* 2000; Nahon 2003). Furthermore, as the most widespread Mesozoic sedimentary formation, the Adigrat Sandstone, is diachronous, exhibits rapid changes in thickness (rises 3 – 20m in 50m) and is entirely absent in places (see figure 7.3), laterites may have begun to form at the same time as and alongside Mesozoic sediments. This would give them a maximum Middle Triassic to Middle Jurassic age limit. This could only happen if laterite development outstripped erosion, which continued throughout the Mesozoic. In other words, for a thick laterite profile to begin and continue on its lengthy evolution to maturity, the progression of chemical weathering and downward migration of the weathering front would have to

exceed the rate of erosion (Nahon 1976; Tardy 1997; Butt *et al.* 2000).

Laterite development continued into the Cenozoic and the cluster of new radiometric ages for alunite in laterites presented in this study (table 6.1) provide evidence that clay facies were forming during the Eocene (and possibly earlier). Consequently since laterite profiles commonly reflect variations in soil-forming environments, chemical processes and climate during their evolution, the clay zone, 'younger' than both mottled and ferricrete horizons, signals a marked change in conditions. Most authors accept that this change marked the close of the Mesozoic (Vasconcelos *et al.* 2008), another point in favour of 'older' mottled and ferruginous zones being Mesozoic.

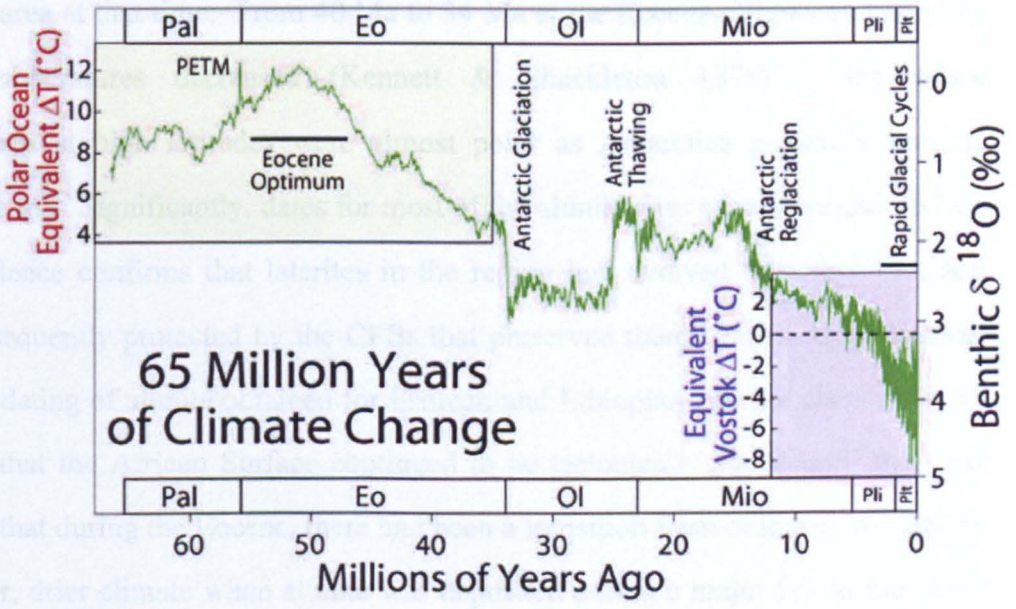


**Figure 7.13** Climatic variability during the Cenozoic (Schrag *et al.* 2010)

Following the hothouse conditions of the Cretaceous, which extended into the early Tertiary, there was a world-wide shift to overall global cooling, greater aridity and shorter episodic climatic oscillation (figure 7.13). This trend was interrupted at the Palaeocene/Eocene boundary (~56 Ma) by a pulse of global warming during which there was a global increase in the deposition of kaolinite on the ocean floor

(Thiry 2000; Bolle & Adatte 2001; Banerjee *et al.* 2012). Banerjee *et al.* (2012) find a sudden rise in the proportion of kaolinite (a higher kaolinite:smectite ratio) in marine sediment cores from offshore eastern USA, just before the C-isotope signature of the warming pulse. They use oxygen-isotope data to show that kaolinite was more likely to have been produced by erosion of products of earlier lateritisation - most likely Cretaceous - than if the kaolinite had been produced by increased weathering during the Palaeocene-Eocene global warming. They attribute the increased supply of kaolinite in the early North Atlantic to an increase in seasonal rainfall and erosion of the continental surface. However, the clay zone in the Eritrean-Ethiopian study area is the most extensively preserved of the upper three laterite horizons in the profile and shows no evidence that lateritisation was interrupted or that profiles were truncated in the study area at that time. From 40 Ma to 34 Ma at the Eocene-Oligocene boundary global temperatures decreased (Kennett & Shackleton 1976). Sea-surface temperatures at high latitudes were almost polar as Antarctica gradually became covered in ice. Significantly, dates for most of the alunite ages cluster around 40 Ma. Field evidence confirms that laterites in the region had evolved to completion and were subsequently protected by the CFBs that preserved them in their original state. $^{40}Ar/^{39}Ar$ dating of alunite obtained for Eritrean and Ethiopian lateritic clays not only indicates that the African Surface continued to be tectonically stable until the CFB event but that during the Eocene, there had been a transition from hothouse conditions to a cooler, drier climate when alunite was deposited during a major fall in the water table as the clays underwent desiccation. Furthermore, even though alunite is precipitated from ground water at low temperatures and is only susceptible to argon release at very high temperatures so ages are not easily reset (Vasconcelos *et al.* 1994; Itaya *et al.* 1996), its position deep within the profile (figure 7.14) ensures that any geochronological data are reliable and not subject to distortion in the same way as unprotected laterites of West Africa and Western Australia.

The appearance of alunite in the youngest part of the laterites, nowhere later than ~35 Ma and for the most part 5 or more million years beforehand, probably marked

the end of lateritisation in Eritrea and Tigray. Extreme weathering processes require saturation of the land surface with groundwater and desiccation would have halted laterite formation. At 30 Ma in the study area the products of chemical weathering, laterites, were sealed off from weathering by repeated volcanic eruptions and an up to 2km thick cap of flood basalt. Only a profound tectonic change and massive erosion could have exposed the now 'fossilised' laterites.

Coupled with Ar-Ar basement cooling ages, the clay ages help resolve the debate about which uplift patterns best explains rifting in the Ethiopian-Eritrean Red Sea, Escarpment (figure 7.15; Drury *et al.* 1994, 2006; Ghebreab 1998) and the nature of the topography at the onset of CFB volcanism circa 30 Ma to 34 Ma (section 2.2.4, 6.6, 6.7; Drury *et al.* 2006; Moucha & Forte 2011; Pik 2011). Interpreted in different ways by different authors, the crustal bending hypothesis (Ghebreab & Talbot 2000) is preferred here to the idea of Miocene uplift controlled by a single fault at the foot of the escarpment (Drury *et al.* 1994).

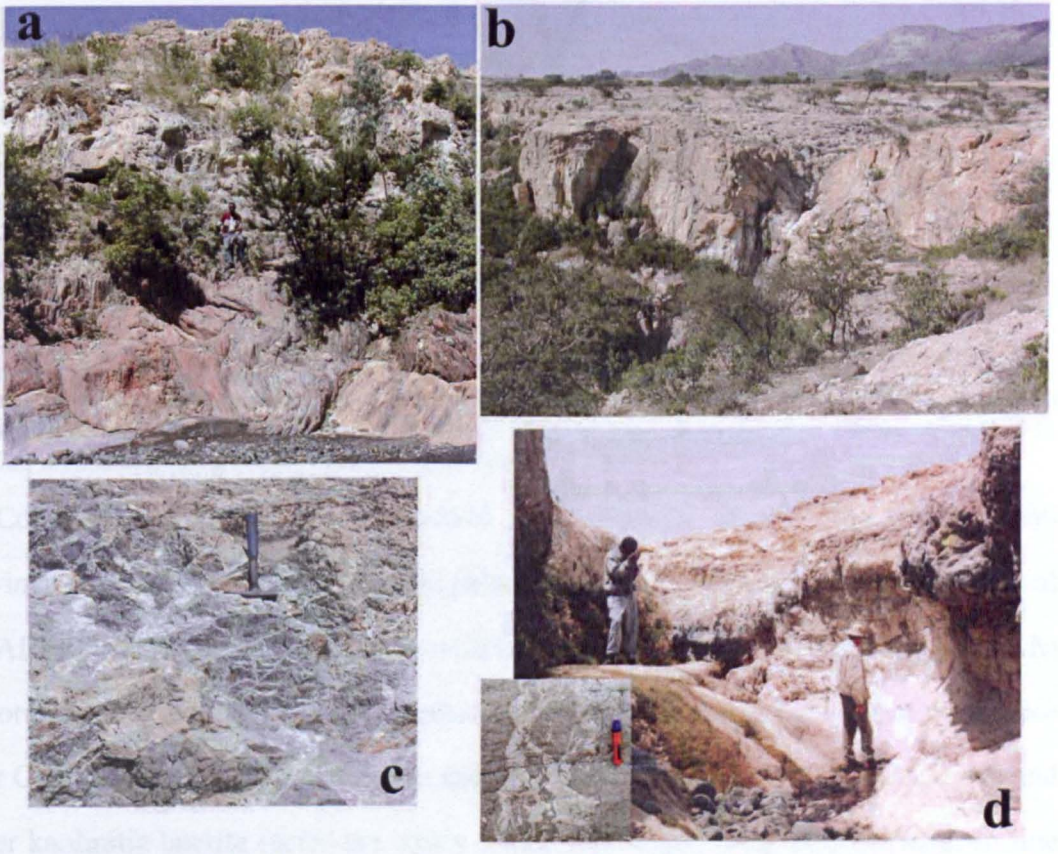


**Figure 7.14** Features of the thick laterite clay zone at Adi Felesti: (a) figure at contact between clay zone and pink saprolite (Horizon 2) developed on granitic basement; (b) terrace developed at the clay-mottled-zone boundary; (c) alunite veining in clay-zone; (d) upper clay zone with alunite veins (inset) – B. Nagassi & Dr S. Drury for scale

As to any change in the surface topography caused by the flood basalts prior to that uplift (section 7.3), recent modelling of mantle convection beneath Africa (Moucha & Forte 2011) attempts to predict how deformation of its pre-existing surface evolved since the Late Oligocene. Their model uses an assumption of initial topography at 30 Ma as a 'point of departure'. They suggest from global modelling of mantle dynamics that Africa was dominated by a broad N-S swell that reached an elevation of ~1.0km trending from what at present is 36°N, 40°E (northern Levant) to 4°N, 36°E (northern Kenya).

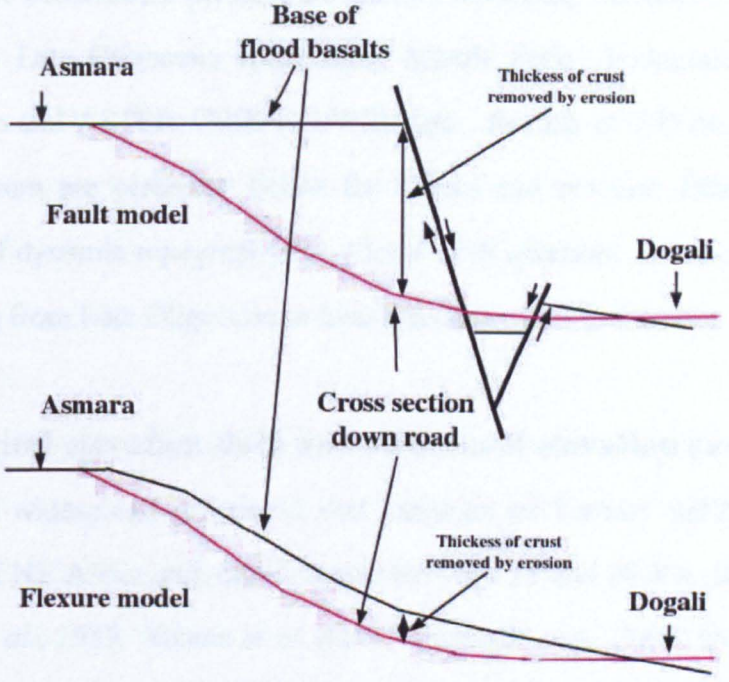


**Figure 7.15** Simple sketches showing two models for Neogene uplift affecting the CFB-laterite datum in the Eritrean-Ethiopian Escarpment. Top: Major fault at base of escarpment (Drury *et al.* 1994); Bottom; monoclinal flexure (Ghebreab & Talbot 2000)

Conveniently, Oligocene continental flood basalts of the Ethiopian-Yemeni province rest conformably on lateritic palaeosols that formed on the northern part of the African Surface. Their extent lies within the postulated regional dome of Moucha & Forte (2011). The CFB-laterite contact forms a datum for tectonics that took place after CFB outpouring. The distinctive spectral properties of the upper ferruginous and lower kaolinitic laterite facies are easily traced regionally using ASTER data. In line with Burke and Gunnell (2008), Moucha and Forte's (2011) starting parameters

predict that the laterites would have been eroded from the crest of the pre-30 Ma topographic swell before CFB outpouring began at ~30 Ma. Mapping the laterites across the Yemen-Eritrea-Ethiopia region should therefore either verify or refute their model. The results presented in Chapters 4 and 5 undoubtedly demonstrate a consistent regional presence of ~40 MA laterites beneath 30 Ma CFBs that suggests the basis on which the above authors (Burke & Gunnell 2008); Moucha & Forte 2011) found their work is flawed.

Having formed on a peneplain close to sea-level the present topographic elevation of laterite occurrences presents a means of modelling the actual topography produced by post- Late Oligocene uplift using Shuttle Radar Topography Mission (SRTM) elevation and ASTER VNIR to SWIR data. Results of 3-D mapping of the laterite-CFB datum are presented below for Eritrea and northern Ethiopia. These test the model of dynamic topography for Africa's NE quadrant and reveal the surface shape resulting from Late Oligocene to Late Miocene uplift in the area.

## 7.3 Digital elevation data and structural elevation surface

There is widespread agreement that initiation of Tertiary uplift and erosion of the whole of NE Africa and Arabia began between 25 and 20 Ma (Bohannon *et al.* 1989; Omar *et al.*, 1989; Abbate *et al.* 2001; Ghebreab *et al.* 2002; Drury *et al.* 2006). Yet little is known about the surface expression of uplift, which is thought to be a result of the Afar Plume and tectonic readjustment of the crust. Identification of the kaolinite-rich clay zone in laterites using Landsat 742 or ASTER 631 images (see Chapter 4), allows for mapping of the variation in height of the base of the laterites, given suitable topographic elevation data. There are two global data sets that map elevation, derived from ASTER data and from the Shuttle Radar Topography Mission (SRTM) that are useful for this purpose (section 4.8). ASTER scenes with minimal cloud cover are used to produce digital elevation models in 1° latitude by 1° longitude subdivisions, for the Earth's land surface between 83°N and 83°S. The elevations in the ASTER DEM have a precision of about ±20m.

SRTM topographic elevation data are available for land areas between 60° N and 56° S. They were generated using radar interferometry during a dedicated mission of NASA's Space Shuttle in February 2000 (Farr *et al.* 2007). Although processed to give a 1 arc second (~30m) horizontal resolution, data for areas outside the USA are available only at 3 arc second (~90m) resolution. The precision of elevation values is between ±6 and 9 m, i.e. considerably better than the ASTER DEM. Because of the greater vertical precision, data from the SRTM were used in estimating variations in the elevation of laterite occurrences: the lower horizontal resolution of SRTM has no bearing on these measurements as they were spaced at least 2-3km apart.

ASTER 631 or Landsat 742 images were displayed over SRTM data using TNTmips desktop mapping software, so that elevation values were shown for points over which the cursor was placed. Occurrences of the distinctive sky-blue kaolinitic clay zone in the laterite profile were sought in the images. In some areas, distinctive small patches of kaolinite-rich saprolite remain on the tops of hills, offering some opportunity to extend the coverage of digitised points. The UTM co-ordinates and elevation were digitised for each selected occurrence (figure 7.16). This was done for much of the Eritrean and northern Ethiopian plateaus and the lower plains to the west of them between 12.5° and 18° N, where there are outcrops of both flood basalts and the underlying laterites.

Between 9.4° and 11° N, in the middle reaches of the Blue Nile, laterites beneath the flood basalts are ubiquitous. From 11° to 12.5° N the geology of the Ethiopian Highlands is totally dominated by flood basalts, younger shield volcanoes and Miocene to Pliocene sediments and volcanics of the Lake Tana basin, so laterites are completely obscured by younger rocks. This results in a major gap in points showing elevations of the laterite datum (figure 7.16). The mountainous area of northern Eritrea, north of 15.5° N is effectively a dissected plateau, with relics of former drainage courses etched into it (S.A. Drury, personal communication 2001), from which the laterites have been almost completely eroded. However, in the eastern and north-western parts of this highland area there are several relic plateaus, locally

known as *rora* that are up to 2700m high. Drainages from them contain fragments of ferricrete and there are small outcrops of laterite above late Palaeozoic glaciogenic strata (A. Kibreab, personal communication, 1998). A high proportion of the *rora* surface is deeply weathered saprolite that supports isolated agricultural communities. Elevations in this area were digitised for points on the *roras* and for intervening isolated peaks, in an attempt to model a surface that represents the minimum possible elevation of the laterite datum.

A surface was fitted to the digitised points with TNTmips Minimum Curvature software that computes a minimum tension surface. The method fits a two-dimensional cubic spline surface to the input points (Smith 2009). A bendable plastic ruler is an analogue version of a one-dimensional spline that allows a smooth curve to be fitted through points plotted on a graph of two variables, with the minimum amount of curvature necessary for a fit. A two-dimensional spline function is analogous to a sheet of rubber fabric 'stretched over' points distributed in three-dimensional space to form a smooth surface. The 'tension' of this 'rubber sheet' determines the smoothness of the fitted surface. In practice the Minimum Curvature algorithm depends on a number of parameters being set carefully. As it uses an iterative approach that works from coarse to finer sizes of output cells, the initial grid size chosen is critical. Because tension (between 0.0 and 1.0) determines the smoothness with which the final surface is 'stretched over' the data points, low values of tension can overly emphasise inaccuracies and produce a 'rough' fitted surface full of 'pits' and 'spikes'. High values of tension produced a more useful surface. The selected surface was fitted with a grid size of 500m, using a 50-cell search radius, a tension of 0.75 and an initiating grid size of 16 cells.

The absence of data between 11° to 12.5° N makes it inappropriate to place any reliance on the fitted surface between those areas that are rich in points (figure 7.16). As there are only a few occurrences of laterite and CFBs in the Red Sea lowlands and the Afar Depression, they only emphasise the sudden change in elevations of the datum between the Highland and Eastern Lowland, separated by the 10-20km wide

escarpment (Drury *et al.* 1994).

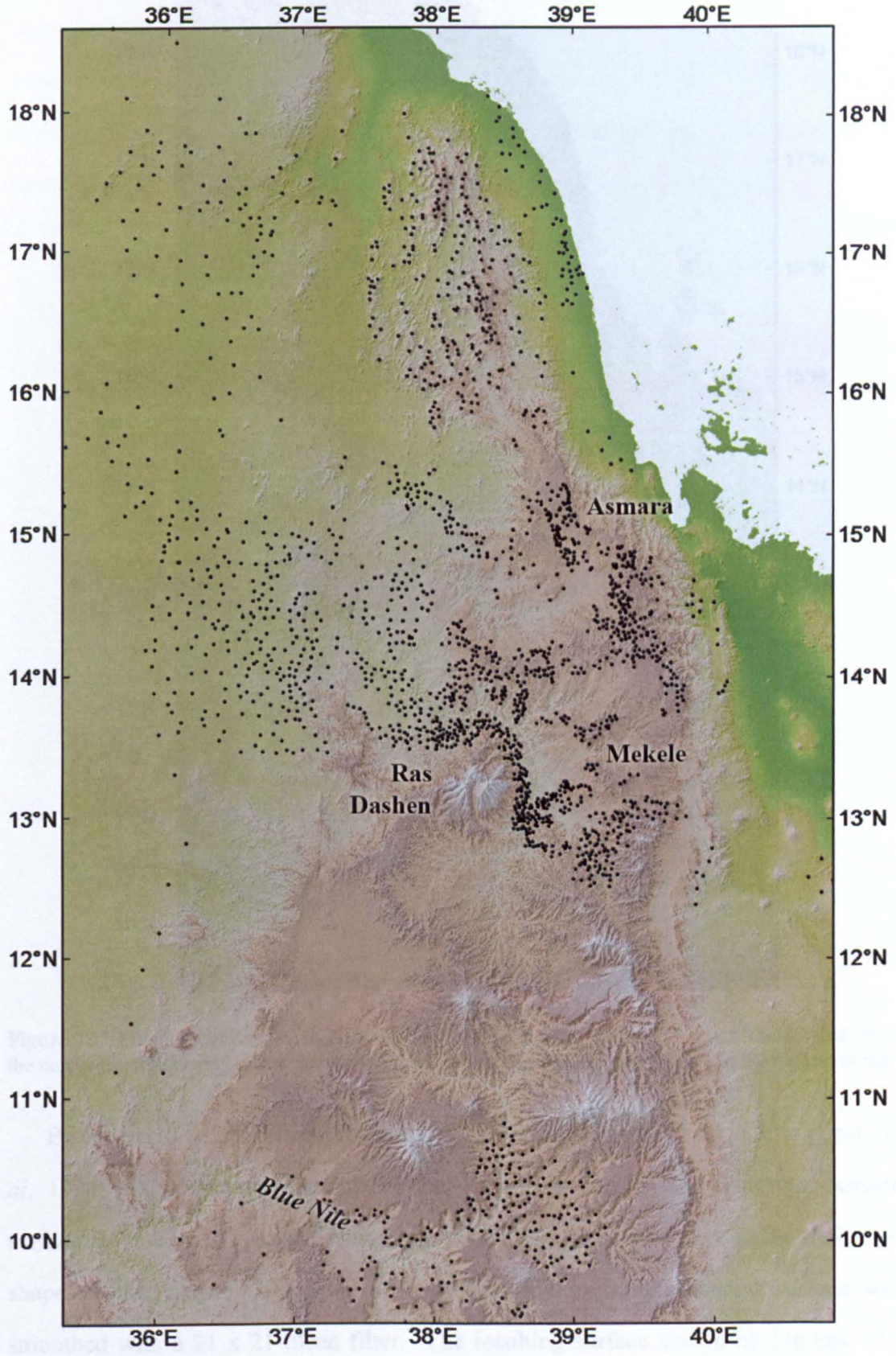


**Figure 7.16** Points where elevations of laterite occurrence were digitised (black dots) displayed over colour-coded SRTM elevation data illuminated from the north-west

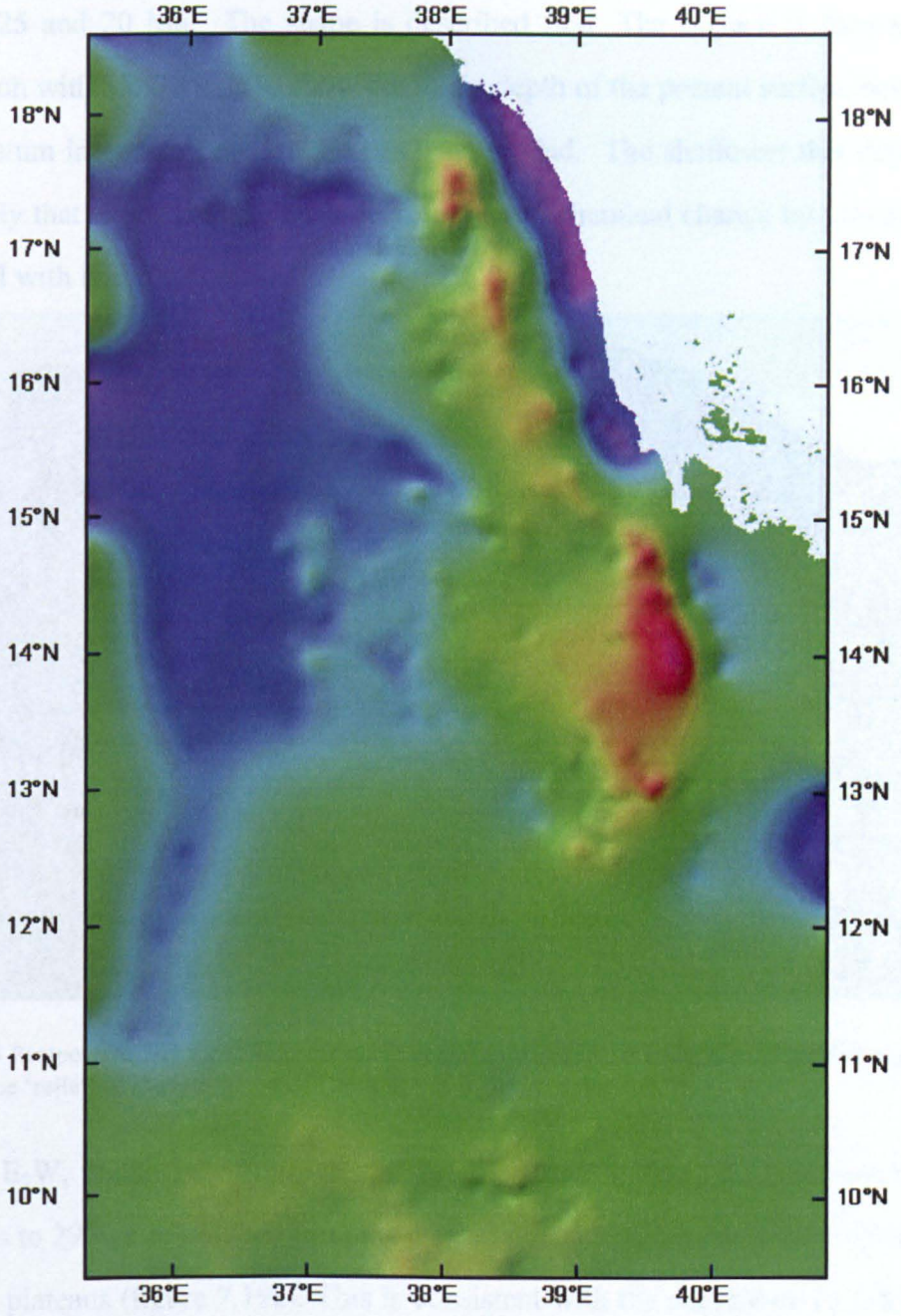


**Figure 7.17** Minimum tension surface for the base of the laterites, colour coded and 'illuminated' from the northwest. The lowest values are in purple, higher values in rainbow sequence to the highest in red

Because many small normal faults with throws of the order of 10 to 50m (Drury *et al.* 1994, 2001) displace the laterite and overlying basalts, the minimum tension surface is 'noisy'. To reduce noise and emphasise broad variation in the deformed shape of the laterite datum, the output from the minimum tension surface was smoothed with a 21 x 21 mean filter. The resulting surface shown by Figures 7.17 and 7.18 represents the shape of the datum imposed by tectonic uplift that began

between 25 and 20 Ma. The shape is described first. The surface is then used in conjunction with SRTM data to show the likely depth of the present surface below the laterite datum in areas where laterite has been eroded. The shallower that depth, the more likely that exposed rocks have been subject to chemical change by groundwater associated with lateritisation.

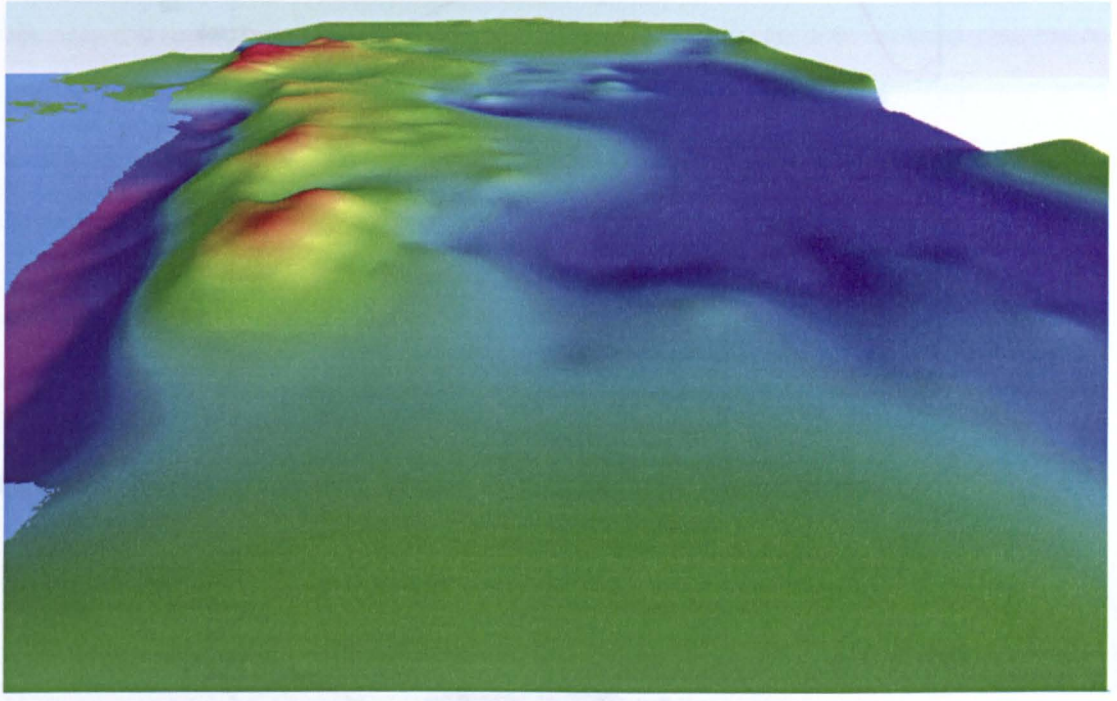

**Figure 7.18** Perspective 3-D view from the north of the data in Figure 7.17, with vertical exaggeration of the surface 'relief' of the laterite base. The Red Sea is shown at the left.

From E-W, the shape of the laterite surface between 18° to 13°N shows a steep rise (100m to 2900m in ~60km) from the coastal plains to the crest of the Eritrean and Ethiopian plateaus (figure 7.19a). This is consistent with the suggestion by Ghebreab and Talbot (2000) that erosion in the Ethiopian-Eritrean Escarpment was by a broad east-dipping crustal monocline, an idea supported by the apatite-fission age profile through the Eritrean Escarpment (Ghebreab *et al.* 2002). The surface dips gently westwards from the Escarpment towards the western lowlands (figure 7.19a). The crest of the regional structure defined by the laterite datum shows a NNW to SSE trending sequence of domes and basins (figures 7.17, 7.18 and 7.19b). Drury *et al.* (2001) suggested that such structures superimposed on regional uplift and bending of brittle upper crust could account for a series of very prominent E-W dilatational

fracture zones that occur from northern Eritrea to the border with Ethiopia and form major fractured-basement aquifers.

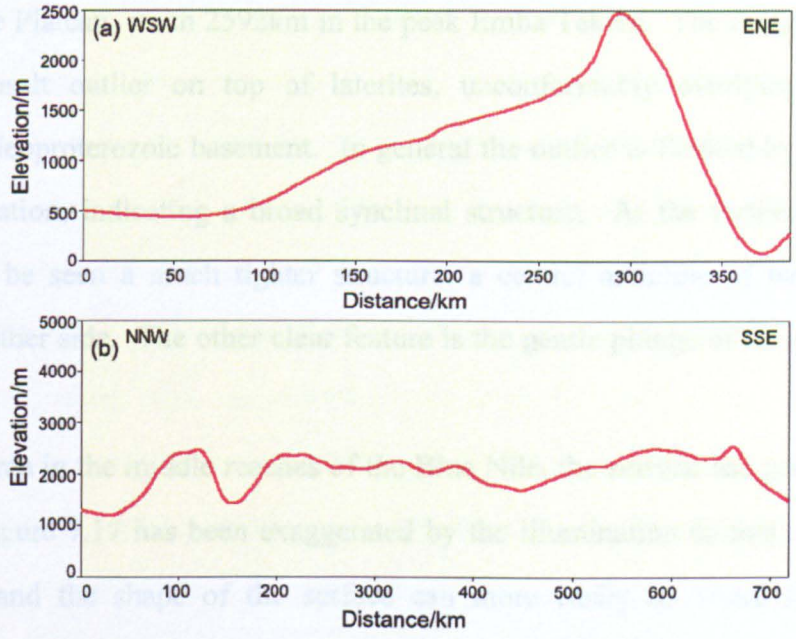


**Figure 7.19** Profiles (a) across and (b) along the main axis of the regional structure

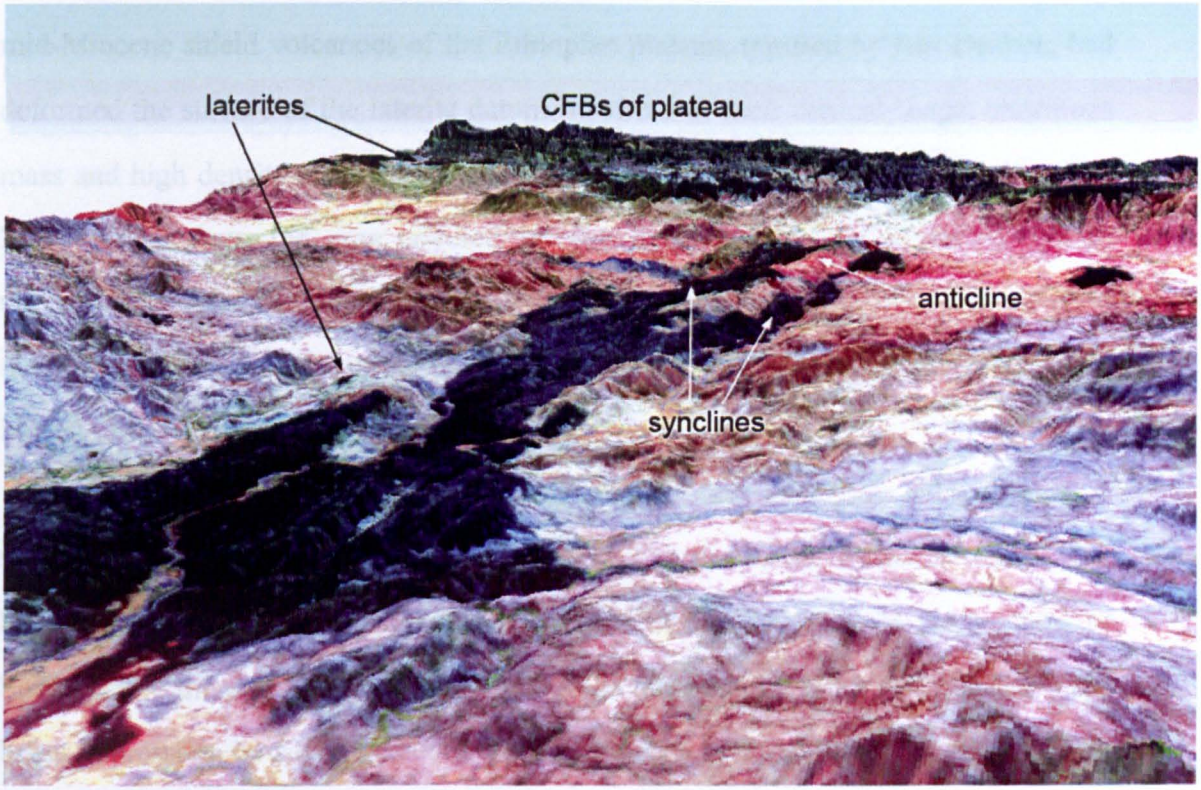


**Figure 7.20** ASTER 631 image of the lowlands to the west of the Eritrean Plateau draped over an ASTER DEM to simulate a perspective aerial view of one of the prominent linear basalt outliers of the Western Lowlands

The laterite datum is indeed spectacularly folded in places (see figure 7.20), as a

simulated perspective view looking NE across the trend of one of the prominent linear outliers of basalt west of the Eritrean Plateau illustrates. On the skyline, the main CFBs of the Plateau, reach 2592km in the peak Emba Tekera. The foreground shows a linear basalt outlier on top of laterites, unconformably overlying the highly deformed Neoproterozoic basement. In general the outlier is flanked by basement at higher elevation, indicating a broad synclinal structure. At the furthest end of the outlier can be seen a much tighter structure: a central anticline of basement with synclines either side. The other clear feature is the gentle plunge of the outlier to the west.

In the area in the middle reaches of the Blue Nile, the surface has gentle 'relief' - note that Figure 7.17 has been exaggerated by the illumination so that shadowing is prominent and the shape of the surface can more easily be visualised. This is expected for areas far from the main axis of late Tertiary uplift along the western flanks of the Red Sea and Afar Depression. It was hoped to test the idea that the later, mid-Miocene shield volcanoes of the Ethiopian plateau, typified by Ras Dashen, had deformed the surface of the laterite datum by virtue of their conical shape, enormous mass and high density relative to the basement beneath the entire volcanic pile. The lack of data from the area covered by the flood basalts and shield volcanoes unfortunately ruled out any definitive test. However, approaching Ras Dashen from the north and east the base of the laterites can clearly be seen to dip gently towards the largest of the shield volcanoes.

A linear depression can be seen in the western part of Figure 7.17, extending southwards from the broad, low area in western Eritrea and northeastern Sudan. The broad low is well defined by points, especially in the Tekesse and Gash plains of Sudan where there are abundant outcrops of the lateritic clay zone in drainages. The linear depression, however, is an artefact produced by surface fitting. It follows a line of points in western Ethiopia where there are only sparse outcrops of laterite at the base of the flood basalts separated from the rest of the data by a large area devoid of points.

### 7.3.1 Exploration potential of the modelled laterite surface

Subtracting the surface defined by the laterite datum from the regional topographic elevation gives a measure of the amount of rock remaining above the laterite after erosion. These are given positive values and usually comprise outliers of CFBs. Negative values indicate the amount of incision into the underlying crust after laterite erosion that exposes the Neoproterozoic basement and Mesozoic sediments.

In his compendium of mineral occurrences in Eritrea, Ethiopia and Somalia, Usoni (1952) noted that in the Eritrean gold mines, operated during the Italian colonial occupation, high concentrations of gold in the near-surface workings consistently petered out below about 150m depth. He also documented a large number of gold mines and gold occurrences in basement lithologies on the Hamasien Plateau, part of the original African Surface from which the laterites had been eroded. Moreover, he noted that several gossans that cap volcanic massive sulfide (VMS) deposits in the basement occur in direct contact with the base of the laterites.

In the course of examining several laterite sections, it was clear that successful gold panning operations (figure 7.21) were being conducted in stream beds a few tens of metres below the base of the laterites and that artisanal mining had become an important focus for commercial exploration. Gold is mobilised during tropical weathering as a complex chloride ion, which results in secondary enrichment below the water table, often in the form of nuggets (Butt 1998). Gossans also form by the breakdown of iron sulfide in VMS deposits at the oxidation - reduction boundary associated with the water table. In Eritrea and Tigray, primary mineralisation formed in the Neoproterozoic basement during the eruption of island-arc volcanic lavas and pyroclastics and the deposition of sea-floor sedimentary rocks, as VMS and other sea-floor exhalative deposits. During, or shortly after, the Pan African deformation and metamorphism, hydrothermal fluids scavenged the upper crust and formed innumerable quartz-pyrite veins, some of which are gold bearing (Barrie *et al.* 2007). Few of the VMS or hydrothermal gold deposits are world class but several are sufficiently productive to have encouraged an exploration boom in Eritrea and Tigray

since the mid-1990s (Eritrean Ministry of Energy & Mines 1997; Tesfamichael Keleta, pers. comm.1998).

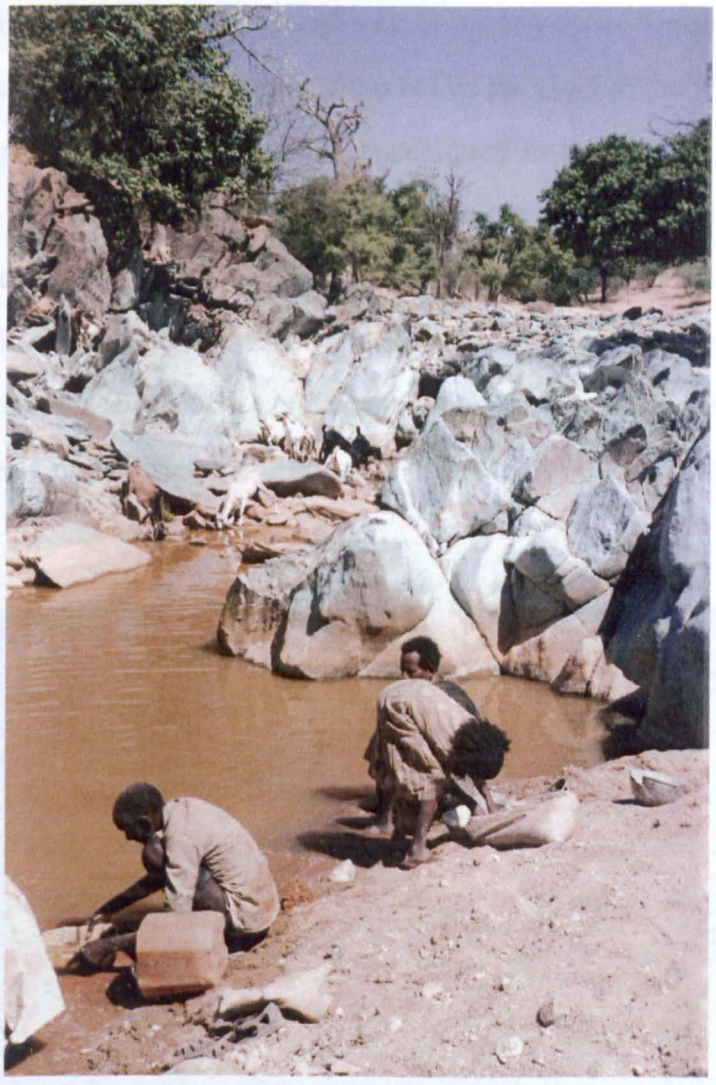

**Figure 7.21** Artisanal miners in SW Eritrea panning alluvial sediments for gold. The stream is just below laterites, as indicated by suspended iron oxy hydroxides colouring the pond water. The stream bed is full of core stones derived from the saprolite zone

The hypothesis that secondary enrichment is due to lateritisation is tested by matching known gold and gossan occurrences to those parts of the land surface that are less than 250m below the former level of the now-eroded laterite. Figures 7.22 and 7.23 show that the bulk of gold occurrences and gossans reported by Usoni (1952) do indeed lie in areas where the present land surface is less than 250m below the former surface of the laterite. This suggests that although the deposits originally formed during the Neoproterozoic, they were probably enriched by circulation of

groundwater from the zone of deep weathering associated with lateritisation. Figures 7.22 and 7.23 illustrate two distinct former mining and exploration prospects as dense clusters on the Eritrean plateau near Asmara and in the low-relief Western Lowlands respectively. These appear to be less than 250m below the level of the former laterite surface. Of the gold occurrences that are concentrated in the Asmara area, 20 lie more than 250m below the level of prediction. One is associated with the Alid volcano (A. Kibreab, pers. comm. 1998) and is probably a product of hot spring activity associated with the now dormant volcanism. The gold occurrences in the escarpment are in fact placer deposits concentrated in the courses of torrential streams draining the plateau immediately to the west (Tesfamichael Keleta, pers. comm. 1998).

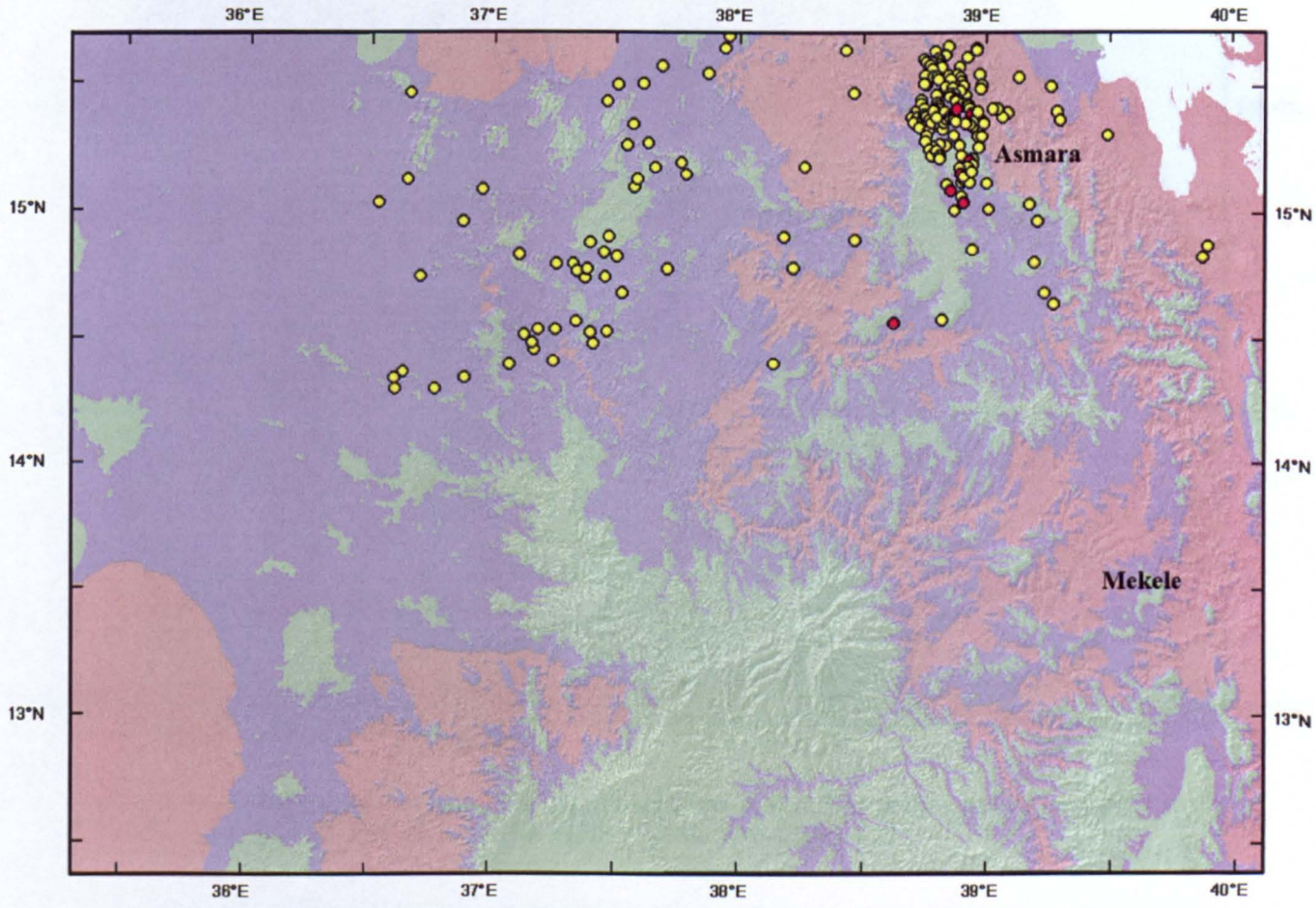


**Figure 7.22** Map of the elevation difference between the present land surface and the surface fitted to the laterite datum, with gold and gossan occurrences (yellow and red dots, from Usoni 1952). Green areas indicate positive values, i.e. outliers of rocks overlying laterite. Pink areas are more than 250 m below the former level of laterites. Lilac areas lie between 20m above and 250m below the former level of laterites. See Figure 7.23 for detail of the Asmara area

Figure 7.22 shows very large areas of the surface that are now less than 250 m below the formed level of the laterites. These may be areas where future exploration for gold and secondarily enriched VMS deposits will prove most fruitful. But success in both cases depends on the nature of the exposed, pre-lateritisation rocks, since primary mineralisation is a product of processes during the Neoproterozoic. Except in the areas where laterites developed on Mesozoic sediments the rocks exposed will be Neoproterozoic. Most of the mineralisation in the basement is associated with metavolcanics of felsic composition and associated metasediments. So, exploration planning would need to delineate such promising host rocks in the basement as well as reject areas that have, or once had, thick sequences of Mesozoic strata.

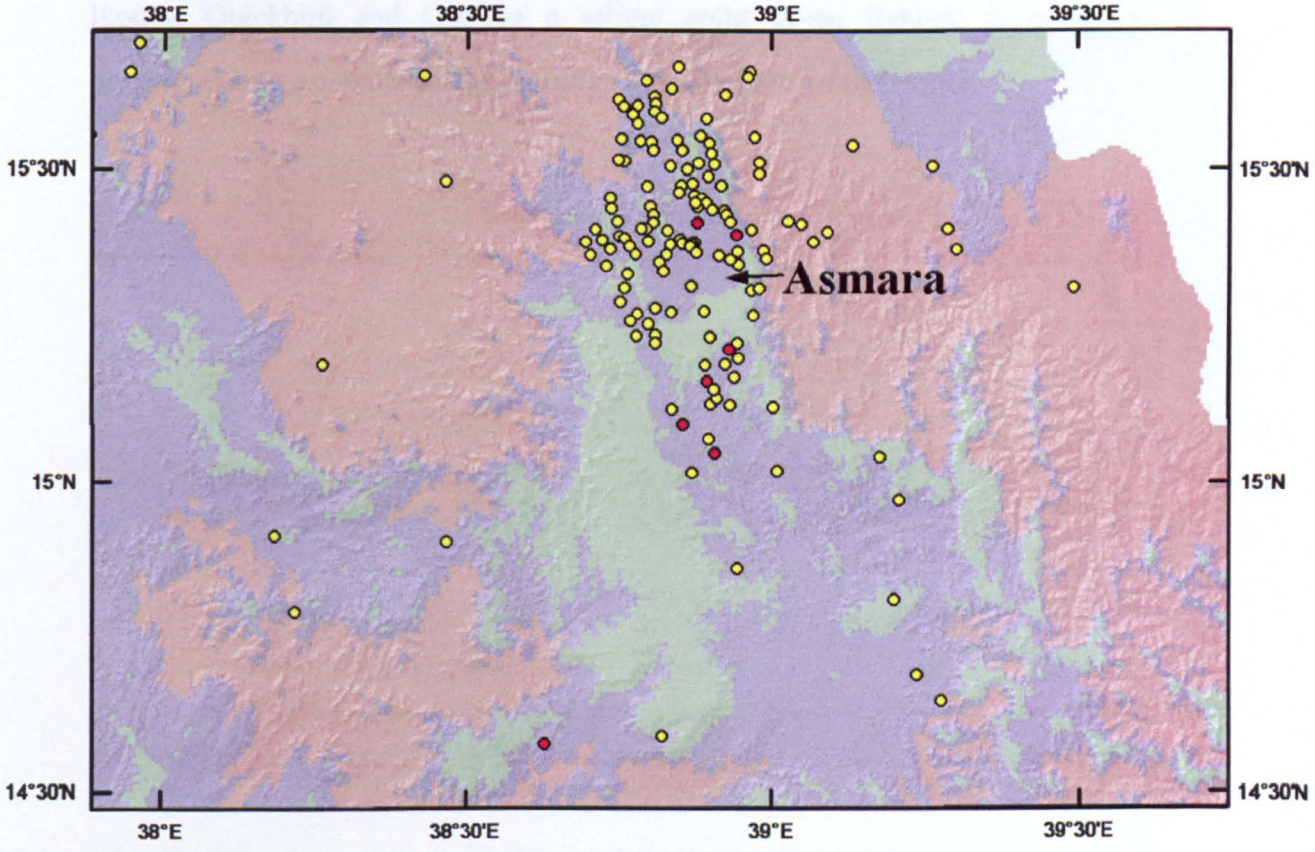


**Figure 7.23** Map of the elevation difference between the present land surface and the surface of the laterite datum, for the Asmara area. Symbols and colours as on Figure 7.22

It is important to note the limitations of using RS for reconnaissance exploration. Location of the laterite datum on remotely sensed images such as ASTER or Landsat ETM is accurate to less than 100m. Moreover, the laterites have been eroded and

there is no longer clear evidence of their former elevation. Reliance on the datum is therefore critical as late Tertiary faults with throws up to 100m also displace the laterites where they occur (Drury *et al.* 1994; Mohr 2001). Although the SRTM elevation data is by no means an exact representation of the present topography (it has a vertical precision of about ± 10m and a cell size of 90m), in rugged terrain it is useful for determining the approximate shape of the former laterite surface. These results are promising. Ideally digital elevation data with 10 times better horizontal and vertical precision, together with more closely digitised points would produce a better model of the shape of the former laterite surface. Such data are available, but at considerable cost, from high-resolution (<1m) stereoscopic images produced by the Ikonos, Quickbird and GeoEye a salient point given funding is being cut in government departments and universities in many parts of the world.

CHAPTER EIGHT

# Living with laterites - societal ramifications and economics

Laterites have a marked effect on landscape and the people who live in this terrain. Perhaps one important aim of research is to understand and benefit humanity. Such an aim could never be achieved in this work; what is attempted though, is to provide four case studies - the first in the form of a published paper - which may prove useful to indigenous populations. Each study may be read as a stand-alone piece and its layout conforms with the rest of the thesis.

*Space technology for disaster management: data access and its place in the community*

M.E. Andrews Deller

Published in: Teeuw, R. M. (ed.) *Mapping Hazardous Terrain using Remote Sensing.* Geological Society, London, Special Publications, 283, 149–164.

*Abstract:* The ways in which remotely sensed data can be used to manage and alleviate the consequences of natural disasters have never been fully exploited. If prediction of impending disaster is to be useful, those affected by catastrophe and those who come to their aid must work together. A global strategy based on a vision for disaster management will fail if those affected by hazards are not involved in their own disaster preparation, relief efforts and rehabilitation. Local people are experts in ground knowledge; all that is needed is for those with expertise in remote sensing to pass on their skills, knowledge and data in a way that can be understood and valued. To do this, those threatened by catastrophe must understand how disaster relates to their lives, how satellite data can be used with confidence to prepare for local hazards and how to apply information that can help lessen the effects of catastrophe. This can be achieved by making available remotely sensed images with simple explanations that enhance vegetation, topography and geology. With timely, reliable information, preventative measures can be taken, surface features identified on satellite images can guide refugee placement and hazards can be anticipated and contained.

## 8.1 Introduction

Although the mapping of hazardous terrain using remote sensing is well-documented

(King *et al.* 1981; King 1984, 1994; Massonnet 1995; Bjorgo 2000; Drury & Andrews Deller 2002a; Huang & Fu 2002; Hunt 2002; Wright *et al.* 2002; Kerle *et al.* 2003; Oštir *et al.* 2003; Marsh 2004; Ramsay & Flynn 2004; UNOOSA 2004), its application in the hands of people who live and work in these areas is limited. With minimal training and easily understood satellite images however, local inhabitants and relief workers can quickly become proficient in simple image interpretation and competent at producing their own informative maps and information. Examples of the general public's fascination with remotely sensed images are not hard to find, for instance:

- *'When the first satellite image posters of Southern California and Los Angeles went on sale several years ago they were extremely popular. From what I saw, the public was quick to see them as a new type of map, with new information, in addition to the aesthetic aspects of the imagery. People would gather around the displays at the shopping mall and be amazed at what they saw.'* (R.E. Crippen, NASA/JPL, pers. comm. 2006);
- *'In 1998 I did a compilation of satellite images covering Eritrea and had it printed at A1 size so the Eritrean Water Resources Department could sell it to expatriates to raise funds for water exploration but copies ended up in schools, public offices and tiny fuel stations throughout the country.'* (S.A. Drury, Open University, pers. comm. 2001; see also Drury 1997);
- *'We've been developing a project called TerraLook [formerly the Protected Area Archive] to make it easy for "ordinary" people to get images of sites they have an interest in. Originally it was geared towards Ecosystem and Park managers but now it is really for anybody.'* (M. Abrams & G.N. Geller, NASA/JPL, pers. comm. 2006; see also Table 8.2).

Specific reports of people's capacity to use satellite data are also available, for example:

- *'As to people's ability to use images...our experience has been that people with ground knowledge can very quickly orient themselves to an image and start using*

*it -- in fact, they much enjoy doing that. The image is generally treated as an extension of their ground knowledge -- for example, they may have known that there was agricultural encroachment into their park but did not know how much. An image can tell them that. In fact, that ground knowledge usually seems to act as pre-existing ground truth, greatly aiding interpretation.*' (M. Abrams & G.N. Geller, NASA/JPL, pers. comm. 2006; see also Abrams & Geller 2005);

- '*Several years ago some of us at JPL were doing aerial reconnaissance over the Mojave Desert from a NASA airplane, looking at earthquake faults. There was some difficulty telling the pilots exactly where we wanted to go. I had Landsat images of the area for our use, but quickly realised that the pilots would better understand the geography if I supplied them with images too. The pilots' maps [contour lines, etc.] looked not much like the view out the window but the satellite images showed them what to seek.*' (R.E. Crippen, NASA/JPL, pers. comm. 2006);
- '*I found Tanzanian farmers could well read satellite images (Landsat 3 RBV) and understand their value better than some government officials.*' (R.B. King, pers. comm. 2006, regarding a project funded by the British Overseas Development Authority, the International Developmental Research Centre and the US Agency for International Development (USAID); see also King 1981).

Yet, the ways in which remote sensing data can be used to manage and alleviate the consequences of disasters have never been fully exploited. This problem is exemplified in areas like the Horn, one of Africa's most disaster-prone regions with poor map coverage, insufficient roads or funds, endemic drought, famine and disease, unreliable rainfall and inhospitable terrain (Andrews Deller 2005). In such territory, the importance of multispectral remote sensing in geological and environmental applications, many of which relate directly to natural hazards, is unsurpassed (Vincent 1997). Given cheap, efficient means of acquiring appropriate data (Abrams 2000; Andrews Deller 2000, 2002; Goossens 2002a) and the potential uses of satellite technologies for disaster relief (J. McCluskey, Oxfam, pers. comm. 2000 - see Table 8.4), remotely sensed material provides a way forward in that it can be used to aid

local communities. As such its socio-economic value is considerable, since much of the rapidly growing archive of data (Drury 1998) required to enable ordinary people to manage the hazards that affect them is freely available (Andrews Deller 2004, 2006).

## 8. 2 Data and materials

Several operational satellite systems provide image data that can be used with simple interpretation to manage the effects of catastrophe. The most notable are the Enhanced Thematic Mapper Plus (ETM+) deployed on Landsat-7 and the Advanced Spaceborne Thermal Emission and Reflection Radiometer (ASTER) (Abrams 2000). Complementing ASTER and ETM+, the Shuttle Radar Topography Mission (SRTM), with near-global coverage, provides free, moderate to high-resolution (90 and 30 m) topographic elevation data useful for detailed terrain mapping (Jenson & Domingue 1988, Crippen 2001).

From the wealth of data on offer, images selected as appropriate for raising public awareness of natural hazards should be clear and simple and ought to include the following:

- Perspective views based on SRTM digital elevation model (DEM) data with images draped over them – these provide natural-looking renditions of familiar landscapes or specific localities (Jenson & Domingue 1988; Goossens 2002b);
- Stereo anaglyphs using co-registered left and right images of stereopairs [such as those from ASTER] as red and cyan components of red, green, blue (RGB) images, viewed using simple colour filters (Crippen & Blom 2000) - these simulate 3-dimensional (3-D) models of natural landscape (Abdallah *et al.* 2005);
- Landsat ETM+ bands 7, 4 and 2 (742) and ASTER bands 6, 3 and 1 (631) displayed as RGB respectively - these display vegetation in natural-looking colours and provide a good basis for general geological interpretation of terrain.

The above data sets are free or low cost and can be easily appreciated by people of all cultures. Accessed from sites listed in Table 8.2, images printed by individuals or

personnel from government departments, local surveys, educational establishments, non-governmental organisations (NGOs) or United Nations (UN) agencies may be used for training or distribution in local communities via schools, places of worship, relief agencies and administrative buildings.

Even though cheap Landsat ETM+, ASTER and SRTM data for the Earth's land surface are easy to obtain (table 8.2) and the price of image processing software, computers and peripherals has dropped considerably, costs are still prohibitively high for most people affected by disasters. Websites such as Google Earth, which use satellite data and vector maps and are '*well accepted as a new way to understand places*' (R.E. Crippen, NASA/JPL, pers. comm. 2006) are useful for getting information about a given region quickly, but few people in the Third World have access to such digital data. Relief workers may have computers in the field, together with some skills and software for image display and interpretation, but the local population will probably not. In these cases, colour lithographic printing offers a solution. It is cheap and an excellent source of educational aid (Andrews Deller *et al.* 2004, 2005). A good all-in-one printer-photocopier-scanner costs no more than UK£65 (US$121 or 94 euros at 2006 rates), a price which continues to fall. A good quality colour-printed A4 page costs just over one penny or roughly 2 US cents. In durable form [e.g. with plastic laminated protection] images and explanations of image features that indicate hazards of different kinds can be delivered to at-risk communities as warnings and sources of valuable information for educational purposes. Lower-cost copies [e.g. colour newsprint], suitable for individual families, might also be considered.

Geoscientists who use hard-copy satellite images notice the interest shown in such data by local people world-wide and their ability to grasp the information about the terrain displayed (King 1981; Drury 1998; Setzer 2004; Abrams & Geller 2005). Before global positioning system (GPS) receivers became available, Drury and Berhe report getting lost topographically and geologically when using Landsat TM images to map the geology of remote western Eritrea, while working with Oxfam in 1990.

**Table 8.1** Potential Uses for Satellite Technologies for Disaster Relief (modified from table provided by J. McCluskey, Oxfam UK)

| NATURAL DISASTERS | Maps | Migration | Site Planning | Environmental Degradation | Communications/ Infra-structure | Vector Control | Food Security/ Agriculture |
|---|---|---|---|---|---|---|---|
| **Floods** | Flood prediction - flood prone areas. Flood progress monitoring. areas affected | Where populations have moved to in order to facilitate assistance | Mapping of potential flood shelter locations - out of flood risk | Effect of flood on drinking water supply and installations | Effect on road/rail/ river network. Alternative access | Monitoring duration of flood - sustained environmental/ ecological changes | Destruction of crops; recovery of crops |
| **Drought** | Progress of drought | If populations and livestock have migrated out of area | Locating new water resources | Mapping of soil/land degradation<br><br>Change in water bodies – reduction & quality. Change in groundwater levels | | Potential for increase in vector breeding sites i.e. pools of water instead of flowing water in rivers | Effect on crop production; change in cultivated area; change in crops; availability of pasture for animals |
| **Earthquake & Tsunamis** | Extent of quake for assessment purposes<br><br>Map of tsunami potential effect | Where populations have moved to in order to facilitate assistance | Mapping of seismically stable areas - locations for camps and unsuitable locations | Mapping of areas at risk from aftershocks, rockfalls, landslides etc.<br><br>Effect of saline intrusions due to tsunami on water supply | Effect on roads/rail/ bridges.<br><br>Alternative access. Extent of building damage | | Effect of saline intrusions due to tsunami on agriculture |
| **Cyclone/ Hurricane/ Tropical Depression** | +/- Real-time tracking of weather event | Where populations have moved to in order to facilitate assistance | Mapping probable affected and safe areas | Mapping of areas at risk from mudslides.<br><br>Effect of saline intrusions on water supply | Effect on roads/rail/ bridges.<br><br>Alternative access. Extent of building damage | | Effect of saline intrusions on agriculture |

**Table 8.2** Free and low-cost remotely sensed data

| Web site | Brief description of available data |
|---|---|
| landsat.usgs.gov | Landsat 7 ETM+ to purchase, browse and ordering faci |
| glcfapp.umiacs.umd.edu:8080/esdi/index.jsp | Free Landsat TM and ETM+ 742 compressed mosaics; free Landsat TM and ETM+ scenes for selected dates (often post-wet and dry seasons) |
| zulu.ssc.nasa.gov/mrsid/ | Free Landsat TM and ETM+ 742 compressed mosaics |
| edcimswww.cr.usgs.gov/ pub/imswelcome/ | Low-cost or free ASTER, MODIS & AVHRR data; other data, browse and ordering facilities |
| ftp://e0mss21u.ecs.nasa.gov/srtm/ | Free SRTM Digital elevation data |
| www.maproom.psu.edu/ dcw/ or http://www.libraries.psu.edu/ crsweb/maps/ | Free on-line Digital Chart of the World |
| www.ngdc.noaa.gov/mgg/image/2minrelief.html | Digital elevation data |
| edcdaac.usgs.gov/gtopo30/gtopo30.html | Free ~1km resolution digital elevation data |
| www.oosa.unvienna.org/SAP/stdm | Links to web sites such as the International Charter "Space and Major Disasters", maps, satellite images and other data at UNOOSA |
| http://www.geodata.gov/gos | US government's Geospatial One-Stop E-Gov Initiative - free high resolution maps and images for search, rescue disaster areas |
| ftp://ftp.glcf.umiacs.umd.edu/glcf/SRTM/ | Free ~90m resolution SRTM Digital elevation data |
| http://earth.google.com/ | Google Earth - Free on-line, global Landsat TM natural colour, perspective views of topography, high-resolution data available in some areas |
| http://www.nasa.gov/home/ | Directory and links to many NASA sites. |
| http://edcimswww.cr.usgs.gov/pub/imswelcome/ | NASA Earth Observing System Data Gateway (EROS Data Center): low-cost or free ASTER, MODIS & AVHRR data; other data, browse and ordering facilities |
| http://asterweb.jpl.nasa.gov/paa | TerraLook make it easy for ordinary people to get images |
| www.nws.noaa.gov | NOAA National Oceanic and Atmospheric Administration sites - weather, tropical storms, climate etc. |
| http://www.ncdc.noaa.gov/onlineprod/drought/ xmgr.html | CLIMVIS: Online access to drought, precipitation and temperature data |
| http://TerraWeb.wr.usgs.gov/projects/eolian/ | USGS TerraWeb: Use of Remotely Sensed Images for Eolian and Rainfall Mapping, detection active dust storms and/or detection and mapping areas vulnerable to aeolian erosion |

Their guide, a semi-nomadic herdsman intervened, pointing out on the image the ridge on which they stood, the same rock type occurring on two further ridges to the west, landscape features, their destination and a nearby gold-bearing stream (S.A. Drury & S.M. Berhe, Open University, pers. comm. 1998). Across the globe, *'a company named Solid Terrain Modelling... in Fillmore, California, created a new process to drape satellite images onto high-density foam blocks that are carved into the shape of a DEM'*. Amongst their customers, *'lawyers who need to get the jury to understand the geography of a court case... found that imagery, especially in 3-D, is well understood by the general public'* (R.E. Crippen, NASA/JPL, pers. comm. 2006).

## 8.3 User-friendly images

People affected by disaster are generally unaware of the potential of space technology and the usefulness of remotely sensed images in the field, so starting with the familiar can instil confidence. This can be achieved by making available images that clearly enhance features of the local environment [vegetation, water, roads, topography and geology], as well as those features that typify hazards [volcanoes, landslides, active faults, flash floods and areas desiccated by drought] (Andrews Deller 2004, 2005). Indigenous peoples readily appreciate images in printed form and the basic information about the features depicted, a fact confirmed by the author's experience on several occasions. For example, Alamou, a guide, driver and navigator in Ethiopia, (2002) proved an excellent image interpreter; anticipating and guiding geologists to clay- and iron-rich localities noted on ASTER 631 images of the country.

A good starting point and an image that mirrors many people's general perception of their surroundings therefore, is ASTER 631 combined as RGB. Equivalent to Landsat TM 742 (Andrews Deller 2006), it simulates natural-looking vegetation and highlights rock differences (figure 8.1). A clear informative image, it is easily understood by relief workers and local people (Andrews Deller *et al.* 2004, 2005). Linking the familiar with what can be seen on the image, vegetation is green [not an aesthetically disturbing red tone (Drury 1993) as on standard false-colour ASTER 321

images] and iron-rich rocks and soils are red, as they are with human vision, so there is no confusion. This type of image bears out experience and encourages trust in Earth observation for assessing resources or potential hazards.

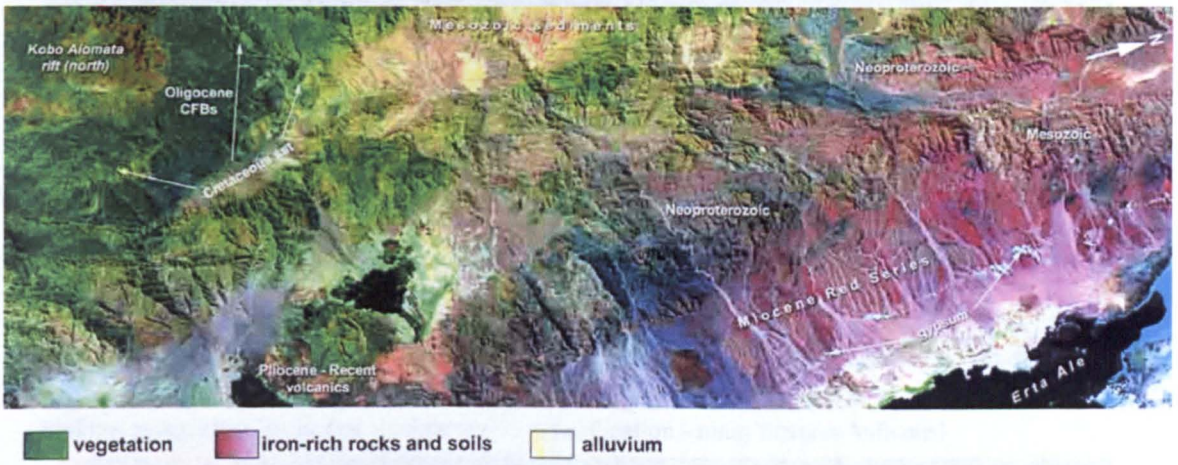


**Figure 8.1** ASTER 631 combined as RGB simulates natural-looking vegetation and enhances rock differences in the Ethiopian Escarpment. (Key shows colours of various elements of the terrain; CFBs = continental flood basalts)

Equally useful, an ASTER 631 image combined with SRTM DEM data (figure 8.2) produces a natural-looking perspective view which can be used for location and realistic graphic representation of landscape. Such 3-D renditions of Earth observation data are more easily understood than 2-D prints. The positive as well as the dangerous can be highlighted on this image. The combination of bands clearly distinguishes outcrop - high-ground basalt, clay and multicoloured basement - from green vegetation. Abundant vegetation indicates sources of water and land fit for agriculture whereas the distinct blue clay horizons warn of potential land slippage and areas best avoided for buildings, roads or grain storage. Early signs of trouble can be noted and once features observed on the image are understood in the context of hazardous geological processes, potential disasters can be avoided.

An ASTER 631 image and stereo anaglyph of part of the Ogaden, Ethiopia (figure 8.3) makes the point. Failure of the clay zones (blue in figure 8.3, left) produces landslides that range in size from a few square kilometres to thousands of square kilometres (Temesgen *et al.* 2001; Andrews Deller 2002, 2004; Singhroy & Molch 2004; Abdallah *et al.* 2005). Images like this not only identify areas that are

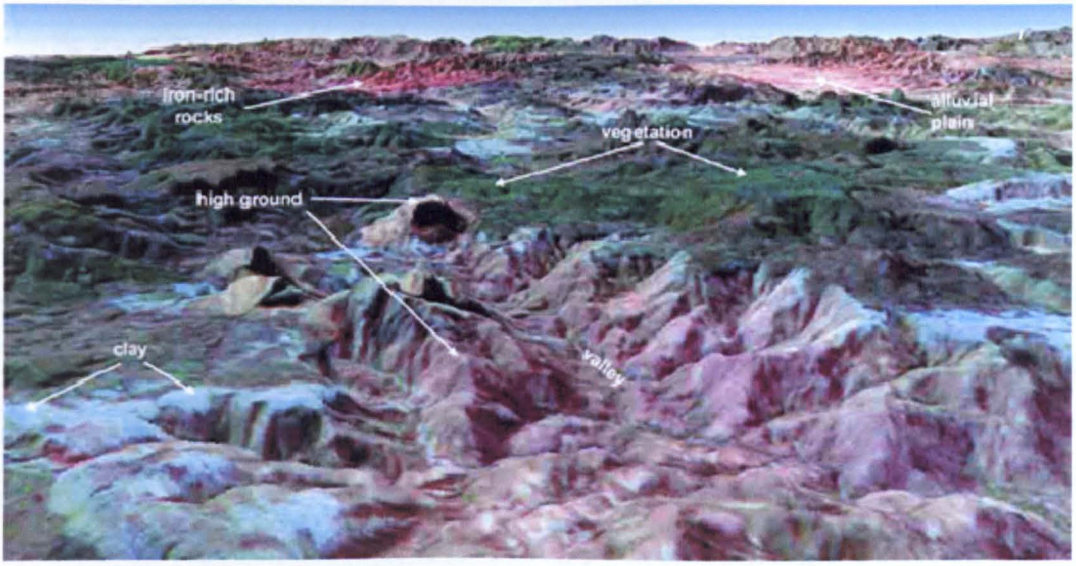


**Figure 8.2** The Areza area, Eritrea: ASTER 631 draped over SRTM DEM data, produces a natural-looking perspective landscape used for terrain visualization - main features indicated

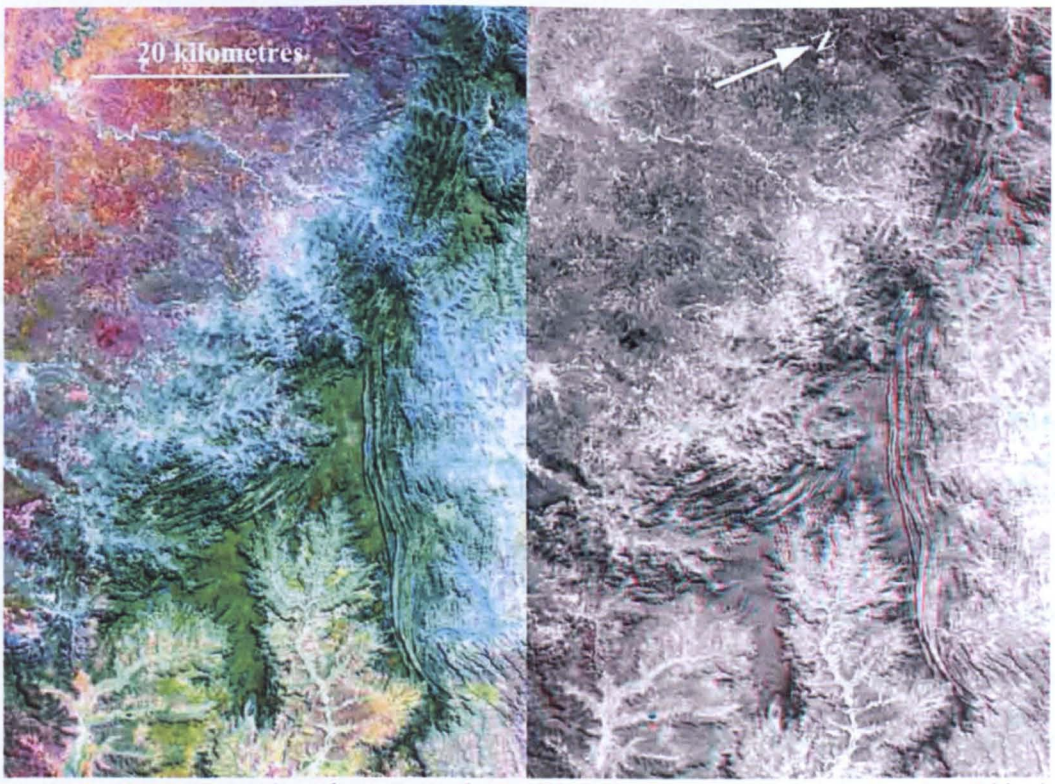


**Figure 8.3** ASTER 631 (left) and stereo anaglyph (right) showing landslides in the Ogaden, Ethiopia

potentially hazardous, but provide visually stimulating ways of teaching entertainingly. Using a 20 pence (~40 cents) anaglyph viewer, adults and children are fascinated by the dramatic features of landslides that take on 3-dimensional form before their eyes. Furthermore a serious point is made that such hazards, highlighted by remote sensing, can be mitigated by local government planning and by individuals taking precautions.

Sadly this was not the case on the 26 December 2004 when one of the biggest natural disasters in recorded history took place (see McCluskey & Choudhury 2005). Tragically, no one was prepared for the tsunamis of the northern Indian Ocean (see Drury 2005). Small signs, such as the receding coastal waters that might have alerted many and saved lives, were not understood. Fascinated by the withdrawal of water, people walked towards the sea rather than run to higher ground. The need for any foreknowledge of both disaster-affected districts and those areas where people have found refuge in the past has been noted by many relief teams (e.g. Sartori *et al.* 2000; HAIC Secretariat 2001; Sanyal & Lu 2006), particularly in regions affected by severe flooding. Even moderate-resolution DEMs from SRTM data (figure 8.4) provide useful indicators of safe and unsafe localities, whilst such information derived from stereoscopic, high-resolution satellite image data e.g. Ikonos and Quickbird, far surpass the topographic maps of most Third World countries.

Figure 8.4 displays coastal areas of the Nicobar Islands below 15m elevation in magenta, red and orange (Drury 2005; see also http://www.geodata.gov/gos - Indian Ocean Disaster link). These areas, clearly identifiable on the image correlate with the tsunamis' worst effects. Remotely sensed data of this kind, which can be understood by anyone, are instructive and alert local people to possible hazards. They indicate areas to avoid when warnings of imminent danger are forecast, highlight areas of safety when disaster strikes and mark out areas in which to concentrate relief efforts should a tsunami strike again. Understandably people are attracted to areas with fertile soils or other useful attributes on which their livelihoods depend, even when fully aware of the associated risks from local natural hazards. Nevertheless, educational measures outlined above increase their chances of surviving disasters where legislation for safe siting of dwellings is lacking.

At their most useful, remotely sensed images indicate what geologists know or believe to have happened and what might happen again. Large-scale topographic maps derived from DEM data are ideal for highlighting land surface features related to active faults and volcanoes, whereas multispectral remote sensing data distinguish

vegetation and rock type nicely.

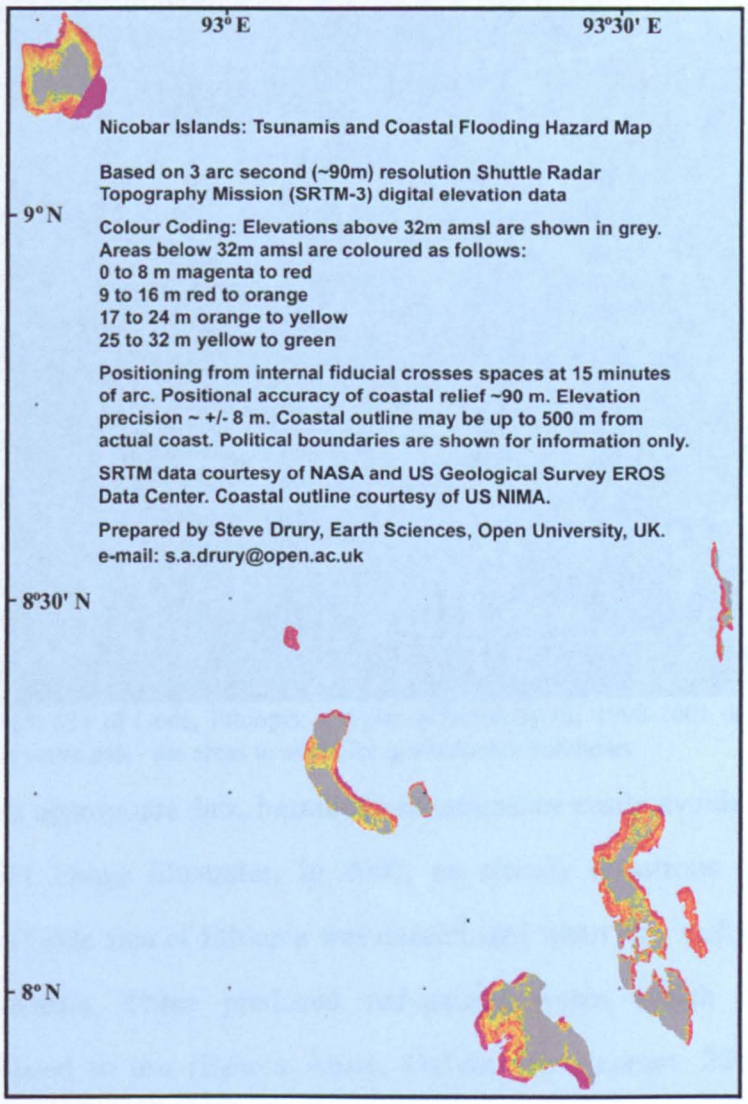


**Figure 8.4**. Coastal Flooding Hazard Map of the Nicobar Islands, Bay of Bengal, based on SRTM DEM data

Examples of areas that ought to be highlighted on images include:

- steep slopes with thick soil or debris, prone to landslides and debris flows (Jordan *et al.* 2000b);
- low-lying inland or coastal areas liable to flood (Drury 2005; Sanyal & Lu 2006);
- highly vegetated areas prone to forest fire when dry (e.g. Setzer 2004);
- sparsely vegetated or poor kaolinitic soils prone to drought (Andrews Deller 2002, 2006);
- areas where geology dictates that groundwater will endanger life (e.g. McArthur *et al.* 2001);
- recent lava flows and volcanic gas emissions (Wright 1999; Alvarez *et al.* 2000);
- active fault lines (Kaya *et al.* 2004; Fu *et al.* 2004).

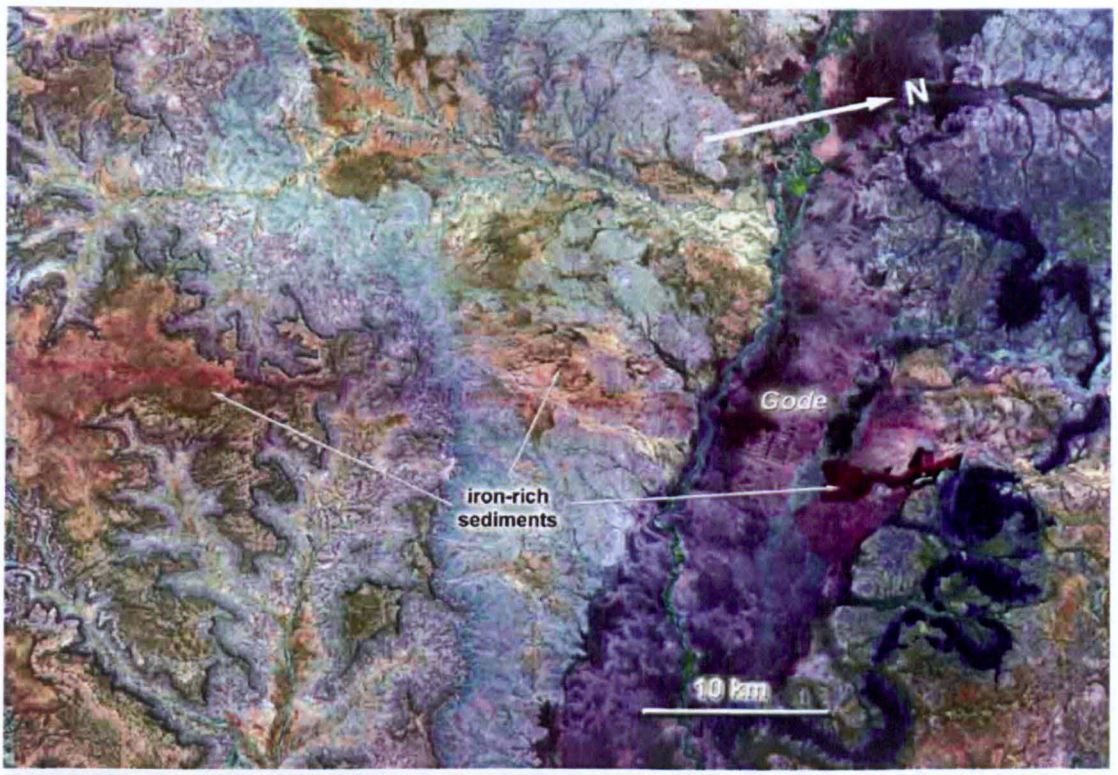


**Figure 8.5**. ASTER 631 of Gode, Ethiopia: a region affected by the 1998-2001 drought: red colour indicates iron-rich sediments - the areas to avoid for groundwater boreholes

Armed with appropriate data, hazardous situations are easily avoided as Figure 8.5, an ASTER 631 image illustrates. In 2000, an already disastrous situation in the drought-ridden Gode area of Ethiopia was exacerbated when new wells were drilled in iron-rich sediments. These produced red-stained water, which the indigenous population refused to use (Eshetu Abate, Oxfam, pers. comm. 2001). The image clearly shows areas that should be avoided as water sources because of the presence of iron-rich rocks. These are highlighted in red because of the spectral properties of iron (III) oxy-hydroxides (Andrews Deller 2006). Such knowledge could have facilitated strategic placing of more suitable wells for people already desperate for clean water (Andrews Deller 2002). However, given that disaster relief situations are often already desperate, as in the continuing humanitarian crisis in Darfur, Sudan (Buchanan-Smith 1997), remote sensing can be used to alleviate worsening conditions and help relocate relief camps near clean water.

Compressed Landsat ETM+ 742 mosaics (e.g. figure 8.6), freely available from the University of Maryland Global Land Cover Facility, are useful for planning access and provision of clean drinking water. A case in point is Figure 8.6, showing part of

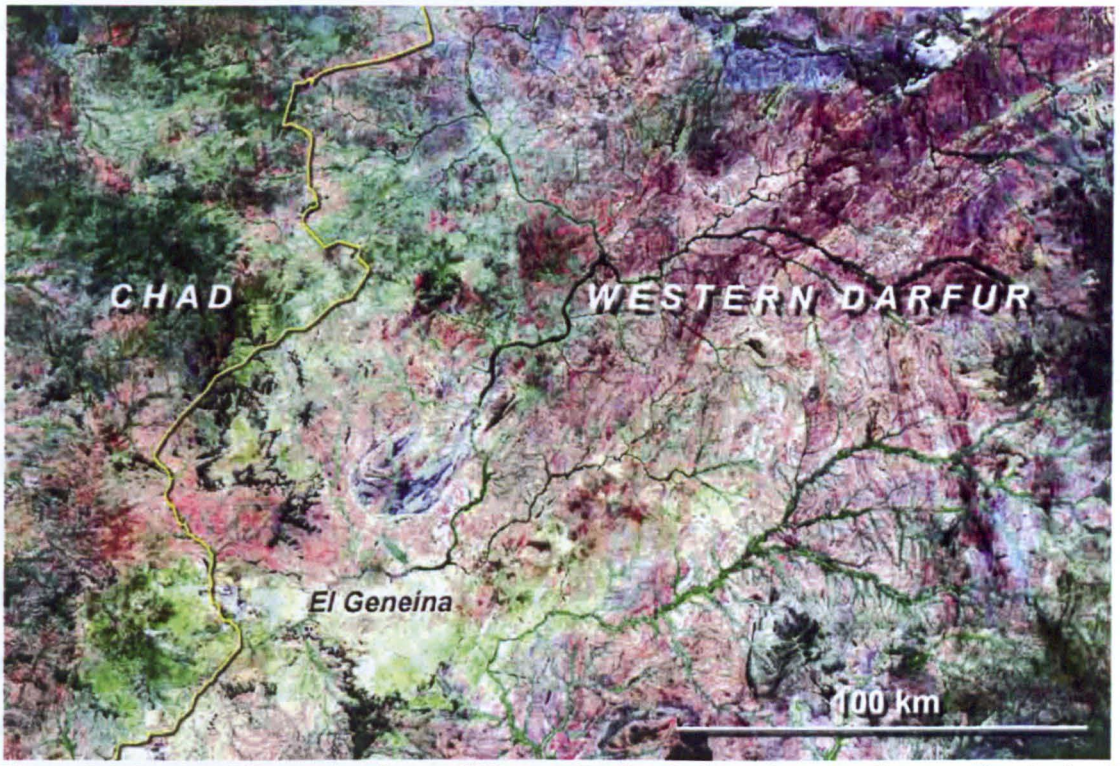


**Figure 8.6**. Landsat 742 mosaic of part of Western Darfur, Sudan, where excellent aquifers in fossil dunes (linear features in NE) could help in the siting of relief camps

Western Darfur, downloaded from glcfapp.umiacs.umd.edu:8080/esdi/index.jsp and prepared in one hour. Roads can be added to the image in 30 minutes, using the free, on-line Digital Chart of the World and VMAP as rough guides, until more accurate road mapping data can be accessed from UN humanitarian information centres (table 8.2). Natural features enhanced on the image can be used to locate sources of water. In the NE quadrant of Figure 8.6, for example, fossil sand dunes, which form excellent aquifers and could provide new sources of water within walking distance of overcrowded established camps, show up clearly as pale thin linear features with vegetation following them. As a result of only half a day's analysis, ASTER-derived geological maps of all water sources in areas around camps can be compiled to help refugees, aid workers and local people cope better with limited water supplies (Drury & Andrews Deller 2005).

## 8.4 Disaster mitigation and preparedness: infrastructure, water and education

'*Many areas of the world are poorly mapped by conventional topographic mapping so*

*satellite images are a big advantage when working in such terrains and are absolutely essential for determining location, geological features of interest such as faults and contacts, as well as the zones of rock alteration that may be the first indicators of economic concentrations of metals*' (D. Taranik, Anglo American, pers. comm. 2006).

Dealing with disasters is important, but improving people's normal living conditions is more so. A person's ability to survive disasters is enhanced if he or she has good food, water, financial security and a safe environment. The usefulness of remote-sensing technologies in long-term planning and economic management should not be underestimated. With basic training, local people can use satellite images to plan infrastructure: the best routes for roads, the whereabouts of building materials, agricultural possibilities, the management of mineral wealth to finance projects, areas best avoided because of risk from natural hazards and safe water supplies. Once the geology of an area is mapped, its resource potential is clear. Figure 8.7, a geological map of laterite facies in the Asmara area, Eritrea, based on image data for the region (Andrews Deller 2000, 2004, 2006), provides a simple example. The uppermost ferricrete provides aggregate for roads and the mottled zone building material for houses. The clay zone with its infertile, poorly draining, kaolinitic soils susceptible to land slippage, is best avoided for agriculture. The weathered basement, easily pinpointed on Figure 8.7 as sub-laterite regolith where the process of lateritisation has rotted primary minerals in the underlying bedrock, together with lateritic ferricretes and the mottled zone are potential aquifers whose waters can be beneficial (Andrews Deller 2002, 2006). Strategic siting of boreholes is crucial however, as ground water in some lateritised terrain may have high levels of arsenic, concentrated fluoride that leads to dental fluorosis (Zerai 1996), excessive levels of magnesium sulphate and sodium chloride which cause diarrhoea and high ferric hydroxide content that results in pipe blockages. With very little input, specialist and non-specialist can use remotely sensed data for positive ends within the community.

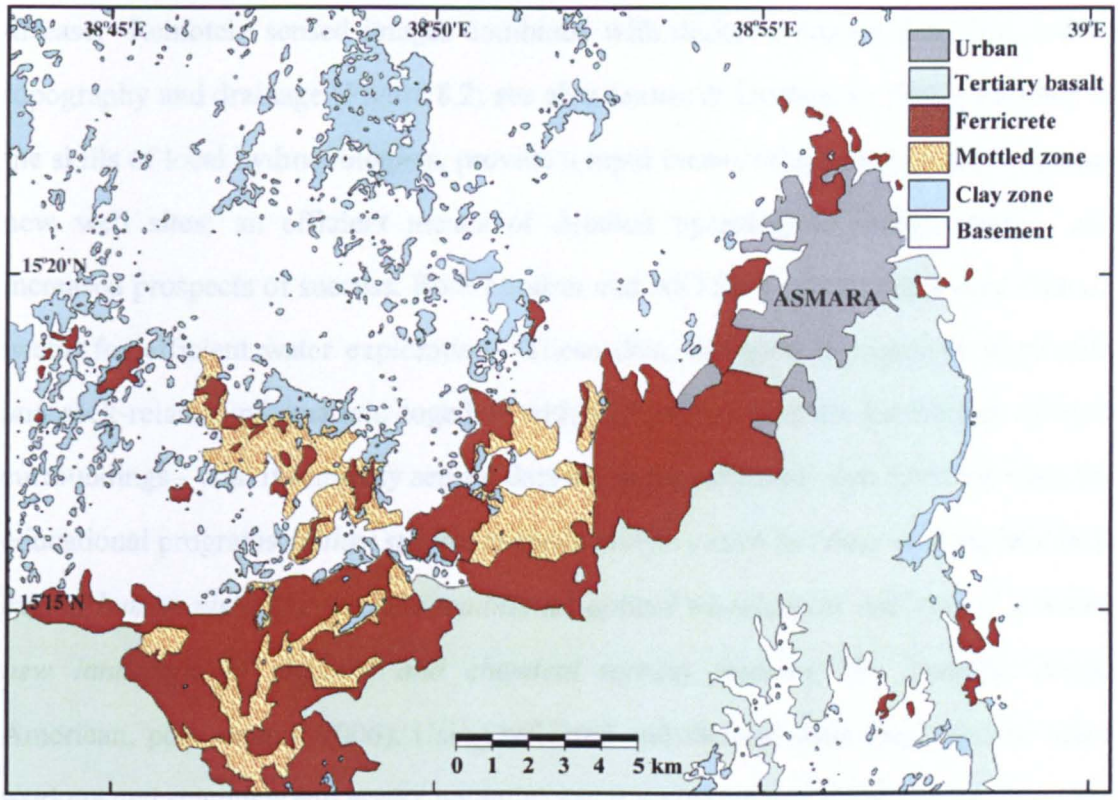


**Figure 8.7**. Geological map of Eritrean laterite facies near Asmara, Eritrea, interpreted from Landsat TM and ASTER data (Andrews Deller 2006)

Adequate planning to manage disasters that come with little or no warning is often difficult - earthquakes (Ellsworth 2006) and volcanic eruptions are cases in point. But drought and famine are entirely foreseeable, even though the new millennium began with nearly 20% of the world drought-stricken (Kogan 2005). Drought, desertification and crop yield monitoring data (Chavez *et al.* 2002) are available, as are comprehensive Drought Early Warning (DEW) and Famine Early Warning (FEW) systems with alerts and appropriate data collections that can be used to provide timely warning (Davies *et al.* 1991; Buchanan-Smith 1997), (Table 8.2). Discernible deterioration of vegetation captured over time on satellite images, coupled with local people's expertise in ground information can facilitate strategic planning for disaster mitigation months before drought takes hold.

However, central to any disaster that disrupts infrastructure and displaces people from their homes is the need for rapid provision of clean drinking water, an even greater priority than food and shelter because of the ever-present threat of epidemic

disease. Remotely sensed images combined with digital elevation data that display topography and drainage (Figure 8.2; see also Jenson & Domingue 1988), matched to the skills of local hydrogeologists, provide a rapid means of assessing and prioritising new well sites; an efficient means of detailed hydrological reconnaissance and increased prospects of success. Both Landsat and ASTER provide image data that are useful for efficient water exploration. These data, designed to highlight vegetation and rock-related information, together with indigenous people's knowledge of their surroundings - vital if remotely sensed data are to be validated - can form the basis for educational programs. '*Other special purpose imagery such as radar and thermal help extend human vision beyond the traditional optical wavelengths and reveal a whole new landscape of physical and chemical terrain features*' (D. Taranik, Anglo American, pers. comm. 2006). Using reflected and thermal data, local people, relief workers and scientists can assess potential water resources and work out the best sites for extraction, storage and distribution.

ASTER 631 and TM 742 images illustrate the use of remote sensing for groundwater exploration the most simply. On these images green vegetation can be traced along spring lines, an elementary observation that allows for the best placing of wells. Whilst TM data allow some discrimination of potential aquifers, ASTER data have the spectral capabilities to identify sediments likely to have high yields (Drury & Andrews Deller 2002a & b). Major aquifers are rocks and superficial deposits rich in quartz and feldspar and/or carbonates. These minerals produce porous and permeable conditions in sediments, but also in crystalline rocks that have been pervasively fractured. Quartz and feldspar have unique red to magenta signatures (Drury 1998) in the standard multispectral thermal image combination of ASTER bands 14, 12 and 10 as RGB and can be identified easily because of that colouration. Quartz- and feldspar-rich alluvial sediments therefore are often the most easily found aquifers and readily pinpointed where the ground is not obscured by thick vegetation. It is true that thermal images are darkened by vegetation, but the predicted hues still show unless vegetation cover is dense. Carbonates show in yellow hues on images that combine

ASTER bands 5,6 and 8 as RGB, but so too do epidote- and chlorite- bearing rocks, which have to be checked according to their spectral 'signatures' in other band combinations. ASTER 631 images are ideal for such screening as carbonates show as pale grey to white because of their flat visible and near-infrared (VNIR) to short-wave infrared (SWIR) spectra, whereas chlorite and epidote show up in shades of red to magenta (Drury & Andrews Deller 2002b, 2004). Use of these two ASTER images therefore identifies carbonates effectively. ASTER 631 images can also be used to screen quartz- and feldspar-rich sediments for low permeability due to pore-clogging by clays and white micas, which show up as cyan or sky-blue, and by detrital chlorite that gives a magenta tint (Drury & Andrews Deller 2005).

Moreover, both TM and ASTER instruments have sufficient resolution to delineate major joint systems and large fracture zones (Drury *et al.* 2001). Fracture zone mapping is most easily achieved using stereoscopic ASTER bands 3N and 3B in anaglyph form. For example, International Committee of the Red Cross (ICRC) relief workers in Eritrea, '*with diverse backgrounds and no remote sensing experience*', quickly grasped the essentials of image interpretation and proficiently targeted '*locations for sinking wells on simple 3-band images and ASTER anaglyphs. ... An Eritrean ICRC drilling team produced even quicker responses using images in the field*' (S.A. Drury, Open University, pers. comm. 2006). To determine water table depth, field follow-up with geophysical methods is necessary (Drury *et al.* 2001), but remote sensing efficiently narrows the areas of search and increases the prospects of finding water dramatically. Observation borne out by successful experience instils confidence and none of the observations made above, essential for water exploration, are beyond local people. In rural areas, where individuals specialise in locating near-surface water supplies, their expertise coupled with a remote sensing approach can benefit all.

Perhaps a key to successful community-based disaster management is education (Andrews Deller *et al.* 2004, 2005). Long-term and emergency water supplies, important at all times and crucial during periods of disaster and post-crisis recovery,

might be a topic used to raise public awareness of the usefulness of space technology for disaster management and a starting point for training adults and children. Students and school children assimilate new ideas quickly, whilst older people, who are experts in ground truth, have a great respect for education in less-developed and rural areas. Blaut *et al.* (2003), Plester *et al.* (2002) and Sowden *et al.* (1997) report on pre-school children's innate ability to recognise terrain features and navigate using aerial photos. This is borne out by the author's experience in rural Eritrea (2003) with young children who mastered aerial photos and ASTER images within an hour and selected appropriate samples correctly all over the locality - a pre-school child even located a house made out of the correct material. '*Nothing can replace field observation as a basis for building up knowledge in depth*' (Marsh 2000). Local people of all ages at any standard of education, given motivation, are quite capable of collecting and locating data (Delson 2006; see also Ferreira 1792; Dehaene *et al.* 2006) that can add to hazard early warning by reporting instances of:

- unusual changes in the level of water in wells - a common precursor of seismic events in earthquake-prone areas;
- ground fracturing on and near unstable slopes - an indication of landslides;
- recent fumarole activity and ground changes in the vicinity of volcanoes - common precursors to volcanic eruption.

Moreover, in areas prone to flooding, tsunamis, seismic activity, landslides or volcanism, people with ready access to graphic remotely sensed images that indicate potential refuge, can prepare themselves with greater confidence to escape future hazards.

In the long term, data distribution on a global level is being addressed by the United Nations Office for Outer Space Affairs (UNOOSA), NASA, NOAA, the USGS EROS Data Centre (Table 8.2) and the Integrated Global Observing Strategy (IGOS) (Marsh 2003). Training opportunities in remote sensing are available through organisations like the UN Development Programme, the World Bank, USAID, ICRC and the British Department for International Development (Drury 1998). However,

space technology for disaster management is often centred round specific problem areas or hazards and few people in disaster-prone areas currently benefit from accurate regional information, data, training or funding (HAIC Secretariat 2001; Rochon *et al.* 2005).

## 8.5 Conclusion

The place for remotely sensed data and access to it should be within local communities and at the disposal of the indigenous populations. Yet, '*developing countries still do not have wide access to space-based technologies used for early warning and emergency response, not only during the disaster response phase, but also during the more important preparedness phase of the disaster cycle, which invariably results in unnecessary loss of life and property when disaster strikes*' (Stevens 2005). Country-specific information and guidance on the use of appropriate cost-effective remote sensing data (Jordan *et al.* 2000a) are available. But the fact

**Table 8.3** Useful types of satellite imagery for assessing geohazards

| Geoscientific hazard | Useful remotely sensed data for unmapped terrains |
|---|---|
| Volcanic | ASTER stereo (bands 3N & 3B in anaglyph form – landform overview), MODIS (near real-time thermal mapping), AVHRR (near real-time thermal mapping), MODIS and AVHRR (visible - near real-time emission mapping), perspective views (ASTER 631 or ETM+ 742 draped over SRTM DEM) |
| Seismic | ASTER stereo (bands 3N & 3B in anaglyph form – landform overview, active fault mapping), ASTER or Landsat ETM+ (631 or 742 - clay-rich strata prone to liquefaction), perspective views (ASTER 631 or ETM+ 742 draped over SRTM DEM) |
| Landslide | ASTER stereo (bands 3N & 3B – landform overview), SRTM (DEM – slope mapping), ASTER or Landsat ETM+ (631 or 742 - clay-rich lubricant strata), perspective views (ASTER 631 or ETM+ 742 draped over SRTM DEM) |
| Flood & tsunamis | SRTM (DEM – mapping flood-prone areas, slope and drainage assessment for flash floods) |
| Drought (water provision) | ASTER (631 – geological and vegetation mapping; 568 and 14 12 10 – discrimination of quartz- and carbonate rich aquifers; bands 3N & 3B in anaglyph form – fracture zone mapping); SRTM (DEM – fracture zone mapping) |

that multispectral remote sensing data remain little understood by local people,

emergency relief workers and civil protection agency personnel is indicative of the lack of communication between specialists in space technology and the people who need their help. The problem is not small but can be tackled. Remote sensing applications provide an opportunity for progress. Given the chance, local people and those involved in humanitarian relief readily grasp the essentials of image interpretation in the context of their lives or duties. Once dialogue between locals, relief workers and specialists is established, all those who have a common interest in safety and the improvement in living conditions can work together. Easily understood images in printed form can be used to assess geohazards in mapped and unmapped terrain. Free or low-cost ASTER, MODIS, Landsat ETM+, SRTM-DEM and AVHRR data can be used to enable local people to deal with the water requirements where they live and the dangers of floods, tsunamis, landslides, volcanic or seismic hazards and drought and famine (Table 8.3). As a result local people can take charge of their own lives. Environmental factors affecting human health and wellbeing can be catered for, hazards contained and remotely sensed data used by ordinary people to address the problems they face.

*Acknowledgements*

Special thanks go to W.S. Deller and S.A. Drury who helped and encouraged me with this work. My thanks also go to D. Stevens and A. Teklegiorgis for their support, to R. M. Teeuw for asking me to contribute my work to this publication and to the Eritrean and Ethiopian children and peoples.

## 8.6 Case Study 2 - Geochemistry of well water

Water was sampled from 34 wells within a 60km radius of Asmara (figure 8.8) in order to answer the questions below:

- What chemical hazards are posed by well waters in the most populous part of Eritrea?
- Do waters from wells in different lithologies have different chemical compositions?

The iron -rich facies of laterites form aquifers for many village wells. These facies are rich in goethite [$Fe(OH)_3$], a sorbent for many elements (including arsenic) (Manning *et al.* 1997) which can affect drinking water. Reductive dissolution of goethite, leading to contamination of well waters with arsenic levels above the World Health Organisation (WHO) recommended maximum (10 $\mu g\ l^{-1}$) in latertised terrain

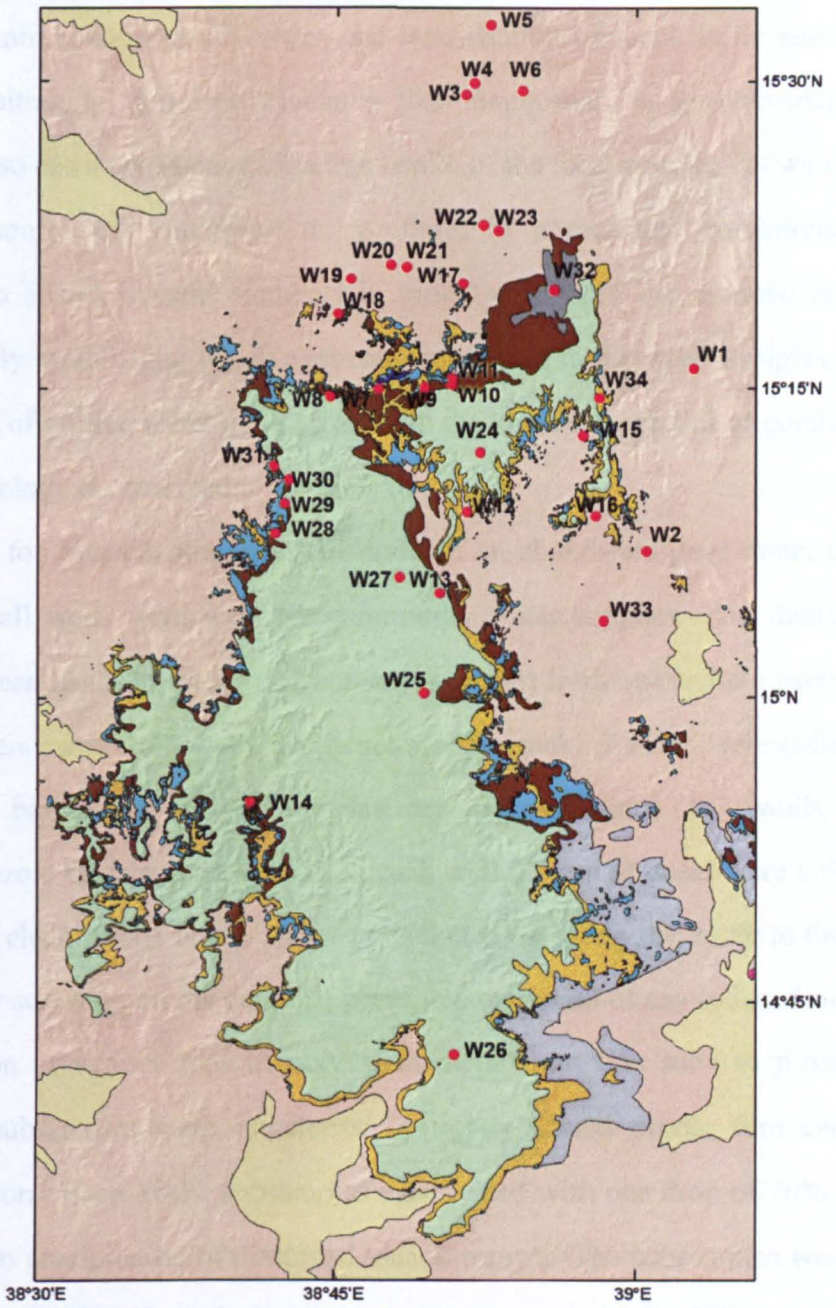


**Figure 8.8** Locations of well water samples in Eritrea (red dots) in relation to regional geology (see Chapter 4/5 Map Legend)

in Ghana (Smedley *et al.* 1996; Smedley 1996) and Bangladesh (Kinnigburgh & Smedley 2001), may also be a problem in Eritrea. In Bangladesh though, goethite forms a thin film coating sedimentary grains, but in Eritrea and Ethiopia, it is a dominant mineral in areas underlain by laterites. The study area has pervasive hydrothermal mineralisation in lateritised areas and is dominated by low-grade gold, which has been mined for decades. Arsenopyrite and arsenic may therefore occur in high concentrations in groundwater and lateritisation of local mafic and ultramafic rocks, resulting in dissolved elements like magnesium in groundwater used for drinking also has a detrimental effect on health of the local people. As well as being a potential source of contamination, goethite, in appropriate conditions, has the potential to adsorb several elements in groundwater and can remove contaminant elements. By establishing which elements are present in the water samples, a realistic assessment of ground water quality based on the known properties of goethite and the relevant geology is presented.

Except for two samples from the drain of an abandoned gold mine, the sample points for all wells were used for community water supplies. No distinction was made between hand-dug wells and boreholes. Apart from one sample from alluvium, all the waters came from wells that penetrated bedrock. Results were collected from the flood basalts (6 wells); the laterites beneath them (17 wells) and the Neoproterozoic basement (9 wells). At each well 2 litres of water were collected and placed in a clean plastic bottle. Air was excluded by filling the bottle to the brim and then tightly screwing on the cap; this prevented oxidation of any reduced samples and precipitation of various ions of polyvalent metal ions. As soon as possible, 50ml duplicate subsamples were transferred to tightly sealed plastic film canisters for transportation. Each of the subsamples was treated with one drop of 70% nitric acid to ensure no precipitation of dissolved ions in transit. The subsamples were used for ICP-AES and ICP-MS analysis (see below) on return to the UK. On the day of collection, subsamples for field testing were pipetted from the main samples into small test vessels provided with the test kits.

### 8.6.1 Semi-quantitative tests for potential toxicity


**Figure 8.9** Merckoquant test strip for cobalt and calibration chart

**Table 8.4** Concentration steps analysed by using the Merckoquant semi-quantitative strips, in mg $l^{-1}$ (ppm), except for arsenic (As) in µg $l^{-1}$ (ppb)

| **Element** | | | | | | |
|---|---|---|---|---|---|---|
| Al mg $l^{-1}$ | 0 | >10 | >25 | >50 | >100 | |
| Fe mg $l^{-1}$ | 0 | >10 | >30 | >100 | >300 | >1000 |
| Mn mg $l^{-1}$ | 0 | >2 | >5 | >20 | >50 | >100 |
| Ca mg $l^{-1}$ | 0 | >10 | >25 | >50 | >100 | |
| K mg $l^{-1}$ | 0 | >250 | >450 | >700 | >1000 | >1500 |
| Cl mg $l^{-1}$ | 0 | >500 | >1000 | >1500 | >2000 | >3000 |
| Co mg $l^{-1}$ | 0 | >10 | >20 | >100 | >300 | >1000 |
| Ni mg $l^{-1}$ | 0 | >10 | >25 | >100 | >250 | >500 |
| Cu mg $l^{-1}$ | 0 | >10 | >30 | >100 | >300 | |
| Zn mg $l^{-1}$ | 0 | >10 | >40 | >100 | >250 | |
| As µg $l^{-1}$ | 0 | >10 | >25 | >50 | >100 | >500 |

Merckoquant semi-quantitative paper test strips aimed at environmental monitoring of surface and groundwater for 11 elements were used. The strips for each element are impregnated with a compound that undergoes a colour change in the presence of ions of the element. The chemistry involved in this colorimetric method is often very complex, but has where possible been simplified so that merely dipping a strip in water shows a colour change according to several rages of concentration (Merck Millepore 2012). In some cases the pH of the sample has to be set to a particular value by adding acid or alkaline reagent with a calibrated dropper. The

most complex of these tests is that for arsenic, which requires any arsenic present in solution to be converted to arsine gas, to which the test strip reacts. Most of the colour changes are in the intensity of a single colour, the strip being matched to a stepwise, calibrated chart (figure 8.9). Table 8.4 shows the steps in concentration analysed using the strips and Appendix C the semiquantitative analyses of well water samples.

### 8.6.2 Accurate, quantitative water analysis

An opportunity arose to analyse the well-water samples to a much higher level of precision at the NERC Inductively Coupled Plasma Spectrometry Facility, using an Inductively Coupled Plasma-Atomic Emission Spectrometer (ICP-AES) at Royal Holloway University of London and an Inductively Coupled Plasma Mass Spectrometer (ICP-MS) at Kingston University (Lynge 2005; Lynge & Jarvis 2009). More than a check of the validity of the strip analyses conducted in the field, these analyses aimed at examining any differences in water chemistry between wells in different lithologies. Data for 9 major elements (Ca, Na, Mg, K , Fe, Al, Si, S and Mn) and strontium (Sr) are from the ICP-AES instrument. The ICP-MS provided analyses for 27 trace elements (see below[1]). Of these cobalt (Co), rubidium (Rb), tin (Sn), antimony (Sb), tungsten (W), thallium (Tl) and bismuth (Bi) are not considered because their concentrations fell close to or below the ICP-MS detection limits.

Table 8.5 summarises the water analyses as means and ranges of concentration for each element, grouped according to the lithology (laterite, basalt or basement) in which wells were constructed. Three extra analyses were carried out on unusual wells ('Others'). Of the last three, two (samples 22a and 22b) are mine drainage waters and the third is water from a well in alluvium overlying laterite that quickly precipitated iron hydroxide on exposure to the air. These three were considered likely to have the most toxic dissolved contents. For comparison, Table 8.5 also shows means and ranges for 55 different bottled mineral waters from Europe (Misund *et al.* 1999)

[1] Li, B, Al, P, Ti, V, Cr, Co, Ni, Cu, Zn, As, Se, Rb, Mo, Ag, Cd, Sn, Sb, Ba, W, Au, Hg, Tl, Pb, Bi, U

analysed at several laboratories using ICP-AES and ICP-MS with comparable detection limits to those used in this study.

The detailed analyses confirms that the Merckoquant strip tests performed as specified, with neither 'false positives' nor 'false negatives' values. Mean values of the Eritrean data compare reasonably well with those for bottled European mineral waters, and are either lower or less than an order of magnitude higher than those for European waters. The notable exceptions are aluminium, vanadium and zinc.

It has been suggested, but not proven, that aluminium is a risk factor in the onset of Alzheimer's disease (Martyn *et al.* 1989; Sharp 2001) however, only three Eritrean samples exceed the 200 ppb maximum for Al in the World Health Organisation guidelines for drinking water-water (WHO 2004, 2008). Two (samples 1 and 6) of the three samples were only a few ppb over the limit and the third (samples 9) at 1400 ppb was seven times over the WHO guideline maximum and perhaps hazardous. Sample 9 is from a protected spring rising from the top of the laterite clay zone, i.e. from a highly aluminous source that under slightly acid conditions may yield Al ions to solution. Figure 8.10 shows the range of Al and Na ion concentrations in the samples. Aluminium concentrations are scaled logarithmically to show detail at low and high concentrations and, except for those noted above, all the waters are similar to European mineral waters. Sodium is completely within the range of mineral waters, although there are reports that some wells in saprolitic basement (Horizon 4) are noticeably salty in the more arid parts of northern Eritrea (Tesfamichael Keleta, personal communication 2003).

**Table 8.5** Means and ranges of element concentrations in waters from wells in laterites, basalts and basement rocks. The 'others' category shows concentrations in waters from atypical wells. Sample 6 showed iron hydroxide precipitate after 2 hours. Samples 22a and 22b are waters draining from an abandoned gold mine. Concentrations by volume are shown in ppm (mg $l^{-1}$) for major elements, and ppb (μg $l^{-1}$) for trace elements. The means and ranges for 55 European bottled mineral waters are shown for comparison (Misund *et al.* 1999). WHO limits (guidelines for maximum acceptable concentrations in drinking water) are from WHO (2008). **n.d.** not detected

| **Major elements (ppm)** | | | | | | | | | | | **Trace elements (ppb)** | | | | | |
|---|---|---|---|---|---|---|---|---|---|---|---|---|---|---|---|---|
| | **Ca** | **Na** | **Mg** | **K** | **Fe** | **Al** | **Si** | **S** | **Mn** | **Sr** | | **Li** | **B** | **Al** | **P** | **Ti** |
| | | | | | | | | | | | **Det lim** | 0.2 | 0.6 | 0.09 | 1.3 | 0.2 |
| **WHO limits** | | | | | | | | | 0.4 | | **WHO lims** | | | **200** | | |
| **55** | **mineral** | **waters** | | | | | | | | | | | | | | |
| **European** | | | | | | | | | | | | | | | | |
| Mean | 69 | 27 | 25 | 5.8 | 0.0 | 0.0 | 5.5 | 32.0 | 0.0 | 0.45 | | 16 | 92 | 6 | <100 | 0.9 |
| max | 488 | 1723 | 215 | 30.3 | 0.4 | 0.1 | 20.2 | 1067 | 0.2 | 12.2 | | 3100 | 10096 | 147 | 1380 | 6.3 |
| min | 26 | 1 | 0 | 0.3 | 0.0 | 0.0 | 1.4 | 0.9 | 0.0 | 0.01 | | 0 | 5 | 0 | <100 | 0.0 |
| **Laterite** | | | | | | | | | | | **Laterites** | | | | | |
| Mean | 61 | 48.2 | 32 | 10.1 | 0.2 | 0.1 | 16.5 | 12.2 | 0.04 | 0.33 | mean | 8 | 49 | 103 | 63 | 3.8 |
| Max | 85 | 223 | 64 | 134.0 | 2.8 | 2.3 | 31.4 | 26.3 | 0.21 | 1.07 | max | 84 | 189 | 1400 | 162 | 30.1 |
| Min | 16 | 11 | 1 | 0.4 | 0 | 0 | 1.4 | 2.6 | 0.00 | 0.10 | min | 0 | 8 | 8 | 11 | 0.9 |
| **Basalt** | | | | | | | | | | | **Basalts** | | | | | |
| mean | 82.3 | 51 | 44 | 2.3 | 0.1 | 0 | 19 | 15.3 | 0.02 | 0.27 | mean | 92 | 39 | 44 | 73 | 3.3 |
| max | 111 | 79 | 73 | 4.9 | 0.4 | 0.2 | 26.7 | 22.4 | 0.04 | 0.77 | max | 282 | 50 | 176 | 153 | 7.8 |
| min | 63 | 14 | 16 | 0.7 | 0 | 0 | 10.3 | 9.6 | 0.00 | 0.04 | min | 0 | 25 | 7 | 29 | 2.1 |
| **Basement** | | | | | | | | | | | **Basement** | | | | | |
| mean | 110 | 77 | 47 | 2.2 | 0.3 | 0.1 | 13.7 | 34.9 | 0.14 | 0.59 | mean | 8 | 93 | 72 | 48 | 3.2 |
| max | 171 | 201 | 96 | 4.2 | 0.7 | 0.4 | 20.0 | 86.2 | 0.51 | 1.14 | max | 57 | 168 | 247 | 78 | 7.2 |
| min | 53 | 10 | 14 | 0.3 | 0.1 | 0 | 8.9 | 3.3 | 0.00 | 0.14 | min | 0 | 22 | 4 | 21 | 1.5 |
| **Others** | | | | | | | | | | | **Others** | | | | | |
| sample 6 | 47 | 13 | 15 | 0.8 | 16 | 0.3 | 8.1 | 3.4 | 0.14 | 0.21 | sample 6 | 0 | 22 | 214 | 387 | 6.6 |
| sample 22a | 101 | 27 | 23 | 2.1 | 0.2 | 0 | 11.2 | 8.7 | 0.33 | 0.39 | sample 22a | 147 | 52 | 52 | 40 | 2.5 |
| sample 22b | 60 | 7 | 15 | 1.4 | 1 | 0 | 6.6 | 1.8 | 0.88 | 0.25 | sample 22b | 0 | 22 | 35 | 26 | 2.2 |

**Table 8.5** (cont.)

| **Trace elements (ppb)** | | | | | | | | | | | | | | | |
|---|---|---|---|---|---|---|---|---|---|---|---|---|---|---|---|
| | **V** | **Cr** | **Ni** | **Cu** | **Zn** | **As** | **Se** | **Mo** | **Ag** | **Cd** | **Ba** | **Au** | **Hg** | **Pb** | **U** |
| **Det lim** | 0.01 | 0.02 | 0.02 | 0.08 | 0.05 | 0.08 | 0.8 | 0.02 | 0.02 | 0.04 | 0.8 | 0.03 | 0.06 | 0.05 | 0.02 |
| **WHO limits** | | **50** | **20** | **2000** | **3000** | **10** | **10** | **70** | | **3** | **70** | | **2** | **10** | |
| **55** | **mineral waters** | | | | | | | | | | | | | | |
| **European** | | | | | | | | | | | | | | | |
| Mean | 0.6 | 2.9 | 2.5 | 0.6 | 3 | 0.5 | 0.6 | 0.3 | 0.0 | 0.0 | 26 | n.d. | 0.0 | 0.0 | 0.1 |
| Max | 31 | 28.9 | 14.4 | 30.7 | 271 | 21.6 | 49.3 | 14.7 | 7.2 | 0.2 | 2000 | n.d. | 0.3 | 0.5 | 9.5 |
| Min | 0.0 | 0.0 | 0.2 | 0.0 | 0.0 | 0.0 | 0.0 | 0.0 | 0.0 | 0.0 | 1.4 | n.d. | 0.0 | 0.0 | 0.0 |
| **Laterite** | | | | | | | | | | | | | | | |
| Mean | 11.3 | 2.4 | 2.2 | 4.0 | 53 | 0.6 | 2 | 1.1 | 0.5 | 0.2 | 71 | 0.2 | 0.1 | 0.7 | 0.8 |
| Max | 49.9 | 7.8 | 10 | 12.9 | 658 | 2.8 | 4.9 | 5.4 | 2.7 | 0.3 | 239 | 0.3 | 0.2 | 2.3 | 2.4 |
| Min | 0.3 | 0.8 | 0.5 | 0.8 | 5 | 0.1 | 0.7 | 0.1 | 0 | 0.1 | 8.8 | 0.1 | 0.1 | 0.3 | 0 |
| **Basalt** | | | | | | | | | | | | | | | |
| Mean | 16.1 | 2.2 | 1.7 | 4 | 15 | 0.3 | 2.5 | 0.5 | 0.4 | 0.2 | 32 | 0.2 | 0.1 | 0.9 | 1.1 |
| Max | 25 | 3.2 | 2.6 | 9.5 | 24 | 0.5 | 5.3 | 0.6 | 0.7 | 0.4 | 83 | 0.3 | 0.2 | 2.3 | 3.5 |
| Min | 2.4 | 0.8 | 1 | 1.4 | 7 | 0.2 | 1.5 | 0.3 | 0.1 | 0.1 | 3.5 | 0.1 | 0 | 0.3 | 0.2 |
| **Basement** | | | | | | | | | | | | | | | |
| Mean | 5.1 | 2.3 | 1.6 | 2.1 | 12 | 1.2 | 3.6 | 1.7 | 0.3 | 0.1 | 60 | 0.2 | 0.2 | 0.5 | 8.7 |
| Max | 16.9 | 3.7 | 3 | 4.1 | 32 | 3.6 | 5 | 5.6 | 1.1 | 0.2 | 77 | 0.4 | 0.5 | 0.6 | 31.1 |
| Min | 0.9 | 1.2 | 0.8 | 0.7 | 5 | 0.2 | 1.5 | 0.1 | 0 | 0.1 | 19 | 0.1 | 0.1 | 0.1 | 0.1 |
| **Others** | | | | | | | | | | | | | | | |
| sample 6 | 1.5 | 5 | 3 | 214 | 1067 | 0.5 | 0.7 | 0.3 | 0.4 | 0.2 | 18 | 0.3 | 0.2 | 34.9 | 0.1 |
| sample 22a | 1.7 | 2.8 | 1.7 | 6 | 17 | 0.8 | 2.5 | 1.5 | 0.5 | 0.2 | 72 | 0.2 | 0.2 | 2.3 | 1.5 |
| sample 22b | 0.4 | 1.4 | 1.8 | 0.8 | 3 | 0.5 | 1 | 0.2 | 0 | 0.2 | 40 | 0.1 | 0.1 | 0.2 | 0.3 |

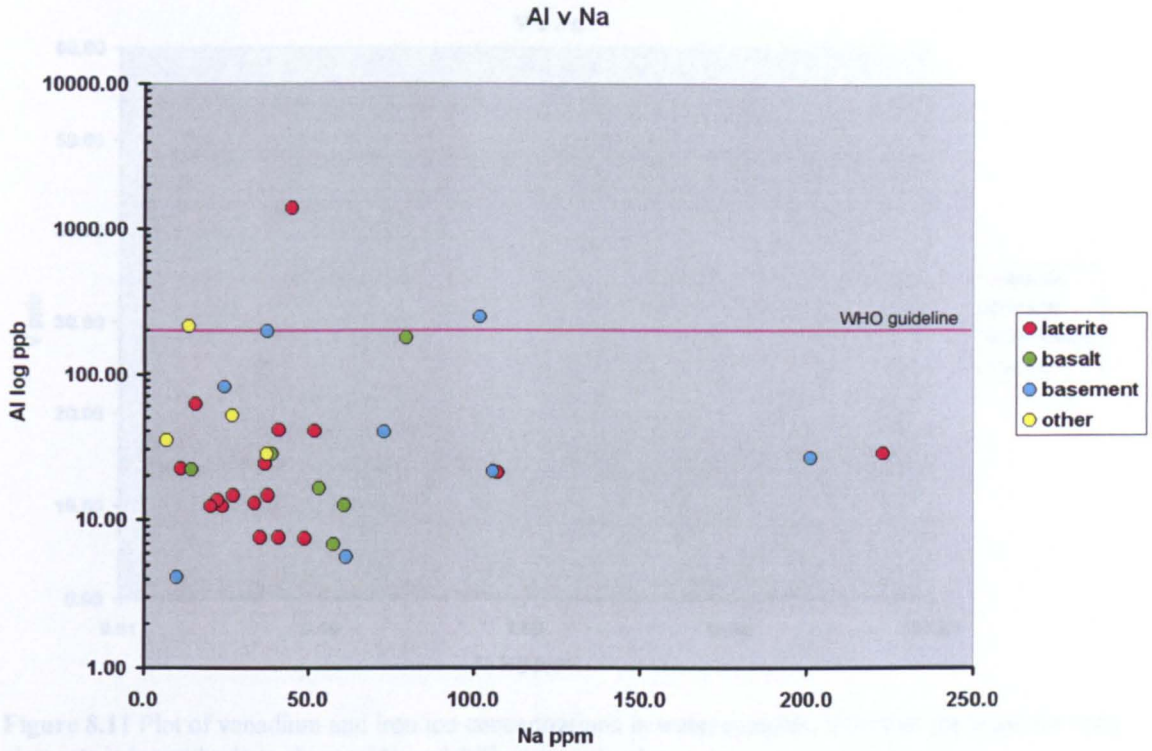


**Figure 8.10** Plot of aluminium and sodium ion concentrations in water samples. Note that the scale for Al is logarithmic to show wide variability more clearly. The WHO guideline maximum for Al (200 ppb) is shown for reference

The high mean for vanadium (V) compared with the European mineral waters is apparent in 11 with V concentrations above 10 ppb (Figure 8.11), but none had values higher than 50 ppb. However the remainder although still significantly higher than the European mean concentration, pose no known hazard at concentrations up to 50 ppb in drinking water. Indeed WHO has set no guideline maximum though some explanation is needed for the high concentrations found. Vanadium is concentrated in the mottled zone of laterites (Chapter 2) yet depleted in ferricretes, reflecting its ready dissolution in aerated waters. Five of the V-rich waters are from wells driven in laterites. Vanadium is more abundant in mafic igneous rocks than other common crustal rocks, borne out by the fact that 5 of the 6 waters from wells in basalt have V >10 ppb. Figure 8.11 shows little correlation between V and Fe, although the highest V concentration is in water from a laterite well with high Fe content. There is little apparent correlation between V and any other element.

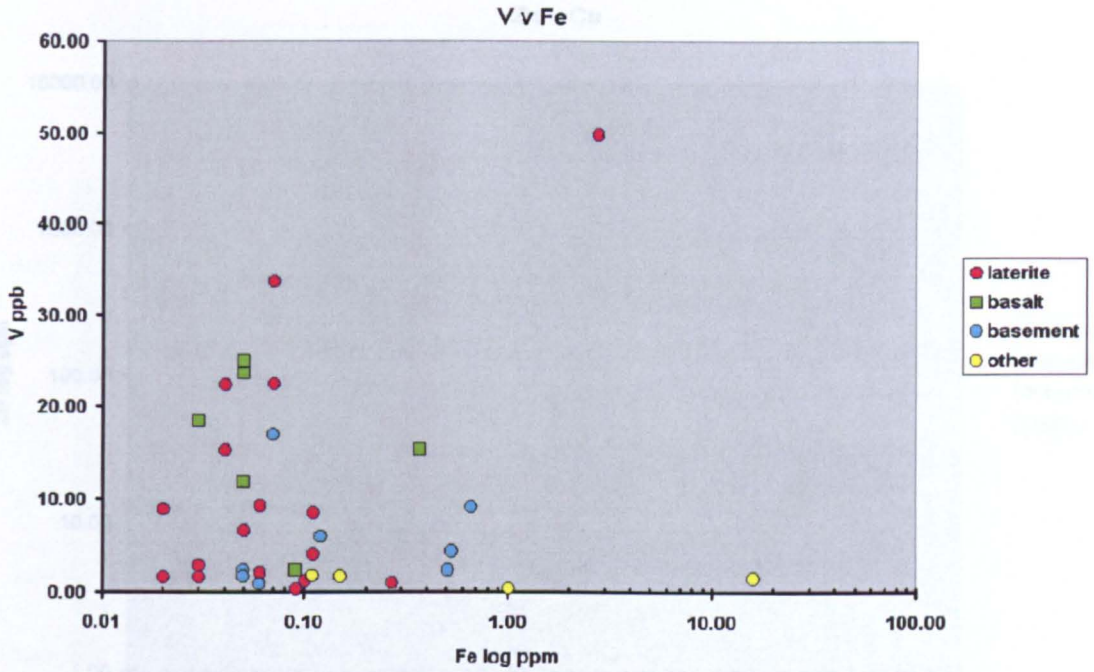


**Figure 8.11** Plot of vanadium and iron ion concentrations in water samples. Note that the scale for both elements is logarithmic to show wide variability more clearly

Figure 8.12 showing zinc and copper concentration aims to highlight any influence in well waters of weathered sulfides or release of heavy metal ions from reduced conditions acting on ferricretes, goethite in which may concentrate them by adsorption. Two samples have far higher contents of Zn ions than the others (sample 6 and 7, at 1067 and 658 ppb respectively). Although the element is consistently at higher concentrations than the European mineral water mean of 3 ppb, but below the WHO guideline maximum of 3000 ppb, Zinc is not toxic but at high concentration creates a noxious taste in water. Only one sample (6) contains notably high Cu (214 ppb) however this is far below the WHO guideline maximum of 2000 ppb. Sample 6 is from an alluvial well whose concrete pump pedestal was deeply iron-stained. Soon after exposure to air this water sample turned brownish as Fe(II) ions became oxidised and precipitated as Fe(III) hydroxide.

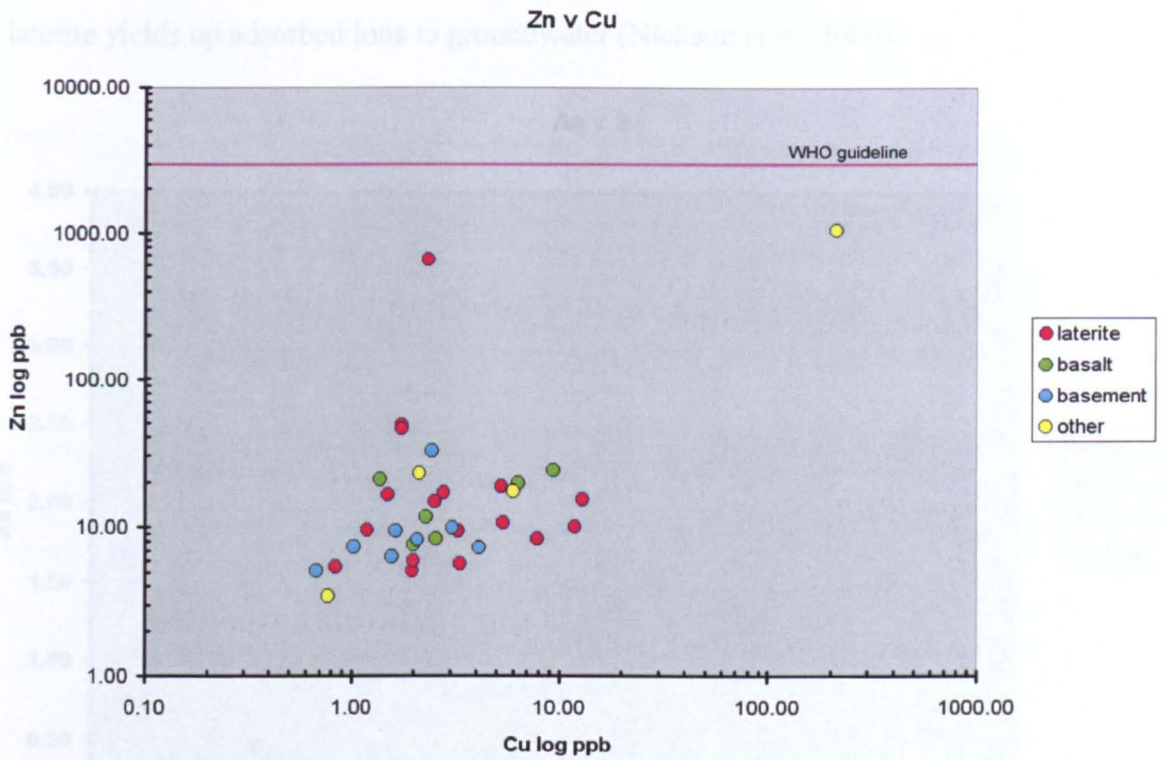


**Figure 8.12** Plot of zinc and copper ion concentrations in water samples. Note that the scale for both elements is logarithmic to show wide variability more clearl.

Arsenic is the most worrying element adsorbed by goethite is, as it causes a variety of cancers and unsightly skin lesions (WHO 2004; Drury 2006). A vital part of this study was to check waters for As contamination in an area with large tracts of laterite an experiment justified by discovery of the high concentrations of the element in ferricrete (Chapter 2). Thankfully, not a single well yielded water with close to the WHO guideline maximum of 10 ppb for As. Sample 6 demonstrates that shallow modern groundwater in Eritrea can be highly reduced to result in conditions under which goethite may be dissolved, whereas bleached zones in the upper laterite profile show that such waters have affected ferricretes and the mottled zone in the past. Yet, no sign of arsenic enrichment is present nor any correlation with Fe content in waters. There is a weak correlation between As and S (figure8.13). Ironically low As concentrations may be due to the superabundance of lateritic goethite in the environment and its extremely high capacity for adsorption. If any adsorbed ions are released by goethite dissolution, any remaining goethite will take up those ions

readily indicating that perhaps only complete reductive dissolution of goethite in laterite yields up adsorbed ions to groundwater (Nickson *et al.* 2000).

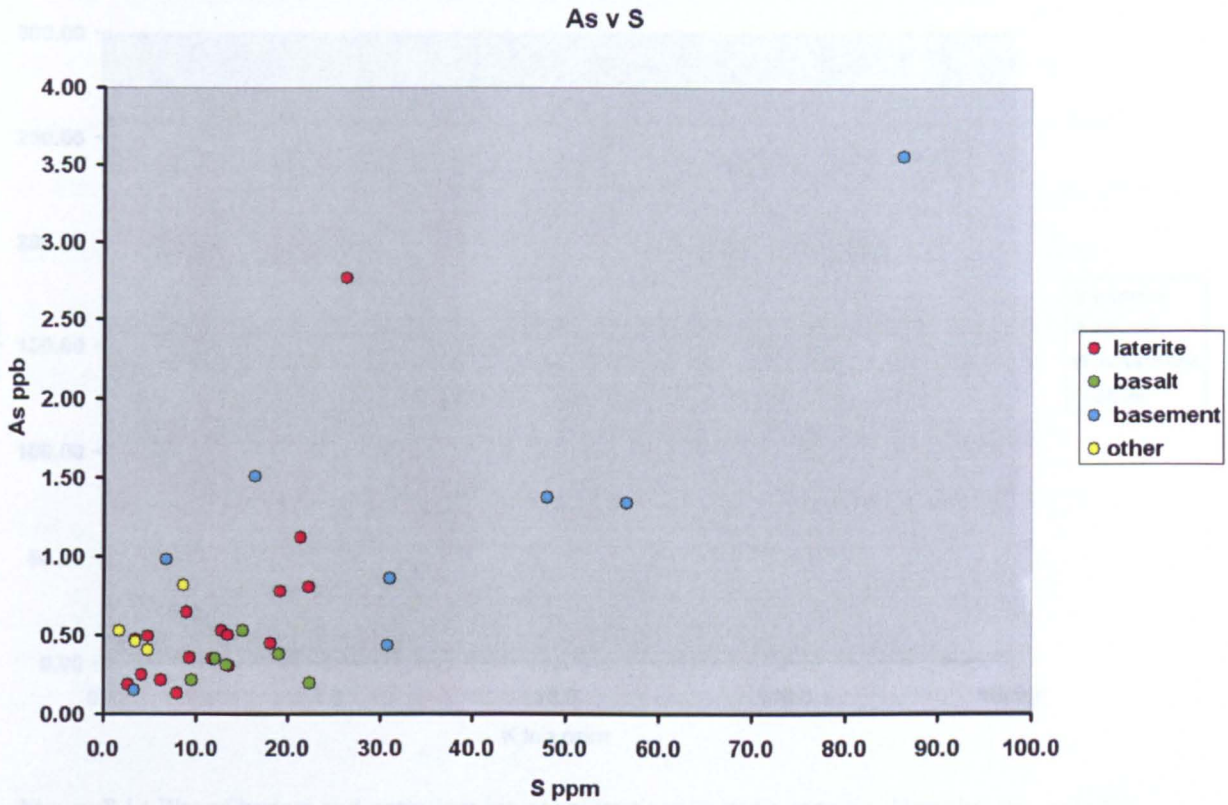


**Figure 8.13** Plot of arsenic and sulfur ion concentrations in water samples

The major concerns resulting from the well water analyses centred on 12 samples that had barium concentrations above the WHO guideline maximum. Six were from wells in laterite, 1 came from a basalt well and 5 originated from wells in basement. Although barium sulfate is commonly used as a filler in paper and in the barium 'meal' ingested by patients having gastrointestinal X-rays, no ill effects are known from ingestion of barium in that form ($BaSO_4$) which is highly insoluble. However, dissolved barium ions do pose a hazard. They affect the central nervous system and act as a muscle stimulant lowering the amount of potassium in the blood (McCain 1997) so significantly increasing the mortality rate in the 65+ age group as Ba-rich water if drunk habitually causes cardiovascular disease. For this reason the WHO guideline maximum is 70 $\mu g\ l^{-1}$ (ppb) in drinking water, which in12 Eritrean well waters (6 from laterite areas, 5 from basement rocks and one from basalt) was

exceeded (figure 8.14).

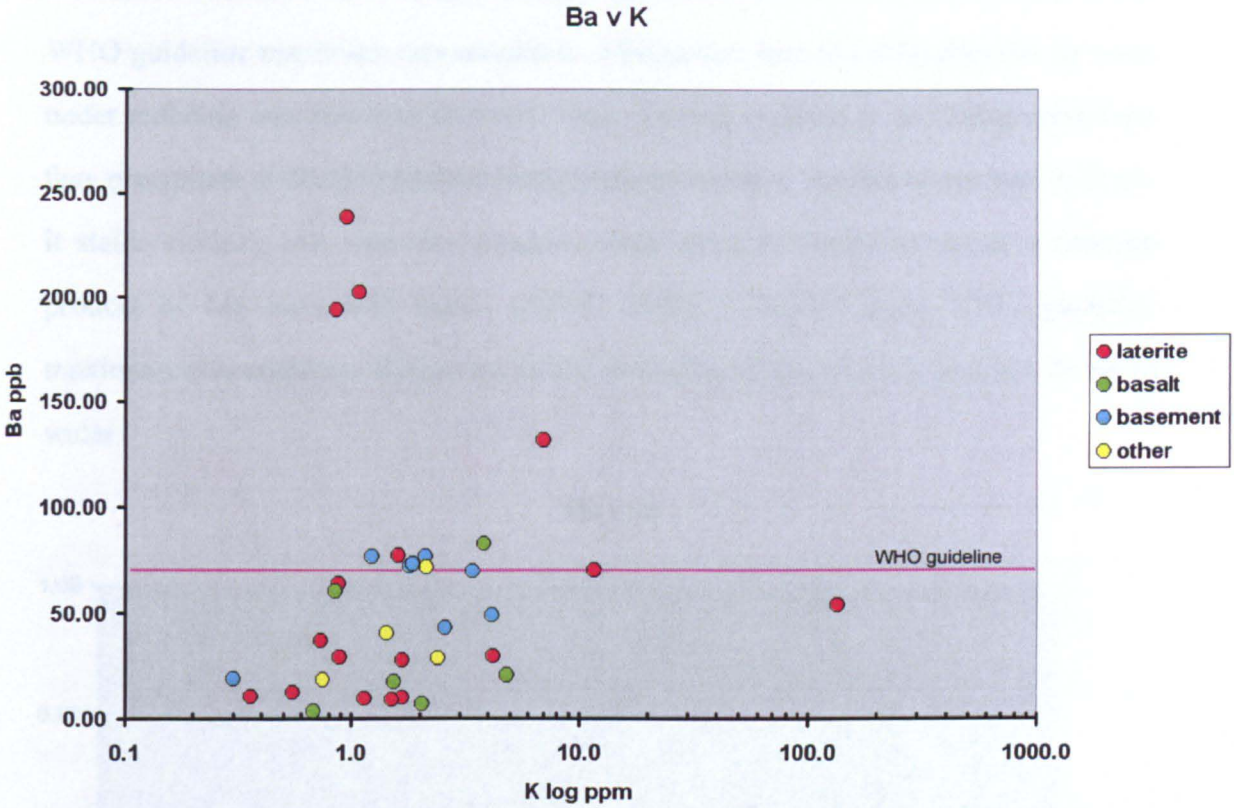


**Figure 8.14** Plot of barium and potassium ion concentrations in water samples. Note that the scale for potassium is logarithmic to show wide variability more clearly

Barium closely follows potassium and sulfur in the analysed laterite rock samples (Chapter 2) and reaches a maximum in the clay zone either substituting for K in alunite or being present in some other sulfate mineral like barite. Nevertheless, the high incidence of Ba-rich waters from 6 wells in laterite is not supported by any correlation of Ba with K or S. Granites containing K-feldspar, yet of the 5 high-Ba waters from the basement are the most Ba-rich basement rocks. Only two basement (samples 2 and 33) came from wells in granite, the others came from chlorite schist (sample 16), amphibolite (sample 19) and an abandoned gold mine workings (sample 22a). Only one sample from a well sunk in basalt exceeds the WHO maximum. The Ba concentrations in well waters seem to show no clear correlation with any other analysed element, so the process responsible for a potential hazard from barium in well water is not obvious.

Several samples with unusually high manganese contents compared with those in commercial mineral waters (figure 8.15) were collected. Two were well above the WHO guideline maximum concentration. Manganese ions (Mn(II)) dissolve in water under reducing conditions as do Fe(II) ions. During exposed to oxidising conditions they precipitate as Mn(IV) to form manganese hydroxide. As this compound is black, it stains clothing and may also produce black slime in coffee or tea as a reaction product of Mn ions with tannin (APEC 2009). The 0.4 ppm WHO guideline maximum concentration is ascribed to the aesthetic effects of even low Mn levels in water.

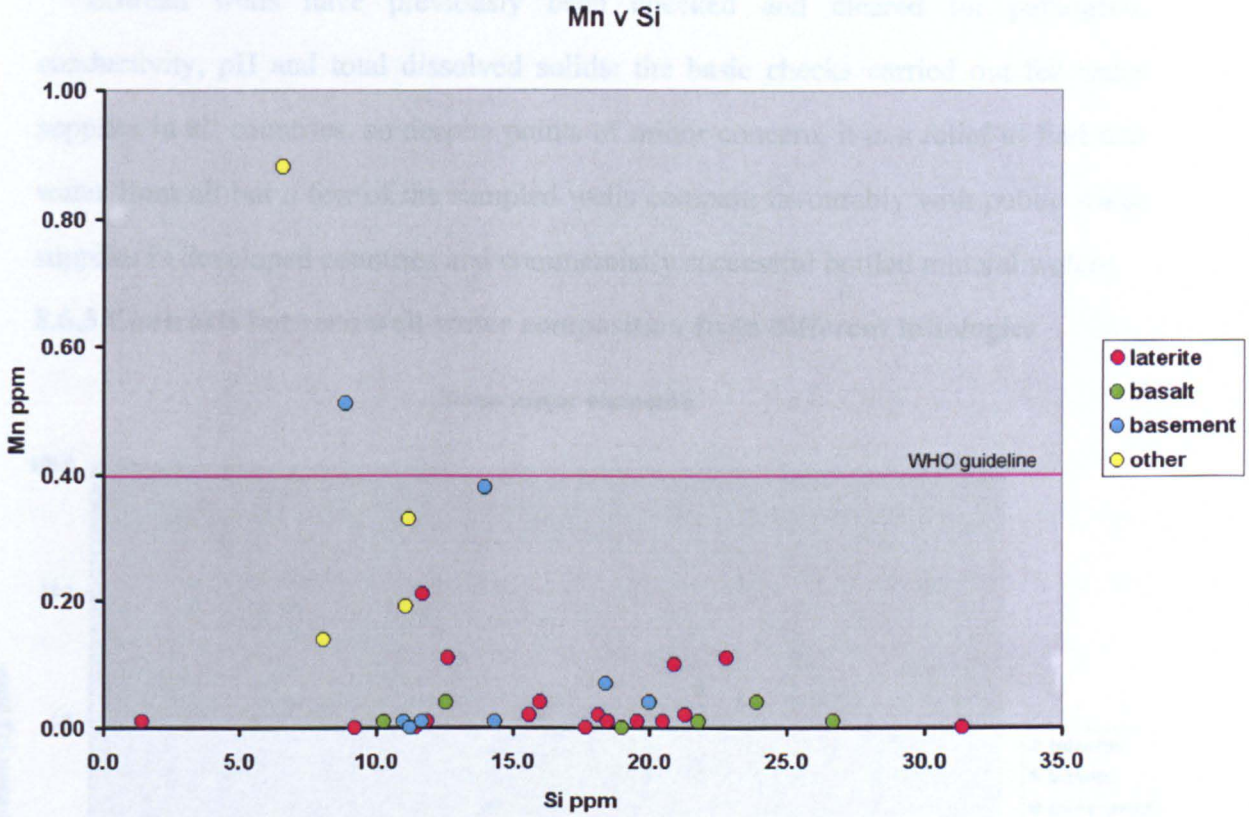


**Figure 8.15** Plot of manganese and silicon ion concentrations in well waters

However, neurological impairment with symptoms akin to those of Parkinson's Disease (WHO 2004) can result from protracted ingestion of manganese, producing 'manganism'). One such sample that contained Mn above the WHO guideline was (22b) that came from a disused mine working, the other from a well in fresh

granodiorite in the basement.

Chromium and Nickel too, with a WHO guideline maxima of 50 and 20 ppb respectively, are potentially carcinogenic if inhaled. None of the samples contain Cr or Ni ions above the WHO guideline. Finally, Selenium has a dual effect on humans; it is an essential trace element but at high concentrations it poses a variety of risks, such as hair loss and nerve damage leading to arthritis. The WHO guideline concentration for Se in drinking water is 10 ppb and none of the samples exceed that value. Concentrations of the potentially toxic elements Cd, Hg and Mo also fall consistently well below the WHO guidelines.

Eritrean wells have previously been checked and cleared for pathogens, conductivity, pH and total dissolved solids: the basic checks carried out for water supplies in all countries, so despite points of minor concern, it is a relief to find that water from all but a few of the sampled wells compare favourably with public water supplies in developed countries and commercially successful bottled mineral waters.

### 8.6.3 Contrasts between well-water composition from different lithologies

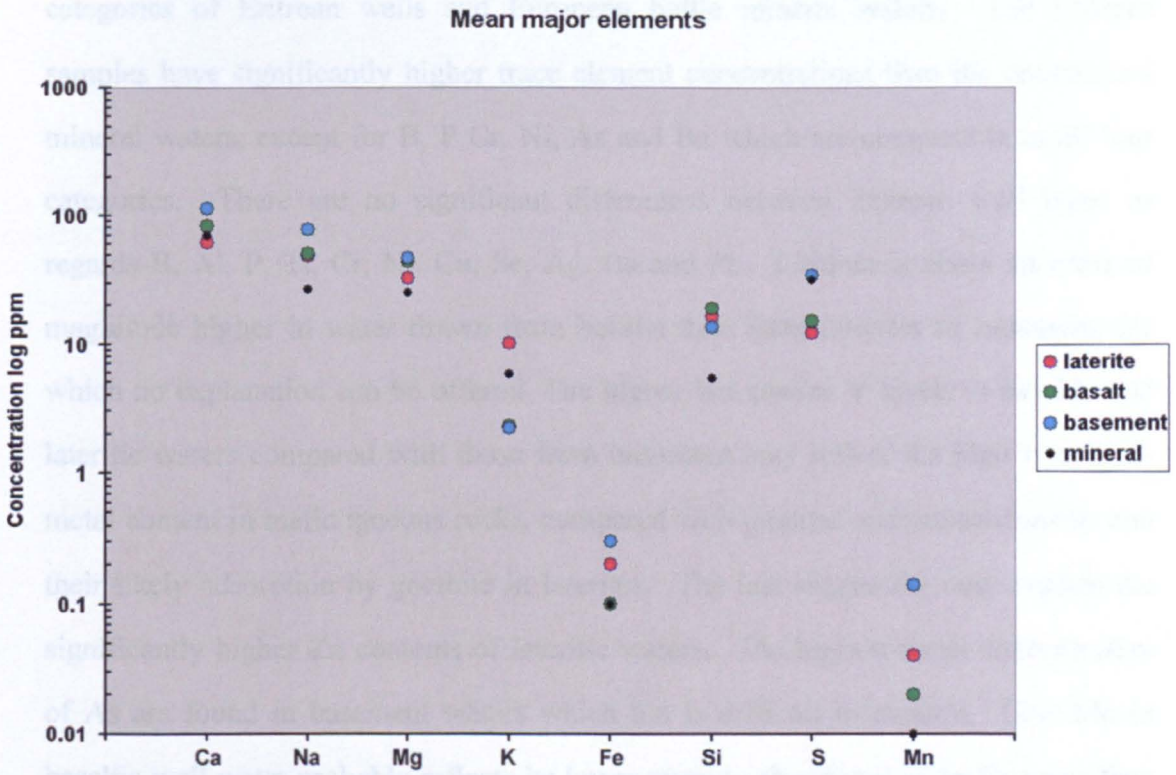


**Figure 8.16** Mean concentrations of some major elements in Eritrean well waters and European bottled mineral waters. Note that the concentration scale is logarithmic to show wide variability more clearly

It is difficult to discern from Table W.3 if waters from wells in laterites, basalts or the Precambrian basement can be considered to have significantly different geochemistry, in terms of their means and ranges of concentrations. Figure 8.16 compares the means for 8 major elements in each category of Eritrean wells and in European bottled mineral waters. Considering the number of samples and the ranges of concentrations, there are probably no significant differences in terms of Ca, Na, Mg, and Si. As might be expected from the known presence of the sulfate alunite in laterites, well waters from them are clearly more K-rich than those from basalts and unaltered basement, in which K is in insoluble silicate minerals. Wells in basalts are less Fe-rich than those in basement. However, some of the basement wells are in Fe-rich chlorite schists that also contain readily oxidised pyrite. This may explain the abundance of S in water from basement wells, in the form of $SO_4^{2-}$ ions produced by such oxidation. Basement wells also show significantly higher mean Mn concentrations than basalt and laterite wells.

Figure 8.17 compares trace element concentrations in waters from the three categories of Eritrean wells and European bottle mineral waters. The Eritrean samples have significantly higher trace element concentrations than the commercial mineral waters, except for B, P Cr, Ni, As and Ba which are comparable in all four categories. There are no significant differences between Eritrean well types as regards B, Al, P, Ti, Cr, Ni, Cu, Se, Ag, Ba and Pb. Lithium is about an order of magnitude higher in water drawn from basalts than from laterites or basement, for which no explanation can be offered. The higher but similar V levels in basaltic and lateritic waters compared with those from basement may reflect the high transition-metal content in mafic igneous rocks, compared with granites and metasediments and their likely adsorption by goethite in laterites. The last suggestion may explain the significantly higher Zn contents of lateritic waters. The highest mean concentration of As are found in basement waters which too is difficult to explain. Low Mo in basaltic well water probably reflects its lower average abundance in mafic rocks than in granites. Low values for Mo in laterite well waters show little evidence for its

possible release from adsorption on goethite. Uranium concentration in basement waters is an order of magnitude above those in waters drawn from laterites and basalts, which may reflect low abundance in mafic igneous rocks and the high solubility of U ions leading to them being leached from laterites during their formation.

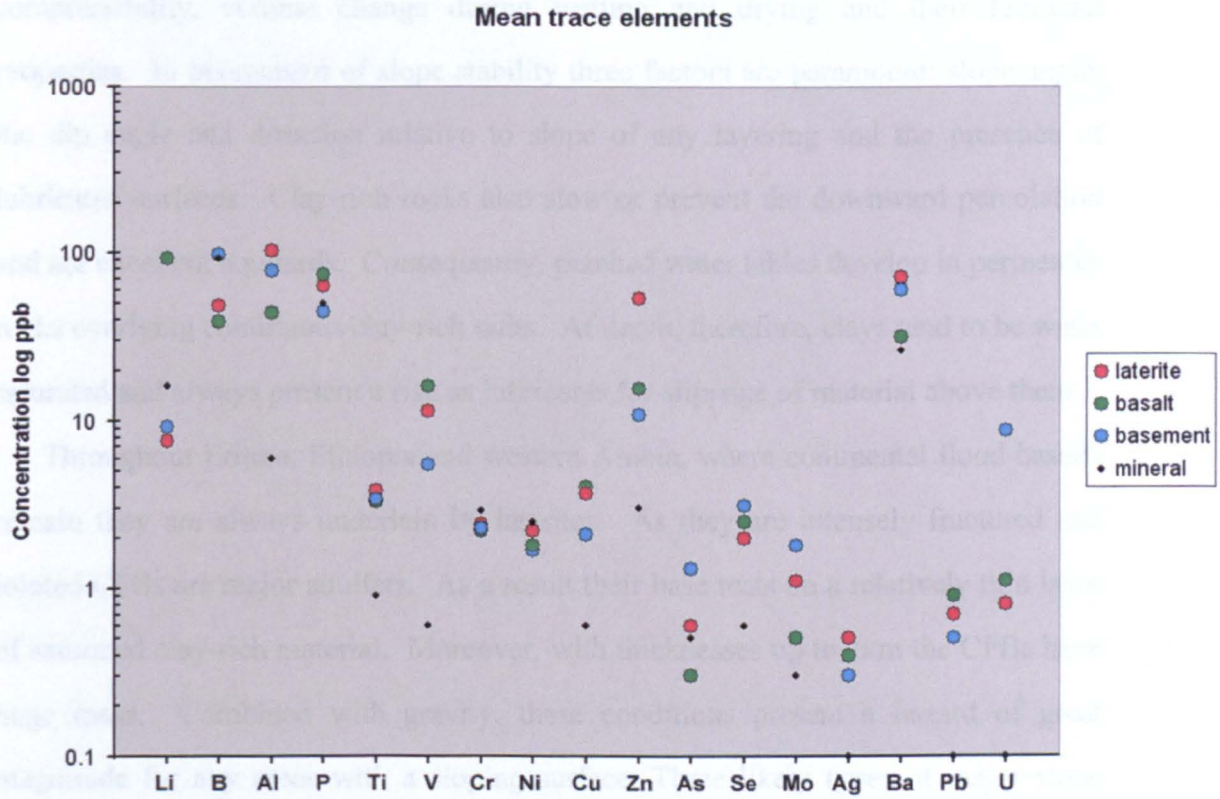


**Figure 8.17** Mean concentrations of some trace elements in Eritrean well waters and European bottled mineral waters. Note that the concentration scale is logarithmic to show wide variability more clearly

It is likely that significant differences between mean concentrations of elements arises from individual samples with unusually high values. This is borne out by the clustering at lower concentrations of waters from all source lithologies on the bi-element plots (figures 8.10 to 8.15). One possible distinguishing feature is the disproportionate tendency for wells in laterite to contain high Ba and K (figure 8.14).

This regional sampling of Eritrean well waters is not, of course comprehensive. However, results from the 17 wells in laterites seem to suggest that, despite the possibility of goethite dissolution under reducing conditions, contamination of well water by arsenic and other toxic elements that it adsorbs is not a problem.

## 8.7 Case Study 3 - Laterites and landslips

Every horizon in the laterite profile contains kaolinite, which is the dominant mineral in Horizons 3 and 4, the clay and mottled zones. When water-saturated, the porosity, fine grain and platy mineral structure of all clays renders them excellent lubricants. To a civil engineer clay-rich rocks present several important hazards because of their compressibility, volume change during wetting and drying and their lubricant properties. In assessment of slope stability three factors are paramount: slope angle; the dip angle and direction relative to slope of any layering and the presence of lubricated surfaces. Clay-rich rocks also slow or prevent the downward percolation and are excellent aquitards. Consequently, perched water tables develop in permeable rocks overlying continuous clay-rich units. At depth, therefore, clays tend to be water saturated and always present a risk as lubricants for slippage of material above them.

Throughout Eritrea, Ethiopia and western Arabia, where continental flood basalts remain they are always underlain by laterites. As they are intensely fractured and jointed CFBs are major aquifers. As a result their base rests on a relatively thin layer of saturated clay-rich material. Moreover, with thicknesses up to 2km the CFBs have huge mass. Combined with gravity, these conditions present a hazard of great magnitude for any areas with a sloping surface. Three likely types of major slope failure under wet conditions are shown in Figure 8.18

Laterites are themselves quite capable of being affected by slope failure wherever they are exposed in escarpments. Figure 8.19 shows small ferricrete masses that have slid and rotated on the underlying clay zone in the escarpment that faces the Western Lowlands in Eritrea.

With a simple and reliable remote sensing approach (Chapter 4) it is now easily possible to detect the presence of clay-rich laterite facies, especially from their distinctive sky-blue hues on TM 742 and ASTER 632 images. Even small surface occurrences of the lateritic clay zone – perhaps the greatest hazard-prone unit - can be detected. Their relation to thick basalt cover is easily assessed too on these images and slope is readily calculated from digital topographic elevation data, such as SRTM.

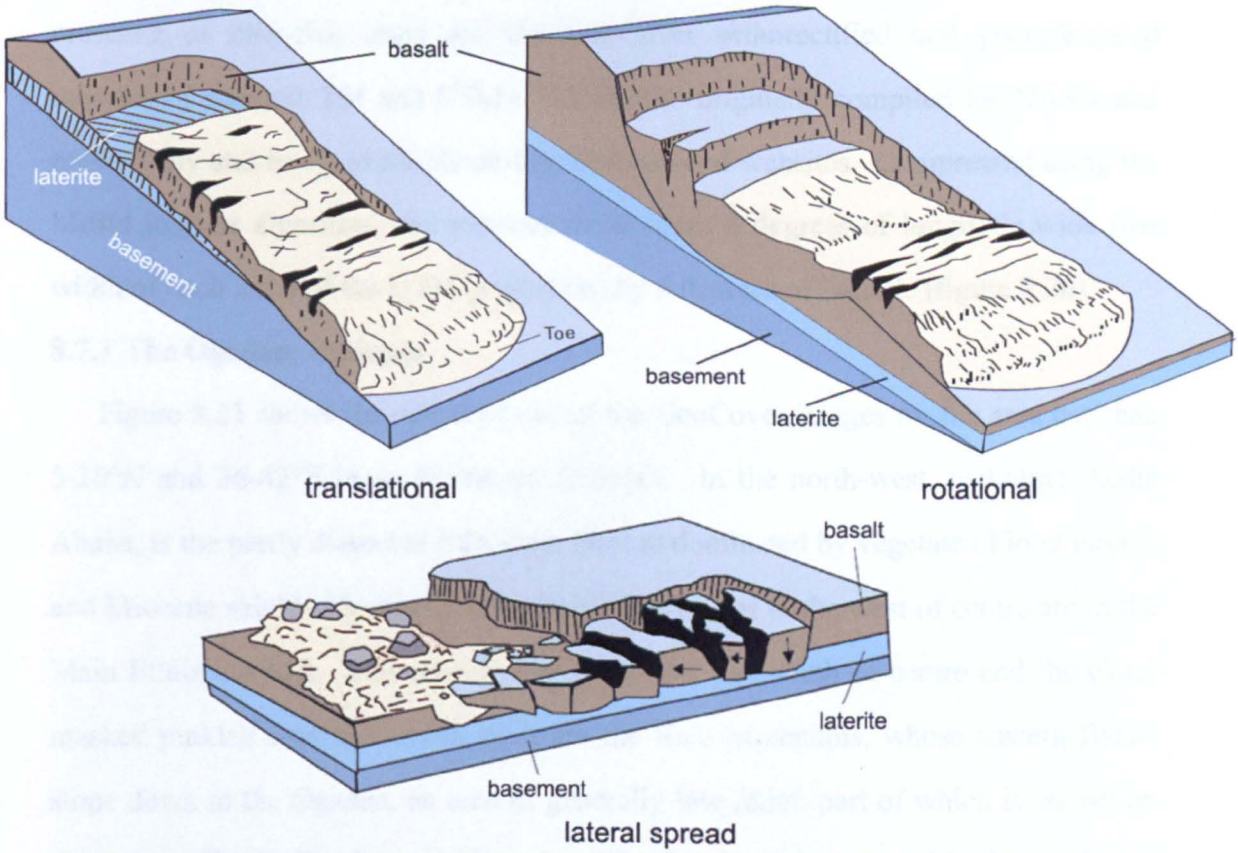


**Figure 8.18** Three types of major slope failure that may occur in layered sequences (after Highland & Bobrowsky 2008)

**Figure 8.19** Small landslips and rotated blocks (mid-right) affecting ferricrete and mottled zone above clay zone in the west-facing escarpment of central Eritrea

As well as individual TM and ASTER scenes, a useful tool in rapid assessment of the presence of clay-rich units are the GeoCover orthorectified and georeferenced mosaics of Landsat TM and ETM+ 742 images originally compiled for NASA and now widely and freely available on-line from several websites. Compressed using the MrSid lossless algorithm, the mosaics cover areas 6 degrees of longitude wide (the width of each Zone of the UTM projection) by 5 degrees of latitude (figure 8.20).

**8.7.1 The Ogaden, Ethiopia**

Figure 8.21 shows the extent of one of the GeoCover images for the area between 5-10°N and 36-42°E in south-eastern Ethiopia. In the north-west, including Addis Ababa, is the partly dissected Ethiopian Plateau dominated by vegetated Flood basalts and Miocene shield volcanoes. The string of lakes just to the west of centre are in the Main Ethiopian Rift. The densely vegetated area just south of centre and the cloud masked pinkish area to the east of it are the Bale Mountains, whose eastern flanks slope down to the Ogaden, an area of generally low relief, part of which is shown on the image. The buff to brownish terrain of the Ogaden is interrupted in the south-east part of the image by several darker upland areas that show hints of blue green. Figure 8.3 zooms into that area. Figure 8.3 reveals a large number of curvilinear patterns that seem to have developed around several plateaus, the most prominent of which is just to east of centre and has a dense cover of vegetation. The geological Map of Ethiopia reveals that the plateaus are composed of the mid-Oligocene flood basalts, which show in brown where vegetation is sparse. The curved features separate narrow ridges of the basalts, those in the north where vegetation cover is sparse are associated with obviously sky-blue surfaces in the features themselves. Although this area was not visited and is extremely remote it was seen from the air. It clearly represents a large outlier of CFBs underlain directly by laterites, of which the clay zone is the most easily recognisable part. While this observation bears out the conclusions drawn in Chapter 7, in its local context it demonstrates the direct relationship between laterites and one of the world's largest, but yet to be documented, systems of landslides.

Figure 8.22 illustrates part of the Ogaden landslide complex with sky-blue laterite clay zone in the troughs between rotated linear blocks of basalt. The undisturbed basalt plateaus at upper right suggest that the CFBs were originally almost horizontal. In this case the likely mechanism of failure is that of lateral spread (figure 8.18). It was probably initiated during the dissection of the CFBs when lateral restraint of movement had been eliminated by erosion. Once set in motion, progressive removal of sliding block would have propagated further failure.

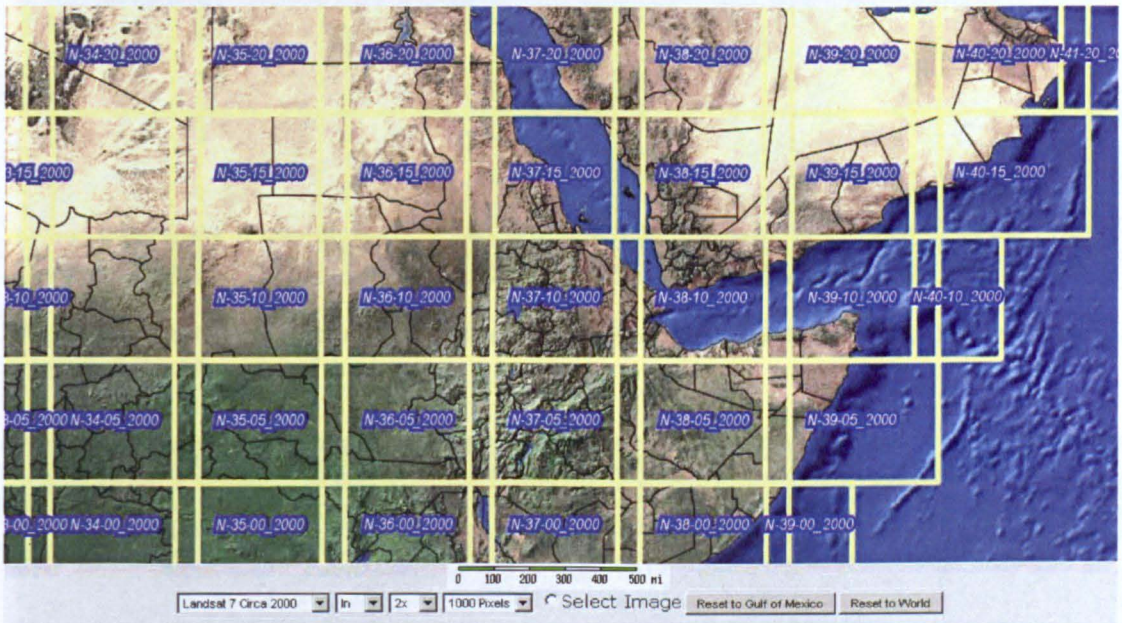


**Figure 8.20** GeoCover Landsat TM 742 mosaics of the Horn of Africa and surroundings


**Figure 8.21** GeoCover Landsat TM 742 mosaic N-37-O5 of part of central Ethiopia. Figure 8.3 zooms into the south-eastern part of this image

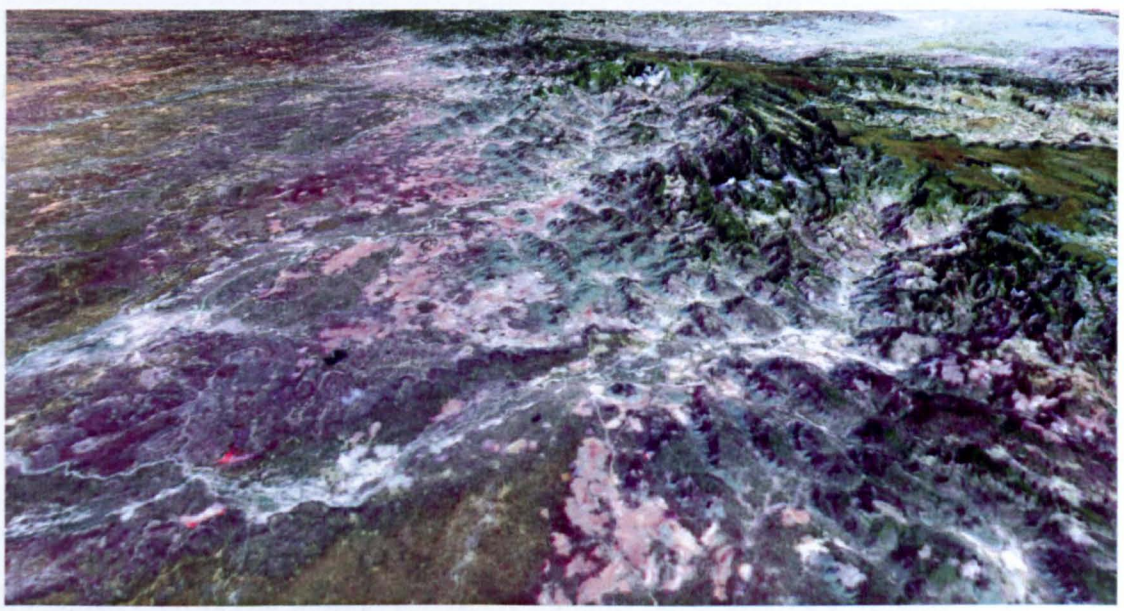

**Figure 8.22** Oblique perspective view of the Ogaden landslides with Landsat TM 742 image draped over SRTM elevation data, viewed from the SE with a 1.5 times vertical exaggeration for clarity

The same stratigraphic relationship as above is demonstrated in Eritrea about 750-1000km to the NNW. There, Miocene uplift in the Eritrean-Ethiopian Escarpment created sufficient gravitational energy to detach blocks of CFBs (above the laterite

sequence) by translational and rotational sliding (figure 8.18). River systems, such as the Nile and Tekesse have dissected the Ethiopian plateau creating canyons which has also resulted in large-scale landslides. The western part of the modelled shape of the laterite-basalt contact (Chapter 7) dips gently westwards from the Eritrean Plateau towards the Western Lowlands, descending ~2km over a distance of ~250km between Adi Caieh and the Sudanese border. Major denudation in the area has removed the CFBs and laterites though some large outliers at elevations between 500 to 1200m remain. Apart from the Ogaden landslide terrain, there have been some reports of large-scale landslides in the region (e.g. Chorowicz *et al. 1999*; Ayalew & Yamagishi 2004; Ayenew & Barbieri 2004; Abebe *et al.*2010) although many local ones are apparent from road traverses in Northern Ethiopia.

### 8.7.2 Three terrains

Using the laterite facies maps (Chapter 4) and Landsat TM 742 images with SRTM elevation data all three terrains were searched for examples of large-scale landslides since the Miocene opening of the Afar Depression and uplift of the Eritrean-Ethiopian Plateau. Various hypotheses have been suggested for the form that the extensional tectonics took. The most comprehensive account to date is that by Chorowicz *et al.* (1999; see also Collet *et al.* 2000), whose model includes the Pliocene development of crustal scale rotational slips to create a series of large marginal basins in the Ethiopian Escarpment.

*West flank of the Afar Depression*

Figure 8.23 shows a foreground dominated by pinkish basement with lightly vegetated outliers of Adigrat sandstone. Dark brown surfaces in the dissected Ethiopian Plateau and Escarpment in the west are undisturbed but uplifted CFBs. The centre is marked by reddish brown alluvium and colluvium of the K'Obo-Alomata marginal basin, flanked to the east by fault-bounded blocks of Mesozoic sandstones that are buff where unvegetated. At the northern apex of the basin dark greyish basalts, which in vertical view are seen to be intensely fractured. At their base in the

**Figure 8.23** Oblique perspective view of Landsat TM 742 image draped over SRTM elevation model, looking south down the K'Obo-Alomata marginal basin with the Ethiopian Escarpment south of Mekele in the west. The mid-ground of the image is ~70km wide. Note the white capping in parts of the Escarpment is cloud on the image draped over the elevation data

north are isolated patches of sky-blue laterite clay zone (not seen in this distant view). Interestingly, the basalts (at lower elevation) can be seen to wrap around a lightly vegetated, buff-hued hill of Mesozoic sandstones to the east of centre. The combination of features suggests that the gently east dipping mass of heavily fractured basalt floored by a laterite is a huge slipped mass from the Escarpment, which maintained its integrity (except for internal fracturing) and slid on the lubricant surface of the underlying laterites.

*The Blue Nile Gorge*

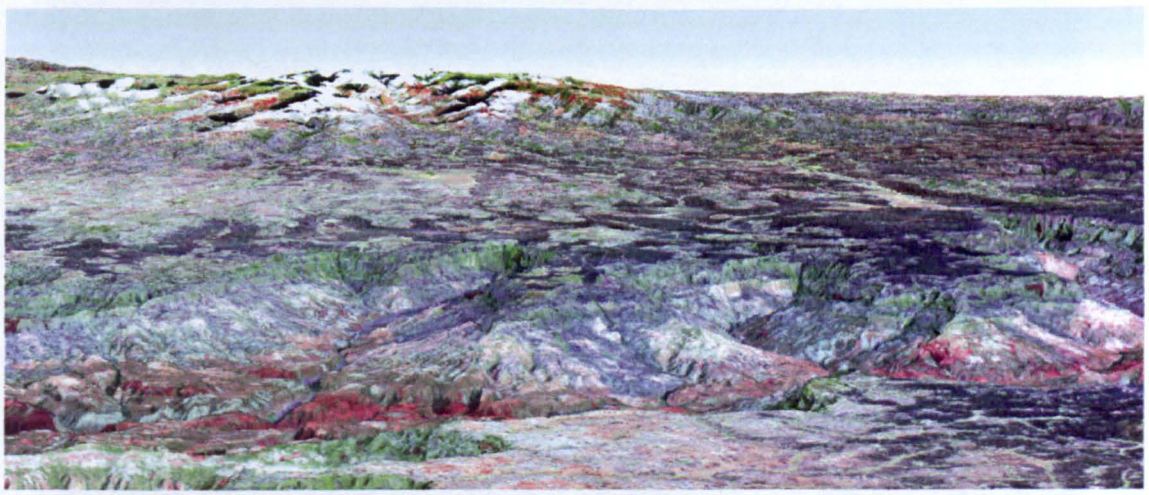

**Figure 8.24** Oblique perspective view of Landsat TM 742 image draped over an SRTM elevation model, looking north over the Blue Nile Gorge towards the shield volcano Choke. The width at centre is ~40 km The white areas on Choke are clouds on the TM image

The upper reaches of the Blue Nile and its tributaries occupy a huge canyon system whose flanks are topped by CFBs underlain by laterites. This has created conditions in which landslides and debris flows from them present expected hazards. Figure 8.24 illustrates the Blue Nile Gorge below the town of Dejen on the main road from Lake Tana to Addis Ababa.

In the foreground, the southern rim of the Gorge shows the flat topography typical of the lower flows of the Ethiopian Traps. The full thickness of the CFBs in this area is shown from the northern rim of the Gorge to the lower slopes of Choke. Black areas on the regional terrace beyond the northern rim are *tselima* soils derived from basalts whereas at the lip of the Gorge fresh, purplish basalts can be seen in cliffs, below which are large basaltic debris flows in which prominent patches of sky-blue lateritic clay zone are prominent.

*Western Eritrea*

To the west of the main area of CFBs in Eritrea are a number of large outliers of basalt. Unlike the CFBs of the Eritrean Plateau these occur at a variety of elevations and the dip of flows varies in amount and direction. The main Eritrean CFBs show in the upper part of Figure 8.25. In the foreground are three large outliers, all at lower elevations than those on the plateau. The central, outlier gently dipping westwards

**Figure 8.25** Oblique perspective view of Landsat TM 742 image draped over SRTM elevation model looking east towards the Eritrean Plateau from the Western Lowlands

defines a small plateau and is clearly at a substantially higher elevation than the larger ones to either side. The elongated outlier to the south is flanked by pinkish basement at higher elevations. Its overall form is irregular and parts of it are synclinal. Unlike the basalts of the main Plateau laterites below this outlier are not continuously visible on images, and only occur in isolated pockets. Although it proved impossible to visit the area, these broad characteristics strongly suggest that these basalt occurrences occupy a former valley descending to the west. This part of Eritrea is far from the major tectonic disturbances in the western flank of the Red Sea Rift and there are few signs of any major Tertiary faults. It is possible that the low-elevation linear outliers are relics of huge translational landslips lubricated by laterite clays and formed once the gently west-dipping basalts of the area were incised. Their linear form and signs of bending to a broad synclinal shape suggests that such slides filled pre-existing post-uplift valleys, the plateau-forming outlier between them probably remaining in place, as does a larger outlier to the west of this view.

## 8.8 Case Study 4 - Exploration - other aspects

This section examines secondary supergene enrichment of sulfidic mineralisation during lateritisation. It considers a means of detecting such occurrences using remote sensing based on the methodology developed for laterite facies discrimination (see Chapter 4). Currently, mineral explorationists' interests lie in the basement terrains of Eritrea and northern Ethiopia. They target polymetallic (Cu-Pb-Zn-Au), volcanogenic sulfide deposits and gold in sulfidic quartz-vein deposits. Both types of mineralisation are prone to secondary enrichment, given suitable conditions.

### 8.8.1 Secondary or supergene enrichment

In tropical oxidising conditions sulfides are extremely unstable. The higher the proportion of sulfides (e.g. pyrite and base-metal sulfide ores), the greater is the potential for acid conditions during lateritic weathering of sulfidic rocks during aqueous oxidation (e.g. eqn 8.1).

$$4CuFeS_2(s) + 10H_2O(l) + 17O_2(aq) = 4Fe(OH)_3(s) + 4Cu^{2+}(aq) + 8SO_4^{2-}(aq) + 8H^+(aq) \quad \text{Eqn 8.1}$$

Chalcopyrite oxidising rainwater goethite

$$2KAlSi_3O_8(s) + 2H^+(aq) + H_2O(l) = Al_2Si_2O_5(OH)_4(s) + 2K^+(aq) + 4SiO_2(aq) \quad \text{Eqn 8.2}$$

K-feldspar acid groundwater kaolinite

On one hand this increases the potential for hydrogen ions to break down silicates in common basement rocks in zones of economic mineralisation concentration (e.g. eqn 8.2). On the other hand, it helps form those ions that allow base metals and gold to enter solution in chemically altered groundwater, such as chloride ($AuCl_2^-$) and thiosulfate ($Au(S_2O_3)_2^{3-}$) complexes in the case of gold (Butt 1998).

Prolonged lateritisation results in palaeosol profiles >50 metres thick on schistose, granitic and metavolcanic rocks by fundamentally transforming their mineralogy. This is the ideal mechanism for secondary enrichment of any sulfide-bearing mineralisation in the basement (figure 8.26).

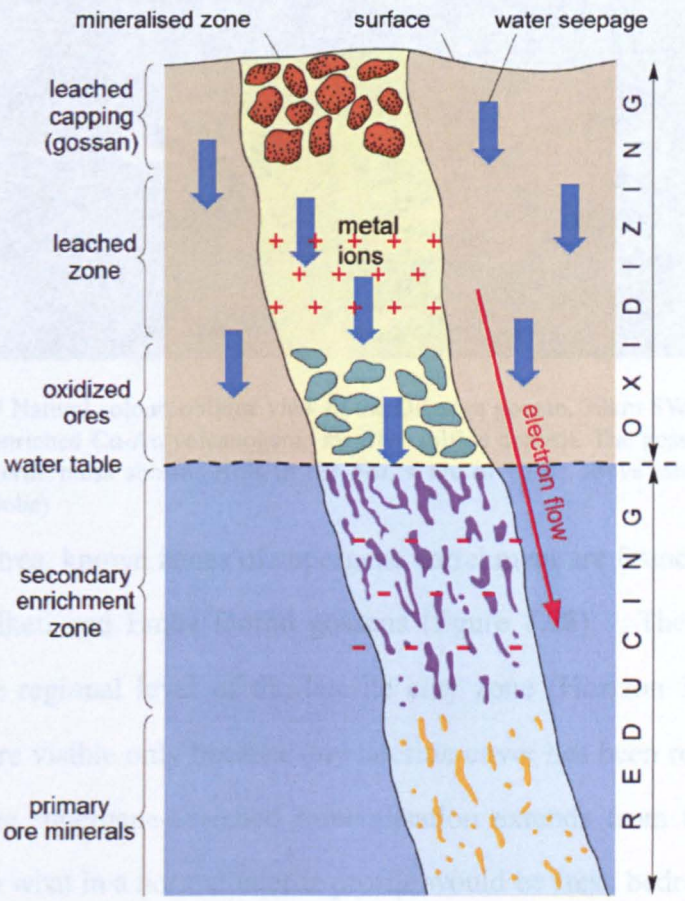


**Figure 8.26** Schematic cross section through a mineralised zone that has been subjected to supergene alteration, showing the various zones of alteration, leaching and mineral precipitation. (from Figure 3.9 in Webb 2006)

Although gold re-precipitates under oxidising conditions, it may also be concentrated through volume reduction in the higher oxidised zones (Anand *et al.* 2010; Butt 1998; Butt *et al.* 2000). Electron mobility related to redox processes reaches extremes in supergene alteration of sulfide-bearing mineralisation, to such an extent that the entire alteration system conducts electricity, a process that is the natural equivalent of a Voltaic cell or battery. Some of the freed metal ions precipitate out under oxidising conditions. However, much of the secondary enrichment takes place below the water table under reducing conditions (figure 8.26).

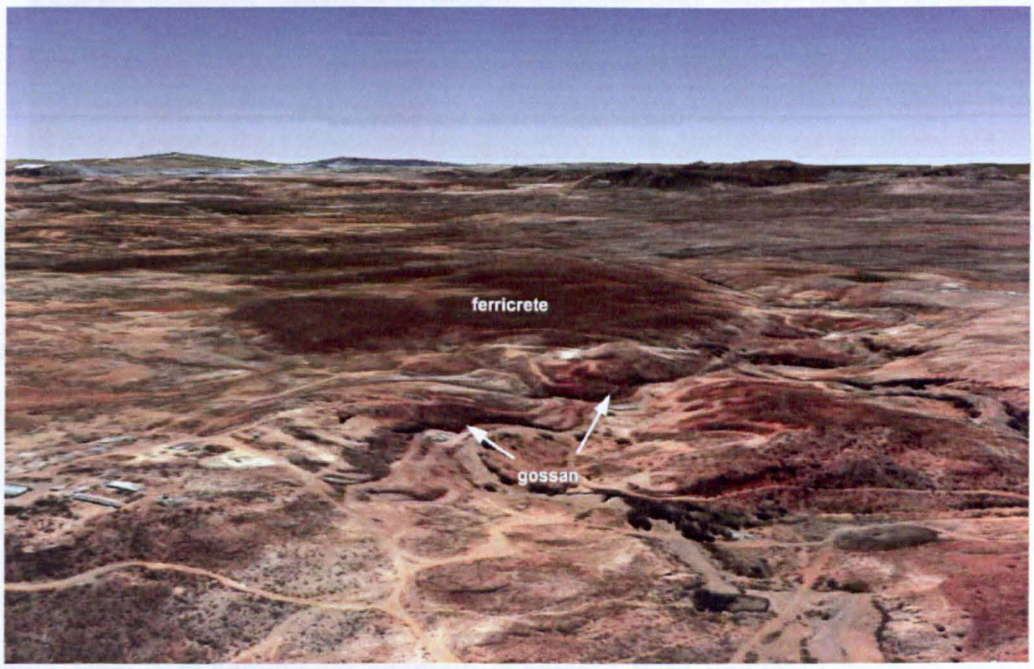


**Figure 8.27** Natural colour, oblique view of the Dibarwa gossan, 30km SW of Asmara Eritrea, above a supergene enriched Cu-Au volcanogenic massive sulfide deposit. The gossan is topographically lower than the laterite mesa shown. Hills in the disnce are of CFBs above laterite. (Google Earth, image ©Digital Globe)

In Eritrea, known zones of supergene enrichment are found at the Dibarwa (figure 8.27), Shiketi and Emba Dorho gossans (figure 8.28). The gossans occur >10 m below the regional level of the laterite clay zone (Horizon 3). In each case these gossans are visible only because ~~any~~ lateritic cover has been removed and the highest part of the supergene-enriched mineralisation extends from the level of Horizon 2 down into what in a normal laterite profile would be fresh bedrock.

The abundance of hydrogen ions produced by oxidative weathering of sulfide-rich rock during lateritisation can be expected to have locally increased the volume and


**Figure 8.28** Natural colour, vertical view of the Emba Dorho gossan, 15km NW of Asmara Eritrea, above a supergene enriched Zn-Pb volcanogenic massive sulfide deposit. The gossan is approximately 50m below the local level of laterites (Google Earth, image ©GeoEye)

depth of basement rocks prone to breakdown of silicate minerals compared with the relatively thin veneer affected by regional, general lateritisation. This creates an alteration 'halo' similar to those formed by low-temperature hydrothermal processes (Carranza & Sadeghi 2012). The likely production of abundant clay minerals together with goethite and other oxidised iron minerals in such a supergene alteration halo would form a mineralogical anomaly compared with unaltered bedrock below the general influence of regional lateritisation. Moreover, in a mineral-spectral sense it would be similar if not identical to a familiar part of the laterite profile: Horizon 4, the mottled zone. As discussed in Chapter 4, the iron oxy-hydroxide – kaolinite mixture is uniquely discriminated using a band-ratio technique (figures 8.29, 4.5). The release of large amounts of sulfate ions from the oxidation of sulfides in basement mineralised zones creates the conditions for such a halo, together with abundant jarosite and alunite, widely recognised as 'indicator' minerals for various kinds of mineralisation involving hydrolysis. Both minerals are easily targeted using multispectral remote sensing (Chapter 5).

Section 7.3 suggests that using the elevation model for the regional laterite datum

and digital terrain elevation data, such as SRTM data, is a means of broadly indicating where supergene-enriched mineralisation may be found in areas from which the laterite cover over basement has been removed. In this section some examples drawn from remotely sensed data are given for possible occurrences of supergene enrichment in such areas, based on the band-ratio technique (Chapter 4).

### 8.8.2 Remote sensing reconnaissance for supergene enrichment

The combined spectral effect of mixtures of iron oxy-hydroxides and kaolinite on RGB combinations of Landsat TM band ratios 5/4, 3/2 and 7/5 or ASTER ratios 4/3, 3/1 and 6/4 is to render such mixtures in yellow-orange hues on false-colour images (Chapter 4). Figures 8.29 to 8.32 show some notable occurrences of possible supergene-enriched mineralised zones in basement terrains.

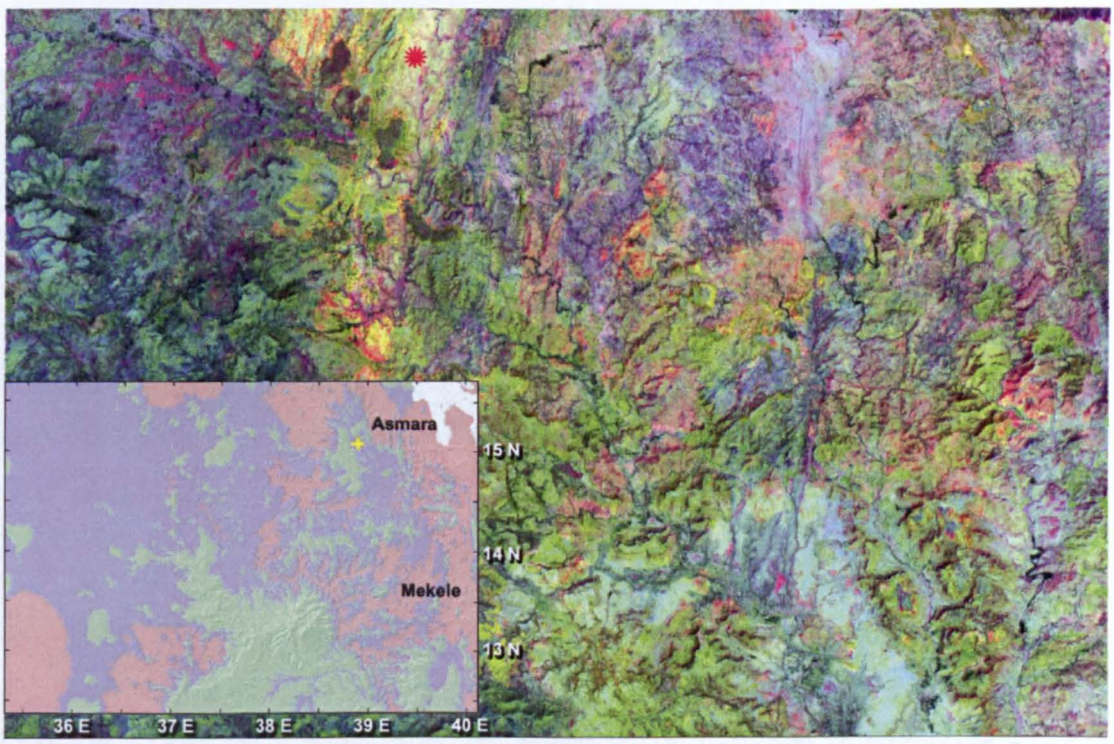


**Figure 8.29** Landsat TM band ratios 5/4, 3/2 and 7/5 as RGB for Gaala valley S of Asmara. Red star marks Adi Nifas mineralisation. Inset shows the elevation difference between the present land surface and the surface fitted to the laterite datum (Figure 7.22) – lilac areas show values between 20 m above and 250 m below laterites. The location of the Landsat image shown by yellow cross. Image width = 40km

On the main image of Figure 8.29 the dark-green – purple area to the west is flood basalt with laterite occurrences on its east flank in red-browns (ferricrete) yellow – orange (mottled zone) and light green (clay zone) the dissected Gaala valley has

abundant clay-zone areas plus several prominent orange patches suggestive of supergene alteration of sulfide rich basement rocks. A known area with oxidized copper mineralisation (malachite and azurite staining) occurs near the village of Adi Nifas, marked with a red star. There are however, several more substantial signs of supergene-enriched sulfidic basement.

Figure 8.30 like the previous figure depicts an area close to eroded laterite. The eastern part shows CFBs in dark green and purple. The most distinctive laterite horizon in this case is the particularly well-developed clay zone on large terraces, which shows in pale green. Ferricrete is dark red-brown. The arrowed area in basement between two laterite outliers is one of several possible occurrences of supergene alteration of sulfidic basement. About 10km to the north is a small area of similar hue where artisanal miners pan for alluvial gold nuggets.

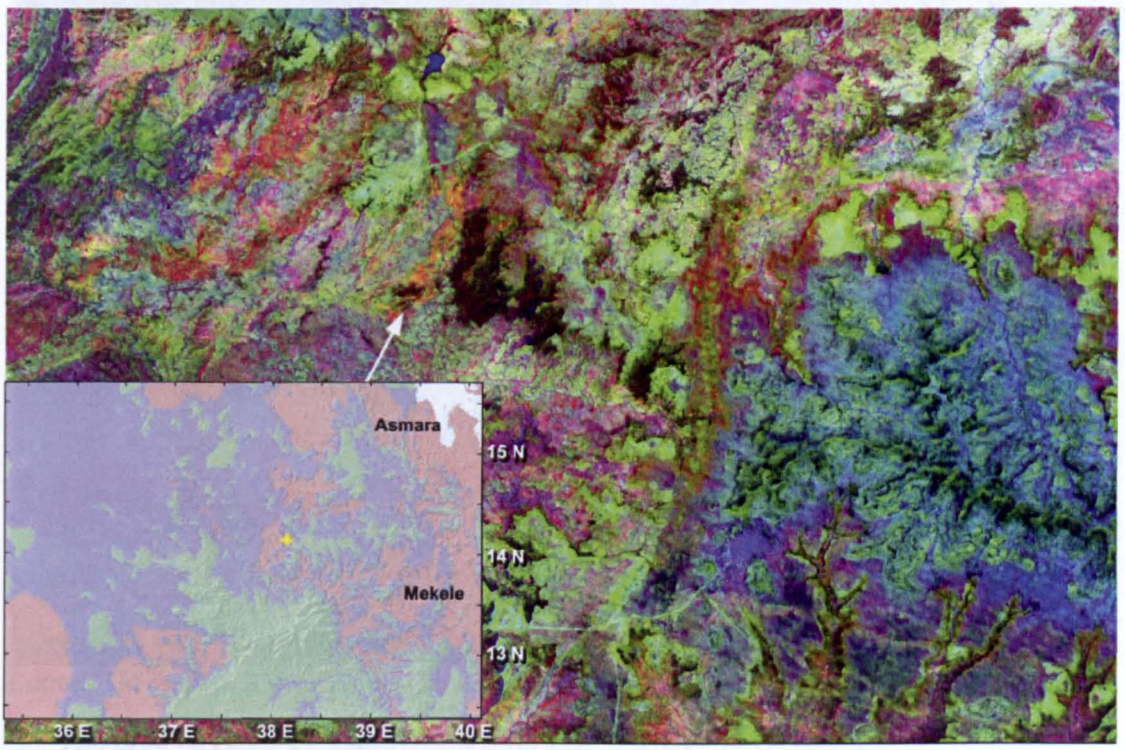


**Figure 8.30** ASTER 4/3, 2/1, 6/4 ratio image of an area to the north of Shire, Tigray. The location of the ASTER image is shown by a yellow cross on the inset. Image width = 40km

Figure 8.31 is a Landsat TM ratio image of an area far from any laterite occurrences. However, modelling of the former shape of the laterite-basalt datum suggests that the present land surface is less than 250m below the former level of the

datum (lilac on inset), i.e. it is in 'prospective ground' in terms of that model. The river in the east is the Gash and apart from alluvial and colluvial sediments the remaining outcrop is of Neoproterozoic basement rocks that is lithologically and structurally complex. A large fold is obvious in the SE corner while green coloration, on some of the peaks, indicates a high proportion of kaolinite in colluvium, which may indicate that the highest points are close to the former level of the datum. Arrows indicate locations of small, but sharply defined yellow – orange zones that are clear signs of sulfide alteration and kaolinisation of silicates in the host rocks. The area is currently covered by several mineral-exploration concessions awarded by the Eritrean Ministry of Energy and Mines.

**Figure 8.31** Landsat TM ratio image of an area of Neoproterozoic basement to the south of Haycotta, Eritrea. The location is shown by a yellow cross on the inset. Image width = 40km

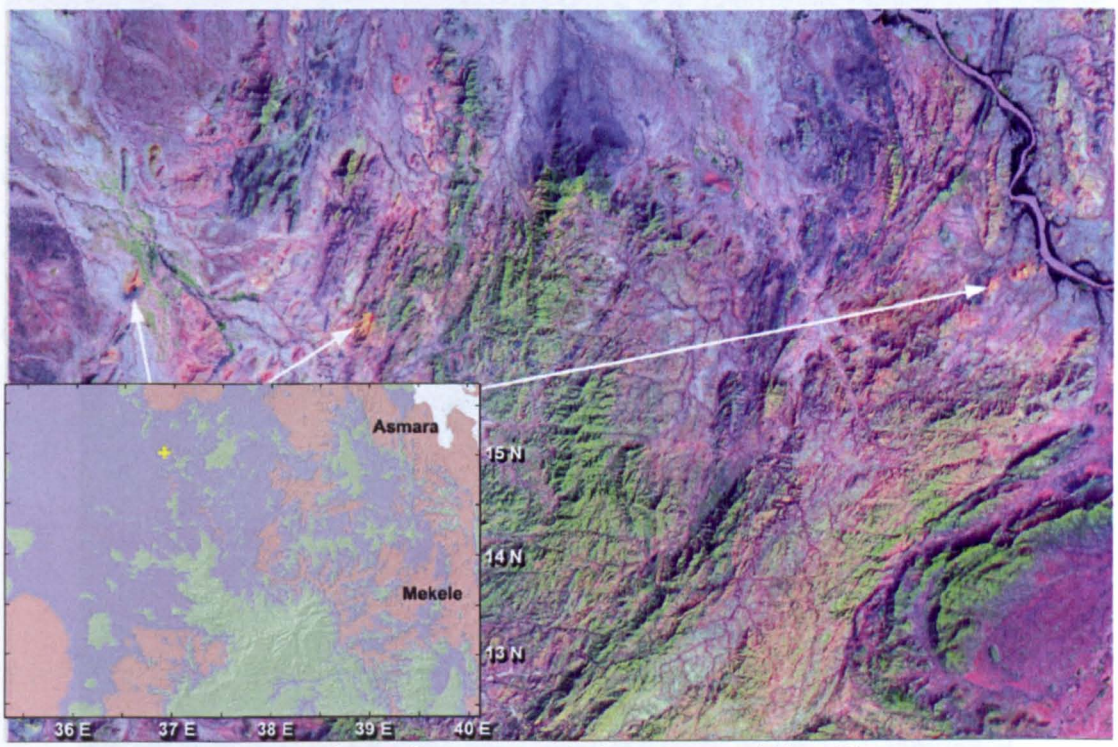


The area covered by Figure 8.32 contains Eritrea's only operating mine, the Bisha Au-Ag-Cu-Zn supergene-enriched, volcanogenic massive sulfide deposit that commenced production in February 2011. Reserves are said to be 330 thousand ounces of gold, 10 million ounces of silver, 390 thousand metric tons of zinc and 860 thousand tonnes of copper (Nevsun 2011), occurring in oxidised, supergene-enriched

and primary mineralised zones (see figure 8.26).

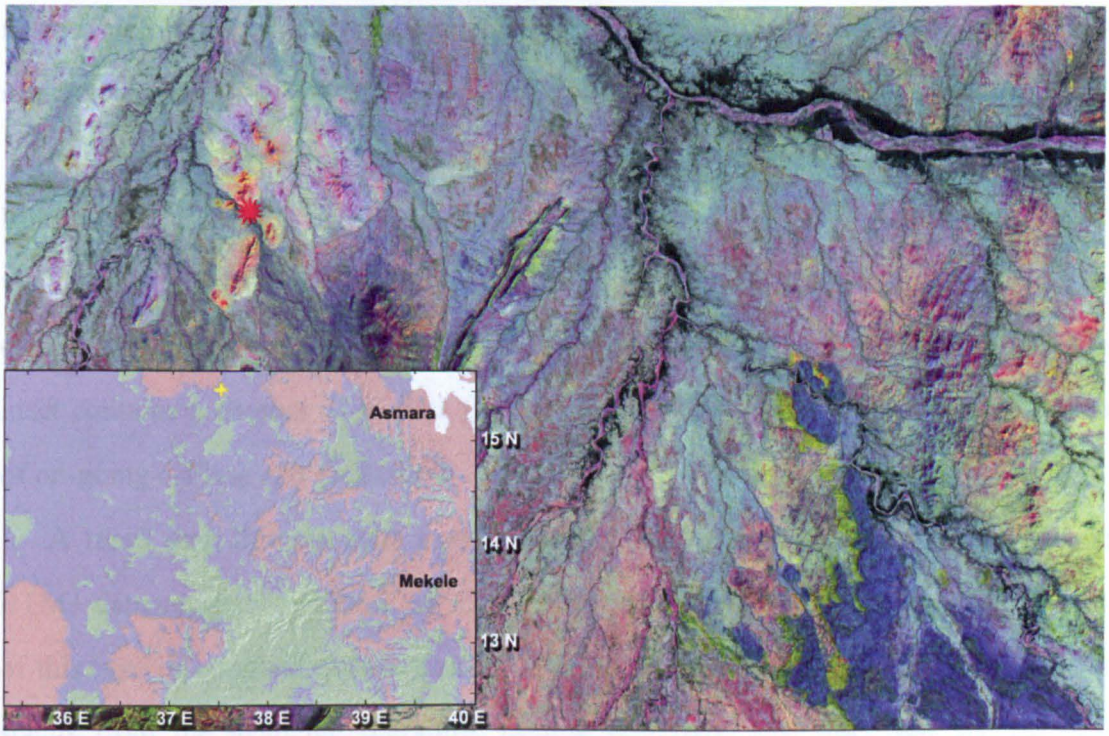


**Figure 8.32** Landsat TM ratio image of an area to the west of Akordat, Eritrea. Red star marks the centre of the Bisha mining project. The location is shown by a yellow cross on the inset. Image width = 40km

The TM data used in Figure 8.32 was acquired by Landsat 5 in January 1986, well before any exploration had begun in Eritrea. The data therefore provide an excellent

**Figure 8.33** The Bisha open pit in 2011. (from Nevsun 2011)

test of concept for the methodology suggested here. The Nevsun concession area for

the Bisha project encloses the cluster of yellow – orange 'anomalies' above the inset map which correspond with outcrops of gossan and a variety of altered and mineralised rocks (Reddy & Brisebois 2004; Barrie *et al.* 2007).

Figure 8.33 shows the newly excavated open pit at Bisha when production began. It is situated in roughly the position of the red star on Figure 8.32. A gossan is clearly visible on the left margin of the pit and extends into the hillock above – a feature clearly visible just to the north of the red star on Figure 8.32. The area hidden by the inset contains a number of similar yellow – orange 'anomalies', which are the focus of on-going drilling and evaluation.

A rapid scan through ratio images derived from the available Landsat TM and ETM+ data suggests that there are many more prospective areas in Eritrea and Tigray of this type of enriched mineralisation. Yet, apart from Nevsun Resources (2011), it seems from the available literature, mining company web sites and the Eritrean Ministry of Energy and Mines mining concession maps (1997) that few explorationists have used the simple reconnaissance approach suggested here. The only other major projects concern mineralisation known from Italian field surveys in the 1920s and 30s, but due to unprecedented world prices for gold (at the time of writing around US$1600 per troy ounce) mining companies are showing renewed interest in the region.

CHAPTER NINE

# Summary and conclusions

*'Science does not know its debt to imagination'* (Emerson)

This thesis is the result of curiosity about a distinctive regional lateritic landscape that had not been geologically mapped. It uses remote sensing (RS) to improve our understanding of laterites. Each chapter contains substantive conclusions based on the weight of the evidence presented. For the convenience of the reader, the main findings are summarised below and further lines of enquiry are raised.

Initially, lateritic palaeosols of Eritrea and Tigray are viewed in a regional context. Multispectral data, field evidence and laterite mineralogy are combined to produce the first-ever regional map of laterite facies. Scientific, social, economic and environmental issues that may be resolved by RS mapping of laterites in the region are assessed and documented.

## 9.1 Overview

A modern stratigraphic framework for a critical review of the Phanerozoic evolution of the region is presented. This provides the context for petrology, remote sensing, map production and geochronological work on laterites and a reassessment of the timing and setting of the Ethiopian-Yemeni Large Igneous Province (LIP).

Lateritic palaeosols dominate the scenery of Eritrea and northern Ethiopia. They form the base upon which flood basalts of the Ethiopian-Yemeni LIP were erupted throughout the region (figure 9.1). This undermines the common assumption that crustal doming and erosion always precedes plume-generated magmatism. Indeed it supports new geophysical modelling of the gravitational effects of plumes and LIPs on the Earth's surface and lithosphere (Leng & Zhong 2010).

**Figure 9.1** Laterites at the base of the CFBs on the Eritrean Ethiopian border at Senafe, Eritrea

## 9.2 Remote sensing - mapping of laterites

The core of this project centered on a RS strategy for regional geologic mapping of the laterite regolith. Only with such maps is it possible to understand the significance of their distribution and the relationship between laterites, other rocks and tectonics. Multispectral visible to very-near infrared (VNIR) and short-wave infrared (SWIR) data from various Earth observing instruments provide a unique means of mapping laterites that are dominated by kaolinite and ferric oxy-hydroxides. Spectra of these main minerals indicate that particular features in the palaeosols can be analysed so that the contrasting upper three horizons – ferricrete, mottled and clay laterite facies – can be distinguished from each other.

A cheap, efficient method of discriminating distinct horizons from other rocks has been developed using 3-band and band ratio Landsat TM and ASTER red, green, blue (RGB) image renditions. The outcome is the first detailed mapping of laterites and their subdivisions for any weathered terrain globally. Such maps have many potential uses, one of which is to use them as a framework for examining dominant and accessory minerals in laterites with distinct spectral properties.

Using the full range of reflected wavelengths imaged by ASTER, multispectral mineral mapping in the region revealed the following interesting findings backed by ground truth:

- The clay-zone (Horizon 3) throughout the study area is everywhere dominated by the highly evolved clay mineral kaolinite. There is little sign of illite- or smectite-group clays that are characteristic of the early stages of weathering. However, some saponite (a smectite) was detected immediately below Eritrean laterites defining a narrow zone of ultramafic schists in the underlying basement.
- The relative proportions of hematite, goethite and jarosite in ferricretes (Horizon 5) differ. There is a regional dominance of hematite with significantly less goethite and very little sign of jarosite - potassium iron sulfate.
- The potassium aluminium sulfate, alunite, which is potentially datable using the $^{40}Ar/^{39}Ar$ method is detectable in the clay facies. In the field it is extremely difficult to distinguish from kaolinite. However, alunite can be distinguished spectrally from kaolinite by their differing Al-OH vibrational features in the SWIR. The Spectral Angle Mapper mineral mapping algorithm was used to highlight alunite in the clay-zone. This led to successful regional dating of Horizon 3 using the $^{40}Ar/^{39}Ar$ method and a minimum mid-Eocene age being determined for lateritisation in Eritrea and northern Ethiopia. The technique reveals that dating is possible over vast lateritised areas by pin-pointing alunite-rich localities.
- A laterite-CFB datum can be charted using the distinctive appearance of the lateritic clay zone on remotely sensed images. Together with regional topographic elevation data, it has been possible to model the deformation associated with Neogene rifting and uplift in NE Africa for the first time. The method is rigorous enough to apply to future studies of the Arabian Peninsula, or indeed anywhere that laterites mark major planation surfaces. The deformed surface comprises several previously unsuspected swells and swales superimposed on a regional, roughly N-S crustal monocline whose axis follows the lip of the present escarpment.

## 9.3 Phanerozoic geology

Laterites in Eritrea and Tigray were successfully dated regionally as were the basalts. New basement ages were also obtained in Eritrea. This geochronological data are used to constrain events in the geological evolution of the region and determine the genesis of the African Surface (figure 7.3, 9.2).

Minimum ages obtained from the laterites are ~40 Ma. They indicate that deep tropical weathering continued until the early Priabonian. Alunite precipitation that allowed dating of the clay facies was a late-stage event, which possibly represents a period of protracted aridity that halted the water-dependent process of lateritisation. This was at a time of declining global mean surface temperatures that culminated in the earliest known glaciation of Antarctica at the time of the Eocene-Oligocene boundary (~34 Ma).

**Figure 9.2** Vestiges of an ancient landscape - The African Surface

Stratigraphic evidence presented here and drawn from the literature strongly suggests that lateritisation was an ongoing process in the study area from as early as the late Triassic, when sea-level change permitted subaerial conditions on a peneplained African Surface. Progress towards defining a maximum age for the long-lived Eritrean lateritisation depends on future radiometric dating of the oldest part of

the laterite profile, the ferricretes. However, field evidence presented in this study indicates that lateritisation was ongoing throughout the Mesozoic.

Tertiary CFBs and the Palaeozoic basement rocks constrain the age-span of lateritic palaeosols in the region. The earliest flood basalts that everywhere rest conformably on laterites, from the Blue Nile gorge to central Eritrea, are confirmed as being mid-Oligocene (~30 Ma). However, this study shows that flood basalts higher in the Eritrean sequence extend to ~19.3 Ma, which adds to evidence that the Ethiopian-Yemeni LIP was not as short-lived as suggested by some workers. Moreover, the young ages constrain the maximum age for the start of Red Sea extension and uplift as somewhat younger than the ~24 Ma indicated by apatite fission-track estimates from both sides of the Red Sea. Further work is needed to confirm these age constraints. Two areas where modern radiometric dating might focus are identified as Afar and the upper Tekese basin:

- During field reconnaissance an exposure was discovered in the escarpment flanking the western side of the Afar Depression where flood basalts are overlain by thick sandstones, which in turn are overlain by mid-Oligocene flood basalts. The locality lies at the top of a basalt unit referred to as the Ashangi basalts, dated by K-Ar methods as Eocene. This new exposure is an ideal place to establish whether Eocene magmatism did occur in the region as it did in Southern Ethiopia and Kenya.
- Remote sensing of the upper Tekese basin strongly suggests that a spectrally distinctive basal basalt unit, marked as Ashangi on the Geological Map of Ethiopia (Tefera *et* al. 1996) is overlain and overlapped by the equally distinctive 30 Ma Aiba basalts, with a slight angular unconformity.
- Palaeozoic basement rocks unconformably underlie laterites and it is suggested that the unconformity constitutes Lester King's African Surface. A plot of $^{40}Ar/^{39}Ar$ cooling ages of basement granodiorites exhumed by deep erosion in the Eritrean Escarpment strongly suggests an episode of erosion and uplift that roughly coincides with the duration of Carboniferous-Permian glaciation of Gondwana. These events

resulted in a peneplained erosion surface. For the first time in NE Africa the African Surface can be ascribed to this specific long-lived process of planation

## 9.4 Laterite petrology: field evidence, petrography and geochemistry

Lateritisation occurs as a result of two main chemical processes. Hydrogen ions in weakly acid groundwater break down silicate minerals resulting in volume loss through their partial dissolution and the dissolution of silica when groundwater becomes alkaline. The rise and fall of groundwater in the developing soil profile governs redox conditions: oxidising above the water table and reducing below. Both affect the range of major and trace elements in the original soil substrate. Geochemical analysis of the different laterite facies and fresh substrate is required to identify the specific processes involved in their evolution. The development of unusually high concentrations of some elements in the laterite profile is important from both an economic and health standpoint:

- Soluble alkali and alkaline-earth elements are concentrated in the lower part of the profile, probably as a result of desiccation late in the palaeosol evolution. Barium shows unexpectedly high values in some mottled zone and ferricrete samples and has positive correlation with sulfur, which suggests barite ($BaSO_4$) has been precipitated at various levels in the profile.
- Elements, such as zirconium, niobium and yttrium, which are preferentially concentrated in minerals such as zircon and apatite that resist weathering, might be expected to increase in residual soils. However, no such increase in Eritrean laterites is observed and there is random distribution of these elements throughout the profile.
- Variations in redox conditions exert a substantial influence over the movement of the multi-valent metals iron and manganese. Iron is concentrated as oxy-hydroxides in the ferricrete. Goethite acts as a geochemical 'sponge' for a range of metals and non-metals such as arsenic. Results indicate concentration of copper, zinc, lead and arsenic in ferricretes which confirm influence of redox processes and goethite's

adsorptive capacity. Other multivalent metals in the mottled and clay zones show similar susceptibility to redox conditions.

Preliminary results of geochemical and well-water studies of laterites indicate the need for future detailed work in this area.

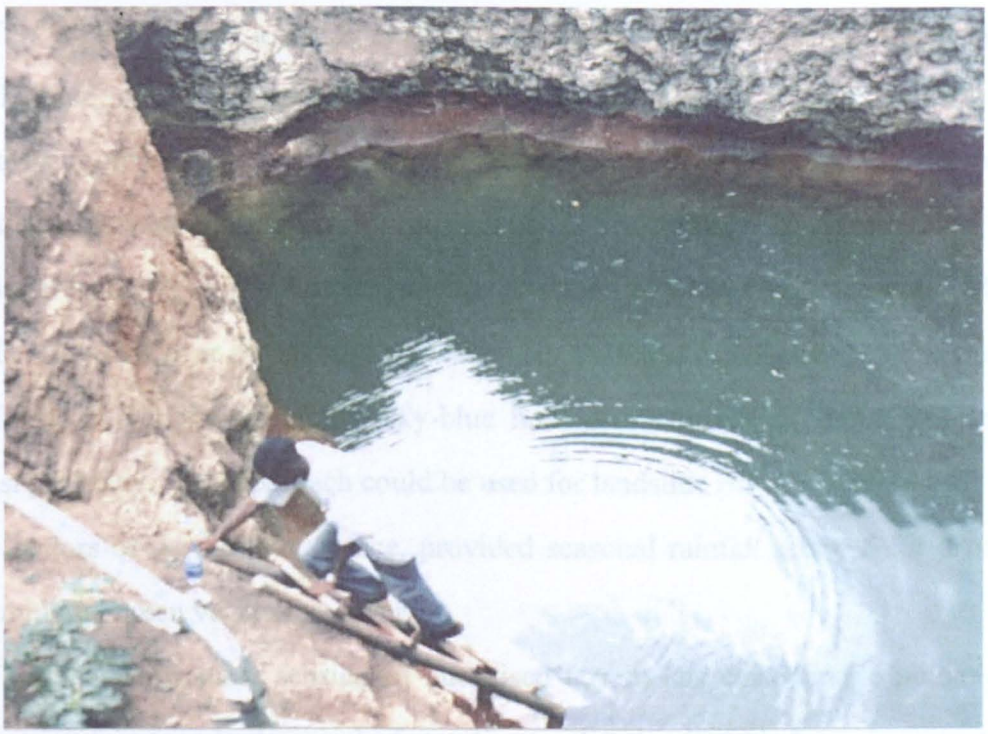

**Figure 9.3** Well at the contact between the CFBs and laterite, near Dibarwa, Eritrea. A distinctive red coloration shows the top of laterite ferricrete just above the water level: laterites form an important aquifer. M. Tesfai for scale.

## 9.5 Socio-economic applications - the ramifications of living with laterites

Three possible applications have been considered, conclusions from which open up related fields for further study. All the work documented in this thesis has been used to aid populations in the region.

- The knowledge that laterites concentrate and can release several toxic elements in groundwater was examined. The chemistry of well waters from laterites and rocks above and below them (figure 9.3) was checked for signs of contamination. Fortunately, even in instances of reducing groundwater, the most dangerous potential contaminant, arsenic, was not found at concentrations above the World Health Organisation's (WHO) guideline maximum. However, a few samples exceeded the guidelines for aluminium and manganese. Four samples had substantially higher

barium concentrations than the WHO guideline maximum and were a cause for concern. Further work is required to address this problem and also to deal with the problem of fluoride in water, whose presence in drinking water gives rise to many health problems.

- The possibility that a widespread unit of clay-rich laterite would form a highly ductile zone of slippage or décollement when wetted beneath younger aquifers was tested using appropriate remote sensing methods. In three cases the laterite-basalt 'package' showed clear signs of large-scale mass wastage by translational and rotational landslide and lateral spread. Using the globally available Landsat TM and ETM+ 742 GeoCover mosaics, it was relatively easy and rapid in arid and semi-arid terrains to detect the distinctive sky-blue hues characteristic of rocks comprising almost pure clay. This approach could be used for landslide risk assessment over very large sectors of the Earth's surface, provided seasonal rainfall allowed for a period with minimal green vegetation cover.
- The idea that remote sensing of lateritised terrain has considerable potential in exploration for secondarily-enriched metal mineralization in underlying basement was explored. Two approaches were considered. The first was a regional reconnaissance of basement areas that were formerly <250m below the level of lateritisation using topological modelling of the laterite-basalt datum from RS and DEM data. Almost all recorded gold occurrences lie within the <250m zone. The second approach was to exploit the similarity between the iron-clay-rich laterite mottled zone and sulfide-rich basement rocks affected by supergene alteration processes during lateritisation. In Eritrea, this approach highlights the supergene enriched zone of the currently mined Bisha volcanogenic massive sulfide deposit and several other unexplored areas.

## 9.6 Final comment

This thesis furnishes the grounds for further lines of enquiry: a remotely sensed global map of laterite facies and a comprehensive geochronological database for laterites, Tertiary basalts and Neoproterozoic basement. Both, as shown in this study, would be

of direct benefit to human populations. However, there are other possibilities for future reseach worth consideration that could not be covered here, though, some mentioned below, may provide a stating point for others.

### 9.6.1 A remotely sensed global map of laterite facies

The now global coverage of ASTER data after more than a decade of operation of the US-Japan *Terra* satellite does seem to promise the possibility of global geological mapping exploiting ASTER's reflected and thermally emitted spectral bands. Laterite facies present an especially clear target because of their dominance by two spectrally distinct types of minerals: clays and iron oxy-hydroxides.

The ideal terrains for laterite mapping are arid and semi-arid deserts together with highly seasonal savannah and steppe. However laterites can also be mapped in terrains characterised by year-round humid climates and perennial vegetation because of the variable resistance to erosion of the different laterite facies results in scarps on the indurated clay- and ferricrete zones. Together with the lack of plant nutrients in these residual palaeosols that lessen vegetation cover whatever the climate, steep scarps encourage at least some bare outcrop that might be detected and mineralogically distinguished. Spectral clues to such occurrences of laterite, combined with mapping of associated scarps using stereoscopic ASTER anaglyphs would enable some mapping in humid terrains, albeit with less accuracy. Without a visible, well developed, mineralogically pure clay zone, the convenience of accurate spectral angle mapping (SAM) of that key horizon is not universally possible. For example the post-Cretaceous laterite cover on the Deccan Traps in western India, where the clay zone is poorly developed could not benefit from SAM. More complex mineral mapping methods, based on spectra of mixed iron minerals and clays may, together with band-ratioing approaches, should enable detection of less highly evolved laterites, especially when combined with 3-D feature mapping using stereoscopic ASTER data.

### 9.6.2 Detection of dateable minerals using remote sensing

The usefulness of the srategy developed in Chapter 5 for using ASTER data for

spectral identification of radiometrically dateable alunite-in laterites may have application in other areas. The K-bearing manganese mineral cryptomelane, used for laterite dating elsewhere, is not such a mineral (Chapter 6) but the distinctive SWIR spectrum of jarosite ($KFe_3(OH)_6(SO4)_2$; see figures 4.3 and 5.17), common in sedimentary rocks and hydrothermal mineralisation, can potentially be targeted in this way. However, jarosite's Ar closure temperature (~140°C; see Kula & Baldwin 2011) is much lower than for alunite. Consequently, post-formation heating may expel some radiogenic argon and corrupt $^{40}Ar/^{39}Ar$ ages. Glauconite ($(K,Na)(Fe,Al,Mg)_2(Si,Al)_4O_{10}(OH)_2$), another possibility, is a green mica-like mineral that can precipitate at low temperatures under reducing conditions in marine sands. Dateable using $^{40}Ar/^{39}Ar$ methods, it also has a distinctive spectral absorption in the SWIR that, together with its green colour, makes it potentially detectable using remote sensing. However, it easily weathers to a variety of iron minerals and loses its spectral distinctiveness at outcrop; not an attribute favourable for practical mineral mapping.

### 9.6.3 Traceable tectonic datums and remote sensing

The ideal datum for assessing tectonic uplift needs to be easily distinguished over the entire area of study, at a known topographic elevation, such as mean sea level. These requirements are satisfied almost perfectly by the clay zone at the base of the laterite (Chapter 7). Whether or not other spectrally distinctive strata would serve the same purpose depends on the size of the area being analysed tectonically. In practice, lateritic palaeosols extend over enormous areas on sub-continental to continental scales, unlike most sedimentary rocks and lavas, even those of CFB provinces. The only comparably extensive rocks are ash horizons from the largest known volcanic eruptions, which too can be precisely dated. Whether or not they are distinctive on remotely sensed images depends on their spectral contrast with rocks above and below them and on their thickness. Outside the close vicinity of their source ashes are rarely more than a few centimetres thick and unlikely to be discernible, even on aerial photographs. Although less extensive, a variety of stratiform rocks are spectrally

distinctive and potentially useful: limestones and gypsum-rich evaporites in the SWIR; quartz sands and flood basalts on multispectral thermal infrared images. The main drawbacks with common, albeit distinctive sedimentary strata and lava flows are: similar rocks of different ages may occur in different parts of the area; individual strata may be diachronous or discontinuous. In the study area limestones are restricted to the Mekele and Blue Nile sedimentary basins and the Adigrat Sandstone is patchy in the north and confused with other quartz-rich sandstones of different ages in the south. While the CFBs once extended over the whole area, individual flows have far smaller extents, the age of the base of the pile may vary over the region and the sheer mass of basalt may have depressed the underlying crust and the surface on which it accumulated.

# THE END or a new beginning

## References

Abbate, E., Albianelli, A., Azzaroli, A., Benvenuti, M., Tesfamariam, B., Bruni, P., Cipriani, N., Clarke, R.J., Ficcarelli, G., Macchiarelli, R., Napoleone, G., Papini, M., Rook, L., Sagri, M., Tecle, T.M., Torre, D. & Villa, I. 1998. A one-million-year-old Homo cranium from the Danakil (Afar) Depression of Eritrea. *Nature*, **393**, 458-460.

Abbate, E., Balestrieri, M.L. & G. Bigazzi 2001. Uplifted rift shoulder of the Gulf of Aden in north-western Somalia: palinspastic reconstructions supported by apatite fission-track data. In: P.A. Ziegler, W. Cavazza, A.H.F Robertson, S. Crasquin-Soleau (Eds) Peri-Tethys Mem. 6: *Rift/wrench basins and passive margins*, Mémoirs du Museum d'Histoire Naturelle., **186**, 629-640.

Abbate, E., Balestrieri, M.L. & Bigazzi, G. 2002. Morphostructural development of the Eritrean rift flank (southern Red Sea) inferred from apatite fission track analysis. *Journal of Geophysical Research – Solid Earth.* **107** DOI:10.1029/2001JB001009.

Abbate, E. & Sagri, M. 1980. Volcanites of the Ethiopian and Somali Plateaus and major tectonic lines. In: *Geodynamic Evolution of the Afro Arabian Rift System.* Accademia Nazionale dei Lincei, **47**, 219-27.

Abdallah, C., Chorowicz, J., Bou Kheir, R. & Khawlie, M. 2005. Detecting major terrain parameters relating to mass movements' occurrence using GIS, remote sensing and statistical correlations, case study Lebanon. *Remote Sensing of Environment*, **99**, 448–461.

Abdelsalam, M.G., Stern, R.J. and Berhane, W.B., 2000. Mapping gossans in arid regions with Landsat TM and SIR-C images: the Beddaho alteration zone of Northern Eritrea. *Journal of African Earth Sciences*, **30**, 903–916.

Abdul-Haggag Y. 1961. *A contribution to the physiography of northern Ethiopia.* London: Athlone.

Abebe, B., Dramis, F., Fubelli, G., Umer, M. & Asrat, A. 2010. Landslides in the Ethiopian highlands and the Rift margins. *Journal of African Earth Sciences*, **56**, 131-138.

Abrams, M. 2000. The Advanced Spaceborne Thermal Emission and Reflection Radiometer (ASTER): data products for the high spatial resolution imager on NASA's Terra platform. *International Journal of Remote Sensing*, **21**, 847–859.

Abrams, M.J., Ashley, R.P., Rowan, L.C., Goetz, A.F.H. & Kahle, A.B.1977, Mapping of hydrothermal alteration in Cuprite mining district, Nevada, using aircraft scanner images for the spectral region 0.46 to 2.34 μm: *Geology*, **5**, 713–718.

Abrams, M. & Geller, G. N. 2005. Increasing access and usability of remote sensing data. The Protected Area Archive Tool applied to UNESCO Heritage Conservation Sites/NASA/Jet Propulsion Lab (JPL). In: 31st International Symposium on Remote Sensing of Environment, Saint Petersburg, Russia, 20–24 June 2005, World Wide Web Address:
(http://www.isprs.org/publications/related/ISRSE/html/papers/308.pdf).

Abrams, M. and Hook, S., 1995, Simulated ASTER data for geological studies. *IEEE Transactions on Geoscience and Remote Sensing*, **33**, 692–699.

Abrams, M.J., Hook, S. & Ramachandran, B. 2002. *ASTER Users Handbook: Version 2*. Jet Propulsion Laboratory, Pasadena.

Abrams, M.J., Rothery, D.A. & Pontual, A. 1988. Mapping in the Oman ophiolite using enhanced Landsat Thematic Mapper images. *Tectonophysics*, **151**, 387-401.

Agnew, P. 2010. Geochemical Exploration in Lateritic Terrains. In: Fourth Brazilian Symposium on Mineral Exploration, Ouro Preto, Brazil, 23-26 May 2010.

Al-Belushi, J.D., Glennie, K.W.& Williams, B.P.J. 1996. Permo-Carboniferous glaciogenic Al Khlata formation, Oman: a new hypothesis for origin of its glaciation. *GeoArabia* 1, 389–404.

Allaby, M. 2008. *A Dictionary of Earth Sciences*. Oxford University Press: Oxford

Alpers, C.N. & Brimhall, G.H. 1988. Middle Miocene climatic change in the Atacama Desert, northern Chile: Evidence from supergene mineralization at La Escondida. *Geological Society of America Bulletin*, **100**, 1640-1656.

Alvarez, R., Ortiz, M. I., Gomez, G. & Vidal, R. 2000. Geographic evaluation of hazardous volcanic emissions of populations: the plumes of Popocatepetl in March, 1996. In: Proceedings of the 14th International Conference on Applied Geological Remote Sensing, Las Vegas, Nevada, USA, 6–8 November 2000. Environmental Research Institute of Michigan, Ann Arbor, MI, 255–262.

Ambrosi, J.P., Nahon, D.B. & Herbillon, A.J. 1986. The epigenetic replacement of kaolinite by hematite in laterite — petrographic evidence and the mechanisms involved. *Geoderma*, **37**, 283-294.

Anand, R.R. & Butt, C.R.M. 2010. A guide for mineral exploration through the regolith in the Yilgarn Craton, Western Australia. *Australian Journal of Earth Sciences*, 57, 1015-1114.

Andersson,. U.B.; Ghebreab, W. & Teklay, M. 2006. Crustal evolution and metamorphism in east-central Eritrea, south-east Arabian-Nubian Shield. *Journal of African Earth Sciences*, **44**, 45-65.

Andrews Deller, M.E. 2000. Facies discrimination in laterites, using Landsat Thematic Mapper(TM) data: An example from Eritrea (NE Africa), in: Proceedings of the 14th International Conference on Applied Geological Remote Sensing, Las Vegas, Nevada, USA 6-8 November 2000, Environmental Research Institute of Michigan, Ann Arbor, MI, 302.

Andrews Deller, M.E., 2002, Facies discrimination in laterites, using remotely sensed data: Landsat TM versus ASTER, ALI and Hyperion data—an example from Eritrea. In Annual General Meeting of the Geological Remote Sensing Group, December 2002, Geological Society London, Burlington House, Piccadilly, London.

Andrews Deller, M.E., 2003, Locating dateable minerals in laterites using remote sensing: an example from Eritrea, NE Africa. In Annual General Meeting of the Geological Remote Sensing Group, December 2003, Geological Society London, Burlington House, Piccadilly, London.

Andrews Deller, M.E. 2004. Locating dateable minerals in laterites using remote sensing: an example from Eritrea, NE Africa, in: Proceedings of the 32nd International Geological Congress, Florence, 20-28 August 2004, 227.

Andrews Deller, M. E. 2004. Space technology for disaster management: data access and its place in the community. In: United Nations International Workshop on the Use of Space Technology for Disaster Management, Munich, 18–22 October 2004. World Wide Web Address: www.zki.caf.dlr.de/events/2004/unoosa_workshop/unoosa_programme_en.html.

Andrews Deller, M. E. 2005. Space technology for disaster management: examples from NE Africa. In: 31st International Symposium on Remote Sensing of Environment, Saint Petersburg, Russia, 20–24 June 2005. World Wide Web Address: (http://www.isprs.org/publications/related/ISRSE/html/papers/592.pdf).

Andrews Deller, M.E. 2006. Facies discrimination in laterites using remotely sensed data. *International Journal of Remote Sensing*, **27**, 2389–2409.

Andrews Deller, M.E. 2007. Space technology for disaster management: data access and its place in the community. In: Teeuw, R.M. (Ed.) *Mapping Hazardous Terrain using Remote Sensing.* Geological Society, London, Special Publication **283**, 149-164.

Andrews Deller, M. E., Deller, W. S., Drury, S. A. & Teklegiorgis, A. 2005. Use of space technology for disaster management: data access and its place in the community. In: United Nations International Workshop on the Use of Space Technology for Disaster Management, Munich, 18–22 October 2004. World Wide Web Address: www.zki.caf.dlr.de/events/2004/unoosa_workshop/unoosa_programme_en.html.

APEC 2009. Website Water problems – manganese. World Wide Web Address: www.freedrinkingwater.com/water_quality/chemical/water-problems-manganese.htm.

Arkin, Y., Beyth, M., Dow, D.B., Levitte, D., Temesgen, H. & Tsegaye, H. 1971. *Geological Map of Mekele Sheet Area ND 37-11, Tigre Province*. Imperial Ethiopian Government, Ministry of Mines, Geological Survey of Ethiopia, Addis Ababa.

Arndt, N. & Menzies, M.A. 2005. January 2005 LIP of the Month: The Ethiopian Large Igneous Province. World Wide Web Address: http://www.largeigneousprovinces.org/05jan

Ashley, R.P. & Silberman, M.L. 1976. Direct dating of mineralization at Goldfield, Nevada, by K-Ar and fission track methods. *Economic Geology*, **71**, 904-924.

Ayalew, L. & Yamagishi, H. 2004. Slope failures in the Blue Nile basin, as seen from landscape evolution perspective. *Geomorphology*, **57**, 95-116.

Ayele, A. & Kulhanek, O. 1997. Spatial and temporal variations of seismicity in the Horn of Africa from 1960 to 1993. *Geophysical Journal International*, **130**, 805–810.

Ayenew, T. & Barbieri, G. 2004. Inventory of landslides and susceptibility mapping in the Dessie area, northern Ethiopia. *Engineering Geology*, **77**, 1-15.

Baker, J., Snee, L. and Menzies, M., 1996, A brief Oligocene period of flood volcanism in Yemen: Implications for the duration and rate of continental flood volcanism at the Afro-Arabian triple junction. *Earth and Planetary Science Letters*, **138**, 39–55.

Bakor, A. R., Gass, I. G. & Neary, C. R. 1976. Jabal Al Wask, northwest Saudi Arabia: an Eocambrian back-arc ophiolite, *Earth and Planetary Science Letters*, **30**, 1-9

Balestrieri, M.L., Stuart, F.M., Persano, C., Abbate, E. & Bigazze, G. 2005. Geomorphic development of the escarpment of the Eritrean margin, southern Red Sea from combined apatite fission-track and (U–Th)/He thermochronometry. *Earth and Planetary Science Letters*, **231**, 97– 110.

Barberi, F., Giglia, G., Marinelli, G., Santacroce, R., Tazieff, H. & Varet, J. 1972. Geological *map of the Danakil Depression (northern Afar Ethiopia) (1:500 000)*, CNRS CNR Geotechnip.

Barisin, I., Leprince, S., Parsons, B & Wright, T 2009. Surface displacements in the September 2005 Afar rifting event from satellite image matching: Asymmetric uplift and faulting. *Geophysical Research Letters*, **36**, Paper L07301

Barnard, P.C., Thompson, S., Bastow, M.A., Ducreux, C. and Mathurin, G. 1992. Thermal maturity development and source rock occurrence in the Red Sea and Gulf of Aden. *Journal of Petroleum Geology*, **15**, 173-186.

Barrie, C.T., Nielsen, F.W. &Aussant, C.H. 2007. The Bisha volcanic-associated massive sulfide deposit, western Nakfa Terrane, Eritrea. *Economic Geology*, **102**, 717-738.

Beamish, D., 1994. Two-dimensional regularised inversion of VLF data. *Journal Applied Geophysics*, **32**, 357-374.

Beauvais, A. & Bertaux, J. 2002. In situ characterization and differentiation of kaolinites in lateritic weathering profiles using infrared microspectroscopy. *Clays and Clay Minerals*, **50**, 314-330.

Berhe, S. M. 1986. Geologic and geochronologic constraints on the evolution of the Red Sea – Gulf of Aden and Afar Depression, *Journal of African Earth Sciences*, **5**, 101-117.

Berhe, S.M., Desta, B., Nicoletti, M. & Teferra M., 1987. Geology, geochronology and geodynamic implications of the Cenozoic magmatic province in W and SE Ethiopia. *Journal of the Geological Society of London*, **144**, 213-226.

Beyth, M. 1972. *The geology of Central Western Tigre*. Ph.D. dissertation, Rheinische Friedrich-Wilhelms Universiteit, Bonn, W. Germany.

Bird, M.J., Chivas, A.R. & Mcdougall, I. 1990. An isotopic study of surficial alunite in Australia 2. Potassium-argon geochronology. *Chemical Geology*, **80**, 133-145.

Bird, M.J. & Chivas, A.R. 1993. Geomorphic and palaeoclimatic implications of an oxygen-isotope chronology for Australian deeply weathered profiles. *Australian Journal of Earth Science*, **40**, 345–358.

Bitom, D., Volkoff, B. & Abossolo-Angue, M. 2003. Evolution and alteration in situ of a massive iron duricrust in Central Africa. *Journal of African Earth Sciences*, **37**, 89-101.

Bjorgo, E. 2000. Using very high spatial resolution multispectral satellite sensor imagery to monitor refugee camps. *International Journal of Remote Sensing*, **21**, 611–616.

Blanford, W.T. 1870. *Observations on the Geology and Zoology of Abyssinia.* MacMillan: London, 198 p.

Blaut, J. M., Stea, D., Spencer, C. & Blades, M. 2003. Mapping as a cultural and cognitive universal. *Annals of the Association of American Geographers*, **93**, 165–185.

Bohannon, R.G. 1986. Tectonic configuration of the western Arabian continental margin, southern Red Sea. *Tectonics*, **5**, 477-499.

Bohannon, R.G. 1989. Style of extensional tectonism during rifting, Red Sea and Gulf of Aden. *Journal of African Earth Sciences*, **8**, 589-602.

Bohannon, R.G., Naesar, C.W., Schmidt, D.L. & Zimmerman, R.A. 1989. The timing of uplift, volcanism and rifting peripheral to the Red Sea: A case for passive rifting. *Journal of Geophysical Research* **94**, 1683-1701.

Bolle M.-P. & Adatte, T. 2001. Palaeocene-early Eocene climatic evolution in the Tethyan realm: clay mineral evidence. *Clay Minerals*, **36**, 249-261.

Bosellini, A., Russo, A., Fantozzi, P.L., Assefa, G. & Solomon, T., 1997. The Mesozoic succession of the Mekele Outlier (Tigre Province, Ethiopia). *Memorie di Scienze Geologiche* **49**, 95–116.

Bosworth, W. 1992. Mesozoic and early Tertiary rift tectonics in East Africa. *Tectonophysics*, **209**, 115-137.

Bosworth, W., 1994. A model for the three-dimensional evolution of continental rift basins, north-east Africa. In: Schandelmeier, H., Stern, R.J., (Eds.), *Geology of Northeast Africa* (Part 2), *Geologische Rundschau*, **83**, 671–688.

Bosworth, W. & Burke, K. 2004. Tectonic evolution of the Red Sea Basin: a synthesis. Proceedings of the Third International Conference on Africa, London: Petroleum Exploration Society of Great Britain

Bosworth, W., Huchon, P. & McClay, K. 2005. The Red Sea and Gulf of Aden Basins. *Journal of African Earth Sciences*. **43**, 334-378.

Bourman, R.P. 1993. Perennial problems in the study of laterite: A review. *Australian Journal of EarthSciences*, **40**, 387-401.

Bourman, R.P. 1993. Modes of ferricrete genesis – evidence from southeastern Australia. *Zeitschrift für Geomorphologie*, **37**, 77 -101

Boyd, W., 1982, *A Good Man in Africa* London: Penguin Books.

Breecker, D. O., Sharp, Z. D. & McFadden, L. D. 2010. Atmospheric $CO_2$ concentrations during ancient greenhouse climates were similar to those predicted for A.D. 2100. *Proceedings of the National Academy of Sciences*, **107**, doi/10.1073/pnas.0902323106

Brown, D.J., Helmke, P.A. & Clayton, M.A. 2003. Robust geochemical indices for redox and weathering on a granitic laterite landscape in Central Uganda. *Geochimica et Cosmochimica Acta*, **67**, 2711-2723

Buchanan, P. 1807. *A journey from Madras through the countries of Mysore, Kanara and Malabar*. East India Co., London, 2:436-461.

Buchanan-Smith, M. 1997. What is a famine early warning system? Can it prevent famine? Internet Journal for African Studies, March 1997, No. 2. World Wide Web Address: http www.bradford.ac. uk/research/ijas/ijasno2/ijasno2.html.

Büdel, J. 1982. *Climatic Geomorphology*. Princeton University Press: Princeton.

Bumby, A.J. & Guiraud, R. 2005. The geodynamic setting of the Phanerozoic basins of Africa. *Journal of African Earth Sciences*, **43**, 1-12.

Bunter, M.A.G., Debretsion, T. & Woldegiorgis, L. 1998. New developments in the pre-rift prospectivity of the Eritrean Red Sea. *Journal of Petroleum Geology*, **21**, 373-400

Burdon, D.J. 1985. Groundwater against drought in Africa. In: *Hydrogeology in the Service of Man*. Memoirs of the 18th Congress of the International Association of Hydrogeologists, Cambridge, 76-91

Burke, K. 1996. The African Plate. *South African Journal of Geology*, **99**, 341-409.

Burke, K. & Gunnell, Y. 2008. *The African Erosion Surface: a continental-scale synthesis of geomorphology, tectonics, and environmental change over the past 180 million years*. Geological Society of America Memoir **201**, 1-66.

Bussert, R. 2007. Late Palaeozoic glacigenic sediments of northern Ethiopia: facies deposition, environment and palaeogeography. Afrikagruppe deutscher Geowissenschaftler conference (7 July 2007): GFZ-Potsdam (2007)

Bussert, R. & Schrank, E. 2007. Palynological evidence for a latest Carboniferous-EarlyPermian glaciation in Northern Ethiopia. *Journal of African Earth Sciences* 49 201–210.

Butt, C.R.M., 1986, A basis for geochemical exploration models for tropical terrains. *Chemical Geology*, **60,** 5-16.

Butt, C.R.M. 1998. Supergene gold deposits. *Journal of Australian Geology and Geophysics*, **17**, 89-96.

Butt, C.R.M., Lintern, M.J. & Anand R.R. 2000. Evolution of regoliths and landscapes in deeply weathered terrain— implications for geochemical exploration. *Ore Geology Reviews*, **16**, p. 167-183.

Butt, C.R.M. and Zeegers, H. (Eds), 1992, *Handbook of Exploration Geochemistry Vol. 4: Regolith Exploration geochemistry in Tropical and Subtropical Terrains*, Elsevier: Amsterdam..

Cahen, L. 1961. Review of geochronological knowledge in Middle and Northern Africa. *Annals of the New York Academy of Sciences*. **91**, 535–567.

Carranza, E.J.M. & Sadeghi, M. 2012. Primary geochemical characteristics of mineral deposits — Implications for exploration. *Ore Geology Reviews*, **45**, p. 1-4.

Carruthers, R.M., Greenbaum, D., Peart, R.J., Herbert, R., 1991. Geophysical investigations of photolineaments in southeast Zimbabwe. *Quarterly Journal of Engineering Geology* **24**, 437-451.

Chandran, P, Ray, S.K., Bhattacharrya, T., Srivastava, P., Krishnan, P. & Pal, D.K. 2005. Lateritic soils of Kerala, India: their mineralogy, genesis, and taxonomy. *Australian Journal of Soil Research*, **43**, 839-842.

Chardon, D., Chevillotte, V., Beauvais, A., Grandin, G. & Boulangé, B. 2006. Planation, bauxites and epeirogeny: one or two palaeosurfaces on the West African margin? *Geomorphology* **82**:273–282

Chastant, L.J., Porcello, L. & Stevenson, J. 1983. Matter-energy interactions in the microwave region. In: R.M. Colwell, *Manual of Remote Sensing (volume 1)*, American Society of Photogrammetry Falls Church, Virginia. 429-47.

Chavez, P. S., MacKinnon, D. J., Reynolds, R. L. & Velasco, M. G. 2002. Monitoring dust storms and mapping landscape vulnerability to wind erosion using satellite and ground-based digital images. *Aridlands Newsletter*, No. 51, May–June 2002. World Wide Web Address: http://ag.arizona.edu/OALS/ALN/aln51/chavez.html.

Chorowicz, J., Collet, B., Bonavia, F. and Korme, T 1999. Left-lateral strike-slip tectonics and gravity induced individualisation of wide continental blocks in the western Afar margin. *Eclogae Geologicae Helv*etiae, 92, 149-158.

Christie, A. 1940. *The Patriotic Murders*. London: Collins Crime Club.

Christie, A. 1990. Discussions on syntax: a philosophical view. *Journal of Applied Philology*. **32**, 227-291.

Chukhrov, F.V., Yermilova, L.P. & Shanin, L.L. 1969. Age of alunite from certain deposits. *Doklady Akademii Nauk SSSR*, **185**, 49-51.

Clark, R.N., Swayze, G.A., Gallagher, A., King, T.V.V. & Calvin, W.M., 1993. *The U.S. Geological Survey, Digital Spectral Library: Version 1: 0.2 to 3.0 microns*. U.S. Geological Survey Open File Report 93-592, 1340 p., World Wide Web Address: http://speclab.cr.usgs.gov/spectral-lib.html

Cloutis, E.A. 1996. Hyperspectral geological remote sensing: evaluation of analytical techniques. *International Journal of Remote Sensing*, **17**, 2215-2242.

CNR-CNRS Afar Team, 1973. Geology of Northern Afar (Ethiopia). *Revue Geographe, Physique Geologic Dynamique*, **2**, 443-490.

Collet, B., Taud, H., Parrot, J.F., Bonavia, F. and Chorowicz, J. 2000. A new kinematic approach for the Danakil block using a Digital Elevation Model representation. *Tectonophysics*, **316**, 343-357.

Collenette, P. & Grainger, D.J. 1994. *Mineral Resources of Saudi Arabia*. Saudi Arabian Directorate General of Mineral Resources Special Publication SP-2, 322 p.

Coltorti, M., Dramis, F. & Ollier, C.D. 2007. Planation surfaces in Northern Ethiopia. *Geomorphology*, **89**, 287-296.

Cornu, S., Cattle, J. A., Samouelian, A., Laveuf, C., Guilherme, L. R. G. & Alberic, P. 2009. Impact of Redox Cycles on Manganese, Iron, Cobalt, and Lead in Nodules. *Soil Society of America Journal*, **73**, 1231-1241.

Coulié, E., Quidelleur, X., Gillot, P.Y., Courtillot, V., Lefevre, J.C. & Chiesa, S. 2003. Comparative K-Ar and Ar/Ar dating of Ethiopian and Yemenite Oligocene volcanism: implications for timing and duration of the Ethiopian traps. *Earth and Planetary Science Letters*, **206**, 477-492.

Courtillot, V., Jaupart, C., Manighetti, I., Tapponnier, P.& Besse, J. 1999. On causal links between flood basalts and continental breakup. *Earth and Planetary Scioence Letters*, **166**, 177-195.

Crippen, R.E., 1989, Selection of Landsat TM band and band-ratio combinations to maximize lithological information in colour composite displays. In Proceedings of 7th Thematic Conference on Remote Sensing for Exploration Geology, 2–6 October 1989, Calgary, Canada (Ann Arbor, MI: ERIM), 917–921.

Crippen,R.E. 2001. Global topography at high resolution: shuttle radar topography mission/Jet Propulsion Lab (JPL). Applications and New Opportunities in Geologic Remote Sensing. Geological Society of America Annual Meeting, 5–8 November 2001. Session 145 (paper no. 145–0). World Wide Web Address: http://gsa.confex.com/gsa/2001AM/finalprogram/abstract_17784.htm.

Crippen, R. E. & Blom, R. G. 2000. Remote sensing in three dimensions: the integration of new global data sets. In: Proceedings of the 14th International Conference on Applied Geological Remote Sensing, Las Vegas, Nevada, USA, 6–8 November 2000. Environmental Research Institute of Michigan, Ann Arbor, MI, 121.

Crosta, A.P. and Moore, J.M., 1989, Enhancement of Landsat Thematic Mapper imagery for residual soil mapping in SW Minas Gerais State, Brazil: A Prospecting case history in greenstone belt terrain. In Proceedings of the 7th Thematic Conference on Remote Sensing for Exploration Geology, 2–6 October 1989, Calgary, Canada (Ann Arbor, MI: ERIM), 1173–1187.

Crowley, J.K., Brickey, D.W. & Rowan, L.C., 1989. Airborne imaging spectrometer data of the Ruby Mountains, Montana: Mineral discrimination using relative absorption band-depth images. *Remote Sensing of Environment*, **29**, 121–134.

Dainelli, G., 1943, *Geologia dell'Africa Orientale*. Rome: Reale Accademia d'Italia.

Davidson A. 1982. Reconnaissance geology and geochemistry of parts of Illubabor, Kefa, Gemu Gofa and Sidamo, Ethiopia. *Ministry of Mines and Energy, Ethiopian Institute of Geological Surveys, Bulletin*, **2.**

Davidson A. & Rex D. C. 1980. Age of volcanism and rifting in southwestern Ethiopia. *Nature*, **283**:657–658.

Davies, M., Parkinson, I. & Rogers, N. 2003. The Origin of High-Ti Picrites from the Ethiopian Flood Basalt Province. Abstracts; Penrose Conference August 25th – 29th, 2003, Hveragerdi, Iceland

Davies, S., Buchanon-Smith, M. & Lambert, R. 1991. *Early warning in the Sahel and Horn of Africa: The state of the art. A review of the literature.* Volume 1. University of Sussex, Research Report, 20.

Davison, I., al-Kadasi, M.A, al-Khirbash, S., al Subbary, A., Baker, J., Blakey, S., Bosence, D., Dart, C., Heaton, R., McClay, K., Menzies, M., Nichols, G., Owen, L., & Yelland, A. 1994. Geological evolution of the southeastern Red Sea Rift margin, Republic of Yemen. *Geological Society of America Bulletin*, **106**, 1474-1493.

Dehaene, S., Izard, V., Pica, P. & Spelke, E. 2006. Core knowledge of geometry in an Amazonian indigene group. *Science*, **311**, 381–384.

Delson, R.M. 2006. Examining knowledge of geometry. *Science*, **312**, 1309–1310.

Delvigne, J.E. 1998. *Atlas of micromorphology of mineral alteration and weathering.* Canadian Mineralogist, Special Publication **3**, pp. 494.

Dixon, C. J. 1979. *Atlas of Economic Mineral Deposits*. London: Chapman and Hall, 143 p.

Dow, D.B., Beyth, M & Hailu, T. 1971. Palaeozoic glacial rocks recently discovered in northern Ethiopia. *Geological Magazine*, **108**, 53-60.

Drury, S.A., 1983. A regional tectonic study of the Archaean Chitradurga greenstone belt, Karnataka, based on Landsat interpretation. *Journal of the Geological Society of India*, **24**, 167-184.

Drury, S.A., 1986. Remote sensing of geological structure in temperate agricultural terrains. *Geological Magazine* **123**, 113-21.

Drury, S.A., 1987. *Image Interpretation in Geology*, first edition. Allen and Unwin, London, pp. 243.

Drury, S.A., 1993, *Image Interpretation in Geology*, second edition Chapman & Hall: London, pp. 283.

Drury, S.A. 1997. The national image mosaic of Eritrea. *International Journal of Remote Sensing*, **18**, 2897–2898.

Drury, S.A. 1998. *Images of the Earth—a Guide to Remote Sensing, 2nd edn.* Oxford University Press, Oxford.

Drury, S.A., 2001, *Image Interpretation in Geology*, third edition Nelson Thornes: London, pp. 290.

Drury, S. A. 2005. Earth Pages News, January 2005 issue. Oxford: Blackwell Science. World Wide Web Address: http://www.earth-pages.co.uk/2005/01/.

Drury, S.A. 2006. *Water and well-being: arsenic in Bangladesh.* Topic 3 in: S250 Science in Context, The Open University: Milton Keynes, UK; ISBN 0 7492 1435 X.

Drury, S.A. 2012. South Asian arsenic update. *Earth Pages (January 2012)* World Wide Web Address: http://earth-pages.co.uk/2011/11/16/south-asian-arsenic-update/

Drury, S. A. & Andrews Deller, M. E. 2002. Remote sensing and locating new water sources. In: United Nations International Workshop for Space Technology and Disaster Management, Addis Ababa, Ethiopia, 1– 5 July 2002. World Wide Web Address: http://www.unoosa.org/pdf/sap/2002/ethiopia/presentations/12speaker01_1.pdf.

Drury, S. A. & Andrews Deller, M. E. 2004. ASTER multispectral thermal data and finding water. In: United Nations International Workshop on the Use of Space Technology for Disaster Management in Munich, 18–22 October 2004. World Wide Web Address: http://www.zki.caf.dlr.de/media/download/unoosa_workshop_presentations/16_pres_session06c_chair-tarabzouni/58_UNOOSA-DLR_Drury_OpenUni v_UK.pdf.

Drury, S. A. & Andrews Deller, M. E. 2005. Advances in groundwater exploration: the roles of ASTER and SRTM data. In: 31st International Symposium on Remote Sensing of Environment, Saint Petersburg, Russia, 20–24 June 2005. World Wide Web Address: (http://www.isprs.org/publications/related/ISRSE/html/papers/661.pdf

Drury, S.A.& Berhe, SM. 1993. Accretion tectonics in northern Eritrea revealed by remotely sensed imagery. *Geological Magazine*, **130**, 177-1 90.

Drury, S.A. & de Souza Filho, C.R. 1998. Neoproterozoic terrane assemblages in Eritrea: review and prospects. *Journal African Earth Sciences*, **27**, 331-348.

Drury, S.A., Ghebreab, W., Andrews Deller, M.E., Talbot, C.J. & Berhe, S.M. 2006. A comment on "Geomorphic development of the escarpment of the Eritrean margin, southern Red Sea from combined apatite fission-track and (U–Th)/He thermochronometry" by Balestrieri, M.L. *et al.* [Earth Planet. Sci. Lett. 231 (2005) 97–110]. *Earth and Planetary Science Letters*, **242**, 428-432.

Drury, S.A. & Holt, R.W., 1980. The tectonic framework of the South Indian craton: a reconnaissance involving Landsat imagery. *Tectonophysics*, **65**, T1-T15.

Drury, S.A. & Hunt, G.A., 1988. Remote sensing of lateritised Archaean greenstone terrain: Marshall Pool area, North-eastern Yilgarn Block, Western Australia. *Photogrammetric Engineering and Remote Sensing*, **54**, 1717-1725.

Drury, S.A. & Hunt, G.A., 1989, Geological uses of remotely-sensed reflected and emitted data of lateritised Achaean terrain in Western Australia. *International Journal of Remote Sensing*, **10**, 475–497.

Drury, S.A., Kelley, S.P., Berhe, S.M., Collier, R.E.Ll. & Abraha, M. 1994. Structures related to Red Sea evolution in northern Eritrea, *Tectonics* **13** 1371-1380.

Drury, S. A., Peart, R. J. & Andrews Deller, M. E. 2001. Hydrogeological potential of major fractures in Eritrea. *Journal of African Earth Sciences*, **32**, 163–177.

Du Bray, E.A., Stoeser, D.B. & McKee, E.H., 1991, Age and petrology of the tertiary As Sarat volcanic field, southwestern Saudi Arabia. *Tectonophysics*, **198**, 155–180.

Ebinger, C.J., Yemane, T., Harding, D.J., Tesfaye, S., Kelley, S.P. & Rex. D.C. 2000. Rift deflection, migration, and propagation: Linkage of the Ethiopian and Eastern rifts, Africa. *Geological Society of America Bulletin*, **112**, 163-176.

Ebinger, C.J., Yemane, T., Woldegabriel, G., Aronson, J.L. & Walter, R.C. 1993. Late Eocene–Recent volcanism and faulting in the southern main Ethiopian rift, *Journal of the Geological Society London*, **150**, 99-108.

Edwards, R. and Atkinson, K. 1986. *Ore Deposit Geology*. Chapman and Hall: London.

Ellsworth, W. L. 2006. Halfway through Reid's cycle and still counting. *Science*, **312**, 203–204.

Ehlers, T.A., Willett, S.D., Armstrong, P.A. & Chapman, D.S. 2003. Exhumation of the central Wasatch Mountains, Utah: 2. Thermokinematic model of exhumation, erosion, and thermochronometer interpretation. *Journal of Geophysical Research – Solid Earth*, **108**, doi:10.1029/2001JB001723

England, P. & Molnar, P. 1990. Surface uplift, uplift of rocks, and exhumation of rocks. *Geology*, **18**, 1173-1177.

Eritrean Ministry of Energy and Mines 1997, *Mineral Prospects of the State of Eritrea*. Eritrean Ministry of Energy and Mines: Asmara.

Eritrean Ministry of Energy and Mines 2009a. *Geological map of the Gash Area (1:250000)*. Eritrean Ministry of Energy and Mines: Asmara.

Eritrean Ministry of Energy and Mines 2009b. *Geological map of the Mai Dima Kohain Area (1:250000)*. Eritrean Ministry of Energy and Mines: Asmara.

Ethiopian Institute of Geological Surveys (EIGS), 1996. *Geological Map of Ethiopia*. Government of Ethiopia, Addis Ababa.

Eyles, N. 1993. Earth's glacial record and its tectonic setting. *Earth-Science Reviews*, **35**, 1-248/

Farr, T. G., Rosen, P. A., Caro, E., Crippen, R., Duren, R., Hensley, S., Kobrick, M., Paller, M., Rodriguez, E., Roth, L., Seal, D., Shaffer, S., Shimada, J., Umland, J., Werner, M., Oskin, M., Burbank, D. & Alsdorf, D. 2007. The Shuttle Radar Topography Mission. *Reviews of Geophysics*, **45**, doi:10.1029/2005RG000183

Fawcett, P.J. & Barron, E.J. 1998. The role of geography and atmospheric $CO_2$ in long-term climate change: Results from model simulations for the Late Permian to present. In Crowley, T.J. & Burke, K. (Eds.), *Tectonic Boundary Conditions for Climate Reconstructions*. Oxford University Press: New York, 21–38.

Feng, Y.X. & Vasconcelos, P.M. 2001. Quaternary continental weathering geochronology by laser-heating $^{40}Ar/^{39}Ar$ analysis of supergene cryptomelane. *Geology*, **29**, 635–638.

Ferreira, A. R. 1792. *Viagem Filosofica pelas capitanias do Grão Pará , Rio Negro, Mato Grosso e Cuiabá , vol. 2, Memorias zoologia e botanica.* Conselho Federal de Cultura, Rio de Janeiro (reprinted 1974).

Firman, J.B. 1994. Paleosols in laterite and silcrete profiles: Evidence from the South East Margin of the Australian Precambrian Shield. *Earth Science Reviews*, **36**, 149-179.

Fletcher, B.J., Brentnall, S.J., Anderson, C.W., Berner, R.A. & Beerling, D.J. 2008. Atmospheric carbon dioxide linked with Mesozoic and early Cenozoic climate change. *Nature Geoscience*, **1**, 45-48.

Fookes, P.G. 1997. Geology for engineers: the geological model, prediction and performance. *Quarterly Journal of Engineering Geology*, **30**, 293-424.

Franklin, J. M., Lydon, J. W. & Sangster, D. F., 1981, Volcanic associated massive sulphide deposits. *Economic Geology*, **76**, 485-627.

Frazier, S.B 1970. Adjacent structures of Ethiopia: that portion of the Red Sea coast including Dahlak Kebir Island and the Gulf of Zula. *Philosophical Transactions of the Royal Society London*, **A267** 131-141.

Fu, B. H., Ninomiya, Y., Lei, X. L., Toda, S. & Awata, Y. 2004 Mapping active fault associated with the Mw 6.6 Bam (SE Iran) earthquake with ASTER 3D images. *Remote Sensing of Environment*, **92**, 153–157.

Fung, A.K. & Ulaby, F.T. 1983. Matter-energy interactions in the microwave region. In: R.M. Colwell, *Manual of Remote Sensing (volume 1)*, American Society of Photogrammetry Falls Church, Virginia. 115-164.

Gaber, A., Koch, M. & El-Baz, F. 2009. Textural and Compositional Characterization of Wadi Feiran Deposits, Sinai Peninsula, Egypt, Using Radarsat-1, PALSAR, SRTM and ETM+ Data. *Remote Sensing*, **2**, 52-75.

Gani, N.D.S. & Abdelsalam, M.G. 2006. Remote sensing analysis of the Gorge of the Nile, Ethiopia with emphasis on Dejen-Gohatsion region. *Journal of African Earth Sciences*, **44**, 135-150.

Garland, C.R., Assefa, A., Amenti, A., Beyth, M., Dow, D.B., Temesgen, H. & Tsegaye, H. 1978. *Geological Map of Adigrat ND 37-7*. Ethiopian Institute of Geological Surveys, Ministry of Mines, Energy and Water Resources, Addis Ababa.

Gass, I. G. 1981. Pan-African (Upper Proterozoic) plate tectonics of the Arabian-Nubian shield. *In:* Kröner, A.(ed.) *Precambrian Plate Tectonics*, Elsevier, Amsterdam, 387-405.

Gaudin, A., Decarreau, A., Noack, Y. & Grauby, O. 2005. Clay mineralogy of the nickel laterite ore developed from serpentinised peridotites at Murrin Murrin, Western Australia. *Australian Journal of Earth Sciences*, **52**, 231-241.

Geological Research Authority of Sudan (GRAS), 1988. *Geological map of Sudan: Port Sudan Sheet* Scale 1:1 000 000. Robertson Research International, Llandudno, UK..

Geological Survey of Eritrea 1998. *Preliminary geological map of Eritrea (1:1 million)*. Eritrean Ministry of Energy and Mines: Asmara.

Geological Survey of Eritrea 2001. *Simplified geological map of Eritrea (1:1 million)*. Eritrean Ministry of Energy and Mines: Asmara.

George, R.M. 1997. *Thermal and tectonic controls on magmatism in the Ethiopian province*. Unpublished Ph.D. thesis, Open University: Milton Keynes, United Kingdom, pp. 235.

George, R.M., Rogers N. & Kelley, S. 1998. Earliest magmatism in Ethiopia: Evidence for two mantle plumes in one flood-basalt province. *Geology*, **26**, 923-926.

Germann, K., Schwartz, T. & Wipki, M. 1994. Mineral deposit formation in Phanerozoic basins of NE-Africa – the contribution of weathering. *Geologische Rundschau*, **83**, 787-798.

Germann, K., Wipki, M. & Schwartz, T. 1993. Cambro-Ordovician bauxitic laterites of NW-Sudan. In: U. Thorweihe & H. Schandelmeier (eds), *Geoscientific Research in Northeast Africa*, 335-340; Balkema: Rotterdam

Getaneh, W. 2002. Geochemistry provenance and depositional tectonic setting of the Adigrat Sandstone northern Ethiopia. *Journal of African Earth Sciences*, **35**, 185-198.

Ghebreab, W., 1998. Tectonics of the Red Sea region reassessed. *Earth Science Reviews*, **45**, 1-44.

Ghebreab, W., 1999, Tectono-metamorphic history of Neoproterozoic rocks in eastern Eritrea. *Precambrian Research*, **98**, 83–105.

Ghebreab, W., Carter, A., Hurford, A.J. & Talbot, C.J., 2002. Constraints for timing of extensional tectonics in the western margin of the Red Sea in Eritrea. *Earth and Planetary Science Letters*, **200**, 107-119.

Ghebreab, W. & Talbot, C.J. 1997. Red Sea detachment and basement core complexes in Eritrea. *Geology*, **25**, 655-658.

Ghebreab, W. & Talbot, C.J., 2000. Red Sea extension influenced by Pan-African tectonic grain in eastern Eritrea. *Journal of Structural Geology*, **22**, 931-946.

Ghebreab, W., Talbot, C.J. & Page, L. 2005. Time constraints on exhumation of the East African Orogen from field observations and $^{40}Ar/^{39}Ar$ cooling ages of low-angle mylonites in Eritrea, NE Africa. *Precambrian Research*, **139**, 20-41.

Gilkes, R.J., Lee, S. & Singh, B. 2003. The imprinting of aridity upon a lateritic landscape: an illustration from southwestern Australia, *Comptes Rendus Geoscience*, **335**, 1207-1218.

Gillespie, A., 1986, Lithologic mapping of silicate rocks using TIMS. In: *Proceedings of the TIMS Data Users' Workshop*, JPL Publication 86-38 (Pasadena: Jet Propulsion Laboratory), 29–44.

Girard, J.P. & Onstott, T.C. 1991. Application of Ar-40/Ar-39 laser-probe and step-heating techniques to the dating of diagenetic K-feldspar overgrowths. *Geochimica et Cosmochimica Acta*, **55**, 3777-3793.

Goossens, M. 2002. ASTER in mineral exploration: A brief review. *Newsletter of the Geological Remote Sensing Group*, Geological Society of London: London, **33**, 16–21.

Government of the State of Eritrea, 1994, *Eritrea National Map*, (Scale 1: 1,000,000) GDE: Berne.

Gradstein, F.M., Ogg, J.G., Smith, A.G., Bleeker, W. & Lourens, L.J. 2004. A new Geologic Time Scale, with special reference to Precambrian and Neogene. *Episodes*, **27**, 83-100.

Grasty, R., Miller J.A. & Mohr, P.A. 1963. Preliminary results of potassium-argon age determinations on some Ethiopian Trap Series basalts. *Bulletin of the Geophysical Observatory*, **6**, 97-102.

Grenne, T., Pedersen, R.B., Bjerkgård, T., Braathen, A & Selassie, M.G. 2003. Neoproterozoic evolution of Western Ethiopia: igneous geochemistry, isotope systematics and U-Pb ages. *Geological Magazine*, **140**, 373-395.

Guiraud, R., Bosworth, W., Thierry, J. & Delplanque, A. 2005. Phanerozoic geological evolution of Northern and Central Africa: an overview. *Journal of African Earth Sciences*, **43**, 83-143

Gunnell, Y. 2003. Radiometric ages of laterites and constraints on long-term denudation rates in West Africa. *Geology*, **31**, 131-134.

Gupta, R.P. 1991. *Remote sensing geology*. Berlin: Springer-Verlag.

Gustafson, L.B. & Hunt, J.P. 1975. The porphyry copper deposit at El Salvador, Chile. *Economic Geology*, **70**, 857-912.

Gutzmer, J. & Beukes, N.J. 1998. Earliest laterites and possible evidence for terrestrial vegetation in the Early Proterozoic. *Geology*, **26**, 263-266.

Haggerty, B.M. 1996. Episodes of flood-basalt volcanism defined by $^{40}Ar/^{39}Ar$ age distributions: correlation with mass extinctions? *Journal of Undergraduate Science*, **3**, 155-164.

HAIC Secretariat, 2001. Establishment of a regional Humanitarian Assistance Information Centre (HAIC). Report of a UNEP and UNDP (Somalia) Workshop, Nairobi, Feb. 1–2, 2001. World Wide Web Address: (http://www.depha.org/proceedings/HAIC%20Proceedings.DOC).

Hénocque, O., Ruffet, G., Colin, F. & Féraud, G. 1998. $^{40}Ar/^{39}Ar$ dating of West African lateritic cryptomelanes. *Geochimica et Cosmochimica Acta*, **62**, 2739-2756.

Highland, L.M. & Bobrowsky, P. 2008. *The Landslide Handbook: A Guide to Understanding Landslides*. Circular 1325, US Geological Survey: Reston VA, USA. World Wide Web Address: http://pubs.usgs.gov/circ/1325

Hofmann, C., Courtillot, V., Feraud, G., Rochette, P., Yirgu, G., Ketefo, E. & Pik, R., 1997. Timing of the Ethiopian flood basalt event: implications for plume birth and global change. *Nature*, **389**, 838–841.

Holmes, A. 1951. *Principles of Physical Geology* (2nd Ed.). Thomas Nelson & Sons: London.

Huang, W. & Fu, B. 2002. Remote sensing for coastal area management in China. *International Journal of Remote Sensing*, **30**, 271–276.

Hubbard, B.E. & Crowley, J.K. 2005. Mineral mapping on the Chilean-Bolivian Altiplano using co-orbital ALI, ASTER and Hyperion imagery: Data dimensionality issues and solutions. *Remote Sensing of Environment*, **99**, 173-186

Hubbard, B.E., Crowley, J.K. & Zimbelman, D.R., 2003, Comparative alteration mineral mapping using visible to shortwave infrared (0.4–2.4 mm) Hyperion, ALI, and ASTER Imagery. *IEEE Transactions on Geoscience and Remote Sensing*, **41**, 1401-1410.

Hunt, G.A. 1991. *Geological applications of reflected and emitted multispectral data over lateritised Archaean terrain in Western Australia*. Unpublished PhD thesis, Open University: Milton Keynes, UK.

Hunt, G.A., Drury, S.A. and Rothery, D.A. 1986. Techniques for choosing the optimum Thematic Mapper channel combination for lithological mapping in semi-arid terrains. *Proceedings of 12th International Conference of the Remote Sensing Society*, Edinburgh, 637-46.

Hunt, J. C. R. 2002. Floods in a changing climate: a review. *Philosophical Transactions of the Royal Society of London, Series A*, **360**, 1531–1543.

Hussey, M.C. 1998. *Surface detection of alkaline ultramafic rocks in semi-arid and arid terrains using spectral geological techniques*. Unpublished PhD thesis, Open University: Milton Keynes, UK

Itaya, T., Aribas, A. & Okada, T. 1996. Argon release systematics of hypogene and supergene alunite based on progressive heating experiments from 100 to 1000°C. *Geochimica et Cosmochimica Acta*, **60**, 4525-4535.

Jardiné, S. 1974. Microflores des formations du Gabon attribuées au Karroo. *Review of Palaeobotany and Palynology*, **17**, 75–112.

Jenson, S. K. & Domingue, J.O. 1988, Extracting topographic structure from digital elevation data for geographic information system analysis. *Photogrammetric Engineering and Remote Sensing*, 54, 1593–1600.

John, C.M., Banerjee, N.R., Longstaffe, F.J., Sica, C., Law, K.R. & Zachos, J.C. 2012. Clay assemblage and oxygen isotopic constraints on the weathering response to the Paleocene-Eocene thermal maximum, east coast of North America. *Geology*, **40**, 591-594

Johnson, P.R. & Woldehaimanot, B., 2003, Development of the Arabian-Nubian Shield: Perspectives on accretion and deformation in the northern East African Orogen. In: M. Yoshida, B.F. Windley & S. Dasgupta (Eds), *Proterozoic East Gondwana: Supercontinent Assembly and Breakup*, Geological Society of London, Special Publication **206** pp. 289–325.

Jordan, C. J., O'Connor, A. P., Passmore, J., Sucre, B. & Chuluum, O. 2000a. Appropriate technology for low-cost geological mapping—the case for publicising geological, mineral and remote sensing information of developing countries to the investor sector via the internet with case studies from Guyana and Mongolia. In: *Proceedings of the 14th International Conference on Applied Geological Remote Sensing, Las Vegas, Nevada, USA, 6–8 November 2000*. Environmental Research Institute of Michigan, Ann Arbor, MI, 303–310.

Jordan, C. J., O'Connor, E. A., Marchant, A. P. *et al.* 2000b. Rapid landslide susceptibility mapping using remote sensing and GIS modelling. In: *Proceedings of the 14th International Conference on Applied Geological Remote Sensing, Las Vegas, Nevada, USA, 6–8 November 2000*. Environmental Research Institute of Michigan, Ann Arbor, MI, 113–120.

Justin-Visentin E., Nicoletti M., Tolomeo L. & Zanettin B 1974. Miocene and Pliocene volcanic rocks of the Addis Abeba-Debra Berhan area (Ethiopia). Geopetrographic and radiometric study. *Bulletin Volcanologique*, **38**, 237–53

Kar, R. K. & Bose, M. N. 1967, Palaeozoic sporae dispersae from Congo: III – Assise des schistes noirs de la Lukuga. *Musée Royal Afrique Centrale Annales*, (Tervuren), ser. 8, no. 54, 3-61.

Karous, M. & Hjelt, S.E. 1983. Linear filtering of VLF dip-angle measurements. *Geophysical Prospecting*, **31**, 782-794.

Kaya, S., Muftuoglu, O. & Tuysoz, O. 2004. Tracing the geometry of an active fault using remote sensing and digital elevation model: Ganos segment, North Anatolian Fault zone, Turkey. *International Journal of Remote Sensing*, 25, 3843–3855.

Kazmin, V. 1972. *Geological map of Ethiopia* (scale 1:2 million), Ministry of Mines, Addis Ababa.

Kazmin, V., Shifferaw, A. & Balcha, T. 1978. The Ethiopian basement: stratigraphy and possible manner of evolution. *Geologische Rundschau* **67**, 531–546.

Keith, M.L. 1939. Selective staining to facilitate Rosiwal analysis. *American Mineralogist*, **24**, 561-565.

Keats, J. 1816. On the Grasshopper and Cricket. In; F.T. Palgrave (Ed) 1999 *John Keats: Poetical Works*. Bartleby.com: New York. World Wide Web Address http://www.bartleby.com/126/28.html

Kelley, S. P. 2002. Excess argon in K–Ar and Ar–Ar geochronology. *Chemical Geology*, **188**, 1–22.

Kelley, S. P., Reddy, S.M. & Maddock, R. 1994. Laser-probe $^{40}Ar/^{39}Ar$ investigation of a pseudotachylyte and its host rock from the Outer Isles thrust, Scotland. *Geology*, **22**, 443-446.

Kenea, N.H., 1997, Improved geological mapping using Landsat TM data, Southern Red Sea Hills, Sudan: PC and HIS decorrelation stretching. *International Journal of Remote Sensing*, 18, 1233–1244.

Kenea, N.H. Ebinger, C.J. & Rex D.C. 2001. Late Oligocene volcanism and extension in the southern Red Sea hills, Sudan. *Journal of the Geological Society, London* **158** 285-294.

Kennedy, W.Q. 1964. The structural differentiation of Africa in the Pan-African (± 500 m.y.) tectonic episode. *Annual Report of the Research Institute of African Geology, University of Leeds*, **8**, 48-49.

Kennett, J. P. & Shackleton, N. J. 1976. Oxygen isotopic evidence for the development of the psychrosphere 38 Myr ago. *Nature*, **260**, 513–515

Kerle, N., Froger, J. L., Oppenheimer, C. & Van Wyk de VriesS, B. 2003. Remote sensing of the 1998 mudflow at Casita volcano, Nicaragua. *International Journal of Remote Sensing*, **24**, 4791–4816.

Kerr, P.F. 1959. *Optical mineralogy*. McGraw-Hill: New York

Kieffer, B., Arndt, N., Lapierre, H., Bastien, F., Bosch, D., Pecher, A., Yirgu, G., Ayalew, D., Weis, D., Jerram, D.A., Keller, F. & Meugniot, C., 2004. Flood and Shield Basalts from Ethiopia: Magmas from the African Superswell. *Journal of Petrology*, **45**, 793-834.

King, L.C. 1948. On the ages of African land-surfaces. *Quarterly Journal of the Geological Society*, **104**, 439-459.

King, L.C. 1950. The study of the world's plainlands: a new approach in geomorphology. *Quarterly Journal of the Geological Society*, **106**, 101-131.

King L.C. 1962. *The Morphology of the Earth*. Oliver and Boyd: Edinbugh.

King L.C. 1967. *The Morphology of the Earth* (2nd Ed). Oliver and Boyd: Edinbugh.

King, L.C. 1973. Tectonics of Africa. *Geographical Journal*, **139**, p. 119-121.

King, R. B. 1981. An evaluation of Landsat 3 RBV imagery for obtaining environmental information in Tanzania. In: Allan, J. A. (ed.) *Matching Remote Sensing Technologies and their Applications*. Proceedings of the 9th Annual Conference of the Remote Sensing Society, London, 16–18 December 1981. Remote Sensing Society, University of Reading, Reading, 85–95.

King, R. B. 1984. *Remote Sensing Manual of Tanzania*, Land Resources Development Centre: Surbiton, Surrey.

King, R. B. 1994. The value of ground resolution, spectral range and stereoscopy of satellite imagery for land system and land-use mapping of the humid tropics. *International Journal of Remote Sensing*, **15**, 521–530.

King R.B., Kikula I.S. & Mascarenhas A.C., 1981. A less developed country's assessment of Landsat as a data source for development. *UN/ECA Remote Sensing Applications and Satellite Communications for Education and Development*, Addis Ababa, 11-19 March 1981.

Kinniburgh D.G. & Smedley, P.L. (Eds), 2001, *Arsenic Contamination of Groundwater in Bangladesh*, British Geological Survey Technical Report WC/00/19 British Geological Survey: Keyworth.

Klein, N., Bussert, R. & Enkurie, D. 2007. Mesozoic vertebrates from the Adigrat Formation of Ethiopia. *Journal of Vertebrate Palaeontology*, **27**, 99A-100A.

Kogan, F. 2005. Remote sensing contribution to early drought detection and monitoring. In: 31st International Symposium on Remote Sensing of Environment, Saint Petersburg, Russia, 20–24 June 2005 (http://www.isprs.org/publications/related/ISRSE/html/papers/454.pdf).

Kröner, A. 1985. Ophiolites and the evolution of tectonic boundaries in the late Proterozoic Arabian-Nubian Shield of Northeast Africa and Arabia. *Precambrian Research*, **27**, 277-300.

Kröner, A. & Stern, R.J. 2005. Africa: Pan-African Orogeny. In: Selley, R.C., Cocks, R.M & Plimer, I.R. (Eds) *Encyclopedia of Geology*. Elsevier: Amsterdam, 1-12.

Kruck, W., Thiele, J., 1983. Late Paleozoic glacial deposits in the Yemen Arab Republic. *Geologisches Jahrbuch*, **B46**, 3–29.

Kruse, F.A., Kierein-Young, K.S. & Boardman, J.W. 1990. Mineral mapping at Cuprite, Nevada, with a 63-channel imaging spectrometer: *Photogrammetric Engineering and Remote Sensing*, **56**, 83–92.

Kruse, F.A., Lefkoff, A. B., Boardman, J.B., Heidebreicht, K.B., Shapiro, A.T., Barloon, P.J., & Goetz, A.F.H., 1993, The Spectral Image Processing System (SIPS)—interactive visualization and analysis of imaging spectrometer data. *Remote Sensing of Environment*, **44**, 145–163.

Kruse, F.A., Boardman, J.W. & Huntington, J.F., 2003. Comparison of airborne hyperspectral data and EO-1 Hyperion for mineral mapping. Institute of Electrical and Electronics Engineers. *Transactions on Geoscience and Remote Sensing*. **41**, 1388–1400.

Kula, J. & Baldwin, S.L 2011. Jarosite, argon diffusion, and dating aqueous mineralization on Earth and Mars. *Earth and Planetary Science Letters*, **310**, 314-318.

Kumpulainen, R.A., Uchman, A., Woldehaimanot, B., Kreuser, T. & Ghirmay, S. 2006. Trace fossil evidence from the Adigrat Sandstone for an Ordovician glaciation in Eritrea, NE Africa. *Journal of African Earth Sciences* **45**, 408–420.

Kusky, T.M. & El-Baz, F. 1998. Structural and tectonic evolution of the Sinai Peninsula, using Landsat data: Implications for ground water exploration. *Egyptian Journal Remote Sensing Space Sciences* **1**, 69-100.

Landis, G.P., Snee, L.W. & Juliani, C. 2005. Evaluation of argon ages and integrity of fluid-inclusion compositions: stepwise noble gas heating experiments on 1.87 Ga alunite from Tapajo´ s Province, Brazil. *Chemical Geology*, **215**, 127-153.

Lang, H. 1999. ATBD-AST-08 algorithm theoretical basis document for ASTER digital elevation models (Standard Product AST14). World Wide Web Address: http://eospso.gsfc.nasa.gov/eos_homepage/for_scientists/atbd/docs/ASTER/atbd-ast-14.pdf.

Lecompte, P. & Zeegers, H. 1992. Humid tropical terrains (rainforests). Chapter III.2 In: Butt, C.R.M. and Zeegers, H. (Eds), 1992, *Regolith exploration geochemistry in tropical and subtropical terrains* Amsterdam and London: Elsevier.

Leng, W. & Zhong, S. 2010. Surface subsidence caused by mantle plumes and volcanic loading in large igneous provinces. *Earth and Planetary Science Letters*, **291**, 207-214.

Lidmar-Bergström, K., Roaldset, E., & Olsson, S. 1999: Relief features and palaeoweathering remnants in formerly glaciated Scandinavian basement areas. In: M. Thiry and R. Simon-Coinçon (Eds), *Palaeoweathering, palaeosurfaces and related continental deposits*.. International Association of Sedimentologists (IAS) Special publication **27**: 275-301.

Linge, K. L. 2005. Recent developments in trace element analysis by ICP-AES and ICP-MS with particular reference to geological and environmental samples. *Geostandards and Geoanalytical Research*, 29(1), 7-22.

Linge, K.L. & Jarvis, K.E. 2009. Quadrupole ICP-MS: Introduction to Instrumentation, Measurement Techniques and Analytical Capabilities. *Geostandards and Geoanalytical Research*, **33**, 445-467.

Loganathan, V.A., Barnett, M.O., Clement, T.P. & Kanel S.R. 2009. Scaling of adsorption reactions: U(VI) experiments and modeling. *Applied Geochemistry*, **24**, 2051-2060.

López-Gamundí, O.R. & Buatois L.A. 2010. Introduction: Late Paleozoic glacial events and postglacial transgressions in Gondwana. In: López-Gamundí, O.R., and Buatois, L.A., eds., *Late Paleozoic Glacial Events and Postglacial Transgressions in Gondwana*: Geological Society of America Special Paper **468**, v–viii.

Loughlin, W.P., 1991, Principal component analysis for alteration mapping. *Photogrammetric Engineering and Remote Sensing*, **57**, 1163–1169.

Lydon, J.W. 1988. Ore deposit models 14: volcanogenic massive sulfide deposits 2: genetic models. *Geoscience Canada*, **15**, 43-65.

MacRae, C.S. 1988. Palynostratigraphic correlation between the lower Karoo sequence of the Waterberg and Pafuri coal-bearing basins and the Hammanskraal plant macrofossil locality, Republic of South Africa. *Memoir of the South African Geological Survey* **75**, 1–217.

Magpie Trial Collaborative Group, 2002, Do women with pre-eclampsia, and their babies, benefit from magnesium sulphate? The Magpie Trial: A randomised placebo controlled trial. *The Lancet*, 359, 1877–1890.

Maheshwari, H.K. 1969. Palaeozoic sporae dispersae from Congo. X. Microfossils from a cliff section at the confluence of Lufupa and Mushyashya rivers, south Katanga. *Koninklijk Museum voor Midden-Afrika, Annalen*, **8**, 115–169.

Maiti, A., Basu, J.K. & De, S. 2010. Removal of arsenic from synthetic and natural groundwater using acid-activated laterite. *Environmental Progress & Sustainable Energy*, **29**, 457-470.

Manighetti, I., Tapponier, P., Courtillot, V., Gallet, Y., Jaques, E. & Gillot, P.-Y. 2001. Strain transfer between disconnected, propagating rifts in Afar. *Journal of Geophysical Research* **106** (B7) 13613-13665.

Manning, B.A. Fendorf, S.E. &Goldberg, SD. 1997. Coordination and stability of arsenic(III) at the goethite-water interface. *Internal report of the US Department of Agriculture, Agricultural Research Service*, 97/023

Marker, M.E., McFarlane, M.J. & Wormald, R.J. 2002. A laterite profile near Albertinia, Southern Cape, South Africa: its significance in the evolution of the African Surface. *South African Journal of Geology*, **105**, 67-74.

Mars, J.C & Rowan, L.C. 2006. Regional mapping of phyllic- and argillic-altered rocks in the Zagros magmatic arc, Iran, using Advanced Spaceborne Thermal Emission and Reflection Radiometer (ASTER) data and logical operator algorithms. *Geosphere*, **2**, 161-186.

Marsh, S. 2000. Remote mapping technologies for temperate, vegetated terrain. In: *Proceedings of the 14th International Conference on Applied Geological Remote Sensing, Las Vegas, Nevada, USA, 6–8 November 2000*. Environmental Research Institute of Michigan, Ann Arbor, MI, 11–17.

Marsh, S. 2004. The IGOS Geohazard Report. In: *United Nations International Workshop on the Use of Space Technology for Disaster Management in Munich, 18–22 October 2004*. World Wide Web Address: http://www.zki.caf.dlr.de/media/download/unoosa_workshop_presentations/05_pres_session03_c hair-wade/12_UNOOSA-DLR_Marsh_BGS_UK.ppt.

Martyn, C.N., Osmond, C. Edwardson, J.A., Barker, D.J.P., Harris, E.C. & Lacey, 1989. Geographical relation between Alzheimer's Disease and aluminium in drinking water. *The Lancet*, **333**, 61-62.

Mason, B. 1966. *Principles of Geochemistry*. John Wiley & Sons.

Massironi, M., Bertoldi, L., Calafa, P., Visona, D., Bistacchi, A., Giardino, C. & Schiavo, A. 2008. Interpretation and processing of ASTER data for geological mapping and granitoids detection in the Saghro massif (eastern Anti-Atlas, Morocco). *Geosphere*, **4**, 736-759.

Massonnet, D. 1995. Application of remote sensing data in earthquake monitoring. *Advances in Space Research*, 15, 37–44.

McCain, M. 1997. Chemtrails and Barium Toxicity. World Wide Web http://www.rense.com/general21/tox.htm

McArthur, J. M., Ravenscroft, P., Safiullah, S. & Thirlwall, M. F. 2001. Arsenic in groundwater: testing pollution mechanisms for sedimentary aquifers in Bangladesh. *Water Resources Research*, **37**, 109–117.

McCain, M. 1997. Chemtrails And Barium Toxicity. *World Wide Web* http://www.rense.com/general21/tox.htm

McCluskey, J. & Choudhury, Z. 2005. Assessment and Scoping Report, Aceh, Indonesia, 4–13 February 2005. World Wide Web Address: http://www.hapinternational.org/pdf_word/908-Aceh%20trip%20report%20QMP%20scoping.pdf.

McDougall, I. 2008. Brief history of isotope geology at the Australian National University. *Australian Journal of Earth Sciences*, **55**, 727-736.

McDougall, I. and Harrison, T. M. 1988. *Geochronology and Thermochronology by the $^{40}Ar/^{39}Ar$ Method*. Oxford Univ. Press, 212 p

McDougall, I. & Harrison, T. M. 1999. *Geochronology and Thermochronology by the $^{40}Ar/^{39}Ar$ Method, 2nd Edn.* Oxford Univ. Press, 269 p

McFarlane, M.J. 1976. *Laterite and Landscape*. Academic Press: London

McFarlane, M.J., 1991. Some sedimentary aspects of lateritic weathering profile development in the major bioclimatic zones of tropical Africa. Journal of African Earth Sciences **12**, 267–282.

Melo, V.F., Singh, B., Schaefer, C.E., Novais, R.F. & Fontes M.P.F. 2001. Chemical and mineralogical properties of kaolinite-rich Brazilian soils. *Soil Science Society of America Journal*, **65**, 1324-1333.

Menzies, M.A., Baker, J., Bosence, D., Dart, C., Davidson, I., Hurford, A., Al_Kadasi, M., McClay, K., Nichols, G., Al_Subbary, A. & Yelland, A., 1992. The timing of magmatism, uplift and crustal extension: preliminary observations from Yemen. In: Storey, B.C., Alabaster, T., Pankhurst, R.J. (Eds.), *Magmatism and the Causes of Continental Break-up*. Geological Society (London) Special Publication **68**, 293–304.

Menzies, M., Bosence, D., el-Nakhal, H.E., al-Khirbash, S., al-Kadasi, M.A, & al Subbary, A. 1990, Lithospheric extension and the opening of the Red Sea: sediment-basalt relationships in Yemen. *Terra Nova*, **2**, 340-350.

Menzies, M., Gallagher, K., Yelland, A. & Hurford, A.J., 1997. Volcanic and nonvolcanic rifted margins of the Red Sea and Gulf of Aden: crustal cooling and margin evolution in Yemen. *Geochimica et Cosmochimica Acta* **61**, 2511–2527.

Merck Millipore 2012. Methodology summaries for Merckoquant test strips. World Wide Web http://www.merckmillipore.co.uk/chemicals/test-strips-merckoquant/c_29.b.s1LRy4AAAEWI.IfVhTI

Merino E., Nahon D. & Wang Y. 1993. The kinetics and mass transfer of pseudomorphic replacement: Application to replacement of parent minerals and kaolinite by Al, Fe, and Mn oxides during weathering. *American Journal of Science*, **293**, 135- 155.

Merla, G. & Minucci, E. 1938. *Missione geologica nel tigrai*. Reale Accademia D'Italia: Rome.

Merla, G., Abbate, E., Canuti, P., Sagri, M. & Tacconi, P. 1973. *Geological map of Ethiopia and Somalia (1:2 million)*, Consiglio Nazionale delle Ricerche, Rome,

Merla, G., Abbate, E., Azzaroli, A., Bruni, P., Fazzuoli, M., Sagri, M. & Tacconi, P., 1979. *A Geological Map of Ethiopia and Somalia: Comment*. Pergamon, pp. 95

Merrihue, C. and Turner, G. 1966. Potassium-argon dating by activation with fast neutrons. *Journal of Geophysical Research* **71**, 2852-2857.

Misund, A., Frengstad, B., Siewers, U. & Reimann, C. 1999. Variation of 66 elements in European bottled mineral waters. *The Science of the Total Environment*, **243/244**, 21-41.

Mock, C., Arnaud, N.O., Cantagrel, J-M. & Yirgu, G. 1999. $^{40}Ar/^{39}Ar$ thermochronology of the Ethiopian and Yemeni basements: reheating related to the Afar plume? *Tectonophysics*, **314**, 351-272.

Mohr, P.A. 1971. *The Geology of Ethiopia*. University College of Addis Ababa Press: Addis Ababa, 268 p.

Mohr, P. 1979. Lithology and structure of the Precambrian rocks of Eritrea, in *Evolution and mineralisation of the Arabian-Nubian Shield*, edited by A.M. Al

Shanti, Bulletin of the Institute of Applied Geology of King Abdul Aziz University, **2**, 7-15.

Mohr, P. 1983. Ethiopian flood basalt province. *Nature*, **303**, 577-584.

Mohr, P., 1991. Structure of Yemeni dike swarms. *Tectonophysics*, **198**, 203-221.

Mohr P., 2001. The Asmara dike swarm, Eritrean plateau: physical parameters of an off-rift olivine dolerite injection zone. *Acta Vulcanologica,* **11**, 177-181.

Mohr, P. & Zanettin, B. 1988. The Ethiopian flood basalt province, in: J.D. McDougall (Ed.), *Continental Flood Basalts*, Kluwer Academic, Dordrecht,

Mondadori, M. (Ed.) 1983. *The MacDonald Encyclopedia of Rocks and Minerals.* MacDonald: London

Morton, W.H. & Black, R., 1975. Crustal attenuation in Afar. In: Pilger, A. & Rosler, A. (Eds.), *Afar Depression of Ethiopia*, Proceedings of an International Symposium on the Afar Region and Rift Related Problems, Bad Bergzabren, Germany, 1974, vol.1. E. Schweizerbart'sche Verlagsbuchhandlung, Stuttgart, Germany, pp. 55–61.

Moucha, R. & Forte, A.M. 2011. Changes in African topography driven by mantle convection. *Nature Geosciences*, 4, 707-712.

Nahon, D.B. 1976. *Cuirasses ferrugineuses et encroûtements calcaires au Sénégal occidental et en Mauritanie : systèmes évolutifs : géochimie, structures, relais et coexistence.* PhD thesis, Institut de géologie, University of Strasbourg, France.

Nahon, D.B. 2003. Weathering in tropical zone. Significance through ancient and still active mechanisms. *Comptes Rendus Geoscience*, **335**, 1109-1119.

Nahon, D.B. and Tardy, Y., 1992 The ferruginous laterites. In C.R.M. Butt and H. Zeegers (Eds), *Regolith Exploration Geochemistry in Tropical and Subtropical Terrains*, 41–56 Elsevier: Amsterdam.

Nash, D.J., Thomas, D.S.G. & Shaw, P.A. 1994. Siliceous duricrusts as palaeoclimatic indicators: evidence from the Kalahari desert of Botswana. *Palaeogeography, Palaeoclimatology, Palaeoecology*, **112**, 279-295.

Neary, C. R., Gass, I. G. & Cavanagh, B. J. 1976. Granitic association of northeastern Sudan, *Geological Society of America Bulletin*, **87**, 1501-1512.

Nevsun Resources 2011. Bisha main: overview. World Wide Web Address: http://www.nevsun.com/projects/bisha-main/

Nickson R.T., McArthur J.M., Ravenscroft P., Burgess W.G. & Ahmed K.M. 2000. Mechanism of arsenic release to groundwater, Bangladesh and West Bengal. *Applied Geochemistry* **15**, 403-413.

Ninomya, Y., Fu, B. & Cudahy, T.J. 2005. Detecting lithology with Advanced Spaceborne Thermal Emission and Reflection Radiometer (ASTER) multispectral thermal infrared 'radiance-at-sensor' data. *Remote Sensing of Environment*, **99**, 127 – 139.

Nyssen, J., Moeyersons, J., Poesen, J., Deckers, J. & Haile, M. 2002. The environmental significance of the remobilisation of ancient mass movements in the Atbara–Tekeze headwaters, Northern Ethiopia. *Geomorphology*, **49**, 303-322.

Oard, M.J. 2011. The remarkable African Planation Surface. *Journal of Creation*, **25**, 111-122.

Ogubazghi G., Ghebreab, W. & Havskov J., 2004 Some features of the 1993 Bada earthquake swarm of southeastern Eritrea. *Journal of African Earth Sciences*, **38** 135-143.

Ohmoto, H. 1996. Evidence in pre-2.2 Ga paleosols for the early evolution of atmospheric oxygen and terrestrial biota. *Geology*, **24**,1135-1138.

Ollier, C.D. & Pain C F 1996 *Regolith, Soils and Landforms.*: John Wiley & Sons: Chichester 316 p.

Ollier, C.D. & Sheth, H.C. 2008. The High Deccan duricrusts of India and their significance for the 'laterite' issue. *Journal of Earth System Science*, **117**, 537-551.

Omar, G.I., Steckler, M.S., Buch, W.R. & P.B. Kohn 1989. Fission-track analysis of basement apatites at the western margin of the Gulf of Suez, Egypt: evidence for synchroneity of uplift and subsidence. *Earth and Planetary Science Letters*, **94**, 316–328.

Omar, G.I. & Steckler, M.S. 1995. Fission track evidence on the initial rifting of the Red Sea: two pulses, no propagation. *Science* **270** 1341-1344.

Oštir, K., Veljanocski, T., Podobnikar, T. & Stančič, Z. 2003. Application of satellite remote sensing in natural hazard management: the Mount Mangart landslide case study. *International Journal of Remote Sensing*, **24**, 3983–4002.

Overstreet, W.C., Stoeser, D.B., Overstreet, E.F. & Goudarzi, G.H. 1977. *Tertiary laterite of the As Sarat Mountains, Asir Province, Kingdom of Saudi Arabia*. Mineral Resource Bulletin, Saudi Arabia Directorate General of Mineral Resources, **21**, 1–30.

Partridge, T.C. 1998. Of diamonds, dinosaurs and diastrophism: 150 million years of landscape evolution in southern Africa. *South African Journal of Geology*, **101**, 167-184.

Pearce, J. 1981. *Surface Processes – Weathering to Diagenesis*. Block 5 in: S237 The Earth: Structure, Composition and Evolution. The Open University: Milton Keynes, UK; ISBN 033516059X

Pédro, G. 1968. Distribution des principaux types d' alteration chimique à la surface du globe – presentation d' une esquisse geographique. *Revue de Geographie Physique et de Geologie Dynamique*, **10**, 457-470.

Petley, D.N. & Reid, S. 1999. Uplift and landscape stability at Taroko, eastern Taiwan. In: Smith, J.B., Whalley, W.B. & Warke, P.A. (Eds), *Uplift, Erosion and Stability: Perspectives on Long-term Landscape Development*. Geological Society, London, Special Publication **162**: 169-181.

Pik, R. 2011. Geodynamics: Africa on the rise. *Nature Geosciences*, **4**, 660-661.

Pik, R., Deniel, C., Coulon, C., Yirgu, G., Hoffman, C. & Ayelew, D. 1998. The northwestern Ethiopian Plateau flood basalts. Classification and spatial distribution of magma types. *Journal of Volcanology and Geothermal Research*, **81**, 91-111.

Pik, R., Marty, B., Carignan, J. & Lavé, J 2003. Stability of the Upper Nile drainage network (Ethiopia) deduced from (U–Th)/He thermochronometry: implications for uplift and erosion of the Afar plume dome. *Earth and Planetary Science Letters*, **215**, 73-88.

Pilger, A. & Rosler, A. (Eds.) 1975. *Afar Depression of Ethiopia*. Proceedings of an International Symposium on the Afar Region and Rift Related Problems, Bad

Bergzabren, Germany, 1974, vol.1. E. Schweizerbart'sche Verlagsbuchhandlung, Stuttgart, Germany

Pillans, B. 2008. Regolith through time. In: K.M. Scott & C.F. Pain (eds), *Regolith Science*, CSIRO Publishing: Collingwood, Australia, 7-29.

Plester, B., Richards, J., Blades, M. & Spencer, C. 2002. Young children's ability to use aerial photographs as maps. *Journal of Environmental Psychology*, 22, 29–47.

Portenga, E.W., Bierman, P.R. & Rizzo, D.M. 2009. A global summary and analysis of exposed bedrock erosion rates estimated using *in situ* $^{10}$Be. *Geological Society of America, Annual Meeting 18-21 October 2009,* Abstract No. 244-1.

Porter, G.S., Bajita-Locke J.B., Hue, N.V., & Strand, D. 2004 Manganese solubility and phytotoxicity affected by soil moisture, oxygen levels, and green manure additions. *Communications in Soil Science and Plant Analysis*, **35**, 99-116

Radloff, K. A., Zheng, Y., Michael, H. A., Stute, M., Bostick, B. C., Mihajlov, I., Bounds, M., Huq, M. R., Choudhury, I., Rahman, M. W., Schlosser, P., Ahmed, K. M. & van Geen, A. 2011. Arsenic migration to deep groundwater in Bangladesh influenced by adsorption and water demand. *Nature Geoscience*, **4**, 793-798.

Raines, G.L. & Wynn, J.C. 1982. Mapping of ultramafic rocks in a heavily vegetated terrain using Landsat data. *Economic Geology*, **77**, 1755-1769.

Rampino, M.R. & Caldeira, K 1993. Major episodes of geologic change: correlations, time structure and possible causes. *Earth and Planetary Science Letters*, **114**, 215-227.

Ramsay, M. S. & Flynn, L. P. 2004. Strategies, insights, and the recent advances in volcanic monitoring and mapping with data from NASA's Earth Observing System. *Journal of Volcanology and Geothermal Research*, **135**, 1–11.

Ramsey, M.H., Potts, P.J., Webb, P.C., Watkins, P., Watson, J.S. & Coles, B.J. 1995. An objective assessment of analytical method precision: comparison of ICP-AES and XRF for the analysis of silicate rocks. *Chemical Geology*, **124**, 1-19.

Ranganathan, N & Jayaram, S. 2006. *Geomorphology of Karnataka*. Karnataka Geologists' Association: Bangalore. ISBN 81-89650-02-5

Reddy, D. & Brisebois, K. 2004. *Technical report on the Bisha Property and resource estimate of the Bisha Deposit Gash-Barka District, Er*itrea. AMEC: Lima, Peru.

Read, H.H. 1962. *Rutley's Elements of Mineralogy (25$^{th}$ Edition)*. Thomas Murby: London

Reid, I. 2003. Making observations and measurements in the field: an overview. In: Clifford & Valentine (Eds.) *Key methods in geography*, Sage Publications, London, 209-222.

Retallack, G.J. 2010. Lateritization and bauxitization events. *Economic Geology*, **105**, 655-667.

Rochette, P., Tamrat, E., Feraud, G., Pik, R., Courtillot, V., Ketefo, E., Coulon, C. Hofmann, C., Vandamme, D. & Yirgu G. 1998. Magnetostratigraphy and timing of the Oligocene Ethiopian traps. *Earth and Planetary Science Letters*, **164**, 497-510

Rivard, B., Arvidson, R. E., Duncan, I. J., Sultan, M. & El Kaliouby, B. 1992. Varnish, sediment, and rock controls on spectral reflectance of outcrops in arid regions. *Geology*, **20**, 295-298.

Rochon, G. L., Quansah, J. E., & Mohamed, M. A. 2005. Applicability of near-real-time satellite data acquisition and analysis & distribution of geoinformation in support of African Development. In: United Nations Economic Commission for Africa: 4th Meeting of the Committee for Development Information, Addis Ababa, Ethiopia, 23–28 April 2005.

Rock, M.L., James, B.R. & Helz, G.R. 2001. Hydrogen peroxide effects on chromium oxidation state and solubility in four diverse, chromium-enriched soils. *Environmental Science and Technology*, **35**, 4054-4059.

Rossetti, D.F. 2004. Paleosurfaces from northeastern Amazonia as a key for reconstructing paleolandscapes and understanding weathering products. *Sedimentary Geology*, **169**, 151-174.

Rothery, D.A. 1982. *The evolution of the Wuqbah Block and the applications of remote sensing in the Oman ophiolite*. Unpublished PhD thesis, Open University: Milton Keynes, UK.

Rothery, D.A. 1984. Reflectance of ophiolite rocks in the Landsat MSS bands: relevance to lithological mapping by remote sensing. *Journal of the Geological Society of London*, **141**, 933-939.

Rothery, D.A. & Drury, S.A., 1984. The neotectonics of the Tibetan Plateau. *Tectonics*, **3**, 19-26.

Rowan, L.C. & Mars, J.C. 2003. Lithologic mapping in the Mountain Pass, California area using Advanced Spaceborne Thermal Emission and Reflection Radiometer (ASTER) data. *Remote Sensing of Environment*, **84**, 350-366.

Rowan, L.C., Hook, S.J., Abrams, M.J. & Mars, J.C. 2003. Mapping hydrothermally altered rocks at Cuprite, Nevada, using the Advanced Spaceborne Thermal Emission and Reflection Radiometer (ASTER), a new satellite-imaging system. *Economic Geology*, **98**, 1019-1027.

Rowan, L.C., Mars, J.C. & Simpson, C.J. 2005. Lithologic mapping of the Mordor, NT, Australia ultramafic complex by using the Advanced Spaceborne Thermal Emission and Reflection Radiometer (ASTER). *Remote Sensing of Environment*, **99**, 105-126.

Rowan, L.C., Schmidt, R.G. & Mars, J.C. 2006. Distribution of hydrothermally altered rocks in the Reko Diq, Pakistan mineralized area based on spectral analysis of ASTER data. *Remote Sensing of Environment* **104**, 74–87.

Ruffet, G., Innocent, C., Michard, A., Feraud, G., Beauvais, A., Nahon, D. & Hamelin, B. 1996. A geochronological Ar-40/Ar-39 and Rb-87/Sr-87 study of K-Mn oxides from the weathering sequence of Azul, Brazil. *Geochimica et Cosmochimica Acta*, **60**, 2219-2232.

Russo, A., Fantozzi, P.L., Solomon, T., Getaneh A., Neri C., Russo F., Asfwossen A., Peccerillo A. & Valera P. 1997. *Geological Map of the Mekele Outlier (Western Sheet)* Addis Ababa University: Addis Ababa.

Sagri, M., Abbate, E., Azzaroli, A., Balestrieri, M.L., Benvenuti, M., Bruni, P., Fazzuoli, M., Ficcarelli, G., Marcucci, M., Papini, M., Reale, V., Rook, L. & Medhin Tecle, T. 1998. New data on the Jurassic and Neogene sedimentation in the Danakil Horst and Northern Afar depression, Eritrea, in: S. Crasquin-Soleau, & É. Barrier (Eds), *Peri-Tethys Mémoire 3: Stratigraphy and evolution of Peri-Tethyan platforms*. Mémoires du Muséum *National* d'Histoire Naturelle, **117**, 193– 214.

Sanyal, J. & Lu, X. X. 2006. GIS-based flood hazard mapping at different administrative scales: A case study in Gangetic West Bengal, India. *Singapore Journal of Tropical Geography*, **27**, 207–220.

Sartori, G., Nembrini, P. G., Jansen, P., Salone, G. L., Werdmuller, M. & Corthésy, P. 2000. An appraisal of data collection methodologies: Somalia flood relief operation 1977 with special reference to using a GIS approach. Interagency Meeting, 18–19 December 2000, Oxfam, Oxford.

Schandelmeier, H. & Reynolds, P.O., 1997. *Palaeogeographic–Palaeotectonic Atlas of North-Eastern Africa, Arabia and Adjacent Areas*. Balkema, Rotterdam, pp. 160.

Schellmann. W. 1981. Considerations on the definition and classification of laterites. In *Proceedings of the International Seminar on Lateritisation Processes, Trivandrum, India*, A.A. Balkema: Rotterdam 1–10

Schellmann, W. 1986. A new definition of laterite. *Geological Survey of India, Memoir* **120**, 1–7.

Schellmann, W. 2003. Discussion of "A critique of the Schellmann definition and classification of laterite" by R.P. Bourman and C.D. Ollier (Catena 47, 117–131). *Catena*, **52**, 77-79.

Schellmann, W. 2003. An introduction in laterite. World Wide Web Address: www.laterite.de

Schulz, M.S. & White, A.F. 1999. Chemical weathering in a tropical watershed, Luquillo Mountains, Puerto Rico III: quartz dissolution rates. *Geochimica et Cosmochimica Acta*, **63**, 337-350.

Schwartz, T & Germann, K. 1999. Weathering surfaces, laterite-derived sediments and associated mineral deposits in North-East Africa. In: Thiry, M & Simon-Coinçon, R. (Eds), *Palaeoweathering, Palaeosurfaces and Related Continental Deposits*, International Association of Sedimentologists, Special Publication **27**, Ch 15.

Scotese, C.R., 1994. Late Carboniferous paleogeographic map. In: Klein, G.D. (Ed.), *Pangea: Paleoclimate, Tectonics, and Sedimentation During Accretion, Zenith, and Breakup of a Supercontinent*. Geological Society Special Paper, **288**, 5.

Scotese, C. & Golonka, J. 1992. *PALEOMAP Paleogeographic Atlas*. PALEOMAP Progress Report No. 20, Department of Geology, University of Texas at Arlington, Arlington, Texas, pp. 34.

Searle, R.C. & Ross, D.A. 1975. A geophysical study of the Red Sea axial trough between 20.5° and 22°N. *Geophysical Journal of the Royal Astronomical Society*. **43**, 555-572.

Setzer, A. 2004. The operational fire alert system of Brazil: a detection and management tool using multiple satellites. In: United Nations International Workshop on the Use of Space Technology for Disaster Management in Munich, 18–22 October

2004. World Wide Web Address:
http://www.zki.caf.dlr.de/media/download/events/2004/unoosa_workshop_presentations/06_pres_session04a_chair-manikiam/19_UNOOSA-DLR_Setzer_INPE.ppt.

Shanin, L.I., Ivanov, I.B. & Shipulin, F.K. 1968. The possible use of alunite in K-Ar geochronometry. *Geokhimiya*, **1**, 109-111.

Sharp, R. (Ed.) 2001. *SXR103 Practicing Science: Study Book.* The Open University: Milton Keynes

Sheffield, C. 1981. *Earthwatch*, Sidgwick and Jackson: London

Shoshani, J., Walter, R.C., Abraha, M., Berhe, S., Tassy, P., Sanders, W.J., Marchant, G.H., Libsekal, Y., Ghirmai, T. & Zinner, D. 2006. A proboscidean from the late Oligocene of Eritrea, a "missing link" between early Elephantiformes and Elephantimorpha, and biogeographic implications. *Proceedings of the National Academy of Sciences*, **103**, 17296-17301.

Schrag, D.P., Hoffman, P.F. & Knoll, A.H. 2010. *Many Planets, One Earth.* Unit 1, Section 9 of *The Habitable Planet.* Annenberg Foundation: Los Angeles. E-learning resource; World Wide Web address: http://www.learner.org/courses/envsci/

Siegal, B.S. & Gillespie, A.R. 1980. *Remote Sensing in Geology.* John Wiley: New York.

Silberman, M.L. & Ashley, R.P. 1970. Age of ore deposition at Goldfield, Nevada, from potassium-argon dating. *Economic Geology*, **65**, 352-354.

Sillitoe, R.H. & McKee, E.H. 1996. Age of supergene oxidation and enrichment in the Chilean porphyry copper province. *Economic Geology*, **91**, 164-179.

Singhroy, V. and Molch, K., 2004, Characterizing and monitoring rockslides from SAR techniques. *Advances in Space Research*, **33**, 290–295.

Smedley, P L 1996. Arsenic in rural groundwater in Ghana. Journal of African Earth Sciences, 22, 459–470.

Smedley, P.L., Edmunds, W.M. and Pelig-Ba, K.B., 1996, Mobility of arsenic in groundwater in the Obuasi area of Ghana. In: J.D. Appleton, R. Fuge and G.J.H. McCall (Eds), *Environmental Geochemistry and Health*, Geological Society Special Publication No.**113**, 163–181, Geological Society: London.

Smith, R.B 2001. *Getting Started: Analysing hyperspectral images.* TNTmips tutorial bookley. MicroImages, Lincoln, Nebraska. World Wide Web Address:
http://www.microimages.com/getstart/index.htm

Smith, R.B. 2009. *Getting Started: Surface Modelling.* TNTmips tutorial booklet, MicroImages Inc., Lincoln, Nebraska. World Wide Web Address:
http://www.microimages.com/getstart/index.htm

Smith, R.E., Anand R.R. & Alley, N.F., 2000, Use and implications of paleoweathering surfaces in mineral exploration in Australia. *Ore Geology Reviews*, **16**, 185–204.

Sowden, S., Stea, D., Blades, M., Spencer, C. & Blaut, J. M. 1997. Mapping abilities of four-year-old children in York, England. *Journal of Geography*, **95**, 107–111.

Spatz, D.M., 1997, Remote sensing characteristics of the sediment- and volcanic-hosted precious metal systems: imagery selection for exploration and development. *International Journal of Remote Sensing*, **18**, 1413–1438.

Stamoulis, V. 2009. Use of night-time thermal infrared (NTIR) for mineral exploration: examples with ASTER and other satellite data. In: Proceedings of the 14th International Conference on Applied Geological Remote Sensing, Las Vegas, Nevada, USA, 6–8 November 2000. Environmental Research Institute of Michigan, Ann Arbor, MI, 127.

Stampfli, G.M. & Borel, G.D. 2002. A plate tectonic model for the Paleozoic and Mesozoic constrained by dynamic plate boundaries and restored synthetic oceanic isochrons. *Earth and Planetary Science Letters*, **196**, 17–33.

Stampfli, G.M., Mosar, J., Favre, P., Pillevuit, A. & Vannay, J.-C., 2001. Permo-mesozoic evolution of the western Tethys realm: the Neo-Tethys East Mediterranean Basin connection. *Mémoir Museum National d'Histoire Naturelle*, **186**, 51–108.

Steiger, R. H. and Jager, E. 1977. IUGS Subcommission on Geochronology: convention on the use of decay constants in geo- and cosmochronology. *Earth and Planetary Science Letters*, **36**, 359-362.

Stern, R. J. 1994. Neoproterozoic (900-550 Ma) arc assembly and continental collision in the East African orogen: Implications for the consolidation of Gondwanaland. *Annual Review of Earth and Planetary Sciences*, **22**, 319-351.

Stephenson, M.H. & Osterloff, P.L. 2002. Palynology of the deglaciation sequence represented by the Lower Permian Rahab and lower Gharif members, Oman. *AASP Contributions Series*, **40**, 1–48.

Stevens, D. 2005. Space-based technologies for disaster management—making satellite imagery available for emergency response in developing countries. In: *Geoscience and Remote Sensing Symposium, 25–29 July 2005, Seoul, S. Korea, IGARSS '05. Proceedings*. 2005 IEEE International 6, 4366–4369.

Stoney, W.E. 2008. *ASPRS Guide to Land Imaging Satellites*. American Society of Photogrammetry and Remote Sensing, Falls Church, Virginia.

Sultana, N.D. & Abdelsalam, M.G. 2006. Remote sensing analysis of the Gorge of the Nile, Ethiopia with emphasis on Dejen–Gohatsion region, *Journal of African Earth Sciences*. **44**, 135-150

Tadesse, S., Milesi, J-P. & Deschamps, Y., 2003, Geology and mineral potential of Ethiopia: a note on geology and mineral map of Ethiopia. *Journal of African Earth Sciences*, **36**, 273–313.

Tadesse, T. 1996. Structure across a possible intra-oceanic suture zone in the low-grade Pan-African rocks of northern Ethiopia. *Journal of African Earth Sciences*, **23**, 375-381.

Tadesse, T., Hoshino, M. & Sawada, Y. 1998. Lithological, structural and geochemical constraints from the Neoproterozoic low-grade rocks of northern Ethiopia: implications for crustal growth in the region. *Journal of African Earth Sciences*, 27, 194-195.

Tadesse, T., Hoshino, M. & Sawada, Y. 1999. Geochemistry of low-grade metavolcanic rocks from the Pan-African of the Axum area, northern Ethiopia. *Precambrian Research*, **96**, 101-124.

Tadesse, T., Hoshino, M., Suzuki, K. & Iizumi, S. 2000. Sm-Nd, Rb-Sr and Th-U-Pb zircon ages of syn- and post-tectonic granitoids from the Axum area of northern Ethiopia. *Journal of African Earth Sciences*, **30**, 313-327.

Tadesse, T., Suzuki, K. & Hoshino, M. 1997. Chemical Th-U-total Pb isochron age from the Mereb Granite in northern Ethiopia. *Journal of Earth and Planetary Sciences, Nagoya University*, **44**, 21-27.

Talbot, C.J. & Ghebreab, W. 1997. Red Sea detachment and basement core complexes in Eritrea. *Geology*, **25**, 655-658.

Tanner, L.H. & Khalifa, M.A. 2009. Origin of ferricretes in fluvial-marine deposits of the Lower Cenomanian Bahariya Formation, Bahariya Oasis, Western Desert, Egypt. *Journal of African Earth Sciences*, **56**, 179-189.

Tangestani, M.H., Mazhari, N, Agar, R. & Moore, F. 2008. Evaluating Advanced Spaceborne Thermal Emission and Reflection Radiometer (ASTER) data for alteration zone enhancement in a semi-arid area, northern Shahr-e-Babak, SE Iran. *International Journal of Remote Sensing*, **29**, 2833-2850.

Taranik, D.L. & Kruse, F.A., 1989, Iron mineral reflectance in Geophysical and Environmental Research Imaging spectrometer GERIS) data. In Proceedings of the 7th Thematic Conference on Remote Sensing in Exploration Geology, 2–6 October 1989, Calgary, Canada (Ann Arbor, MI: ERIM), 445–459.

Taranik, D.L., Kruse, F.A., Goetz, A.F.H. & Atkinson, W.W., 1991 Remote sensing of ferric iron minerals as guides for gold exploration. In Proceedings of the 8th Thematic Conference on Geological Remote Sensing, 29 April–2 May 1991, Denver, CO, USA (Ann Arbor, MI: ERIM), 197–228.

Tardy, Y. 1997. *Petrology of laterites and tropical soils.* A.A. Balkema: Rotterdam.

Tardy, Y., Kobilsek, B. & Paquet, H. 1991. Mineralogical composition and geographical distribution of African and Brazilian periatlantic laterites. The influence of continental drift and tropical paleoclimates during the past 150 million years and implications for India and Australia. *Journal of African Earth Sciences*, **12**, 283–295

Taylor, G. and Eggleton, R.A., 2001, *Regolith Geology and Geomorphology.* John Wiley & Sons: Chichester, UK.

Teeuw, R.M. (Ed.) 2004. *Field Techniques: GIS, GPS and Remote Sensing.* Royal Geographical Society, London.

Teeuw, R.M. (Ed.) 2007. *Mapping Hazardous Terrain using Remote Sensing.* Geological Society, London, Special Publication **283**.

Tefera, M., Chernet, T. and Haro, W., 1996. *Geological Map of Ethiopia (1:2 million).* Geological Survey of Ethiopia, Addis Ababa.

Teklay, M. 1997. *Petrology, Geochemistry and Geochronology of Neoproterozoic Magmatic Arc Rocks from Eritrea: Implications for Crustal Evolution in the Southern Nubian Shield.* Department of Mines Memoir No. 1. 125 p. Asmara: Ministry of Energy, Mines and Water Resources.

Teklay, M., Haile, T., Kroner, A., Asmerom, Y. & Watson, J. 2003. A back-arc palaeotectonic setting for the Augaro Neoproterozoic magmatic rocks of western Eritrea. *Gondwana Research*, **6**, 629-640.

Teklay, M., Hofmann, A.W., Brugmann, G.E. & Lassiter, J.C. 2002. Chemical and Sr-Nd-Os isotope variations in tholeiitic and alkaline flood basalts from Eritrea: evidence for recycled depleted oceanic crust in the Afar plume. *Geochimica et Cosmochimica Acta*, **66**, A767-A767.

Teklay, M., Kröner, A., Mezger, K. & Oberhänsli, R. 1998. Geochemistry, Pb-Pb single zircon ages and Nd-Sr isotope composition of Precambrian rocks from southern and eastern Ethiopia: implications for crustal evolution in East Africa. *Journal of African Earth Sciences*, **26**, 207-227.

Teklay, M., Kröner, A. & Mezger, K. 2002. Enrichment from plume interaction in the generation of Neoproterozoic arc rocks in northern Eritrea: implications for crustal accretion in the southern Arabian-Nubian Shield. *Chemical Geology*, **184**, 167-184.

Temesgen, B., Mohammed, M.U. & Korme, T. 2001. Natural hazard assessment using GIS and remote sensing methods, with particular reference to the landslides in the Wondogenet Area, Ethiopia. *Physics and Chemistry of the Earth, Part C: Solar, Terrestrial & Planetary Science*, **26**, 665–675.

Temgoua, E., Bitom, D., Bilong, P., Lucas, Y. & Pfeifer, H.R. 2002. Old ferricrete landscape dismantling in Central Africa rain forest zone: formation of the present downslope iron accumulations. *Comptes Rendus Geoscience*, **334**, 537-543.

Temgoua, E., Pfeifer, H.R. & Bitom, D. & 2003. Trace element differentiation in ferruginous accumulation soil patterns under tropical rainforest of southern Cameroon, the role of climatic change. *Science of the Total Environment*, **303**, 203-214.

Thiry, M. 2000. Palaeoclimatic interpretation of clay minerals in marine deposits: an outlook from the continental origin. *Earth Science Reviews*, **49**, 201-221.

Thiry, M., Simon-Coinçon, R. & Schmitt J.M. 1999. Kaolinic palaeoweatherings: climatic significance and signature in the sedimentary column. *Comptes Rendus de l'Académie des Sciences - Series IIA - Earth and Planetary Science*, **329**, 853-863.

Thomas, M.F., 1994. *Geomorphology in the Tropics : A Study of Weathering and Denudation in Low Latitudes*. Wiley: New York

Thome, K. 1999. *Algorithm Theoretical Basis Document for ASTER Level 2B1 – Surface Radiance and ASTER Level 2B5 – Surface Reflectance.* Remote Sensing Group, University of Arizon, Tucson.

Thornber, M.R. 1992. The chemical mobility and transport of elements in the weathering environment. In C.M.R. Butt & H. Zeegers (Eds) *Handbook of Exploration Geochemistry Vol. 4: Regolith Exploration geochemistry in Tropical and Subtropical Terrains,* 79-96. Elsevier: Amsterdam.

Tohver, E., Lana, C., Cawood, P. A., Fletcher, I. R., Jourdan, F., Sherlock, S., Rasmussen, B., Trindade, R. I. F., Yokoyama, E., Souza Filho, C. R. & Marangoni, Y. 2012. Geochronological constraints on the age of a Permo-Triassic impact event: U-Pb and $^{40}Ar/^{39}Ar$ results for the 40 km Araguainha structure of central Brazil. *Geochimica et Cosmochimica Acta*, **58**, 214-227.

Trescases, J.-J. 1992. Chemical weathering. In C.M.R. Butt & H. Zeegers (Eds) *Handbook of Exploration Geochemistry Vol. 4: Regolith Exploration geochemistry in Tropical and Subtropical Terrains*, 79-96. Elsevier: Amsterdam.

Tsekhovskii, Y.G., Shchipakina, I.G. & Khramtsov, I.N. 1995. Lateritic eluvium and its redeposition products as indicators of Aptian–Turonian climate. *Stratigraphy and Geological Correlation* **3**, 285–294.

Tucker, M.E. 1985. *Sedimentary Rocks in the Field*. The Open University: Milton Keynes, UK.

Turner, R. 2009. Wassu stone circles. *Local History News*, Issue 93, World Wide Web Address: http://www.balh.co.uk/lhn/article_file_lhn-vol1iss93-5.xml.html

Twidale, C.R. 1992. King of the plains: Lester King's contributions to geomorphology. *Geomorphology*, **5**, 491-509.

Twidale, C.R. 1998. Antiquity of landforms: An 'extremely unlikely' concept vindicated. *Australian Journal of Earth Sciences*, **45**, 657-668.

Twidale, C.R. 2000. Early Mesozoic (?Triassic) Landscapes in Australia: Evidence, Argument, and Implications. *Journal of Geology*, **108**, 537-552

Ukstins, I., Renne, P., Wolfenden, E., Baker, J. and Menzies, M., 2002. Matching conjugate volcanic rifted margins: 40Ar/39Ar chrono-stratigraphy of pre- and syn-rift bimodal flood volcanism in Ethiopia and Yemen. *Earth and Planetary Science Letters*, **198**, 289– 306.

UNOOSA (The United Nations Office for Outer Space Affairs) 2004. In: Proceedings of the United Nations International Workshop on the Use of Space Technology for Disaster Management, Munich, 18–22 October 2004. World Wide Web Address: zki.caf.dlr.de/events/2004/unoosa_workshop/unoosa_ programme_en.html.

US Geological Survey 2009. *On Demand Surface Reflectance - VNIR & Crosstalk Corrected SWIR*. World Wide Web Address: https://lpdaac.usgs.gov/products/aster_products_table/ast_07xt

US Geological Survey. *Spectral library*. World Wide Web Address: http://speclab.cr.usgs.gov/spectral-lib.html.

Usoni, L. 1952. *Risorse mineralie dell'Africa Orientale: Eritrea, Etiopia, Somalia*. Inspettorato Generale Minerario, Rome 553 p.

Vail, J.R. 1985. Pan-African (late Precambrian) tectonic terrains and the reconstruction of the Arabian-Nubian shield, *Geology*, **13**, 839-842.

Vasconcelos, P.M. 1999. K-Ar and $^{40}Ar/^{39}Ar$ geochronology of weathering processes. *Annual Review of Earth and Planetary Sciences*, **27**, 183–229.

Vasconcelos, P.M., Brimhall., G.H. Becker, T.A. & Renne, P.R. 1994. $^{40}Ar/^{39}Ar$ analysis of supergene jarosite and alunite: Implications to the paleo weathering history of western US and West Africa *Geochimica et Cosmochimica Acta*, **58**, 401-420

Vasconcelos, P.M. & Conroy, M. 2003. Geochronology of weathering and landscape evolution, Dugald River valley, NW Queensland, Australia. *Geochimica et Cosmochimica Acta*, **58**, 2913-2930.

Vasconcelos, P.M., Knesel, K. M., Cohen, B. E. & Helm, J.A. 2008. Geochronology of the Australian Cenozoic: a history of tectonic and igneous activity, weathering, erosion, and sedimentation. *Australian Journal of Earth Sciences*, **55**, 865-914.

Vasconcelos, P.M., Renne, P.R., Brimhall. G.H. & Becker, T.A. 1994. Direct dating of weathering phenomena by Ar-40/Ar-39 and K-Ar analysis of supergene K-Mn oxides. *Geochimica et Cosmochimica Acta*, **58**, 1635-1665.

Vincent, R.K., 1997, *Image Fundamentals of Geological and Environmental Remote Sensing*, second edition. Prentice Hall: New Jersey.

Visscher, J.C. 1862. *Letters from Malabar, to which is added An account of Travancore, and fra Bartolomeo's travels in that country* Translated by M.H. Drury. Google Books, World Wide Web: http://books.google.co.uk/books?id=LDUBAAAAQAAJ&redir_esc=y

Visser, J.N.J. & Praekelt, H.E. 1996. Subduction, mega-shear systems and Late Palaeozoic basin development in the African segment of Gondwana. *Geologische Rundschau*, **85**, 632–646.

Warren, A., Yates, Y. M., Damiani, R. J., Goodwin, M. B., Wood, C. B. & Schaff, C. R. 1998. The first temnospondyl amphibian (Stereospondyli: Capitosauroidea) from Ethiopia. *Neues Jahrbuch für Geologie und Paläontologie*, Monatshefte **11**: 694-704.

Waters, P., Greenbaum, D., Smart, P.L. & Osmaston, H. 1990. Applications of remote sensing to groundwater hydrology. *Remote Sensing Reviews*, **4**, 223-264.

Watson, J.S. 1996. Fast, simple method of powder pellet preparation for X-ray fluorescence analysis. *X-Ray Spectrometry*, **25**, 173-174.

Webb, P. 2006. *Metals: Ore Deposits and Their Exploitation.* Book 5 in: Course S278 Earth's Physical resources: origin, Use and Environmental Impact. The Open University: Milton Keynes, UK; ISBN 978 0 7492 1920 8

Webster, J.G., Swedlund P.J. & Webster, K.S 1998. Trace metal adsorption onto an acid mine drainage iron (III) oxy hydroxy sulphate. *Environmental Science and Technology*, **32**, 1361–1368.

Wernicke, B. 1985. Uniform-sense normal simple shear of the continental lithosphere. *Canadian Journal of Earth Sciences*, **22**, 108-125.

White, T.D., Asfaw, B., DeGusta, D., Gilbert, H., Richards, G.D., Suwa, G. & Howell, F.C. 2003. Pleistocene Homo sapiens from Middle Awash, Ethiopia. *Nature*, **423**, 742-747.

Whitten, J.R.V. & Brooks, D.G.A. 1987. *The Penguin Dictionary of Geology.* Penguin Books: Harmondsworth.

WHO (World Health Organisation) 2004. Manganese in drinking-water. Background document for *WHO Guidelines for Drinking-water Quality*. World Wide Web Address: http://www.who.int/water_sanitation_health/dwq/chemicals/manganese.pdf.

WHO 2004. A to Z of background documents for chemical hazards in drinking water World Wide Web Address: http://www.who.int/water_sanitation_health/dwq/chemicals

WHO 2008. Annex 4 Chemical summary tables. In: *Guidelines for drinking-water quality* (3rd edition) World Wide Web Address: http://www.who.int/water_sanitation_health/dwq/GDWAN4rev1and2.pdf

Widdowson, M. & Gunnell, Y. 1999. Lateritization, geomorphology and geodynamics of a passive continental margin: The Konkan and Kanara coastal lowlands of western peninsular India. *Special Publication of the International Association of Sedimentologists*, **27**, 245-274.

Williams, S.N., Gilkes, R.J. & Bernard, N.G. 2000. Waste jarosite and alunite will be ineffective sulfur and potassium fertilisers. *Australian Journal of Soil Research*, **38**, 493-500.

Wopfner, H., Casshyap, S.M., 1997. Transition from freezing to subtropical climates in the Permo-Carboniferous of Afro-Arabia and India. In: Martini, I.P. (Ed.), *Late Glacial and Postglacial Environmental Changes Quaternary, Carboniferous-Permian, and Proterozoic*. Oxford University Press, New York, 192-212.

Woldegabriel, G., Aronson, J.L. & Walter, R.C. 1990. Geology, geochronology, and rift basin development in the central sector of the Main Ethiopia Rift. *Geological Society of America Bulletin*. **102**, 439-458.

Wolfenden, E., Ebinger, C., Yirgu, G., Renne, P.R. & Kelley, S.P., 2005. Evolution of a volcanic rifted margin: southern Red Sea, Ethiopia. *Geological Society of America Bulletin*, **117**, 846-864.

Wood, B. 1997. The oldest whodunnit in the world. *Nature*, **385**, 292-293.

Worash, G. & Valera, R. 2002. Rare earth element geochemistry of the Antalo Supersequence in the Mekele Outlier (Tigray region, northern Ethiopia). *Chemical Geology* **182**,395–407.

Worrall, W.E. & Cooper, A.E. 1966. Ionic composition of a disordered kaolinite. *Clay Minerals*, **6**, 341-344.

Wright, R. 1999. *Infrared satellite studies of Mount Etna volcano: 1991 to 1999*. Unpublished PhD thesis, The Open University.

Wright, R., Flynn, L., Garbeil, H., Harris, A. & Pilger, E. 2002. Automated volcanic eruption detection using MODIS. *Remote Sensing of Environment*, **82**, 135–155.

Wright, T.J., Ebinger, C, Biggs, J., Ayele, A., Yirgu, G., Keir, D. & Stork, A. 2006. Magma-maintained rift segmentation at continental rupture in the 2005 Afar dyking episode. *Nature*, **442**, 291-294.

Xu N., Christodoulatos C. & Braida W. 2009. Modeling the competitive effect of phosphate, sulfate, silicate, and tungstate anions on the adsorption of molybdate onto goethite. *Chemosphere*, **64**, p. 1325-1333.

Zachos, J., Pagani, M. Sloan, L. Thomas, E & Billups, K. 2001. Trends, rhythms, and aberrations in global climate 65 Ma to present. *Science*, **292**, 686-692.

Zanettin B., Bellieni, G., Justin-Visentin E. & Haile, P. 1999 The volcanic rocks of the Eritrean plateau: stratigraphy and evolution. *Acta Volcanologica*, **11**, 183–193

Zanettin, B., Bellieni, G., Visentin, E.J. & Justin, E. 2006. New radiometric age of volcanic rocks in the central Eritrean plateau (from Asmara to Adi Quala): Considerations on stratigraphy and correlations. *Journal of African Earth Sciences*, **45**, 156-161.

Zanettin, B., Gregnanin, A., Justin E., Mezzacasa, G. & Piccirillo, E.M. 1974. Petrochemistry of the Volcanic Series of the Central Eastern Ethiopian Plateau and Relationships Between Tectonics and Magmatology. *Memorie Istituti di Geologia e Mineralogia, Università di Padova*, **31**, 1–34.

Zanettin B., Justin-Visentin E., Nicoletti M. & Piccirillo E. M. 1980. Geodynamic Evolution of the Afro-Arabian Rift System: Correlations among Ethiopian volcanic formations with special references to the chronological and stratigraphic problems of the 'Trap Series'. *Accademia Nazionale dei Lincei*, **47**, 231–252

Zerai, H., 1996. Groundwater and geothermal resources of Eritrea with the emphasis on their chemical quality. *Journal of African Earth Sciences*, **22**, 415-421.

Ziegler, A.M., Hulver, M.L., Rowley, D.B., 1997. Permian world topography and climate. In: Martini, I.P. (Ed.), *Late Glacial and Postglacial Environmental Changes – Quaternary, Carboniferous-Permian, and Proterozoic*. Oxford University Press, New York, 111–146.

Ziegler, P.A., & Stampfli, G.M., 2001. Late Palaeozoic-Early Mesozoic plate boundary reorganization: collapse of the Variscan orogen and opening of Neotethys. *Natura Bresciana*, **25**, 17–34.

Zumbo, V., Feraud, G., Bertrand, H., Chazot, G., 1995. $^{40}Ar/^{39}Ar$ chronology of Tertiary magmatic activity in Southern Yemen during the early Red Sea–Aden Rifting. *Journal of Volcanology and Geothermal Research*, **65**, 265–279.

APPENDIX 1

# Excursions: Eritrea and northern Ethiopia

To aid geological interpretation throughout the region, during field excusrions all samples were logged so that areas with predicted responses on images could be related to exposures of individual laterite facies. Sampled sections with relevant UTM co-ordinates are detailed where appropriate throughout the thesis. Inspection records of the area detailing the lithology (excursions *i – xi see figure 2.27*) where appropriate are briefly summarised below. These initial excursions, on which subsequent field trips were based and new localities targeted using RS data, give an overview of the region and benefit others who may wish to follow-up this research:

*Reconnaissance excursions: i - vi (Ethiopia); vii - xi (Eritrea) indicated on Figure 2.27*

i) Addis Ababa to Alamata traverse: Along the west flank of the Main Ethiopian Rift (MER) and Afar Depression (Wolfenden et al. 2005, Daley *et al.* 2008).

*Lithology*:

Locality 1 [Addis Ababa, the capital of Ethiopia, to Dese] - Rift floor: vast amphitheatre of unconsolidated red iron-rich soils, black cotton soils on basalts and weathered trachytes (Morton et al. 1979).

Locality 2 [Weldiya] - Massive CFB flows: possible Ashangi basalts (troop movements precluded inspection)

Locality 3 [Kobo Alamata] - K'obo Graben: River Aviva - good ground water. Ashangi basalts and laterites in distance beneath CFBs (Kobo Alamata Agricultural Development Project. Geological and Hydro-Geological Reconnaissance Map). Thick sandstones overlie the stratigraphically lowest basalts (Ashangi basalts on Geological Map of Ethiopia, Merla *et al.* 1973, 1979) and in turn to be overlain by laterites and stratigraphically higher basalts (Aiba basalts on Geological Map of Ethiopia, Merla *et al.* 1973, 1979)

ii) Mekele, the capital city of the Tigray Region in northern Ethiopia: The Mekele outlier of Mesozoic to Cenozoic rocks (Beyth 1972).

*Lithology*:

Trap volcanics with lacustrine beds, sandstones, and limestone-shale sequences. Laterite horizons in the Amba Aradam formation (Beyth 1972) reported to be Cretaceous (Russo *et al.* 1997) are abundant below trap basalts at Hagere Selam ~30 km northwest of Mekele city.

iii) Adi Nebrid (figure 2.22): Mafic and ultramafic sequences noting shear and alteration zones and gold prospect areas (figure 2.23)

*Lithology*:

Laterite above Neoproterozoic metamorphosed mafic and ultramafic rocks, metasediments and sheared equivalents, felsic granitic intrusive lithologies widespread.

iv)The Shiraro Lowland: (figure 2.22).

*Lithology*:

Locality 1 [Shiraro] - Laterite on Neoproterozoic metasediments: weakly deformed, polymict conglomerate, sandstone and siltstone, containing well-preserved sedimentary

structures.

Locality 2 [Adi Hageray area] - Laterite on strongly deformed, lineated epiclastic metasediments and chlorite schist, metasediments and metavolcanics shear zones, which contain thrust faults and associated structures, alteration zones and artisanal gold prospecting areas.

v) The Mai Kenetal area:

*Lithology*

Laterite on Neoproterozoic limestones and slates exposed in major syncline and on Permian fluvial deposits and tillites.

vi)Axum (figure 2.22) to Asmara traverse: Eritrean-Ethiopian border area.

*Lithology*:

Locality 1 [20 km north of Adwa] - Laterite on fine-grained, quartz veined, graphitic phyllites grading to quartzite in the west, granitoids.

Locality 2 [Mereb River] - Post tectonic Neoproterozoic granites far below the level of lateritisation.

Locality 3 [Debarwa] - Debarwa massive sulphide deposit - a classic Kuroko deposit (Franklin *et al.* 1981; Lydon 1988;) hosted by dacitic metavolcanics, greywackes, black shales and phyllites. The ore body is capped by a goethitic barite-bearing gossan. The bedded and massive ore contains Cu 7.6%, Zn 1.8%, Ag 809 g $t^{-1}$, Au1-2 g $t^{-1}$(Usoni 1952) Bedded barite lenses are exposed below the gossan while laterite occurs topographically above the gossan. This area is crossed by a major fault system and laterite mesas occur at different levels.

Locality 4 [Shiketi] - Clearly faulted sequence of thick Oligocene flood basalts conformably above laterite derived from Neoproterozoic basement of the central tectonic block of Eritrea, the Nakfa Terrane (figure 2.19) (Drury & Berhe 1993; Drury & De Souza Filho 1998). Faulting in the basalts extends into the laterites clearly displacing the palaeosols (figure 2.21).

vii) Asmara to Agordat traverse: Nakfa terrane (figure 2.19). Volcano-sedimentary island-arc assemblage and granitoids.

*Lithology*:

Locality 1 [Adi Tekelezan] - Laterite on Neoproterozoic porphyritic granitoids that contain 4-6cm long microcline crystals.

Locality 2 [Elabared] - Sheared schists and banded amphibolite gneisses (figure 2.20), faulted deformed host rocks and aplitic dykes with prominent fold axis plunging NW. Fresh basement far below the level of lateritisation.

viii) Agordat to Sawa traverse: Hagar terrane (figure 2.19) volcano-sedimentary and ultramafic rocks. Barka terrane (figure 2.19) high-grade gneisses, far below the level of lateritisation.

*Lithology*:

Locality 1 [Barka River] - Sheared quartzo-feldspathic intrusive rocks (steep west dips) along river.

Locality 2 [11km E of Agordat] - interleaved granitoids and volcanoclastic sediments.

Locality 3 [25km W of Agordat] - Quartzo-feldspathic, biotite gneisses with concordant and discordant aplitic dykes. Folds are parallel to foliation with a lineation plunging NE. Sheared, banded, grey-white marbles form prominent marker units and massive veined pyroxenites of the Hagar terrane mafic-ultramafic complex are abundant.

Locality 4 [the road to Cheru] - Hagar terrane: sheared, folded schists with microfolds, muscovite-sericite schists, sheared serpentinites, epidotic mylonite, sericite-chlorite schists interleaved with metabasalts, chlorite-sericite schists interleaved with granitoids, massive deformed amphibolites and flat-lying interthrust granitoids and gneisses.

Locality 5 [Keru] - Barka terrane: interthrust granitoids and hornblende gneisses.

Locality 6 [Sawa] - Barka terrane: sheared, refolded biotite-hornblende and massive quartzo feldspathic gneisses.

ix) Sawa to Haycota traverse: Southern extension to Barka and Hagar terranes. Far below the level of lateritisation.

*Lithology*:

Flat-lying gneisses and amphibolites with shallow dips to SE.

x) Haycota to Barentu traverse: volcano-sedimentary rocks and the mafic-ultramafic extension of the Hagar terrane. No evidence of laterites on this traverse:

*Lithology*:

Locality 1 - Strongly sheared volcano-sedimentary rocks.

Locality 2 - Metre-thick quartz veins in tuffaceous metavolcanics.

Locality 3 - Massive elliptical ultramafic bodies interbedded with metabasalts.

Locality 4 - Amphibolites of the Hagar terrane.

xi) Asmara to Massawa traverse: The rifted Red Sea Escarpment and Gahtelay gneisses. Laterites rest unconformably on deeply weathered basement. Along the Asmara to

Massawa section, a difference of 2.2 km separates the laterites at the base of the escarpment at Dogali from the nearest occurrence of laterites at the top of the escarpment. Major faults may account for this displacement.

*Lithology*:

Locality 1 [Asmara, the capital of Eritrea] – Basalts clearly overlie laterite on the eastern outskirts of Asmara. Laterite overlies Neoproterozoic basement throughout the city and is well exposed at many recent building sites.

Locality 2 [Gahtelay] - High-grade gneisses affected by Tertiary faulting (fault breccia common) and cut by Tertiary dolerite dykes.

Locality 3 [Dogali] - Laterite / basalt tectonic datum; laterites unconformably overlying gneisses. Basalts unconformably beneath Miocene clastic sediments. Overlying Pliocene (?) coral limestone outcrops elevated during late Tertiary uplift.

# Appendix A: Laterite geochemistry

**Table A.1** Major and trace element data (LOI – loss on ignition)

| Majors | | ferricrete | ferricrete | mottle | mottle | mottle | basement | mottle |
|---|---|---|---|---|---|---|---|---|
| wt. % | Samples | M136 | M136a | M136b | M136c | M136d | M136f | M315a |
| $SiO_2$ | | 21.21 | 19.29 | 72.24 | 32.25 | 79.16 | 47.43 | 71.34 |
| $TiO_2$ | | 1.015 | 0.458 | 1.026 | 0.715 | 0.362 | 0.607 | 1.397 |
| $Al_2O_3$ | | 16.21 | 15.39 | 18.12 | 28.69 | 6.39 | 14.74 | 13.99 |
| $Fe_2O_3$ | | 53.08 | 55.83 | 1.07 | 4.66 | 10.24 | 11.70 | 6.57 |
| MnO | | 0.047 | 0.022 | 0.004 | 0.005 | 0.022 | 0.219 | 0.006 |
| MgO | | 0.05 | 0.09 | 0.17 | 0.25 | 0.10 | 4.61 | 0.15 |
| CaO | | 0.10 | 0.16 | 0.17 | 0.14 | 0.18 | 12.97 | 0.20 |
| $Na_2O$ | | 0.07 | 0.05 | 0.08 | 0.74 | 0.06 | 0.89 | 0.03 |
| $K_2O$ | | 0.02 | 0.05 | 0.16 | 3.24 | 0.04 | 0.43 | 0.16 |
| $P_2O_5$ | | 0.136 | 0.109 | 0.013 | 0.121 | 0.046 | 0.068 | 0.025 |
| LOI | | 7.75 | 7.99 | 7.63 | 25.97 | 4.50 | 6.09 | 6.42 |
| Total | | 99.69 | 99.44 | 100.69 | 96.79 | 101.11 | 99.74 | 100.30 |
| **Traces ppm** | **Det. Lim. ppm** | | | | | | | |
| Rb | 2 | 0 | 1 | 3 | 1 | 2 | 6 | 4 |
| Sr | 2 | 23 | 16 | 17 | 686 | 5 | 77 | 15 |
| Y | 2.0 | 13.2 | 7.5 | 6.1 | 8.9 | 4.0 | 13.7 | 5.7 |
| Zr | 2 | 210 | 107 | 117 | 204 | 36 | 19 | 178 |
| Nb | 1.5 | 11.8 | 4.8 | 6.6 | 10.2 | 3.3 | 1.4 | 8.8 |
| Ba | 12 | 0 | 0 | 83 | 712 | 75 | 79 | 72 |
| Pb | 5 | 69 | 50 | 12 | 157 | 2 | 1 | 0 |
| Th | 4 | 18 | 15 | 2 | 7 | 0 | 0 | 1 |
| U | 3 | 2 | 0 | 1 | 1 | 2 | 0 | 1 |
| Sc | 5 | 0 | 0 | 11 | 56 | 18 | 47 | 10 |
| V | 5 | 0 | 0 | 29 | 153 | 245 | 369 | 147 |
| Cr | 4 | 0 | 0 | 56 | 249 | 249 | 434 | 127 |
| Co | 2 | 0 | 0 | 1 | 0 | 0 | 40 | 0 |
| Ni | 3 | 14 | 0 | 6 | 4 | 14 | 77 | 6 |
| Cu | 3 | 65 | 98 | 12 | 49 | 13 | 46 | 17 |
| Zn | 3 | 23 | 19 | 7 | 14 | 46 | 70 | 9 |
| Ga | 3 | 36 | 40 | 13 | 43 | 14 | 12 | 14 |
| Mo | 2 | 10 | 3 | 3 | 2 | 1 | 0 | 1 |
| As | 5 | 125 | 32 | 1 | 11 | 6 | 3 | 6 |
| S | 50 | 1429 | 3724 | 163 | 29642 | 164 | 17 | 184 |

**Table A.1** (cont.)

| | mottle | mottle | basement | saprolite | saprolite | clay | clay |
|---|---|---|---|---|---|---|---|
| **wt. %** | **M315b** | **M315c** | **M316a** | **M316b** | **M316c** | **M348c** | **M348d** |
| **$SiO_2$** | 62.26 | 60.93 | 66.08 | 66.36 | 48.46 | 73.25 | 77.95 |
| **$TiO_2$** | 0.853 | 0.726 | 0.759 | 0.700 | 0.855 | 0.185 | 0.256 |
| **$Al_2O_3$** | 10.15 | 11.59 | 17.68 | 17.88 | 15.76 | 17.32 | 14.60 |
| **$Fe_2O_3$** | 20.23 | 19.66 | 6.40 | 6.01 | 5.46 | 1.06 | 1.39 |
| **MnO** | 0.018 | 0.009 | 0.021 | 0.023 | 0.208 | 0.003 | 0.004 |
| **MgO** | 0.10 | 0.12 | 1.29 | 1.88 | 3.04 | 0.13 | 0.06 |
| **CaO** | 0.24 | 0.22 | 0.10 | 0.09 | 12.14 | 0.12 | 0.10 |
| **$Na_2O$** | 0.03 | 0.04 | 0.78 | 0.77 | 5.34 | 0.13 | 0.12 |
| **$K_2O$** | 0.04 | 0.17 | 2.55 | 2.37 | 0.17 | 0.09 | 0.40 |
| **$P_2O_5$** | 0.079 | 0.140 | 0.024 | 0.025 | 0.287 | 0.020 | 0.038 |
| **LOI** | 6.21 | 5.95 | 4.36 | 4.02 | 7.57 | 7.53 | 5.47 |
| **Total** | 100.20 | 99.56 | 100.05 | 100.12 | 99.27 | 99.85 | 100.40 |
| | | | | | | | |
| **ppm** | | | | | | | |
| **Rb** | 1 | 4 | 75 | 69 | 2 | 1 | 7 |
| **Sr** | 19 | 473 | 169 | 152 | 526 | 8 | 33 |
| **Y** | 4.7 | 8.1 | 36.5 | 42.1 | 16.5 | 2.1 | 5.2 |
| **Zr** | 111 | 127 | 138 | 131 | 181 | 25 | 119 |
| **Nb** | 6.2 | 6.0 | 7.6 | 7.4 | 12.6 | 2.3 | 4.8 |
| **Ba** | 38 | 302 | 536 | 504 | 107 | 14 | 106 |
| **Pb** | 3 | 19 | 5 | 0 | 6 | 0 | 5 |
| **Th** | 3 | 2 | 6 | 5 | 4 | 0 | 0 |
| **U** | 2 | 0 | 0 | 2 | 2 | 1 | 1 |
| **Sc** | 24 | 13 | 26 | 24 | 21 | 8 | 7 |
| **V** | 426 | 296 | 111 | 103 | 185 | 18 | 22 |
| **Cr** | 231 | 206 | 84 | 82 | 162 | 50 | 14 |
| **Co** | 0 | 0 | 11 | 14 | 18 | 0 | 1 |
| **Ni** | 15 | 5 | 78 | 87 | 60 | 1 | 5 |
| **Cu** | 62 | 40 | 159 | 94 | 48 | 10 | 5 |
| **Zn** | 18 | 12 | 152 | 193 | 72 | 5 | 10 |
| **Ga** | 17 | 18 | 20 | 20 | 19 | 13 | 12 |
| **Mo** | 1 | 0 | 2 | 0 | 1 | 3 | 4 |
| **As** | 30 | 24 | 6 | 0 | 2 | 2 | 2 |
| **S** | 428 | 831 | 59 | 23 | 35 | 356 | 76 |

**Table A.1 (cont.)**

| wt. % | mottle M348e | mottle M349A(f) | mottle M349A(g) | ferricrete M349Q | basement M358a | saprolite M358b | saprolite M358c |
|---|---|---|---|---|---|---|---|
| $SiO_2$ | 71.82 | 76.55 | 74.96 | 58.68 | 76.30 | 75.67 | 80.53 |
| $TiO_2$ | 0.210 | 0.287 | 0.275 | 0.406 | 0.204 | 0.181 | 0.151 |
| $Al_2O_3$ | 16.41 | 14.33 | 15.01 | 6.06 | 12.05 | 13.78 | 10.68 |
| $Fe_2O_3$ | 4.47 | 3.25 | 3.97 | 30.51 | 3.30 | 3.61 | 3.95 |
| MnO | 0.005 | 0.006 | 0.004 | 0.013 | 0.084 | 0.007 | 0.017 |
| MgO | 0.16 | 0.05 | 0.05 | 0.06 | 0.66 | 0.20 | 0.08 |
| CaO | 0.09 | 0.11 | 0.09 | 0.12 | 0.38 | 0.12 | 0.12 |
| $Na_2O$ | 0.06 | 1.40 | 0.45 | 0.06 | 4.80 | 0.10 | 0.04 |
| $K_2O$ | 0.93 | 0.28 | 0.19 | 0.03 | 0.49 | 0.93 | 0.03 |
| $P_2O_5$ | 0.030 | 0.018 | 0.027 | 0.047 | 0.041 | 0.045 | 0.015 |
| LOI | 6.10 | 4.15 | 5.64 | 3.66 | 1.34 | 5.53 | 4.79 |
| Total | 100.30 | 100.44 | 100.66 | 99.63 | 99.66 | 100.17 | 100.41 |
| ppm | | | | | | | |
| Rb | 19 | 5 | 3 | 0 | 8 | 21 | 1 |
| Sr | 9 | 103 | 94 | 16 | 58 | 8 | 12 |
| Y | 16.8 | 12.1 | 15.6 | 7.4 | 28.6 | 3.2 | 2.2 |
| Zr | 92 | 70 | 78 | 104 | 71 | 62 | 50 |
| Nb | 4.9 | 5.6 | 3.4 | 6.1 | 4.2 | 4.9 | 3.2 |
| Ba | 105 | 120 | 92 | 33 | 209 | 319 | 26 |
| Pb | 0 | 2 | 10 | 15 | 0 | 0 | 0 |
| Th | 2 | 1 | 1 | 8 | 0 | 1 | 0 |
| U | 2 | 0 | 0 | 0 | 0 | 1 | 1 |
| Sc | 13 | 12 | 8 | 7 | 13 | 9 | 11 |
| V | 57 | 52 | 41 | 608 | 14 | 57 | 60 |
| Cr | 17 | 18 | 19 | 76 | 3 | 20 | 86 |
| Co | 1 | 0 | 2 | 0 | 3 | 0 | 0 |
| Ni | 3 | 3 | 4 | 9 | 2 | 6 | 3 |
| Cu | 15 | 79 | 48 | 24 | 2 | 11 | 5 |
| Zn | 7 | 19 | 15 | 8 | 56 | 29 | 5 |
| Ga | 11 | 13 | 12 | 11 | 12 | 8 | 7 |
| Mo | 2 | 2 | 2 | 4 | 1 | 2 | 1 |
| As | 3 | 5 | 4 | 102 | 2 | 4 | 6 |
| S | 42 | 57 | 678 | 1198 | 7 | 148 | 67 |

**Table A.1 (cont.)**

| wt. % | saprolite M358d | mottle M358e | ferricrete M358f | basement M359a | saprolite M359b | saprolite M395c?? | clay M359d |
|---|---|---|---|---|---|---|---|
| $SiO_2$ | 78.84 | 74.49 | 28.73 | 62.10 | 65.90 | 78.52 | 11.96 |
| $TiO_2$ | 0.095 | 0.072 | 0.251 | 0.891 | 0.741 | 0.126 | 0.077 |
| $Al_2O_3$ | 13.94 | 16.33 | 8.21 | 18.02 | 16.06 | 13.98 | 31.74 |
| $Fe_2O_3$ | 1.23 | 2.03 | 54.32 | 5.97 | 4.18 | 1.07 | 0.68 |
| MnO | 0.007 | 0.005 | 0.014 | 0.097 | 0.041 | 0.004 | 0.005 |
| MgO | 0.21 | 0.10 | 0.07 | 1.83 | 1.43 | 0.18 | 0.12 |
| CaO | 0.08 | 0.18 | 0.10 | 1.76 | 1.59 | 0.08 | 0.09 |
| $Na_2O$ | 0.05 | 0.05 | 0.03 | 2.32 | 4.63 | 0.11 | 1.30 |
| $K_2O$ | 1.39 | 0.12 | 0.07 | 4.06 | 2.44 | 1.63 | 4.97 |
| $P_2O_5$ | 0.011 | 0.033 | 0.224 | 0.210 | 0.212 | 0.014 | 0.158 |
| LOI | 4.77 | 7.09 | 7.83 | 2.76 | 2.66 | 4.60 | 37.65 |
| Total | 100.61 | 100.49 | 99.86 | 100.02 | 99.89 | 100.31 | 88.75 |
| ppm | | | | | | | |
| Rb | 41 | 3 | 2 | 111 | 72 | 47 | 2 |
| Sr | 15 | 9 | 8 | 325 | 285 | 18 | 1507 |
| Y | 3.8 | 12.8 | 5.9 | 28.6 | 22.6 | 20.8 | 1.8 |
| Zr | 78 | 98 | 96 | 217 | 171 | 149 | 18 |
| Nb | 5.6 | 9.8 | 5.5 | 8.2 | 7.3 | 7.4 | 2.8 |
| Ba | 552 | 45 | 0 | 1572 | 1112 | 434 | 1653 |
| Pb | 10 | 0 | 27 | 7 | 8 | 5 | 111 |
| Th | 1 | 2 | 7 | 8 | 6 | 2 | 3 |
| U | 0 | 2 | 0 | 1 | 1 | 1 | 1 |
| Sc | 4 | 2 | 0 | 17 | 18 | 5 | 190 |
| V | 6 | 16 | 0 | 109 | 107 | 7 | 9 |
| Cr | 9 | 12 | 0 | 30 | 45 | 11 | 22 |
| Co | 0 | 1 | 0 | 10 | 44 | 1 | 1 |
| Ni | 1 | 5 | 2 | 18 | 200 | 1 | 2 |
| Cu | 8 | 13 | 86 | 24 | 37 | 11 | 149 |
| Zn | 12 | 16 | 26 | 69 | 326 | 12 | 8 |
| Ga | 8 | 12 | 35 | 21 | 16 | 11 | 6 |
| Mo | 1 | 2 | 5 | 1 | 1 | 1 | 1 |
| As | 2 | 6 | 37 | 4 | 4 | 3 | 24 |
| S | 85 | 137 | 1477 | 121 | 18 | 121 | 80103 |

**Table A.1 (cont.)**

| | clay | mottle | mottle | mottle | mottle | mottle | ferricrete |
|---|---|---|---|---|---|---|---|
| **wt. %** | **M359d(1)** | **M359e** | **M359e(1)** | **M359f** | **M359g** | **M359h** | **M359k** |
| **$SiO_2$** | 66.11 | 72.41 | 59.64 | 76.36 | 71.72 | 70.28 | 21.48 |
| **$TiO_2$** | 0.750 | 0.556 | 0.862 | 0.542 | 0.648 | 0.533 | 0.501 |
| **$Al_2O_3$** | 16.97 | 12.10 | 21.20 | 11.07 | 15.23 | 12.03 | 9.69 |
| **$Fe_2O_3$** | 4.99 | 3.05 | 5.24 | 3.46 | 4.65 | 10.28 | 55.22 |
| **MnO** | 0.011 | 0.005 | 0.012 | 0.005 | 0.010 | 0.015 | 0.029 |
| **MgO** | 0.46 | 0.22 | 0.63 | 0.30 | 0.18 | 0.12 | 0.32 |
| **CaO** | 0.05 | 0.10 | 0.17 | 0.11 | 0.12 | 0.13 | 0.12 |
| **$Na_2O$** | 0.56 | 0.29 | 0.23 | 0.17 | 0.07 | 0.05 | 0.06 |
| **$K_2O$** | 3.31 | 2.50 | 2.84 | 2.20 | 0.90 | 0.53 | 1.15 |
| **$P_2O_5$** | 0.077 | 0.186 | 0.101 | 0.094 | 0.092 | 0.110 | 1.350 |
| **LOI** | 6.50 | 8.36 | 9.09 | 5.41 | 6.59 | 5.96 | 10.14 |
| **Total** | 99.79 | 99.78 | 100.01 | 99.70 | 100.21 | 100.04 | 100.06 |
| | | | | | | | |
| **ppm** | | | | | | | |
| **Rb** | 52 | 21 | 49 | 34 | 13 | 10 | 34 |
| **Sr** | 116 | 883 | 260 | 346 | 295 | 134 | 63 |
| **Y** | 11.8 | 15.0 | 11.6 | 11.5 | 11.5 | 10.7 | 16.4 |
| **Zr** | 192 | 158 | 204 | 143 | 157 | 129 | 113 |
| **Nb** | 7.4 | 5.8 | 8.0 | 5.6 | 6.6 | 5.3 | 5.0 |
| **Ba** | 517 | 947 | 646 | 794 | 359 | 222 | 0 |
| **Pb** | 6 | 39 | 19 | 9 | 10 | 13 | 16 |
| **Th** | 5 | 8 | 6 | 3 | 5 | 4 | 9 |
| **U** | 2 | 1 | 3 | 1 | 2 | 0 | 7 |
| **Sc** | 14 | 13 | 15 | 13 | 11 | 13 | 0 |
| **V** | 79 | 67 | 94 | 73 | 63 | 126 | 0 |
| **Cr** | 42 | 27 | 31 | 24 | 23 | 42 | 0 |
| **Co** | 3 | 1 | 3 | 0 | 2 | 2 | 0 |
| **Ni** | 5 | 4 | 12 | 3 | 7 | 7 | 37 |
| **Cu** | 14 | 8 | 29 | 8 | 15 | 25 | 258 |
| **Zn** | 15 | 8 | 30 | 11 | 34 | 23 | 355 |
| **Ga** | 16 | 15 | 20 | 13 | 15 | 17 | 20 |
| **Mo** | 6 | 2 | 3 | 2 | 2 | 3 | 5 |
| **As** | 12 | 9 | 9 | 8 | 4 | 8 | 67 |
| **S** | 630 | 10922 | 477 | 4444 | 1230 | 191 | 582 |

**Table A.1 (cont.)**

| wt. % | ferricrete M359N | basement M361a | clay M361b | mottle M361c | ferricrete M361d | silcrete M101c | clay M104 |
|---|---|---|---|---|---|---|---|
| $SiO_2$ | 16.74 | 99.59 | 56.11 | 64.21 | 4.92 | 94.40 | 70.42 |
| $TiO_2$ | 0.940 | 0.075 | 0.416 | 0.418 | 0.025 | 0.805 | 0.037 |
| $Al_2O_3$ | 13.61 | 0.73 | 25.56 | 20.22 | 1.17 | 2.51 | 19.67 |
| $Fe_2O_3$ | 59.52 | 0.23 | 1.74 | 4.30 | 81.72 | 0.32 | 0.79 |
| MnO | 0.016 | 0.002 | 0.004 | 0.007 | 0.020 | 0.002 | 0.002 |
| MgO | 0.21 | 0.04 | 0.08 | 0.80 | 0.10 | 0.03 | 0.05 |
| CaO | 0.27 | 0.03 | 0.04 | 0.06 | 0.06 | 0.08 | 0.18 |
| $Na_2O$ | 0.10 | 0.01 | 0.27 | 0.08 | 0.07 | 0.04 | 0.05 |
| $K_2O$ | 0.30 | 0.05 | 1.24 | 2.32 | 0.02 | 0.21 | 0.12 |
| $P_2O_5$ | 0.348 | 0.012 | 0.084 | 0.030 | 0.104 | 0.053 | 0.022 |
| LOI | 6.61 | 0.58 | 13.89 | 7.64 | 10.56 | 2.05 | 8.40 |
| Total | 98.67 | 101.34 | 99.44 | 100.09 | 98.77 | 100.49 | 99.73 |
| ppm | | | | | | | |
| Rb | 0 | 0 | 2 | 34 | 0 | 1 | 2 |
| Sr | 1030 | 26 | 498 | 120 | 4 | 216 | 29 |
| Y | 19.1 | 5.9 | 9.0 | 7.7 | 62.4 | 7.8 | 5.3 |
| Zr | 217 | 34 | 127 | 103 | 7 | 194 | 19 |
| Nb | 14.1 | 2.2 | 3.3 | 2.2 | 2.4 | 14.2 | 0.2 |
| Ba | 0 | 317 | 387 | 233 | 0 | 86 | 70 |
| Pb | 43 | 0 | 19 | 7 | 17 | 12 | 11 |
| Th | 13 | 0 | 5 | 4 | 1 | 3 | 0 |
| U | 3 | 0 | 1 | 1 | 0 | 1 | 1 |
| Sc | 0 | 2 | 15 | 8 | 0 | 1 | 1 |
| V | 0 | 8 | 41 | 75 | 0 | 24 | 7 |
| Cr | 0 | 160 | 49 | 62 | 0 | 19 | 6 |
| Co | 0 | 0 | 1 | 6 | 0 | 1 | 0 |
| Ni | 8 | 4 | 9 | 98 | 1364 | 0 | 0 |
| Cu | 110 | 5 | 43 | 58 | 98 | 14 | 12 |
| Zn | 23 | 5 | 25 | 120 | 950 | 3 | 4 |
| Ga | 28 | 3 | 28 | 21 | 7 | 5 | 4 |
| Mo | 11 | 2 | 2 | 1 | 1 | 1 | 0 |
| As | 346 | 1 | 8 | 9 | 235 | 8 | 4 |
| S | 31236 | 162 | 8279 | 1808 | 751 | 122 | 278 |

**Table A.1 (cont.)**

| wt. % | clay M109 | clay M110e | clay M110t | clay M113 | clay M113a | clay M113b | clay M113c | clay M114 | clay M121a |
|---|---|---|---|---|---|---|---|---|---|
| $SiO_2$ | 41.97 | 65.79 | 64.66 | 54.88 | 0.31 | 43.25 | 40.08 | 77.83 | 79.05 |
| $TiO_2$ | 0.016 | 1.006 | 1.003 | 1.474 | 0.075 | 0.034 | 0.855 | 0.571 | 0.323 |
| $Al_2O_3$ | 39.09 | 22.05 | 23.31 | 30.21 | 35.53 | 38.51 | 33.03 | 14.82 | 13.58 |
| $Fe_2O_3$ | 0.19 | 0.80 | 0.78 | 1.43 | 1.04 | 0.78 | 0.89 | 0.77 | 1.72 |
| MnO | 0.002 | 0.002 | 0.002 | 0.003 | 0.002 | 0.013 | 0.006 | 0.001 | 0.006 |
| MgO | 0.03 | 0.03 | 0.00 | 0.12 | 0.00 | 0.02 | 0.06 | 0.06 | 0.04 |
| CaO | 0.09 | 0.07 | 0.06 | 0.18 | 0.03 | 0.13 | 0.10 | 0.12 | 0.13 |
| $Na_2O$ | 0.20 | 0.12 | 0.17 | 0.08 | 0.42 | 0.07 | 0.24 | 0.08 | 0.04 |
| $K_2O$ | 0.61 | 0.21 | 0.28 | 0.05 | 8.34 | 0.21 | 2.29 | 0.07 | 0.03 |
| $P_2O_5$ | 0.099 | 0.035 | 0.039 | 0.031 | 0.137 | 0.506 | 0.155 | 0.014 | 0.045 |
| LOI | 17.10 | 9.47 | 10.19 | 11.73 | 41.24 | 15.49 | 21.21 | 6.26 | 6.01 |
| Total | 99.39 | 99.58 | 100.50 | 100.19 | 87.12 | 99.00 | 98.92 | 100.60 | 100.97 |
| ppm | | | | | | | | | |
| Rb | 1 | 1 | 0 | 2 | 1 | 1 | 2 | 2 | 0 |
| Sr | 610 | 194 | 215 | 85 | 4324 | 4677 | 899 | 19 | 70 |
| Y | 2.3 | 16.2 | 16.5 | 17.5 | 0.7 | 3.1 | 15.1 | 13.6 | 2.4 |
| Zr | 6 | 215 | 209 | 367 | 22 | 29 | 221 | 138 | 45 |
| Nb | 0.2 | 7.9 | 7.9 | 19.3 | 0.4 | 0.4 | 8.6 | 4.4 | 1.4 |
| Ba | 221 | 68 | 79 | 58 | 2047 | 616 | 656 | 51 | 98 |
| Pb | 33 | 7 | 9 | 16 | 58 | 30 | 25 | 5 | 20 |
| Th | 0 | 2 | 3 | 8 | 2 | 3 | 7 | 1 | 0 |
| U | 1 | 2 | 1 | 3 | 1 | 0 | 3 | 1 | 0 |
| Sc | 0 | 4 | 5 | 2 | 182 | 33 | 33 | 3 | 5 |
| V | 8 | 15 | 17 | 17 | 737 | 90 | 52 | 12 | 26 |
| Cr | 11 | 46 | 49 | 55 | 276 | 56 | 74 | 22 | 15 |
| Co | 0 | 1 | 1 | 0 | 0 | 1 | 2 | 1 | 1 |
| Ni | 1 | 7 | 6 | 3 | 0 | 6 | 19 | 3 | 6 |
| Cu | 27 | 21 | 20 | 7 | 133 | 29 | 61 | 8 | 6 |
| Zn | 3 | 10 | 10 | 18 | 8 | 4 | 30 | 14 | 9 |
| Ga | 5 | 16 | 16 | 33 | 21 | 12 | 24 | 14 | 12 |
| Mo | 0 | 0 | 0 | 1 | 0 | 0 | 0 | 0 | 0 |
| As | 16 | 32 | 33 | 7 | 37 | 71 | 8 | 3 | 3 |
| S | 3304 | 1358 | 1899 | 62 | 93174 | 1983 | 10890 | 64 | 105 |

**Table A.1 (cont.)**

| wt. % | clay M121b | clay M122a | clay M125 | clay M125a | clay M125d | clay M130 | clay M131 | clay M133 | clay M147 |
|---|---|---|---|---|---|---|---|---|---|
| $SiO_2$ | 81.25 | 76.02 | 40.57 | 18.05 | 31.82 | 84.45 | 93.14 | 71.13 | 78.20 |
| $TiO_2$ | 0.288 | 0.553 | 0.175 | 0.337 | 0.323 | 0.123 | 0.323 | 1.185 | 0.256 |
| $Al_2O_3$ | 12.83 | 15.92 | 21.27 | 32.76 | 23.40 | 10.48 | 5.28 | 19.48 | 14.62 |
| $Fe_2O_3$ | 0.56 | 0.30 | 0.29 | 0.87 | 0.71 | 0.15 | 0.14 | 1.20 | 0.42 |
| MnO | 0.002 | 0.002 | 0.009 | 0.009 | 0.012 | 0.002 | 0.002 | 0.006 | 0.002 |
| MgO | 0.06 | 0.03 | 0.01 | 0.03 | 0.02 | 0.05 | 0.04 | 0.05 | 0.04 |
| CaO | 0.12 | 0.08 | 0.07 | 0.05 | 0.09 | 0.18 | 0.06 | 0.15 | 0.12 |
| $Na_2O$ | 0.04 | 0.31 | 0.17 | 0.18 | 0.22 | 0.03 | 0.03 | 0.04 | 0.69 |
| $K_2O$ | 0.19 | 0.20 | 5.33 | 6.03 | 5.96 | 0.06 | 0.05 | 0.05 | 0.12 |
| $P_2O_5$ | 0.017 | 0.027 | 0.294 | 0.229 | 0.525 | 0.040 | 0.019 | 0.021 | 0.006 |
| LOI | 5.50 | 6.28 | 26.51 | 36.14 | 30.13 | 4.81 | 2.20 | 7.67 | 5.47 |
| Total | 100.85 | 99.72 | 94.70 | 94.70 | 93.21 | 100.38 | 101.29 | 100.98 | 99.94 |
| ppm | | | | | | | | | |
| Rb | 3 | 4 | 2 | 1 | 1 | 2 | 2 | 1 | 2 |
| Sr | 9 | 86 | 1044 | 1647 | 2035 | 106 | 26 | 8 | 89 |
| Y | 4.2 | 11.4 | 2.8 | 4.9 | 5.5 | 2.9 | 8.9 | 1.4 | 0.9 |
| Zr | 79 | 129 | 39 | 86 | 92 | 131 | 241 | 92 | 12 |
| Nb | 3.2 | 3.2 | 2.3 | 3.6 | 3.8 | 1.7 | 4.3 | 11.0 | 0.1 |
| Ba | 78 | 139 | 909 | 2010 | 1355 | 76 | 100 | 52 | 51 |
| Pb | 4 | 12 | 4 | 4 | 16 | 8 | 7 | 3 | 4 |
| Th | 0 | 2 | 3 | 9 | 5 | 1 | 4 | 0 | 0 |
| U | 0 | 3 | 2 | 2 | 3 | 1 | 0 | 2 | 0 |
| Sc | 2 | 2 | 70 | 100 | 77 | 1 | 1 | 2 | 3 |
| V | 11 | 18 | 51 | 59 | 124 | 12 | 15 | 26 | 32 |
| Cr | 5 | 56 | 69 | 177 | 94 | 8 | 17 | 38 | 10 |
| Co | 1 | 1 | 2 | 1 | 1 | 0 | 1 | 1 | 1 |
| Ni | 0 | 0 | 1 | 1 | 1 | 1 | 1 | 5 | 0 |
| Cu | 3 | 5 | 136 | 159 | 343 | 2 | 9 | 5 | 8 |
| Zn | 4 | 2 | 9 | 13 | 13 | 5 | 2 | 5 | 2 |
| Ga | 8 | 14 | 5 | 20 | 12 | 3 | 6 | 15 | 13 |
| Mo | 0 | 0 | 1 | 1 | 0 | 0 | 0 | 0 | 0 |
| As | 2 | 3 | 15 | 22 | 21 | 3 | 4 | 4 | 3 |
| S | 85 | 61 | 36962 | 49094 | 43530 | 53 | 45 | 28 | 62 |

# Appendix B: Radiometric dating

## B.1 Data processing manual for infrared laser-probe mass spectrometry

This guide was compiled for the author's own use from the limited guidance available in the OU Ar-Ar laboratory and the many problems encountered with the MS Excel macro provided for users, but may be helpful for others needing to process or re-process raw data from the OU IR laser probe mass spectrometer.

### B.1.1 Setting up the software

1. **Argon1.xlm** and **Linefitw.exe** should go in **C:\Program Files\Microsoft Office\Office**

**Linefit.dat** and **fit.dat** should go in **C:\windows\temp\FIT.DAT**

If you don't have a directory with that name, create a new one.

2. Start Excel and then open **Argon1.xlm** from C:\Program Files\Microsoft Office\Office\

Click **Enable** when dialog box appears ( from disable, enable or do not open).

Chronplot menu item appears at top of Excel screen.

### B.1.2 Cleaning up data

Open your raw data file.

Several columns are redundant, and need to be deleted

Do this by (1) clicking in grey box labelled **H** first, then **with Ctrl key held down** click grey boxes for columns, **I, L, O, R, U, X & AA** The columns will go black. (b) Select **Edit/Delete** and all remaining columns close-up to left.

**Add column headings**

1. **Click grey box for Row** 1 – all row goes black. Select **Insert/Rows** – a blank row appears above selected row (now this is Row 1)
2. Open **Ar_empty.xls** which has the proper column headings for 2004 data, including the G1 magic\number 37987.00 used in the Day Number\calculation. Highlight Row 1 as above, and use **Ctrl C** to copy row. For other years,G1 should be **37622** (2003), **37257** (2002), **36892** (2001), **36526** (2000) **36161** (1999)

3. Go to new data file, click in top left hand cell (Col A, Row 1) and do **Ctrl V** – pastes the column headings into Row 1. This includes headings for steps and Ar40 to Ar36 blanks – see below

**Formatting**

Some columns might have a ####### in them – that means they are not formatted properly – Col D (Date) is most likely.

1. Left-hold-drag down column to bottom of data from Row 2 to highlight all
2. Do **Format/Cells**. For Col D, select **Date** as Category and whatever **Type** you fancy from the little Format window. When you OK or Enter the #### appear as a date.

**Day number**

1. Click in **Column F, Row 2** which for the moment has a meaningless number in it. As well as in the cell you will see the number in the Formula Bar that is just above the main table. Delete the number and replace it with
2. =D2+E2-$G$1 This is the formula that calculates the day number from cell D2 (actually column D is in days since Jan 1 1900, and col E is in decimals of a day = clock time)
3. Click on the **little = sign next to the Formula bar** - a little box opens with the result. If it looks like 102.76 then that is OK. If not, you got the formula wrong – do 1&2 again
4. Now **click in cell F2** and do **Ctrl C = copy** – gets highlighted with vibrating box
5. Left-hold-drag from cell F3 to bottom of col F, then **Ctrl V = paste** – day numbers should \appear from top to bottom. (If it is the #### you need to format all the cells in Col F as Number (see above)

**B.1.3 Performing blank corrections**

1. First go to bottom right corner of Excel window and find the little grey box with some diagonal lines in it. Just to the left of this is a "raised" line. Move the cursor onto it, until a horizontal, double-headed arrow appears, then left-hold-drag the raised line towards the left. This adds another copy of the table, so you can use the

left-right scroll bars on both to get the sample and date columns always showing at the left hand side and the columns you will be working with showing in the right-hand side – you can scroll at right while left stays still.

2. Now do same at top right – drag the little divider down one cell, so that Row 1 shows above and below. This keeps the column headings in view at all times.
3. Set the right hand part of the table so that you can see Col H (40peak) to Col V (40blank) (use full screen)
4. Select prior blank for each step, and highlight its row between **Cols H and Q**. Do **Ctrl C (copy)** – this is the Ar40 to Ar36 data needed for blank correction.
5. Click in **Col V cells for the following sample step(s)** and do **Ctrl V (paste)**. Repeat for each step and prior blank.
6. Now you need to get rid of the blanks. Quick way – Do **Ctrl A (highlights all cells)**. Select **Data/**Sort. Make sure **Header row** button is dotted. Then select **Sort by Type and Descending**. Press OK. This separate samples and blanks into two blocks. Highlight all rows with blanks (left-hold-drag grey Row numbers). Do **Ctrl X (cut)** Move to Sheet 2, put cursor in cell A1 and do **Ctrl V**.

Now you are ready to do the corrections in Sheet 1. **SAVE AT THS POINT using a different file name**

**Blank correction procedure**

1. **Click in any cell containing Ar data** – ie a number. Do **Chronplot/Subtract**. Select 40peak in First column and 40 blank in Second column. Then OK>
2. Answer **Cancel** to **Change flag settings**.
3. Type in **40Ar** in **New column title** box, then OK – blank-corrected Ar-40 data and error go into columns headed 40Ar and ±.
4. Repeat 1-3 for 39peak and 39blank, creating new columns for 39Ar and another ±. Same for 38, 37 and 36.
5. **SAVE file**

**B.1.4 Setting up Argon part**

1. Click **Chronplot/Argon**

2. First you are asked **which columns contain Day Number, then corrected argons – 36Ar first 40Ar last.** Use the scroller to make the right selections – care needed.
3. Click **Argon/Discrimination**. This asks for the $^{40}Ar/^{39}Ar$ ratio of the atmosphere as measured by the mass spectrometer. **Type in 283**, then OK.

**$^{37}Ar$ decay correction**

This is crucial, and takes account of the decay of $^{37}Ar$ since the irradiation. It starts with the time since irradiation, which is **sample day number minus irradiation day number.**

1. Click **Argon/37Ar decay.**
2. You are asked to "Enter the irradiation completion time as a day number". If the irradiation was the same year as the samples were run, put in the day number from **the Excel irradiation parameters file.** However, if it was the year before, the number of days between the irradiation day number and the end of that year is involved i.e. 365 (or 366 in leap year) minus irradiation day number. This has to be entered as a **negative number** (minus a negative number adds it to the sample-run day number, which is what is required).
3. Enter the Time in the reactor from **the Excel irradiation parameters file** then OK.

**Ca and K corrections**

1. Open **the Excel irradiation parameters file** and scroll down to the bottom set, so you can see the column headings for the J value, its error, two Ca corrections and the K correction
2. Go back to data table, click in any data cell. Select **Argon/Ca correction** In first box type in the value for the **(39Ar/37Ar)Ca**, OK then 0.00 in error box, OK, then value for **(36Ar/37Ar)Ca**, OK then **0.00 in error box** OK. This changes the 40Ar to 36Ar values.
3. Click in any data cell. Select **Argon/K correction.** Type in value for **(40Ar/39Ar)K**, OK then **0.00 in error box** OK. This also changes values in 40Ar etc.

**Age calculation**

1. Select **Argon/Ages.** In first box type in the **J value,** in error box the **error for J.**

You will now have new columns for **40Ar*/39Ar**, its **error (±)** and **Age** with its **error (±)**, for each step.

**Plotting Age against Cumulative $^{39}$Ar as box plots**

You need now to separate all your sample runs into separate blocks, each starting with a row containing the column headings.

1. Highlight the first row of each set of sample steps, and **do Insert/Rows**. Do this five times at the start of each set.
2. Highlight Row 1 of the whole Table (**Col Headings**) and do **Edit/Copy**.
3. Highlight the **blank rows that immediately precede each of the data blocks, by clicking on the row number in grey area at far left, with Ctrl key held down**. When they (and only they) are highlighted, press the Enter Key on keyboard. This puts column headings above each set of sample steps

Now select **Argon/Plotter** - Chronplot Menu appears next to Argon.

1. Click anywhere in a block for one sample, and then do **Chronplot/Plot**
2. Select the **Box Plot** radio button, and **type sample name into Main Graph Title** box.
3. Select **39Ar in Column for X** and **Age (Ma) in Column for Y boxes** respectively - these should appear in X axis title and Y axis title boxes.
4. The plot appears, and two new columns "cummulative [sic] 39Ar" and "±". Cumulative is a good guide to whether you have a plateau or not.

The axes on the plot will probably be wrongly set, so you have to adjust them, which is quite tricky.

Move the cursor around along the Y-axis until a little yellow box saying "value Y axis" appears. Right-click to reveal a menu. Select **Format axis**. Click on the **Scale** tab. change Minimum to 0, Maximum to round number just above maximum age in results (say 50 when the maximum age is 30 Ma), and Major Units to a smaller number (10 in the case of ages less than 100 Ma and 100 for those between 100 and 1000 Ma). Then click on OK.

Now Format X-axis in same way, using Min of 0, Max of 100 and Major and minor units of 20.

**Adding plot to Excel file**

**Left-hold-drag the Chart 1** tab on the plot into the list of Sheet tabs at bottom left of main Excel table – this adds the Chart to the data, and is essential for doing line fitting and age errors etc – You can rename all the Sheets and Charts by right click on their tabs and selecting rename – just type in an appropriate name.

**Saving final workbook**

When you save the file, it should preserve the plots all right. But when you close Excel, say NO when it asks you if you want to save changes to Argon1.xlm. Then, when you want to look at the file again in Excel, it will tell you that the workbook contains automatic links to information in another workbook, and asks if you want to update all the linked information. YOU MUST ANSWER **NO**

**B.1.5 How to calculate total fusion, plateau and isochron ages**

**Ar data correction procedure.**

1. Create Day number columns – create a new column and into the first cell enter a formula adding the date and time (normally in columns D and E) and subtract the date for January 1st of the year of analysis. The easiest way to do this is to type 1/1/04 into another cell and use that cell in the formula. The resulting number should always be less than 365. Get rid of the formula so that the day numbers don't change accidentally if you do anything else like split the samples with a few row spaces. To do that 'copy' the new column and 'paste special' over the same column to paste it back as 'values'. Finally, add another column to the right of the day number column filled with the number 0.01. This just provides an error for the day number.
2. Blanks corrections – use the prior blanks technique to correct for extraction line blank and mass spectrometer background. In this section you should create columns for 40Ar, 39Ar, 38Ar, 37Ar, and 36Ar.
3. Go into the argon section of the macro, selecting each of the Ar columns in the when the macro dialog box asks for them.

4. The general rule for the argon correction menu is start at the top and move progressively down the menu doing the corrections in that order.
5. Discrimination correction – select discrimination correction in the menu, enter 283 for the measured value. This corrects for bias in the mass spectrometer detector.
6. 37Ar decay – it is not always necessary to use the 37Ar correction because in samples that have low Ca (e.g. clays and K-feldspars) it increases the errors. It is always necessary for plagioclase-bearing rocks, such as basalts. However, if you are correcting several different sample types and ages, it is safest to do it on all samples. First look at the 37Ar column and wherever you see a negative number change it to zero. The explanation for this is that if you have a negative number it means the amount of 37Ar is extremely small but if you leave it, the correction for 37Ar decay makes it a larger negative number and it can affect the ages slightly. Select 37Ar decay and enter the 'irradiation day number' and 'time in the reactor' which are both in days and are in the irradiation parameters sheet.
7. Ca corrections – enter the numbers from the irradiation parameters sheet with zero errors in both cases. This corrects 39Ar and 36Ar for Ca interference
8. K corrections - enter the number from the irradiation parameters sheet with zero error. This corrects 40Ar for K interference.
9. Ages – enter the J value and error from the irradiation parameters sheet. This should give you new columns for 40Ar*/39Ar and Age.

**Total gas age calculation**

1. Place cursor in the data as you do for other macro calculations.
2. Select 'totals' from the chronplot menu and select the 40Ar and 36Ar columns so all Ar totals are totalled.
3. A new row with totals appears a couple of rows below your data – be careful because if there are more rows below this will overwrite them.
4. Delete the empty rows between your data and the totals row.
5. Go into the argon corrections menu of the macro in the normal way selecting the columns for the Ar isotopes.

6. Select the 'Ages' and enter the same J value you used for the sample for which you are calculating the total gas age.

The macro will produce new 40Ar*/39Ar and age columns and the total gas age will be at the bottom of the new ages column at the end of the data. You can delete the old 40Ar*/39Ar and age columns because they are the same apart from the total gas age.

## B.2 Results

Figure B.1 gives examples of step plots yielding the three main types of $^{40}Ar/^{39}Ar$ age: "plateau", "total fusion" and "integrated".

The irradiation parameters for the five batches of samples used in this study are shown in Table B.1

Tables B.2 to B.4 contain extracts from the mass spectrometry data corrected for atmospheric argon contamination, $^{37}Ar$, K and Ca.

(a)

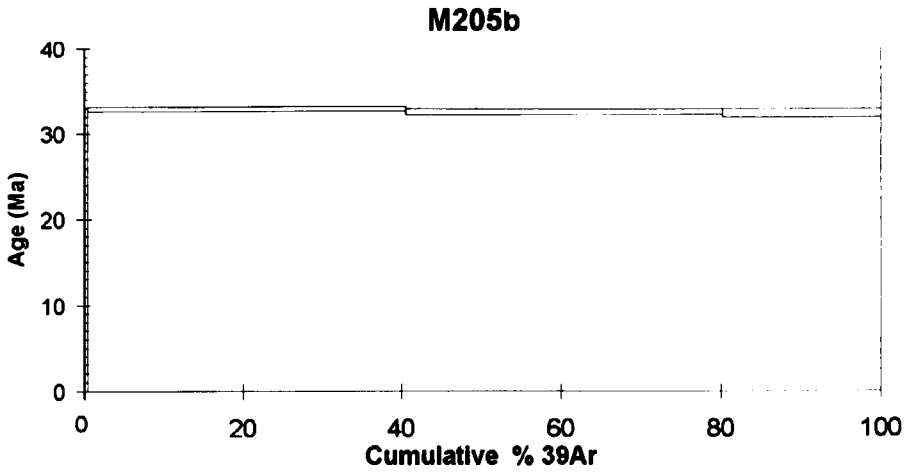


(b)

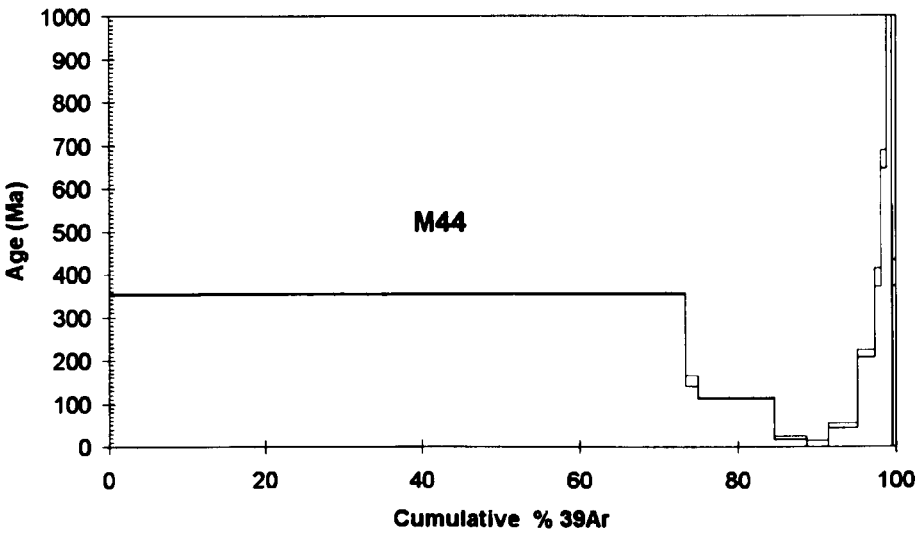


(c)

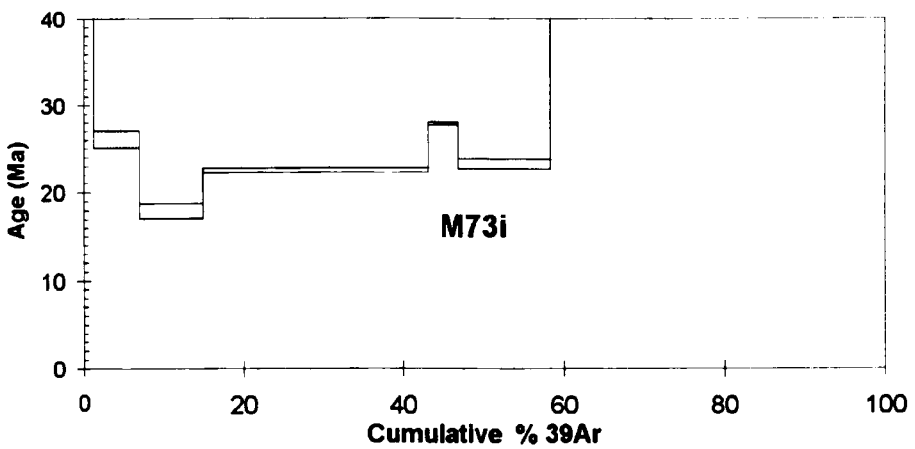


**Figure B.1** Examples of $^{40}Ar/^{39}Ar$ step plots yielding: (a) plateau age (sample M205a); (b) total fusion age (sample M44); (c) integrated age taken from steps between those showing classic excess argon (sample M73i).

**Table B.1** Irradiation parameters

**Irradiation 1** Date: 24 August 1998. Time in reactor: 2.1 days

| Sample | type | J value | J Error | $(^{39}Ar/^{37}Ar)_{Ca}$ | $(^{36}Ar/^{37}Ar)_{Ca}$ | $(^{40}Ar/^{39}Ar)_{K}$ |
|---|---|---|---|---|---|---|
| M33(ii) | basalt | 0.01172 | 0.00006 | 0.00072 | 0.00027 | 0.015 |
| M33(iv) | kaolinite | 0.01172 | 0.00006 | 0.00072 | 0.00027 | 0.015 |
| M48 | kaolinite | 0.01172 | 0.00006 | 0.00072 | 0.00027 | 0.015 |
| M68 | kaolinite | 0.01172 | 0.00006 | 0.00072 | 0.00027 | 0.015 |
| M70a | kaolinite | 0.01172 | 0.00006 | 0.00072 | 0.00027 | 0.015 |
| M70b | kaolinite | 0.01172 | 0.00006 | 0.00072 | 0.00027 | 0.015 |
| M73(i) | basalt | 0.01172 | 0.00006 | 0.00072 | 0.00027 | 0.015 |
| M73(iii) | basalt | 0.01172 | 0.00006 | 0.00072 | 0.00027 | 0.015 |
| M77 | basalt | 0.01172 | 0.00006 | 0.00072 | 0.00027 | 0.015 |

**Irradiation 2** Date: 18 August 2000. Time in reactor: 2.1 days

| Sample | type | J value | J Error | $(^{39}Ar/^{37}Ar)_{Ca}$ | $(^{36}Ar/^{37}Ar)_{Ca}$ | $(^{40}Ar/^{39}Ar)_{K}$ |
|---|---|---|---|---|---|---|
| M18(i) | kaolinite | 0.01270 | 0.00006 | 0.00072 | 0.00027 | 0.015 |
| M19a | kaolinite | 0.01270 | 0.00006 | 0.00072 | 0.00027 | 0.015 |
| M19c | kaolinite | 0.01270 | 0.00006 | 0.00072 | 0.00027 | 0.015 |
| M26(ii) | kaolinite | 0.01270 | 0.00006 | 0.00072 | 0.00027 | 0.015 |
| M29 | kaolinite | 0.01270 | 0.00006 | 0.00072 | 0.00027 | 0.015 |
| M34 | kaolinite | 0.01270 | 0.00006 | 0.00072 | 0.00027 | 0.015 |
| M45(iii) | kaolinite | 0.01270 | 0.00006 | 0.00072 | 0.00027 | 0.015 |
| M48 | kaolinite | 0.01270 | 0.00006 | 0.00072 | 0.00027 | 0.015 |
| M58 | kaolinite | 0.01270 | 0.00006 | 0.00072 | 0.00027 | 0.015 |
| M70B | kaolinite | 0.01270 | 0.00006 | 0.00072 | 0.00027 | 0.015 |
| M79(i) | kaolinite | 0.01270 | 0.00006 | 0.00072 | 0.00027 | 0.015 |

**Irradiation 3** Date: 10 February 2001. Time in reactor: 2.1 days

| Sample | type | J value | J error | $(^{39}Ar/^{37}Ar)_{Ca}$ | $(^{36}Ar/^{37}Ar)_{Ca}$ | $(^{40}Ar/^{39}Ar)_{K}$ |
|---|---|---|---|---|---|---|
| M39 | granodiorite | 0.01231 | 0.00006 | 0.00065 | 0.000264 | 0.0085 |
| M40 | granodiorite | 0.01231 | 0.00006 | 0.00065 | 0.000264 | 0.0085 |
| M41 | granodiorite | 0.01231 | 0.00006 | 0.00065 | 0.000264 | 0.0085 |
| M42 | granodiorite | 0.01231 | 0.00006 | 0.00065 | 0.000264 | 0.0085 |
| M43 | granodiorite | 0.01231 | 0.00006 | 0.00065 | 0.000264 | 0.0085 |
| M44 | granodiorite | 0.01231 | 0.00006 | 0.00065 | 0.000264 | 0.0085 |

**Table B.1 (cont.)**

**Irradiation 4** Date: 29 August 2001. Time in reactor: 1.04 days, , ,

| Sample | type | J value | J Error | $(^{39}Ar/^{37}Ar)_{Ca}$ | $(^{36}Ar/^{37}Ar)_{Ca}$ | $(^{40}Ar/^{39}Ar)_{K}$ |
|---|---|---|---|---|---|---|
| M100T | kaolinite | 0.00577 | 0.00003 | 0.00065 | 0.000264 | 0.0085 |
| M101C | kaolinite | 0.00577 | 0.00003 | 0.00065 | 0.000264 | 0.0085 |
| M109 | kaolinite | 0.00577 | 0.00003 | 0.00065 | 0.000264 | 0.0085 |
| M110E | kaolinite | 0.00577 | 0.00003 | 0.00065 | 0.000264 | 0.0085 |
| M113A | kaolinite | 0.00577 | 0.00003 | 0.00065 | 0.000264 | 0.0085 |
| M113B | kaolinite | 0.00577 | 0.00003 | 0.00065 | 0.000264 | 0.0085 |
| M113C | kaolinite | 0.00577 | 0.00003 | 0.00065 | 0.000264 | 0.0085 |
| M121B | kaolinite | 0.00577 | 0.00003 | 0.00065 | 0.000264 | 0.0085 |
| M122A | kaolinite | 0.00577 | 0.00003 | 0.00065 | 0.000264 | 0.0085 |
| M125 | kaolinite | 0.00577 | 0.00003 | 0.00065 | 0.000264 | 0.0085 |
| M125A | kaolinite | 0.00577 | 0.00003 | 0.00065 | 0.000264 | 0.0085 |
| M125D | kaolinite | 0.00577 | 0.00003 | 0.00065 | 0.000264 | 0.0085 |

**Irradiation 5** Date: 30 August 2003. Time in reactor: 2.1 days

| Sample | type | J value | J Error | $(^{39}Ar/^{37}Ar)_{Ca}$ | $(^{36}Ar/^{37}Ar)_{Ca}$ | $(^{40}Ar/^{39}Ar)_{K}$ |
|---|---|---|---|---|---|---|
| M1 | Laterite | 0.01195 | 0.00006 | 0.00065 | 0.000264 | 0.0085 |
| M2 | basement | 0.01195 | 0.00006 | 0.00065 | 0.000264 | 0.0085 |
| M3 | laterite | 0.01195 | 0.00006 | 0.00065 | 0.000264 | 0.0085 |
| M4 | basalt | 0.01195 | 0.00006 | 0.00065 | 0.000264 | 0.0085 |
| M5 | basalt | 0.01195 | 0.00006 | 0.00065 | 0.000264 | 0.0085 |
| M6 | basalt | 0.01195 | 0.00006 | 0.00065 | 0.000264 | 0.0085 |
| M7 | basement | 0.01195 | 0.00006 | 0.00065 | 0.000264 | 0.0085 |
| M8 | Laterite | 0.01195 | 0.00006 | 0.00065 | 0.000264 | 0.0085 |
| M9 | basement | 0.01195 | 0.00006 | 0.00065 | 0.000264 | 0.0085 |

**Table B.2** $^{40}Ar/^{39}Ar$ data for laterite clays

| Sample | Irrad | J-value | $^{40}Ar$ | error ± | $^{39}Ar$ | error ± | $^{38}Ar$ | error ± |
|---|---|---|---|---|---|---|---|---|
| | | | | | | | | |
| **Laterite clays** | | | | | | | | |
| M18(i) | 1 | 0.01172 | 5.098 | 0.006 | 0.104 | 0.000 | 0.001 | 0.000 |
| M19A | 1 | 0.01172 | 5.622 | 0.002 | 0.165 | 0.000 | 0.002 | 0.000 |
| M19C(pit2) | 1 | 0.01172 | 1.073 | 0.001 | 0.019 | 0.000 | 0.001 | 0.000 |
| M26(ii) | 1 | 0.01172 | 4.139 | 0.002 | 0.120 | 0.001 | 0.002 | 0.000 |
| M29 | 1 | 0.01172 | 4.139 | 0.002 | 0.120 | 0.000 | 0.001 | 0.000 |
| M33(iv) | 1 | 0.01172 | 8.619 | 0.016 | 0.062 | 0.000 | 0.006 | 0.000 |
| M34(pit1) | 1 | 0.01172 | 4.068 | 0.004 | 1.964 | 0.001 | 0.025 | 0.000 |
| M34(pit2) | 2 | 0.01270 | 6.750 | 0.004 | 3.471 | 0.002 | 0.044 | 0.000 |
| M45iii(pit1) | 2 | 0.01270 | 4.501 | 0.002 | 0.110 | 0.000 | 0.002 | 0.000 |
| M48a | 1 | 0.01172 | 8.202 | 0.005 | 4.084 | 0.002 | 0.052 | 0.000 |
| M48 | 2 | 0.01270 | 2.905 | 0.002 | 1.390 | 0.003 | 0.018 | 0.000 |
| M48a(ii) | 2 | 0.01270 | 4.055 | 0.002 | 1.963 | 0.001 | 0.024 | 0.000 |
| M58c(pit2) | 2 | 0.01270 | 0.002 | 0.000 | 0.000 | 0.000 | 0.000 | 0.000 |
| M70a | 1 | 0.01172 | 18.188 | 0.009 | 4.169 | 0.004 | 0.058 | 0.000 |
| M70A | 2 | 0.01270 | 4.670 | 0.010 | 2.344 | 0.001 | 0.028 | 0.000 |
| M70b | 1 | 0.01172 | 22.209 | 0.014 | 2.034 | 0.001 | 0.038 | 0.000 |
| M70B | 2 | 0.01270 | 40.950 | 0.010 | 7.219 | 0.002 | 0.105 | 0.000 |
| M70B(i) | 2 | 0.01270 | | | | | | |
| M79i(pit2) | 2 | 0.01270 | | | | | | |
| M100T | 4 | 0.00577 | 0.174 | 0.003 | 0.018 | 0.000 | 0.000 | 0.000 |
| 101C | 4 | 0.00577 | 0.032 | 0.000 | 0.000 | 0.000 | 0.000 | 0.000 |
| M109 | 4 | 0.00577 | 0.052 | 0.000 | 0.005 | 0.000 | 0.000 | 0.000 |
| M110E | 4 | 0.00577 | 0.253 | 0.001 | 0.018 | 0.000 | 0.000 | 0.000 |
| M113A | 4 | 0.00577 | 18.440 | 0.010 | 4.655 | 0.006 | 0.059 | 0.000 |
| M113A(1) | 4 | 0.00577 | 19.820 | 0.040 | 3.345 | 0.005 | 0.048 | 0.000 |
| M113A(i) | 4 | 0.00577 | 25.266 | 0.008 | 6.609 | 0.005 | 0.085 | 0.000 |
| M113A(i1) | 4 | 0.00577 | 0.174 | 0.001 | 0.013 | 0.000 | 0.000 | 0.000 |
| M113B(i) | 4 | 0.00577 | 0.035 | 0.000 | 0.003 | 0.000 | 0.000 | 0.000 |
| M113C | 4 | 0.00577 | 0.836 | 0.002 | 0.135 | 0.000 | 0.002 | 0.000 |
| M113C(i) | 4 | 0.00577 | 0.802 | 0.002 | 0.131 | 0.000 | 0.002 | 0.000 |
| M121B | 4 | 0.00577 | 13.931 | 0.035 | 0.004 | 0.000 | 0.008 | 0.000 |
| M122A | 4 | 0.00577 | 1.266 | 0.001 | 0.004 | 0.000 | 0.001 | 0.000 |
| M125 | 4 | 0.00577 | 1.170 | 0.001 | 0.156 | 0.001 | 0.002 | 0.000 |
| M125(i) | 4 | 0.00577 | 4.546 | 0.010 | 0.530 | 0.001 | 0.008 | 0.000 |
| M125A | 4 | 0.00577 | 8.444 | 0.008 | 2.012 | 0.003 | 0.026 | 0.000 |
| M125A(1) | 4 | 0.00577 | 5.153 | 0.006 | 1.326 | 0.002 | 0.017 | 0.000 |
| M125A(i) | 4 | 0.00577 | 11.390 | 0.020 | 2.605 | 0.004 | 0.033 | 0.000 |
| M125A(i)b | 4 | 0.00577 | | | | | | |
| M125D | 4 | 0.00577 | 0.310 | 0.000 | 0.049 | 0.000 | 0.001 | 0.000 |
| M125D(i) | 4 | 0.00577 | 1.141 | 0.001 | 0.221 | 0.000 | 0.003 | 0.000 |
| M201 | 5 | 0.01195 | 9.051 | 0.012 | 0.507 | 0.002 | 0.010 | 0.000 |
| M201a | 5 | 0.01195 | 0.212 | 0.002 | 0.052 | 0.000 | 0.001 | 0.000 |
| M211 | 5 | 0.01195 | 0.951 | 0.004 | 0.290 | 0.000 | 0.003 | 0.000 |
| M211a | 5 | 0.01195 | 1.683 | 0.037 | 0.073 | 0.000 | 0.002 | 0.000 |

**Table B.2 (cont.)**

| Sample | $^{37}Ar$ | error ± | $^{36}Ar$ | error +/- | $^{40}Ar^*/^{39}Ar$ | error +/- | Integrated age (Ma) | error ±(Ma) |
|---|---|---|---|---|---|---|---|---|
| | | | | | | | | |
| **Laterite clays** | | | | | | | | |
| M18(i) | 0.004 | 0.000 | 0.001 | 0.000 | 45.434 | 0.127 | **821.83** | **3.63** |
| M19A | 0.004 | 0.000 | 0.002 | 0.000 | 30.874 | 0.057 | **596.82** | **2.58** |
| M19C(pit2) | 0.002 | 0.000 | 0.002 | 0.000 | 20.296 | 0.532 | **413.74** | **9.85** |
| M26(ii) | 0.007 | 0.001 | 0.001 | 0.000 | 31.279 | 0.581 | **563.46** | **9.33** |
| M29 | 0.001 | 0.000 | 0.001 | 0.000 | 31.649 | 0.113 | **609.53** | **3.06** |
| M33(iv) | 0.016 | 0.000 | 0.025 | 0.000 | 20.418 | 0.384 | **387.06** | **6.79** |
| M34(pit1) | 0.022 | 0.001 | 0.002 | 0.000 | 1.843 | 0.006 | **41.12** | **1.12** |
| M34(pit2) | 0.022 | 0.000 | 0.003 | 0.000 | 1.692 | 0.003 | **38.36** | **0.19** |
| M45iii(pit1) | 0.005 | 0.000 | 0.001 | 0.000 | 38.597 | 0.129 | **719.65** | **3.44** |
| M48a | 0.038 | 0.000 | 0.004 | 0.000 | 1.743 | 0.004 | **39.49** | **0.21** |
| M48 | -0.001 | 0.000 | 0.002 | 0.000 | 1.724 | 0.008 | **36.10** | **0.25** |
| M48a(ii) | 0.024 | 0.000 | 0.002 | 0.000 | 1.803 | 0.006 | **40.84** | **0.23** |
| M58c(pit2) | 0.002 | 0.000 | 0.000 | 0.000 | 21.656 | 16.172 | **438.34** | **290.61** |
| M70a | 0.020 | 0.000 | 0.026 | 0.000 | 2.490 | 0.010 | **51.97** | **0.33** |
| M70A | 0.023 | 0.000 | 0.001 | 0.000 | 1.869 | 0.009 | **42.32** | **0.28** |
| M70b | -0.003 | 0.000 | 0.062 | 0.000 | 1.873 | 0.048 | **39.17** | **1.00** |
| M70B | 0.021 | 0.000 | 0.091 | 0.000 | 1.955 | 0.004 | **44.24** | **0.23** |
| M70B(i) | | | | | | | | |
| M79i(pit2) | | | | | | | | |
| M100T | 0.000 | 0.000 | 0.000 | 0.000 | 4.301 | 0.526 | **44.22** | **5.35** |
| 101C | 0.000 | 0.000 | 0.000 | -20.797 | -11.443 | 0.000 | **-230.62** | **135.36** |
| M109 | 0.001 | 0.000 | 0.000 | 0.000 | 3.800 | 1.200 | **39.46** | **12.15** |
| M110E | 0.001 | 0.000 | 0.001 | 0.000 | 4.305 | 0.398 | **44.27** | **4.05** |
| M113A | 0.006 | 0.000 | 0.003 | 0.000 | 3.794 | 0.006 | **39.07** | **0.21** |
| M113A(1) | 0.013 | 0.000 | 0.028 | 0.000 | 3.470 | 0.010 | **35.75** | **0.23** |
| M113A(i) | 0.007 | 0.000 | 0.004 | 0.000 | 3.662 | 0.004 | **37.72** | **0.20** |
| M113A(i1) | 0.001 | 0.000 | 0.000 | 0.000 | 5.300 | 0.400 | **53.89** | **4.12** |
| M113B(i) | 0.001 | 0.000 | 0.000 | 0.000 | 4.996 | 1.506 | **51.27** | **15.24** |
| M113C | 0.001 | 0.000 | 0.001 | 0.000 | 4.010 | 0.060 | **41.24** | **0.61** |
| M113C(i) | 0.000 | 0.000 | 0.001 | 0.000 | 3.878 | 0.058 | **39.93** | **0.63** |
| M121B | 0.001 | 0.000 | 0.046 | 0.000 | 55.346 | 15.752 | **640.44** | **153.45** |
| M122A | 0.000 | 0.000 | 0.003 | 0.000 | 107.682 | 2.217 | **871.82** | **14.68** |
| M125 | 0.003 | 0.000 | 0.002 | 0.000 | 3.980 | 0.050 | **40.94** | **0.59** |
| M125(i) | 0.002 | 0.000 | 0.007 | 0.000 | 4.477 | 0.239 | **46.01** | **2.43** |
| M125A | 0.006 | 0.000 | 0.003 | 0.000 | 3.732 | 0.008 | **38.43** | **0.21** |
| M125A(1) | 0.004 | 0.000 | 0.001 | 0.000 | 3.750 | 0.010 | **38.66** | **0.23** |
| M125A(i) | 0.008 | 0.001 | 0.004 | 0.000 | 3.870 | 0.010 | **39.83** | **0.24** |
| M125A(i)b | | | | | | | | |
| M125D | 0.001 | 0.000 | 0.000 | 0.000 | 4.234 | 0.147 | **43.54** | **1.51** |
| M125D(i) | 0.005 | 0.000 | 0.001 | 0.000 | 4.390 | 0.090 | **45.15** | **0.95** |
| M201 | 2.436 | 0.009 | 0.023 | 0.000 | 4.498 | 0.044 | **94.45** | **1.02** |
| M201a | 0.315 | 0.009 | 0.000 | 0.000 | 2.100 | 0.100 | **45.69** | **2.25** |
| M211 | 0.958 | 0.010 | 0.002 | 0.000 | 1.640 | 0.028 | **35.02** | **0.62** |
| M211a | 0.715 | 0.011 | 0.002 | 0.000 | 14.584 | 0.567 | **289.84** | **10.50** |

**Table B.2 (cont.)**

| Sample | Plateau age (Ma) | error ±(Ma) | MSWD | Cumulative % $^{39}$Ar | Isochron age (Ma) | error ±(Ma) | MSWD | Initial $^{40}$Ar/$^{36}$Ar |
|---|---|---|---|---|---|---|---|---|
| | | | | | | | | |
| **Laterite clays** | | | | | | | | |
| M18(i) | | | | | | | | |
| M19A | | | | | | | | |
| M19C(pit2) | | | | | | | | |
| M26(ii) | | | | | | | | |
| M29 | | | | | | | | |
| M33(iv) | | | | | | | | |
| M34(pit1) | | | | | | | | |
| M34(pit2) | | | | | | | | |
| M45iii(pit1) | | | | | | | | |
| M48a | | | | | | | | |
| M48 | | | | | **38.6** | **1.7** | 45 | 267±68 |
| M48a(ii) | **Single step, 92% $^{39}$Ar released** | | | | | | | |
| M58c(pit2) | **low $^{39}$Ar** | | | | | | | |
| M70a | | | | | | | | |
| M70A | | | | | | | | |
| M70b | **36.80** | **0.98** | 0.39 | 88.40 | **41.90** | **5.90** | 1.01 | 288.5±7.0 |
| M70B | | | | | | | | |
| M70B(i) | | | | | | | | |
| M79i(pit2) | | | | | | | | |
| M100T | | | | | | | | |
| 101C | **low $^{39}$Ar** | | | | | | | |
| M109 | **low $^{39}$Ar** | | | | | | | |
| M110E | | | | | | | | |
| M113A | | | | | | | | |
| M113A(1) | | | | | | | | |
| M113A(i) | | | | | | | | |
| M113A(i1) | | | | | | | | |
| M113B(i) | **low $^{39}$Ar** | | | | | | | |
| M113C | | | | | | | | |
| M113C(i) | | | | | | | | |
| M121B | **low $^{39}$Ar** | | | | | | | |
| M122A | **low $^{39}$Ar** | | | | | | | |
| M125 | | | | | | | | |
| M125(i) | **43.40** | **3.30** | 0.53 | 94.20 | **41.4** | **6.2** | 0.47 | 344±120 |
| M125A | | | | | | | | |
| M125A(1) | **36.50** | **1.30** | 1.14 | 65.60 | **37.5** | **2.6** | 47 | 374±120 |
| M125A(i) | | | | | | | | |
| M125A(i)b | | | | | | | | |
| M125D | | | | | | | | |
| M125D(i) | | | | | | | | |
| M201 | | | | | | | | |
| M201a | **40.0+/-2.6 Ma single step, 52% $^{39}$Ar released** | | | | | | | |
| M211a | **38.2+/-0.8 Ma two steps, 50% $^{39}$Ar released** | | | | | | | |

**Table B.3** $^{40}Ar/^{39}Ar$ data for flood basalts

| Sample | Irrad | J-value | $^{40}Ar$ | error ± | $^{39}Ar$ | error ± | $^{38}Ar$ | error ± |
|---|---|---|---|---|---|---|---|---|
| | | | | | | | | |
| **Basalts** | | | | | | | | |
| M73i | 1 | 0.01172 | 1.053 | 0.000 | 0.559 | 0.000 | 0.007 | 0.000 |
| M73ii | 1 | 0.01172 | 1.175 | 0.000 | 0.562 | 0.001 | 0.011 | 0.000 |
| M77 | 1 | 0.01172 | 0.048 | 0.000 | 0.026 | 0.000 | 0.001 | 0.000 |
| M79i | 2 | 0.01270 | 0.235 | 0.001 | 0.045 | 0.000 | 0.001 | 0.000 |
| M205a | 5 | 0.01195 | 2.537 | 0.006 | 1.486 | 0.001 | 0.014 | 0.000 |
| M205b | 5 | 0.01195 | 1.202 | 0.004 | 0.677 | 0.001 | 0.006 | 0.000 |
| M215a | 5 | 0.01195 | 0.825 | 0.005 | 0.343 | 0.001 | 0.004 | 0.000 |
| M215b | 5 | 0.01195 | 0.100 | 0.001 | 0.032 | 0.000 | 0.000 | 0.000 |
| M222a | 5 | 0.01195 | 0.251 | 0.001 | 0.142 | 0.000 | 0.002 | 0.000 |
| M222b | 5 | 0.01195 | 0.143 | 0.001 | 0.053 | 0.000 | 0.001 | 0.000 |

**Table B.3 (cont.)**

| Sample | $^{37}Ar$ | error ± | $^{36}Ar$ | error ± | $^{40}Ar^*/^{39}Ar$ | error ± | Integrated age (Ma) | error ±(Ma) |
|---|---|---|---|---|---|---|---|---|
| | | | | | | | | |
| **Basalts** | | | | | | | | |
| M73i | 0.025 | 0.000 | 0.002 | 0.000 | 1.090 | 0.010 | **22.90** | **0.30** |
| M73ii | 0.033 | 0.000 | 0.002 | 0.000 | 0.918 | 0.014 | **19.31** | **0.31** |
| M77 | 0.011 | 0.000 | 0.000 | 0.000 | 1.527 | 0.006 | **31.55** | **1.76** |
| M79i | 0.040 | 0.000 | 0.001 | 0.000 | 1.413 | 0.096 | **32.03** | **2.17** |
| M205a | 1.671 | 0.007 | 0.001 | 0.000 | 1.461 | 0.006 | **31.20** | **0.20** |
| M205b | 0.685 | 0.008 | 0.001 | 0.000 | 1.510 | 0.010 | **32.30** | **0.30** |
| M215a | 1.376 | 0.009 | 0.001 | 0.000 | 1.490 | 0.020 | **31.75** | **0.49** |
| M215b | 0.015 | 0.000 | 0.000 | 0.000 | 1.380 | 0.090 | **29.50** | **2.00** |
| M222a | 0.012 | 0.000 | 0.000 | 0.000 | 1.291 | 0.005 | **27.60** | **0.20** |
| M222b | 0.015 | 0.000 | 0.000 | 0.000 | 0.754 | 0.057 | **16.19** | **1.22** |

**Table B.3 (cont.)**

| Sample | Plateau age (Ma) | error ± (Ma) | MSWD | Cumulative % $^{39}Ar$ | Isochron age (Ma) | error ± (Ma) | MSWD | Initial $^{40}Ar/^{36}Ar$ |
|---|---|---|---|---|---|---|---|---|
| | | | | | | | | |
| **Basalts** | | | | | | | | |
| M73i | | | | | | | | |
| M73ii | | | | | | | | |
| M77 | | | | | | | | |
| M79i | | | | | | | | |
| M205a | **32.79** | **0.76** | 0.53 | 99.60 | **34.0** | **1.8** | 8.5 | 119±110 |
| M205b | | | | | **33.7** | **4.3** | 10.3 | 245±220 |
| M215a | | | | | **34.0** | **5.0** | 28 | 253±160 |
| M215b | | | | | | | | |
| M222a | | | | | **31.1** | **5.1** | 51 | 190±130 |
| M222b | **21.7+/-0.3 Ma single step, 74% $^{39}Ar$ released** | | | | | | | |

**Table B.4** $^{40}Ar/^{39}Ar$ data for basement rocks

| Sample | Irrad | J-value | $^{40}Ar$ | error ± | $^{39}Ar$ | error ± | $^{38}Ar$ | error ± |
|---|---|---|---|---|---|---|---|---|
| | | | | | | | | |
| **Basement** | | | | | | | | |
| M39 | 1 | 0.01172 | 9.255 | 0.008 | 0.666 | 0.000 | 0.015 | 0.000 |
| M40 | 3 | 0.01231 | 4.420 | 0.002 | 0.159 | 0.000 | 0.016 | 0.000 |
| M41 | 3 | 0.01231 | 4.117 | 0.003 | 0.286 | 0.000 | 0.008 | 0.000 |
| M42 | 3 | 0.01231 | 6.337 | 0.007 | 0.436 | 0.001 | 0.012 | 0.000 |
| M43 | 3 | 0.01231 | 2.445 | 0.004 | 0.179 | 0.000 | 0.004 | 0.000 |
| M44 | 3 | 0.01231 | 6.971 | 0.009 | 0.417 | 0.000 | 0.011 | 0.000 |
| M68 | 1 | 0.01172 | 2.487 | 0.001 | 0.052 | 0.000 | 0.001 | 0.000 |
| M94 | 5 | 0.01195 | 0.707 | 0.004 | 0.024 | 0.000 | 0.000 | 0.000 |
| M96 | 5 | 0.01195 | 37.072 | 0.037 | 0.934 | 0.002 | 0.010 | 0.000 |

**Table B.4 (cont.)**

| Sample | $^{37}Ar$ | error ± | $^{36}Ar$ | error ± | $^{40}Ar^*/^{39}Ar$ | error ± | **Integrated age (Ma)** | **error ± (Ma)** |
|---|---|---|---|---|---|---|---|---|
| | | | | | | | | |
| **Basement** | | | | | | | | |
| M39 | 0.014 | 0.003 | 0.003 | 0.000 | 12.666 | 0.024 | **261.40** | **1.27** |
| M40 | 0.011 | 0.001 | 0.002 | 0.000 | 23.804 | 0.101 | **463.63** | **2.64** |
| M41 | 0.011 | 0.002 | 0.001 | 0.000 | 13.350 | 0.050 | **274.50** | **1.50** |
| M42 | 0.004 | 0.004 | 0.002 | 0.000 | 13.190 | 0.030 | **271.60** | **1.40** |
| M43 | 0.018 | 0.003 | 0.001 | 0.000 | 12.469 | 0.058 | **257.62** | **1.61** |
| M44 | 0.021 | 0.002 | 0.003 | 0.000 | 14.940 | 0.050 | **304.50** | **1.60** |
| M68 | 0.002 | 0.000 | 0.003 | 0.000 | 30.187 | 0.184 | **546.48** | **3.75** |
| M94 | 0.016 | 0.000 | 0.000 | 0.000 | 24.000 | 0.318 | **454.93** | **5.70** |
| M96 | 1.190 | 0.011 | 0.002 | 0.000 | 39.136 | 0.081 | **692.20** | **3.12** |

**Table B.4 (cont.)**

| Sample | **Plateau age (Ma)** | **error ± (Ma)** | MSWD | Cumulative % $^{39}Ar$ | **Isochron age (Ma)** | **error ± (Ma)** | MSWD | Initial $^{40}Ar/^{36}Ar$ |
|---|---|---|---|---|---|---|---|---|
| | | | | | | | | |
| **Basement** | | | | | | | | |
| M39 | | | | | | | | |
| M40 | **315.8+/-1.8 Ma single step, 55% $^{39}Ar$ released** | | | | | | | |
| M41 | **297.0+/-1.5 Ma single step, 44% $^{39}Ar$ released** | | | | | | | |
| M42 | **292.2+/-1.5 Ma single step, 72% $^{39}Ar$ released** | | | | | | | |
| M43 | **310.4+/-1.8 Ma single step, 68% $^{39}Ar$ released** | | | | | | | |
| M44 | **350.1+/-1.7 Ma single step, 73% $^{39}Ar$ released** | | | | | | | |
| M68 | **weighted mean of 2 steps, 52.6% $^{39}Ar$ released** | | | | | | | |
| M94 | | | | | | | | |
| M96 | | | | | | | | |

# Appendix C: Well-water geochemistry

**Table C.1** Locations and altitudes of sampled wells (UTM Zone 37, WGS84 Datum)

| *Well* | *Easting* | *Northing* | *Altitude/m* |
|---|---|---|---|
| sample 1 | 505121 | 1687744 | 1641 |
| sample 2 | 500863 | 1671401 | 2202 |
| sample 3 | 484710 | 1712370 | 2390 |
| sample 4 | 485460 | 1713371 | 2434 |
| sample 5 | 486858 | 1718758 | 2535 |
| sample 6 | 489747 | 1712737 | 2415 |
| sample 7 | 476968 | 1686003 | 2223 |
| sample 8 | 472549 | 1685237 | 2199 |
| sample 9 | 481043 | 1686101 | 2250 |
| sample 10 | 483488 | 1686364 | 2290 |
| sample 11 | 483543 | 1686918 | 2244 |
| sample 12 | 484831 | 1674999 | 2036 |
| sample 13 | 482384 | 1667671 | 1923 |
| sample 14 | 465466 | 1648862 | 1854 |
| sample 15 | 495249 | 1681817 | 2188 |
| sample 16 | 496355 | 1674606 | 2134 |
| sample 17 | 484438 | 1695353 | 2306 |
| sample 18 | 473241 | 1692727 | 2258 |
| sample 19 | 474405 | 1695785 | 2287 |
| sample 20 | 478011 | 1697030 | 2259 |
| sample 21 | 479389 | 1696852 | 2255 |
| sample 22a | 486260 | 1700588 | 2336 |
| sample 22b | 486260 | 1700588 | 2336 |
| sample 23 | 487642 | 1700106 | 2333 |
| sample 24 | 486047 | 1680243 | 2294 |
| sample 25 | 481050 | 1658773 | 1962 |
| sample 26 | 483735 | 1625944 | 1934 |
| sample 27 | 478827 | 1669074 | 1976 |
| sample 28 | 467622 | 1673057 | 1978 |
| sample 29 | 468435 | 1675738 | 2029 |
| sample 30 | 468859 | 1677835 | 2057 |
| sample 31 | 467502 | 1679056 | 2097 |
| sample 32 | 492588 | 1694808 | 2210 |
| sample 33 | 497108 | 1665169 | 1922 |
| sample 34 | 496653 | 1685123 | 2279 |

**Table C.2** ICP-AES and ICP-MS analyses of well waters. Major elements in parts per million by volume (ppm), trace elements in parts per billion by volume (ppb)

| **Major element** | Ca ppm | Na ppm | Mg ppm | K ppm | Fe ppm | Al ppm | Si ppm | S ppm | Mn ppm | Sr ppm |
|---|---|---|---|---|---|---|---|---|---|---|
| **WHO limit (ppm)** | | | | | | | | | 0.05 | |
| **Laterite** | | | | | | | | | | |
| sample 3 | 67.9 | 23.8 | 17.9 | 0.6 | 0.03 | 0.0 | 11.7 | 8.0 | 0.21 | 0.37 |
| sample 4 | 47.4 | 22.3 | 10.0 | 0.4 | 0.02 | 0.0 | 11.4 | 2.6 | 0.00 | 0.20 |
| sample 7 | 32.8 | 15.6 | 13.3 | 4.2 | 0.10 | 0.0 | 1.4 | 9.0 | 0.01 | 0.17 |
| sample 9 | 73.1 | 44.5 | 47.1 | 0.9 | 2.75 | 2.3 | 22.8 | 19.2 | 0.11 | 0.52 |
| sample 10 | 73.4 | 27.2 | 45.2 | 0.7 | 0.04 | 0.0 | 17.6 | 11.8 | 0.00 | 0.20 |
| sample 11 | 84.8 | 51.7 | 56.6 | 7.0 | 0.11 | 0.0 | 12.6 | 21.3 | 0.11 | 0.47 |
| sample 12 | 80.3 | 35.3 | 52.9 | 1.1 | 0.07 | 0.0 | 21.3 | 4.8 | 0.02 | 0.10 |
| sample 13 | 77.6 | 20.2 | 30.4 | 0.9 | 0.04 | 0.0 | 19.5 | 12.8 | 0.01 | 0.30 |
| sample 14 | 62.8 | 107.2 | 64.4 | 1.7 | 0.07 | 0.0 | 20.5 | 18.2 | 0.01 | 0.12 |
| sample 17 | 15.9 | 223.0 | 0.9 | 11.7 | 0.09 | 0.0 | 31.4 | 26.3 | 0.00 | 1.07 |
| sample 21 | 63.2 | 48.9 | 22.1 | 1.7 | 0.03 | 0.0 | 11.8 | 13.5 | 0.01 | 0.47 |
| sample 28 | 69.8 | 36.6 | 38.6 | 1.0 | 0.06 | 0.0 | 18.1 | 9.4 | 0.02 | 0.15 |
| sample 29 | 69.5 | 37.6 | 43.0 | 1.5 | 0.05 | 0.0 | 16.0 | 6.3 | 0.04 | 0.20 |
| sample 30 | 79.6 | 40.8 | 46.8 | 1.6 | 0.11 | 0.0 | 20.9 | 3.5 | 0.10 | 0.23 |
| sample 31 | 37.1 | 11.1 | 12.3 | 1.1 | 0.06 | 0.0 | 18.5 | 4.2 | 0.01 | 0.23 |
| sample 32 | 40.9 | 40.9 | 29.3 | 134.3 | 0.02 | 0.0 | 9.2 | 22.3 | 0.00 | 0.33 |
| sample 34 | 59.1 | 33.4 | 16.2 | 0.9 | 0.27 | 0.0 | 15.6 | 13.6 | 0.02 | 0.45 |
| **Basalt** | | | | | | | | | | |
| sample 8 | 79.7 | 79.4 | 52.4 | 4.9 | 0.37 | 0.2 | 12.6 | 19.1 | 0.04 | 0.33 |
| sample 23 | 62.9 | 38.9 | 16.0 | 1.5 | 0.09 | 0.0 | 10.3 | 9.6 | 0.01 | 0.27 |
| sample 24 | 78.1 | 14.3 | 40.8 | 0.9 | 0.05 | 0.0 | 26.7 | 13.3 | 0.01 | 0.04 |
| sample 25 | 86.3 | 53.3 | 73.3 | 2.1 | 0.05 | 0.0 | 21.8 | 22.4 | 0.01 | 0.06 |
| sample 26 | 111.4 | 60.9 | 38.2 | 3.8 | 0.05 | 0.0 | 23.9 | 15.1 | 0.04 | 0.77 |
| sample 27 | 75.2 | 57.6 | 42.5 | 0.7 | 0.03 | 0.0 | 19.0 | 12.1 | 0.00 | 0.17 |
| **Fresh basement** | | | | | | | | | | |
| sample 1 | 143.0 | 101.5 | 95.7 | 3.4 | 0.66 | 0.4 | 18.4 | 86.2 | 0.07 | 0.98 |
| sample 2 | 124.6 | 105.6 | 35.9 | 1.8 | 0.06 | 0.0 | 11.0 | 31.0 | 0.01 | 0.76 |
| sample 5 | 64.3 | 10.1 | 17.0 | 0.3 | 0.05 | 0.0 | 11.2 | 3.3 | 0.00 | 0.14 |
| sample 15 | 86.9 | 37.4 | 41.5 | 2.6 | 0.53 | 0.3 | 14.0 | 16.4 | 0.38 | 0.42 |
| sample 16 | 163.5 | 72.7 | 71.6 | 2.1 | 0.12 | 0.0 | 14.4 | 56.6 | 0.01 | 1.14 |
| sample 18 | 53.1 | 24.5 | 14.4 | 4.2 | 0.51 | 0.1 | 8.9 | 6.8 | 0.51 | 0.23 |
| sample 19 | 171.1 | 61.5 | 55.6 | 1.9 | 0.05 | 0.0 | 11.7 | 30.9 | 0.01 | 0.68 |
| sample 20 | 89.5 | 37.3 | 22.6 | 2.4 | 0.11 | 0.0 | 11.1 | 4.9 | 0.19 | 0.33 |
| sample 33 | 101.4 | 201.2 | 40.9 | 1.2 | 0.07 | 0.0 | 20.0 | 48.1 | 0.04 | 0.60 |
| **Others** | | | | | | | | | | |
| sample 6 | 47.5 | 13.4 | 14.6 | 0.8 | 16.02 | 0.3 | 8.1 | 3.4 | 0.14 | 0.21 |
| sample 22a | 100.5 | 26.8 | 23.2 | 2.1 | 0.15 | 0.0 | 11.2 | 8.7 | 0.33 | 0.39 |
| sample 22b | 60.2 | 6.8 | 14.5 | 1.4 | 1.02 | 0.0 | 6.6 | 1.8 | 0.88 | 0.25 |

**Table C.2 (cont.)**

| **Trace element** | $^{7}Li$ | $^{11}B$ | $^{27}Al$ | $^{31}P$ | $^{47}Ti$ | $^{51}V$ | $^{52}Cr$ | $^{59}Co$ | $^{60}Ni$ | $^{62}Ni$ | $^{63}Cu$ |
|---|---|---|---|---|---|---|---|---|---|---|---|
| **Det lim ppb** | 0.15 | 0.58 | 0.09 | 1.26 | 0.21 | 0.01 | 0.02 | 0.01 | 0.02 | 0.09 | 0.03 |
| **WHO limit (ppb)** | | | 200 | | | | 50 | | 20 | 20 | 2000 |
| **Laterite** | | | | | | | | | | | |
| sample 3 | 0.00 | 28.76 | 12.44 | 46.03 | 1.70 | 1.55 | 1.55 | 0.11 | 0.70 | 0.20 | 1.98 |
| sample 4 | 0.61 | 28.35 | 13.53 | 44.17 | 1.63 | 1.63 | 1.36 | 0.08 | 0.50 | 0.24 | 1.50 |
| sample 7 | 0.09 | 22.06 | 61.94 | 15.92 | 0.88 | 1.18 | 0.78 | 0.10 | 1.02 | 0.79 | 2.26 |
| sample 9 | 0.55 | 48.77 | 1399.5 | 85.55 | 30.13 | 49.88 | 7.82 | 3.25 | 9.99 | 9.90 | 7.95 |
| sample 10 | 83.62 | 40.43 | 14.61 | 34.84 | 2.04 | 22.38 | 1.90 | 0.13 | 1.12 | 0.56 | 3.29 |
| sample 11 | 0.26 | 54.65 | 40.38 | 109.34 | 2.62 | 8.42 | 2.41 | 0.55 | 1.40 | 0.76 | 2.19 |
| sample 12 | 0.35 | 29.17 | 7.64 | 94.27 | 2.54 | 33.71 | 4.99 | 0.16 | 1.21 | 0.67 | 1.32 |
| sample 13 | 0.44 | 24.29 | 12.45 | 16.76 | 2.36 | 15.24 | 1.53 | 0.14 | 0.95 | 0.36 | 2.86 |
| sample 14 | 0.31 | 22.52 | 20.80 | 87.77 | 2.53 | 22.53 | 2.90 | 0.22 | 1.26 | 0.84 | 3.22 |
| sample 17 | 34.37 | 189.40 | 28.17 | 10.91 | 3.12 | 0.29 | 2.53 | 0.10 | 0.73 | 1.73 | 2.58 |
| sample 21 | 1.18 | 61.74 | 7.46 | 162.03 | 1.81 | 2.92 | 1.81 | 0.15 | 4.70 | 4.39 | 13.21 |
| sample 28 | 1.23 | 14.44 | 23.95 | 50.32 | 2.33 | 9.24 | 1.73 | 0.17 | 0.71 | 0.41 | 1.88 |
| sample 29 | 0.20 | 10.48 | 14.69 | 58.39 | 2.10 | 6.56 | 2.19 | 0.24 | 5.54 | 5.01 | 11.92 |
| sample 30 | 1.23 | 10.54 | 41.22 | 42.32 | 3.22 | 4.09 | 2.74 | 0.54 | 4.11 | 3.69 | 5.50 |
| sample 31 | 0.75 | 7.77 | 22.37 | 35.60 | 2.13 | 2.07 | 0.86 | 0.14 | 2.12 | 1.95 | 5.20 |
| sample 32 | 0.62 | 186.88 | 7.59 | 153.69 | 1.41 | 8.86 | 1.80 | 0.15 | 1.33 | 0.97 | 3.51 |
| sample 34 | 2.63 | 45.24 | 12.92 | 27.09 | 2.02 | 0.95 | 1.42 | 0.16 | 0.65 | 0.37 | 1.86 |
| **Basalt** | | | | | | | | | | | |
| sample 8 | 0.01 | 30.09 | 176.28 | 29.36 | 7.84 | 15.35 | 2.47 | 0.66 | 2.19 | 1.66 | 3.01 |
| sample 23 | 267.84 | 50.31 | 28.01 | 50.20 | 2.10 | 2.39 | 0.79 | 0.22 | 1.53 | 1.03 | 6.65 |
| sample 24 | 0.64 | 25.06 | 21.77 | 102.90 | 2.63 | 25.04 | 3.00 | 0.20 | 2.60 | 2.14 | 9.56 |
| sample 25 | 281.59 | 46.71 | 16.49 | 41.55 | 2.28 | 23.63 | 3.15 | 0.17 | 1.02 | 0.43 | 2.24 |
| sample 26 | 0.63 | 45.99 | 12.69 | 153.18 | 2.81 | 11.87 | 1.83 | 0.29 | 1.43 | 0.65 | 1.66 |
| sample 27 | 0.26 | 33.30 | 6.88 | 62.47 | 2.31 | 18.38 | 2.07 | 0.14 | 1.20 | 0.80 | 2.61 |
| **Fresh basement** | | | | | | | | | | | |
| sample 1 | 1.09 | 168.11 | 247.22 | 66.38 | 7.19 | 9.12 | 3.59 | 1.12 | 3.00 | 2.13 | 4.57 |
| sample 2 | 56.67 | 134.83 | 21.31 | 20.90 | 1.77 | 0.91 | 1.55 | 0.20 | 1.46 | 0.70 | 1.52 |
| sample 5 | 0.33 | 21.48 | 4.12 | 25.06 | 1.59 | 2.41 | 3.73 | 0.10 | 0.94 | 0.48 | 1.49 |
| sample 15 | 1.28 | 70.34 | 197.82 | 62.84 | 5.38 | 4.36 | 2.84 | 0.93 | 2.25 | 1.79 | 2.20 |
| sample 16 | 1.90 | 92.14 | 39.69 | 42.66 | 3.73 | 5.95 | 1.76 | 0.30 | 1.54 | 0.60 | 3.39 |
| sample 18 | 0.62 | 44.83 | 81.25 | 41.56 | 3.28 | 2.35 | 1.18 | 1.05 | 2.10 | 1.80 | 2.49 |
| sample 19 | 0.30 | 81.88 | 5.62 | 32.71 | 1.53 | 1.73 | 1.47 | 0.25 | 1.28 | 0.24 | 0.89 |
| sample 20 | 0.07 | 56.35 | 27.73 | 77.64 | 2.07 | 1.76 | 1.81 | 0.36 | 1.04 | 0.34 | 2.31 |
| sample 33 | 10.66 | 162.49 | 26.29 | 61.46 | 2.66 | 16.90 | 2.52 | 0.19 | 0.83 | 0.45 | 2.99 |
| **Others** | | | | | | | | | | | |
| sample 6 | 0.38 | 21.64 | 214.13 | 387.22 | 6.60 | 1.49 | 5.03 | 0.83 | 3.04 | 2.89 | 209.56 |
| sample 22a | 146.64 | 51.68 | 51.78 | 39.71 | 2.48 | 1.68 | 2.75 | 0.46 | 1.65 | 1.04 | 6.13 |
| sample 22b | 0.07 | 22.16 | 34.75 | 25.67 | 2.22 | 0.40 | 1.38 | 0.60 | 1.81 | 1.13 | 0.74 |

**Table C.2 (cont.)**

| Trace element | $^{65}Cu$ | $^{66}Zn$ | $^{68}Zn$ | $^{75}As$ | $^{77}Se$ | $^{82}Se$ | $^{85}Rb$ | $^{95}Mo$ | $^{107}Ag$ | $^{111}Cd$ | $^{118}Sn$ |
|---|---|---|---|---|---|---|---|---|---|---|---|
| **Det lim ppb** | 0.08 | 0.54 | 0.36 | 0.08 | 4.14 | 0.78 | 0.01 | 0.02 | 0.02 | 0.04 | 0.01 |
| **WHO limit (ppb)** | 2000 | 3000 | 3000 | 10 | 10 | 10 | | 70 | | 3 | |
| **Laterite** | | | | | | | | | | | |
| sample 3 | 1.95 | 5.16 | 6.02 | 0.13 | 2.81 | 1.55 | 0.20 | 0.32 | 0.10 | 0.09 | 0.01 |
| sample 4 | 1.49 | 16.68 | 16.04 | 0.19 | 3.65 | 1.03 | 0.18 | 0.10 | 0.40 | 0.11 | 0.01 |
| sample 7 | 2.32 | 658.07 | 597.40 | 0.64 | 2.24 | 0.72 | 0.56 | 0.85 | 0.07 | 0.08 | 0.00 |
| sample 9 | 7.79 | 8.31 | 21.39 | 0.77 | 3.93 | 3.41 | 0.80 | 0.79 | 0.30 | 0.11 | 0.01 |
| sample 10 | 3.25 | 9.48 | 11.77 | 0.35 | 5.08 | 4.94 | 0.37 | 0.53 | 0.11 | 0.16 | 0.09 |
| sample 11 | 1.98 | 5.99 | 14.44 | 1.11 | 1.25 | 1.69 | 1.30 | 1.80 | 0.22 | 0.09 | 0.01 |
| sample 12 | 1.18 | 9.62 | 9.40 | 0.49 | 2.54 | 2.42 | 0.57 | 0.45 | 0.00 | 0.18 | 0.02 |
| sample 13 | 2.76 | 17.06 | 20.35 | 0.53 | 4.19 | 4.50 | 0.35 | 0.29 | 0.23 | 0.12 | 0.01 |
| sample 14 | 2.49 | 14.99 | 14.06 | 0.45 | 2.21 | 2.44 | 0.83 | 1.96 | 2.70 | 0.13 | 0.02 |
| sample 17 | 0.84 | 5.45 | 9.80 | 2.77 | 1.31 | 0.81 | 28.53 | 3.66 | -0.02 | 0.15 | 0.07 |
| sample 21 | 12.90 | 15.51 | 15.48 | 0.50 | 1.80 | 1.67 | 0.63 | 0.34 | 0.68 | 0.16 | 0.02 |
| sample 28 | 1.73 | 48.85 | 60.73 | 0.36 | 2.96 | 1.60 | 2.45 | 0.60 | 0.23 | 0.14 | 0.01 |
| sample 29 | 11.83 | 10.07 | 10.03 | 0.21 | 1.77 | 1.54 | 0.47 | 0.41 | 0.20 | 0.19 | 0.03 |
| sample 30 | 5.36 | 10.73 | 15.18 | 0.47 | 1.98 | 1.22 | 0.79 | 0.89 | 1.46 | 0.22 | 0.04 |
| sample 31 | 5.24 | 18.84 | 32.34 | 0.24 | 1.83 | 0.91 | 0.41 | 0.15 | 0.33 | 0.26 | 0.02 |
| sample 32 | 3.32 | 5.69 | 8.67 | 0.80 | 2.00 | 1.19 | 28.32 | 5.42 | 0.38 | 0.23 | 0.03 |
| sample 34 | 1.73 | 46.37 | 43.26 | 0.30 | 2.63 | 2.51 | 0.10 | 0.43 | 0.38 | 0.22 | 0.02 |
| **Basalt** | | | | | | | | | | | |
| sample 8 | 2.56 | 8.35 | 9.14 | 0.38 | 5.16 | 5.25 | 1.97 | 0.37 | 0.24 | 0.09 | 0.01 |
| sample 23 | 6.40 | 19.55 | 18.86 | 0.21 | 2.49 | 1.53 | 0.57 | 0.55 | 0.68 | 0.20 | 0.05 |
| sample 24 | 9.47 | 24.04 | 25.26 | 0.31 | 3.28 | 2.54 | 0.39 | 0.31 | 0.40 | 0.39 | 0.09 |
| sample 25 | 2.00 | 7.67 | 7.62 | 0.19 | 1.28 | 1.78 | 0.77 | 0.56 | 0.14 | 0.16 | 0.02 |
| sample 26 | 1.37 | 20.91 | 24.35 | 0.53 | 2.25 | 1.67 | 2.03 | 0.56 | 0.59 | 0.18 | 0.03 |
| sample 27 | 2.28 | 11.63 | 10.83 | 0.35 | 2.73 | 2.05 | 0.55 | 0.39 | 0.17 | 0.16 | 0.01 |
| **Fresh basement** | | | | | | | | | | | |
| sample 1 | 4.13 | 7.26 | 11.14 | 3.56 | 6.88 | 4.96 | 0.39 | 1.42 | 0.17 | 0.14 | 0.03 |
| sample 2 | 1.03 | 7.41 | 11.75 | 0.85 | 3.68 | 2.00 | 0.52 | 4.39 | 0.18 | 0.06 | 0.01 |
| sample 5 | 1.56 | 6.34 | 7.48 | 0.15 | 2.84 | 1.45 | 0.21 | 0.06 | 0.00 | 0.07 | 0.07 |
| sample 15 | 2.08 | 8.28 | 10.46 | 1.50 | 4.93 | 4.20 | 0.44 | 0.55 | 0.08 | 0.11 | 0.01 |
| sample 16 | 3.09 | 9.89 | 13.54 | 1.33 | 2.14 | 3.25 | 0.78 | 1.33 | 0.36 | 0.13 | 0.05 |
| sample 18 | 2.45 | 32.40 | 32.14 | 0.97 | 2.66 | 1.50 | 0.84 | 0.97 | 0.24 | 0.16 | 0.04 |
| sample 19 | 0.67 | 5.12 | 9.17 | 0.43 | 4.30 | 3.48 | 0.34 | 0.23 | 0.07 | 0.20 | 0.01 |
| sample 20 | 2.13 | 22.81 | 21.91 | 0.40 | 1.66 | 0.93 | 0.96 | 0.58 | 0.02 | 0.19 | 0.07 |
| sample 33 | 1.63 | 9.42 | 13.50 | 1.37 | 3.31 | 3.85 | 0.60 | 5.58 | 1.11 | 0.21 | 0.02 |
| **Others** | | | | | | | | | | | |
| sample 6 | 214.31 | 1066.4 | 966.45 | 0.46 | 0.66 | 0.68 | 0.25 | 0.34 | 0.37 | 0.24 | 3.26 |
| sample 22a | 6.04 | 17.28 | 20.16 | 0.82 | 2.40 | 2.50 | 0.84 | 1.45 | 0.51 | 0.17 | 0.22 |
| sample 22b | 0.78 | 3.44 | 5.76 | 0.53 | 1.88 | 1.03 | 0.27 | 0.24 | 0.03 | 0.17 | 0.00 |

**Table C.2 (cont.)**

| Trace element | $^{121}Sb$ | $^{137}Ba$ | $^{182}W$ | $^{197}Au$ | $^{202}Hg$ | $^{205}Tl$ | $^{208}Pb$ | $^{209}Bi$ | $^{238}U$ |
|---|---|---|---|---|---|---|---|---|---|
| **Det lim ppb** | 0.02 | 0.79 | 0.02 | 0.03 | 0.06 | 0.01 | 0.05 | 0.01 | 0.02 |
| **WHO limit (ppb)** | | 70 | | | 2 | 2 | 10 | | |
| **Laterite** | | | | | | | | | |
| sample 3 | 0.03 | 12.67 | 0.01 | 0.11 | 0.19 | 0.01 | 0.39 | 0.00 | 0.18 |
| sample 4 | 0.02 | 10.43 | 0.02 | 0.13 | 0.13 | 0.01 | 0.29 | 0.00 | 0.26 |
| sample 7 | 0.07 | 29.23 | 0.04 | 0.17 | 0.16 | 0.01 | 2.25 | 0.01 | 0.11 |
| sample 9 | 0.03 | 194.03 | 0.00 | 0.15 | 0.06 | 0.02 | 1.03 | 0.00 | 1.59 |
| sample 10 | 0.04 | 36.76 | 0.30 | 0.14 | 0.05 | 0.01 | 0.52 | 0.00 | 0.80 |
| sample 11 | 0.05 | 131.45 | 0.03 | 0.34 | 0.23 | 0.01 | 0.39 | 0.00 | 2.36 |
| sample 12 | 0.03 | 9.58 | 0.02 | 0.15 | 0.10 | 0.01 | 0.97 | 0.00 | 1.22 |
| sample 13 | 0.04 | 63.63 | 0.02 | 0.10 | 0.08 | 0.02 | 0.58 | 0.00 | 0.28 |
| sample 14 | 0.03 | 10.12 | 0.01 | 0.11 | 0.11 | 0.01 | 0.45 | -0.01 | 1.18 |
| sample 17 | 0.48 | 69.96 | 9.21 | 0.15 | 0.24 | 0.03 | 0.53 | 0.01 | 0.04 |
| sample 21 | 0.14 | 27.58 | 0.00 | 0.15 | 0.07 | 0.02 | 1.21 | 0.00 | 1.45 |
| sample 28 | 0.05 | 238.46 | 0.01 | 0.12 | 0.08 | 0.03 | 0.52 | 0.00 | 0.82 |
| sample 29 | 0.02 | 8.81 | 0.01 | 0.11 | 0.09 | 0.01 | 0.73 | 0.00 | 0.87 |
| sample 30 | 0.04 | 76.90 | 0.05 | 0.24 | 0.20 | 0.01 | 0.83 | 0.02 | 0.42 |
| sample 31 | 0.03 | 202.35 | 0.05 | 0.22 | 0.18 | 0.02 | 0.95 | 0.00 | 0.13 |
| sample 32 | 0.07 | 53.97 | 0.03 | 0.11 | 0.05 | 0.02 | 0.26 | 0.00 | 0.90 |
| sample 34 | 0.06 | 28.72 | 0.01 | 0.11 | 0.12 | 0.01 | 0.59 | 0.00 | 0.53 |
| **Basalt** | | | | | | | | | |
| sample 8 | 0.06 | 20.45 | 0.04 | 0.16 | 0.19 | 0.01 | 0.33 | 0.00 | 1.27 |
| sample 23 | 0.11 | 17.55 | 0.07 | 0.13 | 0.09 | 0.02 | 1.25 | 0.00 | 0.46 |
| sample 24 | 0.08 | 59.99 | 0.01 | 0.12 | 0.16 | 0.03 | 2.31 | 0.10 | 0.21 |
| sample 25 | 0.05 | 6.80 | 0.03 | 0.10 | 0.09 | 0.00 | 0.60 | 0.00 | 0.61 |
| sample 26 | 0.04 | 82.71 | 0.02 | 0.33 | 0.12 | 0.02 | 0.36 | 0.00 | 3.52 |
| sample 27 | 0.02 | 3.51 | 0.01 | 0.09 | 0.04 | 0.01 | 0.43 | 0.00 | 0.59 |
| **Fresh basement** | | | | | | | | | |
| sample 1 | 0.13 | 69.72 | 0.05 | 0.39 | 0.50 | 0.01 | 0.56 | 0.01 | 2.44 |
| sample 2 | 0.09 | 72.25 | 0.10 | 0.21 | 0.30 | 0.02 | 0.27 | 0.00 | 31.10 |
| sample 5 | 0.01 | 18.96 | 0.01 | 0.12 | 0.08 | 0.02 | 0.52 | 0.02 | 0.14 |
| sample 15 | 0.05 | 42.60 | 0.01 | 0.15 | 0.20 | 0.02 | 0.60 | -0.01 | 1.63 |
| sample 16 | 0.05 | 76.53 | 0.02 | 0.33 | 0.25 | 0.02 | 0.50 | 0.00 | 4.63 |
| sample 18 | 0.07 | 48.81 | 0.45 | 0.12 | 0.33 | 0.02 | 0.47 | 0.00 | 0.54 |
| sample 19 | 0.03 | 73.04 | 0.18 | 0.14 | 0.10 | 0.02 | 0.12 | 0.00 | 1.71 |
| sample 20 | 0.13 | 28.40 | 0.03 | 0.16 | 0.11 | 0.02 | 0.72 | 0.00 | 1.34 |
| sample 33 | 0.06 | 76.64 | 0.07 | 0.20 | 0.13 | 0.01 | 0.56 | 0.00 | 27.13 |
| **Others** | | | | | | | | | |
| sample 6 | 0.35 | 18.41 | 0.04 | 0.26 | 0.23 | 0.01 | 34.90 | 0.02 | 0.09 |
| sample 22a | 0.11 | 71.87 | 0.03 | 0.21 | 0.16 | 0.02 | 2.30 | 0.01 | 1.53 |
| sample 22b | 0.06 | 40.20 | 0.00 | 0.11 | 0.10 | 0.01 | 0.20 | 0.00 | 0.25 |

**1:250 000 Geological Maps**
**Sheets ND 37-2, -3, -6, -7**
(see figure 4.22)

**Anaglyph viewer**